THE UNIVERSITY of EDINBURGH

Title	Observations of large-scale structure in the Universe from the Edinburgh/Durham Southern Galaxy Catalogue
Author	Nichol, Robert Clive
Qualification	PhD
Year	1992

To my parents and family

Observations of Large–Scale Structure in the Universe from the Edinburgh/Durham Southern Galaxy Catalogue

Robert Clive Nichol

Presented for the Degree of Doctor of Philosophy

at the University of Edinburgh

1992

This thesis is my own composition, except where specifically indicated in the text.

May 1992

Abstract

The study of the large–scale structure in the universe places tight constraints on theories of galaxy formation. On scales greater than $10h^{-1}$Mpc, the conditions in the early universe should still be imprinted on the large–scale structure we see today. However, these studies have been hampered by the lack of a reliable, homogeneous catalogue of galaxies and clusters of galaxies over a large area of the sky. Previous catalogues have been built from visual scans of photographic plates (*e.g.* the Lick galaxy catalogue and the Abell cluster catalogue) and many authors believe the large–scale structure seen in these catalogues is an artifact of the subjective manner in which they were constructed.

This thesis is concerned with the scientific analysis of the Edinburgh/Durham Southern Galaxy Catalogue (EDSGC), the Edinburgh/Durham Cluster Catalogue (EDCC) and the Edinburgh/Milano (EM) cluster redshift survey. The first of these databases was objectively constructed from COSMOS scans of 60 UK Schmidt IIIa–J survey plates and contains 1.5 million galaxies covering over 1500 degrees square of the sky centred at the South Galactic Pole. The EDSGC is therefore, ideal for studying the large–scale structure in the universe free from the criticisms levelled at previous catalogues.

The other two databases were constructed from the EDSGC and are described in detail in this thesis. The EDCC was constructed from the EDSGC using a peak–finding algorithm to locate the galaxy overdensities, followed by a pseudo–Abell style analysis to classify the clusters. In total, 737 groups or clusters were detected and the EDCC was found to be complete to a limiting magnitude of $m_{10}(b_j) = 18.75$ ($z = 0.13$). When compared to the Abell catalogue over the EDCC area, over 80% of the Abell clusters were found in the EDCC to the completeness limits of both the catalogues. However, only 50% of the EDCC clusters, to the respective completeness limits, were found. The EM survey was constructed from the EDCC and consists of 103 cluster redshifts, each with an average of 10 galaxy redshift measurements. Over 70% of the clusters were found to have some level of interloper contamination and $\sim$ 10% of the clusters were defined as spurious. These figures are much higher than previously thought. From the EM survey, a 90% redshift complete sample of cluster was selected using an Abell radius of $1.0\,h^{-1}$Mpc.

The distribution of galaxies and clusters seen in the EDSGC and the EM survey were investigated using the two–point correlation function. The angular galaxy correlation function was calculated for the whole EDSGC and was found to have significantly more power on angular scale greater than 5 degrees than the canonical value derived from the Lick galaxy catalogue. The EDSGC angular correlation function is inconsistent (3σ at 5 degrees) with the popular model of biased Cold Dark Matter galaxy formation and is a major constraint on the theory. The spatial cluster correlation function of the EM 90% redshift complete sample of clusters was computed and was found to have less power on all scales compared to correlation functions computed from the Abell catalogue. On investigating the radial and transverse components of the EM correlation function separately, it was observed to be isotropic on scales of less than $30\,h^{-1}$Mpc. By comparison, correlation functions computed from the Abell catalogue show strong anisotropies in the redshift direction which suggests that the catalogue is

contaminated by projection effects. The EM cluster correlation function is consistent with predictions from CDM models of galaxy formation and has removed one of the last conflicting observations with this theory.

The new observations presented in this thesis show that our previous knowledge of the large–scale structure in the universe was biased because of systematic errors in prior object catalogues. Presently, no single theory of galaxy formation can explain these new observations.

Acknowledgements

I've waited a long time to write this page. First, I'd like to thank everyone at the Royal Observatory Edinburgh for putting up with my violent mood swings over the last six months. All I can say is, if it was bad on you imagine what it was like on me!

A massive thank you must go to Chris Collins who has been an excellent supervisor over the last three years. More than that, he has become a great friend and has taught me all I know about golf, women and Astronomy; in that order. I wish him all the best with his future projects and students. In addition, during this project I have been very lucky to work with Stuart Lumsden and Luigi Guzzo. Again, both have become good friends and we have shared many a laugh together. A special thank you must go out to Luigi and Clara for making my trips to Italy so enjoyable, especially the food Clara.

The work presented in this thesis has benefitted from stimulating conversations with many people. I apologise in advance if anyone feels they have been left out, I'm sure it wasn't intentional. At the ROE, these include Lance Miller, Alan Heavens, John Peacock, Andy Connolly, Bob Mann, Mike Hawkins, Karl Glazebrook, Phil James, Peter Brand, Pippa Goldschmidt, Kathy Romer and Tom Broadhurst. Thanks to you all for answering my questions and for lending me your calculators. Outside the ROE, I thank Andy Taylor, Tony Banday, Bob Kirshner, Gordon Stewart, Mel Ulmer, John Huchra, Ann Zabludoff and the Durham crew (Tom Shanks, Dick Fong & Duncan Hale–Sutton). A special thanks must go to Ann for being the perfect hostess during my visit to the CfA in 1991 and to Mel for having faith in me so early on in my Ph.D. I am look forward to working with you in Chicago Mel.

Over the past 3 years, I have made many friends at the ROE, although none of them would admit it. Long gone and departed are Steve from Canada, Paul from Liverpool and Keef from the West Country. I am also much indebted to Neil from Coventry for constructing the EDSGC so well. Still at the ROE are Andy, Bob, Chrispy, Caroline, Ant, Mike, Pippa, Isabelle, Ruth, the 2 Phils and the rest of the students (there is no special order behind this list!).

Away from the ROE, I am grateful to many close friends. First, cheers to Chrispy, Ant, Mike, Bob and Andy (the lads in the flat) for all the laughs, beers and rounds of golf. Life won't be the same without you (I say that as a 90's caring man). I must say thanks to Jon from London and Steve from Wales for all the beers, and Cotsie and Craig for all the food and all the beers. Thanks also to Rowena, who has become a close and loyal friend over the last few years and was kind enough to invite me to all her dinner parties. I am indebted to Kathy for her support and understanding during the last few months in Edinburgh. Finally, thanks to Monica for her long and endearing friendship. I look forward to all of you visiting me in Chicago.

This thesis is dedicated to my parents and family. It is a direct result of their love, support and enthusiasm. I hope they are as proud of me as I am of them. Thank you and take care.

I am very grateful to Chris Collins, Lance Miller, Bob Mann, Andy Connolly, Stuart Lumsden, Luigi Guzzo, Phil James and Rowena McDonald–Young for reading parts of this thesis over and over again during the last few months. I thank Harvey MacGillivray, the COSMOS team and the UK Schmidt team for their excellent support throughout the construction of the EDSGC. Finally, I acknowledge SERC for adequate funding during my studentship and Lloyds Bank for always being there for me.

Contents

Chapter 1

Introduction

Overview

This thesis is concerned with the scientific analysis of the Edinburgh/Durham Southern Galaxy Catalogue (EDSGC) and the Edinburgh/Milano cluster redshift survey (EM survey). The motivation behind these projects was to examine the distribution of galaxies and clusters free from the errors inherent in previous visually constructed catalogues. The construction of the EDSGC was started over 7 years ago by Chris Collins & Harvey MacGillivray at the Royal Observatory Edinburgh, and Tom Shanks at the University of Durham. Neil Heydon–Dumbleton joined the team shortly afterwards as a student and was instrumental in the construction of the EDSGC. He obtained his Ph.D. in January 1989, which was based on the techniques used in the construction of the EDSGC and on his departure from the project the EDSGC had been effectively completed (Heydon–Dumbleton 1989).

Upon my arrival, the EM cluster redshift survey had just begun with its first allocation of telescope time. In addition, Stuart Lumsden joined the team and supervised the construction of the Edinburgh/Durham Cluster Catalogue (EDCC) from the EDSGC. Both these catalogues have now been completed and are soon to be released to the astronomical community.

This thesis is divided into 6 main chapters. Chapter 1 introduces the reader to the general cosmological framework within which the work presented in this thesis fits. This is achieved through a summary of the standard big bang theory and a review of popular models of galaxy formation. This is followed by an outline of the Lick and Abell catalogues, both of which have been heavily used in the study of the large–scale structure in the universe. The chapter concludes with a detailed description of the EDSGC and the techniques used in its construction.

The computation of the galaxy angular correlation function from the whole EDSGC is given in Chapter 2. In addition, a full study of the possible systematic errors and biases that could affect this calculation is carried out *i.e.* the effect of plate–matching errors, extinction and different estimators of the galaxy angular correlation function. Finally, the EDSGC correlation function is compared to previous observations in the astronomical literature and the implications for certain galaxy formation theories are

discussed.

The construction of the EDCC is presented in Chapter 3 and is one of the first objective cluster catalogues to be assembled. The methods used in detecting the clusters from within the EDSGC are explained, along with the measures taken to reduce the problems of projection effects. The chapter concludes with a comparison of the full EDCC and the Abell catalogue. Chapter 4 presents the subset of EDCC clusters selected for multiple object spectral observations, which allowed for an unambiguous determination of the cluster redshift. The methods used in reducing the galaxy spectra are detailed, along with the strict criteria used in defining the cluster redshift. This subset of observed clusters is known as the EM cluster redshift survey.

Chapter 5 investigates the large scale distribution of clusters seen within the EM survey. This is performed through the re–estimation of the cluster spatial correlation function whose form and amplitude have been powerful constraints on theories of galaxy formation. The chapter concludes with a comparison of the EM correlation function with other observed cluster correlation functions and the implications for galaxy formation theories are discussed.

Finally, the last chapter draws together the main observations within the thesis and discusses their relevance to certain galaxy formation theories. The chapter ends with a brief summary of the thesis and a look forward to future work on all the projects. The work presented here has already resulted in 4 papers in the astronomical literature. These are: Collins, Nichol & Lumsden (1992) on the galaxy angular correlation function; Nichol, Collins, Guzzo & Lumsden (1992) on the cluster spatial correlation function; Guzzo, Collins, Nichol & Lumsden (1992) on the distribution of clusters in the EM survey and Lumsden, Nichol, Collins & Guzzo (1992) on the construction of the EDCC. A copy of these papers is presented in Appendix G.

1.1 Standard Big Bang Cosmology

1.1.1 Introduction

At the beginning of this century, a major debate was taking place over the exact nature of the non–stellar nebulae seen in the sky. This discussion culminated in the famous

debate between Shapley and Curtis at the National Academy of Science in Washington in 1920. Shapley proposed that the nebulae were galactic, while Curtis argued that they were systems like our own Galaxy but at a great distance. The observations by Hubble in 1924 of Cepheid variable stars in the Andromeda Nebula showed that this nebula was extragalactic and settled the argument in Curtis's favour. Further observations of other nebulae by Hubble showed that they were also galaxies similar to our own and in 1929 Hubble published his discovery that their distances d were proportional to their recession velocities v as determined from the observed shift in their spectra, *i.e.* $v = H_o d$, where H_o was a constant which is known as the Hubble Constant. By the late 1930s, Hubble and others had shown that this relationship was universal over the whole sky and that on the largest scales, the universe appeared to be homogeneous.

Einstein's theory of General Relativity (GR) forms the theoretical framework within which the evolution of the universe is described. His great insight came from treating space and time as dependent upon each other, which he called the concept of 'space–time'. This was contrary to the classic Newtonian approach which treated the two entities as absolute and independent. In addition to this, his theory went on to explain gravity as the effect of changes in the structure of space–time and not as a direct Newtonian force.

In 1917 Einstein applied his field equations to the universe as a whole under the assumptions that: *i)* The universe was homogeneous and isotropic, so it appeared the same irrespective of an observers place or direction in the universe (the Cosmological Principle); *ii)* The universe was unchanging, with its mean density being constant. However, the solution he obtained predicted an unstable expanding universe which was contrary to popular belief at that time and his original assumptions. He therefore, introduced a cosmological constant which acted as a repulsive force and thus produced a static universe. A decade later, the observations of Hubble described above forced him to retract the constant which he called "the biggest blunder of my life".

Friedmann and Lemaitre were the first to formally derive non–static cosmological solution to Einstein's gravitational field equations. They assumed that the geometry of

the universe was described by the line metric

$$ds^2 = -dt^2 + R(t)^2 \left[\frac{dr^2}{1 - kr^2} + r^2(d\theta^2 + \sin^2\theta d\phi^2) \right], \tag{1.1}$$

where r, θ and ϕ are fixed co–moving spatial coordinates and t is the proper time. In this equation, $R(t)$ is the scale factor of the universe and describes its expansion, while k is the index of curvature which is normalised to have the values of 0, -1 or $+1$. The signature of k describes the spatial geometry of the universe, with positive curvature having a spherical geometry, negative having a hyperbolic geometry and zero being a flat geometry. On substituting this metric into Einstein's field equations and assuming the universe was a pressure–less fluid, they obtained the following differential equation for the scale factor $R(t)$,

$$\left(\frac{\dot{R}(t)}{R(t)} \right)^2 = \frac{8\pi G\bar{\rho}(t)}{3} - \frac{k}{R(t)^2}, \tag{1.2}$$

where $\bar{\rho}$ is the mean density of the universe. Therefore, the Friedmann–Lemaitre equation directly related the curvature of space–time (k) to the contents of the universe.

Equation 1.1 is known as the Robertson–Walker metric and is the most general possible line element for any homogeneous and isotropic universe (Robertson 1935, Walker 1936). The metric fixes the proper time or distance interval between two points in space–time in terms of the coordinate intervals between the points. For example, if two points are separated by the intervals $dt = d\theta = d\phi = 0$ and $dr > 0$ (along the line of sight), then the proper distance (dl) between the points can be written as $dl = R(t)dr/\sqrt{(1 - kr^2)}$. Therefore, the proper distance to a nearby galaxy from our own is $l = R(t)r$ (where local space is assumed to be flat, $k = 0$) and as the radial coordinate distance r is fixed, the recession velocity of that galaxy from our own can be written as

$$v = \frac{dl}{dt} = \dot{R}(t)r = \frac{\dot{R}(t)}{R(t)} l = Hl, \tag{1.3}$$

which is Hubbles Law, with H being the Hubble Constant defined as $\dot{R}(t)/R(t)$. Present day values of H, $R(t)$ and $\dot{R}(t)$ are symbolised by a suffice o *i.e.* $H_o = \dot{R}_o/R_o$.

If the universe is assumed to be flat with $k = 0$, equation 1.2 reduces to

$$\frac{3H_o^2}{8\pi G} = \rho_c\,, \tag{1.4}$$

where ρ_c is known as the critical density. If Ω_o is defined as $\Omega_o = \rho_o/\rho_c$, then equation 1.2 becomes

$$k = R_o^2 H_o^2(\Omega_o - 1)\,, \tag{1.5}$$

where the curvature of the universe is directly related to the mean density of the universe. For $\Omega_o < 1$, the spatial geometry of the universe is hyperbolic since k is negative, while for $\Omega_o > 1$, the geometry of the universe is spherical. In the case of $\Omega_o = 1$, the universe is flat. Moreover, the mean density of the universe scales as

$$\left(\frac{\bar{\rho}(t)}{\rho_o}\right) = \left(\frac{R_o}{R(t)}\right)^3\,, \tag{1.6}$$

where again, the suffice o denotes present day values. By defining $R_o = 1$, then equations 1.2, 1.5 and 1.6 can be combine together to give the following expression,

$$\dot{R}(t)^2 = \frac{H_o^2\Omega_o}{R(t)} - H_o^2(\Omega_o - 1)\,. \tag{1.7}$$

Therefore, for $\Omega_o < 1$, $\dot{R}(t)$ is always greater than zero and the universe will continue to expand forever. For the $\Omega_o > 1$ case, $\dot{R}(t)$ has a maximum value beyond which $\dot{R}(t)$ becomes negative and the universe collapses in on its self. In the case of $\Omega_o = 1$, $\dot{R}(t) = H_o^2\Omega_o/R(t)$ and $\dot{R}(t)$ tends to zero as $R(t)$ tends to infinity, meaning the universe stops expanding at infinite proper time t. These three cases are known as the open, closed and flat Friedmann models of the universe. Clearly, the dynamical evolution of the universe is governed by two constants, H_o and Ω_o, whose exact value are still unknown today, with $50 < H_o < 100\,\mathrm{km\,s^{-1}Mpc^{-1}}$ † and $0.1 < \Omega_o <$ a few.

† Throughout this thesis, the value of $H_o = 100h\,\mathrm{km\,s^{-1}\,Mpc^{-1}}$ is used, where h accounts for observed differences in the Hubble Constant ($0.5 < h < 1.0$).

1.1.2 The Standard Model

This model was first proposed by Gamow (1946) to explain the observed abundance of light elements and this section highlights some of the important features of this model as it stands today. There now exists an extensive collection of historical, popular and scientific reviews of this model *e.g.* Weinberg (1972 & 1977), while the alternatives to this model are discussed by Arp *et al.* (1990) and Peebles *et al.* (1991).

In the standard model, the universe is proposed to be an isotropic, uniformly expanding fluid which began $\sim 15 \times 10^{10}$ years ago as a singularity. During the early stages of its expansion, the universe was a hot relativistic gas, whose temperature decreases inversely proportional to the scale factor *i.e.* $T \propto 1/R(t)$. For temperatures in excess of $kT > m_\mu$, where m_μ is the mass of the muon, the universe was in thermal equilibrium composed of photons, neutrinos, electrons, muons, anti–particles and a small contamination of neutrons and protons.

As the universe continued to expand, its temperature dropped below $T \sim 10^{13}$ K ($R \sim 10^{-13}$ or $t \sim 10^{-5}$ seconds) causing the number density and the reaction rates of the muons to reduced by a factor of $\exp(-m_\mu/kT)$. Consequently, the muons annihilated and the neutrinos and anti–neutrinos were allowed to free stream away, leaving the other particles in thermal equilibrium.

As the universe expanded further, its temperature fell below $T \sim 5 \times 10^9$ K ($kT \simeq m_e$, the rest mass of the electron & positron), which resulted in the electrons and positrons annihilating each other to form photons, $e^- + e^+ \rightarrow \gamma + \gamma$. This effectively left the universe as a sea of photons, neutrinos and anti–neutrinos, with a small fraction of electrons, protons and neutrons. By $T \sim 10^9$ K ($R \sim 10^{-3}$, $t \sim 180$ seconds), the universe was cool enough to allow the neutrons to fuse with the protons producing a trace of heavy elements.

At a temperature of ~ 4000 K, the temperature was low enough to allow hydrogen atoms to form resulting in the capture of the remaining electrons. This caused the matter and radiation to decouple since the photons could no longer be held within

the plasma by electron scattering. This represented the epoch of last scattering, more commonly known as recombination, which is the origin of the Cosmic Microwave Background (CMB, see below). Coincidently, at roughly the same temperature the energy density of the photons, neutrinos and anti–neutrinos fell below that of the baryonic matter and the universe became matter–dominated. The universe then evolved as described by the Friedmann–Lemaitre equation above.

The ability of the standard model to predict the formation of the elements and the CMB is seen as its greatest successes. Detailed analysis of the nuclear reactions that took place in the early universe show that it can accurately predict the relative observed abundances of hydrogen, deuterium, helium, lithium and other heavier elements (Wagoner 1973). In addition to this, the nucleosynthesis of these elements in the standard model constrains the density of baryonic mass to be $\Omega_b \lesssim 0.035h^{-2}$ (Yang *et al.* 1984).

The discovery of the CMB by Penzias and Wilson in 1965 provided strong evidence that the universe had evolved from a hot, dense initial state and represented the redshifted remnant of the epoch of last scattering. Since then, extensive observations have confirmed the existence over the whole sky of the CMB and shown that it has a black–body spectrum of temperature 2.736 ± 0.017 K (Mather *et al.* 1990). It is interesting to note that in his original papers on the hot big bang model, Gamow (1946, 1948) had presented the temperature of the universe as a function of time, but he did not make a direct prediction for the present temperature of the CMB. However, by substituting the estimated age of the universe into his relationship, the present day temperature of the CMB is predicted to be $\sim$ 10K.

Since the discovery of the CMB, much effort has been invested in measuring the homogeneity of the CMB over the whole sky. Any observed fluctuations in its temperature (neglecting the observed CMB dipole which is due to the motion of the Earth) would directly constrain the amplitude of fluctuations in the matter, since the two were in equilibrium at a redshift of $z \sim 1000$ ($T(z) = T_o(1+z)$ with T_o being the present temperature of the CMB). To date, there has been no convincing measurement of any intrinsic fluctuations in the CMB on any angular scale[‡], but upper limits on the am-

[‡]On April 24th this year, it was announced that the satellite COBE (Cosmic Background Explorer)

plitude of these fluctuations are $\Delta T/T < 10^{-4}$ on large angular scales ($\theta > 10°$) and $\Delta T/T < 10^{-5}$ on intermediate to small angular scales ($\theta < 10°$, Efstathiou 1990).

The smoothness of the CMB is a major constraint on models of galaxy formation. For example, on large angular scales the major contribution to fluctuations in the CMB is from gravitational–potential fluctuations (Sachs & Wolfe 1967). At the epoch of last scattering, a photon from a perturbed region of the gravitational potential field ($\Delta\phi$) will be gravitationally redshifted ($\propto \Delta\phi/c^2$) as it decouples from the matter, resulting in a small change in its frequency. This can be written as

$$\Delta T/T \sim \frac{\Delta\phi}{c^2} \sim \frac{G\delta M}{c^2 R} \sim \frac{v^2}{c^2}\,, \tag{1.8}$$

where δM is the mass of the fluctuation. Considering a typical rich cluster with a velocity dispersion v of 1000 km s^{-1}, then the size of the effect is $\sim 10^{-5}$ on arcminute scales. This is already close to the observed upper limit of $\Delta T/T$ on these scales (above) and demonstrates the importance of observations of the large–scale structure in the universe, as via models of galaxy formation they predict fluctuations in the CMB that can be directly related to the observed upper limits.

Finally, Guth (1981, 1986) proposed that the universe went through a rapid exponential growth stage some 10^{-35} seconds after its birth, which expanded the universe by a factor of 10^{50}. This 'inflation' was caused by spontaneous symmetry breaking, where the Strong force separated from the other unified forces. The incentives behind introducing this expansion is that it resolves two problems with the standard model. These are the flatness problem, which is a need to explain why Ω_o is close to unity, and the horizon problem, which is the need to explain why the universe is so homogeneous when different volumes of the universe are only now becoming causally connected. Theoretical justifications for introducing inflation are that it predicts $\Omega_o = 1$ and Gaussian, adiabatic fluctuations with a scale–invariant power spectrum.

---

had measured fluctuations in the temperature of the CMB of $16 \pm 3 \times 10^{-6}$ K on angular scales of 10 degrees. If this measurement is confirmed, then it will have a profound effect on theories of galaxy formation

1.2 The Formation of Structure

The large–scale structure observed in the universe is proposed to have formed via gravitational instability in a uniformly expanding Friedmann universe (above). On top of this uniform background is assumed to be a primordial power spectrum of density fluctuations of the form

$$| \delta_k |^2 = Ak^n , \tag{1.9}$$

where δ_k is the Fourier transform of the density fluctuations $\delta\rho/\bar{\rho}$ and k is the wavenumber of the spatial frequencies. The normalisation constant A is the amplitude of the fluctuations and should be large enough to produce the structure we see today but smaller than the observed limits on the CMB fluctuations. In addition, the density fluctuations are assumed to have random phases which then forces them to obey Gaussian statistics (Efstathiou 1990).

In equation 1.9, the index n must lie within the range, $-3 < n \leq 4$. The lower limit comes from the fact that perturbations in the space–time metric diverge for $n < -3$, causing the mass in the universe to tend to zero (Barrow 1980), while the upper limit is due to values of $n > 4$ naturally tailing off to the limit of $n = 4$ (Peebles 1974a). Apart from these restrictions, n is a free parameter that has to be determined from observations although certain cosmological models predict specific indices *e.g.* for inflation $n = 1$ (Brandenberger 1990), which was originally discussed by Harrison (1970) & Zel'dovich (1972) and is favoured because it is scale–invariant.

As the universe expands, longer wavelengths enter the horizon and the primordial power spectrum is amplified or damped causing different wavelengths to grow at different rates. These changes to the power spectrum can be represented by

$$| \delta_k(t) |^2 = T(k) | \delta_k |^2 , \tag{1.10}$$

where $| \delta_k |^2$ is the primordial power spectrum from equation 1.9 and $T(k)$ is the transfer function which is dependent on the contents of the universe. Once the universe became

matter–dominated, the density fluctuations present are thought to collapse via self–gravitation to form the structures we see today.

If the universe is composed of only baryons, then the transfer function takes on two distinct forms. The first is for adiabatic perturbations where the entropy per baryon is constant. During recombination, the coupling between the photons and the electrons is imperfect leading to Silk damping of density fluctuations of masses smaller than $M_D \sim 10^{12}(\Omega h^2)^{-\frac{3}{2}} M_\odot$ (Peebles 1981). If the constraint on Ω_b from nucleosynthesis is included, $\Omega_b \lesssim 0.035$ (Yang *et al.* 1984), then the damping mass increases to $M_D \sim 10^{15}\, M_\odot$. This corresponds to the observed mass of superclusters and therefore, after recombination, the largest structures form first followed by fragmentation into smaller structures. The second form is for isothermal density fluctuations where the temperature per baryon is constant. These fluctuations emerge from recombination unaffected with no preferred length of clustering. However, just after recombination the Jeans mass is $M_J \sim 10^6(\Omega h^2)^{-\frac{1}{2}}(\delta\rho/\bar{\rho})^{-\frac{1}{2}} M_\odot$ which corresponds to the mass of globular clusters and therefore, small structures form first which aggregate to form the larger structures in a hierarchical fashion.

However, adiabatic baryonic models predict fluctuations in the CMB that are in excess of the observed upper limits (Wilson & Silk 1981, Uson & Wilkinson 1984), while isothermal models are within the limits only if $n > -2$ (Efstathiou & Bond 1987). In addition, if the processes of inflation ($\Omega_o = 1$) and nucleosynthesis are correct then the universe must be dominated by dark non–baryonic matter. Due to these problems, much interest over the past decade has focused on non–baryonic models, with a host of candidates available from particle physics.

1.2.1 Non–Baryonic Models

If the universe is dominated by non–baryonic elementary particles then the transfer function above would be dominated by two processes. The first process is the damping of free–streaming particles before they become non–relativistic, which produces an upper limit in the power spectrum of $k \propto$ mass of the particle $\propto (\Omega h^2)$. The second is known as the Meszaros effect, which freezes out small fluctuations entering the horizon in the radiation dominated era (Meszaros 1975). This causes the power spectrum to

bend from its original index n to $n-4$ on scales smaller than the size of the horizon at matter–radiation equality.

The exact interaction between these processes and the particles is dependent upon the thermal energy of the particles and therefore, non–baryonic galaxy formation models are commonly divided into 3 classes; Cold (CDM), Warm (WDM) and Hot (HDM). The individual power spectra of these 3 cases are shown in Figure 1.1 where the y–axis is related to the rms density fluctuation on a scale of k, the wavenumber (x–axis). These 3 models are described below under the assumption that they have an adiabatic, scale–invariant ($n = 1$) primordial power spectrum.

1. HDM

   A prime candidate for hot dark matter is the neutrino with a mass of $m_\nu \sim$ 30eV. Neutrinos in the early universe start with a velocity close to c, but as the universe expands their velocity decreases until they become non–relativistic ($3kT_\nu \sim m_\nu c^2$). Therefore, the transfer function is dominated by damping of free–streaming particles with a characteristic scale of $\sim 40h^{-1}$Mpc (Frenk 1986). This corresponds to a peak in the power spectrum as shown in Figure 1.1. Similar to the adiabatic baryonic universe, the largest structures form first and then fragment into galaxies.

   With the claimed measurement of the neutrino mass (Lyubimov *et al.* 1980) at the start of the 1980s, the neutrino dominated HDM scenario became extremely popular. However, detailed analysis of the model found that it produced too much large–scale coherence compared to the observed universe (White *et al.* 1983, 1984 & White 1986). Furthermore, for the model to stay below the fluctuation limits in the CMB the amplitude A in equation 1.9 had to be low, forcing galaxy formation to start at very recent epochs, $z \sim 2$ (Frenk 1986). Finally, recent observations of the neutrino mass have not supported earlier claims of a massive neutrino which removes the most attractive feature of this galaxy formation picture (see review by Jelley 1986).

   In a WDM dominated universe, structures would form in a similar way to that described above for HDM, but with a characteristic scale length of the order

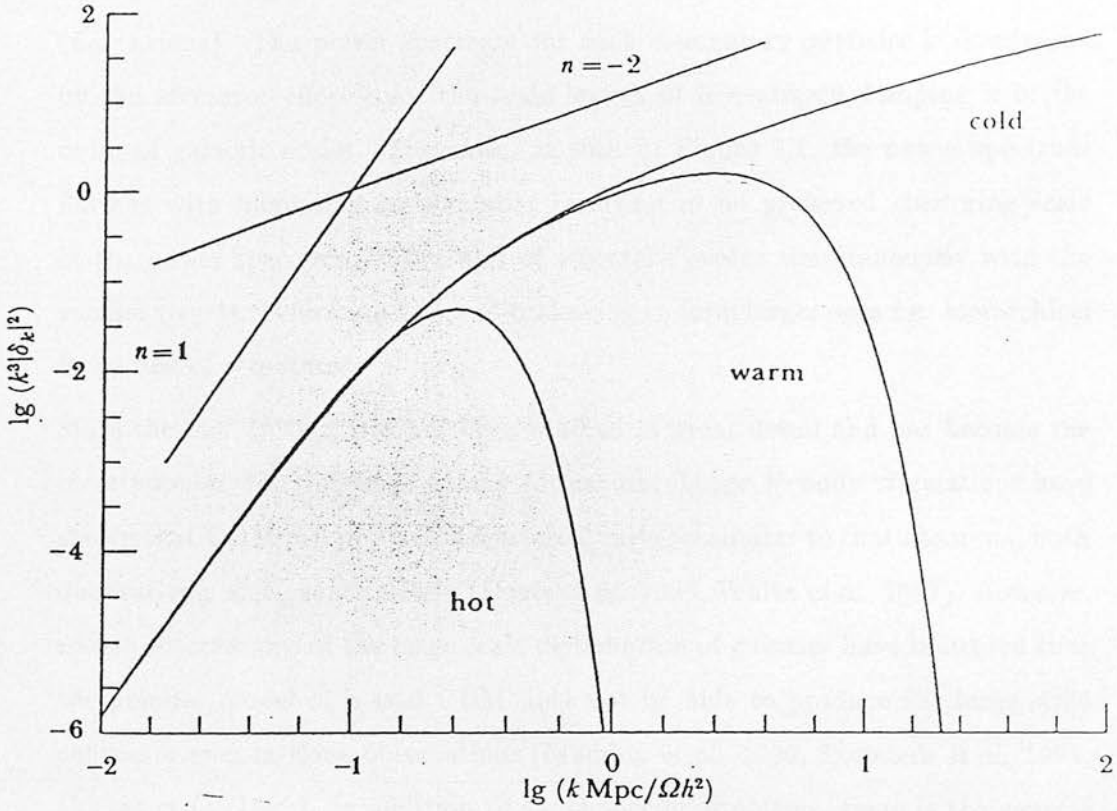

Figure 1.1: The power per decade as a function of spatial frequency for different types of density fluctuations after recombination (Frenk 1986). The curves are discussed in the text.

of galactic scales (Bond & Szalay 1983). This scenario of galaxy formation has received little attention and therefore, there are few hard predictions for the model. The main reason for this is that no strong particle candidate exists from elementary particle physics.

2. CDM

   Particle physics provides an array of possible candidates for CDM, either a host of weakly interacting massive particles with low thermal velocities because of their mass (*i.e.* gravitinos) or lighter particles created with low thermal velocities (*i.e.* axions). The power spectrum for such elementary particles is dominated by the Meszaros effect since the scale length of free–stream damping is of the order of galactic scales. Therefore, as seen in Figure 1.1, the power spectrum flattens with increasing wavenumber resulting in no preferred clustering scale in the power spectrum. All scales of structure evolve simultaneously with the smaller structures forming first and coalescing to form larger ones *i.e.* hierarchical formation of structures.

   Since the mid 1980s CDM has been studied in great detail and has become the most popular description of galaxy formation. Large N–body simulations have shown that CDM can produce a clustered universe similar to that observed, both qualitatively and quantitatively (Davis *et al.* 1985, White *et al.* 1987). However, recent observations of the large scale distribution of galaxies have indicated that the popular model of biased CDM may not be able to produce the large scale coherence seen in these observations (Maddox *et al.* 1990, Saunders *et al.* 1991, Collins *et al.* 1992). In addition to these specific problems, there is the general uneasiness that the whole model relies on unobserved particles.

1.3 The Large Scale Structure in the Universe

As illustrated in the last section, galaxy formation models predict very different histories of structure formation and by comparing these models with the observed universe, important constraints can be placed upon them. For example, computer simulations of HDM universes produce too much large scale coherence compared to the observed universe (White *et al.* 1983), while until recently CDM simulations were in good

agreement (Davis *et al.* 1985). Moreover, on scales $> 10h^{-1}$Mpc, the universe should still be imprinted with the initial power spectrum of the density fluctuations since peculiar velocities have not had enough time to destroy it. On scales greater than this, $\xi(r) \sim \delta\rho/\rho < 1$ and linear theory can be used to describe the evolution of the density field. The large scale clustering can be directly related to the Fourier transform of the two–point correlation function of the mass (x) by the expression

$$\xi(x) = \sum_{\mathbf{k}} \mid \delta_{\mathbf{k}} \mid^2 e^{i\mathbf{k}.\mathbf{x}} = \frac{V}{2\pi^2} \int_o^\infty \mid \delta_{\mathbf{k}} \mid^2 \frac{\sin kx}{kx} k^2 dk \,, \tag{1.11}$$

where V is the volume of the universe considered (Efstathiou 1990). Therefore, using some prescription of how the light we observe traces the underlying mass, observations on large scales can be used to constrain the initial power spectrum of density fluctuations. This is illustrated by Peebles (1974b), who showed that the slope γ of the observed spatial two–point correlation function was related to n, the index of the power spectrum in equation 1.9, by $\gamma = (9 + n)/(5 + n)$, which gives $n \sim 0$ for $\gamma = 1.8$.

Observations of the large–scale structure in the universe have predominately come from clustering studies of large area 2–dimensional galaxy and cluster catalogues. The Abell Catalogue (Abell 1958, Abell *et al.* 1989) and the Lick Catalogue (Shane & Wirtanen 1967, Seldner *et al.* 1977) have been the two most extensively used catalogues. However, as detailed below, both these catalogues were constructed over several years from visual scans of photographic plates and may contain large systematic errors. Therefore, it is unclear whether the structure seen in these catalogues is due to real clustering (which has been used to constrain galaxy formation theories) or is an artifact of their construction. In the following section, these two catalogues are discussed in detail along with the major observations draw from them on the large–scale structure in the universe.

1.4 Catalogues of Galaxies and Clusters of Galaxies

1.4.1 The Lick Catalogue

The Lick Catalogue was constructed over a period of seven years by C. D. Shane and C. A. Wirtanen. In total, they counted over 800000 galaxies on 1246 photographic plates

taken at the Lick Observatory. These plates were originally taken as part of a proper motion study and therefore, each image on the plates was accompanied by an objective prism spectrum. Moreover, the plates were taken with no restrictions on the observing conditions and were developed carelessly which resulted in large discrepancies between the plates in their sensitivity, depth and quality.

Shane and Wirtanen counted galaxies in 10 arcminute pixels using a travelling microscope and their criterion for including galaxies was defined by the observers' confidence that a particular image represented a galaxy. The raw galaxy counts were then corrected for differences in the counting efficiency of the observers and for differences in the plates' depths. This they claimed produced a catalogue with a uniform global limiting magnitude and a counting error of $1.13N^{-\frac{1}{2}}$ compared to $N^{-\frac{1}{2}}$ from normal Gaussian statistics.

The Shane & Wirtanen galaxy counts were re–analysed in 1977 by Seldner, Siebers, Groth and Peebles. They re–determined the correction factor for each plate in the survey by globally minimising the factors using the plate overlap regions. They also included 3 new correction factors to account for atmospheric extinction, the north–south bias and to ensure that the total galaxy count over the survey was consistent with the original count. These correction factors were then applied to each plate and the final catalogue was used to study the large scale distribution of galaxies (Groth & Peebles 1977, GP77).

GP77 analysed the distribution of galaxies within the Lick Catalogue using the two–point ($w(\theta)$) and three–point angular correlation functions (see Chapter 2 for a full discussion of the two–point angular correlation function). They found that $w(\theta)$ was well approximated by a power–law of slope $\gamma = -0.77$ with a sharp break to zero at angular separations of $\theta \simeq 2.5°$. They interpreted this as a preferred length of clustering which corresponded to a spatial scale of $\sim 9h^{-1}$Mpc. In addition, they deprojected the angular correlation functions and obtained an estimate for the spatial two–point correlation function of $\xi(r) \simeq (5\,h^{-1}\mathrm{Mpc}/r)^{1.77}$ over the range $0.05\,h^{-1}\mathrm{Mpc} < hr < 9\,h^{-1}\mathrm{Mpc}$. These results soon became the bench–mark for studies of the galaxy distribution and were widely used to constrain theory (see Figure 1.2).

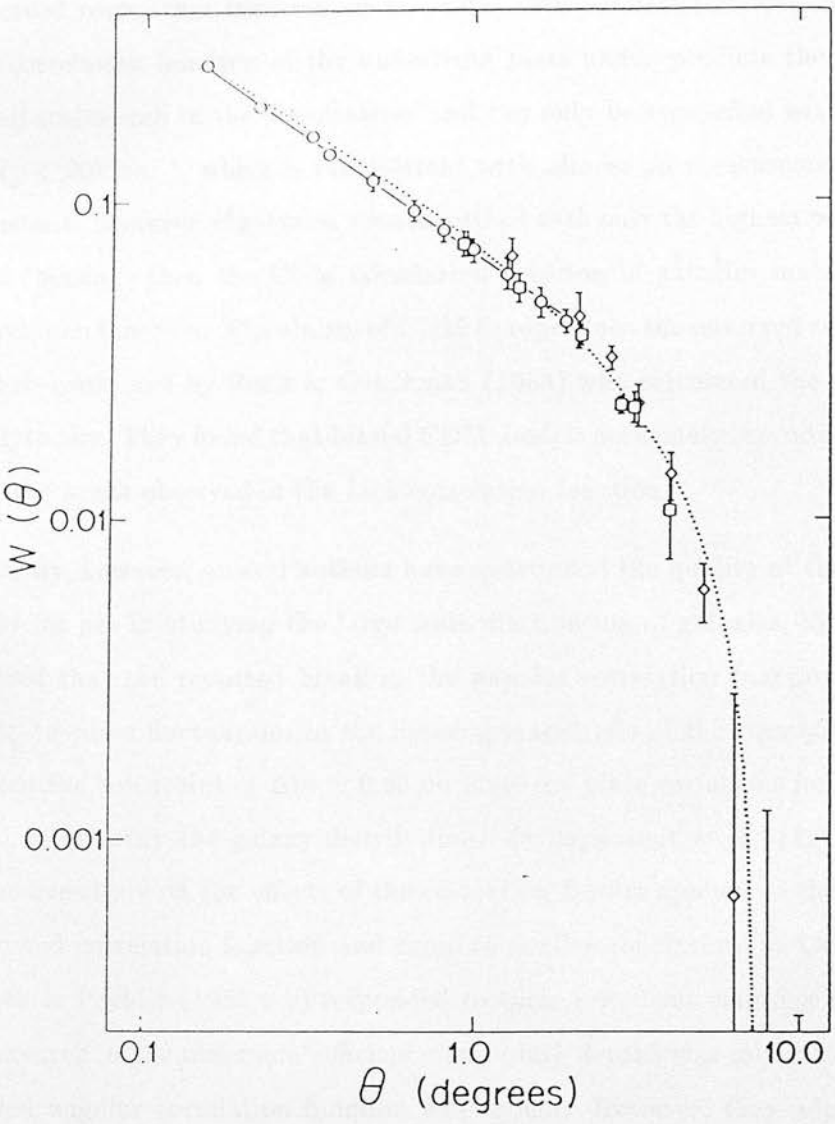

Figure 1.2: The averaged angular galaxy correlation function calculated by Groth & Peebles (1977) for the smoothed Lick galaxy counts. The different symbols are for the inter–plate and intra–plate estimations (Chapter 2). The break in the correlation function is clearly visible.

The consequences of these observations for popular theories of galaxy formation are summarised by White (1986). He shows that the spatial correlation function obtained from large simulations of a HDM universe grossly over–predicts the amplitude of the observed correlation function on all scales. For a CDM universe, he comments that the correlation function of the underlying mass under–predicts the amount of power on all scales seen in the observations and can only be reconciled with the observations if $H_o < 20\mathrm{km\,s^{-1}}$, which is inconsistent with almost all measurements of the Hubble Constant. However, if galaxies were identified with only the highest peaks in the density field (biasing) then the CDM correlation function of galaxies matched the observed correlation function. The ability of CDM to reproduce the observed correlation function was re–confirmed by Bond & Couchman (1988) who calculated the expected function analytically. They found that biased CDM models accurately reproduced the amplitude and the break observed in the Lick correlation function.

Recently, however, several authors have questioned the quality of the Lick data, especially for use in studying the large scale distribution of galaxies. Geller *et al.* (1984) showed that the reported break in the angular correlation function could be due to plate–to–plate fluctuations in the limiting magnitude of the survey. In addition, they placed the constraint of $\Delta m \simeq 0.05$ on plate–to–plate variations for future catalogues used to quantify the galaxy distribution. de Lapparent *et al.* (1986) carried out an extensive study on the effects of the correction factors applied to the Lick data on the observed correlation function and came to similar conclusions as Geller *et al.* (1984). Groth & Peebles (1986 a,b) responded to these criticisms claiming that the effects of differences in the observers' efficiency and plate depths was minimal and that the observed angular correlation function was robust. However, they admitted that "with today's technology it is certainly possible to improve on the Lick survey. Thus we strongly believe in the need for new galaxy catalogs"

Table 1.1 lists the details of several correlation functions computed from galaxy catalogues produced objectively using plate–measuring machines *i.e.* COSMOS & APM. The Lick correlation function is also included for comparison. In general, the automated surveys have confirmed the existence of the break in the Lick correlation function but its exact scale varies between authors by an order of magnitude. More significant though,

is the clear trend of increasing break angle with increasing contiguous area of the survey which demonstrates that the finite area of most of the automated surveys has systematically affected the observed correlation function. However, for the two largest surveys in Table 1.1 (APM & Lick) the break scale differ significantly, with the APM finding a scale of $\simeq 20\,h^{-1}$Mpc compared to the GP77 result of $\simeq 9\,h^{-1}$Mpc. Standard models of CDM cannot predict the large scale power seen in the APM correlation function (Maddox *et al.* 1990).

Area ($\deg^2$)	Break (h^{-1}Mpc)	References
14	3	Shanks *et al.* 1980
22	3	Stevenson *et al.* 1985
36	7	Hewitt 1982
100	7	Collins *et al.* 1988
110	5	Stevenson *et al.* 1988
500	9	Collins *et al.* 1988
680	9	Maddox *et al.* 1988
2800	$\simeq 20$	Maddox *et al.* 1990
3000	9	Groth & Peebles 1977

Table 1.1: The scale of the break observed in the angular correlation function computed from automated galaxy catalogues.

1.4.2 Abell Catalogue

The most efficient way of studying the universe on large scales is to use clusters of galaxies as tracers since they are typically separated by $\sim 10h^{-1}$Mpc. The most extensively used survey for such purposes has been the Abell catalogue (Abell 1958, Abell *et al.* 1989).

George Abell constructed his catalogue of rich clusters by visually scanning 896 Palomar Observatory Sky Survey plates in search of galaxy overdensities. In total, he found 2712 clusters covering two–thirds of the sky down to a declination limit of $-27°$. Of these,

he selected 1682 clusters as a "statistical sample".

When Abell had found a cluster, he determined its centre by eye and included the cluster in his catalogue only if it satisfied the 3 criteria listed below.

1. Richness

   The cluster had to contain at least thirty galaxies within the magnitude range of $m_3 \rightarrow m_3 + 2$, where m_3 was the magnitude of the third brightest member in the cluster. Abell omitted obvious foreground galaxies. The magnitudes were obtained from direct comparisons with galaxies of known magnitude on overlying film copies.

2. Compactness

   The cluster had to be compact so that all the galaxies defining its richness were within $1.5h^{-1}$Mpc of the cluster centre. The angular size of this fixed radius was determined from the redshift–m_{10} relationship where m_{10} was the magnitude of the tenth brightest cluster member. The Abell radius, in terms of angle subtended on the sky, was given by the formula

   $$\theta = \arctan\left(\frac{150}{cz}\right) , \tag{1.12}$$

   where z was the estimated redshift of the cluster.

3. Distance

   Clusters were included only if their redshifts were within the range $6000 < z < 60000\,\mathrm{km\,s^{-1}}$, where again, the redshifts were estimated from the magnitude of the tenth brightest cluster member.

He estimated that the standard error on the cluster richness was 17%, while the error on the redshift was 26%. He divided his clusters into distance and richness classes with the separations between the bands equal to 3.5 times the quoted errors. Table 1.2 shows the classification scheme employed by Abell.

Finally, Abell defined a 'statistical sample' which simply consisted of all clusters with a richness class $RC \geq 1$ at high galactic latitudes (see Table 1 of Abell 1958). This

Richness Intervals (RC)					
Richness class	Counts	Richness class	Counts	Richness class	Counts
0	30 – 49	2	80 – 129	4	200 – 299
1	50 – 79	3	130 – 199	6	> 300
Distance Intervals (D)					
Distance class	Mag. (R band)	Distance class	Mag. (R band)	Distance class	Mag.
1	13.3 – 14.0	4	15.7 – 16.4	6	17.3 – 18.0
2	14.1 – 14.8	5	16.5 – 17.2	7	> 18.0
3	14.9 – 15.6				

Table 1.2: The richness and distance classes as defined by Abell (1958)

sample of clusters has been extensively used in the study of the distribution of clusters, but it should not be forgotten, as with the Lick catalogue, that the catalogue was constructed from visual searches of photographic plates.

Recently, Corwin and Olowin completed the Abell catalogue over the whole sky by visually scanning plates taken of the Southern Skies (Abell *et al.* 1989, ACO). They implemented a very similar scheme to Abell's and classified their clusters using the same selection criteria. In closing, ACO remarked; "We hope this will be the last such catalogue prepared by visual scans of photographic plates, and we urge future investigators to compile cluster catalogues using high–speed microphotometric scanning machines and objective selection criteria".

The most startling result obtained from the Abell catalogue was the spatial two–point correlation function for clusters obtained by Bahcall & Soneira (1983, BS83). They found that the function had the form

$$\xi_{cc}(r) \simeq \left(\frac{25\, h^{-1}\mathrm{Mpc}}{r} \right)^{1.8}, \tag{1.13}$$

over the range $r < 150\, h^{-1}$Mpc for a redshift survey of 104 Abell $RC > 1$ $D \leq 4$

clusters at high galactic latitudes (Figure 1.3). Since 1983, the original BS83 result has been confirmed by several larger Abell cluster redshift surveys (Postman *et al.* 1986, Huchra *et al.* 1990). In particular, Postman *et al.* (1992) have found the same amplitude of clustering using a survey of 351 Abell clusters selected from the original Abell catalogue.

These observations indicate that clusters are more strongly clustered than galaxies, with $\xi_{cc} \simeq 15\xi_{gg}$ over the same scales. Therefore, both cannot be fair tracers of the underlying mass distribution. The most significant implication of the high amplitude of the cluster correlation function is that the biased CDM models described earlier underpredict the amplitude of the cluster correlation function (White *et al.* 1987) and remains one of the few observations unexplained by the model.

To account for this observed discrepancy, Kaiser (1984) proposed a general scheme of biased cluster formation which identified rich clusters with rare high peaks in the underlying density field. He showed that if the amplitude of primordial density fluctuations in spheres of $r \sim 6 - 10h^{-1}$Mpc was estimated from the observed galaxy distribution, then clusters of richness $RC \geq 1$ had an amplification of $\xi_{clusters} \simeq 9 - 16\xi_{density}$. However, in specific models like CDM, the amplification is usually not this great. White *et al.* (1987) show that in a CDM dominated universe, clusters would only be biased compared to the underlying mass by a factor of five and by a factor of two compared to the galaxies. This is inconsistent with the observed discrepancy quoted above.

1.4.3 Projection Effects

BS83 and Bahcall *et al.* (1986) noted that ξ_{cc} was significantly elongated along the line–of–sight with close angular pairs of clusters having very different redshifts. Bahcall *et al.* (1986) interpreted this as large cluster peculiar velocities of the order $v \simeq 2000\,\mathrm{km\,s^{-1}}$ which were in clear disagreement with standard galaxy formation models.

However, Sutherland (1988) proposed that the observed elongation was caused by projection effects which he generally defined as "angular correlations that are not due to genuine clustering in redshift space". He claimed that the haloes of rich nearby clusters had boosted the richness of more distant clusters, close on the sky, into the Abell

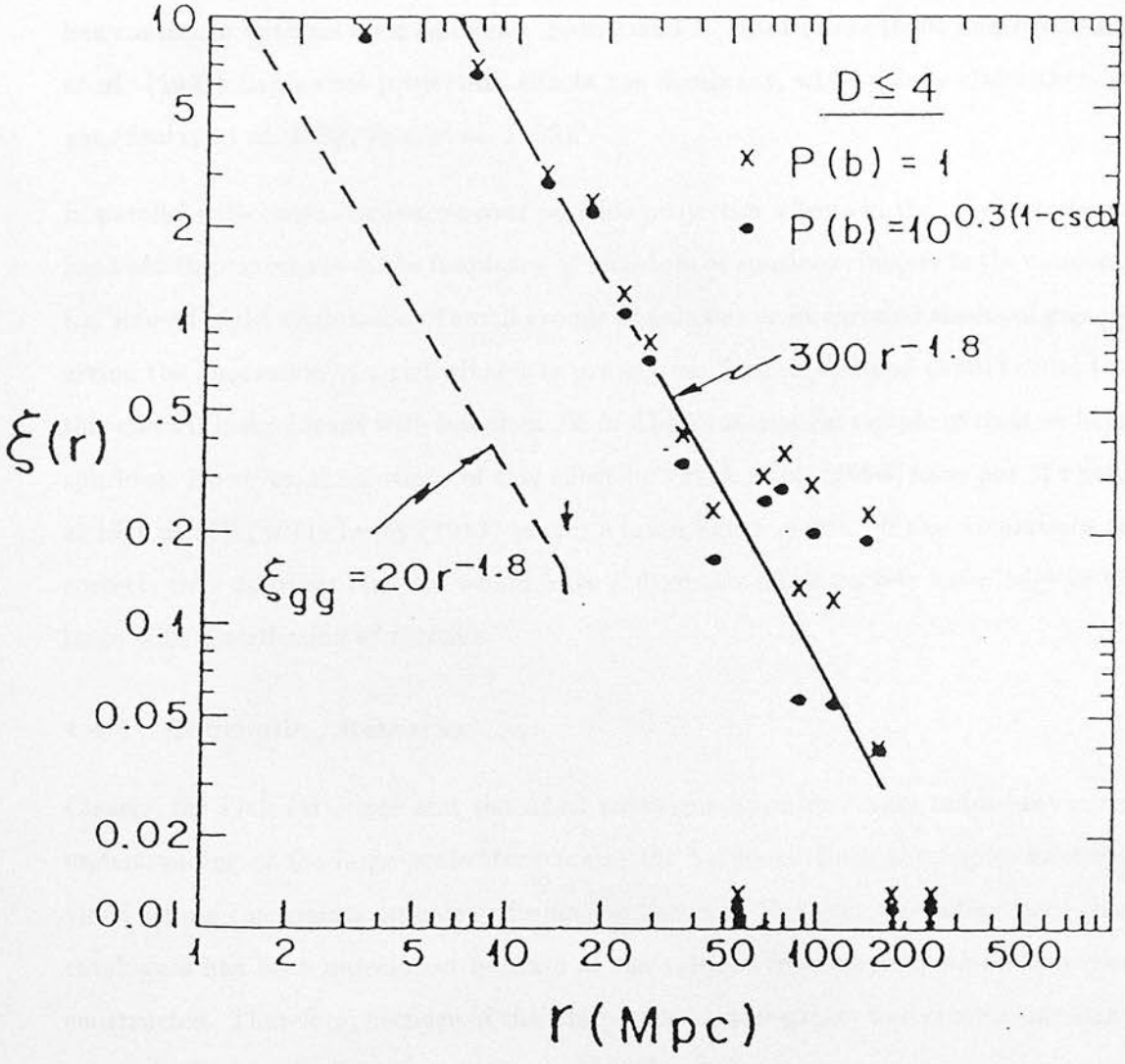

Figure 1.3: The spatial cluster correlation function calculated by Bahcall & Soneira (1983). The • and × symbols refer to two different extinction corrections and the dashed line is the observed galaxy spatial correlation function (GP77) with the break indicated by the arrow.

catalogue. Correcting for these projection effects reduced the correlation length of the correlation function from $25h^{-1}$ Mpc to $14h^{-1}$ Mpc, a value not too discordant with CDM models.

Since then, the debate over the reality of the elongation in the redshift direction of ξ_{cc} has continued with no clear outcome. Sutherland & Efstathiou (1990) and Efstathiou *et al.* (1992) claim that projection effects are dominant, while others claim they are not (Szalay *et al.* 1989, Jing *et al.* 1992).

In parallel with these discussions over possible projection effects in the Abell catalogue, has been the concern over the frequency of phantom or spurious clusters in the catalogue *i.e.* line–of–sight alignments of small groups of galaxies or foreground sheets of galaxies giving the impression of a rich cluster in projection. Struble & Rood (1991) claim that this effect is insignificant with less than 3% of Abell's statistical sample of clusters being spurious. However, simulations of this effect by Frenk *et al.* (1990) have put the value as high as 50%, while Lucey (1983) quotes a lower figure of 30%. If the simulations are correct, then spurious clusters would have a dramatic effect on our knowledge of the large scale distribution of clusters.

1.4.4 Concluding Remarks

Clearly, the Lick catalogue and the Abell catalogue have been very important in our understanding of the large–scale structure in the universe. Both catalogues have provided strong constraints on galaxy formation theories. However, the integrity of these catalogues has been questioned because of the subjective manner in which they were constructed. Therefore, because of their importance, new galaxy and cluster catalogues constructed objectively are needed to resolve the above discrepancies.

The remainder of this thesis is concerned with such catalogues, the Edinburgh/Durham Southern Galaxy Catalogue, the Edinburgh/Durham Cluster Catalogue and the Edinburgh/Milano cluster redshift survey.

1.5 The Edinburgh/Durham Southern Galaxy Catalogue

The Edinburgh/Durham Southern Galaxy Catalogue (EDSGC) is one of the first fully automated objective galaxy catalogues to be constructed. It covers an area of $\sim$ 1500 degrees square centred at the South Galactic Pole (SGP) and contains extensive information on over one million galaxies. The majority of the work involved in its construction was carried out by Neil Heydon–Dumbleton and Chris Collins at Edinburgh and has been presented in several papers (Collins *et al.* 1988, Heydon–Dumbleton *et al.* 1989, Heydon–Dumbleton 1989). This section summarises the data and the methods used in the catalogue's construction and presents some of the tests implemented on the completed EDSGC.

1.5.1 The Raw Data

The UK Schmidt Telescope (UKST) at Siding Springs in Australia was commissioned in late 1973 to carry out a systematic photographic survey of the southern hemisphere. The UKST has a 1.8m diameter mirror with a 1.2m aperture which provides a large field of view making it ideal for the construction of such a large–area survey. The photographic plates used by UKST subtend an area of $6.4^\circ \times 6.4^\circ$ on the sky with a plate scale of 67.12 arcseconds per millimetre. For all the surveys carried out by UKST, the centres of the plates are separated by 5° which provides a substantial overlap between them and removes the need to use the plate edges which are heavily vignetted (vignetting is negligible within 2.7° of the plate centre).

The EDSGC is based on plates taken from the ESO/SERC Atlas. This atlas consists of glass copies of the SERC J survey which was the first survey to be completed by UKST and covers the whole southern sky below a declination of -17° (606 plates in total). The passband of the SERC J survey is defined by the response of the emulsion (Kodak IIIA–J) combined with a Schott GG395 filter. This provides an almost uniform sensitivity in the wavelength range 3500$\AA$ to 5400$\AA$ and is close to the standard Kron–Cousins B passband. Image magnitudes on the plates are usually referred to as b_j magnitudes.

Both the original J survey plates and the atlas copies were taken using a strict set

of criteria to minimise systematic errors between different plate exposures and, more importantly, to ensure that the process was highly repeatable. For example, survey plates were only taken in dark time, good seeing (less than 3 arcseconds) and with the sun $> 18^{\circ}$ below the horizon to avoid astronomical twilight. During the exposure, each plate was held in a curved holder and was flushed with nitrogen to reduce the effects of differential desensitisation over the plate. The developing and copying of the plates were also carried out with a high degree of consistency to ensure that systematic differences between plates were not introduced. Finally, quality control checks were carried out on all plates and each was graded either A, B or C. Therefore, this atlas represented the most homogeneous catalogue of photographic plates available at that time. The reader is referred to the UK Schmidt Telescope Unit Handbook (1983) for a description of the procedures used in taking the original plates, Cannon *et al.* (1978) for full details of the processing of the plates and Bruck & Waldron (1984) for a discussion of the copying process.

In total, 60 A grade plates were used in the final EDSGC and most are listed in Table 2.2. These plates were extracted from the ESO/SERC Atlas held in the UK Schmidt Library at the Royal Observatory Edinburgh and scanned by COSMOS, also at the Royal Observatory Edinburgh. The COSMOS machine is a high–speed flying spot microdensitometer, specifically designed and constructed for scanning astronomical photographic plates. The whole machine sits on a plinth driven 35 feet into the ground which separates it from the rest of the building thus preventing vibrations of any sort from affecting the scans. In addition, COSMOS and the UKST plate library are kept in a dust–free environment, thus reducing the chances of contamination on the plates.

Plates are loaded into COSMOS with their south side at the top of the plate carriage holder and raster scanned using a beam of light from a cathode ray tube of width 8 microns. As the plate moves in the y direction, the beam scans in the x direction with a pixel size of 16 microns. In total, an area of 287mm $\times$ 287mm is scanned each time which corresponds to an area of $5.35^{\circ} \times 5.35^{\circ}$ on the sky. For each pixel, a transmission value is calculated by comparing the light measured passing through the plate with a reference signal. This in turn, is converted into a measured intensity using a Baker

density calibration curve (MacGillivray & Stobie 1984).

COSMOS can operate in two modes; mapping or threshold. The first records all the pixel information on a plate and therefore, requires a vast amount of computer storage. The second records only pixels that are a certain percentage above the sky background of the plate. This is determined beforehand by scanning the plate with a much lower resolution (32 microns) to measure the large scale variations over the plate which are usually due to a combination of large nearby stars, vignetting and differential desensitisation. After scanning, the pixel data is passed into the COSMOS image analyser (Thanisch *et al.* 1984) which connects all adjacent pixels producing a final set of objects for each plate. Each image is assigned 27 individual image parameters such as the image magnitude, position and both the intensity weighted and unweighted moments of the pixel distribution (Stobie 1980). Plates used in the EDSGC were scanned in threshold mode, with a threshold of 8% to 10% above the sky background. This ensured that there were approximately the same number of objects in each scan and was found by MacGillivray & Dodd (1982) to be an acceptable level for maximising the number of true images compared to 'noise' images.

The magnitudes returned by COSMOS were isophotal magnitudes and the threshold quoted above for the EDSGC corresponded to a final isophote of 25 magnitudes per arcsecond squared in b_j. For images brighter than $b_j = 20.5$, the magnitudes were effectively total magnitudes (MacGillivray & Dodd 1982). In addition, the image magnitudes depended upon the sky background magnitude of the scanned plate and adopting a fixed detection threshold for all the plates introduced large variations between the zero–point magnitudes of the plates. Therefore, it was imperative to obtain external photometry to calibrate the magnitude scale of each plate (below).

All the COSMOS scans used in the EDSGC were analysed using the COSMOS deblending software (Beard *et al* 1990), which involved re–thresholding each image in intensity space at 8 progressively higher thresholds in search of saddle–points in the image's intensity distribution. If such saddle–points were found, the separate peaks were fitted by a Gaussian and split into their daughter images. At the SGP, the number of blended objects was found to be $\sim$ 10% at all magnitudes and implementing

the deblending software substantially reduced this number *e.g.* at a surface density of 20 arcminutes^{-2} (cores of rich clusters) the number of real objects detected increased by over 30% because of deblending (Heydon–Dumbleton *et al.* 1989). Deblending of the images was vital to the EDSGC for two reasons. First, faint star–star mergers near the plate limit imitated galaxies because their combined shape appeared elliptical and they had a lower surface brightness compared to a single star. If these were not deblended, then there would have been a significant contamination of false galaxies at faint magnitudes. Secondly, the EDSGC was used in the construction of an automated cluster catalogue (Chapter 3). If deblending had not be implemented, the cores of rich clusters would have appeared as single large objects and therefore, would not have been detected by the automated cluster detection algorithm.

1.5.2 Star–Galaxy Separation

A COSMOS scan of a typical Schmidt plate contains on average 2×10^5 objects. To the plate limit, over 90% of these objects are stars which clearly must be removed to produce a reliable and meaningful galaxy catalogue. For the EDSGC, this was achieved using 3 parameters defined during the scanning of the plates. Each parameter worked over a different magnitude range and their combined effect covered the full range of magnitudes observed on a plate.

1. The G classifier: magnitudes brighter than $b_j \sim 16$.

   This was defined as,

   $$G = \frac{A}{\pi ab} \tag{1.14}$$

   where A was the area of the image and a, b were the unweighted major and minor axes. This parameter effectively measured how well the image filled the ellipse fitted to it. For stars brighter than $b_j \sim 15.5$, diffraction spikes dominate the fitted ellipse but they have a relatively small area, while galaxies at this magnitude tend to fill their fitted ellipse. Objects were selected as galaxies if G was greater than 0.9.

2. The $\log_{10}A$ classifier: intermediate magnitudes $16.0 < b_j < 19.5$.

   This classifier relied on the fact that galaxies have a lower surface brightness than stars. This difference was helped by the fact that stars brighter than $b_j \sim 19.0$ were saturated on the plates. Therefore, all the images were plotted on a $\log_{10}A$ (area) versus magnitude graph and the two populations were separated by a single straight line fit.

3. The S classifier: magnitudes fainter than $b_j \sim 20$.

   This classifier was defined by

   $$I_{th} = I_{max} \exp\left(\frac{-A}{2\pi S}\right) , \tag{1.15}$$

   where A was the area of the image and I_{th} & I_{max} were the threshold and maximum intensities of the object respectively. S was the Gaussian width fitted to the image. Even at faint magnitudes, S was smaller for stars than for galaxies due to the point–spread function of the stars. Therefore, on a plot of S against magnitude the two populations were clearly separated.

Near the limit of the plates, star–galaxy separation became extremely difficult. Therefore, COSMOS scans used in the EDSGC were cut at a COSMOS magnitude of -1.0, which roughly corresponded to $b_j = 21.0$ for most plates. For a much fuller discussion of these classifiers and their effective magnitude ranges, the reader is referred to either Heydon–Dumbleton *et al.* (1989) or Heydon–Dumbleton (1989).

To test the reliability of the star–galaxy separation, visual checks were carried out on 5 plates spread across the EDSGC. For each plate, 300 classified galaxies and 300 classified stars over a broad range in magnitude were randomly selected and eyeballed. The result of this test was a $> 95\%$ completeness for the galaxies at all magnitudes with $\sim 5\%$ stellar contamination. Similar results were obtained for visual checks on images selected before and after deblending.

1.5.3 Galaxy Photometry

As stated above, COSMOS only returned the magnitude of objects relative to the background magnitude of the plate. Therefore, it was essential to obtain external pho-

tometry to calibrate all the galaxies in the EDSGC by determining the sky background magnitude or zero–point magnitude of the plates. For galaxies, the relationship between the COSMOS magnitude and the b_j magnitude is linear over a wide range of magnitudes and can be represented by

$$b_j = m_{cos} + m_{sky}\,, \tag{1.16}$$

where m_{cos} is the COSMOS magnitude and m_{sky} is the constant sky background of the plate.

The EDSGC was calibrated using CCD direct images obtained at CTIO and SAAO. In total, 30 calibration sequences were taken across the whole EDSGC and were spaced in a checkerboard fashion *i.e.* plates either had a sequences on them or overlapped with two or more plates with a sequence on. Each CCD frame was centred on a loose cluster which resulted in $\sim$ 15 usable galaxies per frame for the calibration. For the plates with a sequence, the COSMOS magnitudes of the observed galaxies were plotted against their CCD magnitudes and from the fit (with the slope fixed at 1.0) m_{sky} was obtained. This zero–point was then used to calibrate the whole of the plate with a uncertainty of $\sim$ 0.05 magnitudes. For plates without a sequence, m_{sky} was calculated using the galaxies in the overlap regions with plates with a sequence (typically 1000$-$3000 galaxies in each overlap). On average, each uncalibrated plate overlapped with 2–3 calibrated plates which prevented erroneous calibrations from propagating through the survey. Figure 1.4 shows the histogram of measured plate magnitude offset between adjacent plate zero–points and the best fit Gaussian to this distribution has a dispersion of 0.08 magnitudes. This implies a calibration uncertainty of 0.05 magnitudes on each plate (*i.e.* $0.08/\sqrt{2}$). This is within the limits set by Geller *et al.* (1984) for plate matching errors for any new galaxy catalogue used in measuring the large scale distribution of galaxies.

Once again, the reader is referred to Heydon–Dumbleton (1989) or Collins & Nichol (1992) for a more detailed description of the photometric calibration of the EDSGC and a full discussion of the errors.

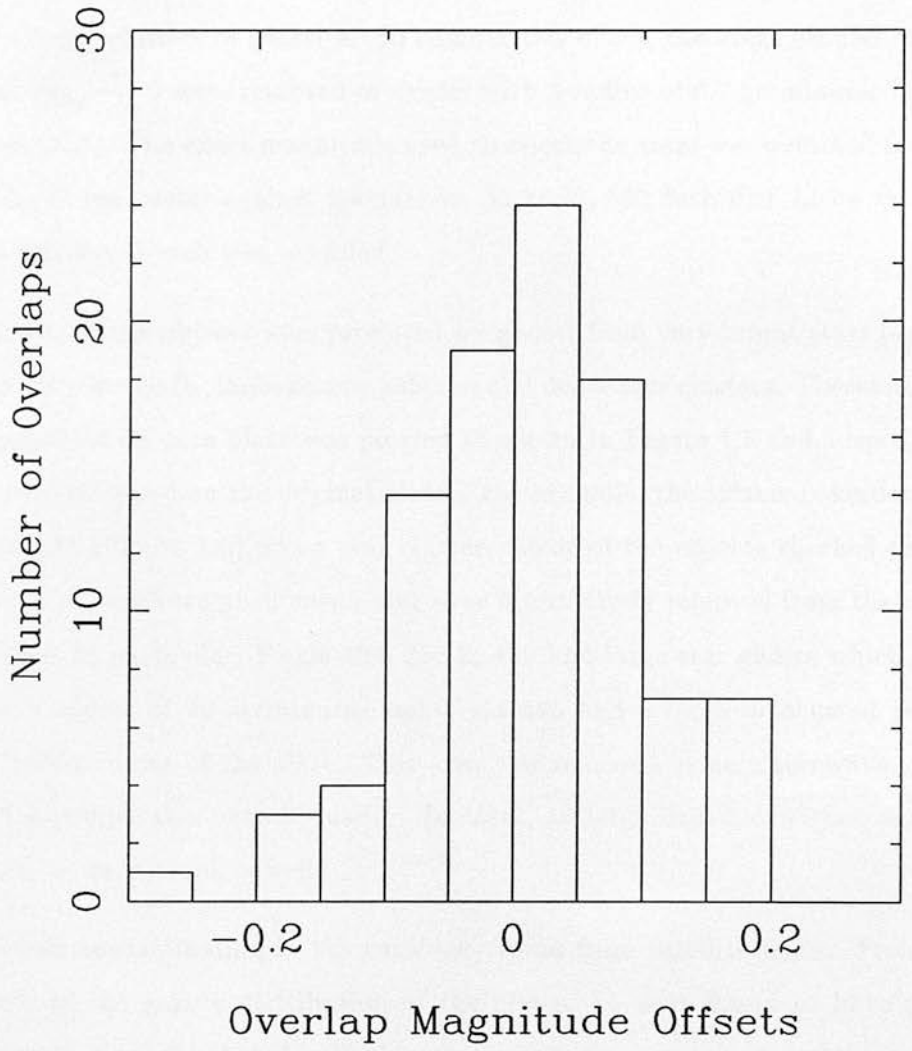

Figure 1.4: Histogram of magnitude offsets between fields in the EDSGC. For each pair of plates the magnitude offset was calculated from the galaxies in the overlap region. The best–fit Gaussian gives a 1σ width of 0.08 magnitudes.

1.5.4 Construction of the EDSGC

Before the plates were joined to form one homogeneous catalogue, the individual COSMOS scans were cleaned of spurious objects. The main source of such objects was from the deblending of star haloes around bright stars in the field ($b_j < 12$) which tended to mimic rich clusters of galaxies. To combat this effect, the areas around stars brighter than $m_{cos} \sim -9$ were removed or *drilled* with a radius of 6.7 arcminutes (UKST handbook 1983). The exact magnitude used to select the stars was obtained from the plots of the G parameter against magnitude. In total, 553 such drill holes were made and the position of each was recorded.

Other spurious objects were produced by ghosts from very bright stars ($b_j \sim 6$) in the field, satellite trails, large nearby galaxies and dense star clusters. Therefore, the galaxy distribution on each plate was plotted as shown in Figure 1.5 and suspicious features were investigated on the original plates. For example, the extreme overdensity seen on Field 531 (Figure 1.5) was a star cluster. Most of the objects checked turned out to be one of the above phenomena and were interactively removed from the catalogue by drilling. In particular, Fields 404, 356 & 469 had large star ghosts which were drilled with a radius of 40 arcminutes and Field 466 had a large defocussed region in the northwest corner of the plate. This area was removed as no alternative plate existed with a comparable overall quality. In total, 10 large drill holes were used and their positions were noted as well.

A severe contamination in the catalogue came from satellite trails. From the visual checks of the galaxy distribution of the plates, 11 were found to have this form of contamination. Combined with this, there were also spurious galaxies associated with the deblending of diffraction spikes of stars. Both these types of spurious image were removed using the fact that they had preferentially aligned position angles *i.e.* diffraction spikes of stars were aligned with the edges of the plate and therefore, their position angles were always 0°, 90° or 180°. In addition, these images have high ellipticities and filled their fitted ellipse well. Therefore, on the plates in question, all the objects were plotted in the eccentricity (minor over major axis) versus position angle plane which separated the satellite trails from the majority of other objects. A cut was made in

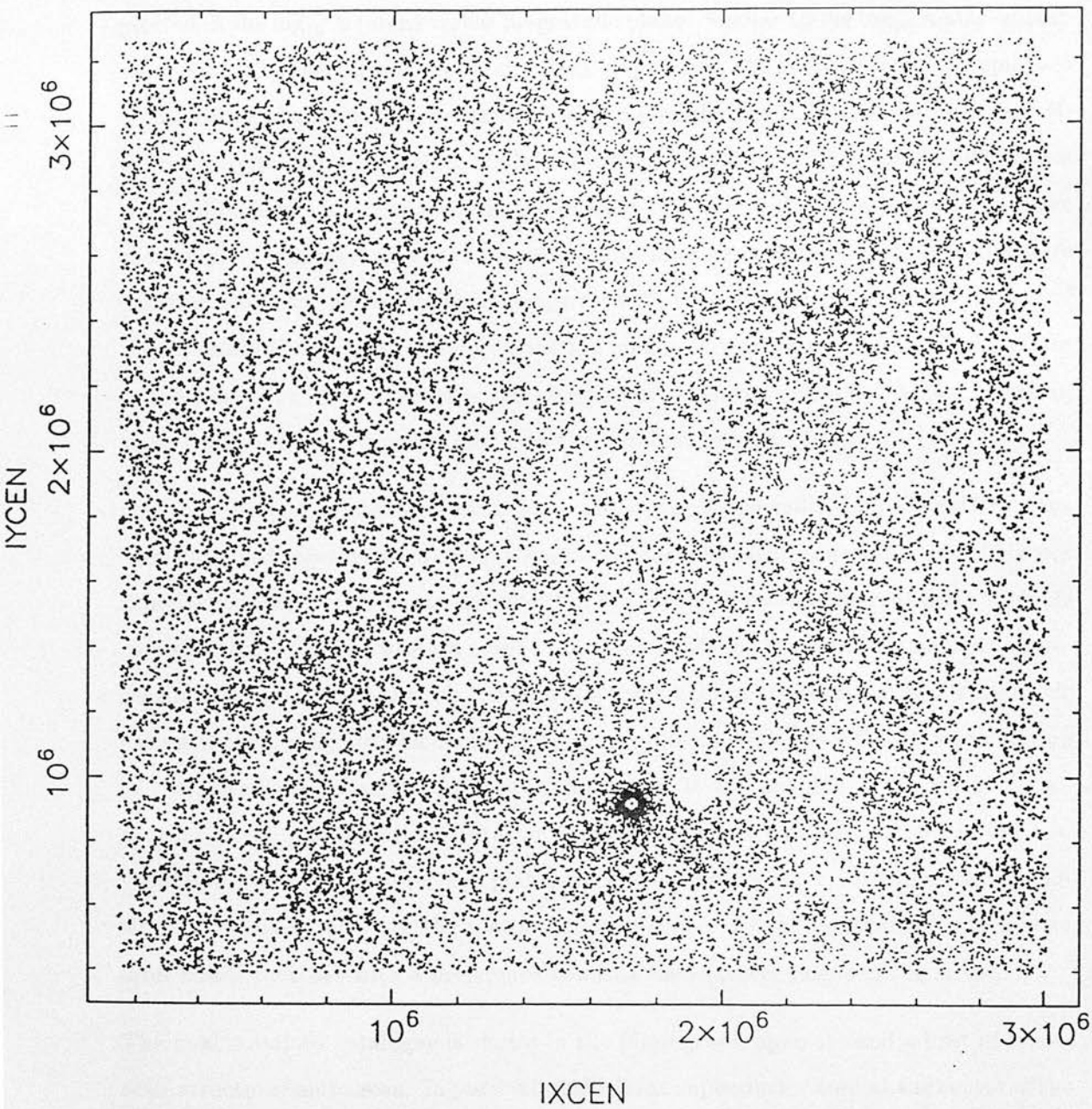

Figure 1.5: The distribution of galaxies before cleaning on Field 531 in the EDSGC. The x and y axes refer to the actual measured coordinates of the galaxies on the plate (microns).

eccentricity (typically $0.3 \sim 0.4$) and all objects with a lower value than the cut were plotted in the $\log_{10}$ A (area) versus magnitude plane. Similar to the $\log_{10}$ A star–galaxy separation classifier above, the real galaxy population stood away from the spurious population and the two were separated with a straight line. This method was very effective at removing the satellite trails and diffraction spikes, with typically 500 images removed on each plate. As a check, the objects both rejected and re–accepted into the catalogue by this method were inspected on 5 plates. For rejected images, $\sim 8\%$ were galaxies, while for the accepted images, over 95% were galaxies. Due to the success of the method in removing residual diffraction spikes, it was performed on all the plates in the EDSGC and on average ~ 100 images were removed per plate. Visual checks of these rejected objects were in line with the numbers quoted above.

Once all the plates had been calibrated and cleaned, the individual COSMOS scans were mosaiced together to produce a final homogeneous catalogue of galaxies. This was achieved interactively because the extent of the overlap between different pairs of plates varied extensively. The western edges of the plates suffered the worst vignetting and desensitisation (UKST handbook 1983), while the northern edges displayed a systematic excess of faint galaxies which seemed to be a problem with the COSMOS calculation of the plate background intensity near that edge. It was not due to the image classification or the photometric calibration because the effect was still present in the raw COSMOS scans. Therefore, the plates were attached together with a preference towards the eastern edges of the plates into long strips of fixed declination, which were later added together with a preference towards the southern edges of the strips.

The final mosaiced catalogue is shown in the photograph opposite and a host of large–scale structure can be seen. In particular, the large supercluster seen at the centre of the EDSGC corresponds to the Sculptor supercluster (Seitter *et al.* 1989). This structure, along with others seen in the EDSGC, are discussed in greater detail in Chapter 5. In addition to these structures, the large drill holes described above are visible, especially the two on Field 469. Also seen is the area removed from Field 466 (left–hand edge of the EDSGC) because of the defocussed region. The smaller drills are not visible because the catalogue has been binned into 10 arcminute pixels.

It should be noted, that the removal of the satellite trails and diffraction spikes was carried by myself and for that reason, the methods used are presented in more detail that other techniques used in the construction of the EDSGC.

1.5.5 External Checks of the Photometric Calibration

Extensive checks of the internal photometric calibration of the EDSGC were carried out by Neil Heydon–Dumbleton and are presented in his thesis (Heydon–Dumbleton 1989). These checks centred around the examination of galaxies in the overlap regions of plates and on the galaxy number counts as a function of Right Ascension and galactic latitude. He concluded that there was no evidence for systematic calibration errors in the catalogue.

However, with the recent publication of the APM CCD photometric calibration sequences (Maddox *et al.* 1990b), a valuable external check on the EDSGC photometry was carried out by myself and Chris Collins. This check was supplemented by two extra sequences kindly supplied by Matthew Colless at the IOA, Cambridge. Galaxies in common between the external CCD sequences and the EDSGC were extracted (tolerance of 6 arcseconds in the matching) and the results of the pairing are shown in Figures 1.6 and 1.7.

Figure 1.6 shows the difference in magnitude of all galaxies found in common between the EDSGC and the APM, as a function of mean magnitude. At the bright end (mean $b_j < 17.0$), the scatter in magnitude is large with a typical difference between the two of ± 0.2 magnitudes. However, the majority of the data are for galaxies fainter than a mean magnitude of $b_j = 18.0$. Over a range of 3 magnitudes, the data are consistent with the expected scatter due to the APM & COSMOS machine measuring errors ($\sim$ 0.1 magnitudes). The main result of the comparison is an overall 0.2 magnitude shift at all magnitudes between the two surveys, with the APM being the brighter of the two. However, the comparison of the EDSGC with the Colless sequences (Figure 1.6) does not show any systematic displacement between the two and is consistent with the expected scatter about zero of the COSMOS machine measuring error.

In terms of the correlation analysis presented in Chapter 2, a simple shift in the global

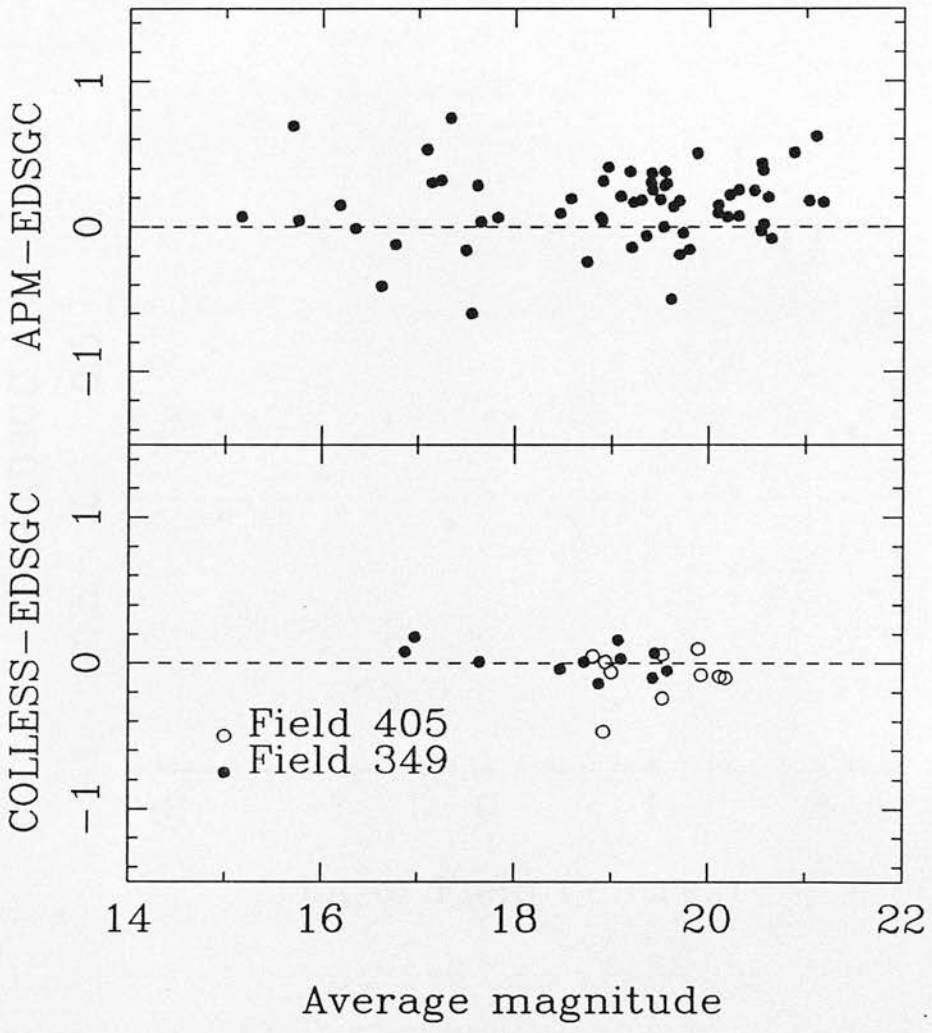

Figure 1.6: The top plot shows the measured offset of galaxies in common between the APM CCD sequences and the EDSGC. The bottom plot shows the measured offset of galaxies in common between the Colless CCD sequences and the EDSGC.

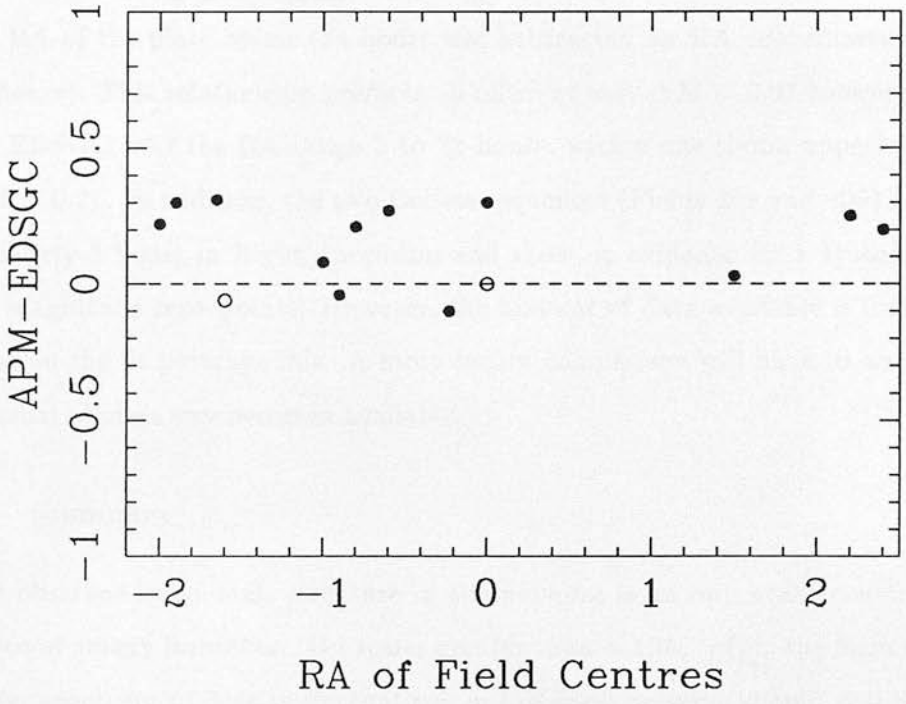

Figure 1.7: The mean offset between the APM and EDSGC calibrations for individual plates as a function of RA (24 hours has been subtracted from the plate RA coordinate if its RA was greater than 12 hours). No significant gradient can be seen.

magnitude calibration between catalogues is not a significant problem, since correlation functions are usually scaled using the number density of galaxies. A potentially more serious problem is the existence of a variable magnitude shift as a function of plate position or Right Ascension, as this would introduce large scale gradients. To test for this, the mean magnitude shift of EDSGC plates with an APM sequence were investigated as a function of Right Ascension. Figure 1.7 shows this comparison and the global 0.2 magnitude shift is still present. However, there are no signs of a systematic variation in the shift across the survey. This is supported by a linear fit to the data, which gives $\Delta m_{APM-COSMOS} = -(1.59 \pm 2.80) \times 10^{-2}\,\alpha + 0.179 \pm 0.041$, where α is the RA of the plate centre (24 hours was subtracted for RA coordinates greater than 12 hours). This relationship predicts an offset of only $\Delta M = 0.07$ between the ends of the EDSGC over the RA range 3 to 22 hours, with a one sigma upper offset limit of $\Delta M = 0.21$. In addition, the two Colless sequences (Fields 349 and 405) are separated by nearly 2 hours in Right Ascension and show no evidence for a systematic shift in the magnitude zero–points. However, the amount of data available is limited and the error on the fit portrays this. A more secure comparison will have to wait until more external photometry becomes available.

1.6 Summary

The observed large–scale structure in the universe is an important constraint on scenarios of galaxy formation. On scales greater than $\sim 10h^{-1}$Mpc, the form of the initial power spectrum of density fluctuations in the early universe should still be imprinted on the structures we see today. Therefore, by observing the universe on scales greater than this, important information about the early universe can be obtained.

However, previous observations of the large–scale structure in the universe have come from detailed analysis of visually compiled galaxy and cluster catalogues. The subjective manner in which these catalogues have been constructed has undermined many of these observations. The Edinburgh/Durham Southern Galaxy Catalogue (EDSGC) presented at the end of this chapter is a new galaxy catalogue constructed from COSMOS scans of photographic plates using strict objective criteria. The final catalogue contains well over a million galaxies with $< 95\%$ galaxy completeness and $> 5\%$ stellar

contamination at all magnitudes. The photometric calibration of the catalogue is homogeneous with a rms plate–to–plate magnitude error of $\Delta m = 0.05$. The EDSGC is therefore, ideally suited for studying the distribution of galaxies and clusters on large scales, free from the systematic errors in previous catalogues.

Chapter 2

The Galaxy Angular Correlation Function

The galaxy angular correlation function, $w(\theta)$, has been one of the most popular statistics used in quantifying the large scale distribution of galaxies in the universe. The classic study by Groth & Peebles which used the Lick galaxy catalogue to determine $w(\theta)$ has become the bench–mark for such studies. In recent years however, this work has been undermined by claims of possible subjective errors within the Lick catalogue, leading to many authors' distrusting the form of the observed correlation function.

This chapter is concerned with the full analysis of $w(\theta)$ derived from the EDSGC. The prime motivation behind the construction of this catalogue was to estimate $w(\theta)$ free of the aforementioned problems. All the possible systematic errors that could affect the observed function were investigated and at the end of the chapter, the EDSGC $w(\theta)$ is compared to previous observations and is used to constrain theories of galaxy formation.

2.1 Definitions and Estimators

Large 2–D galaxy catalogues have been essential in our understanding of how galaxies are clustered, even though they lack the vital third dimension, that of distance. The sheer numbers of galaxies available, over large areas of the sky, makes them unique and powerful tools in probing the large–scale structure in the universe. The galaxy angular correlation function, $\mathrm{w}(\theta)$, has been the most popular statistic used in quantifying the clustering seen in these 2–D catalogues, because it is extremely simple to compute and can be directly related to theoretical predictions (Chapter 1).

The angular correlation function is defined in two ways;

$$\delta P = n[1 + \mathrm{w}(\theta)]\delta\Omega \tag{2.1}$$

and

$$\delta P_{12} = n^2[1 + \mathrm{w}(\theta_{12})]\delta\Omega_1\delta\Omega_2\,, \tag{2.2}$$

where n is the surface density of galaxies and $\delta\Omega$ is an infinitesimal search solid angle. The first is the probability of finding another galaxy, a certain angular separation θ, away from a randomly chosen galaxy, while the second is the joint probability of finding a galaxy in both search solid angles ($\delta\Omega_1$ and $\delta\Omega_2$) simultaneously. In both cases, for $\mathrm{w}(\theta) = 0$, the probability becomes the expected value for a Poissonian distribution of objects. Therefore, $\mathrm{w}(\theta)$ is a measure of the deviation from a random distribution as a function of angular scale.

To use these definitions of $\mathrm{w}(\theta)$, they must first be redefined in terms of measurable quantities. This is performed separately below for each definition. In the following derivations, n always represents the surface density of galaxies, while N_g is the total number galaxies and Ω is the total solid angle subtended by a survey.

1. Consider a ring centred on a randomly chosen galaxy, which subtends a solid angle of $\delta\Omega$ fully within Ω, and has an angular radius of θ to $\theta + \delta\theta$. The expected

number of galaxies, $\langle n \rangle$, within this ring can be written as

$$\langle n \rangle = n[1 + \mathrm{w}(\theta_1)]\delta\Omega\,, \tag{2.3}$$

where θ_1 is the angular separation from the chosen galaxy to $\theta + \frac{\delta\theta}{2}$. For any particular angle (θ_1), and distribution of galaxies, both $\langle n \rangle$ and $\mathrm{w}(\theta_1)$ are constant. In addition, $\langle n \rangle$ is simply the number of pairs with an angular separation of θ_1 for that chosen galaxy. Summing equation 2.3 over all the galaxies in the sample [†], the following expression is obtained

$$\sum_{i=1}^{N_g} \langle n \rangle = \sum_{i=1}^{N_g} n[1 + \mathrm{w}(\theta_1)]\delta\Omega\,, \tag{2.4}$$

or

$$2n_p = n[1 + \mathrm{w}(\theta_1)] \sum_{i=1}^{N_g} \delta\Omega\,, \tag{2.5}$$

where n_p is the number of distinct pairs with the separation θ_1. The factor of two is present due to the double counting of pairs in the sum above *i.e.* for N_g galaxies the total number of distinct pairs is $N_g(N_g - 1)/2 \simeq N_g^2/2$ for large N_g. Finally, if the sum of $\delta\Omega$ is replaced by $N_g\langle\delta\Omega\rangle$, where $\langle\delta\Omega\rangle$ is the average solid angle subtended by a ring, equation 2.5 becomes

$$[1 + \mathrm{w}(\theta_1)] = \frac{2n_p}{nN_g\langle\delta\Omega\rangle} = \frac{2n_p\Omega}{N_g^2\langle\delta\Omega\rangle}\,. \tag{2.6}$$

This is now expressed in measurable quantities. The number of pairs, n_p, can be computed for any separation angle θ_1, while the other terms are constants for a particular survey (Ω, N_g). The only unknown is $\langle\delta\Omega\rangle$.

Several methods of estimating $\langle\delta\Omega\rangle$ have been discussed in the astronomical literature. Hauser and Peebles (1973) estimated $\langle\delta\Omega\rangle$ by restricting their choice of galaxies and separation angles to galaxies whose $\delta\Omega$ always remained within the boundaries of their survey. This made the calculation of $\langle\delta\Omega\rangle$ straightforward, but

[†]It is actually a sum over $N_g - 1$ galaxies since the last galaxy will have had all its pairs already counted. For large N_g this can be ignored.

was wasteful in rejecting galaxies near the edges and restricted the range of angles over which $w(\theta)$ could be computed. Seldner (1977), however, had the advantage of a very large survey with simple boundaries, so $\langle \delta\Omega \rangle$ could be calculated from simple geometrical arguments. Peebles (1980) states that the easiest method of computing $\langle \delta\Omega \rangle$ is to use a Monte Carlo simulation which involves generating a random catalogue within the same boundary as the survey concerned, *i.e.*

$$\frac{1 + w(\theta_1)_{galaxies}}{1 + w(\theta_1)_{random}} = \frac{2n_{gg}\Omega}{N_g^2\langle \delta\Omega \rangle} \Big/ \frac{2n_{rr}\Omega}{N_r^2\langle \delta\Omega \rangle} = \frac{n_{gg}}{n_{rr}} \frac{N_r^2}{N_g^2} . \qquad (2.7)$$

As stated above, $w(\theta)$ for a random distribution is zero and therefore, equation 2.7 simplifies to

$$1 + w(\theta_1) = \frac{n_{gg}}{n_{rr}} \frac{N_r^2}{N_g^2} , \qquad (2.8)$$

where n_{gg} and n_{rr} are the respective number of pairs in the galaxy and the random catalogues, with a separation of θ_1. N_g and N_r are the respective number of objects in each catalogue. Another major advantage of this technique is that any systematic effect or bias within the original survey *e.g.* drill holes, can be built into the random catalogue, thus compensating for them.

By similar arguments, the denominator in equation 2.8 can be replaced by n_{gr}, the number of cross pairs between the galaxy and the random catalogue. $W_{gr}(\theta)$ is also zero, since the distribution of random points around each galaxy is still random. Equation 2.8 becomes

$$1 + w(\theta_1) = \frac{2n_{gg}}{n_{gr}} \frac{N_r}{N_g} , \qquad (2.9)$$

where the factor of 2 has returned because the total number of discrete galaxy pairs for n_{gg} is $N_g^2/2$, while for the cross pairs it is $N_g N_r$.

Both the above estimators can be used on binned or individual galaxy positions. On large scales ($>$ the binsize), the two methods give the same result. Of the two estimators, the n_{gr} estimator is the more accurate for reasons that will be explained in Section 2.3.4. It is recommended that this estimator be used in preference to the n_{rr} estimator.

2. Consider a survey of N_g galaxies subtending a solid angle of Ω, which is divided into X pixels each with a solid angle of Ω_c. By integrating equation 2.2, the following expression is obtained

$$\langle N_1 N_2 \rangle = \int_\Omega n^2 \delta\Omega_1 \delta\Omega_2 + \int_\Omega n^2 \mathrm{w}(\theta_{12}) \delta\Omega_1 \delta\Omega_2 \,, \qquad (2.10)$$

where $\langle N_1 N_2 \rangle$ is the total number of pairs with a separation of θ_{12} within the survey. This is converted to the number density of pairs per pixel by dividing through by Ω_c^2/Ω^2, and equation 2.10 becomes

$$\langle n_1 n_2 \rangle = \langle n \rangle^2 + \langle n \rangle^2 \int_\Omega \mathrm{w}(\theta_{12}) \frac{\delta\Omega_1 \delta\Omega_2}{\Omega^2} \,. \qquad (2.11)$$

In this equation, $\langle n \rangle$ is the expected number of galaxies per pixel and n_1, n_2 are the number of galaxies in individual pixels. By rearranging equation 2.11 and replacing the left–hand side of the equation by $\langle (n_1 - \langle n \rangle)(n_2 - \langle n \rangle) \rangle$, the final equation derived is

$$\frac{\langle (n_1 - \langle n \rangle)(n_2 - \langle n \rangle) \rangle}{\langle n \rangle^2} = \mathrm{w}(\theta_{12}) \int_\Omega \frac{\delta\Omega_1 \delta\Omega_2}{\Omega^2} \,, \qquad (2.12)$$

where $\mathrm{w}(\theta)$ has been removed from the integral as it is constant for a particular angular separation θ_{12}.

The integral on the right–hand side of equation 2.12 is the average solid angle subtended within the boundary of the survey for a separation of θ_{12}, and is the same as the quantity $\langle \delta\Omega \rangle$ described above. The left–hand side of equation 2.12 is the variance of counts in the pixels and because of this, equation 2.12 is usually known as the variance estimator of $\mathrm{w}(\theta)$.

It is worth noting here, that equation 2.12 assumes that the pixels, and their subtended search areas, are independent *i.e.* $\theta_{12} \neq 0$. If this is not the case, the following equation must be used

$$\langle (n_1 - \langle n \rangle)(n_2 - \langle n \rangle) \rangle = \int_\Omega \langle n \rangle \delta(\theta_1 - \theta_2) + \langle n \rangle^2 \mathrm{w}(\theta_{12}) \int_\Omega \frac{\delta\Omega_1 \delta\Omega_2}{\Omega^2} \,, \qquad (2.13)$$

where θ_1 and θ_2 are the subtended angles of the two pixels in question and $\delta(\theta_1 - \theta_2)$ is a delta function. Clearly, when $\theta_1 \neq \theta_2$, the integral of the delta function is

zero, returning equation 2.13 to equation 2.12. The reader is referred to Landau & Lifshitz (1959) for a concise derivation of this equation.

There are numerous references within the astronomical literature to the variance estimator of $w(\theta)$ *e.g.* Limber (1953) and Totsuji & Kihara (1969) for the original definition, Peebles (1973) for a thorough mathematical discussion and Sharp (1979), Peebles (1980) and Hewett (1982) for various practical considerations. The variance estimator of $w(\theta)$ has also been expressed in slightly different ways (Hewett 1982). Two other forms of the same estimator are

$$w(\theta) = \frac{\langle n_1 n_2 \rangle}{\langle n \rangle^2} - 1 , \tag{2.14}$$

and

$$w(\theta) = \frac{\langle n_1 n_2 \rangle}{\langle n_1 \rangle \langle n_2 \rangle} - 1 . \tag{2.15}$$

Clearly, equations 2.9 and 2.12 have quite distinct advantages and weaknesses. For example, the Monte Carlo estimator (equation 2.9) is effective in accounting for edge effects, while care must be taken when using the variance estimator (section 2.3.2). Both estimators were used to compute $w(\theta)$ for the EDSGC and a comparison of the two is given in section 2.3.4.

2.2 The Mechanics of Estimating $w(\theta)$

Table 2.1 shows the largest contiguous area within the boundaries of the EDSGC used in calculating $w(\theta)$. Table 2.2 lists all the survey fields within this area. The positions of all the galaxies within this area and to a specified magnitude limit were extracted from the EDSGC and converted into radians. These were then binned on a true sky projection with a pixel size of 20 arcminutes, which reduced the computation time for a single $w(\theta)$ considerably, as the number of pair calculations dropped from $\sim 10^{12}$ for individual galaxy positions (magnitude limit $b_j = 20.3$) to $\sim 10^8$ for binned positions (57×204 data array). During the binning, each pixel was assigned a plate identification number if all the galaxies within that pixel were from the same plate, otherwise, the pixel was flagged. Figure 2.1 shows an example of the binned data.

The next stage of the calculation depended upon the estimator being used.

	Hours	Degrees	Radians	Radians
	RA	Dec.	RA	Dec.
min	3	-42	-0.5148	0.4014
max	22	-23	0.7755	0.7212
binsize	20 arcminutes		5.817×10^{-3}	
area	1182 degrees^2		0.338 steradians	

Table 2.1: The area used to compute w(θ), which represents the largest rectangular area within the EDSGC. **Note:** All the galaxy positions were converted to radians and in addition, if the RA of a galaxy was greater than 12 hours, then 24 hours was subtracted from its RA coordinate. This resulted in a continuous RA range for the galaxies between ~ -0.7 and ~ 0.7 radians. All the declination coordinates were converted to positive declinations. These conversions were carried out simply for convenience.

- The Monte Carlo estimator

  As described at the start of the chapter, this estimator compares the observed galaxy distribution to that of a random distribution. Therefore, several random catalogues were generated over exactly the same area as shown in Table 2.1. All the drill holes around bright stars, as described in Chapter 1, were incorporated into the random catalogues and in total 458 such holes were used. Each random catalogue contained over a million galaxy positions and was constructed using a non–repeatable NAG routine (GO5DAF). These catalogues were binned in exactly the same way as the galaxy data and as a check, they were cross–correlated against each other. As expected, w(θ) was zero on all scales. The correlation function was calculated using equation 2.9, which involved calculating the number of galaxy–galaxy pairs (n_{gg}) and the number of galaxy–random pairs (n_{gr}) as a function of separation angle. For binned data, this was achieved by simply multiplying the number of galaxies in pixel i (n_i), by the number in pixel j an angle θ away, to give $n_i n_j$ pairs. Finally, the two functions were divided and normalised by N_g/N_r to give w(θ).

- The Variance estimator

Field	Plate	Centre		Field	Plate	Centre	
		RA	DEC			RA	DEC
293	J3578	0^h0^m	$-40°$	411	J11341	0^h46^m	$-30°$
294	J3551	0^h26^m	$-40°$	412	J3516	1^h9^m	$-30°$
295	J2712	0^h52^m	$-40°$	413	J3774	1^h32^m	$-30°$
296	J3524	1^h18^m	$-40°$	414	J3579	1^h55^m	$-30°$
297	J3593	1^h44^m	$-40°$	415	J4607	2^h18^m	$-30°$
298	J3560	2^h10^m	$-40°$	416	J4608	2^h41^m	$-30°$
299	J3588	2^h36^m	$-40°$	417	J3818	3^h4^m	$-30°$
300	J3536	3^h2^m	$-40°$	466	J5113	21^h51^m	$-30°$
467	J3514	22^h14^m	$-30°$	344	J6144	22^h6^m	$-40°$
468	J6436	22^h37^m	$-30°$	345	J3538	22^h32^m	$-40°$
469	J3508	23^h0^m	$-30°$	346	J8022	22^h58^m	$-40°$
470	J3508	23^h23^m	$-30°$	347	J2413	23^h24^m	$-40°$
471	J6138	23^h46^m	$-30°$	348	J3592	23^h50^m	$-40°$
472	J3428	0^h0^m	$-25°$	349	J6145	0^h0^m	$-35°$
473	J3566	0^h22^m	$-25°$	350	J4601	0^h24^m	$-35°$
474	J6277	0^h44^m	$-25°$	351	J8046	0^h48^m	$-35°$
475	J8031	1^h6^m	$-25°$	352	J6124	1^h12^m	$-35°$
476	J8823	1^h28^m	$-25°$	353	J3596	1^h36^m	$-35°$
477	J3785	1^h50^m	$-25°$	354	J4630	2^h0^m	$-35°$
478	J2708	2^h12^m	$-25°$	355	J5304	2^h24^m	$-35°$
479	J5522	2^h34^m	$-25°$	356	J5462	2^h48^m	$-35°$
480	J3649	2^h56^m	$-25°$	404	J5104	22^h0^m	$-35°$
405	J6231	22^h24^m	$-35°$	532	J3420	22^h0^m	$-25°$
406	J9529	22^h48^m	$-35°$	533	J6091	22^h22^m	$-25°$
407	J6468	23^h12^m	$-35°$	534	J6489	22^h44^m	$-25°$
408	J10342	23^h36^m	$-35°$	535	J6114	23^h6^m	$-25°$
409	J2693	0^h0^m	$-30°$	536	J3421	23^h28^m	$-25°$
410	J2696	0^h23^m	$-30°$	537	J8030	23^h50^m	$-25°$

Table 2.2: The fields in the area detailed in Table 2.1.

This estimator uses the variance of counts between cells to compute the correlation function and therefore, no random catalogues were required. However, the drill holes in the galaxy data must still be accounted for and this was achieved by removing pixels that fell, either fully or partly, within a hole. In total, 1135 out of 10641 pixels were lost. The correlation function was calculated using equation 2.12, which involved calculating the variance of each pair of pixels, compared to the mean number per pixel, as a function of angular separation. The edge correction, $\int_\Omega \frac{\delta\Omega_1 \delta\Omega_2}{\Omega^2}$, is discussed in section 2.3.3.

The number of correlation bins used for both estimators was always kept at 60 (binsize 5.8×10^{-3} radians) with a maximum separation of $\theta = 0.3461$ radians. This corresponded to a maximum separation of 20° and a binsize of 20 arcminutes. This allowed for easy comparison between the individual correlation functions as no rebinning was necessary. The maximum separation was set at 20° as beyond this angle the number of pairs started to decrease because the EDSGC is only 20° wide in declination.

The *raw* correlation functions calculated using the Monte Carlo estimator to the magnitude limits of $b_j = 17.5, 18.5, 19.5$ and 20.3 are shown in Figure 2.2. The number of galaxies binned were 15617, 61978, 231310 and 686348 respectively. Figure 2.3 shows $w(\theta)$ calculated using the variance estimator and an all-pairs estimator[‡] compared to an appropriate Monte Carlo estimation. The all–pairs result is in perfect agreement with the binned Monte Carlo estimation, indicating that binning the data had no systematic effect on the final result. However, the variance estimation differs significantly. This observed difference is discussed fully below.

[‡] $w(\theta)$ was calculated using equation 2.9 on unbinned data *i.e.* using all the individual pairs. In comparison, this computation took 4 days of computer processing time instead of 2 hours for the binned data.

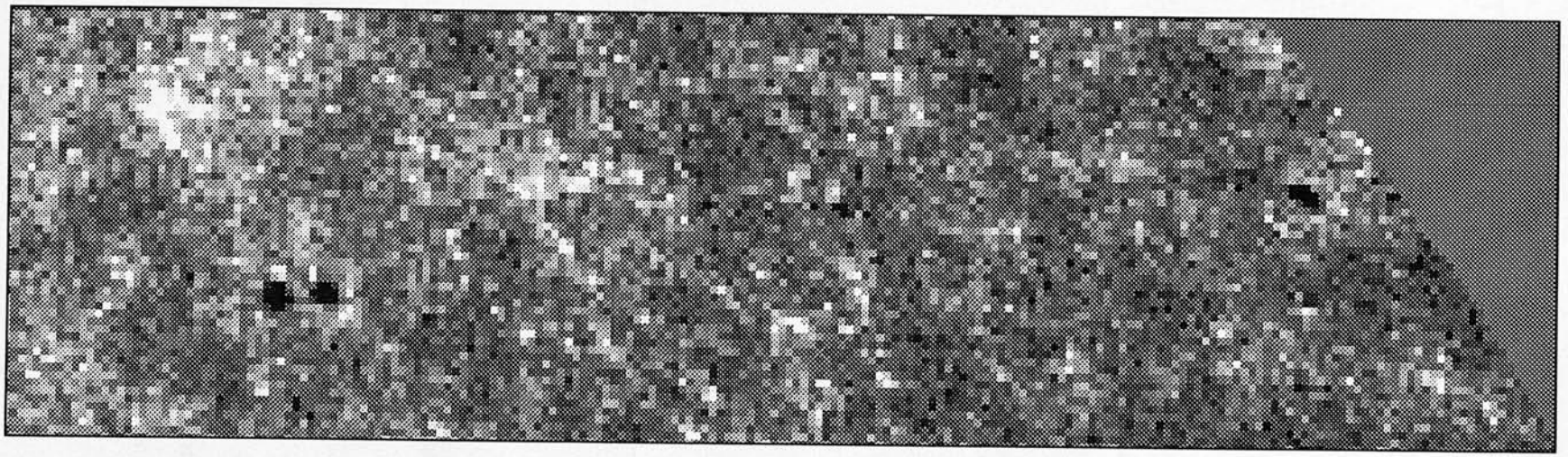

Figure 2.1: All galaxies to the magnitude limit of $b_j = 19.5$ binned into a 57×205 data array with 20 arcminute pixels. This is a true sky projection, so the number of pixels per declination row decreases as a function of declination. Therefore, only 10641 of the 11628 pixels were used. This figure clearly illustrates the host of large–scale structure seen within the EDSGC. Also visible are 3 large drill holes around bright stars in the field (*e.g.* 2 holes very close together in the bottom left hand corner of the array).

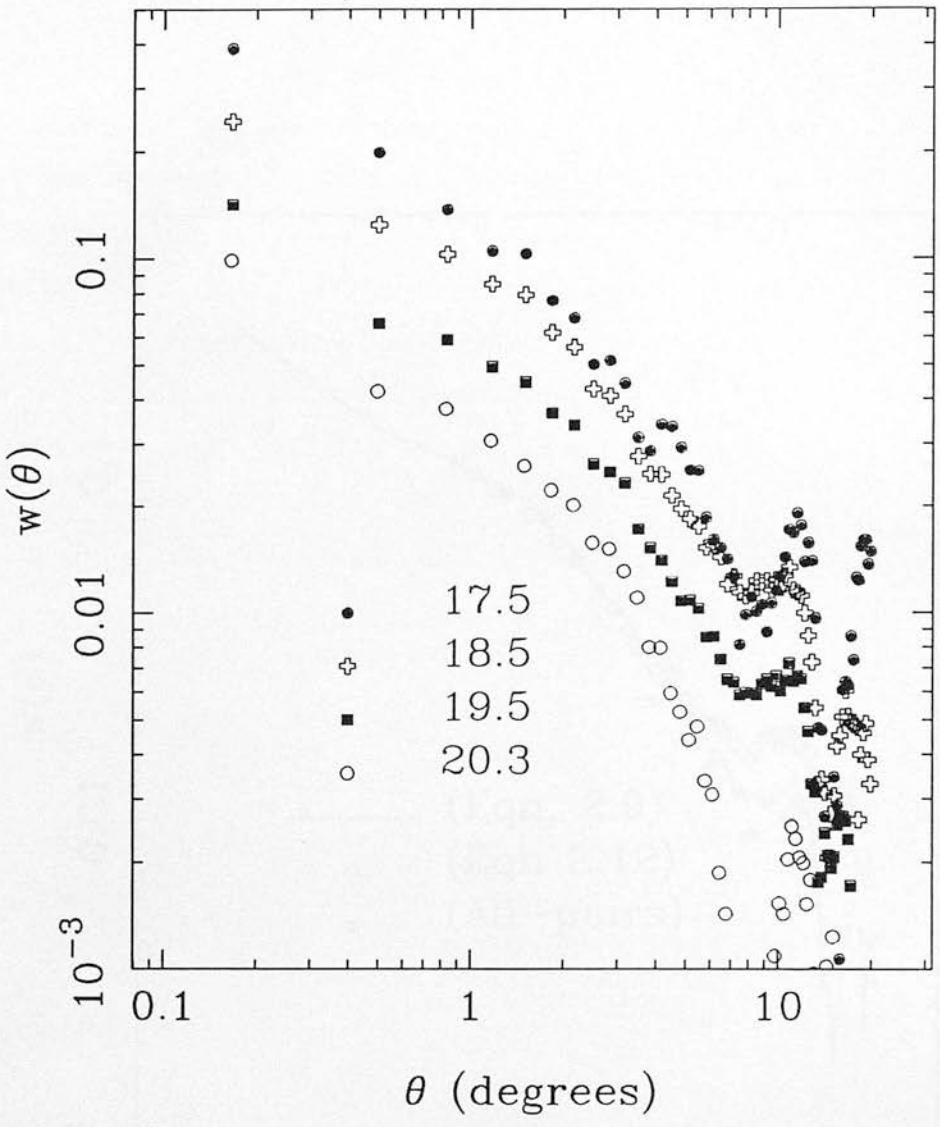

Figure 2.2: The raw EDSGC correlation functions calculated using equation 2.9.

2.3 Bias and Corrections

The correlation function is subject to two main forms of bias; the integral constraint and edge effects. These biases take slightly different forms for the different estimators. In this section, these biases are outlined along with the methods used to correct for them.

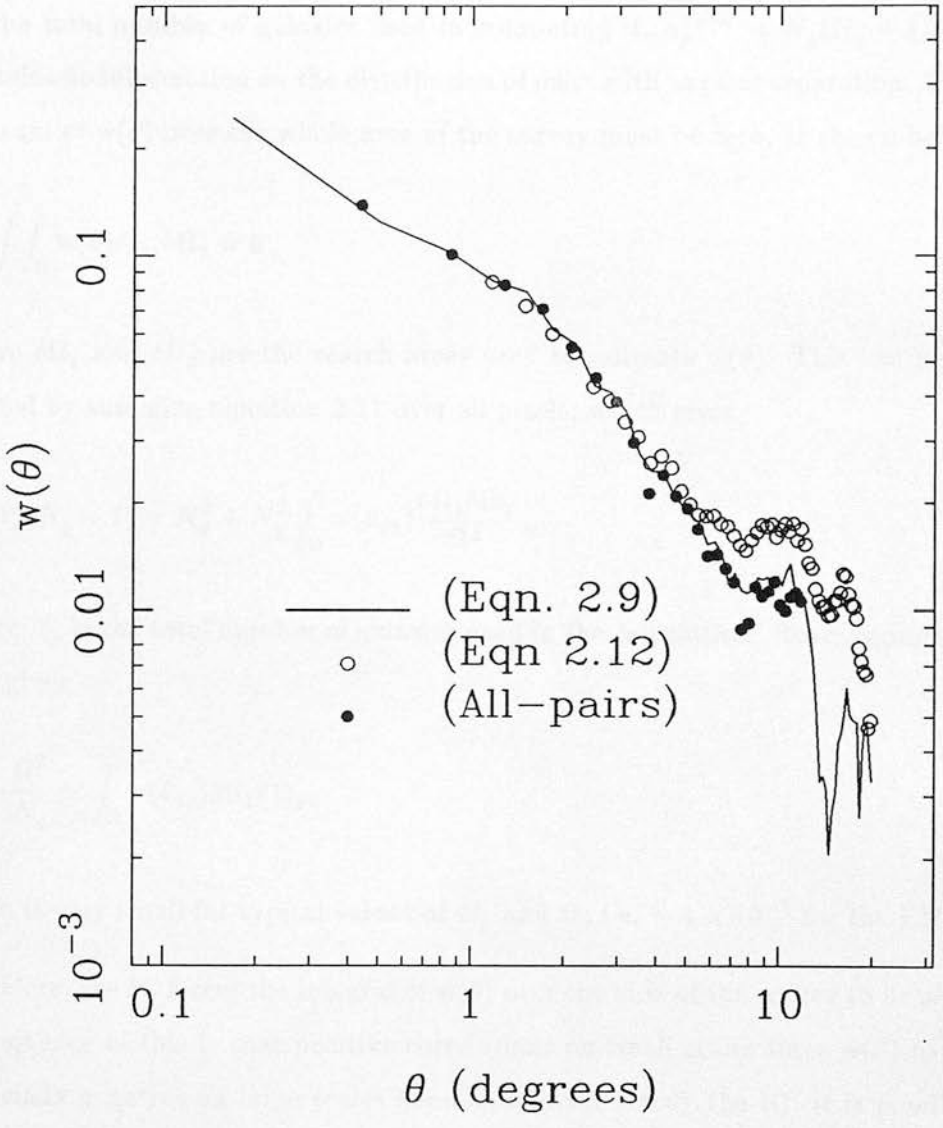

Figure 2.3: A comparison of the Monte Carlo estimation of w(θ) at $b_j = 18.5$ with that of the variance estimation and an all–pairs estimation (using equation 2.9) to the same depth.

2.3.1 The Integral Constraint

All the estimators of the correlation function are subject to an integral constraint (IC). This is due to the mean number density used in estimating $w(\theta)$ being a biased measure of the true number density of the universe. Moreover, the total $w(\theta)$ is directly related to the total number of galaxies used in computing it, $n_p^{Total} = N_g(N_g - 1)/2$, which contains no information on the distribution of pairs with angular separation. Therefore, the sum of $w(\theta)$ over the whole area of the survey must be zero, as shown below

$$\int\int_{\Omega} w(\theta)\delta\Omega_1\delta\Omega_2 = 0\,, \tag{2.16}$$

where $\delta\Omega_1$ and $\delta\Omega_2$ are the search areas used to estimate $w(\theta)$. This can be demonstrated by summing equation 2.11 over all pixels, which gives

$$N_g(N_g - 1) \simeq N_g^2 + N_g^2 \int_{\Omega} w(\theta_{12})\frac{\delta\Omega_1\delta\Omega_2}{\Omega^2}\,, \tag{2.17}$$

where N_g is the total number of galaxies used in the calculation. Rearranging equation 2.17 gives

$$-\frac{\Omega^2}{N_g} \simeq \int_{\Omega} w(\theta_{12})\delta\Omega_1\delta\Omega_2\,, \tag{2.18}$$

which is very small for typical values of N_g and Ω, *i.e.* $\sim 1 \times 10^{-7}$ for the EDSGC.

Therefore, the IC forces the integral of $w(\theta)$ over the area of the survey to be zero. The consequence of this is that positive correlations on small scales force $w(\theta)$ to become artificially negative on large scales because it must satisfy the IC. It is possible that the break reported in previous estimations of $w(\theta)$ (Table 1.1) could simply be due to the IC. In fact, the observed trend of larger break scales with larger survey areas is the trend one would expect if the IC had not been fully corrected for.

The obvious answer would be to integrate $w(\theta)$ over the survey, thus directly calculating the IC. However, this is a difficult task, as the exact nature of the true $w(\theta)$ is not known and it is the function we wish to calculate. Therefore, an *a priori* form of $w(\theta)$ must

be assumed and used to estimate the size of the IC. The most commonly used form of $w(\theta)$ is

$$w(\theta) = A\theta^{-\delta} \qquad \theta \leq \theta_c$$

$$w(\theta) = 0 \qquad \theta > \theta_c ,$$

where $w(\theta)$ is zero beyond some break angle θ_c and A, δ are constants. Integrating the true correlation function over the area of the survey *i.e.*

$$\int_\Omega w_{true}(\theta) d\Omega = 0 , \tag{2.19}$$

and putting in the model for $w(\theta)$, the equation becomes

$$\int_0^{\theta_r} (A\theta^{-\delta} + B) d\Omega = 0 , \tag{2.20}$$

where B is the value of the IC. For small values of θ, $d\Omega = 2\pi\theta d\theta$, equation 2.20 becomes

$$2\pi A \int_0^{\theta_c} \theta^{1-\delta} d\theta + 2\pi \int_0^{\theta_r} B\theta d\theta = 0 , \tag{2.21}$$

$$2\pi \left[\frac{A}{2-\delta} \theta_c^{2-\delta} \right] = 2\pi \left[\frac{B\theta_r^2}{2} \right] , \tag{2.22}$$

$$B = \frac{2A}{2-\delta} \frac{\theta_c^{2-\delta}}{\theta_r^2} , \tag{2.23}$$

where θ_r is the effective radius of the survey, *i.e.* $\pi\theta_r^2$ = area of the survey. The above equation can be used for any observed $w(\theta)$. However, as already stated, the observed form of $w(\theta)$ is subject to an IC itself and any break seen may be a consequence of the IC. Therefore, it was unclear what values of A, δ and particular θ_c should be used in the computation of the IC.

To investigate the range of values allowed for A, δ and θ_c, and to examine the effect of different models on the calculation, the uncorrected observed correlation functions were fitted to three models of $\mathrm{w}(\theta)$ using χ^2 fitting. The first of these models was the one described above, while the other two are detailed here.

1. A two power–law model, where the slope of the power law changed at θ_c. This model was represented by

$$\mathrm{w}(\theta) = A_1\theta^{-\delta_1} + B \quad (\theta \leq \theta_c)$$

$$= A_2\theta^{-\delta_2} + B \quad (\theta > \theta_c)\,.$$

   Using this model, the IC becomes

$$B = \frac{2}{\theta_r^2}\left(\frac{A_1\theta_c^{2-\delta_1}}{2-\delta_1} + \frac{A_2\,(\theta_r^{2-\delta_2} - \theta_c^{2-\delta_2})}{2-\delta_2}\right).$$

2. An exponential break model represented by

$$\mathrm{w}(\theta) = A\theta^{-\delta}e^{-\theta/\theta_c} + B\,.$$

   The IC in this case becomes

$$B = \frac{2A}{\theta_r^2}\int_0^{\theta_r}\theta^{1-\delta}e^{-\theta/\theta_c}d\theta = \frac{2A}{\theta_r^2\theta_c^{2-\delta}}\,\gamma(2-\delta,\theta_r/\theta_c)\,,$$

   where $\gamma(2-\delta,\theta_r/\theta_c)$ is an incomplete gamma function.

All the models were fitted to $\mathrm{w}(\theta)$ at the magnitude limits of $b_j = 17.5, 18.5$ and 19.5. Figure 2.4 shows the fits for exponential model, as an example, while Table 2.3 gives the statistics for all the fits. The error bars plotted in Figure 2.4 were calculated internally and are explained in section 2.7 To check the fits, the APM $\mathrm{w}(\theta)$ (Chapter 1) was used as well, since it was computed over a larger area than the EDSGC and should therefore, have a lower IC. In addition, the error bars on the APM $\mathrm{w}(\theta)$ were much smaller. The APM fits are also detailed in Table 2.3 and an example is shown in Figure 2.4.

Original Model				
	17.5	18.5	19.5	APM
A	0.1345	0.0752	0.0425	0.0213
δ	0.6241	0.7241	0.6578	0.4765
θ_c	12.4766	24.6543	34.6456	14.3467
$\tilde{\chi}^2$	0.4545	1.5421	1.6310	2.6646
Two Power Law Model				
A_1	0.1867	0.1663	0.0653	0.0219
δ_1	0.4986	0.3573	0.5012	0.7837
A_2	12.8243	8.2334	10.2723	0.8338
δ_2	2.0688	18.0607	2.2613	1.1195
θ_c	20.3143	18.9312	16.9823	20.1181
$\tilde{\chi}^2$	0.3709	1.7492	0.6532	7.3395
Exponential Model				
A	0.1661	0.1759	0.0844	0.0214
δ	0.5323	0.3297	0.3939	0.7903
θ_c	18.1100	93.9472	74.2171	18.0454
$\tilde{\chi}^2$	0.3966	2.7321	2.4310	7.2646

Table 2.3: The above table shows the statistics of the fits for all the models of $w(\theta)$. θ_c is in degrees and $\tilde{\chi}^2$ is the reduced minimum χ^2 for the fits.

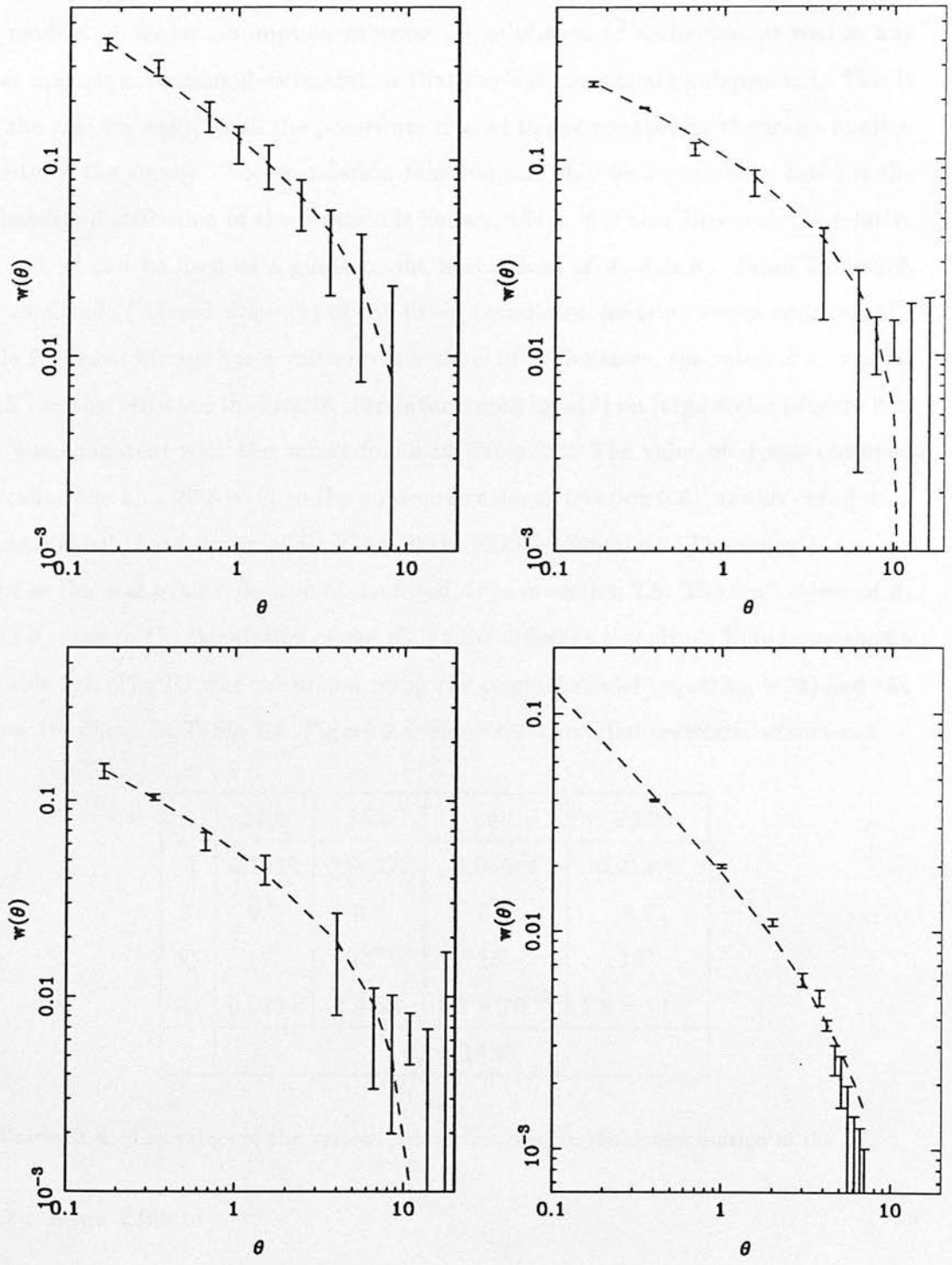

Figure 2.4: The minimum χ^2 fits for w(θ) using the exponential model of w(θ) . The data used was b_j = 17.5, 18.5, APM, 19.5 (clockwise from the the top–left plot). The correlation functions have been rebinned in log space so as to uniformly sample w(θ).

Unfortunately, the $\tilde{\chi^2}$ shown in Table 2.3 have little absolute meaning to the fits of the models. A major assumption in using the minimum χ^2 technique, as well as any other maximum likelihood estimator, is that the data points are independent. This is not the case for $w(\theta)$, as all the points are related to one another by the mean number density of the survey. The correlation function can only be successfully fitted if the probability distribution of the function is known, which it is not. However, the relative fits and $\tilde{\chi^2}$ can be used as a guide to the best values of A, δ & θ_c. From Table 2.3, the amplitude (A) and slope (δ) of the fitted correlation function varies considerably, while θ_c almost always has a value greater than 10°. Therefore, the value of θ_c was set at 15°, as this reflected the lack of correlations seen in $w(\theta)$ on large scales (Figure 2.2) and was consistent with the values found in Table 2.3. The value of A was obtained by scaling the $b_j = 20.3\ w(\theta)$ to the appropriate depth (section 2.6), as this correlation function should have the smallest IC of all the EDSGC functions. The slope, δ, was set at 0.7 as this was a fair reflection of the fitted slope in section 2.8. The final values of A, δ and θ_c used in the calculation of the IC, at the different magnitude limits, are shown in Table 2.4. The IC was calculated using the original model (equation 2.23) and the values are shown in Table 2.4. Figure 2.5 shows the corrected correlation functions.

	17.5	18.5	19.5	20.3
A	0.1312	0.06372	0.03044	0.01396
δ	0.7	0.7	0.7	0.7
θ_c	15°	15°	15°	15°
IC	0.0234	0.0120	5.7×10^{-3}	1.8×10^{-3}
	$\theta_r = 16.6°$			

Table 2.4: The values of the various parameters used in the determination of the IC.

2.3.2 Edge Effects

Apart from an all–sky survey, any catalogue of galaxies used to calculate the angular correlation function is subject to an edge correction. The exact form of this effect is dependent on the estimator used to determine $w(\theta)$. There are two distinct forms of edge effect; the amount of solid angle subtended by a pair of galaxies within the bounds

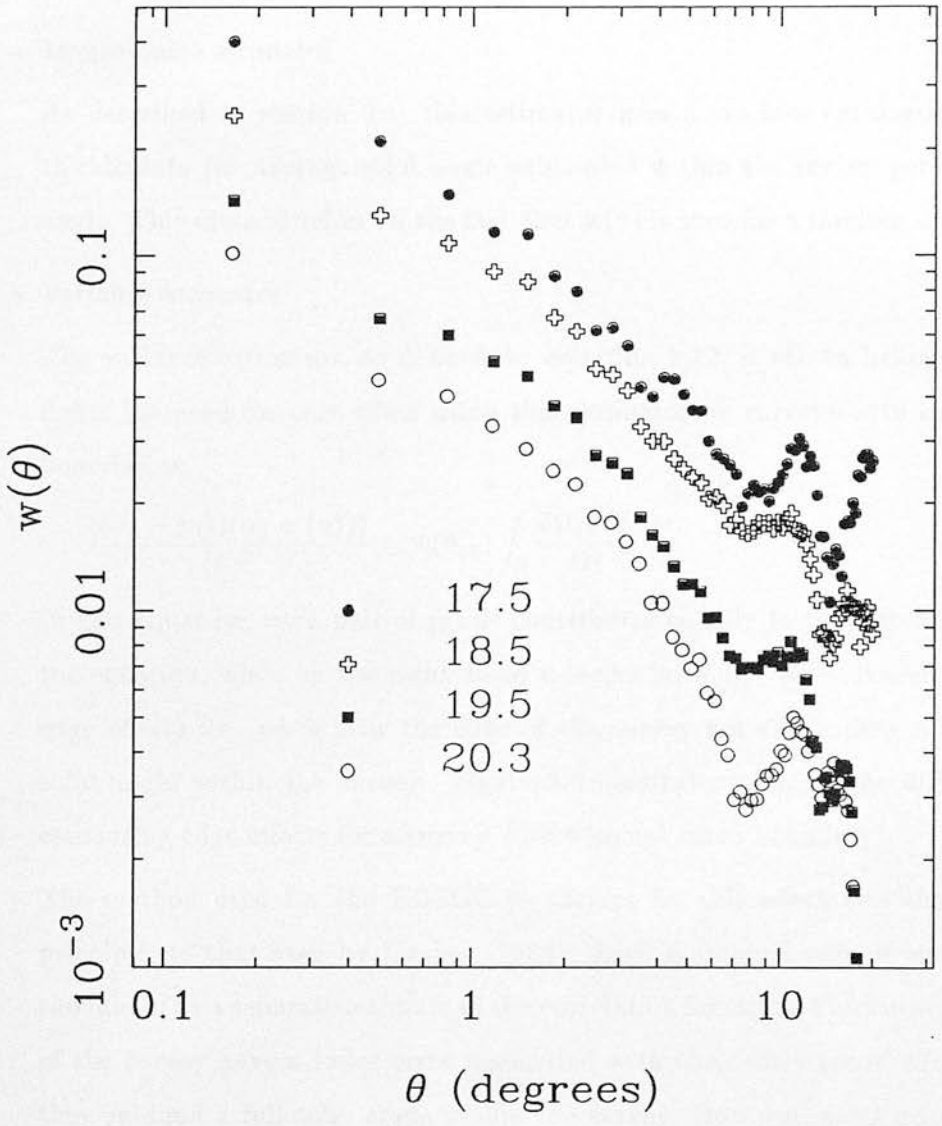

Figure 2.5: The EDSGC correlation functions from Figure 2.2 with integral constraints added.

of the catalogue (see section 2.1) and actual galaxy clustering on or near the boundary of the survey. The two are discussed separately below with respect to the different estimators.

2.3.3 Estimation of $\langle \delta\Omega \rangle$

- Monte Carlo estimator

  As described in section 2.1, this estimator uses a random catalogue of points to calculate the average solid angle subtended within the survey per separation angle. This method relies on the fact that $w(\theta)$ is zero for a random distribution.

- Variance estimator

  The variance estimator, as defined by equation 2.12, is shown below and highlights the need for care when using this estimator on surveys with complicated boundaries;

$$\frac{\langle (n_1 - \langle n \rangle)(n_2 - \langle n \rangle) \rangle}{\langle n \rangle^2} = w(\theta_{12}) \int_\Omega \frac{\delta\Omega_1 \delta\Omega_2}{\Omega^2} . \qquad (2.24)$$

  In this equation, each pair of pixels contributes equally to the left–hand side of the equation, while on the right–hand side the term $\int_\Omega \frac{\delta\Omega_1 \delta\Omega_2}{\Omega_2}$, corrects $w(\theta)$ for edge effects *i.e.* pairs near the edge of the survey not subtending a full search solid angle within the survey. Figure 2.6 illustrates some of the difficulties in estimating edge effects for a survey with a complicated boundary.

  The method used for the EDSGC to correct for this effect was the same, in principle, to that used by Limber (1953). Each individual pair of pixels can be thought of as a separate estimate of the correlation function. Pairs near the centre of the survey have a lower error associated with their estimate of $w(\theta)$ because they subtend a full solid angle within the survey. However, pairs near the edge have a higher error because part of their solid angle falls outside the survey. These pairs of pixels are *not* biased low, but simply have a high error associated with their individual estimate of $w(\theta)$.

  Therefore, instead of averaging over all pairs with equal weight, each pair was weighted relative to its distance from the boundary. Equation 2.24 therefore, becomes a weighted mean,

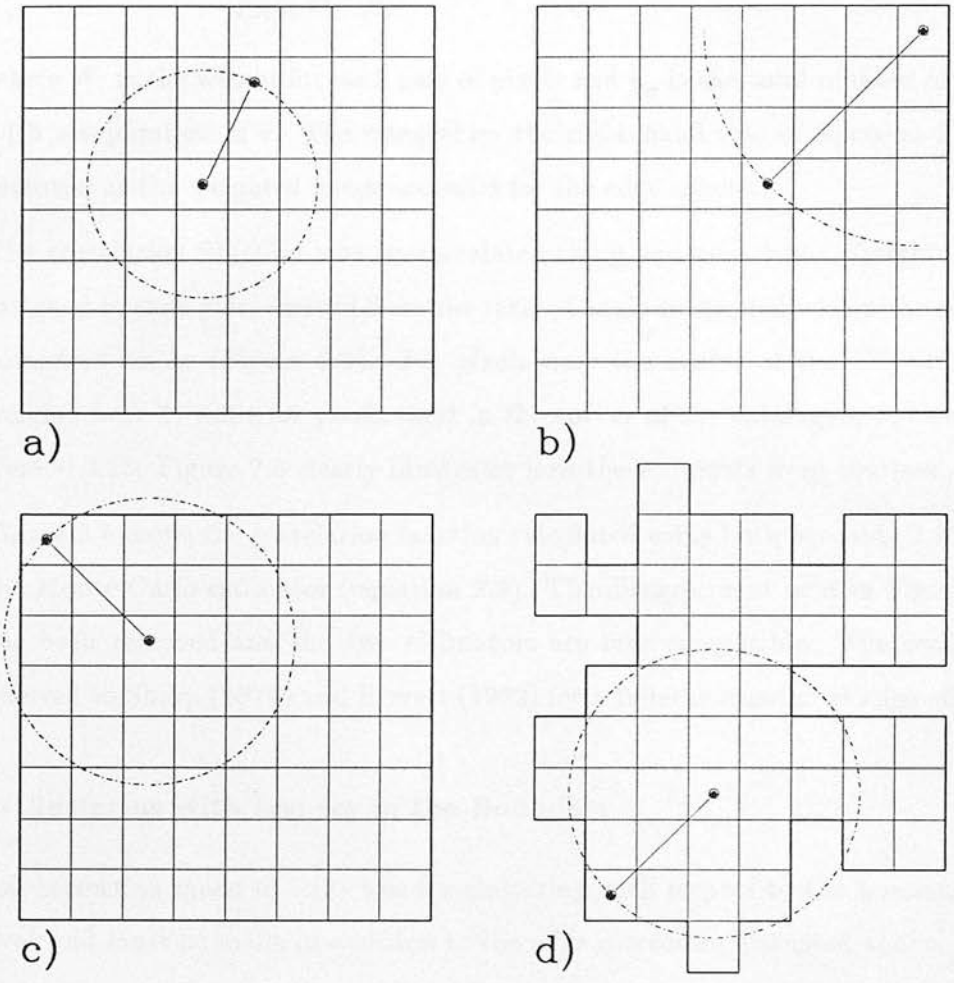

Figure 2.6: These diagrams illustrate the relationship between the boundary shape and the amount of angle subtended by a pair of pixels within the survey region. A weight was assigned to each pair of pixels equal to the amount of angle subtended within the region divided by 2π. (a) For central pixels and small separations the weight was 1. (b) & (c) Near the edges of the survey the value of the weight became harder to estimate since the angle within the survey depended uniquely on the geometry of the boundary and the distance of the object pixel from the boundary. The angle subtended within the survey was approximately calculated by summing all the small angles subtended by the individual pixels cut by the arc. For (b) the weight was 0.25 while for (c) the weight was 0.75. (d) The calculation of a weight clearly becomes complicated if the survey boundary is irregular.

$$w(\theta) = \frac{\sum_{i=1}^{n_p} W_i^2 (n_1 - \langle n \rangle)(n_2 - \langle n \rangle)}{\sum_{i=1}^{n_p} W_i^2 \langle n \rangle^2}, \qquad (2.25)$$

where W_i is the weight for each pair of pixels and n_p is the total number of pairs with a separation of θ. The integral on the right-hand side of equation 2.24 is removed as the weighted mean accounts for the edge effects.

The correlation function was re-calculated using equation 2.25. Weights were assigned to each pair, derived from the ratio of angle subtended within the survey compared to 2π (Figure 2.6). For pixels near the centre of the EDSGC, the weights were 1, while for pixels right in the corner of the catalogue, the weights were ~ 0.25. Figure 2.6 clearly illustrates how these weights were obtained.

Figure 2.7 shows the correlation function calculated using both equation 2.25 and the Monte Carlo estimator (equation 2.9). The disagreement seen in Figure 2.3 has been removed and the two estimators are now compatible. The reader is referred to Sharp (1979) and Hewett (1982) for a fuller discussion of edge effects.

2.3.4 Clustering with respect to the Boundary

The final correction made to $w(\theta)$ was for clustering with respect to the boundary of the survey and must be made in addition to the edge correction discussed above. This bias originates from the fact that $w(\theta)$ is defined to be symmetrical *i.e.* $w_{12} = w_{21}$. The final $w(\theta)$ should be independent of the starting point of the estimation. However, this is often not the case. For example, a cross-correlation between a random and a clustered dataset often results in $w_{cr} \neq w_{rc}$, because the clustered dataset interacts with the boundary, while the random dataset has no relation to the boundary.

The effect was corrected for as follows;

- Monte Carlo estimator

  As mentioned in section 2.1, the n_{gr} estimator was used in preference to the n_{rr} estimator because it directly accounted for this effect, as the correlation function is normalised using w_{gr}. The difference between the two forms of the Monte Carlo estimator is shown in Figure 2.8 and this difference is solely due to clustering on or

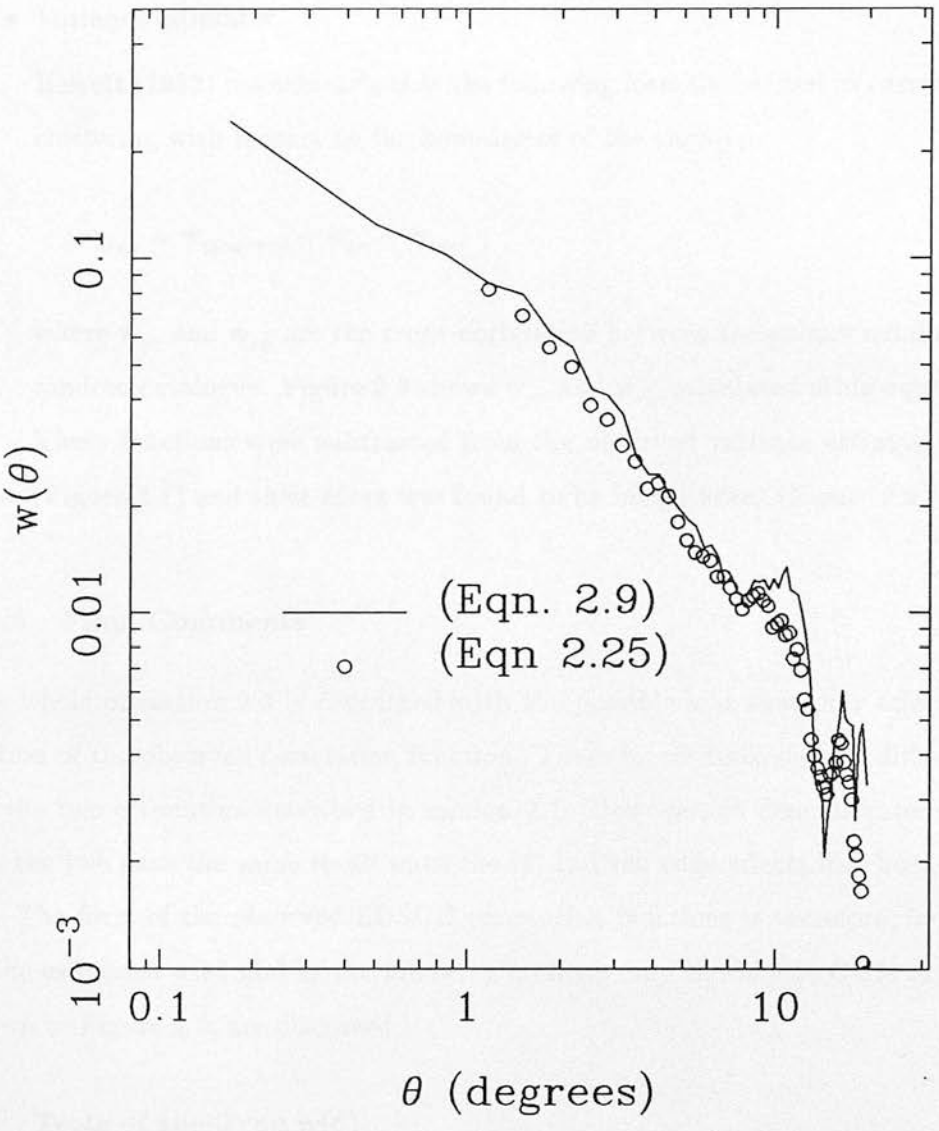

Figure 2.7: A comparison between the Monte Carlo estimator of w(θ) (equation 2.9) and the variance estimator with weights (equation 2.25). Both estimates were calculated to the magnitude limit of $b_j = 18.5$.

near the boundary of the survey. If the n_{rr} estimator is used, then w_{gr} should be subtracted from the estimate of $w(\theta)$. The reader is referred to Davis & Peebles (1983) for a fuller discussion of this.

- Variance estimator

  Hewett (1982) recommends that the following formula be used to correct $w(\theta)$ for clustering with respect to the boundaries of the survey,

$$w_{true} = w_{observed} - w_{gr} - w_{rg}\,, \tag{2.26}$$

  where w_{gr} and w_{rg} are the cross–correlation between the galaxy catalogue and a random catalogue. Figure 2.9 shows w_{gr} and w_{rg} calculated using equation 2.25. These functions were subtracted from the observed variance estimation of $w(\theta)$ (Figure 2.7) and their effect was found to be insignificant (Figure 2.9).

2.3.5 Final Comments

The whole of section 2.3 is concerned with the possible bias that may affect the estimation of the observed correlation function. These biases took slightly different forms for the two estimators described in section 2.1. However, as demonstrated in Figure 2.7, the two gave the same result once the IC and the edge effects had been corrected for. The form of the observed EDSGC correlation functions is therefore, independent of the estimator used and in the following sections only the Monte Carlo estimations, shown in Figure 2.5, are discussed.

2.4 Tests of the True $w(\theta)$

2.4.1 Plate–to–Plate Simulations

The only way at present to produce a large–area galaxy catalogue to cosmologically interesting depths is to mosaic together either photographic plates or large–format CCD frames. Geller *et al.* (1984) highlight the need for care when constructing such a catalogue from individual plates and demonstrate that the break seen in the Lick $w(\theta)$

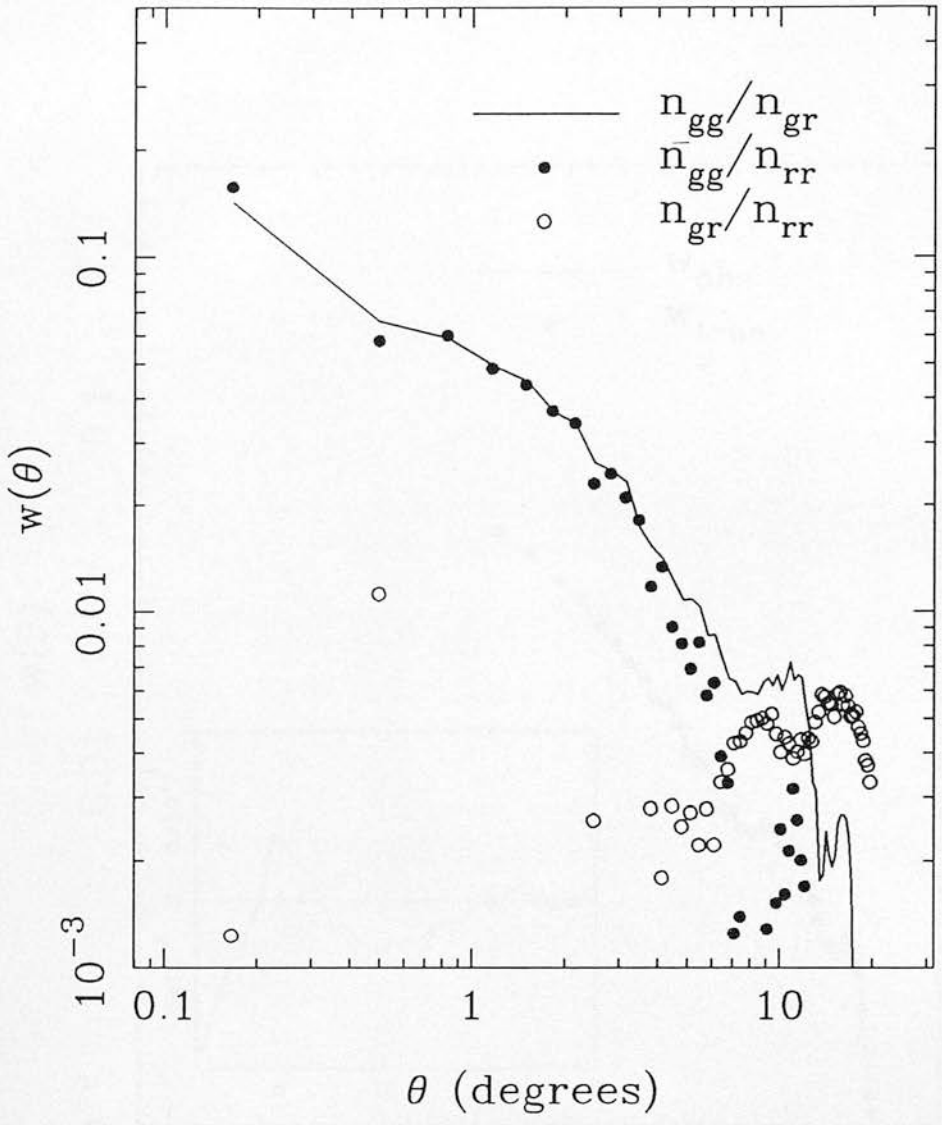

Figure 2.8: A comparison between the two Monte Carlo estimators of w(θ), equation 2.8 & 2.9. The difference between the two is the effect of clustering on or near the edges of the EDSGC. This is illustrated by the symbols o, which represent an estimate of the edge effects and was calculated using the formula

$$1 + \mathrm{w}_{gr}(\theta) = \frac{n_{gr}}{n_{rr}} \frac{2N_g}{N_r},$$

which is derived using similar arguments as those given in section 2.1. As stated in the text, n_{gg}/n_{gr} compensates for edge effects during the computation of w(θ), as it normalises the galaxy–galaxy pairs by the corresponding number of galaxy–random pairs. The n_{gg}/n_{rr} estimator must be corrected for edge effects by subtracting w_{gr}, the function shown above (Note: In fact, $-\mathrm{w}_{gr}$ is plotted above since most of the function was negative). All the correlation functions were calculated at a depth of $b_j = 19.5$.

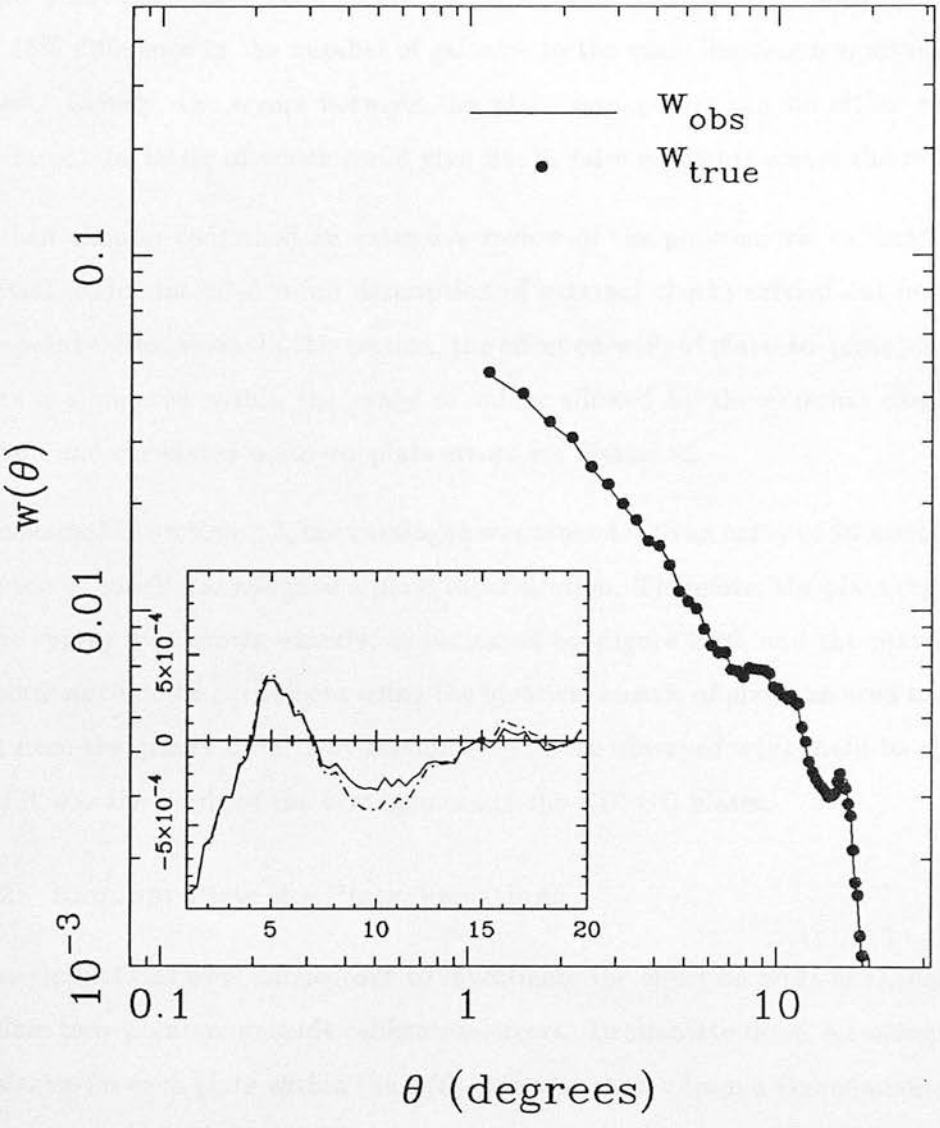

Figure 2.9: The edge corrections for the variance estimator. Inset is a linear plot of w_{gr} (solid line) and w_{rg} (dot–dashed line). These were subtracted from the observed $w(\theta)$ using equation 2.26 as described by Hewett (1982).

(GP77) could be due to plate matching errors. The main concern is that the zero–point magnitude calibrations between plates are not matched correctly, thus leading to systematic shifts between the magnitudes of galaxies on different plates. For example, a zero–point magnitude error of $\Delta m = 0.1$ between two adjacent plates would result in a 15% difference in the number of galaxies to the same limiting magnitude on both plates[§]. Clearly, the errors between the plate zero–points can be either random or correlated, the latter of which could give rise to false gradients across the catalogue.

The last chapter contained an extensive review of the photometric calibration of the EDSGC, which included a full description of external checks carried out on the plate zero–point calibrations. In this section, the effect on $w(\theta)$ of plate–to–plate photometric errors is simulated within the range of values allowed by the external checks. Both random and correlated plate–to–plate errors are discussed.

As explained in section 2.2, the catalogue was binned into an array of 20 arcminute pixels, each of which was assigned a plate identification. Therefore, the plate organisation of the survey was known exactly, as indicated by Figure 2.10, and the plate–to–plate simulations could be carried out using the identical mosaic of plates as used to calculate $w(\theta)$ from the galaxy data. Any feature seen in the observed $w(\theta)$ could be checked to see if it was the result of the arrangement of the EDSGC plates.

2.4.2 Random Plate–to–Plate Variations

These simulations were carried out to investigate the effect on $w(\theta)$ of random plate–to–plate zero–point magnitude calibration errors. To simulate these, a random number of galaxies for each plate within the $w(\theta)$ area was chosen from a Gaussian distribution with a mean of 2000 galaxies. The dispersion of the Gaussian dictated the rms variation between the plates and for these simulations was set at 10%, 20% and 30%. The number of galaxies on each plate was then normalised by the ratio of pixels on the plate compared to the average number per plate (200 pixels). This prevented plates with a smaller area than normal, and therefore, a few number of pixels, having an artificially high number density. Finally, the average galaxy count per pixel was calculated for each

[§]Assuming a number–magnitude relationship of $n(m) \propto 10^{0.6m}$, then $\frac{n_1}{n_2} = 10^{0.6\Delta m}$. Using $\Delta m = 0.1$, $\Delta n = n_1 - n_2 = 0.15 n_2$ *i.e.* $\frac{\Delta n}{n} = 15\%$.

plate. Figure 2.10 shows an example of an individual realisation of the 10% simulations and should help to clarify the procedure described above.

For each percentage variation, approximately 50 realisations were made. The correlation function was calculated, using equation 2.9, for each of these realisations and then averaged together to give a single $w(\theta)$ for each percentage. The individual realisations were not scaled to the same number density because, overall, each had approximately 70000 galaxies (section 2.6). The number density fluctuations between realisations was small, $1\sigma \sim 0.9\%$, and could not account for the large variation seen between their correlation functions. Figure 2.11 shows all the individual correlation functions for the 20% simulation, along with the final averaged $w(\theta)$.

For a fair comparison, the observed galaxy angular correlation function for the EDSGC was re–calculated with a similar number density of galaxies as used in the simulations *i.e.* 69456 galaxies to a magnitude limit of $b_j = 18.65$ compared to $\sim$ 70000 for a single realisation. This removed the need to rescale any of the correlation functions. In addition, the same pixels that were removed from the simulations *e.g.* on plate edges, were removed from the galaxy data array to ensure that these pixels did not bias the observed $w(\theta)$.

The averaged plate simulated correlation functions were subtracted from the observed $w(\theta)$ as described by Geller *et al.* (1984). They were subtracted because they represent a component of the observed $w(\theta)$ that may be due to plate–matching errors. Figure 2.12 shows the averaged correlation function for each of the simulations, while Figure 2.13 shows the effect of subtracting these functions from the observed $w(\theta)$. This was achieved using the formula given by Geller *et al.* (1984), which is presented here;

$$w_{obs} = w_p w_{corr} + w_p + w_{corr}, \qquad (2.27)$$

$$w_{corr} = \frac{w_{obs} - w_p}{1 + w_p}, \qquad (2.28)$$

where w_p is the simulated correlation function, w_{obs} is the observed correlation function, and w_{corr} is the corrected $w(\theta)$. The integral constraint was not a problem, since it had the same value for the simulations and the observed $w(\theta)$.

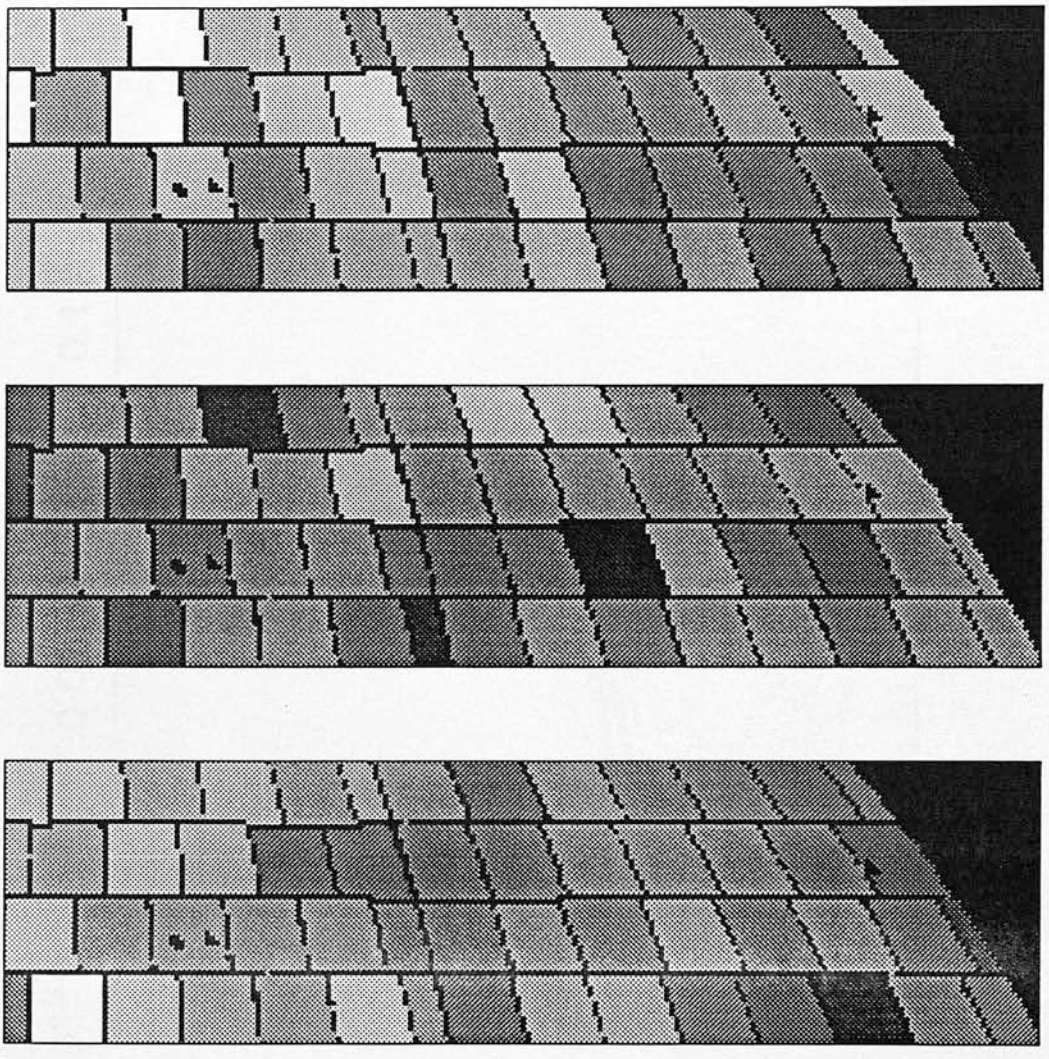

Figure 2.10: Examples of the plate–to–plate simulations. The plots are a true sky projection of all the plates in the area used to compute $w(\theta)$. The top plot shows the distribution of actual plate number densities within the EDSGC, the middle one is an example of a 10% random plate–to–plate realisation and the bottom plot is an example of a $\Delta m = 0.015$ correlated plate–to–plate realisation. Pixels on the boundaries of plates were flagged as shown and were not used in the calculation of $w(\theta)$. Drill holes were also included in the simulations.

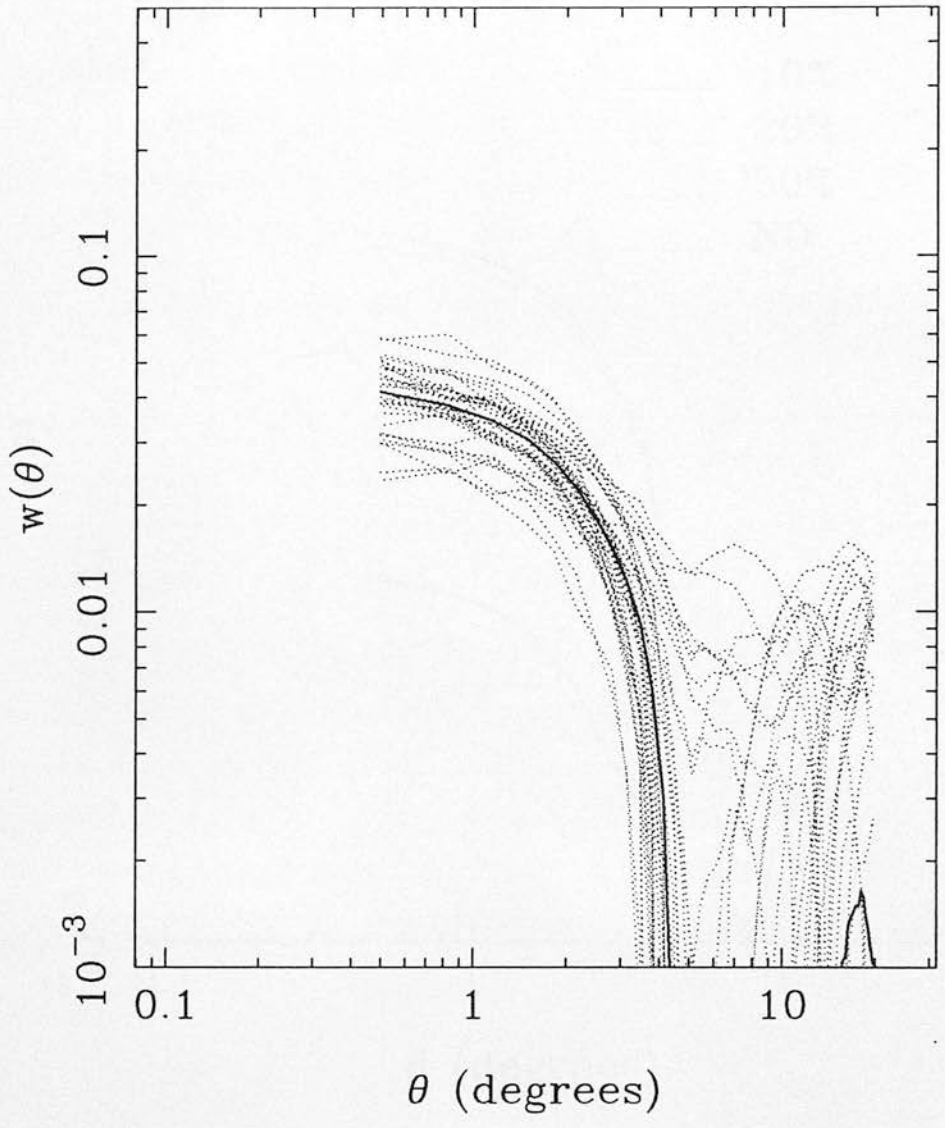

Figure 2.11: All 37 individual 20% random plate–to–plate correlation functions. The average of these correlation functions is shown in bold.

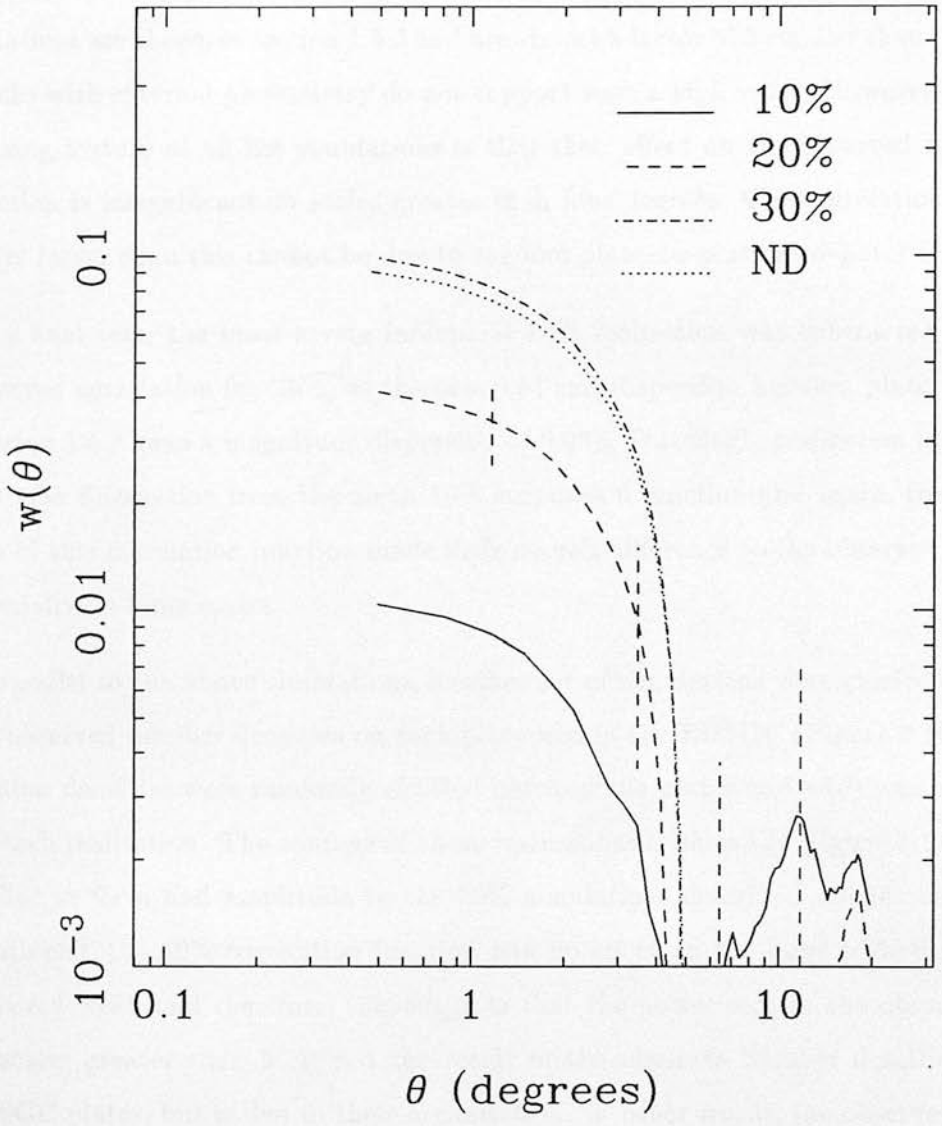

Figure 2.12: This plot shows the averaged 10%, 20% and 30% correlation functions for the 3 sets of random plate–to–plate simulations carried out. In addition, the averaged w(θ) for the shuffled number density simulations is shown (ND).

Figure 2.13 clearly demonstrates that both the 10% and 20% random plate–to–plate simulations have little effect on the observed correlation function. Only above these variations does it become significant. This would correspond to random fluctuations in the plate zero–points of $\Delta m \geq 0.14$. The measured rms plate–to–plate magnitude variations are shown in section 1.5.3 and are almost a factor of 3 smaller than this, while checks with external photometry do not support such a high value. However, the most striking feature of all the simulations is that their effect on the observed correlation function is insignificant on scales greater than four degrees. The correlations seen on scales larger than this cannot be due to random plate–to–plate zero–point errors.

As a final test, the most severe individual 10% realisation was subtracted from the observed correlation function, as the observed rms dispersion between plates was 11% (section 1.5.3 gave a magnitude dispersion of 0.08). This single realisation represented a $\sim 2.5\sigma$ fluctuation from the mean 10% correlation function and again, the subtraction of this correlation function made little overall difference to the observed function, especially on large scales.

In parallel to the above simulations, another set of simulations were carried out using the observed number densities on each plate within the EDSGC (Figure 2.10). These number densities were randomly shuffled between the plates and $w(\theta)$ was calculated for each realisation. The average of these realisations is shown in Figure 2.12 and was similar in form and amplitude to the 30% simulations described above. As already mentioned, the 30% correlation function had no effect on the large scale form of the observed $w(\theta)$, and therefore, this suggests that the power seen in the observed $w(\theta)$ on scales greater than 5° is not the result of the absolute number densities on the EDSGC plates, but is due to their organisation. In other words, the observed angular correlation function is measuring large coherent structures that spanned several plates.

2.4.3 Correlated Plate–to–Plate Variations

Hale-Sutton *et al.* (1992) claim that correlated plate–to–plate zero–point magnitude errors can have a significant effect on the observed angular correlation function. They argue that a $\Delta m = 0.01$ systematic magnitude shift between plates could produce the large scale power seen in the APM $w(\theta)$ (Maddox *et al.* 1990). When they remove this

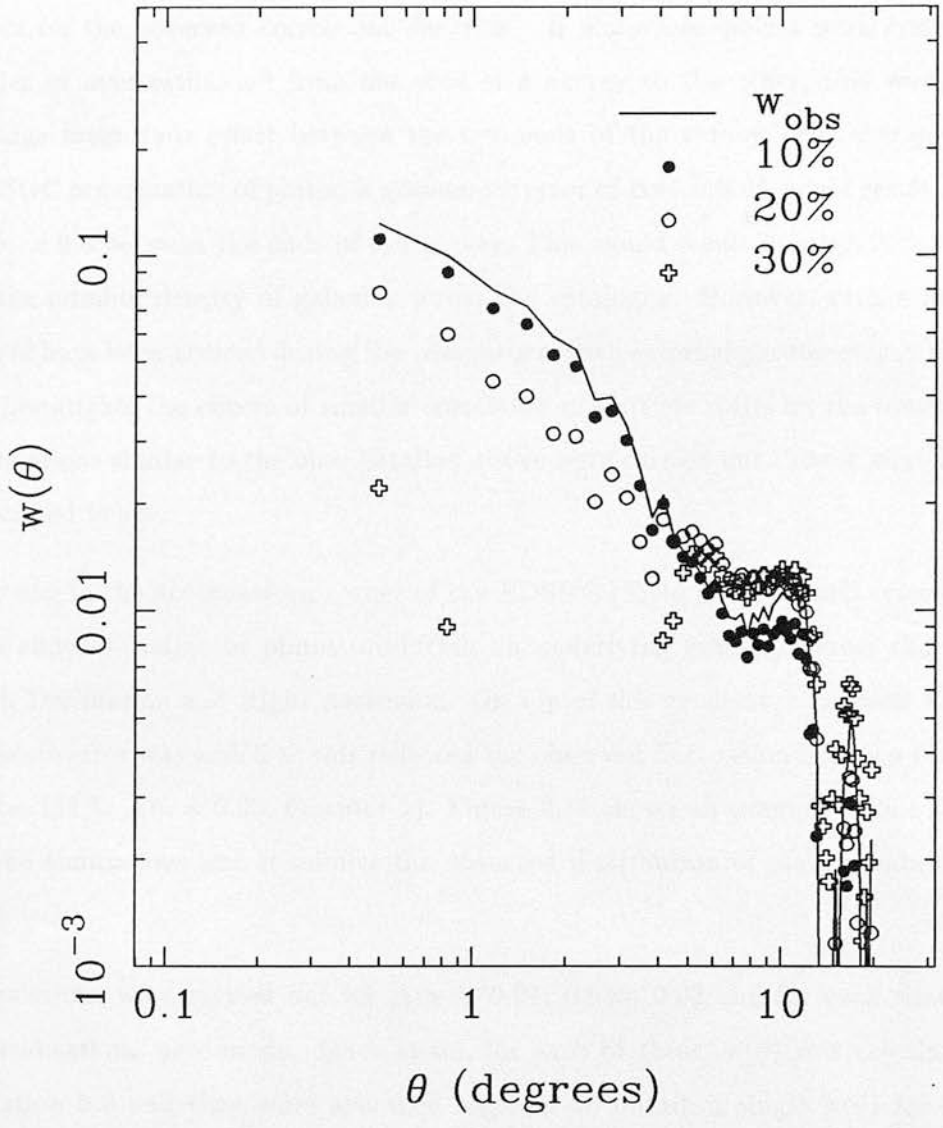

Figure 2.13: The effect of subtracting the random plate–to–plate simulations from Figure 2.12 from the observed $w(\theta)$ at $b_j = 18.65$. The effect of subtracting the number density simulations has not been plotted as it was very similar in shape and amplitude to the 30% simulation.

effect, they find that the APM w(θ) is in good agreement with the Lick w(θ) *i.e.* no power beyond 3°.

It is easy to envisage that correlated plate–to–plate errors could have a significant effect on the observed correlation function. If plate zero–points were systematically under or over estimated from one side of a survey to the other, this would lead to a large magnitude offset between the two ends of the survey. For example, for the EDSGC organisation of plates, a systematic error of $\Delta m = 0.05$ would result in a offset of $b_j = 0.6$ between the ends of the survey. This would result in a significant gradient in the number density of galaxies across the catalogue. However, such a large offset would have been noticed during the comparison with external photometry in Chapter 1. To investigate the effects of smaller correlated magnitude shifts on the observed w(θ), simulations similar to the ones detailed above were carried out. These simulations are described below.

Starting in the northeastern corner of the EDSGC (Field 532), a small systematic Δm was added to adjacent plates producing an underlying gradient across the survey in both Declination and Right Ascension. On top of this gradient, a random 10% plate–to–plate error was added as this reflected the observed fluctuation between the EDSGC plates (11%, $\Delta m = 0.08$, Chapter 1). Figure 2.10 shows an example of one realisation of the simulations and it mimics the observed distribution of plate number densities very well.

Simulations were carried out for $\Delta m = 0.01$, 0.015, 0.02 and for each simulation $\sim$ 50 realisations were made. Once again, for each of these, w(θ) was calculated using equation 2.9 and they were averaged together to obtain a single w(θ) for each Δm shift. It should be noted here, that each of the individual correlation functions was scaled to the mean number of galaxies used in all the realisations ($\sim$ 70000), removing any differences due to the varying number densities between the realisations. Each simulation was subtracted from the observed correlation function using equation 2.28 and the results are shown in Figure 2.15. A magnitude shifts of $\Delta m = 0.01$, used by Hale–Sutton *et al.* (1992) above, had no effect on the EDSGC w(θ). The same was true of the $\Delta m = 0.015$ shift. However, a shift of $\Delta m = 0.02$ was able to remove all the

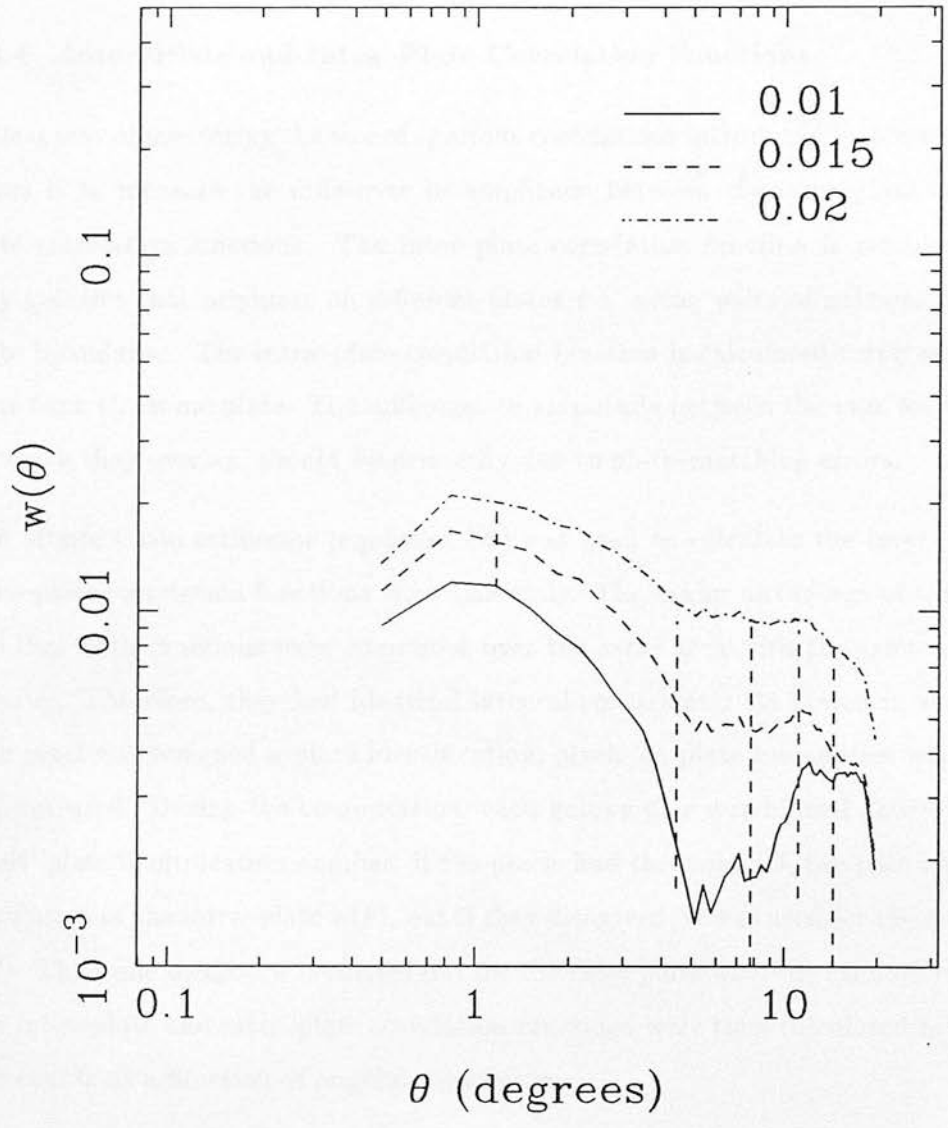

Figure 2.14: This plot shows the averaged correlation functions for the correlated plate–to–plate simulations with $\Delta m = 0.01, 0.015$ & 0.02. One σ error bars have been plotted.

large scale power seen in the observed $w(\theta)$. This shift would represent a magnitude offset between the ends of the EDSGC of 0.3 in Right Ascension and 0.1 in Declination. From the external checks carried out in Chapter 1, it is unlikely that an offset of this size would have gone unnoticed.

2.4.4 Inter–Plate and Intra–Plate Correlation Functions

A clear way of measuring the size of spurious correlations introduced by plate–matching errors is to measure the difference in amplitude between the inter–plate and intra–plate correlation functions. The inter–plate correlation function is calculated using only galaxies that originate on different plates *i.e.* using pairs of galaxies that cross plate boundaries. The intra–plate correlation function is calculated using only galaxy pairs from the same plate. The difference in amplitude between the two, for the scales on which they overlap, should be primarily due to plate–matching errors.

The Monte Carlo estimator (equation 2.9) was used to calculate the inter–plate and intra–plate correlation functions simultaneously. The major advantage of this scheme was that both functions were computed over the same area with the same number of galaxies. Therefore, they had identical integral constraints. As stated in section 2.2, each pixel was assigned a plate identification, pixels on plate boundaries were flagged and not used. During the computation, each galaxy pair was binned according to its pixels' plate identification number: if the pixels had the same ID, the pair was used in calculation of the intra–plate $w(\theta)$, but if they disagreed, it was used for the inter–plate $w(\theta)$. The same method was carried out for the cross pairs with the random catalogue. The intra–plate and inter–plate correlation functions were then calculated using these pair counts as a function of angular separation.

Figure 2.16 shows the two functions calculated to a depth of $b_j = 19.5$, along with the global correlation function to the same depth. No integral constraints were added. The mean offset between the two, in the range $1.0^\circ \leq \theta \leq 3.5^\circ$, was 4.66×10^{-3} which can be translated to a magnitude error using the formula

$$\delta w \sim \left(\frac{\delta n}{n}\right)^2 \sim (b \ln(10) \Delta m)^2 \sim 2(\Delta m)^2 , \qquad (2.29)$$

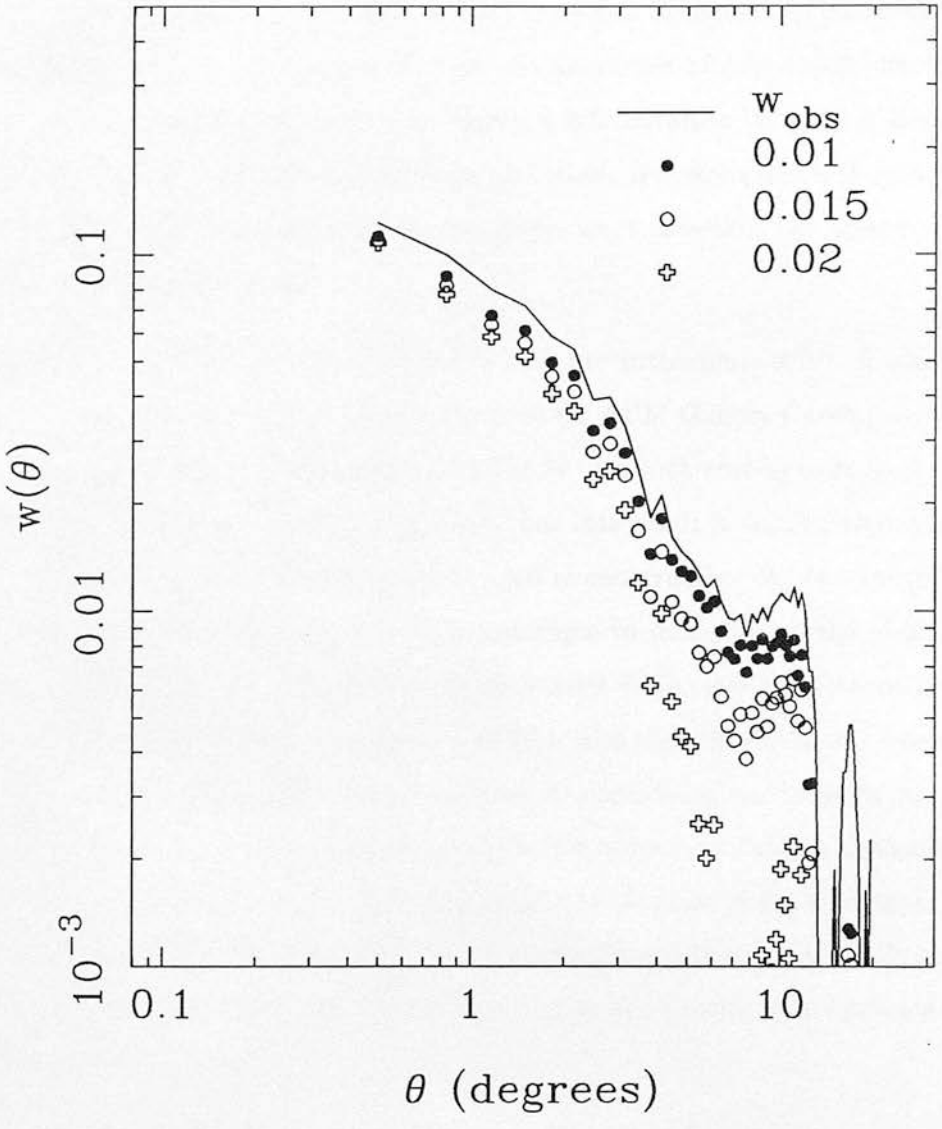

Figure 2.15: The effect of subtracting the correlated plate–to–plate simulations in Figure 2.14 from the observed w(θ) at $b_j = 18.65$.

where b is the slope of the number–magnitude relationship, $n(m) \propto 10^{bm}$ (Geller *et al.* 1984). Using the above formula with $b = 0.6$, the variation in number densities between the EDSGC plates was $\sim 6\%$, or $\Delta m = 0.05$ and is within the limit set by Geller *et al.* (1984) for any galaxy survey used to measure $\bar{w}(\theta)$. Furthermore, it is in excellent agreement with the error derived from the histogram of plate offsets shown in section 1.5.3, which gave an rms plate–to–plate error of $\Delta m = 0.05$. In the context of the random simulations described above, a 6% variation in number density would have no effect on the observed correlation function. However, this test is insensitive to correlated magnitude errors between the plates as it measures the absolute difference between neighbouring plates.

The offset between the inter–plate $w(\theta)$ and the intra–plate $w(\theta)$ obtained for the EDSGC can be compared to the offset quoted for APM Galaxy Catalogue (Maddox *et al.* 1990). They quote a mean offset of 1.7×10^{-3}, which corresponds to an rms magnitude error of ~ 0.03. It is not surprising that this result is smaller than the EDSGC result, considering the different methods used in constructing the two catalogues. The APM group initially used a boot–strap technique to minimise all the plate offsets simultaneously and then calibrated the whole survey using external photometry. For the EDSGC, individual plates were calibrated first, and then all the plates were mosaiced together. Clearly, the APM method will lead to a smaller plate–to–plate rms variation compared to the EDSGC method, since the latter introduces external information, and therefore, external error at the beginning of the construction of the catalogue. However, by calibrating individual plates first, the chances of introducing large scale gradients is greatly reduced and therefore, the APM survey is more prone to large scale gradients than the EDSGC.

2.5 Galactic Extinction

The effect of galactic extinction on extragalactic astronomy has long been debated in astronomical literature. Large clouds of hydrogen and dust within our own Galaxy significantly redden the colours of objects and obscure them. The most accepted method of estimating the extinction is to use the distribution of neutral hydrogen as an extinction tracer, as it can be mapped accurately using its characteristic 21cm emission which

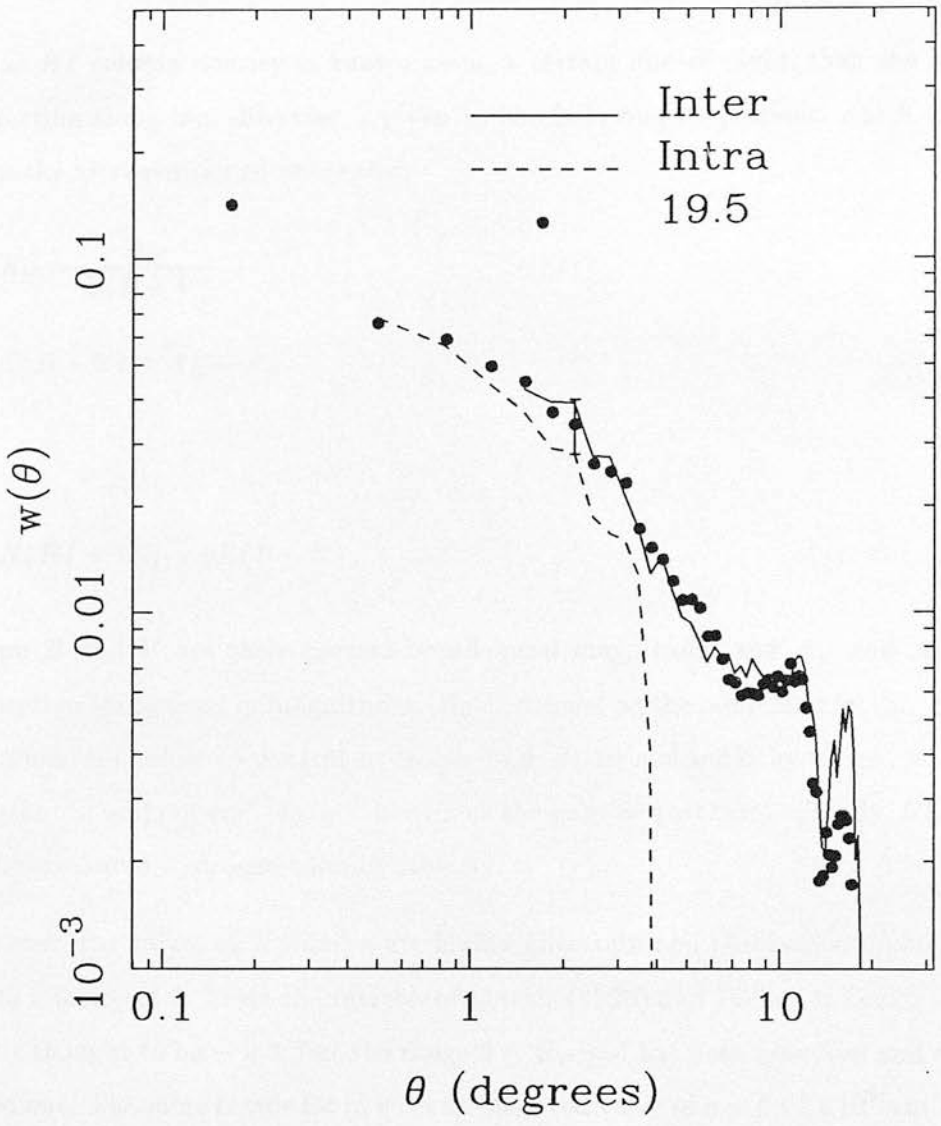

Figure 2.16: The inter–plate and intra–plate correlation functions calculated to a depth of $b_j = 19.5$. Also plotted is the global correlation function calculated to the same depth. The error bar plotted was calculated internally as described in section 2.7

is itself unaffected by extinction. Two excellent reviews of galactic extinction and the methods used to correct for it are: Rowan–Robinson (1985) and Mathis (1990). As a further test of the observed angular correlation function, the effects of extinction were investigated and the results are shown below.

If the HI column density is known along a certain line–of–sight, then the amount of extinction along that direction is given by the following 3 equations, which were taken from the aforementioned references;

$$R_V = \frac{A_V}{E(B-V)}, \tag{2.30}$$

$$E(B-V) = A_B - A_V \tag{2.31}$$

and

$$N(HI + H_2) = \eta E(B-V), \tag{2.32}$$

where B and V are their normal broad–band magnitudes and A_V and A_B are the respective extinctions in magnitudes. R_V is defined as the reddening factor. In the last equation, HI refers to neutral hydrogen and H_2 to molecular hydrogen, while η is a constant in units of $\mathrm{cm}^{-2}\,\mathrm{mag}^{-1}$ known as the gas–to–dust ratio. Finally, $N(HI+H_2)$ is the measured hydrogen column density.

However, the values of R_V and η are highly uncertain and observed estimates vary by up to a factor of 2. From the reviews of Mathis (1990) and Dickey & Lockman (1990), R_V is thought to be ~ 3.5, but the range $3 \leq R_V \leq 6$ has been observed and cannot be ruled out. The same is true for η, with an observed value of $\eta = 6 \pm 2 \times 10^{21}\,\mathrm{cm}^{-2}\,\mathrm{mag}^{-1}$.

An alternative approach, is to map the distribution of dust directly, since this is the cause of the extinction. Rowan–Robinson *et al.* (1991) used data from the Infrared Astronomy Satellite (IRAS) to do just this, and using a sophisticated dust model derived a relationship between the observed infrared dust emission and the extinction. This relationship is presented here

$$A_V = 0.06\, I(100), \tag{2.33}$$

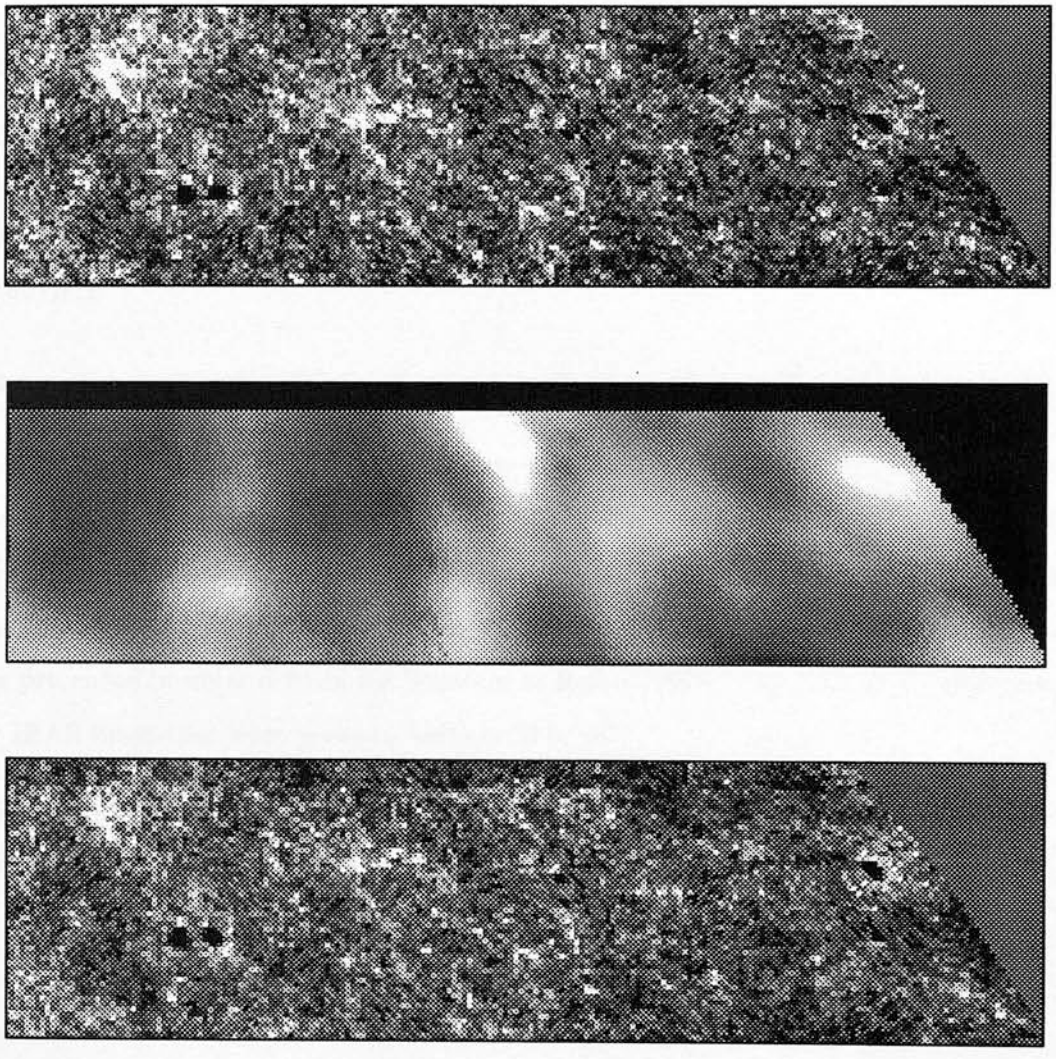

Figure 2.17: The top plot is the EDSGC binned into 20 arcminute pixels as shown in Figure 2.1. The middle plot is a map of the extinction derived from the *HI* column density over the same area of the EDSGC and binned in the same way. There appears to be a general anti–correlation between the two. The bottom plot shows the EDSGC after it has been corrected for extinction as described in the text.

or

$$A_B = 0.08\, I(100)\,, \tag{2.34}$$

for $R_V = 3.5$. $I(100)$ is the observed IRAS 100 micron flux density. They also compared the distribution of dust with that of the HI and found a fair correlation between the two. However, this method of estimating the extinction is dependent on the dust model used and the observed 100 micron flux density is extremely temperature dependent *e.g.* $I(100) \propto T^4$

2.5.1 Correction for Extinction

The EDSGC was corrected for extinction using both the methods described above. The HI data was obtained from the recently published Stark *et al.* (1992) map, which covers most of the sky down to a Declination of $-40°$, while the IRAS data was kindly provided by Mark Jones of Queen Mary & Westfield College, London. The Stark data was presented in units defined by Burstein & Heiles (1978, BH), $2.2 \times 10^{18}\mathrm{cm}^{-2}$ and the IRAS intensities were given in units of MJy sr^{-1}.

The B band extinction to hydrogen column density can be obtained by simple manipulation of the 3 equations above,

$$A_B = \frac{N_{hyd}}{\eta}(1 + R_V) = \tau N_{hyd}, \quad \text{where} \quad \tau = \frac{1 + R_V}{\eta}\,. \tag{2.35}$$

As stated, typical values for the variables were taken from Mathis (1990) and Dickey & Lockman (1990), being $R_V = 3.25$ and $\eta = 5.2 \times 10^{21}\mathrm{cm}^{-2}\,\mathrm{mag}^{-1}$. This translated to $\tau = 8.2 \times 10^{-22}\mathrm{cm}^2\,\mathrm{mag}$, or $\tau = 0.0018$ in $(\mathrm{BHunits})^{-1}\,\mathrm{mag}$.

The HI data, within the EDSGC area, was extracted from the Stark map and converted to extinction using equation 2.35. The data was then binned in exactly the same way as described earlier and Figure 2.17 shows this extinction map along with the binned EDSGC data to a depth of $b_j = 19.5$. A general anti–correlation between the extinction and the galaxy density can be seen, although it is not a strong one as there are areas of high extinction which correspond to areas of high galaxy density and vice versa.

The peak HI column density within the EDSGC area is $3.8 \times 10^{20}\mathrm{cm}^{-2}$ (at $\alpha \sim 0$hrs and $\delta \sim -40°$), which corresponds to a peak extinction of $A_B = 0.3$ using the typical values in equation 2.35. The mean HI column density is $1.6 \times 10^{20}\mathrm{cm}^{-2}$ which gives an extinction estimate of $A_B = 0.12$, again using the typical values of R_V and η. At the SGP, the extinction was $A_B = 0.1$. All the above values are in good agreement with those obtained using the IRAS data.

To investigate the effect of this anti–correlation on $\mathrm{w}(\theta)$, all the galaxies within the EDSGC were corrected for extinction. This was performed 3 times using the following methods and extinction values:

1. Using the Stark HI data with $R_V = 3.25$ and $\eta = 5.2 \times 10^{21}\mathrm{cm}^{-2}\,\mathrm{mag}^{-1}$, which gave $\tau = 0.0018$ in $(\mathrm{BHunits})^{-1}\,\mathrm{mag}$. These were the typical values given in the astronomical literature.

2. Using the Stark HI data with $R_V = 6$ and $\eta = 4 \times 10^{21}\mathrm{cm}^{-2}\,\mathrm{mag}^{-1}$, which gave a $\tau = 0.0038$ in $(\mathrm{BHunits})^{-1}\,\mathrm{mag}$. These were the most extreme values quoted by Mathis (1990). The peak extinction within the EDSGC quoted above increased to $A_B = 0.6$, while the mean became $A_B = 0.24$.

3. Using the IRAS 100 microns data. An appropriate τ value was obtained using the conversion $I(100) = 0.85 \times 10^{-20} N_{hyd}$ (Rowan–Robinson *et al.* 1990), which gave $\tau = 0.0019\,(\mathrm{BHunits})^{-1}\,\mathrm{mag}$.

In each case, the catalogue was re–selected to the depth of $b_j = 19.5$ and binned. The number of galaxies binned was 252021, 300994 and 266820 respectively. Figure 2.17 shows the EDSGC after the extinction correction.

The correlation functions for these 3 cases are shown in Figure 2.18. The slight discrepancy seen between the amplitudes of the correlation functions on small scales is due to the different number densities used in their calculation and could be removed by scaling the functions to the same number density as described in section 2.6. The most striking feature of Figure 2.18 is that the observed large scale power seen in $\mathrm{w}(\theta)$ is still present, irrespective of the extinction correction used.

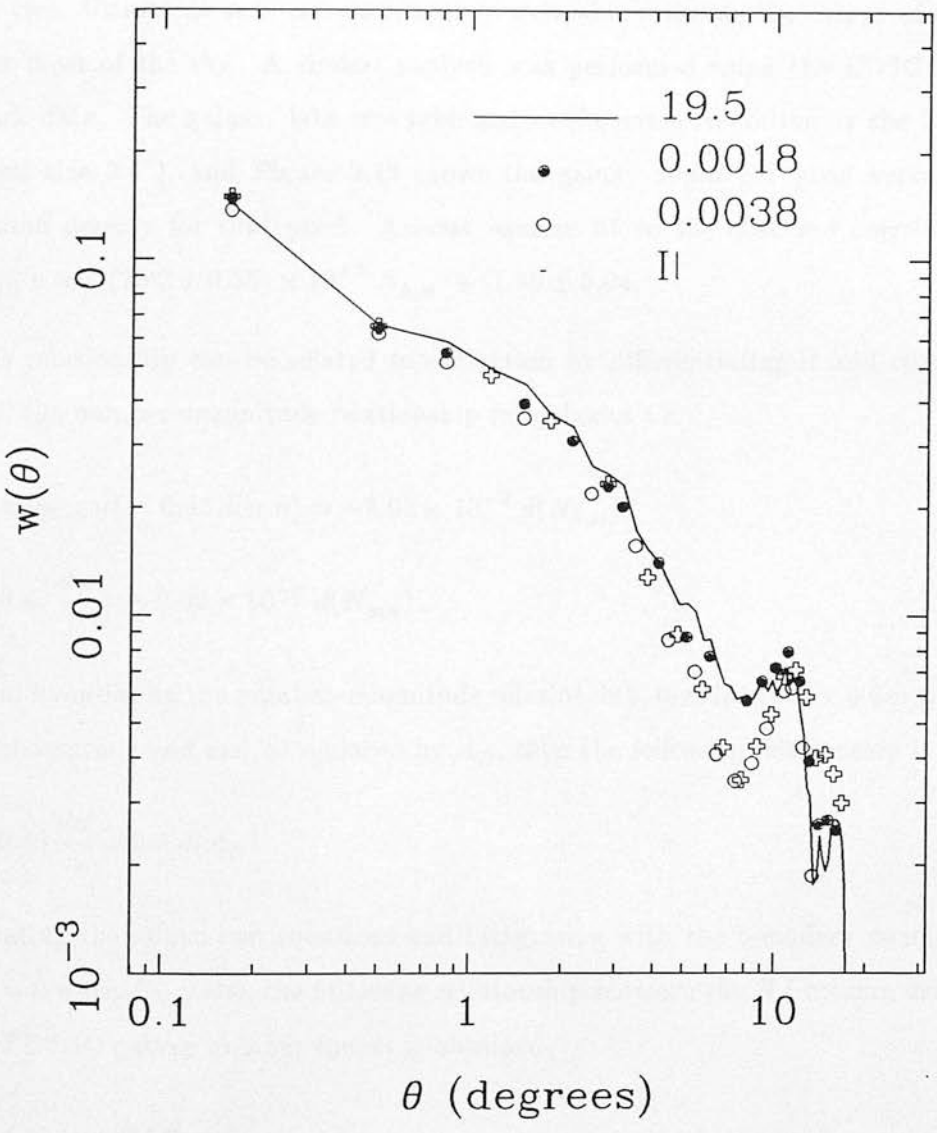

Figure 2.18: A comparison between the observed w(θ) at $b_j = 19.5$ for the whole EDSGC and the 3 extinction corrections described in the text. Only a third of all the points have been plotted to avoid overcrowding.

2.5.2 Correlation between HI Column Density and Galaxy Counts

In the classic study of Burstein & Heiles (1978), they cross–correlated the Lick galaxy counts with maps of HI column density and found a significant anti–correlation between the two. Using this anti–correlation, they were able estimate the extent of extinction over most of the sky. A similar analysis was performed using the EDSGC and the Stark data. The galaxy data was rebinned to the same resolution as the Stark data (pixel size 3.5°), and Figure 2.19 shows the galaxy count per pixel versus the HI column density for that pixel. A least–squares fit to the observed correlation gave $\log_{10} n = -(2.02 \pm 0.55) \times 10^{-3}\ N_{hyd} + 1.49 \pm 0.04$.

This relationship can be related to extinction by differentiating it and comparing it with the number–magnitude relationship for galaxies *i.e.*

$$d(\log_{10} n) = 0.43\, d(\ln n) = -2.02 \times 10^{-3}\ d(N_{hyd})\,, \tag{2.36}$$

$$0.43\, \frac{dn}{n} = -2.02 \times 10^{-3}\ d(N_{hyd})\,. \tag{2.37}$$

By differentiating the number–magnitude relationship, $0.43 \ln n(m) \propto 0.6m$ where m is the magnitude and can be replaced by A_B, then the following relationship is obtained

$$0.43\, \frac{dn}{n} = 0.6\ d(A_B)\,. \tag{2.38}$$

Equating the above two equations and integrating with the boundary condition that $A_B = 0$ when $N_{hyd} = 0$, the following relationship between the HI column density and the EDSGC galaxy number counts is obtained,

$$A_B = 0.0034 N_{hyd}\,, \tag{2.39}$$

which is a τ value of 0.0034 in equation 2.35. This is the same factor of τ as used in correction 2 above, *i.e.* the most extreme values recorded in the literature. This is extremely worrying for studies of galactic extinction, since it is unlikely that both R_V and η should have their observed upper limits. However, in terms of $w(\theta)$, it has already been demonstrated that this amount of extinction does not significantly alter the observed correlation function. The large scale power still remained.

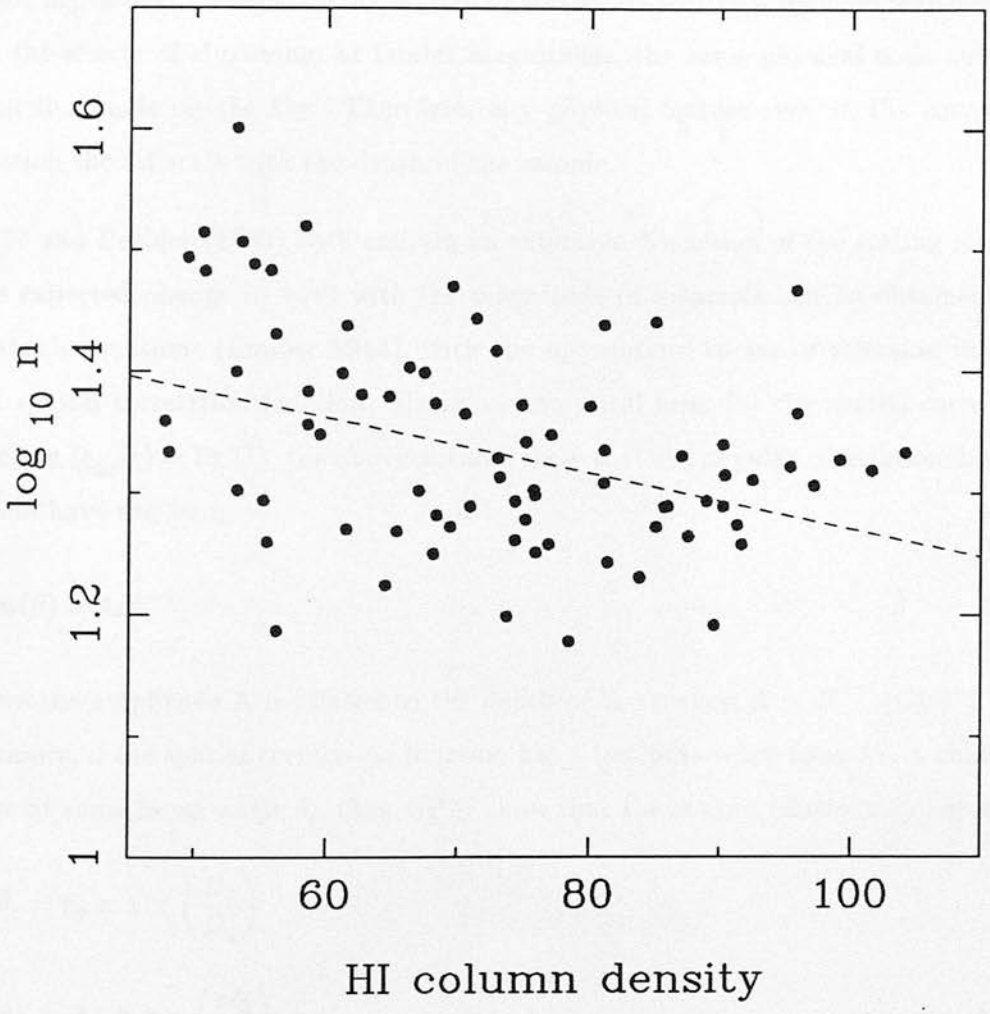

Figure 2.19: The correlation between the number per pixel and the corresponding *HI* column density for that pixel. The galaxy data was taken from the EDSGC binned on 3.5° scales, while the *HI* data was taken from the Stark *HI* map binned to the same resolution. The line is a least–square fit of slope -2.02×10^{-3} and intercept 1.49. The y-axis is plotted in Burstein & Heiles (1978) units.

2.6 Scaling Test

An essential test of the galaxy angular correlation function is the scaling of the function with apparent magnitude *i.e.* number density. The amplitude of $w(\theta)$ decreases with the depth of the sample used as illustrated in Figure 2.5. There are two reasons for this: as the depth of the sample increases, more galaxies are seen in projection which washes out the effects of clustering; at fainter magnitudes, the same physical scale subtends a smaller angle on the sky. Therefore, any physical feature seen in the correlation function should scale with the depth of the sample.

GP77 and Peebles (1980) both contain an extensive discussion of the scaling relation. The expected change in $w(\theta)$ with the magnitude of a sample can be obtained from Limber's equations (Limber 1953), with the appropriate choice of selection function and spatial correlation function. Using an analytical form for the spatial correlation function ($\xi_{gg}(r) = Br^{-\gamma}$), the above authors show that the angular correlation function should have the form

$$w(\theta) = A\theta^{1-\gamma}, \tag{2.40}$$

where the amplitude A is related to the depth of the survey, $A \propto D^{-\gamma}$ (GP77). Furthermore, if the spatial correlation function has a two power–law form *i.e.* a change of slope at some break angle θ_b, then GP77 show that the scaling relationship becomes

$$\theta_1 = \theta_2 \times x \times \left(\frac{D_2}{D_1}\right) \tag{2.41}$$

$$A_1 = A_2 \times y \times \left(\frac{D_2}{D_1}\right), \tag{2.42}$$

where the subscripts 1 and 2 refer to the two different samples, or catalogues, which have the depths D_1 and D_2. The factors x and y change with the relative depths of the samples and contain most of the cosmological effects. For modest sample depths, they are both unity. The relative depth of the samples, or between different catalogues, can be derived from their respective number densities *i.e.*

$$\left(\frac{D_2}{D_1}\right) = \left(\frac{n_2}{n_1}\right)^{\frac{1}{3}}, \tag{2.43}$$

where n_1 and n_2 are the number densities of the two samples being compared. Finally, GP77 show that for apparent magnitudes brighter than $m = 21$ the above scaling relationships are insensitive to the details of the model used.

The four EDSGC correlation functions shown in Figure 2.5 were all scaled to the depth of the Lick catalogue, $b_j \simeq 18.6$ or $n = 1.77 \times 10^5$ galaxies per steradian. This allowed for easy comparison with the Lick w(θ) and the values of x and y were available from GP77, Shanks *et al.* (1980) and Heydon–Dumbleton (1989) (Table 2.5). Figure 2.20 shows the scaled correlation functions along with the average of these functions.

Mag.	x	y	n
17.5	1.34	1.00	44223
18.5	1.00	1.00	175507
19.5	0.91	1.00	655058
20.3	0.82	0.97	1599241

Table 2.5: Table of values used in the scaling of the EDSGC correlation functions. The values of x and y were taken (or interpolated) from GP77, Shanks *et al.* (1980) and Heydon–Dumbleton (1989). The last column, n, is the number of galaxies per steradian at the corresponding depths. Drill holes were taken into account when calculating n.

The EDSGC correlation functions scale well with depth, with excellent agreement on small scales ($< 6°$). On large scales, the amplitude of w(θ) scales, but the individual features within each w(θ) do not. This indicates that the bump/dip feature seen on large scales is not physical. In addition, this feature is prominent in the n_{gr}/n_{rr} estimator shown in Figure 2.8, which is a measure of the edge effects. The presence of the feature suggests that some residual edge effects remain. This explanation is supported by the fact that the fully corrected variance estimator (Figure 2.7) does not show this feature as strongly. However, the error on w(θ), on these scales, is larger than the amplitude of this feature, so it can be ignored within the errors bars (section 2.7).

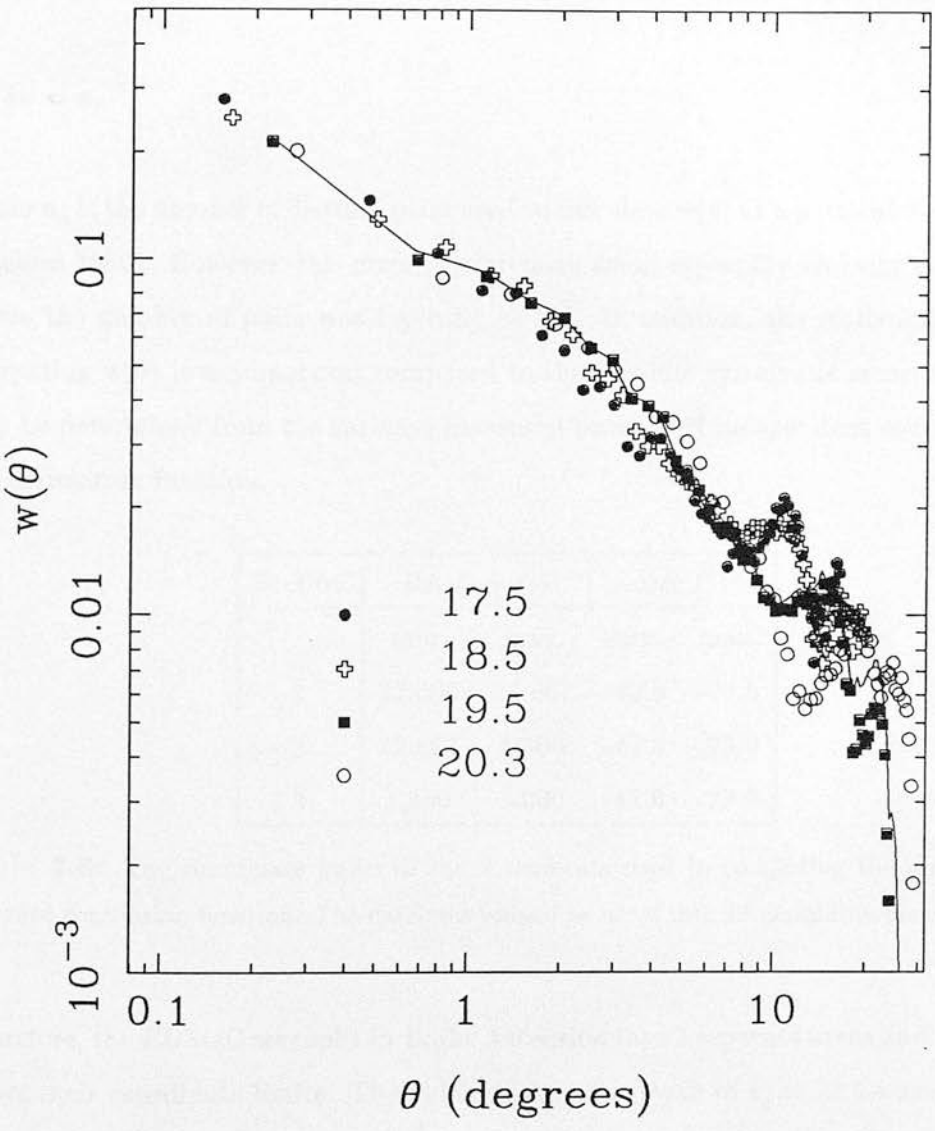

Figure 2.20: The EDSGC correlation functions from Figure 2.5 scaled to the Lick depth, $b_j \simeq 18.6$. The solid line represents the average of the four scaled functions.

2.7 The Error on w(θ).

The exact statistical error on estimating w(θ) can be determined, but it is a complicated expression of higher–order correlation functions *i.e.* the four–point correlation function. If the objects are assumed to be uncorrelated, then the relation simplifies greatly to

$$\delta \mathrm{w} = n_p^{-\frac{1}{2}}, \tag{2.44}$$

where n_p is the number of distinct pairs used to calculate w(θ) at a particular separation (Peebles 1980). However, this error is extremely small especially on large separations where the number of pairs was typically $\sim 10^9$. In addition, the statistical error on computing w(θ) is unimportant compared to the possible systematic error, which can only be determined from the variance measured between N independent estimations of the correlation function.

Section	RA (hours)		Dec.(°)	
	min.	max.	min.	max.
1	22.000	23.667	-42.0	-23.0
2	22.667	1.300	-42.0	-23.0
3	1.300	3.000	-42.0	-23.0

Table 2.6: The coordinate limits of the 3 segments used in computing the error on the observed correlation function. The data was binned as usual into 20 arcminute pixels.

Therefore, the EDSGC was split in Right Ascension into 3 separate areas and Table 2.6 shows their coordinate limits. The galaxy data to a depth of $b_j = 18.5$ was extracted for each area and binned into 20 arcminute pixels as described earlier. The correlation function was calculated for each area using equation 2.9 and an integral constraint was added. The average of the three functions was computed along with the variance between them. Figure 2.21 shows this average and a representation of the 1σ error bars on the points. Clearly, the errors on the small scale w(θ) are insignificant, but on scales approaching the width of the EDSGC ($\sim 20°$) the errors increase. In fact, on scales greater than $\sim 15°$, the error bars are large enough to make w(θ) consistent with zero.

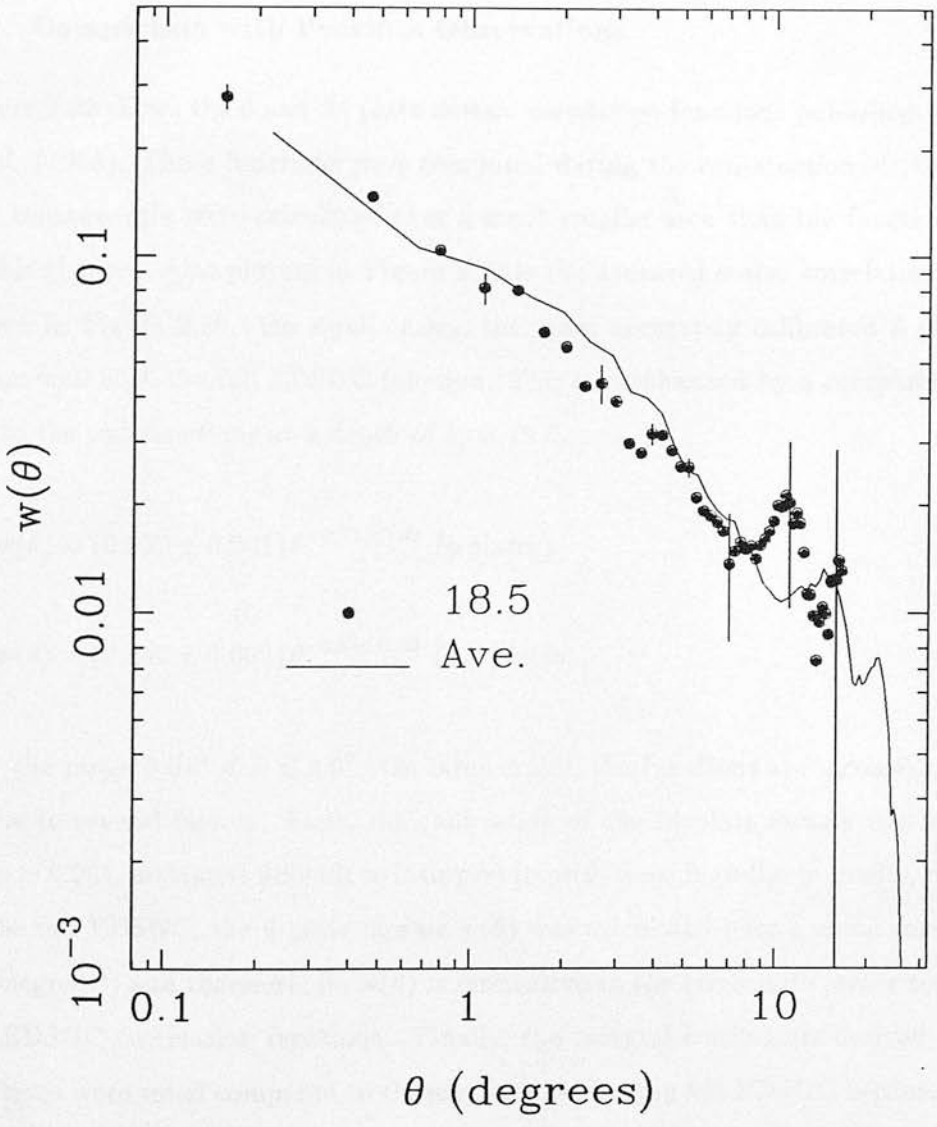

Figure 2.21: The typical error on the observed $b_j = 18.5$ EDSGC correlation function. The error bars were obtained by splitting the EDSGC into 3 separate segments. Also shown is the averaged w(θ) from Figure 2.20.

As stated above, the bump/dip feature is well within the noise on $w(\theta)$. The errors on $w(\theta)$ were examined at all other magnitude limits and were found to be comparable to those shown in Figure 2.21.

2.8 Comparison with Previous Observations

Figure 2.22 shows the 6 and 24 plate mosaic correlation functions published by Collins *et al.* (1988). These functions were computed during the construction of the EDSGC and consequently were calculated over a much smaller area than the functions shown in this chapter. Also plotted in Figure 2.22 is the averaged scaled correlation function shown in Figure 2.20. On small scales, the more accurately calibrated 6 plate $w(\theta)$ agrees well with the full EDSGC function. This is emphasised by a comparison of the fits to the two functions at a depth of $b_j = 19.5$,

$$w(\theta) = (0.039 \pm 0.001)\,\theta^{-0.71\pm0.02} \text{ (6 plates)}$$

$$w(\theta) = (0.042 \pm 0.002)\,\theta^{-0.67\pm0.03} \text{ (All plates)},$$

over the range $0.01^\circ < \theta < 2.0^\circ$. On large scales, the functions are inconsistent. This is due to several factors. First, the calibration of the 24 plate mosaic was very poor ($\Delta m \simeq 0.25$), making it difficult to interpret its $w(\theta)$ meaningfully. Secondly, compared to the full EDSGC, the 6 plate mosaic $w(\theta)$ was calculated over a much smaller area (100degrees^2) and therefore, its $w(\theta)$ is insensitive to the large scale power seen in the full EDSGC correlation functions. Finally, the integral constraints derived for both functions were small compared to those computed for the full EDSGC because a break angle of 2.5° was used in equation 2.23. The integral constraint for both areas would increase significantly if a break scale of 15° was used instead.

In addition to the reasons mentioned above, there is the trend observed in Table 1.1 of Chapter 1, where the scale of the break in $w(\theta)$ increases with survey area. This trend is a combination of the integral constraint and too small a survey area to sample the large scale power in the true correlation function. Therefore, to check whether a large enough area had been sampled using the full EDSGC area, the correlation functions shown in

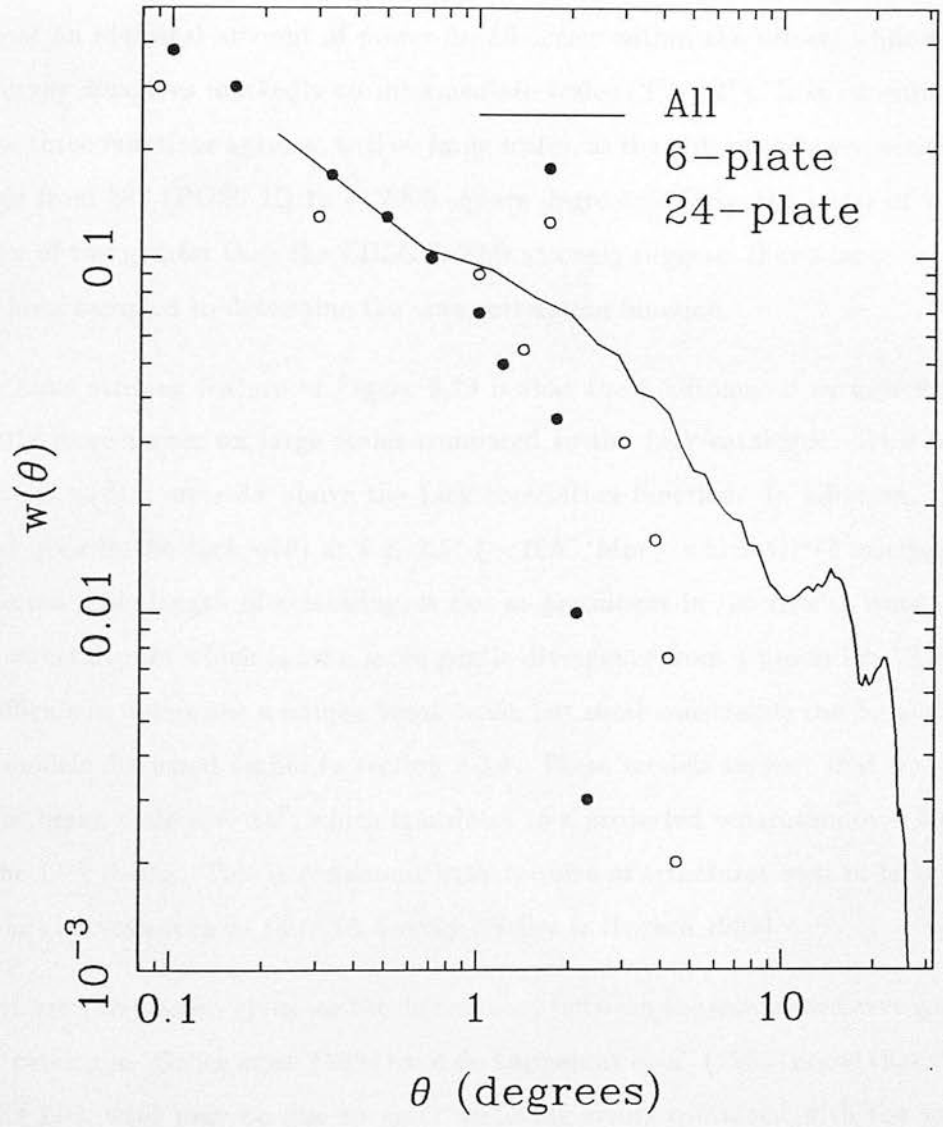

Figure 2.22: A comparison between the 6 and 24 plate mosaic correlation functions published by Collins *et al.* (1988) and the averaged correlation function from Figure 2.20. All the correlation functions have been scaled to the Lick depth.

Figure 2.20 were compared to the APM (Maddox *et al.* 1990), Lick (GP77) and POSS II (Picard 1991) correlation functions, which constitute the 3 largest surveys available in the literature. Figure 2.23 shows this comparison and all the functions are in perfect agreement on small scales ($< 1.0°$). The EDSGC and APM correlation functions find almost an identical amount of power on all scales within the errors, while the POSS II survey disagrees markedly on intermediate scales ($2° \rightarrow 4°$). It is encouraging that these three functions agree so well on large scales, as the area of their respective surveys range from 386 (POSS II) to $\sim$ 2000 square degrees (APM), the latter of which is a factor of two greater than the EDSGC. This strongly suggests that a large enough area has been sampled to determine the true correlation function.

The most striking feature of Figure 2.23 is that the 3 automated surveys find significantly more power on large scales compared to the Lick catalogue. At $\theta = 5°$, the EDSGC w(θ) is over 3σ above the Lick correlation function. In addition, the sharp break seen in the Lick w(θ) at $\theta \simeq 2.5°$ ($\sim 10h^{-1}$Mpc), which GP77 interpreted as a preferred scale length of clustering, is not so prominent in the results from the automated catalogues which show a more gentle divergence from a power law. This makes it difficult to determine a unique break scale, but some constraints can be placed using the models discussed earlier in section 2.3.1. These models suggest that a lower limit to the break scale is $\sim 15°$, which translates to a projected separation of $\sim 50h^{-1}$Mpc at the Lick depth. This is consistent with the size of structures seen in fully sampled redshift surveys such as the CfA Survey (Geller & Huchra 1989).

There are two reasons given for the discrepancy between the automated surveys and the Lick catalogue. Geller *et al.* (1984) and de Lapparent *et al.* (1986) argue that the break in the Lick w(θ) may be due to plate matching errors combined with the subjective nature of the catalogue. This prompted Groth & Peebles (1986a,b) to defend their earlier result, but they were unable to identify a specific systematic error that would lead to the break. They themselves admitted that the inherit subjective nature of the catalogue could be responsible. Secondly, Maddox *et al.* (1990) claim that the smoothing carried out on large scales by GP77 removed the large scale component of clustering seen in the automated catalogues. In fact, this is clearly illustrated in Figure 2.24, where the EDSGC averaged correlation function is compared to the unfiltered

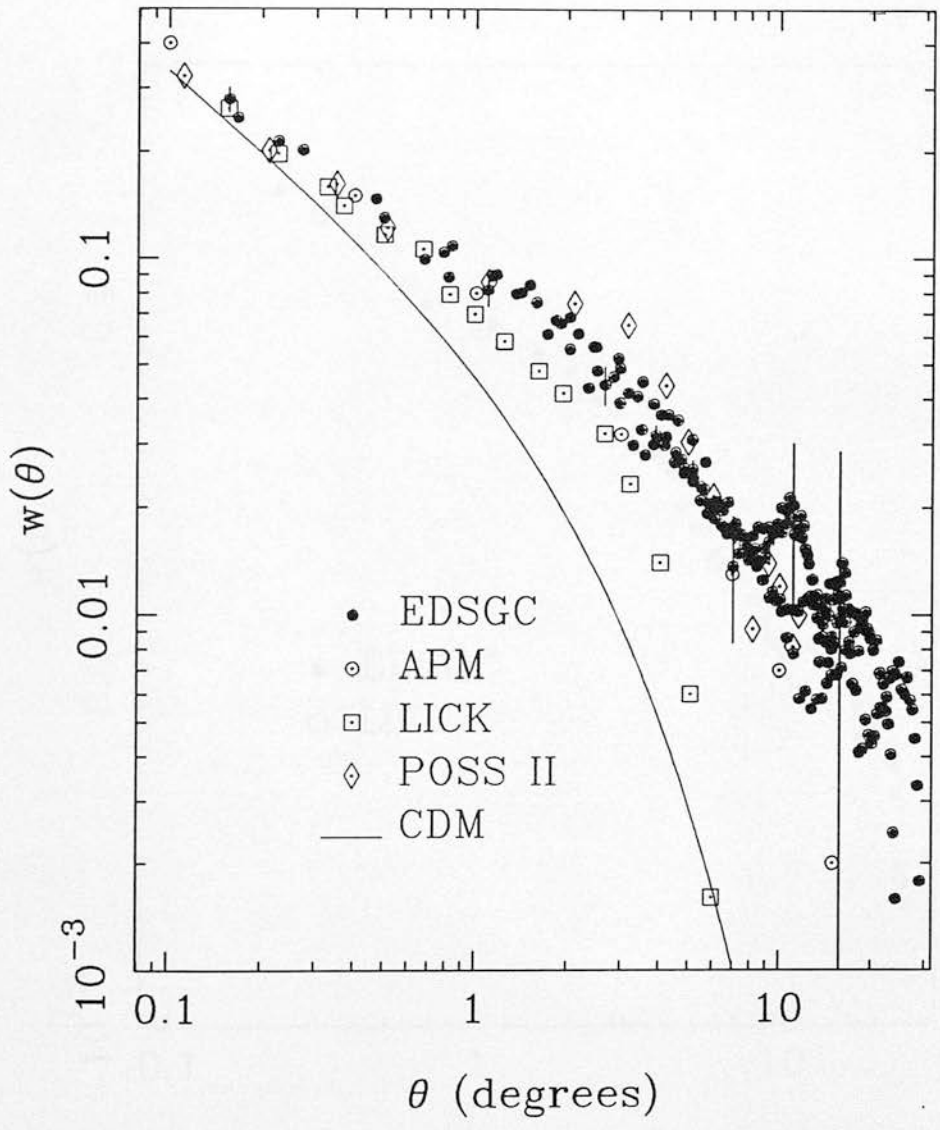

Figure 2.23: A comparison of the EDSGC correlation functions and the APM (Maddox *et al.* 1990), Lick (GP77) and POSS II (Picard 1991) correlation functions. They have all been scaled to the Lick depth. In addition to the observed correlation functions, the predicted angular correlation function for CDM ($h = 0.5$) is plotted (Maddox *et al.* 1990).

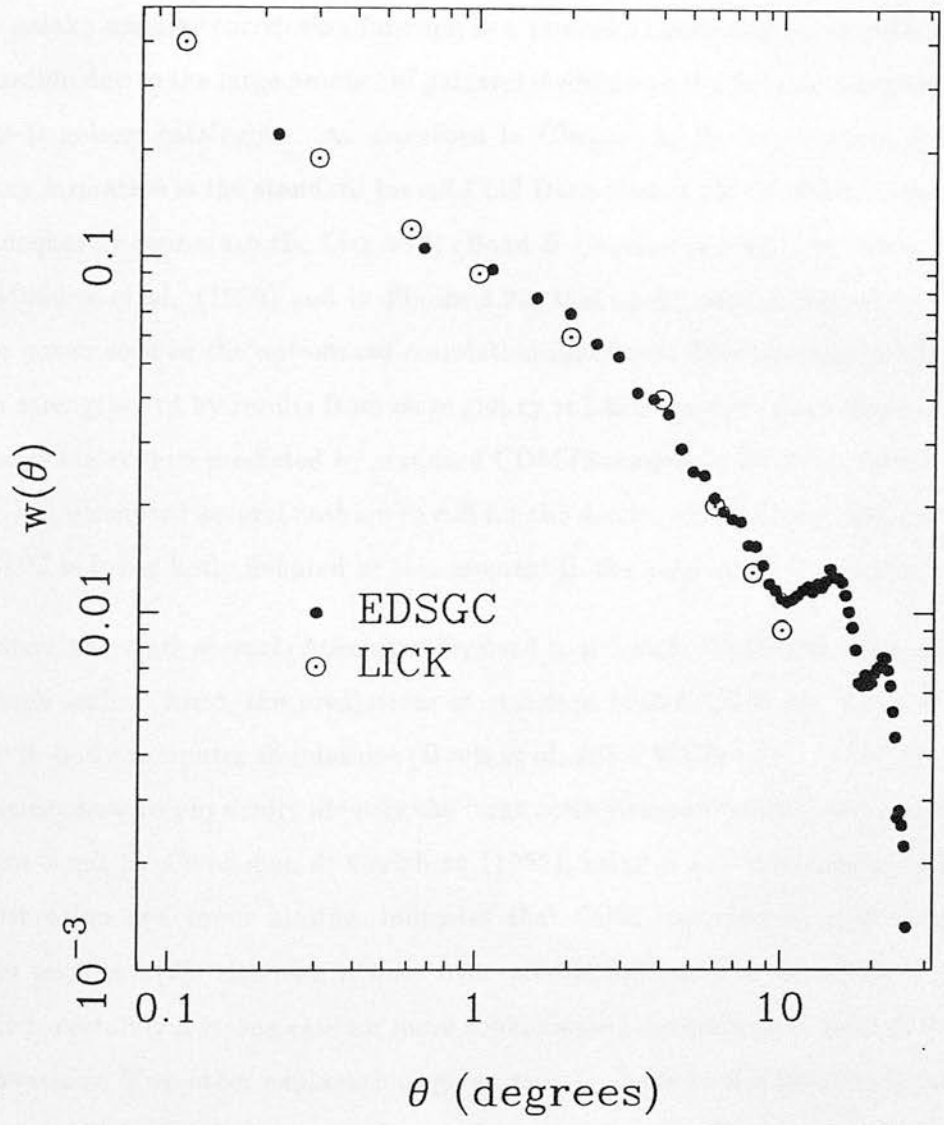

Figure 2.24: A comparison between the averaged EDSGC w(θ) and the unfiltered Lick correlation function. They are both at the Lick depth.

Lick $w(\theta)$ given by GP77. The agreement between the two is excellent on all scales (GP77 only presented data for $\theta < 10°$).

2.9 Discussion

The galaxy angular correlation function is a powerful constraint on theories of galaxy formation due to the large number of galaxies studied and the volumes of space sampled by 2–D galaxy catalogues. As described in Chapter 1, the most popular theory of galaxy formation is the standard biased Cold Dark Matter model (CDM) which is able to adequately reproduce the Lick $w(\theta)$ (Bond & Couchman 1988). However, as shown by Maddox *et al.* (1990) and in Figure 2.23, this model cannot reproduce the large scale power seen in the automated correlation functions. This conclusion has recently been strengthened by results from large galaxy redshift surveys which find more power on large scales than predicted by standard CDM (Saunders *et al.* 1991, Loveday 1991). This has prompted several authors to call for the demise of the theory and the survival of CDM is being hotly debated at this moment in the astronomical literature.

However, there are several options put forward to reconcile CDM with the observations on large scales. First, the predictions of standard biased CDM are based mainly on large N–body computer simulations (Davis *et al.* 1985, White *et al.* 1987), for which it is unclear how to physically identify the large scale structure within these simulations. Recent work by Couchman & Carlsberg (1992), using a new prescription for galaxy identification and lower biasing, indicates that CDM can reproduce the large scale power seen in $w(\theta)$, although it does over–predict the peculiar velocities of galaxies. There is certainly a strong case for more sophisticated simulations in light of these new observations. Two other explanations given recently have been a positive cosmological constant which would give more time to form structure in the universe (Efstathiou *et al.* 1990) and the decay of the 17 keV neutrino on a timescale of 1 to 5 years which would boost the structure seen on large scales (Bond & Efstathiou 1991). Finally, a host of solutions to the problem can be obtained from removing the initial assumption that the primordial power spectrum was scale–invariant. For example, cosmic textures which are unwinding topological knots can give rise to preferred large wavenumbers in the power spectrum. For a fuller discussion on the fate of CDM, the reader is referred

to an article by Davis *et al.* (1992).

In physical terms, the large scale power seen in w(θ) can be related to the size of density inhomogeneities on these scales. More relevantly, the large–scale structure seen can be used to predict the amplitude of the peculiar velocity field on large scales, which is an active area of research at the present time. Clutton–Brock & Peebles (1981) carried out such a calculation by relating the power seen in the Lick w(θ) on large scales to the peculiar velocity field. They predicted rms peculiar velocities of $\langle v^2 \rangle^{\frac{1}{2}} \simeq 300 e^{\pm 0.10} \Omega^{0.6} \mathrm{km\,s^{-1}}$ on scales of $\sim 65 h^{-1}$Mpc, which was inconsistent with the large scale galaxy streaming motions observed by Rubin *et al.* (1976a,b). However, as discussed above, the EDSGC w(θ) finds significantly more power on large angular scales compared to the Lick result and therefore, should predict higher peculiar velocities on the same scales.

To investigate the proposed effect of the large scale power seen in the EDSGC w(θ) on peculiar velocities, a similar analysis was carried out as described by Clutton–Brook & Peebles (1981). In their paper, they showed how the angular correlation function could be related to the J_3 integral, which in turn, could be directly related to the peculiar velocity field using linear theory. As described in this chapter, the EDSGC w(θ) can be approximated, at the Lick depth, by the function

$$\mathrm{w}(\theta) = 0.07\,\theta^{-0.71}\,e^{-\frac{\theta}{\theta_c}}, \qquad (2.45)$$

where $\theta_c = 15^\circ$ and the function is zero beyond $\theta < 30^\circ$ (Figure 2.23). Using the prescription laid out by Clutton–Brook & Peebles, the EDSGC w(θ) predicts rms peculiar velocities of $\langle v^2 \rangle^{\frac{1}{2}} \simeq 610 e^{\pm 0.12} \Omega^{0.6} \mathrm{km\,s^{-1}}$ on scales of $\sim 65 h^{-1}$Mpc. This prediction is in excellent agreement with recent observations of galaxy streaming velocities, which are $\sim 600\,\mathrm{km\,s^{-1}}$ on scales of $\sim 50 h^{-1}$Mpc (Dressler *et al.* 1987, Lynden–Bell *et al.* 1988, Willick 1990, Matherson *et al.* 1992.) and is consistent, within the error, with larger observed peculiar velocities quoted by Rubin *et al.* (1976a,b) and Collins *et al.* (1986).

2.10 Conclusions

The galaxy angular correlation function was used to quantify the large scale clustering seen within the Edinburgh/Durham Southern Galaxy Catalogue. The resultant $w(\theta)$ was corrected for edge effects and the integral constraint before extensive tests were carried out to ensure that the observed function was real. The angular correlation function was checked for spurious clustering due to plate–to–plate magnitude matching errors and for the effects of variable extinction. During all the tests, the large scale power seen on scales $> 5^\circ$ in $w(\theta)$ remained. Finally, the scaling of the function with depth strongly suggests that the power seen on large scales is real.

The EDSGC correlation function was compared to previous observations and was found to be in good agreement on small scales. On scales $> 5^\circ$, the functions derived from automated galaxy catalogues found significantly more power than the GP77 Lick $w(\theta)$. At present, these observations of large scale power in $w(\theta)$ are the strongest evidence for excess clustering on these scales ($\delta\rho/\rho \sim 0.4$ on scales of $r \sim 10\,h^{-1}\,\mathrm{Mpc}$) and is inconsistent with the popular theory of standard biased Cold Dark Matter. Finally, the observed angular large scale structure predicts peculiar velocities of $\simeq 600\mathrm{km\,s^{-1}}$, which agrees well with the observed large scale peculiar velocity field.

Chapter 3

The Edinburgh/Durham Cluster Catalogue

The Abell cluster catalogue has been extensively used in the study of the distribution of clusters in the nearby universe, which have provided powerful constraints on theories of galaxy formation. Many authors, however, have expressed concern over the Abell catalogue's completeness and reliability, as it was constructed from visual scans of the Palomar Sky Survey. Results obtained from the catalogue have been seriously undermined by the potential subjective errors and biases that may be within the catalogue. With the advent of large area automated galaxy catalogues, it is now possible to construct new objective cluster catalogues free of the problems that have plagued previous visually compiled cluster catalogues.

This chapter describes the construction of one of the first fully automated objective cluster catalogues, the Edinburgh/Durham Cluster Catalogue (EDCC). At the end of the chapter, a full comparison of the EDCC and the Abell catalogue is presented and used to assess the completeness of the respective catalogues. The full EDCC is presented in Appendix A.

3.1 Introduction

The work presented in this Chapter was carried out in collaboration with Dr. Stuart Lumsden and has been accepted for publication in the Monthly Notices of the Royal Astronomical Society. The purpose of this Chapter is to outline the methods used in detecting the clusters and is included in this thesis for completeness. For a more detailed explanation of the construction of the EDCC, the reader is referred to Lumsden *et al.* (1992). The main motivations behind the construction of this catalogue are summarised below:

- To present the community with an optical cluster catalogue covering a large area of the sky, that is free from the *eyeball* systematics that have plagued previous optical catalogues.
- To investigate and minimise the effects of projections, as discussed in Chapter 1.
- To use the catalogue to investigate the completeness and the potential systematic errors within the Abell catalogue, thus providing the first independent external check of this catalogue.
- To study the distribution of clusters in the nearby universe and place tighter constraints on models of galaxy formation.

3.2 Cluster Candidates

The EDCC was constructed from the Edinburgh/Durham Southern Galaxy Catalogue (EDSGC), which was described in detail in the Chapter 1. The objective nature of this catalogue made it an ideal database from which to build a new cluster catalogue. The galaxy data from the EDSGC was binned into equal area pixels on a true sky projection. This was performed three times to three different magnitude limits, $b_j = 18.5, 19.5$ and 20.5, which prevented a fixed pixel size imposing a preferential angular scale on the cluster detection and maximised the number of candidates found. The pixel sizes used for the three selections are shown in Table 3.1. In each case, the pixel size was chosen so that the mean number of galaxies per pixel was unity.

The three data arrays *i.e.* the three magnitude slices, were smoothed with a filter the same as that used by Shectman (1985) which has the weights

$\frac{1}{16}$	$\frac{1}{8}$	$\frac{1}{16}$
$\frac{1}{8}$	$\frac{1}{4}$	$\frac{1}{8}$
$\frac{1}{16}$	$\frac{1}{8}$	$\frac{1}{16}$

where the number of galaxies in the central pixel of the filter is distributed as shown. The 'Shectman' filter is effectively a Gaussian filter and therefore, matches the cluster density profile well. This smoothing reduced the binning noise within the data arrays and ensured that a true galaxy overdensity was detected irrespective of where it fell within the original bin. To check the validity of this method and to check the effect of residual binning noise, the bin centres for the three data arrays were shifted by half a pixel and re–analysed. No significant differences were found in the candidates selected, thus indicating that the selection was insensitive to the exact form of the binning and smoothing. In addition, this argument is strengthened by the observed distribution of angular sizes of clusters in the final EDCC catalogue, as shown in Figure 3.1. The observed distribution shows that, on average, no preferred angular size of cluster was selected and it agrees well with the expected distribution of angular sizes for clusters selected using the standard Abell radius (Chapter 1, equation 1.12) with a number–magnitude relationship of slope 0.6.

Run	Mag. limit (b_j)	Binsize (arcminutes)	Threshold (galaxies/bin)	No. of cands.
1	18.5	8	$1.5\,(2.3\sigma, \sigma = 0.65)$	438
2	19.5	5	$2.5\,(3.9\sigma, \sigma = 0.64)$	491
3	20.5	3	$3\,(4.6\sigma, \sigma = 0.65)$	633

Table 3.1: Details of the three selection runs used in the construction of the EDCC.

The next step was to determine at what threshold, above the mean pixel level, should a galaxy density peak justify the tag of a candidate cluster. Two types of threshold were considered: *i)* a global threshold across the whole EDCC corresponding to a

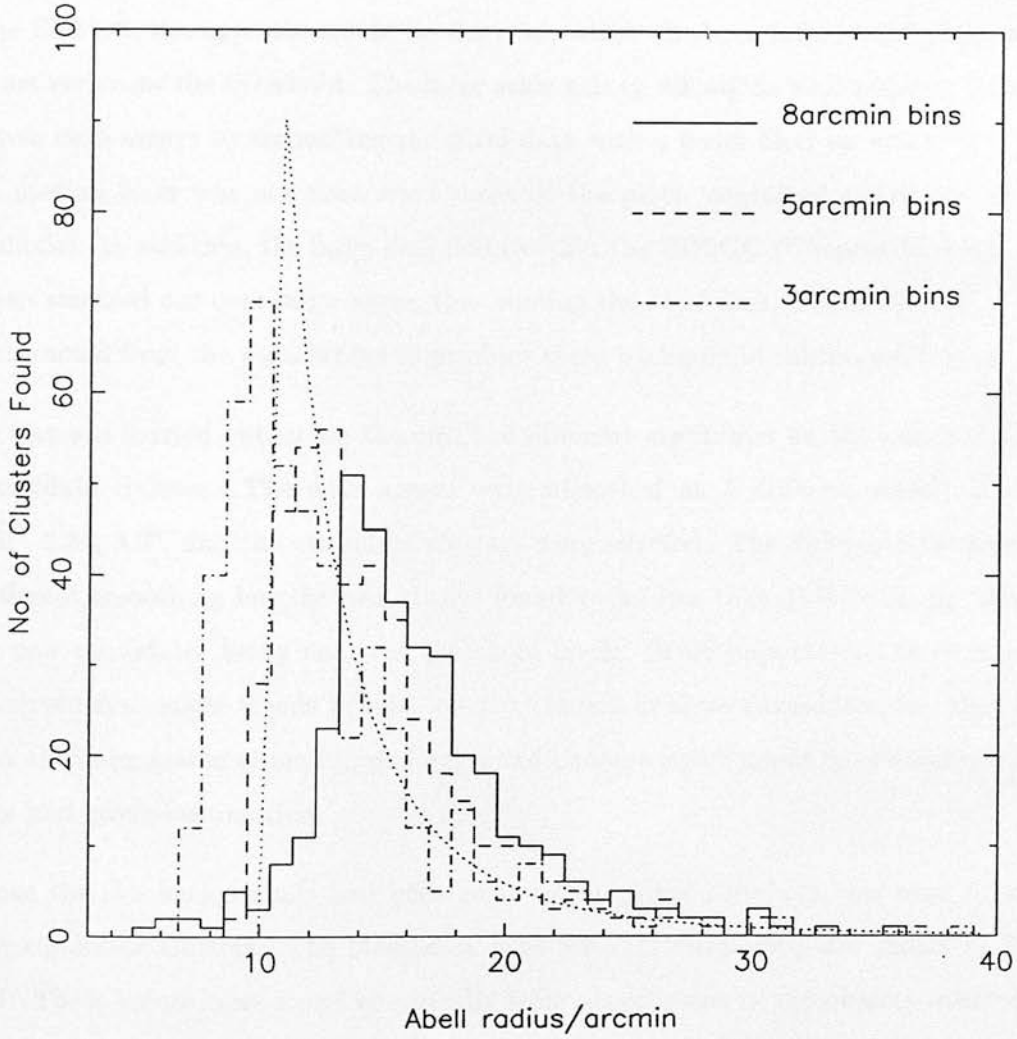

Figure 3.1: Comparison of the expected distribution of angular sizes of Abell–type clusters to that seen in the EDCC (dotted line). The 3 individual runs of the EDCC are shown separately. The expected distribution was computed using a number–magnitude relationship of slope 0.6.

DC level above the mean pixel values (Shectman 1985); *ii)* a local threshold which depended upon the large scale environment of the density peak (Dodd & MacGillivray 1986). The second of these was chosen, as it removed any environmental biases from the detection of the galaxy peaks. For example, a global threshold would have missed density peaks in and around large underdense regions of the catalogue because the base level of the peaks would already be far below the threshold. In high density regions of the EDSGC, the opposite would be the case, where the base level of the peaks would start very near the threshold. The large scale galaxy variations were removed from the three data arrays by smoothing the pixel data with a mean filter on scales of $\sim 1.5°$. A median filter was not used since most of the pixels contained either one or zero galaxies. In addition, the large drill holes within the EDSGC (Chapter 1) would have been smeared out over large areas, thus ruining the *sky* frame. These *sky* frames were subtracted from the data arrays to produce three background subtracted frames.

A test was carried out to see the effect of different *sky* frames on the selection of the candidate clusters. The data arrays were smoothed on 5 different scales; 1°, 1.5°, 2.0°, 2.5°, 3.0°, and the candidate clusters were selected. The difference between the different smoothing lengths was always found to be less than 10%, with the missing or new candidates being near the threshold levels. More importantly, there were no observed systematic trends behind the distribution of these candidates, *i.e.* they were not all concentrated around large foreground clusters which might have dominated the sky background estimation.

Once the sky backgrounds had been removed, a global threshold was used to select the candidate clusters. The thresholds used for each data array are shown in Table 3.1. These values were found empirically from visual scans of the objects selected for different threshold levels; the threshold with the highest fraction of true to spurious or 'noise' clusters was chosen. On average, for the accepted thresholds, only 5% of the objects selected were classified from visual inspections as 'noise' clusters. The COSMOS image analysing software (Thanisch *et al.* 1984, Beard *et al.* 1990) was then used to connect all pixels above the chosen thresholds in the three data arrays. This produced a list of candidate clusters for each data array, along with the pixels within those candidates which were used in the next stage of the selection.

Projection effects were discussed in Chapter 1 and clearly any new optical cluster catalogue must be constructed with these in mind. Therefore, to reduce the problem of overlapping cluster radii, the candidates in the three selections were deblended. This involved re–thresholding the pixel–data of a candidate cluster at 20 progressively higher thresholds above the background, in search of saddle–points. If one was found, the pixel data was split into two (or more) 'daughter' candidates, the boundaries of which were defined by fitting Gaussian profiles to the separate peaks. In total, $\sim 30\%$ of the candidates were deblended. This deblending was analogous to the standard image deblending carried out by COSMOS on merged objects. However, the EDCC deblender worked in density space, while the COSMOS deblender worked in log space (Beard *et al.* 1990).

In total, over the whole area of the EDSGC, 1562 candidate clusters were detected, while for the three individual runs; $b_j = 18.5$ produced 438, $b_j = 19.5$ 491 and $b_j = 20.5$ found 633 candidates. Obviously, there was considerable overlap between these candidates.

3.3 Abell Analysis

The candidate clusters selected above contained little information about galaxy over-densities they corresponded to. Therefore, they were analysed using similar criteria as those used by Abell, which were described in detail in Chapter 1. This also allowed for a fair comparison to be carried out between the EDCC and the Abell catalogue and presented the EDCC in a familiar framework.

All the galaxies within a candidate cluster's pixel data were extracted from the EDSGC and used to define the clusters centroid. From this galaxy listing, the magnitude of the tenth brightest galaxy (m_{10}) was found and the Abell radius calculated using equation 1.12 from the first Chapter. The value of m_{10} was corrected for background/foreground contamination using the number–magnitude relationship of galaxies in a $4^\circ \times 4^\circ$ area centred on the cluster. This relationship was used to compute the expected number of field galaxies within the Abell radius that would be brighter than m_{10}. These were then removed by counting further down the galaxy listing to m_{10+x}, where x was the number of contaminating galaxies. A new Abell radius was calculated and the whole

process was iterated until it converged, which was usually rapid ($\sim$ 3 iterations). The iteration process was stopped when the difference between the values of m_{10} in turns was within 1%. Clusters were removed from the catalogue for the following reasons: *i)* m_{10+x} lay below the EDSGC limit, *ii)* the centroid of the cluster moved by more than a quarter of the original Abell radius during iteration, *iii)* the process did not converge after 10 iterations.

It should be noted at this stage, that Abell did not systematically background correct his values of m_{10} by subjectively removed 'obvious' foreground galaxies. A correction was made to the final richness of the Abell clusters, using either a global luminosity function (Abell *et al.* 1989) or by examining a region of the plate devoid of clusters (Abell 1958). Neither of these two methods is satisfactory since the first was a global correction, which made no allowance for the local sky contamination, while the second systematically underestimated the contamination as, by definition, the area was free of clusters and/or galaxies.

The richness of a cluster was derived using the final value of the Abell radius and Abell's definition of richness *i.e.* the number of galaxies within the magnitude range m_3 to $m_3 + 2$. The final centroid of a cluster was then defined using all the galaxies in the cluster. Similar background corrections were made to both the value of m_3 and the richness using the number–magnitude relation calculated above. For each of the three runs a list of clusters, each with their coordinates, m_{10}, m_3, richness and Abell radius, was produced.

3.4 The Edinburgh/Durham Cluster Catalogue

The final catalogue of clusters was constructed from the three runs described above. As mentioned, there was considerable overlap between the clusters detected, as well as differences in the statistics assigned to these clusters. Therefore, all the clusters detected in total in the three runs were added together. This list was then searched for overlapping clusters *i.e.* if the centroid of a cluster was within another cluster's Abell radius. Clusters that did not overlap, were passed straight through into the final EDCC list. Overlapping clusters were flagged.

The background–subtracted magnitude distributions of the flagged clusters were compared using a two–sided Kolmogorov–Smirnov test (KS test). This checked, within a particular significance, if the two distributions were the same. The level of significance was determined by the respective separations of the two clusters; 10% if both the centroids WERE within the others Abell radii, 20% if only one centroid was within an Abell radius and 40% if the Abell radii just overlapped. This last requirement catered for the case where two clusters were connected by a common third cluster. These significances were determined empirically from visual inspections of the clusters before and after the test. It was found that if only one significance was used then either too few or too many blends were created depending upon the particular significance chosen. To check the robustness of these significances, a test was carried out on a typical EDCC cluster *i.e.* richness of 40, $m_{10}(b_j) = 18$. The cluster was shifted in m_{10} and richness and compared to its original self using the KS test. Only after a shift of 0.2 in m_{10} ($z \simeq 0.01$) or 60% in richness did the test fail at the 10% level. This indicated that substructure was unlikely to cause the KS test to fail and thus fragment the cluster. Clusters with less of an overlap required a smaller shift in m_{10} or richness to fail the KS test.

If the two clusters were found to have the same magnitude distribution, then their galaxies were added together and an Abell analysis was carried out on the single cluster. If the clusters failed the KS test, then they were seen as separate clusters and were passed through into the final EDCC listing. Once a final list of distinct clusters had been created, the question of projection effects had to be addressed once more. The list of clusters was again searched for overlaps and since the KS test had shown that they were separate clusters, deblending was applied to ensure that each galaxy was assigned to one cluster only. This deblending was only carried out for the galaxies in the overlap region. A Gaussian profile was fitted to the two (or more) clusters and the galaxies were assigned to the cluster with the largest Gaussian amplitude at its location. Once all the galaxies had been assigned, the individual cluster statistics (richness, m_3, m_{10}) were recalculated.

Overall, 769 clusters were detected over the whole area of the EDSGC, 255 of which were deblended in the final stages of the construction (33% of the clusters). The full EDCC list is presented in Appendix A. All the clusters detected are within this list,

no cut in richness or distance (m_{10}) is imposed as the catalogue is based around the location of local peaks in the galaxy density. The following information for each cluster is presented in Appendix A:

- Right Ascension and Declination (Epoch 1950).
- The magnitude of the first, third and tenth brightest galaxy in the cluster.
- The richness of the cluster as defined by Abell, *i.e.* within the magnitude strip of m_3 to $m_3 + 2$. The background contamination count is also presented.
- The Abell radius in degrees, which was also used in the estimation of the cluster's richness.
- The number of the UK Schmidt survey field the cluster was detected on.
- Whether the cluster was deblended in the final stages of the construction of the EDCC.
- Any match–up with the Abell catalogue.

It is worth noting that all the 769 clusters were visually checked by Dr. Lumsden, Dr. Collins and myself. Only clear errors in the cluster catalogue were removed from the main catalogue and have been placed in a separate table in Appendix A (32 clusters). The errors were usually bright nearby stars or galaxies that had been deblended into a cluster of small images, satellite trails or diffraction spikes. This left 737 real galaxy overdensities. In addition, possible errors in the statistics of these clusters were recorded during the visual checks and these have been highlighted in the final list. Obviously, these may be highly subjective estimates and should be treated with caution.

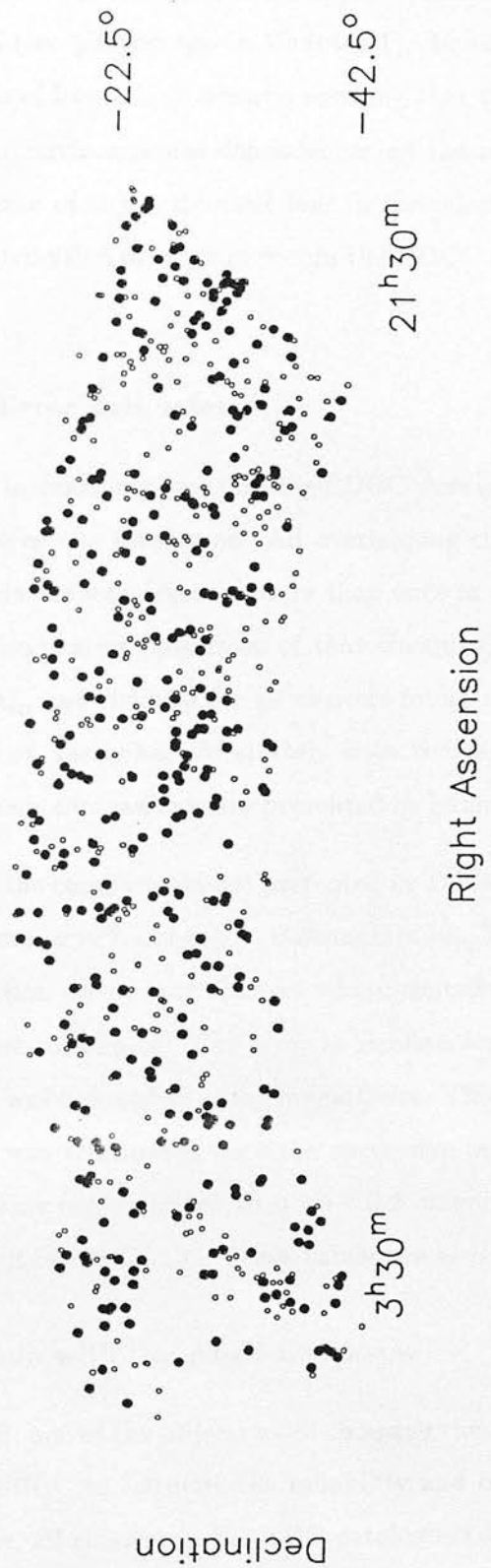

Figure 3.2: The sky distribution of all the EDCC clusters. The • symbols represent clusters with greater than 30 members, while the ◦ symbols represent clusters with less than 30 members. The coordinate limits of the EDCC are marked.

Figure 3.2 shows all the EDCC clusters in projection, which follows the galaxy distribution very well (see photograph in Chapter 1). In addition, clusters were evidently detected in areas of low galaxy density, showing that the sky background subtraction helped to remove environmental dependences on the selection of the clusters. There is no clear evidence of any systematic bias in the selection of the clusters. Chapter 5 discusses the distribution of clusters within the EDCC and the reader is referred there for more detail.

3.5 Internal Error Estimates

Estimates of the internal errors within the EDCC were obtained from the clusters found in common between the three runs. All overlapping clusters that passed the KS test were used. If a cluster was detected more than once in a single run and/or in different runs, then the two nearest detections of that cluster were used. Figure 3.3 shows the comparison of m_{10} and richness for all clusters found in common. A comparison was also carried out on the subset of clusters with richness greater than 30. The main conclusions of these comparisons are presented in Lumsden *et al.* (1992).

The statistics of the comparisons are presented in Table 3.2, but the scatter in richness for all the clusters is $\sigma \sim 7$ and $m_{10} \sim 0.2$ magnitudes. To estimate the minimum error, or intrinsic selection error, only clusters whose centroids were separated by less than 2 arcminutes were considered. The error in richness was reduced to ~ 5 galaxies and the error in m_{10} was reduced to ~ 0.1 magnitudes. This error was due to the iteration procedure, as it was terminated once the successive magnitude iterations had agreed to within 1%. This corresponded to $0.1 \rightarrow 0.2$ magnitudes for a typical m_{10} at the completeness limit of the EDCC. These values are also shown in Table 3.2.

3.6 Comparison with the Abell Catalogue

As already stated, one of the objectives of choosing the Abell classification of a cluster, was to use the EDCC to estimate the reliability and completeness of the Abell catalogues. Therefore, all clusters in the ACO catalogue (Abell *et al.* 1989), the northern Abell catalogue (Abell 1958) and the Abell supplementary catalogue (Abell *et al.* 1989), that were within the EDCC area, were extracted. Clusters within 20 arcminutes of the

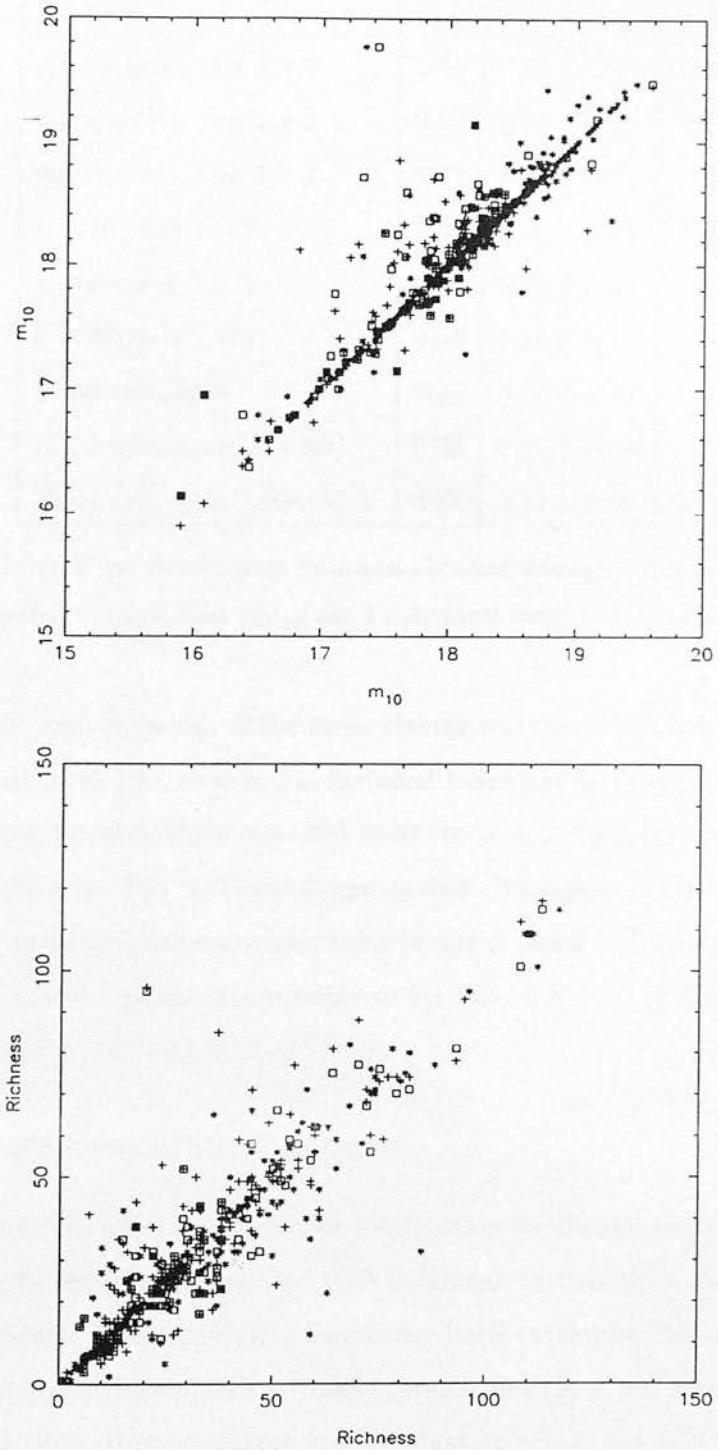

Figure 3.3: Scatter plots showing the comparison in m_{10} (top) and Richness (bottom) for the three individual EDCC selection runs. All the EDCC clusters are plotted. The symbols are; + for run 1 against run 2, □ for run 1 against run 3 and ∗ for run 2 against run 3. The lower numbered run is always plotted on the x–axis.

Sample	σ_{m1}	σ_{m3}	σ_{m10}	σ_{counts}
All clusters: run 1 v 2	0.54	0.36	0.24	10.4
All clusters: run 1 v 3	0.52	0.31	0.34	9.2
All clusters: run 2 v 3	0.42	0.31	0.26	9.5
$r > 30$: run 1 v 2	0.57	0.24	0.15	10.4
$r > 30$: run 1 v 3	0.60	0.24	0.19	8.2
$r > 30$: run 2 v 3	0.46	0.16	0.15	9.5
Final catalogue	0.34	0.23	0.18	6.9
Final catalogue: $r > 30$	0.38	0.15	0.15	6.5
Final catalogue: offset $< 2'$	0.32	0.14	0.08	4.6

Table 3.2: Table of the various error estimates obtained from the comparison of the statistics of clusters detected in more than one of the 3 individual runs. r is the richness of the cluster.

boundary were also included. If the same cluster was found in both the ACO and the northern Abell catalogue, then it was included twice and both detections were used in the comparison. In total, there were 339 ACO clusters, 228 Supplementary clusters and 87 northern clusters. The ACO catalogue quoted all magnitudes in the V band, while the northern catalogue quoted magnitudes in the R band. The following conversions were used to convert all the magnitudes to b_j; *i)* $b_j - V = 0.77$ (Heydon-Dumbleton 1989), *ii)* $b_j - R = 1.07$ (Abell *et al.* 1989).

3.6.1 Completeness of the Catalogues

Figure 3.4 shows the number–magnitude relationship for clusters with a richness greater than 30 in both the EDCC and the ACO catalogue as described above (transformed to b_j magnitudes). The cumulative counts for both catalogues are also plotted. The EDCC appears to be incomplete at bright magnitudes ($b_j < 16$) when compared with the ACO catalogue. However, there are few clusters within the EDCC area that have an m_{10} brighter than this value. Using the ACO catalogue, the EDCC was only missing three bright clusters. On examining these clusters, one was in a drilled region (Chapter 1) and the other two had been deblended. It was difficult to prevent the software from

deblending these clusters, as they had such large Abell radii (1.0 $\rightarrow$ 0.5 degrees) and overlapped many other clusters.

The fit to the slope of the EDCC number–magnitude relationship was 0.65, but values of 0.55 and 0.75 could not be ruled out because of the incompleteness at bright magnitudes. However, if the ACO catalogue was assumed to be complete at these magnitudes and was used to correct the EDCC counts, then the fit to the slope of the number counts was 0.65 ± 0.05. This is encouraging as it is close to the expected slope for a homogeneous distribution at low redshifts with minimal curvature or K – correlations. The completeness limit of the EDCC was estimated as $b_j = 18.75$, where number–magnitude relation of the clusters starts to decline. This is expected since the definition of richness $(m_3 + 2)$ begins to reach the limit of the EDSGC. The Abell catalogue appears to be complete to the same magnitude limit, yet this makes no account of the subjective nature of its construction.

Figure 3.5 shows the number–richness relationship for the EDCC and the ACO clusters in the EDCC area (above). The EDCC is complete at all richnesses compared to the ACO catalogue, which appears to be incomplete for richnesses of less than 40. This could be due to two factors; either they systematically overestimated their richnesses or they were insensitive to such low richness systems. Also evident in Figure 3.5 is a global offset between the two catalogues which again suggests that the Abell richnesses are over–estimated compared to the EDCC richnesses.

3.6.2 Comparison of the Catalogues

One of the major differences between the EDCC and the Abell catalogue was in the method used to estimate the background contamination of a cluster. As stated, in the northern catalogue, a region devoid of clusters was chosen, while in the ACO catalogue, the Rainey (1977) luminosity function was used. For the EDCC, the background was estimated from a $4^\circ \times 4^\circ$ area around the cluster. Using the prescription described by ACO, the original galaxy count (cluster plus background) was reconstructed for each Abell cluster and the data from the EDSGC used to estimate its background. This background was then subtracted from the Abell cluster to give it a new Abell richness,

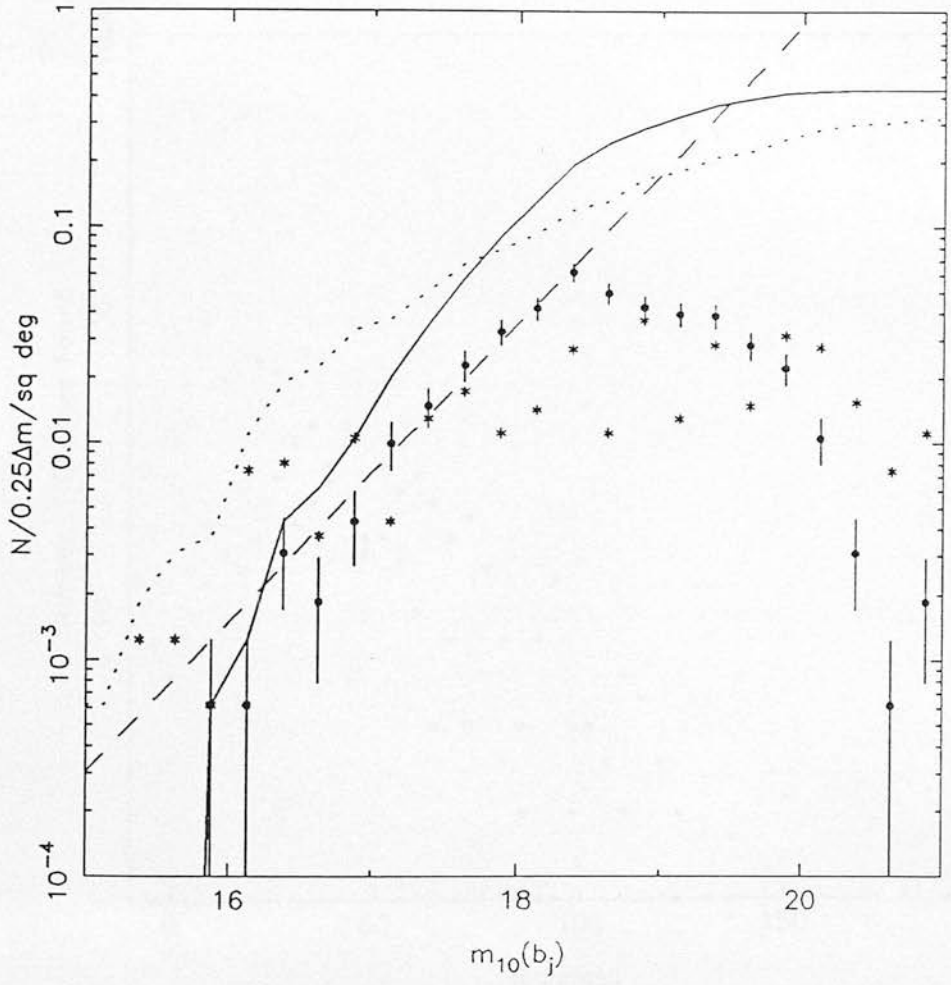

Figure 3.4: The number–magnitude counts for the EDCC and ACO catalogue in the EDCC area (see text). The symbol • represents the EDCC differential counts, while the symbol $*$ are the Abell differential counts. The solid and dotted lines are the respective cumulative counts. The dashed line is a fit to the EDCC data between $15.9 < b_j < 18.9$ with a slope of 0.65 ± 0.05. Poissonian error bars are plotted

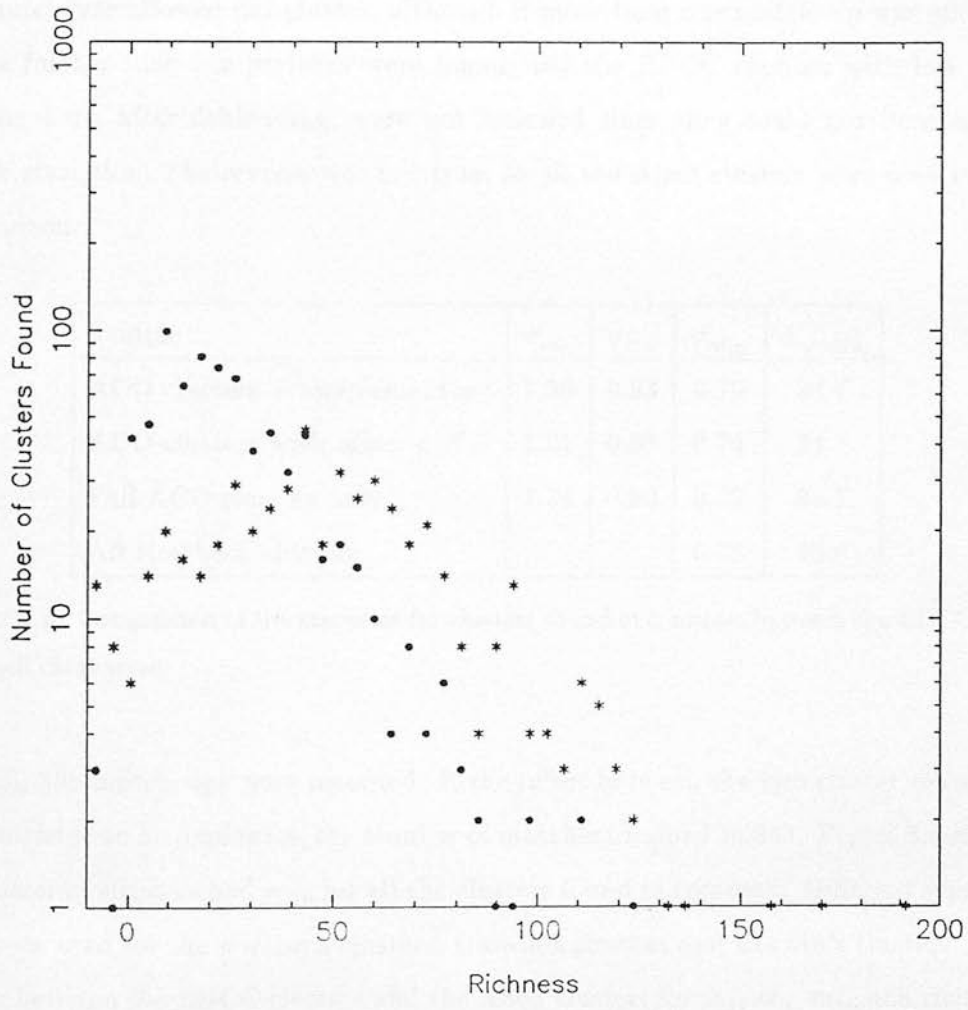

Figure 3.5: The number–richness counts for the EDCC and ACO clusters in the EDCC area. The same symbols are plotted as in Figure 3.4

similarly defined to that of the EDCC. The original Abell richness was used for the clusters that were within 20 arcminutes of the boundary.

A match–up between any Abell cluster and an EDCC cluster was defined as follows: *i)* both centroids of the clusters had to lie within the others' cluster radius; *ii)* only one match was allowed per cluster, although if more than one match–up was allowed, only a further nine comparisons were found; *iii)* the EDCC clusters with less than ten members, after deblending, were not included since they could not be assigned cluster statistics. The reverse was not true, so all the Abell clusters were used in the comparison.

Sample	σ_{m_1}	σ_{m_3}	$\sigma_{m_{10}}$	σ_{counts}
ACO clusters + supplementary	1.30	0.93	0.79	34.7
ACO clusters with offset $< 5'$	1.21	0.88	0.74	34.4
Full ACO clusters only	1.34	0.90	0.72	36.7
All Northern clusters			0.78	40.4

Table 3.3: Comparison of the statistics for clusters found in common between the EDCC and the Abell catalogues.

In total, 308 match–ups were recorded. If the offset between the two cluster centroids was restricted to 5 arcminutes, the number of matches dropped to 243. Figure 3.6 shows the scatter in richness and m_{10} for all the clusters found in common. Different symbols have been used for the northern clusters, Olowin's clusters and Corwin's clusters. The scatter between the EDCC clusters and the Abell clusters for m_1, m_3, m_{10} and richness are shown in Table 3.3. The general findings of these comparisons are detailed below:

- For all the clusters, the scatters were $m_1 \sim 1.3$ mags, $m_3 \sim 0.93$ mags, $m_{10} \sim 0.79$ mags and in the counts ~ 35. These did not change significantly if the comparison was restricted to clusters with an offset of less than 5 arcminutes or if individual comparisons were carried out on the two separate Abell catalogues.

- No correlation was seen between the richnesses of the clusters in common, although there was a general trend for the Abell clusters to have a higher richness

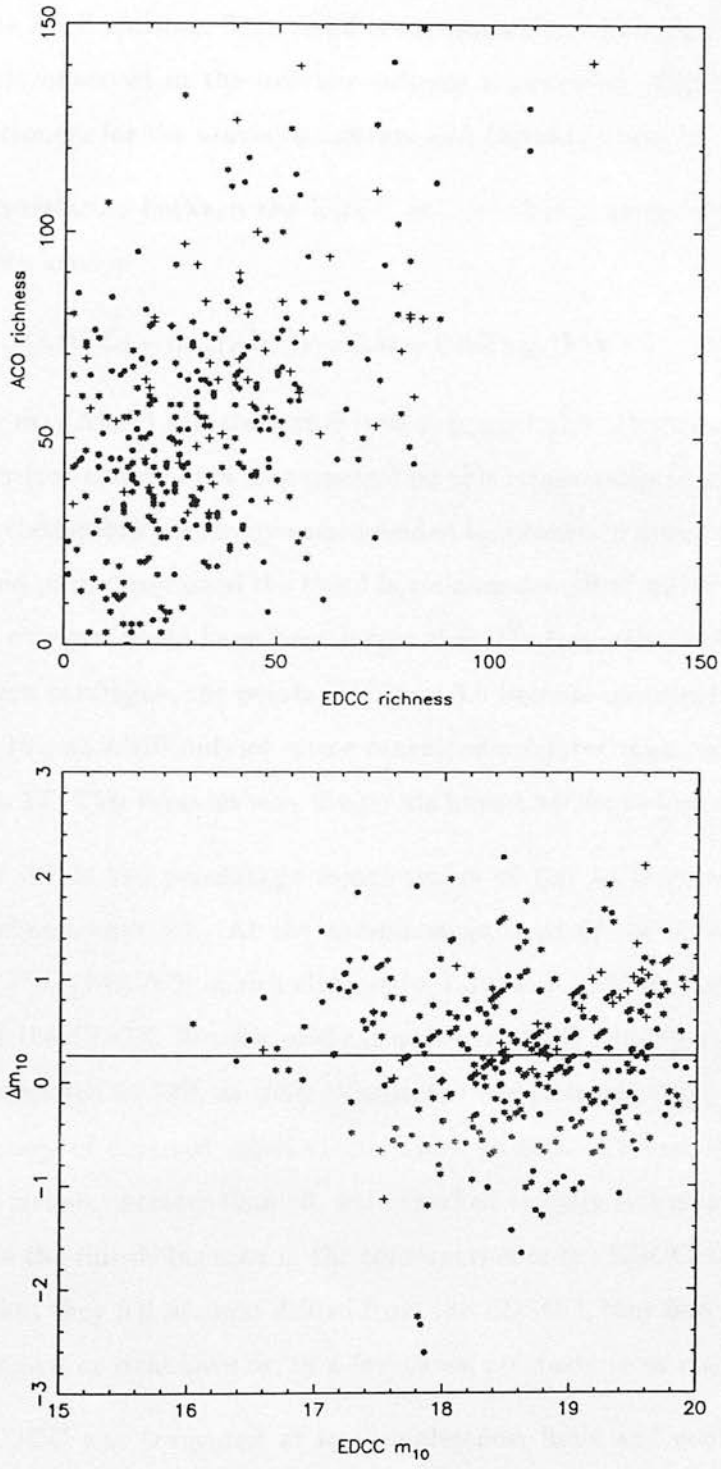

Figure 3.6: The top plot shows the comparison of the richnesses for all the clusters found in common between the Abell catalogue and the EDCC. The different symbols are; • for Corwins cluster's, $*$ for Olowin's clusters and $+$ for the northern Abell clusters. The bottom plot is similar to the top plot, but for the comparison of m_{10}. All magnitudes were converted to b_j.

by $\sim 30\%$. This was still seen if the original background corrections were used for the Abell clusters. This trend could explain the discrepancy of lower richness clusters observed in the number–richness relationship (Figure 3.5). The trend was stronger for the northern clusters and Corwin's clusters.

- The correlation between the EDCC and Abell m_{10} values was characterised by the relationship

$$m_{10}(\mathrm{EDCC}) - m_{10}(\mathrm{Abell}) = 0.31 + 0.03(m_{10}(\mathrm{EDCC}) - 18), \qquad (3.11)$$

where $m_{10}(\mathrm{Abell})$ was converted into b_j magnitudes. However, there was a large scatter (see above ~ 0.8 magnitudes) on this relationship as shown in Figure 3.6. This relationship effectively corresponded to a constant offset of 0.31 between the two and partly explained the trend in richness described above, as the radii of the Abell clusters would have been larger than the respective EDCC radii. For the northern catalogue, the points in Figure 3.6 become meaningless beyond $R \sim 17$ ($b_j \sim 18$), as Abell did not quote magnitudes fainter than this, setting them all to $R = 17$. This explains why the points have a 45° slope beyond this magnitude.

- Figure 3.7 is the percentage completeness of the ACO catalogue for 4 different richness cuts (c). At the completeness limit of the ACO catalogue ($b_j \simeq 17.75, V \sim 17.0$) 70% of rich clusters ($c > 30$) and 65% of all clusters were found within the EDCC. For the original northern Abell catalogue, the completeness was estimated at 70% as well. Within the completeness limit of the EDCC, the percentage of detected Abell clusters rose to 80%. The missing Abell clusters, with a richness greater than 30, were checked visually and most were found to be close to the thresholds used in the construction of the EDCC. Other explanations were that they fell in areas drilled from the EDSGC, they had grossly inaccurate magnitudes or richnesses or, in a few cases, no cluster was visible.

- The EDCC was truncated at its completeness limit and compared once again with the Abell catalogue. Only 42% of EDCC clusters were found. For EDCC clusters with a richness greater than 30, the number increased to 58%. These missing EDCC clusters were visually checked and most where found to be true overdensities.

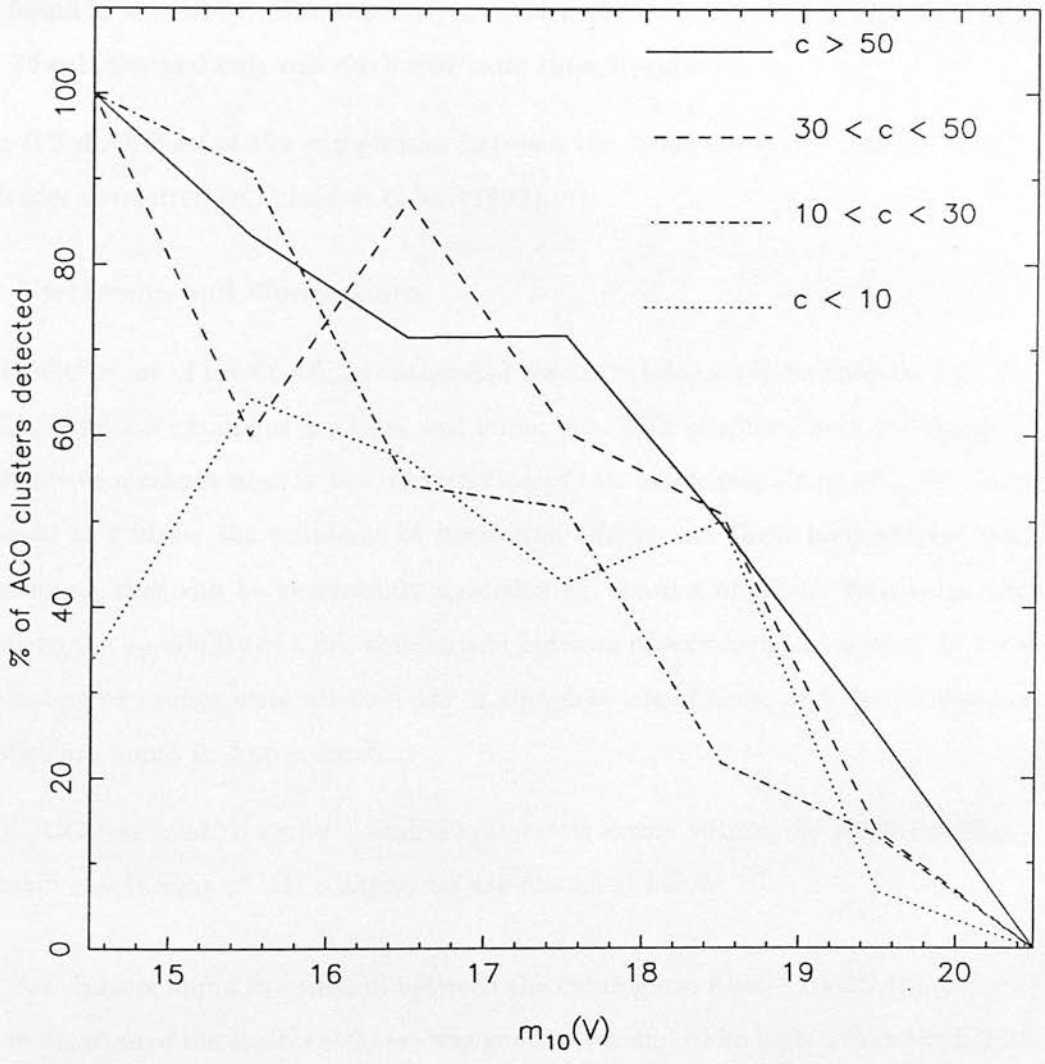

Figure 3.7: The detection rate of ACO clusters as a function of richness (c). The data has been binned with a binwidth of one magnitude.

Finally, a comparison was carried out between the EDCC and the Abell 'statistical' sample of clusters. This was defined in Chapter 1, but constituted all the high galactic latitude Abell clusters with a distance class $D \leq 4$ and richness class $RC \geq 1$ (50 galaxies). This sample has been the most frequently used set of Abell clusters for studies of the cluster distribution. All but 5 of the sample, within the EDCC area, were found in the EDCC. However, only one third of the clusters had a richness greater than 30 galaxies and only one sixth had more than 50 galaxies.

For a full discussion of the comparison between the Abell catalogue and the EDCC, the reader is referred to Lumsden *et al.* (1992).

3.7 Discussion and Conclusions

The EDCC is one of the first fully automated cluster catalogues to be constructed. The benefits of such a catalogue are clear and numerous. This chapter presented details on the objective methods used in the construction of this catalogue, along with the efforts employed to address the problems of projection effects. As these methods are well–documented, they can be successfully modelled by theories of galaxy formation, thus leading to the possibility of a fair comparison between observation and theory. In total, 737 clusters or groups were selected and a complete list of these and their individual statistics are found in Appendix A.

The EDCC was used to assess possible systematic errors within the Abell catalogue. The main conclusions of this comparison are discussed below:

1. For clusters found in common between the catalogues, Abell's (ACO & northern) estimation of the cluster richness was generally found to be higher than the EDCC estimation. It may be argued that this trend could be the result of several steps implemented during the construction of the EDCC. For example; the m_{10} magnitudes of the EDCC clusters were corrected for contamination, thus leading to preferentially fainter m_{10} magnitudes and smaller Abell radii; the methods used to correct the richnesses of the clusters for contamination were very dissimilar for all the catalogues; or the magnitude conversions used to correct all the magnitude to b_j could be in error. However, Scaramella *et al.* (1991) also concluded

that the ACO clusters were systematically richer compared to the Abell northern clusters, both in terms of individual clusters in common in the overlap region and in the percentage of clusters found in the high richness classes. In addition, ACO themselves show that there were large systematic differences between the richness estimates of clusters observed by all three observers. This is illustrated in Figure 3.6. This suggests that the Abell clusters are systematically richer compared to external estimates and that it is observer–dependent.

2. The Abell 'statistical' sample of clusters has been the most frequently used sample of Abell clusters because it is assumed to be the most robust. Struble & Rood (1991) carried out an extensive study of the internal errors within this sample and concluded that only two clusters of lower richness (< 50 galaxies) had been boosted into the whole sample. Moreover, they concluded that the individual cluster statistics were reliable. An external comparison of the EDCC with this sample showed that over two–thirds of the clusters had a richness of less than 30 galaxies, thus suggesting that the sample was not free of the errors detailed above.

3. The observed scatter in richness for clusters in common between the EDCC and Abell catalogues was found to be greater than 30 galaxies, irrespective of the sample used and its richness class. This error is almost twice the final standard deviation quoted by ACO, which was 18 galaxies for both the northern and southern catalogues. This observed scatter could easily move clusters across more than one richness class. In comparison, the EDCC internal richness error was found to be 7 galaxies.

4. Similar conclusions were obtained for the scatter seen in the magnitude estimates. ACO quoted an error of ~ 0.3 on their m_{10} values, while the comparison with the EDCC, suggested that the error was more than double this. Again, this could easily shift clusters across more than one distance class. The internal EDCC error on m_{10} was 0.18.

5. Finally, to the completeness limits of the EDCC and the Abell catalogue, 80% of the Abell clusters were detected. Assuming that 10% of the Abell clusters

were seriously in error in their classification (obtained from visual checks), the EDCC was 90% complete for Abell-type clusters. In comparison, nearly 60% of the EDCC clusters brighter than $m_{10}(b_j) = 18.5$ were new. These results are in direct conflict with the findings of Struble & Rood (1991) who estimated that the Abell catalogue was only missing 3% of existing rich clusters and consistent with the findings of Lucey (1983) who estimated, using simulations, that the percentage of missing rich clusters was 30%.

Clearly, the external checks detailed above indicate that the Abell catalogue is unsuitable for statistical studies of the large scale distribution of clusters. In contrast, the EDCC is statistically complete, but more importantly, the methods used in its construction are objective and therefore, can be reproduced exactly.

The main objective of this thesis was to study the distribution of clusters in the nearby universe. Sutherland (1988) has shown that our knowledge of this distribution may be seriously undermined by the uncertainties within the Abell catalogue. In Chapter 5, the distribution of clusters is investigated using the two–point spatial correlation function.

Chapter 4

The Edinburgh/Milano Cluster Redshift Survey

The Edinburgh/Milano cluster redshift survey (EM) was constructed over the last 5 years using clusters selected from the EDCC. The primary goal of this survey was to measure the cluster spatial correlation function free of the systematic errors that have plagued previous measures of this function (Chapter 1). The EM survey contains redshifts for $\sim$ 100 rich clusters, with an average of 10 galaxy redshifts measurements per cluster. This provides an unambiguous determination of the cluster redshift and can be used to estimate the frequency of cluster interlopers and phantom clusters. It will later be used to study the distribution of cluster velocity dispersions and the cluster luminosity function.

This chapter details the observations made during the construction of the EM survey and reviews the instruments used. A complete explanation of the data reduction methods are given, which includes a full discussion of the cross–correlation technique implemented in obtaining the galaxy redshifts. Finally, the chapter ends with a description of the objective criteria used in defining a cluster's redshift and an assessment of the frequency of interlopers and phantom clusters.

4.1 Introduction

The motivation behind the construction of the EM survey was to re–estimate the cluster spatial correlation function free from the criticisms that have been levelled at previous estimations in the literature. These criticisms have mainly been concerned with the quality of the original two–dimensional cluster catalogue used in their estimation. The most frequently used catalogue has been the Abell catalogue; problems regarding its reliability and completeness were detailed in Chapter 1 and Chapter 3. The EDCC is a new objective cluster catalogue, which clearly answers many of the aforementioned criticisms and is an ideal database from which to construct a new cluster redshift survey

A full discussion of projection effects was given in Chapter 1, but it would be beneficial to remind the reader here of its definition. Sutherland (1988) suggested that the richnesses of distant clusters, close on the sky to rich nearby cluster, were artificially boosted because of foreground contamination. This would result in many close angular pairs of clusters having very different redshifts and could explained the observed elongation in the redshift direction of ξ_{cc}. Combined with this proposed effect, is the problem of cluster interlopers and phantom clusters caused by the alignment, along the line–of–sight, of small groups of galaxies. The first of these points was addressed in the construction of the EDCC, as the deblending of the clusters should help in reducing the *Sutherland effect.* However, the other point can only be addressed by taking multiple redshift measurement towards the cores of the clusters. The majority of existing cluster redshift surveys are based mainly on one or two galaxy redshift measurements per cluster. For example, the two largest cluster redshift surveys to date, the APM (Dalton *et al.* 1992) and Postman Abell (Postman *et al.* 1992) surveys, contain significant fractions of single or double cluster redshift measurements. The APM survey contains $\sim$ 200 clusters, of which $\sim$ 70% are based on 1 or 2 galaxy redshifts; while for the Postman sample, the figure is $\sim$ 50%. As demonstrated at the end of this chapter, phantom clusters cannot be detected with so few redshifts, while for real clusters, there is a reasonable chance that the redshift of an interloper will be measured and assigned to the cluster.

Therefore, the strategy behind the construction of the EM survey was to measure,

on average, 10 galaxy redshifts per cluster towards the centres of the hundred richest clusters selected from the EDCC. The main motivations behind the survey were: *i)* to unambiguously determine the redshift of the cluster and estimate the true frequency of interlopers and phantom clusters; *ii)* to calculate ξ_{cc} from a robust, clean and objective sample of clusters; *iii)* to investigate the distribution of cluster velocity dispersions; *iv)* to study the luminosity function of clusters; *v)* finally, to investigate the reality of claimed cluster alignments (West *et al.* 1989).

This thesis is primarily concerned with the study of clustering of galaxies and clusters within the EDSGC and EM survey. The other topics will not be expanded on here. These studies are being carried out at the present time and will be published elsewhere.

4.2 The Sample

During the construction of the EM survey, two improvements were made to the selection of the clusters within the EDCC. The first was to correct the values of m_{10} and m_3 for background contamination and the second was to implement deblending of the candidate clusters and the final clusters. The result of these changes, and the continued improvement of the EDCC during the 5 years of the project, was that the priority of certain clusters within the EDCC changed. The consequence of this is that no richness–limited or magnitude–limited subsample of EDCC clusters has been completely observed.

The EM survey clusters corresponded to high galaxy density peaks seen at the initial candidate cluster selection stage (Chapter 3), but subsequent analysis of some of these peaks caused several of them to fall outside any statistically significant sample of clusters. However, at the end of this chapter, a selection of clusters is presented that represents a 90% complete sample of redshift measurements. In addition, this sample has been rigorously selected using a smaller than usual Abell radius (Chapter 3), making it ideal for examining the statistical distribution of rich clusters (Chapter 5).

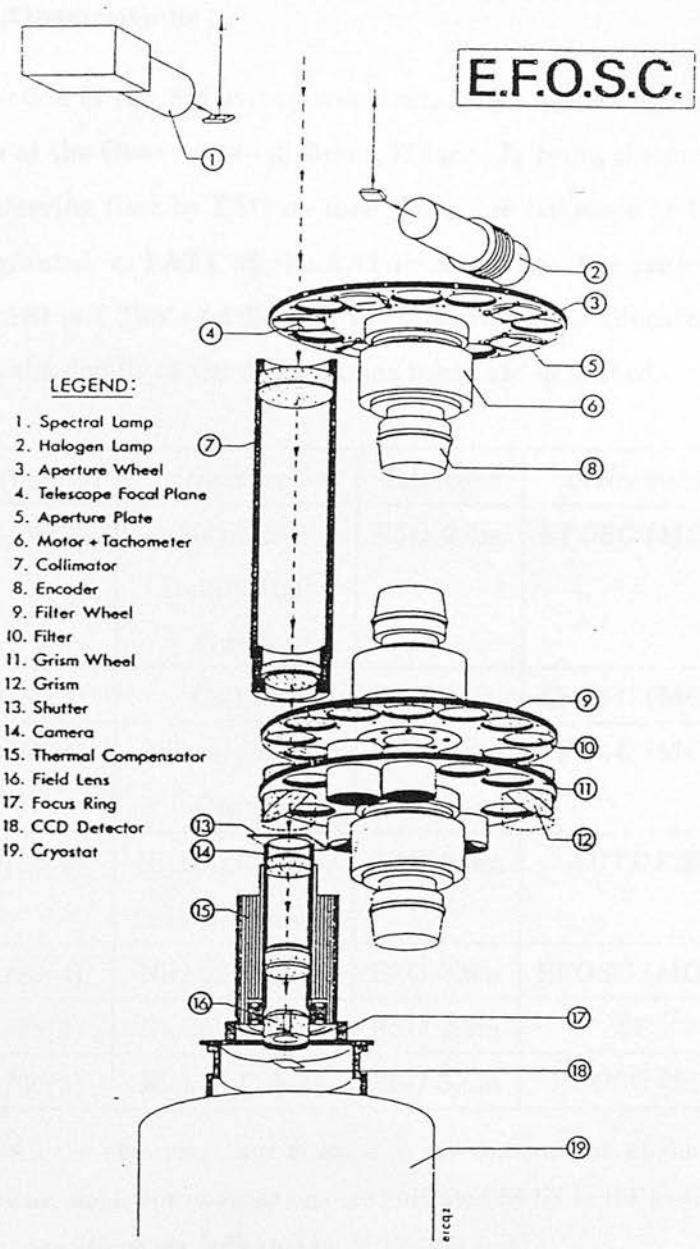

Figure 4.1: The optical and mechanical layout of the ESO Faint Object Spectrograph and Camera (EFOSC). The details of the instrument are described in the text. This illustration was taken from the EFOSC user manual written by Dekker and D'Odorico.

4.3 The Observations

The construction of the EM survey was started over 5 years ago in collaboration with Luigi Guzzo at the Osservatorio di Brera, Milano. In total, the project was granted 20 nights of observing time by ESO on their 3.6 metre telescope at La Silla, Chile and 6 nights was granted by PATT on the AAT in Australia. The project was completed in November 1990 and Table 4.1 lists all the observing time allocated to the project. In this section, the details of the observations taken are described.

Dates (nights)	Observers	Telescope	Instrument	Weather
06/08/88(3)	Heydon-Dumbleton, Guzzo	ESO 3.6m	EFOSC (MOS)	Clear
03/10/88(3)	Collins	ESO 3.6m	EFOSC (MOS)	Clear
05/08/89(4)	Nichol, Collins, Guzzo	ESO 3.6m	EFOSC (MOS)	Cloud on night 2.
01/10/89(6)	Nichol, Collins, Dalton, Maddox	AAT 3.9m	AUTOFIB	Bad weather
02/11/89(4)	Nichol, Collins	ESO 3.6m	EFOSC (MOS)	Clear
06/11/89(3)	Nichol, Collins	ESO 2.2m	SS	Cloudy
09/11/90(3)	Nichol, Collins	ESO 3.6m	EFOSC (SS)	Clear

Table 4.1: All the observing time devoted to the construction of the EM survey. For the ESO observations, single slit observations are indicated by SS in the instrument column, while multi-object observations are indicated by MOS (see text).

4.3.1 MOS with EFOSC

Over 70% of all the observations made in the construction of the EM survey were carried out using the ESO Faint Object Spectrograph and Camera (EFOSC) on the 3.6 metre telescope at La Silla. Figure 4.1 shows the general layout of EFOSC. Light entering the instrument, first passes through the aperture wheel which sits at the Cassegrain focus of the telescope. A collimator placed behind the wheel produces a beam of diameter

40mm which then passes through the filter and grism wheel respectively. An f/2.5 camera focuses the beam onto a thinned, back–illuminated RCA CCD chip of size 520×320 pixels. The pixel size is 30 μm which corresponds to 0.675 arcseconds on the sky.

The aperture wheel has 12 positions, 9 of which were free for the observer to use. EFOSC was mainly used in multi–object spectroscopic mode (MOS), which entailed producing masks of the clusters which were then inserted into these free positions (see below). The other 3 positions were kept constant and contained an empty position for direct imaging, a 1.0 arcsecond slit and a 1.5 arcsecond slit (3.6 arcminutes in length). The filter wheel contained all the standard Bessell and Gunn filters, but these were not used in any of the observations. The grism wheel held a variety of grisms, but the B300 grism was found to be best suited to our observations because it had a peak efficiency at 4400Å with a dispersion of 230Å per millimetre, which corresponded to a wavelength coverage of 3600Å $\rightarrow$ 7000Å with 6.4Å per pixel. This wavelength window was ideal suited to our galaxy observations, since a typical galaxy spectrum has many absorption and/or emission features in this range (Table 4.2). For example, elliptical galaxies usually have strong features at 3968Å and 3933Å (Calcium H & K), at 4000Å (break feature), at 4304Å (G band) and at 5175Å (Magnesium B band), while spiral galaxies often have strong emission lines of [O II] at 3727Å, Hβ at 4861Å and [O III] at 4958Å and 5007Å. At the typical redshift of the observed galaxies ($z < 0.2$), these features were not shifted out of the wavelength window. Another advantage of this window was that the sky emission was relatively low, containing few lines or features, so sky–subtraction was not crucial (Figure 3). Therefore, the B300 grism was used throughout the project. Finally, the RCA chip was cosmetically clean and had a relatively low read–out noise of 45 electrons per pixel. The peak quantum efficiency of the chip was at 4800Å and remained $> 60\%$ efficient over the observed wavelength range.

4.3.2 Observing with EFOSC

During all the observing runs, dome flats, halogen lamp flats and bias frames were taken at the beginning and the end of each night. Before and after each scientific observation, a Helium–Argon calibration arc was taken. The Helium arc was typically exposed for

Absorption						Emission	
λ_0	Line	Vis.	λ_0	Line	Vis.	λ_0	Line
3798.6	Hθ	3	4383.9	Fe	3	3727.3	[*O II*]
3835.6	Hη	3	4863.9	Hβ	2	4101.7	Hδ
3933.7	K	10	5175.3	MgI	5	4340.4	Hγ
3968.5	H	10	5168.6	MgI	5	4861.4	Hβ
4101.7	Hδ	2	5183.3	MgI	5	4958.9	[*O III*]
4226.7	CaI	2	5268.9	Ca+Fe	5	5006.8	[*O III*]
4304.4	G	5	5892.5	Na	7	6562.8	Hα

Table 4.2: The major emission and absorption features seen in a typical galaxy spectrum. In the table, λ_o is the rest wavelength in Angstroms and Vis. is the relative visibility of the line. Note: H & K refer to Calcium transitions and G refers to a blend of 3 lines caused by various CH molecular transitions. For a complete list of galaxy spectral features the reader is referred to Corwin & Emerson (1982) and Costero & Osterbrook (1977).

30 seconds and the Argon arc for 120 seconds (these values varied slightly between runs). This gave many calibration lines throughout the whole wavelength window.

Using EFOSC in MOS mode, masks of the candidate clusters had to be made to place in the aperture wheel. This was achieved by spending the first night of each run imaging all the candidate clusters. These images were later used in the construction of the masks, so time was invested in maximising the number of galaxies within each image. The position of the image (and therefore mask) within the cluster radius was chosen beforehand from visual inspections of Schmidt plates and usually coincided with the centre of the cluster. During the following days, these images were analysed using dedicated software at the telescope. Slits 2 arcsecond in width and $5 - 15$ arcseconds in length were placed on the galaxies seen within the image. The choice of galaxies to observe was dictated by an attempt to cover a wide range of apparent magnitude (without going too faint and increasing the integration time), their position within the image and the possibility of placing a sky slit near the object. Once the image had been processed, the slit positions were down–loaded to a punching machine which produced

the masks.

On average, each mask contained 10 object slits and 10 sky slits, with a maximum of 20 for A2755. Care was taken to ensure that these slits did not overlap when dispersed. Clearly, the wavelength coverage of each spectrum depended upon the position of its slit within the mask. For example, slits near the top of the mask (high y coordinate) had the red end of their spectrum clipped as it fell outside the chip, and vice versa for slits near the bottom of the mask. The arc calibration and flat–field frames were taken through the same masks. Figure 4.2 shows a typical example of a MOS exposure.

Before twilight each day, the masks required that night were loaded into the aperture wheel and imaged using a Halogen lamp. During the night, the telescope was slewed to exactly the same position WHERE the image was taken (these positions were carefully recorded when the image was taken) and a quick direct image was taken. Using dedicated software, this image and the image of the mask taken at the start of the night were compared and small telescope offsets WERE obtained which perfectly aligned the mask. Once aligned, a spectroscopic exposure was taken. On most nights a bright spectroscopic velocity standard (galaxies whose redshifts were measured from 21cm observations or radial standards from the Astronomical Almanac) was taken and overall 17 such standards were observed.

EFOSC + MOS proved to be a highly successful instrument, with an average of 8 clusters observed per night. The final run on the 3.6m telescope was devoted to single slit observations, as this increased the total number of clusters observed, but decreased the number of galaxy redshifts per cluster. This did not compromise our observing strategy of detecting possible projection effects, as an average of 5 galaxies per cluster were still measured.

4.3.3 The ESO 2.2m Telescope

Four nights in November 1989 were granted by ESO to start a galaxy redshift survey constructed from the EDSGC. This project was terminated before the run because of the lack of manpower and the significant advantages other groups had in terms of telescope time already granted. In addition, such a large project was better suited to

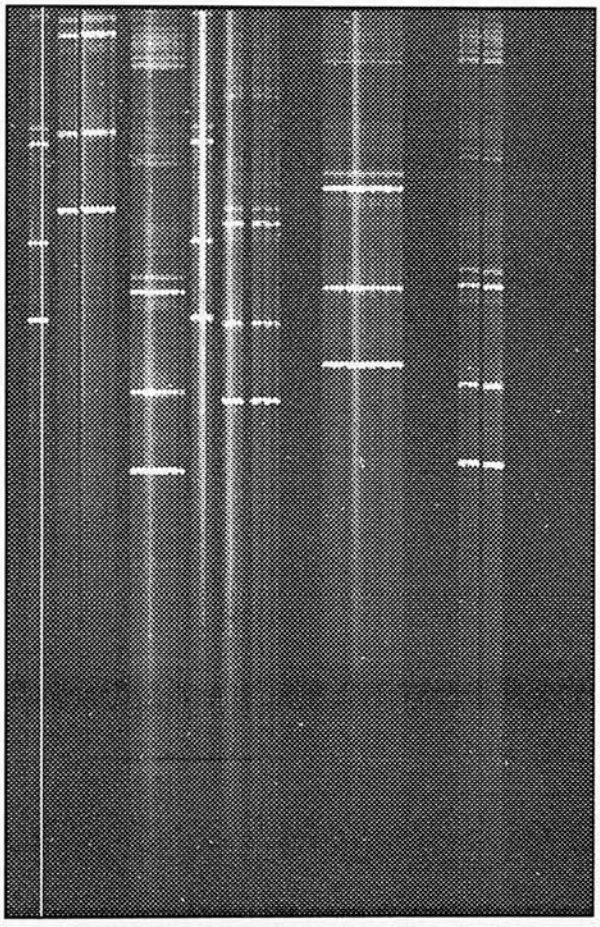

Figure 4.2: A MOS exposure taken of cluster 732. The shifts in the dispersion direction described in the text can be easily seen.

the automated multi–fibre systems that, at the time, were planned but not available. Only in the past 2 years, have such systems become available on large telescopes. The EDSGC is at present supporting three such galaxy redshift surveys (Chapter 6).

Therefore, the time allocated was used for the EM survey, yet most of the run was affected by bad weather which constrained the observations to very bright galaxies within the clusters. Many of the galaxies observed were the brightest cluster member and had been observed previously, but the choice of candidate galaxies was dictated by the weather and their zenith angle.

The Boller & Chivens Spectrograph was used in conjunction with a 2 arcsecond slit which gave a spectral coverage of $3000\mathring{A} \rightarrow 9000\mathring{A}$ with a resolution of $10\mathring{A}$ per pixel (grating 13). An RCA CCD was used (662×1024 pixels) binned 3×1 in the spatial and dispersion direction respectively. The usual flats and biases were taken and a Helium–Argon calibration was taken before and after each observation.

4.3.4 AUTOFIB on the Anglo–Australian Telescope

One allocation of AAT time was awarded to this project in collaboration with the APM group (Maddox *et al.* 1990). Six nights in October 1990 were shared equally between the two groups. The instrument used for the observations was AUTOFIB, which is a multi–fibre system developed jointly between the Anglo–Australian Observatory and Durham University. AUTOFIB consists of 60 user fibres that are automatically positioned by robot arms. The whole instrument sits at the Cassegrain focus of the 3.9m Anglo–Australian Telescope and has a circular areal coverage of 40 arcminutes in diameter. The telescope is guided using 6 special fibre bundles which are usually placed on nearby stars.

The object fibres are fed into the RGO Spectrograph through a special slit and arranged in a line 33.5 millimetres in length. The light from these fibres is transmitted directly into an f/6 collimator which is blazed to the grating. During the 6 night run, several different combinations of the grating angle, grating and detector were used to find the most efficient combination in terms of wavelength coverage and throughput. The best combination was found to be the 600V grating in conjunction with the IPCS. Table 4.3

summarises the detectors and the instrument details used during the whole run.

Night	Grating	Grating angle	Wavelength coverage	detector	Seeing
		Degrees	Angstroms		Arcseconds
01/10/89	250B	23.67 23.86	3700 – 5500 3550 – 5350	GEC CCD	2.0 → 10.0
02/10/89	250B	23.67 23.01	3700 – 5500 3900 – 5800	GEC CCD	∼ 2.5
03/10/89	250B	23.55	3700 – 5500	GEC CCD	∼ 1.5
04/10/89	600V	18.39	3800 – 5600	IPCS	∼ 2.0
05/10/89	600V	18.39	3800 – 5600	IPCS	1.5 → 3.0
06/10/89	600V	18.39	3800 – 5600	IPCS	1.5 → 4.0

Table 4.3: Details of the AAT instrument set–ups used during the 6 night run in October 1989. The GEC detector size was 584 × 386 pixels. Due to the fibres, the IPCS was constrained to 1024 × 480 lines.

4.3.5 Observing with AUTOFIB

Before observing, each cluster field had to be configured. This was achieved using dedicated software at the telescope which read in the coordinates of all the target galaxies in the cluster and allowed the observer to interactively place the fibres on the required galaxies. The positions of the target galaxies were taken from the EDSGC, since their positional accuracy was a few tenths of an arcsecond, while the fibres were 2 arcsecond in diameter. One of the main advantages of AUTOFIB was its large field–

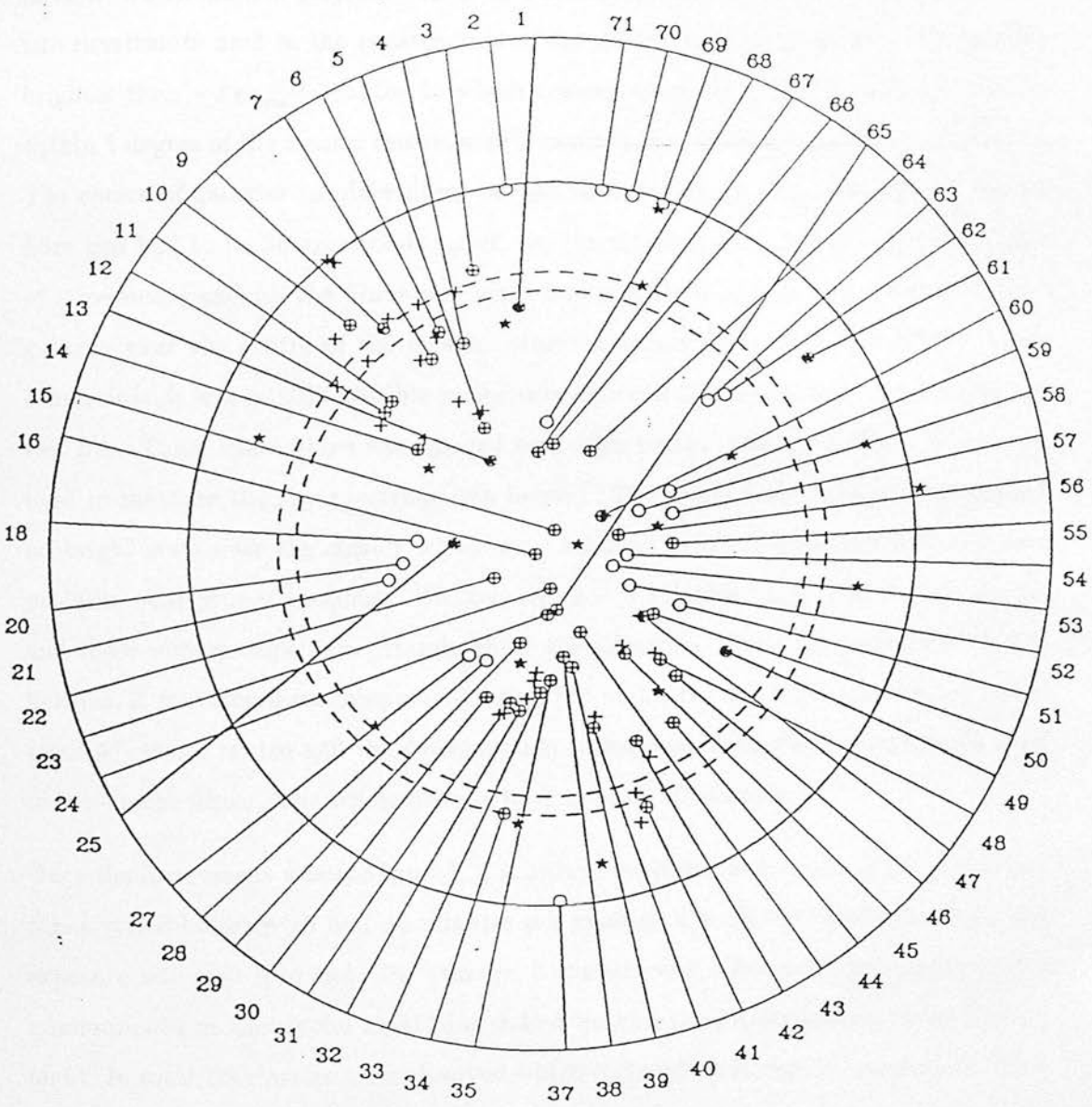

Figure 4.3: A typical AUTOFIB configuration taken from Glazebrook (1991). Although this configuration does not represent one of the EM survey cluster observations, it does illustrate some of the constraints imposed during the positioning of the fibres. Crosses indicate the target objects and stars indicate possible guide stars in the field. Thin lines represent the object fibres, while thicker lines represent the special fibre bundles used for guiding the telescope. The dotted lines show the position of a metal plate which the fibres rest on.

of-view, which allowed galaxies well away from the cluster centre to be observed. The two constraints used in the construction of the galaxy target list were; *i)* all galaxies brighter than $-3\,m_{cos}$ (Chapter 1) which corresponded to $b_j \simeq 19$, and *ii)* galaxies within 1 degree of the cluster centre, which resulted in ~ 80 target galaxies per cluster. The choice of galaxies to place fibres on was dictated by; *i)* their magnitude, *ii)* the fibre tips had to be 30 arcseconds apart, *iii)* the robot arms only had a limited range of movements and *iv)* the fibres and arms had restricted crossover positions. Bright galaxies near the centre of the cluster were obviously given priority. Within these constraints, it was usually possible to position between $30-40$ of the fibres, leaving the rest free. These spare fibres were placed near high concentrations of object fibres and used to measure the sky spectrum (see below). The guide fibre bundles were placed on bright stars near the cluster which were selected from CHART and had accurate positions and proper motions. On average, $2-3$ suitable stars were found nearby and these were enough to accurately guide the telescope. Once the configuration was finished, it was stored on computer. During the night, the telescope was slewed to the required cluster centre and the configuration called back from the computer and used to set–up the fibres. The whole process took around 15 minutes.

Once the instrument was configured, a scientific exposure was taken. The integration times varied between 15 and 30 minutes per cluster. For the CCD observations, the exposure was split into two. On average, 5 clusters were observed each night, with a minimum of 3 on the second night (due to bad weather) and a maximum of 8 on the last night. In total, 29 clusters were observed which included 4 clusters in common between the EM survey and the APM, 12 EM survey clusters and 13 APM clusters. Most of the APM clusters were outside the area of the EM survey and will not be discussed in this thesis, although the data has been reduced. The standard bias frames (CCD) and flat–fields were taken at the beginning and end of each night. Also, a variety of sky frames and twilight sky frames were taken, with the fibres configured in a circle or configured as though observing a cluster. For each scientific exposure, a 200 second calibration arc (copper, iron and argon) was taken before and after. Finally, most nights a radial velocity standard star was observed through several of the fibres to use as a template in the cross–correlation technique described below.

4.4 Data Reduction

In this section, the techniques used to reduce all the telescope data to one–dimensional, wavelength calibrated spectra are detailed. The ESO data was reduced by Luigi Guzzo, while the AUTOFIB data was reduced by myself. Therefore, only a summary of the ESO data reduction is presented at the end of this section. The data reduction software package FIGARO was used extensively throughout the reduction of the AUTOFIB data, but several new programs had to be written as AUTOFIB was, at that time, a relatively new instrument. These new programs are described where necessary, while existing FIGARO programs are highlighted in capital letters.

4.4.1 AUTOFIB Data

Table 4.3 shows that the 6 nights awarded to the project were split equally between the IPCS and the GEC CCD detectors. In this section, the two detectors are discussed simultaneously.

4.4.2 Bias Subtraction and Flat–Fielding

For the CCD observations, the bias frames taken at the beginning and end of each night were examined together. It was found that the bias level remained constant throughout the whole run, with no gradients across the chip. A typical bias frame contained 80 ± 2 counts and was completely flat with no signs of major chip defects. Therefore, the bias frames were not subtracted since we were only interested in detecting galaxy absorption or emission features in the spectra and uninterested in the absolute flux calibration of the spectra. The subtraction of the bias frames would have only introduced random noise which could have hindered the detection of the spectral features.

Once the spectral response of the lamp had been removed from the flat–fields, they were found to be very smooth with $\sim$ 1% pixel–to–pixel variations. Again, since absolute flux calibration was not required, it was decided that dividing through by the flat–fields would have just added in random noise. Therefore, neither the CCD or IPCS data were flat–fielded. This was consistent with the findings of Nicholson (1991), who found $\sim$ 2% flat–field variations for the same AAT IPCS detector.

4.4.3 Cleaning and Extraction

Cosmic ray cleaning was only carried out on the CCD data. For each object, the CCD data was usually split into 2 separate integrations, which decreased the number of cosmic ray events per data frame and, in principle, could have been compared to remove these events. This proved impractical for only 2 frames per object and each frame was cleaned interactively using CLEAN.

Each data frame contained between 55 and 60 fibres depending upon the detector used. The fibre spectra were extracted from the data frame using FINDSP and POLEXT. These programs had been specifically written to optimally extract AUTOFIB fibres from the data frames and were extremely user–friendly. They accounted for any curvature effects or distortions in the dispersion direction (x–direction) by fitting an n^{th} order polynomial. The fibre positions were found to be very stable throughout the night, so a single frame was used to find the spectra and its fit was then used to extract the fibres from all the other data frames taken that night. Usually the twilight sky data frame was used since it had the highest signal–to–noise spectra and all the fibres were visible. The final product of the extraction was a reduced data frame, within which each x row corresponded to a separate extracted fibre. For the CCD data, the 2 individual integrations per object were added after they had been cleaned and extracted, since shifts in the dispersion direction were negligible (see below).

4.4.4 Wavelength Calibration

This was certainly the most important part of the data reduction. Accurate wavelength calibration was essential because the galaxy spectra were to be used to measure the redshift of the galaxies. Each scientific observation was accompanied by two calibration arcs, either side of the exposure. The theory behind this strategy was to account for any changes in the dispersion of the spectra as the telescope slewed from object to object. On examining various pairs of calibration arcs taken over a night, it was found that the temporal shifts in the arcs were much smaller than the fibre–to–fibre shifts in any one individual arc calibration ($\sim$ 0.05 pixel shifts over a night compared to $\sim$ 1 fibre–to–fibre pixel shifts). In addition, the individual arc calibrations contained many

low signal–to–noise lines, especially near the edges of the wavelength window. This restricted the number of arc lines that could be used in the calibration and reduced its confidence, particularly near the edges. Therefore, all the arc calibration frames taken on the same night were added together. This increased the signal–to–noise of the faint lines and removed the need for long and laborious individual frame calibration.

The central row from the master arc calibration frame was extracted and ARC was used to interactively identify as many lines as possible. These lines were then supplemented by an automatic search which resulted in 40–50 identified lines spread almost evenly throughout the wavelength window. A 4th order polynomial was then fitted to the wavelength/pixel number relationship of the identified lines to obtain a wavelength calibration for the whole spectrum. The typical rms deviation between the fitted and observed values of these lines was $\sim 0.3\AA$ for the IPCS data and $\sim 0.7\AA$ for the CCD data; the maximum deviations were usually twice these values. The benefits of adding all the arcs for a particular night together can be illustrated by comparing the rms deviations obtained from a single arc with that obtained from the master arc. For example, on night 5 of the run, 10 arcs were taken; the summed arc gave an rms deviation of $0.4\AA$ while an individual arc gave $\sim 1.5\AA$. This agrees with the expected $\sqrt{N}$ improvement for the master arc, $0.4\AA \times \sqrt{10} \simeq 1.3\AA$. Also, the improvement in the signal–to–noise was reflected in the number of lines that were confidently identified, ~ 15 for an individual arc compared to ~ 40 in the master arc.

A quick qualitative check of the wavelength calibration can be obtained by estimating the accuracy to which the identified lines had been centroided. For a good signal–to–noise arc, it is possible to centroid lines to a tenth of a pixel (Andrew Connolly, private communication). The resolution of the IPCS data was $1.8\AA$ per pixel and for the CCD data it was $3.3\AA$ per pixel. Using these values and the rms deviations quoted above, the lines were centroided to a fifth of a pixel, which is reasonable. This small error in the wavelength calibration translates to a redshift error of ~ 0.0001, which is insignificant. A more robust method of checking the wavelength calibration was carried out once all the data frames for a particular night had been calibrated. The wavelength of the strong [O I] sky line at $5577\AA$, which is present in almost all the spectra, was checked and found to be at the correct wavelength within the rms deviations quoted above.

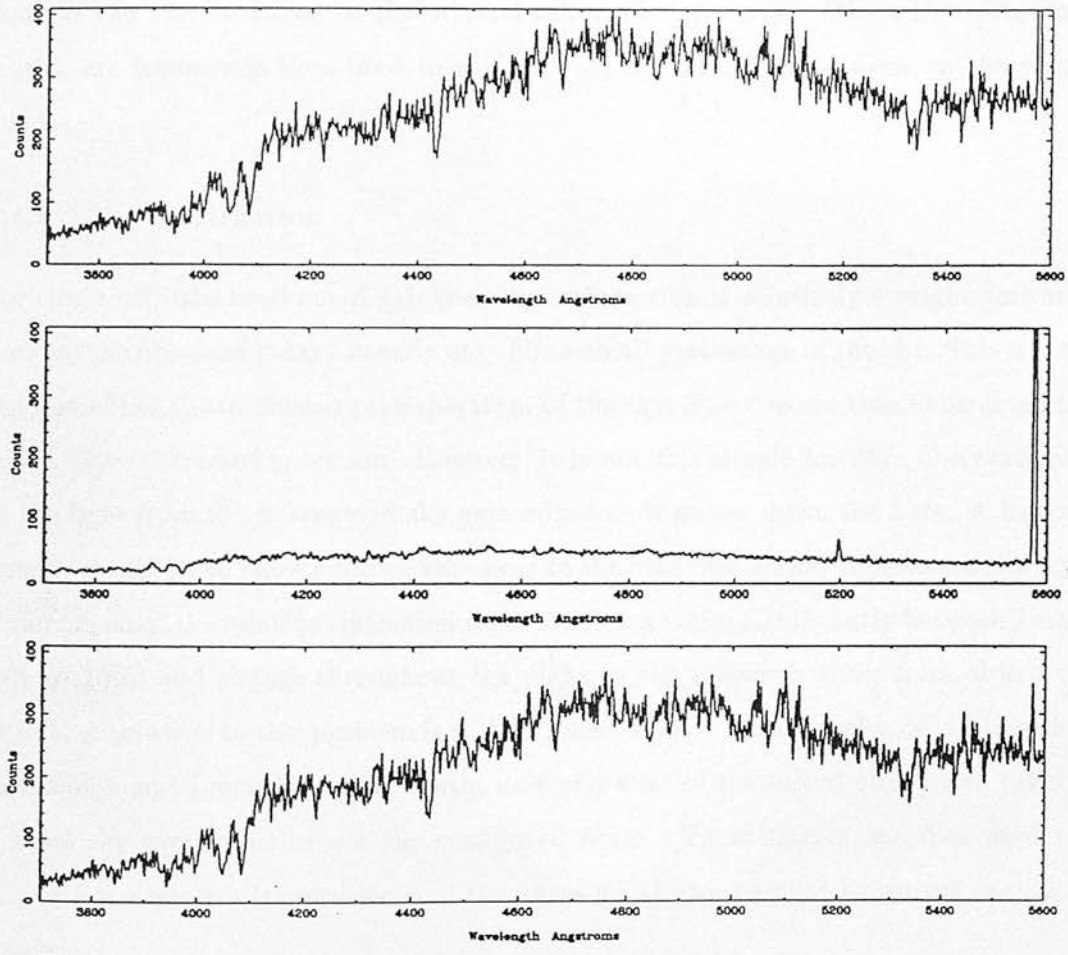

Figure 4.4: Sky subtraction of spectrum 10 observed with AUTOFIB for cluster E348. The top frame has not been sky-subtracted and contains the strong $[O\,I]$ sky line at 5577$\mathring{A}$ (total of 1154 counts) The middle spectrum is the median sky for the cluster scaled by the ratio of the heights of this oxygen line (see text). The bottom spectrum shows the result of subtracting the two. As stated throughout this chapter, the spectrum of the sky contained few features and had a low continuum level. This is illustrated by the middle spectrum.

Once the central spectrum had been calibrated, it was used to calibrate the other spectra in the master arc frame. This was achieved using IARC which took the single calibrated arc and calibrated each x-row in turn by shifting the calibrated spectrum until it found the best fit for each row. This removed the fibre–to–fibre shifts highlighted above. The rms deviation for each fibre within the master arc was approximately the same as the rms deviation in the original calibration spectrum. The fully calibrated master arc frame was then used to calibrate all the data frames taken on the same night.

4.4.5 Sky Subtraction

For single–slit observations of galaxies, sky–subtraction is relatively straight–forward because the observed galaxy usually only fills a small percentage of the slit. This leaves the rest of the slit to measure the spectrum of the sky. The two are then subtracted to give a sky–subtracted spectrum. However, it is not this simple for fibre observations, as the light from the galaxy and sky gets mixed as it passes down the fibre. A logical remedy would be to place another fibre near to the observed galaxy to measure the sky. Unfortunately, the relative transmissions of the fibres varies significantly between fibres (5% to 10%) and change throughout the night as the telescope slews from object to object. A solution to this problem is to take 'offset skies'. These involve off–setting the telescope a small amount north, south, east and west of the initial object and taking a short sky exposure through the configured fibres. These frames are then used to measure the relative transmissions of the fibres which can be used to correct the data frames.

During our run, it was decided not to take offset skies. There were several reasons for this. First, it increased the observing time of each cluster by around 10 minutes. This was comparable to the time spent configuring the fibres and taking the calibration arcs. Inclusion of offset skies would have pushed the overheads per cluster over the actual time spent observing the cluster. By neglecting them, we were able to observe an extra cluster per night. Secondly, sky–subtraction was not crucial. The wavelength window used during the observations contained very few sky features. Within the observed range of $3500\mathring{A} \rightarrow 6000\mathring{A}$, the sky contained only strong emission lines at $5577\mathring{A}$ (O I)

and 5199Å (N I) and no significant absorption features. These lines were irrelevant since we were only interested in observing broad absorption features in the galaxy spectrum (Figure 4.4). Finally, the sky emission was small compared to the signal from the galaxy. It was found that the sky emission was only $\sim 10\%$ of the signal passing down the fibre.

A crude sky–subtraction was performed using the fibres that had not been placed on target galaxies. First, the vignetting function was estimated and removed using the twilight sky frames. By summing all the pixels in the dispersion direction for each spectrum, the relative transmissions of the fibres was measured as each fibre was exposed to the same bright source *i.e.* the sky. A low order polynominal was fitted to the distribution of total fibre counts in the twilight sky frame and used to remove the large scale variation between the fibres in all the data frames taken that night. Figure 4.5 shows the total counts per fibre for a typical twilight sky frame and illustrates the presence of the vignetting function. Secondly, all the sky fibres in a particular data frame were extracted and divided through by the median pixel count of that spectrum. This removed differences between the continuum levels of the sky spectra. The median of these sky spectra was taken and effectively represented a model sky spectrum. The problem still remained that this sky spectrum had to be scaled appropriately to account for the small scale transmission variations between the fibres (5% to 10%). The twilight frame could not be used since the relative fibre–to–fibre transmissions varied according to the telescope position. Therefore, the ratio of the heights of the strong oxygen sky line at 5577Å was used to scaled the model sky spectrum to galaxy spectrum. Once scaled, the median sky was subtracted from the galaxy spectrum. Finally, to guard against residual sky lines in the galaxy spectrum, the pixels at and next to the 5577Å and 5199Å lines were set to the galaxy continuum level. The whole of the sky–subtraction was carried out using new computer code written by myself and is demonstrated in Figure 4.4.

4.4.6 Final Comments

Flux calibration was unnecessary as the galaxy spectra were only to be used for determining the redshift of the galaxy. Using the cross–correlation technique, only the

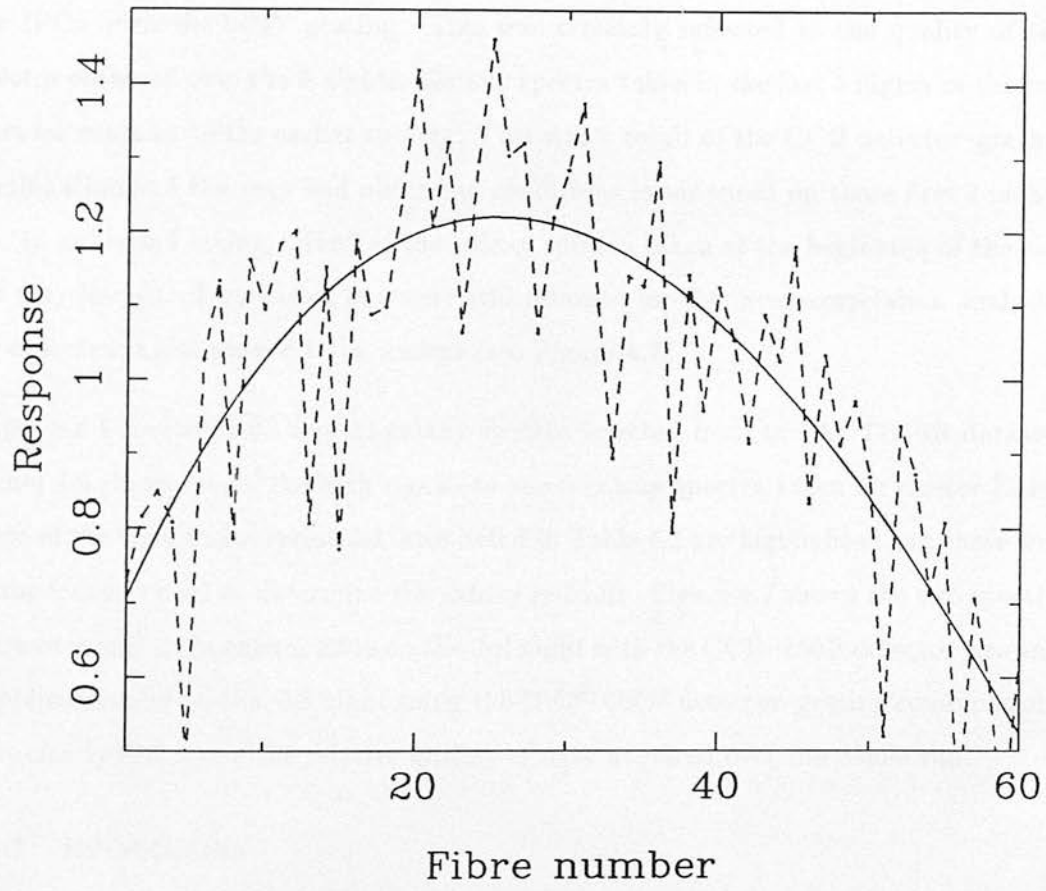

Figure 4.5: The vignetting function of a typical twilight sky frame. On the y-axis is plotted the response of the fibre compared to the mean, while the x-axis is the corresponding fibre number. This plot illustrates the presence of a strong vignetting function, which has been fitted with a 4th order polynomial, and the existences of large individual fibre–to–fibre variations in the transmission.

relative wavelength separations of certain galaxy features are important. In preparation for cross–correlation, the continuum level of the galaxy spectrum was subtracted thus rendering absolute flux calibration pointless (see below).

The individual galaxy spectra for the AUTOFIB clusters were extracted from the data frames, producing $\sim$ 400 spectra, all of which were sky–subtracted and wavelength calibrated. As stated above, the best detector–grating combination was found to be the IPCS with the 600V grating. This was certainly reflected in the quality of the spectra obtained over the 6 nights. Galaxy spectra taken in the last 3 nights of the run were far superior to the earlier spectra. This was a result of the CCD detector–grating combination and the very bad observing conditions experienced on those first 3 nights *i.e.* 10 arcsecond seeing. Many of the galaxy spectra taken at the beginning of the run are very low signal–to–noise, but were still retained for the cross–correlation analysis. As expected, most proved to be useless (see Figure 4.7).

Appendix C contains 25 typical galaxy spectra selected from the AUTOFIB dataset. Figure 4.6 shows one of the high signal–to–noise galaxy spectra taken for cluster E348. Some of the strong absorption features listed in Table 4.2 are highlighted and these will be the features used in determine the galaxy redshift. Figure 4.7 shows the two spectra taken of galaxy 41 in cluster E519 on the 3rd night with the CCD–250B detector–grating combination and on the 4th night using the IPCS–600V detector–grating combination. This clearly illustrates the relative quality of data acquired over the whole run.

4.4.7 EFOSC data

This data was reduced to one-dimensional, sky–subtracted, wavelength calibrated spectra by Luigi Guzzo. On my arrival in Edinburgh, he had already begun the reduction of the 1988 EFOSC data and had written several new computer programs within the ESO MIDAS software reduction package to extract and wavelength calibrate the multi–slit data. Therefore, he continued to reduce the data from subsequent EFOSC observing runs and a summary of his data reduction chain follows.

1. Bias subtraction and cleaning

The bias frames taken on a particular night were averaged together and subtracted from all the data frames taken the same night. The CCD chip varied little throughout the entire project and remained cosmetically clean with no gradients or major defects. The typical count per bias frame was $\simeq 200 \pm 3$. Each object observation was usually split into 2 or more exposures. Within MIDAS, these individual exposures were averaged together using k–sigma clipping which removed most of the cosmic rays events.

2. Slit extraction

   The exact position of each slit within a mask was marked interactively using the profile of the object frame as seen in the mask's spatial direction (x–direction). These slit positions were then used to extract the slit spectra from the object frame, the corresponding arc calibrations taken either side of the object frame and the flat–field frame taken of that mask. This produced 4N 2-D spectra for each mask, where N was the number of slits in the mask.

3. Flat–fielding and wavelength calibration

   The spectral response of the lamp was removed from each flat–field spectrum leaving the pixel–to–pixel variations. These variations proved to be very small ($\sim$ 2%), but as a precaution the object and arc spectra were divided through by the appropriate slit flat–field. The final redshift results were insensitive to whether the spectra had been flat–fielded or not. For each arc calibration spectrum, several lines were manually identified and supplemented by an automatic search resulting in $\sim$ 20 lines spread evenly across the wavelength window. Using a 4th order polynominal, these identified lines were used to calculate the pixel–to–wavelength relationship for the spectrum. This resulted in a typical rms wavelength calibration error of $\sim 0.3\text{Å}$. This fit was then used to calibrate the 2–D object spectra using a MIDAS program similar to IARC in FIGARO (see above).

4. Sky–subtraction

   Each object 2–D spectrum was examined and the position of the galaxy within the spectrum marked interactively. The galaxy was then collapsed to a 1–D

spectrum, averaging over the number of columns in the galaxy. For galaxies with a separate sky slit, this slit was collapsed to 1–D by averaging over the number of columns in that slit. If enough sky spectrum existed in the object slit, this was used by once again collapsing it to an averaged 1–D spectrum. For galaxy spectra without a suitable sky estimation, another sky estimation from within the same frame was used. Finally, the sky spectrum was subtracted from the galaxy spectrum.

5. Final comments

   All the spectra were inspected and any residual sky lines or cosmic rays were removed by linear interpolation of the galaxy continuum across the line.

Over the six ESO observing runs, a total of $\sim$ 500 galaxy spectra were observed. Appendix D shows 25 typical galaxy spectra selected from the ESO database. Figure 4.5 shows an example of a high signal–to–noise galaxy spectrum taken for cluster E198. Some of the strong features in Table 4.2 are highlighted.

4.5 Redshift Determination

4.5.1 The Redshift of a Galaxy

The definition of redshift is given by the formula

$$z = \frac{\lambda_{obs} - \lambda_{rest}}{\lambda_{rest}}, \tag{4.1}$$

where λ_{rest} is the rest wavelength and λ_{obs} is the measured wavelength of a line or feature in the galaxy spectrum. This definition can be related to the recession velocity, v, of a galaxy by the non–relativistic Doppler relationship ($v << c$)

$$z = \frac{\lambda_{obs}}{\lambda_{rest}} - 1 = \frac{v}{c}, \tag{4.2}$$

where c is the speed of light. Clearly, the redshift of a galaxy can be determined by simply examining the galaxy spectrum and measuring the wavelength shift of one particular feature. Unfortunately, this is usually not possible because the galaxy spectrum

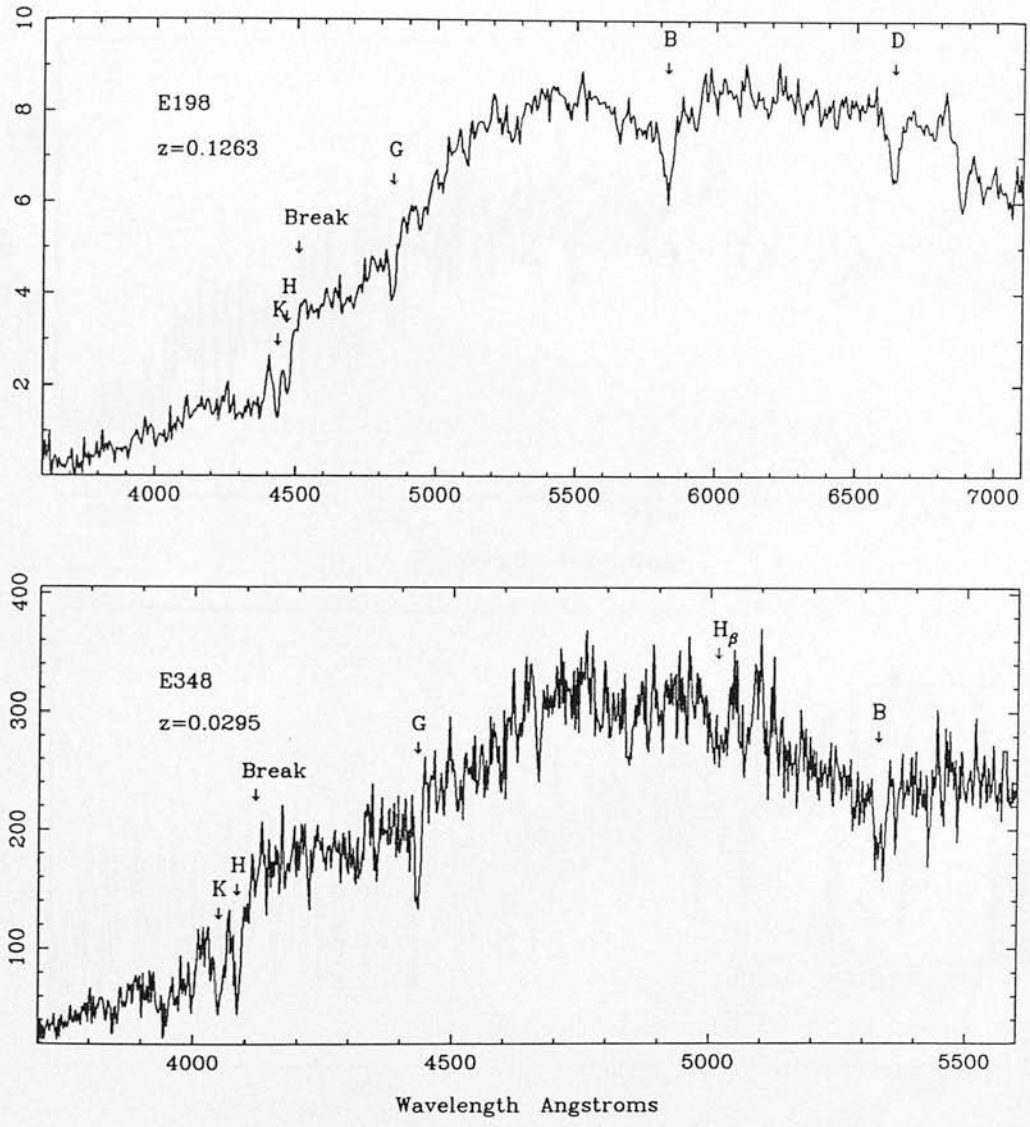

Figure 4.6: The top spectrum was observed with EFOSC and some of the strong absorption features from Table 4.2 are highlighted. H & K refers to the calcium H & K transitions, Break refers to the 4000Å break feature, G is a belend of CH molecules, B is the MgI triplet and D is NaI. These are the main galaxy features used by cross–correlation to derive the redshift of the galaxy. The bottom spectrum was observed with AUTOFIB. Again, the main galaxy absorption features are highlighted. (Note: the y–axis in the top plot is counts per minute, while the bottom plot is total counts.)

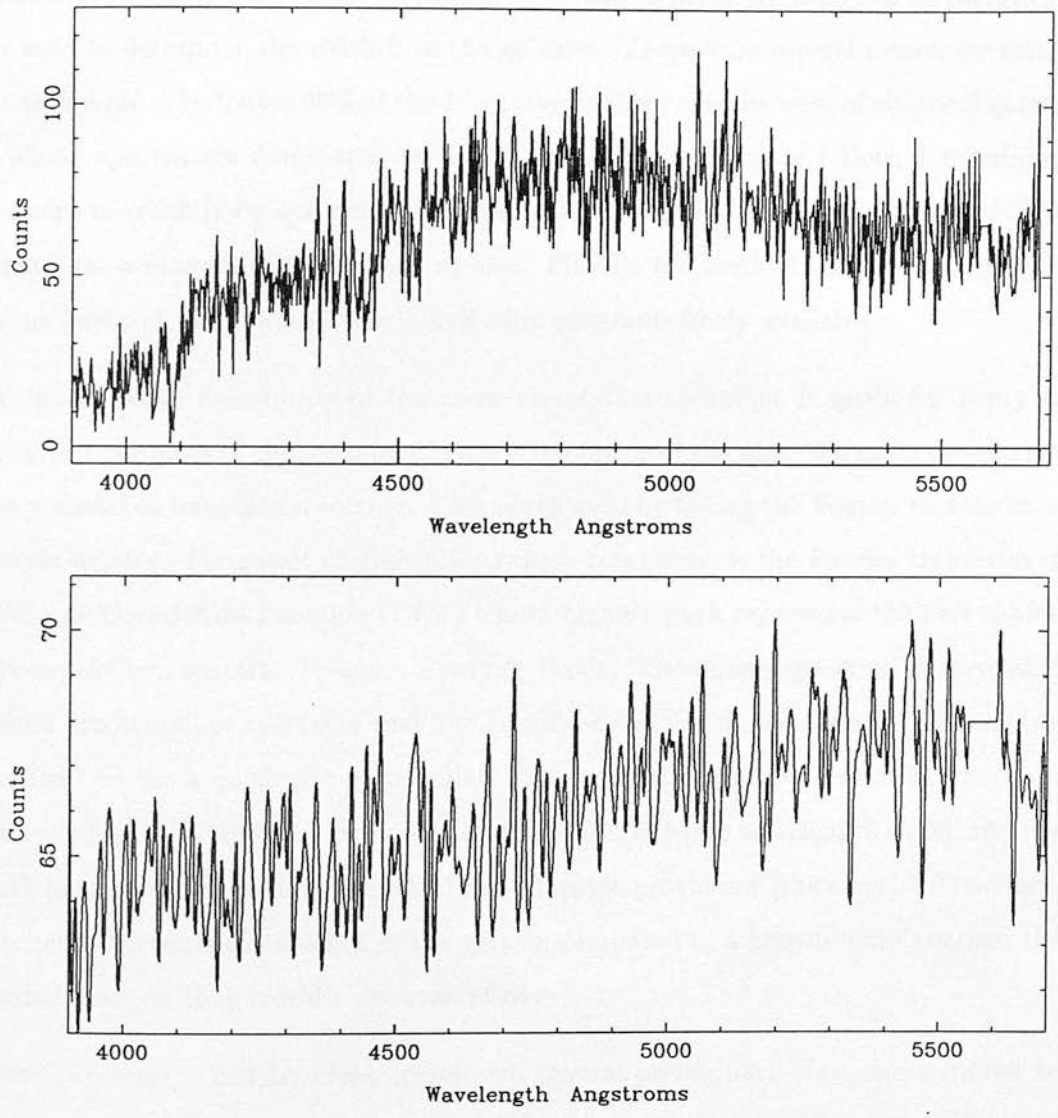

Figure 4.7: A comparison of spectrum 41 in cluster E519 taken with AUTOFIB. The top spectrum was observed on night 4 using the 600V grating with the IPCS. The bottom spectrum was observed on night 3 using the 250B grating with the CCD (bad weather as well). The relative quality of the data is evident. The top spectrum gave a redshift $z = 0.03023 \pm 0.00005$ with a confidence of 1.0. The bottom spectrum gave a redshift $z = -0.04806 \pm 0.00011$ with a confidence of 0.56. Figure 4.8 presents the cross–correlation functions of these two spectra.

does not possess one high signal–to–noise unambiguous line or feature. In addition, the accuracy with which a visual wavelength shift can be determined is low.

Therefore, the cross–correlation technique described in detail by Tonry & Davis (1979) was used to determine the redshift of the galaxies. There were several reason for using this technique. First, over 90% of the EM survey galaxy spectra were of elliptical galaxies whose spectra are dominated by broad absorption features and thus, determining an accurate redshift by eye would be impossible. Secondly, the sheer volume of data meant that a manual approach was unwise. Finally, the method was commonly used and understood, with many cross–correlation programs freely available.

A comprehensive description of the cross–correlation technique is given by Tonry & Davis, but the basis of the technique is the convolution of the observed galaxy spectrum with a model or template spectrum. This is achieved by taking the Fourier transform of the two spectra. The result of multiplying these transforms is the Fourier transform of the Cross–Correlation Function (CCF) whose highest peak represents the best match between the two spectra. To quote Tonry & Davis, "the galaxy spectrum is correlated against the template spectrum and the resultant peak is fit by a smooth symmetric function (we use a quadratic polynomial). The central height of this fit determines α [the scale factor between the two spectra], the center is δ [the wavelength shift], and the width in conjunction with the width of the template provides σ [the error]." Therefore, this method returns the redshift of the galaxy, compared to a known template, and the internal error on that redshift determination.

Before the spectra can be cross–correlated, several preliminary steps are required to prepare the spectra. These are described below.

1. The continuum level of the galaxy spectrum had to be removed, which was achieved by fitting a 4th order polynomial to the spectrum and subtracting it. In addition to this, the wavelength coverage of the spectrum was cut, purely for convenience, to the range $3800\mathring{A} \rightarrow 5500\mathring{A}$ for the AUTOFIB data and to $3800\mathring{A} \rightarrow 6500\mathring{A}$ for the ESO data. The final redshift of the galaxy was found to be insensitive to the order of polymonial used in the continuum subtraction and to the exact wavelength coverage of the spectrum. Finally, any emission lines or

residual sky lines in the galaxy spectrum were removed by linear interpolation across the line. The presences of lines in the spectrum was usually indicated by a "strange" initial cross–correlation *i.e.* most of the templates gave a very confident high redshift, $z \sim 0.3$ (see below).

2. Often after continuum subtraction, the edges of the spectrum were non–zero thus leading to a discontinuity in the galaxy spectrum which could be identified as a real feature. For example, it could easily be mis–interpretated as the 4000Å break feature which is also seen as a distinct shear in the galaxy spectrum. Therefore, the spectrum was multiplied by a cosine–bell function which is unity for most of the wavelength window, but falls smoothly to zero at the edges. This has the required effect of smoothing the galaxy spectrum to zero at the ends. The FIGARO command COSBELL was used to perform this task.

3. The spectrum was rebinned into logarithmic bins

$$\mathrm{n} = \mathrm{A} \ln \lambda + \mathrm{B}, \tag{4.3}$$

where n was the bin number and λ was its wavelength. Therefore, the shift of a particular feature in the spectrum can be written as

$$\Delta \mathrm{n} = \mathrm{A} \ln \frac{\lambda_1}{\lambda_2}, \tag{4.4}$$

and if λ_2 is the rest wavelength of that feature, then equation 4.4 becomes

$$\Delta \mathrm{n} = \mathrm{A} \ln (1 + z), \tag{4.5}$$

which gives the redshift of the galaxy directly. However, λ_2 is usually not the rest wavelength of the feature, but the wavelength it appears in the template spectrum. Therefore, equation 4.5 becomes

$$\Delta \mathrm{n} = \mathrm{A} \ln \left[\frac{(1 + z_o)}{(1 + z_t)} \right], \tag{4.6}$$

where z_t is the known redshift of the template and z_o is the unknown galaxy redshift. The FIGARO program SCRUNCH was used to rebin all the spectra

into 2000 logarithmic bins. For the ESO data, this corresponded to a velocity binwidth of $84.5\mathrm{km\,s^{-1}}$, while for the AUTOFIB data it was $57.9\mathrm{km\,s^{-1}}$. The redshift of the galaxy was found to be insensitive to the exact binwidth chosen.

4.5.2 The Template Spectra

The major advantage of the cross–correlation technique is that it is able to determine the redshift of a galaxy using several features simultaneously. For instance, if a galaxy spectrum contains many low signal–to–noise features, then a visual inspection is unlikely to determine its redshift. However, cross–correlation can detect the combined presence of these features and therefore, determine the redshift. The major disadvantage of the cross–correlation technique is that it can be easily fooled and will give an answer irrespective of the signal–to–noise of the spectrum (Figure 4.7). Therefore, checks must be implemented to guard against false correlations. One such check is to cross–correlate the galaxy spectrum with as many different templates as possible, which will highlight marginal or false correlations.

During the course of the project, 27 templates were observed. In addition, a modest library of templates already existed at the Royal Observatory Edinburgh. In total, ~ 35 suitable templates were available covering a wide range of object type and resolution. To cross–correlate the galaxy spectra against all these templates would have been impractical and therefore, time was invested in selecting the most suitable templates for our observations.

Of the 27 EM survey templates observed, 10 were taken at the AAT using AUTOFIB and 17 at ESO using EFOSC in single slit mode. These spectra were reduced as described above. Fifteen of the ESO templates were bright nearby galaxies taken from Da Costa *et al.* (1984) and their redshifts were known accurately from 21cm observations (errors $\sim 10\mathrm{km\,s^{-1}}$). The other two were radial standard stars taken from the Astronomical Almanac. The AUTOFIB templates were all radial standards, again extracted from the Astronomical Almanac. On examining all the template spectra, it became clear that the ESO single slit spectra were far superior, in terms of signal–to–noise, compared to the AUTOFIB spectra, and since the number of usable templates was not a problem, the AUTOFIB templates were discarded.

To check the reliability of the ESO templates, they were cross–correlated against each other to obtain the redshift of each template with respect to the other 16 templates. For each template, the difference between its published redshift and the measured redshifts from the other 16 templates were plotted against the template used. By examining these plots, rogue templates were easily spotted (Appendix B). For example, N5134 systematically underestimated the redshift of other templates by $\sim 100\mathrm{km\,s^{-1}}$, while its redshift was constantly overestimated by a similar amount suggesting that its published redshift was in error. Once a problem template had been discovered, it was removed from the list. Overall, seven of the original seventeen ESO templates were selected for use in the cross–correlation technique. See Appendix B for a fuller discussion of this selection procedure.

Of the archive templates available, two were chosen on the basis of their previous reliability and high signal–to–noise (Parker *et al.* 1987). In addition, they were stellar templates which was advantageous since the seven chosen ESO templates were all galaxies. The final template chosen was the high signal–to–noise spectrum of galaxy 10 taken as part of the AUTOFIB observation of E348. The reason for including this template was to avert any possible problems during cross–correlation because of differences in the instruments used to observe the AUTOFIB galaxies and the templates. In fact, the AUTOFIB data was found to cross–correlate to a higher confidence and regularity with the ESO galaxies than with template E348.

The ten final templates are listed in Table 4.4 along with their published redshifts. Plots of the templates can be found in Appendix B. All these templates were prepared for cross–correlation as described above.

4.5.3 Cross–Correlation of the Spectra

Cross–correlation was carried out using the FIGARO command XCORR. The advantage of this program was that it had been extensively checked by Karl Glazebrook who had found an error in the original program concerned with the calculation of the redshift (Glazebrook 1991). In addition, the program was highly automated and could be left to cross–correlate hundreds of spectra at once.

Name	RA (hours)	Dec. (°)	mag.	$v\,(\mathrm{km\,s^{-1}})$
N5740	14.6983	1.8833	12.5	1575 ± 20
N5746	14.7066	2.1667	11.5	1801 ± 33
N5921	15.3250	5.2500	12.0	1480 ± 10
N6070	16.1233	0.8333	12.5	2005 ± 7
N6118	16.3200	-2.1667	12.0	1578 ± 15
N6958	20.7583	-38.1816	12.2	2742 ± 50
N7793	23.9633	-32.5833	9.1	231 ± 7
A4038	23.7522	-28.4169	13.7	8813 ± 65
HD171391	18.5769	-10.9836	5.1	6.9 ± 0.2
HD35410	5.3656	-0.9377	5.2	20.5 ± 1.0

Table 4.4: The final 10 templates selected for use with the cross–correlation technique. The last 2 are stellar templates taken from Parker *et al.* 1987. The others were observed during the construction of the EM survey and their published redshifts were taken from Da Costa *et al.* (1984).

The cross–correlation technique offered two useful options during its estimation of the redshift. The first of these was the opportunity to bandpass filter the Fourier transforms of the galaxy and template spectra which removed the low frequency and high frequency components of the transforms. The low frequency components were usually due to residual continuum left in the spectra, while the high frequency components were due to binning noise. On experimenting with various spectra, it was found that filtering the spectra reduced the internal error on the redshift determination because the width of the CCF peak had been artificially expanded by the low order frequencies. In addition, it was found that these spurious low frequencies had boosted the height and therefore, significance, of the chosen CCF peak. Figure 4.8 shows the CCFs for the galaxy spectra shown in Figure 4.7 and illustrates the above points.

The second option was the ability to place a confidence level on the chosen CCF peak by comparing its height with that expected for a random noise peak in the CCF. Tonry & Davis explained that if the CCF had $2B$ positive and negative peaks over its entire range, whose heights had roughly a Gaussian distribution, then the probability of a noise peak having a particular height h can be calculated. In addition, if the wavelength range of the chosen peak was constrained to a fraction f of the entire range *i.e.* only positive redshift peaks with $z < 0.2$, then the confidence C on a chosen peak is given by

$$C = \left(1 - \int_r^\infty \mathrm{P(r)dr}\right)^{fB}, \tag{4.7}$$

with

$$\mathrm{P(r)dr} = \frac{2}{\sqrt{2\pi}} \exp\left(-\frac{r^2}{2}\right) \mathrm{dr} \tag{4.8}$$

being the normalised probability distribution of a random noise peak of height $h > 0$ (Tonry & Davis 1979, equations 29 & 30) and r being the ratio of the peak height to the noise (σ) seen in the CCF *i.e.*

$$\mathrm{r} = \frac{h}{\sqrt{2}\sigma}. \tag{4.9}$$

Therefore, for high signal–to-noise spectra where the CCF peak height is large, the probability of a noise peak having such a height is low and the confidence level should be near unity. Clearly, the opposite is the case for low signal–to–noise spectra.

The XCORR program was modified to include a confidence level estimate on the redshifts obtained. The prepared galaxy spectra were cross–correlated against the 10 templates described above and a confidence level was assigned to each cross–correlation. Spectra with 5 or more templates in agreement (within the errors on the redshifts) with confidence levels above 0.95 ($\sim 2\sigma$) were passed as secure. Spectra that did not satisfy these criteria were inspected by eye. Most of these spectra had between 2 and 4 templates in agreement and the visual inspection often supported this lower level of agreement. Spectra were discarded if there was no agreement between the templates and a visual inspection could not determine the redshift.

At this stage, 2 checks were carried out. First, all spectra that gave a redshift greater than $z = 0.15$ were examined by eye to check the reality of such a redshift and to see if any spurious feature, such as emission lines and/or residual sky lines, were influencing the cross-correlation. This was found to be the case for $\sim 5\%$ of the spectra and on the removal of these lines the true redshift of the galaxy was obtained. Secondly, a subset of the spectra were cross–correlated against a typical sky spectrum and one of the templates. As expected, the sky and template redshifts disagreed and the confidence level on the sky estimate was very low.

Once a spectrum had been accepted as secure (visually or with > 5 templates), the template redshift with the highest confidence level was assigned to the galaxy. If several templates had the same confidence, then the one with the lowest returned internal error was used. For high signal–to–noise spectra, it was common to find all the templates agreeing with a confidence level of 1.0, with a typical scatter of $\Delta z \sim 0.0002$ between the templates. Lower signal–to–noise spectra had a typical scatter of $\Delta z \sim 0.0003$ between the templates in agreement.

During the course of the reduction, it was noted that templates HD35410, N5921 and N6118 consistently gave the best confidence levels and the lowest internal errors. For high signal–to–noise spectra where all the templates agreed, the scatter between these

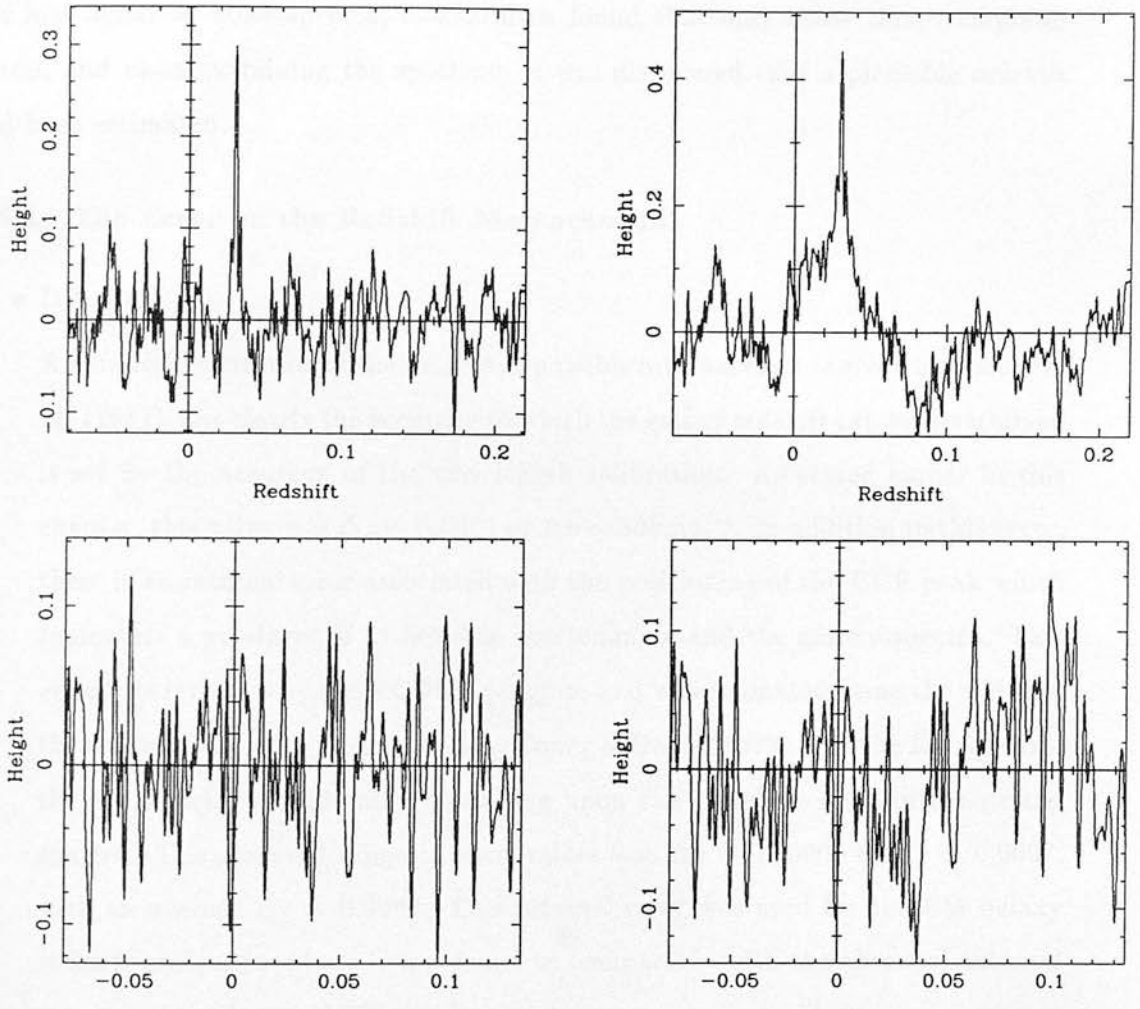

0.03023 ± 0.00005	0.03028 ± 0.00013
Confidence = 1.0	Confidence = 1.0
Filtering	No filtering
-0.04806 ± 0.00011	0.09873 ± 0.00038
Confidence = 0.56	Confidence = 0.46
Filtering	No filtering

Figure 4.8: The cross–correlation functions (CCF) for the two spectra show in Figure 4.7. The top two correspond to the IPCS data, while the bottom two are the CCD data. The left hand pair have been filtered and demonstrate the advantages of filtering the Fourier transforms during the cross–correlation. Filtering removes the low–order frequencies preventing them from artificially boosting the significance of the CCF peak and increasing its width (error). This can be seen in the right hand pair of plots. The CCD data illustrates the need for cross–correlating each spectrum with several templates and the need for assigning a confidence level to the CCF peak. Cross–correlation will always return a peak, no matter how insignificant. The confidence levels quoted in the table help to quantify the importance of the chosen CCF peak.

3 was usually a factor of 2 lower than between the whole 10 templates ($\Delta z \sim 0.0001$). For low signal–to–noise spectra, it was often found that only these three templates agreed and upon examining the spectrum it was discovered that a plausible redshift had been estimated.

4.5.4 The Error on the Redshift Measurements

- **Internal**

  A detailed description of the sources of possible internal error is given by Parker *et al.* (1987), but clearly the accuracy to which the galaxy redshift can be determined is set by the accuracy of the wavelength calibration. As stated earlier in this chapter, this value was $\Delta z \sim 0.0001$ or $\Delta v \sim 30 \mathrm{km\,s^{-1}}$. In addition to this error, there is an internal error associated with the positioning of the CCF peak which represents a goodness of fit between the template and the galaxy spectra. This error was returned by the XCORR program and was estimated using the width of the chosen CCF peak as described by Tonry & Davis (1979). For the EM spectra, the error varied considerably depending upon the signal–to–noise of the galaxy spectra. The observed range of error values was $\Delta z \simeq 0.00005$ to $\Delta z \simeq 0.0007$, with an average $\Delta z \sim 0.0002$. This internal error was used for the EM galaxy redshift measurements as it was found to comparable with the observed external error on the galaxy redshifts (below).

  Two alternative method of estimating the internal error on a redshift determination are either to use the galaxies with both emission and absorption features, or, to use the observed scatter between the templates in agreement. The first of these, however, relies on the assumption that these features originate from the same part of the galaxy and therefore, the rotation of the galaxy is negligible. The second method is undesirable since each template represents a different model spectrum which is fitted to the galaxy spectrum. The scatter between these models will therefore, not be a good measure of the error on the best fit between a particular template and the galaxy spectrum.

- **External**

Throughout the course of the project, several repeat observations were carried out. In fact, due to the bad weather during the ESO 2.2m run, we were often forced to re–observe certain bright cluster galaxies that had already been observed on other telescopes. These repeat observations were used to estimate the external error on determining a galaxy redshift.

To ensure an honest comparison, these repeated observations were only brought together after they had been reduced and cross–correlated. Table 4.5 shows the redshift estimates for the repeats using the same template. The mean offset between all the redshift measurements is $164 \pm 251 \mathrm{km\,s^{-1}}$. If uncertain redshifts are excluded (the 3 indicated in the table), the mean offset drops to $53 \pm 49 \mathrm{km\,s^{-1}}$ or $\Delta z = 0.00017$. This is comparable to the internal error returned by XCORR quoted above.

4.5.5 Emission Line Galaxies

A small fraction of the EM survey spectra were identified as emission line galaxies with no identifiable absorption features. These spectra were detected by their "strange" initial cross–correlation (above). The redshift of these galaxies was initially calculated using the program EMLINES, which interactively shifted the position of known galaxy emission lines until a best visual fit was obtained. The program then returned an approximate redshift and indicated which emission lines had been confidently identified (~ 2 lines per galaxy). These lines were then fitted individually with a Gaussian profile and their central wavelengths determined (GAUSS). A redshift was finally calculated from the mean of these lines, with a typical error of $\Delta z \sim 0.0008$.

4.5.6 The Galaxy Spectra and Redshifts

Appendix B contains details of the reduction of the EM survey templates, while Appendices C and D contains all the galaxy redshifts used to determine of the cluster redshifts. Finally, Appendix E contains a pictorial representation of where the observed galaxies are located within each cluster, with respect to the unobserved galaxies used to define that cluster.

RA (hrs)	Dec. (°)	b_j	z_1	z_2	Temp.	Δv	Comments
0.1233	-35.9531	19.51	0.12330	0.12385	N5921	164.8	
0.1238	-35.9522	18.91	0.12271	0.12236	N6070	104.6	
0.1235	-35.9591	19.09	0.12210	0.12208	HD35410	6.0	
0.1238	-35.9771	18.97	0.12071	0.11747	N5921	970.4	Low S/N.
0.1471	-29.1327	15.03	0.06096	0.06098	N5927	11.4	
1.5009	-31.3492	15.65	0.07117	0.07128	N5921	33.5	
1.6977	-35.5162	16.81	0.08616	0.08592	N5921	70.6	
1.9748	-33.2266	18.18	0.09597	0.09509	HD35410	261.3	Star?
2.9070	-24.9099	16.32	0.10985	0.11052	HD35410	199.1	Low S/N.
3.1545	-27.1195	15.96	0.06830	0.06847	HD35410	51.4	
3.3418	-41.5253	18.34	0.06467	0.06466	N6118	3.6	
22.9984	-33.6197	17.23	0.08744	0.08733	N5740	31.0	
23.7481	-28.3864	14.14	0.02664	0.02656	HD171391	26.2	
23.7523	-28.4170	13.77	0.02861	0.02834	HD171391	82.1	

Table 4.5: The repeat observations carried out during the construction of the EM survey (see text). The units of Δv are $\mathrm{km\,s^{-1}}$, while b_j is in magnitudes.

4.5.7 The Redshift of a Cluster

The redshift of a cluster was defined in an objective manner which removed any subjective "eyeball" determination of whether a galaxy was in a cluster or not and provided a set of well–defined selection criteria that could be reproduced exactly. In addition, these criteria were used to quantify the contamination due to cluster interlopers and used to determine the frequency of phantom clusters. The objective approach taken was similar to that described by Struble & Rood (1991) and is detailed below.

1. The mean and standard deviation of all the galaxy redshift measurements for a single cluster were calculated. The most discrepant galaxy redshift was temporarily removed from the galaxy listing and the mean redshift and standard deviation (σ_r) were re–calculated. This prevented σ_r from being dominated by a

single highly discrepant galaxy redshift. If σ_r was found to be outside the range $700 < \sigma_r < 2800 \mathrm{km\,s^{-1}}$, then it was set to the nearest of these limits which prevented clusters with a large scatter in their redshift measurements having an excessive σ_r and clusters with a small scatter having an unrealistic σ_r.

2. All the galaxy redshifts taken for a particular cluster were binned in redshift with a binwidth of $700 \mathrm{km\,s^{-1}}$. This binwidth corresponded to the median velocity dispersion quoted by Zabludoff *et al.* (1991) for the largest sample to date of observed clusters.

3. The cluster redshift distribution was searched for its highest peak. Once found, other peaks in its vicinity were located and merged if they were less than one σ_r away from the original peak. Various multiples of σ_r were tried, but it was found empirically that one gave the most realistic results. All the galaxy redshift measurements that had been merged into this one peak were written out and removed from the galaxy listing. This procedure was repeated until all the redshift peaks had been located, which produced a list of redshift concentrations for the cluster which could vary from a single galaxy to all the galaxies observed in that cluster.

4. For each concentration, the mean redshift and the fraction of observed galaxies within that concentration were calculated. The concentration with the highest fraction was assigned to the redshift of the cluster.

5. If a cluster had a secondary concentration within its distribution that contained more than a third of the observed galaxies and was separated by more than $1500 \mathrm{km\,s^{-1}}$ *i.e.* 2 binwidths, from the largest concentration mentioned above, then the cluster was defined as a projection effect or phantom cluster. If the peaks were separated by less than $1500 \mathrm{km\,s^{-1}}$, then they were merged together and re–analysed (Stage 4). This guarded against clusters with subclustering and/or high velocity dispersions being broken up and classed as spurious. All the remaining redshift concentrations for a cluster were defined as interlopers. These values of acceptance were found empirically

The main advantage of these criteria was that they could be used on all the clusters irrespective of the number of observed galaxies in a cluster. In addition, they were insensitive to the type of cluster observed and did not fragment clusters with a high velocity dispersion and/or subclustering. Finally, the criteria were easily understood and were based only on the redshift information of the cluster.

However, there were two potential problems with these criteria. First, clusters with a small scatter between measured galaxy redshifts would have a small σ_r and therefore, peaks in the vicinity of the highest peak (Stage 2), would not be merged. This would lead to them being defined as interlopers, yet in reality, they would not be too discordant from the cluster redshift. Secondly, although the definition of a phantom cluster was clear and concise, there may have been a few instances where the definition broke down. Examples of this are clusters E408 & E482.

All the EM survey clusters were analysed using these criteria and their cluster redshifts determined. Appendix C contains details of the AUTOFIB observations, while Appendix D contains details of the ESO observations. The interlopers, as defined above, are presented in Table 3 of both the above Appendices. In Appendix E, 27 cluster redshift histograms are shown along with the angular distribution of the observed galaxies with respect to all the galaxies in the EDSGC used to define the original cluster. These plots should help the reader to visualise the criteria used and illustrate the amount of contamination that exists along the line–of–sight towards the clusters.

4.5.8 Interlopers and Phantom Clusters

The objective criteria described above lead to a natural definition of an interloper and a phantom cluster. The statistics associated with these phenomena are still highly uncertain and could be used to estimate the expected contamination for previous and future cluster observations. Therefore, the ESO EM survey clusters were used to estimate the frequency of interloper contamination and determine the number of interlopers per observation. The ESO data was used in preference to the AUTOFIB data because of its small field–of–view. With AUTOFIB, the field–of–view was 40 arcminutes which meant that galaxy redshifts well away from the cluster core were measured, while for

the ESO observations, the EFOSC field–of–view was only 5 arcminutes and thus the observations were constrained to the cores of the clusters.

For all the observed ESO clusters, excluding phantom ones, the percentage of clusters that had any amount of interloper contamination was 73%. For these clusters, the percentage of sampled redshifts per cluster defined as interlopers was 25 ± 16 %. These figures represent an upper limit on the interloper contamination because of the simple methods used in defining them and as stated above, the slight problem with low σ_r clusters. If a more sophisticated set of criteria had been used involving the magnitudes of the galaxies and their radial distance from the cluster centre, these numbers would undoubtably be reduced. However, from an examination of the cluster redshift histograms (*i.e.* Appendix E), these figures were found to be in good agreement with a visual estimation of the interloper contamination and indicates that even towards the cores of rich clusters, the probability of measuring an interloper could be as high as $\sim 20\%$. For cluster redshifts based on a single galaxy observation, there is a reasonable chance of this galaxy not being in the cluster.

The number of clusters defined as spurious out of the total 103 observed EM survey clusters was 14, *i.e.* 13.5%. For the complete sample described at the end of this chapter, 9 out of 97 clusters were classified as phantom *i.e.* 9%. These figures indicate that $\sim$ 10% of rich clusters seen in projection on the sky are spurious rich cluster. However, this should also be taken as an upper limit as no account has been made for distance or richness effects. The statistics derived for both the frequency of interlopers and phantom clusters have been based on simple arguments and a more robust method of defining the two is presently being investigated.

These figures compare to $\sim 15\% \rightarrow 25\%$ quoted by Lucey (1983) from Monte Carlo simulations and $\sim 50\%$ derived by Fesenko (1979) from an analytical model. Struble & Rood (1991) used redshift measurements to estimate that only $\sim 3\% \rightarrow 5\%$ of Abell clusters were superpositions and thus spurious. However, they were mainly concerned with estimating the effects of interloper contamination on the richness of the cluster and whether a cluster could be boosted up into Abell's statistical sample. Therefore, they set out with the a priori assumption that they were clusters of some form or another.

Their result is probably a lower limit and used in conjunction which the EM survey] contamination constrains the frequency of phantom clusters to 5% → 10%, which is well below the contamination derived from models and simulations.

4.5.9 Literature Search for Cluster Redshifts

The astronomical literature was searched for possible cluster redshift observations of any of the EDCC clusters. This was helped greatly by the existence of several large computer databases and cluster lists. The largest of these was the NASA/IPAC Extragalactic Database (NED) based at Caltech. This database contains 150,000 objects taken from over 30 major catalogues *i.e.* cluster catalogues, x-ray catalogue, quasar catalogues and galaxy catalogues. Other lists that were available were; Andernach's cluster list, the radio galaxy observations of Nicholson (1991), Huchra's galaxy and cluster lists and various published galaxy redshift surveys. Several authors were kind enough to provide unpublished data and they are gratefully acknowledged (Tom Shanks, Alison Broadbent, John Huchra, John Peacock, Quentin Parker, Diego Lambas). The EDCC cluster positions were cross–correlated against all these lists and below is a table of the EDCC clusters found, with references to the original redshifts. It should be noted, that this search was carried out specifically to find clusters in the small Abell radius sample (section 4.6) and therefore, several match–ups with the full EDCC cluster list may have been missed. A more rigorous literature search is underway at the moment.

4.5.10 The Error on a Cluster Redshift

The error on a cluster redshift was calculated from the scatter seen between the individual galaxy observations and is quoted in Appendices C & D for each cluster. The average error on a cluster was $\Delta z \sim 0.0015$. If a cluster is virialised, then the measured error on its redshift should be related to its velocity dispersion σ_v by $\Delta z \sim \sigma_v/\sqrt{N}$, where N is the number of measured redshifts in that cluster. Zabludoff *et al.* (1991) found that the median velocity dispersion for a large sample of clusters was $\sim$ 750km s^{-1}, which translates to an error of $\Delta z \sim 0.001$ for an average of 10 redshifts per cluster. This is in good agreement with the measured error quoted above, but as a precaution,

ID	z	No.	Refs.	ID	z	No.	Refs.
4	0.0653	1	da Costa *et al.* 1991.	38	0.0934	2	Muriel *et al.* 1990.
86	0.0940	1	Loveday (1991).	124	0.1457	30	Colless & Hewett 1987.
129	0.0349	2	Loveday (1991).	160	0.1510	149	Teague *et al.* 1990.
173	0.0569	?	Peacock.	176	0.0570	1	Nicholson 1991.
188	0.0671	2	Muriel *et al.* 1990.	190	0.0664	1	CfA Redshift Survey.
231	0.1351	1	CfA Redshift Survey.	246	0.0635	1	CfA Redshift Survey.
258	0.1119	2	Struble & Rood 1984.	258	0.1118	1	CfA Redshift Survey.
261	0.1170	3	Peacock.	279	0.0840	1	Nicholson 1991.
307	0.0547	2	Vettolani *et al.*, 1989.	335	0.0701	1	Olowin *et al* 1988.
356	0.0432	1	CfA Redshift Survey.	360	0.0624	1	CfA Redshift Survey.
361	0.0271	1	CfA Redshift Survey.	366	0.0732	2	Muriel *et al.* 1990.
370	0.0285	1	CfA Redshift Survey.	377	0.0592	1	Broadbent.(P. Com.)
381	0.1016	2	Muriel *et al.* 1990.	394	0.0488	4	CfA Redshift Survey.
396	0.0678	2	Muriel *et al.* 1990.	400	0.1142	3	CfA Redshift Survey.
400	0.1160	32	Colless & Hewett 1987.	407	0.0489	3	Henry *et al.* Preprint.
410	0.0616	1	CfA Redshift Survey.	419	0.1209	1	CfA Redshift Survey.
431	0.0923	2	Muriel *et al.* 1990.	447	0.1085	1	CfA Redshift Survey.
448	0.1074	1	Parker. (P. Com.)	480	0.0540	1	CfA Redshift Survey.
482	0.1100	2	Stevenson. 1985.	495	0.1110	2	Stevenson. 1985.
507	0.1130	2	Stevenson. 1985.	520	0.1590	1	CfA Redshift Survey.
533	0.0193	1	CfA Redshift Survey.	557	0.0803	2	Cappi *et al.* 1991.
683	0.1350	?	Peacock.	695	0.0200	1	CfA Redshift Survey.
700	0.1120	?	Peacock.	712	0.1151	1	CfA Redshift Survey.
729	0.0665	2	Sandage 1978.	735	0.0678	1	CfA Redshift Survey.
735	0.0688	2	Cappi *et al.* 1991.	747	0.0785	1	CfA Redshift Survey.
758	0.0644	2	Muriel *et al.* 1990.	758	0.0687	1	CfA Redshift Survey.
763	0.1030	?	Peacock.				

Table 4.6: Table of some of the literature redshifts found for EDCC clusters. Redshifts with the reference, CFA Redshift Survey, were taken from the full up–to–date CfA Redshift Survey and were kindly provided by John Huchra. Cluster with the reference, Peacock, were taken from a large database of cluster redshifts compiled by John Peacock at Edinburgh. The redshifts for clusters 448 and 377 were provided from unpublished data and are warmly acknowledged. Note: ID is the EDCC identification number and No. is the number of measured redshifts for that cluster.

clusters with 2 independent observations were compared and the average error or offset between the redshifts computed. For 20 clusters, usually literature against EM cluster, the mean difference between the redshift measurements was $\Delta z \simeq 0.0017$, which again, is in good agreement with the expected error quoted above. This error is insignificant to statistical studies of the cluster distribution as this represents an error of $0.2\,h^{-1}$ Mpc in the radial distance to a cluster.

4.5.11 The m_{10}–log z Relationship

This relationship has been used by many authors to predict the distance of a cluster. The relationship uses the correlation found between the magnitude of tenth brightest cluster galaxy (m_{10}) and the cluster's redshift. However, the error on a predicted redshift from a cluster m_{10} magnitude is very high *i.e.* 25%.

The $\log_{10} - m_{10}(b_j)$ relationship was derived for a subsample of 80 EM clusters, all of which had a robust redshift measurement. A least–squares fit to the data gave

$$\log_{10} z = -(4.702 \pm 0.139) + (0.2015 \pm 0.0004) m_{10}, \tag{4.10}$$

with a reduced χ^2 of 1.21. In Chapter 3, the completeness limits of the EDCC were quoted as $15.5 < m_{10}(b_j) < 18.75$. This corresponds to a redshift completeness of $0.03 < z < 0.13$. These limits will be used later in Chapter 5.

Zamorani *et al.* (1991) examined the $m_{10} - \log_{10} z$ relationship for a large sample of Abell clusters and found a better fit to the data using $(m_3 + m_{10})/2$ instead of m_{10}. Therefore, for the EM clusters, several combinations of m_1, m_3 and m_{10} were tried. The best combination was found to be

$$log_{10} z = -(3.929 \pm 0.090) + (0.1671 \pm 0.0003) \left(\frac{m_1 + m_{10}}{2} \right), \tag{4.11}$$

which gave a reduced χ^2 of 1.13. The error on a redshift, calculated from the error on the fit, was $\sim 20\%$.

Clearly, a better method of predicting the cluster redshift can be obtained by using all the available information within the EDSGC. It is possible to construct the apparent

magnitude distribution of the whole cluster and use this instead of the simple m_{10} magnitude. However, the error on any estimated redshift will always be high, making it difficult to use meaningfully.

4.6 The Small Abell Radius Selection

As already stated, the main motivation behind the construction of the EM survey was to re–estimate the spatial correlation function free from systematic errors and biases that have plagued previous estimates. One of the major problems has been the effects of projections in the catalogues used. Chapter 1 gave a full discussion of these projection effects and the reader is referred there for details.

One of the easiest ways of reducing projection effects is to reduce the size of the counting radius within which the cluster is defined. This would reduce the number of cluster overlaps and thus prevent distant clusters in the haloes of nearby clusters being boosted into the catalogue. In the Abell catalogue, a radius of $1.5h^{-1}$ Mpc was used to define the clusters (Chapter 1). Many authors believe this is an overestimate for the size of clusters and even George Abell, in his original paper, commented that his radius maybe 30% too large.

The EDCC was constructed using the standard Abell radius mentioned above, as this allowed for a fair comparison between it and the Abell catalogue (Chapter 3). For the computation of the cluster correlation function, a new sample of clusters was selected from the EDCC using a smaller radius of $1.0h^{-1}$ Mpc. This reduced the number of overlaps from 30% in the standard EDCC to 8% in this sample and constrained the clusters to be more centrally condensed.

The final sample used to calculated the correlation function was selected using the following criteria.

1. Clusters with a galaxy richness, R, greater or equal to 22, after background correction, within an Abell radius of $1.0h^{-1}$ Mpc.

2. A background corrected $m_{10}(b_j)$ of less than 18.75 which corresponds to the completeness limit of the EDCC.

3. Within the coordinate limits of 21.88hrs < RA < 3.59hrs and $-42.4° <$ Dec $< -22.88°$. This prevented clusters near the edge of the survey being included as their statistics were often uncertain.

By comparing clusters in common between this sample and the Abell catalogue, the $R \geq 22$ richness cut corresponded to a richness cut of 40 for Abell clusters. This meant that this small Abell radius sample of clusters was equivalent to a richness between the Abell $RC = 0$ and $RC = 1$ richness classes as defined in Chapter 1.

Appendix F contains all the details of the sample. In total, 97 clusters were selected, of which 71 had a redshift from the EM survey and 16 from the literature. This corresponded to a redshift completeness of 90%. Clusters without a redshift had their redshifts estimated using the $\log_{10} z - m_{10}$ relationship above and are negative in Appendix F. For the 71 clusters measured as part of the EM survey, 9 were rejected as projection effects and these are clearly marked. The analysis of this sample is explained in the next chapter along with the larger EM survey.

4.7 Summary

The EM survey was constructed over 5 years using both the AAT in Australia and the ESO 3.6m telescope in Chile. On average, 10 galaxies were observed per cluster allowing the redshift of the cluster to be determined unambiguously. The individual galaxy redshifts were calculated using the cross–correlation technique described by Tonry & Davis (1979) and had an accuracy of $\sim 50 \mathrm{km\,s^{-1}}$. The cluster redshifts were calculated using a set of well–defined objective criteria. The error on the cluster redshifts were in good agreement with that expected from the velocity dispersions of clusters.

The objective criteria used resulted in a natural definition of an interloper and a phantom cluster. It was found that $\sim 70\%$ of the clusters had some amount of interloper contamination and for these clusters $\sim 25\%$ of the sampled galaxy redshifts were defined as interlopers. This means that there is a 20% probability of a measured galaxy redshift being an interloper.

The EDCC was re–analysed using a smaller Abell radius and the number of cluster

overlaps was reduced by a factor of 3. This new sample of 97 clusters was found to be 90% complete in redshift measurements, with 71 from the EM survey and 16 from the literature. Nine clusters were classed as spurious. This sample is used extensively in the next chapter.

Chapter 5

The Large Scale Distribution of Clusters

Over the last 10 years, there has been much discussion in the astronomical literature over the true distribution of galaxy clusters in the nearby universe. Our knowledge of this distribution has mainly come from detailed studies of the Abell catalogue of rich clusters. However, many authors believe that the hidden systematics within this catalogue have undermined our understanding of the cluster distribution.

This chapter examines the spatial distribution of clusters within the EM survey. This is carried out in two ways. First, an examination of the size and distribution of structures within the survey is performed, along with an investigation of the recently reported Broadhurst *et al.* phenomenon. Secondly, the spatial cluster correlation function ($\xi_{cc}(r)$) is estimated and compared to previous estimates of the cluster correlation function. The implications of these observations on models of galaxy formation are discussed.

5.1 Introduction

The main motivation behind the construction of the EM cluster redshift survey was to study the spatial distribution of clusters free from the systematic errors and biases that have plagued previous catalogues of galaxy clusters. In Chapter 3, the methods used to objectively detect clusters of galaxies from the EDSGC were outlined, while Chapter 4 detailed the techniques used in constructing the EM survey. In addition, Chapter 4 presented the full EM survey and a 90% redshift complete sample of clusters constructed using a smaller than usual Abell radius. This chapter is concerned with the scientific analysis of the EM survey and the subsequent conclusions drawn from that analysis.

This analysis is split into 2 sections. The first is a presentation of the EM survey to identify certain large structures, which are then related to the periodicity in the galaxy distribution reported by Broadhurst *et al.* (1990). The second part is concerned with the estimation of ξ_{cc} from the EM survey.

5.2 Clusters as Tracers of the Large–Scale Structure

5.2.1 The Observed Distribution of Clusters

Clusters of galaxies are key tracers of the large–scale structure in the universe. Since their typical separation is $\sim 10h^{-1}$ Mpc, they represent an efficient method of tracing structures over hundreds of megaparsecs. Over these scales, the use of galaxies as tracers would require a large investment of telescope time. Previous studies of the large scale distribution of clusters have been based upon cluster catalogues visually compiled from photographic plates *i.e.* the Abell catalogue (Oort 1983, Bahcall 1988). However, many authors believe that the systematic biases and errors within these catalogues have given a false view of the distribution of clusters (Postman 1986, Sutherland 1988).

The RA and Declination coneplots for the full EM survey (104 clusters, 87 clusters after phantom clusters have been removed and 17 new redshifts from the literature) are shown in Figures 5.1 and 5.2 respectively. For comparison, the RA coneplot of the 90% complete sample of clusters defined in Chapter 4 and presented in Appendix F is

shown in Figure 5.3. The most impressive features of these diagrams are highlighted below.

1. The huge supercluster at $z = 0.11$ corresponds to the Sculptor Supercluster (Seitter *et al.* 1989). This structure contains over 20 systems extending over $\sim 70h^{-1}$ Mpc in RA and $\sim 140h^{-1}$ Mpc in Declination and is one of the most massive structures seen in the nearby universe (Corona Borealis Supercluster contains 15 Abell clusters with a diameter $\sim 300h^{-1}$ Mpc, while the Hercules Supercluster contains only 8 Abell clusters and has a diameter $145h^{-1}$ Mpc, Oort 1983).

2. The large spherically shaped supercluster at $z \sim 0.06$ is identified as the BS1 Supercluster (Bahcall & Soneria 1984). This structure also contains many clusters and has a radius of $\sim 100h^{-1}$ Mpc.

3. At the edge of the survey (RA $\sim$ 3 hours), a large void of clusters is evident (diameter $\sim 150h^{-1}$ Mpc) which has not been identified with any previously observed void. As well as this large void, several other underdensity regions are present, particularly between BS1 and the Sculptor Supercluster.

4. All these structures are seen in the complete well–defined 90% redshift complete selection of clusters (Chapter 4)

The most striking result of this visual presentation of the EM survey is shown in Figure 5.4. This is a plot of the redshift distribution for 3 different volumes within the EM survey (3.5 $\rightarrow$ 1.2 hours, 1.2 $\rightarrow$ 23.4 hours, 23.4 $\rightarrow$ 21.5 hours and Declination range of $-22.5° \rightarrow -42.5°$). The middle plot (b) is in the direction of the SGP and includes the two superclusters described above. The markers are the positions of the observed Broadhurst *et al.* (1990) peaks in the galaxy distribution which they claimed was periodic (period of $128h^{-1}$ Mpc) out to redshifts of ~ 0.3 towards the Galactic Poles (SGP & NGP). This result caused much controversy in the astronomical literature and if true, would revolutionise our understanding of the distribution of galaxies in the universe.

There is a clear correspondence between the cluster structures and the Broadhurst peaks in both the full and 90% redshift complete samples. The position of the Broadhurst

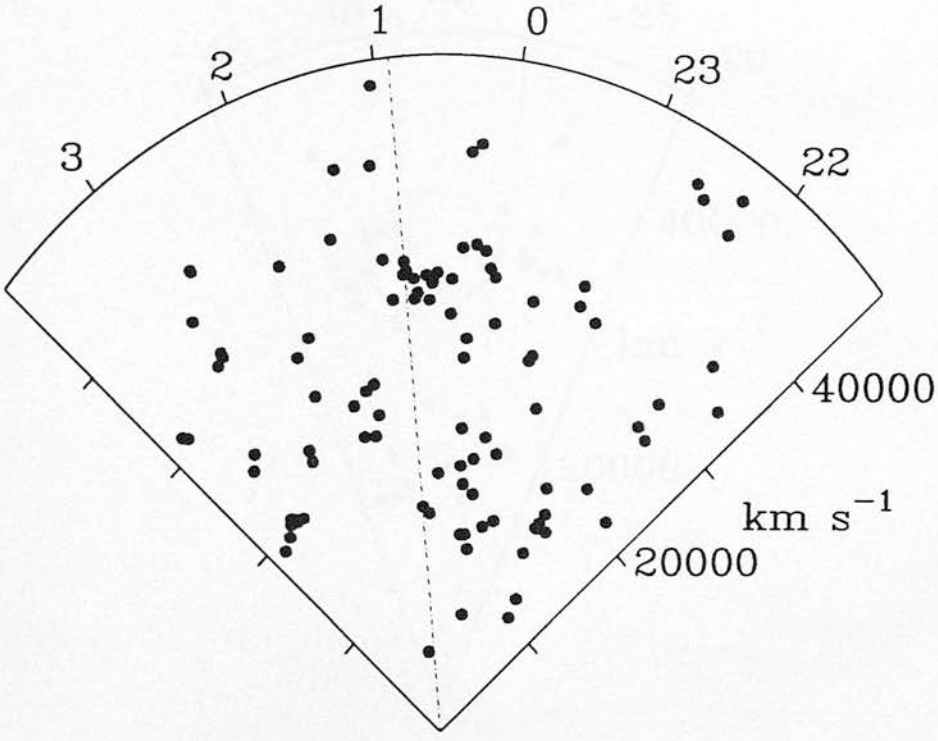

Figure 5.1: The Right Ascension cone diagram for the whole EM survey. The structure at $z = 0.11$ is the Sculptor Supercluster, while the structure at $z = 0.06$ is known as the BS1 Supercluster. The dot–dashed line corresponds to the line–of–sight towards the SGP and is the direction observed by Broadhurst *et al.* (1990). See text for discussion.

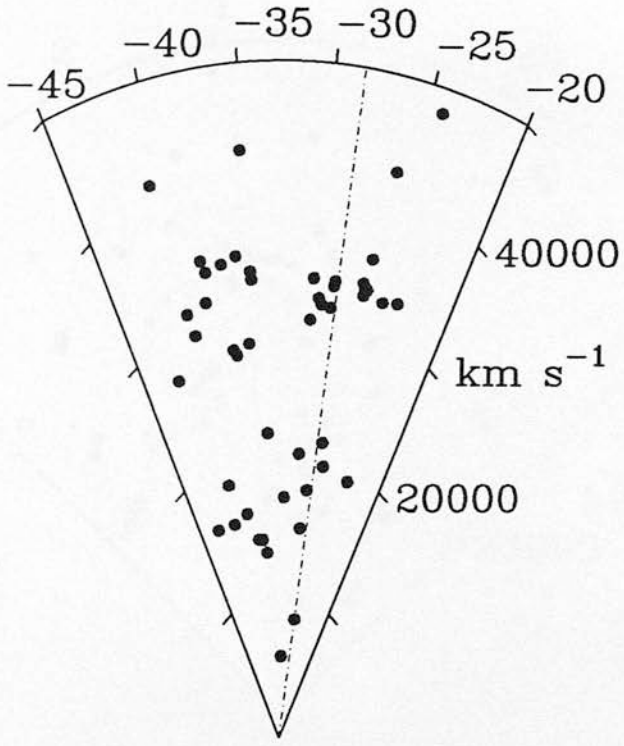

Figure 5.2: The Declination cone diagram for the whole EM survey with the RA constrained to 1.2 → 23.4 hours (48 clusters). The Sculptor and BS1 superclusters are easily identified. The dot–dashed line corresponds to the line–of–sight towards the SGP and is the direction observed by Broadhurst *et al.* (1990). See text for discussion.

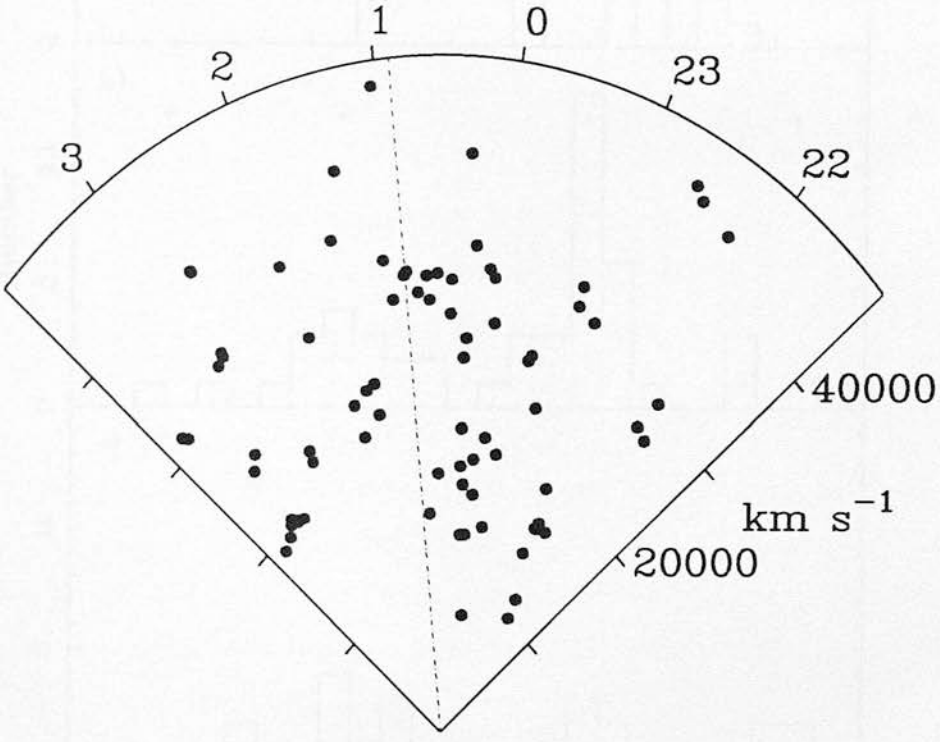

Figure 5.3: The Right Ascension cone diagram for the 90% redshift complete sample of clusters from the EM survey (Chapter 4). The structure at $z = 0.11$ is the Sculptor Supercluster, while the structure at $z = 0.06$ is known as the BS1 Supercluster. The dot–dashed line corresponds to the line–of–sight towards the SGP and is the direction observed by Broadhurst *et al.* (1990). See text for discussion.

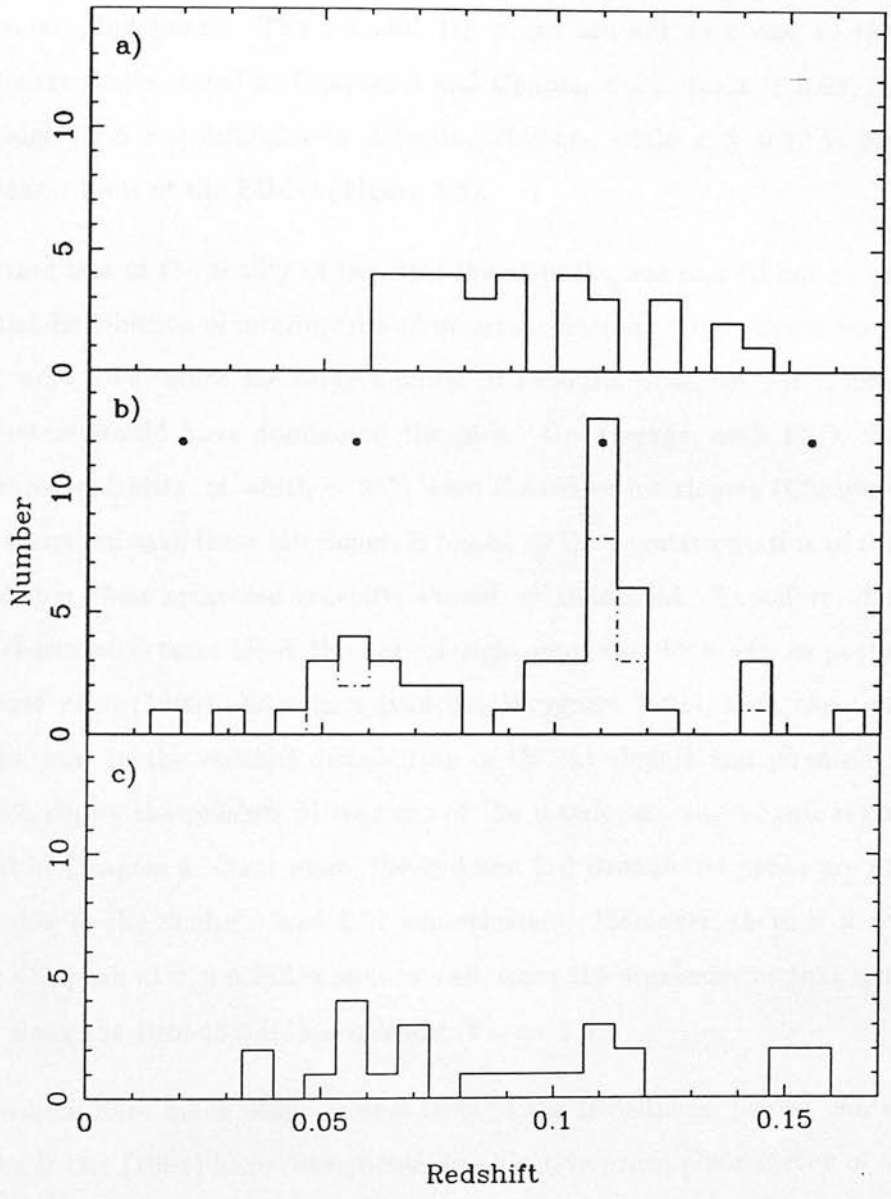

Figure 5.4: The redshift histograms for the RA ranges: a) 3.5 → 1.2 hours, b) 1.2 → 23.4 hours and c) 23.4 → 21.5 hours taken from Figure 5.1. The data plotted is the full EM survey discussed in Chapter 4. Panel b) also shows the redshift histogram for the 90% redshift complete sample (dot–dashed line). The • symbols represent the positions of the observed Broadhurst *et al.* (1990) peaks (see text).

line–of–sight is shown in Figures 5.1, 5.2 & 5.3 and passes straight through the centre of the Sculptor Supercluster (3rd peak), while clipping the outer regions of the BS1 Supercluster (2nd peak). The 1st and 4th peaks are not seen due to the redshift completeness limits stated in Chapter 3 and Chapter 4 *i.e.* for $z < 0.02$, the cluster finding algorithm has difficulty in detecting clusters, while $z > 0.13$ is beyond the completeness limit of the EDCC (Figure 3.4).

One further test of the reality of the Broadhurst peaks was carried out by examining the spatial distribution of interlopers and phantom clusters. Only the clusters observed at ESO were used, since the large number of redshifts observed per cluster for the AAT clusters would have dominated the plot. On average, each ESO cluster had 10 measured redshifts, of which $\sim 25\%$ were classed as interlopers (Chapter 4). The angular distribution of these interlopers is biased by the angular selection of the clusters observed, but their measured redshifts should be unaffected. Therefore, if there are regular sheets/structures along the line–of–sight separated by voids, as postulated by Broadhurst *et al* (1990) and others (van der Weygaert 1991), then these structures should be seen in the redshift distribution of the interlopers and phantom clusters. Figure 5.5 shows the redshift histograms of the interlopers and phantom clusters as discussed in Chapter 4. Once more, the 2nd and 3rd Broadhurst peaks are prominent and are due to the Sculptor and BS1 superclusters. Moreover, there is a suggestion that the 4th peak at $z \simeq 0.165$ is seen as well, since the 4 galaxies at that redshift are directly along the Broadhurst line–of–sight (Figure 5.5).

Other authors have made observational tests of the Broadhurst peaks. For example, Schuecker & Ott (1991) have constructed an objective prism plate survey of $\sim 40,000$ galaxies centred on the SGP. The survey probes to a depth of $z \sim 0.3$ and is therefore, ideal for testing the reality of the Broadhurst peaks. However, they found no such peaks, but the large observational error on their redshifts must certainly have smear out the structures. To test this, the EM survey redshifts in Figure 5.1 were convolved with a Gaussian of width $\sigma_z = 0.013$, which is equal to the redshift error quoted by Schuecker & Ott (1991). As suspected, the peaks were no longer visible above the mean of the redshift distribution (this is demonstrated in Figure 5.6). Tully *et al.* (1992) also investigated the Broadhurst phenomenon using clusters from the Abell catalogue

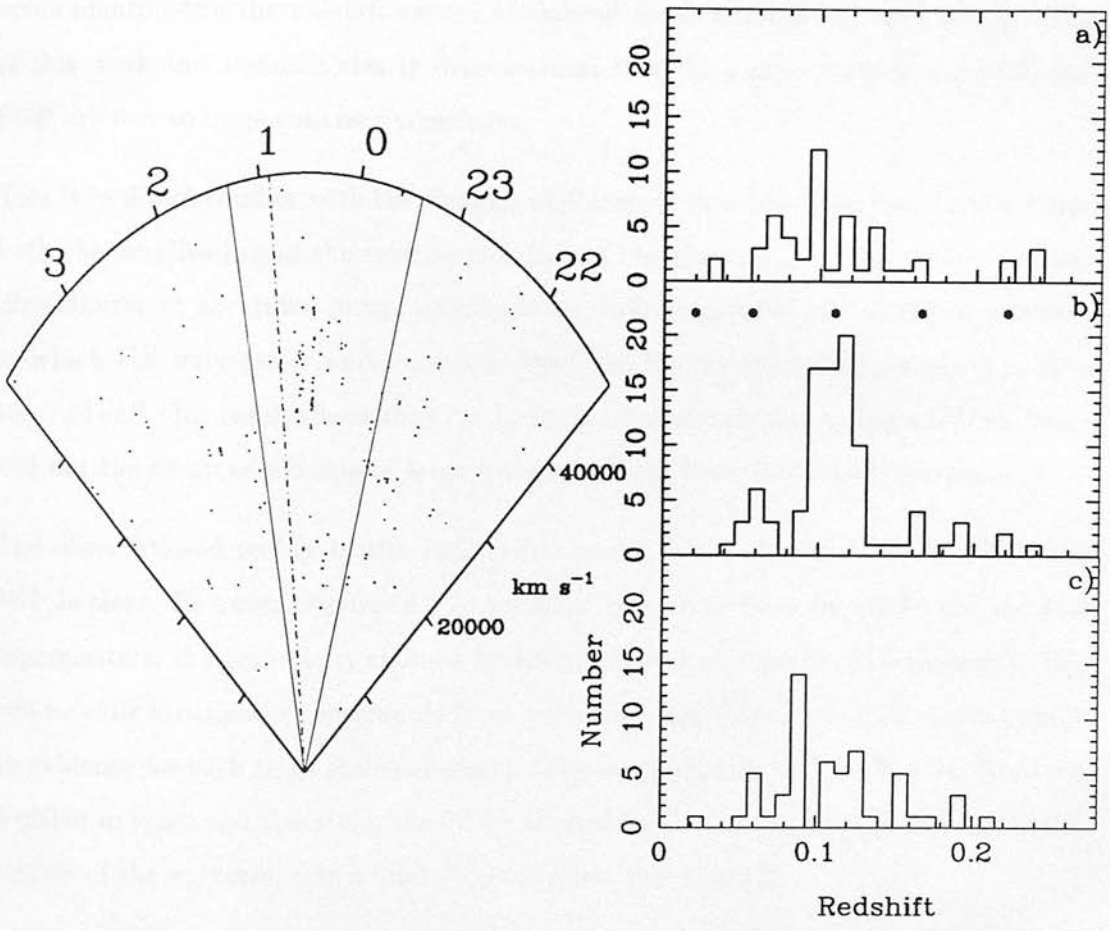

Figure 5.5: The RA coneplot and redshift histograms for the ESO interlopers. The coneplot shows 184 galaxies defined as cluster interlopers or phantom clusters (redshift cut of 0.17). Several 'finger of God' effects can be seen and these are due to small groups of galaxies aligned along the direction of sight appearing as rich clusters (phantom clusters). The dashed line is the Broadhurst *et al.* (1990) line–of–sight. The two large superclusters discussed in the text are clearly visible. The redshift histograms are for the RA ranges: 3.5 → 1.2 hours, 1.2 → 23.4 hours and 23.4 → 21.5 hours (faint lines drawn on the coneplot). These histograms contain all the ESO interlopers, which is 203 galaxies in total. Again, the Broadhurst peaks are present in panel (b) but absent in panels (a) and (c).

(mainly estimated redshifts) and found a tentative agreement between the peaks and cluster overdensities. Finally, Bahcall (1991) found a clear coincidence between the Broadhurst peaks towards the North Galactic Pole (NGP) and known superclusters and voids identified in the redshift survey of Bahcall & Soneira (1984). The combination of this work and Bahcalls clearly demonstrates that the peaks towards the NGP and SGP are due to large coherent structures.

This is in direct conflict with the findings of Kaiser & Peacock (1991) who claim "that both the amplitude and the relative isolation of the peak at $\lambda = 128\,h^{-1}$Mpc in their [Broadhurst *et al.* 1990] power spectrum are well consistent with a null hypothesis in which the universe is uniform apart from the known clustering on scales $\sim 1 - 10h^{-1}$Mpc." Our result shows that the Broadhurst peaks are due to large superclusters and not the result of aliasing of large scale structures from small scale clustering.

The observational reality of the Broadhurst peaks in the direction of the NGP and SGP is clear. However, Figures 5.1 & 5.4 show that away from the SGP, and the two superclusters, the periodicity claimed by Broadhurst *et al.* changes or disappears. The two redshift histograms constructed from volumes either side of the SGP volume show no evidence for such large scale coherence. This suggests that the NGP–SGP direction is either unique, and therefore, should be studied further, or, in the context of cellular models of the universe, was a 'lucky' initial guess (see below).

5.2.2 Discussion

The visual presentation of the EM survey above shows that the Broadhurst peaks are the result of large superclusters along the line–of–sight. Models of the large–scale structure which incorporate a cellular or foam type structure have tried to explain the Broadhurst periodicity in terms of skewers through the walls of much larger structures (Coles 1990, Kurki-Suonio *et al.* 1990, Ikeuchi & Turner 1991, van de Weygaert 1991). In principle, the EM survey can be used to distinguish between these models by placing constraints on the frequency of the periodicity as away from the direction of the SGP the periodicity either changed or disappeared (Figure 5.4).

Kurki-Suonio *et al.* (1990) proposed a model in which the galaxies populated the

surfaces of bubbles or sheets whose centres were anticorrelated. In such a model, they showed that there was a $\sim 80\% - 85\%$ probability of observing regular periodicity in the galaxy distribution along any line–of–sight. On the other hand, in the Voronoi cellular model of van de Weygaert (1991) there is only a 15% probability of any line–of–sight showing periodicity similar to that reported by Broadhurst *et al.* (1990).

From the EM survey, the probability of a random line–of–sight intersecting both the Sculptor and BS1 superclusters and therefore, producing the Broadhurst peaks is $\sim$ 20%. At face value, the EM survey is consistent with Voronoi models of the galaxy distribution and is definitely inconsistent with bubble and/or sheet models. However, a detailed analysis of the Voronoi model by Williams (1992) shows that this model cannot simultaneously account for the recent observations of the galaxy angular correlation function (Chapter 2, Collins *et al.* 1992), the spatial cluster correlation function (this chapter, Nichol *et al.* 1992) and the periodicity of Broadhurst *et al.* (1990).

5.3 The Spatial Cluster Correlation Function

The two–point correlation function is the most popular statistic used to quantify the distribution of galaxies and clusters of galaxies. The spatial correlation function ($\xi(r)$) is defined as

$$dP = N^2(1 + \xi(r))dV_1 dV_2 , \qquad (5.1)$$

where N is the number density of galaxies or clusters. It is the excess probability (dP) of finding 2 galaxies or clusters in volume elements dV_1, dV_2 separated by a distance r compared to a random distribution. This is the direct equivalent of the definition given in Chapter 2 for the angular two–point correlation function. Using similar arguments as given in Chapter 2, ξ can be defined as

$$\xi(r) = \frac{2N_r}{N_d}\frac{n_{dd}}{n_{dr}} - 1 , \qquad (5.2)$$

where n_{dd} is the number of data–data pairs with a separation r, and n_{dr} is the number of data–random pairs with the same separation. N_r and N_d are the number of random

and data objects respectively. The factor of two is present in the numerator because the pairs are double counted compared to the denominator (Chapter 2). A full discussion of the spatial correlation function can be found in Peebles (1980) and Davis & Peebles (1983).

Although Chapter 1 contained a review of the major estimates of the spatial correlation function, it is worth summarising the main points here. The observed spatial correlation function can be characterised by

$$\xi(r) = (r_o/r)^{\gamma}, \tag{5.3}$$

where r is the spatial separation, r_o normalises the correlation function and γ is the slope. For galaxies, $r_o \simeq 5h^{-1}$ Mpc ($\gamma = 1.8$), while for clusters, $r_o \simeq 25h^{-1}$ Mpc ($\gamma = 1.8$). The discrepancy between the clustering strengths (r_o) of the galaxies and clusters has caused much debated in the astronomical literature.

5.3.1 The Mechanics of Estimating $\xi_{cc}(r)$

The cluster correlation function was calculated for the 90% redshift complete sample of clusters defined in Chapter 4 using equation 5.2. Table 5.1 shows the limits used in computing ξ_{cc}. It was important to accurately define the limits on the data as these limits were used in the construction of the random catalogues (below). The angular limits on the data were dictated by the size of the EDSGC. The upper redshift limit was set at the highest observed cluster redshift (below), while the lower redshift limit was placed at $z = 0.02$ as the methods used in detecting the clusters were unable to find clusters this close.

Coordinate	Upper limit	Lower limit
Right Ascen.(Hours)	21.89	3.59
Declination (degs.)	−22.88	−42.40
Redshift	0.16	0.02

Table 5.1: Table of data limits used in the estimation of ξ_{cc}.

The advantage of using equation 5.2 in calculating ξ_{cc} is that any systematic errors or biases in the data can be included into the random catalogue. In addition, the effect of the edges of the survey are reduced (Chapter 2). The first major problem in estimating ξ_{cc} was in the construction of the random catalogue as care must be taken to include the data selection function into the random catalogue. During the construction of the EDCC, much effort was invested in making the selection of clusters throughout the survey as homogeneous as possible. The implementation of sky background subtraction substantially reduced environmental dependences on the angular detection of clusters (*i.e.* patchy extinction). Therefore, the angular selection function of clusters was assumed to be flat across the survey.

However, the redshift selection function of the data was unknown. Therefore, to remove the need for modelling this function, the redshifts of the random clusters were drawn from the data redshift histogram after it had been smoothed with a Gaussian of dispersion 3000km s^{-1}. This smoothing reduced the effects of binning noise and lowered the significance of certain strong structures seen in the redshift distribution (section 5.2). In addition, using the data redshift histogram removed the need to have a fixed upper redshift limit to the data as the random catalogue was constrained to have the same redshift distribution. Figure 5.6 shows the redshift histograms for the data and a typical random catalogue constructed from that data.

Each random catalogue was generated with one hundred times the number of clusters as in the data. Each random cluster was assigned a random Right Ascension and Declination within the limits shown in Table 5.1, while its redshift was drawn from the smoothed data redshift distribution, again within the limits shown in Table 5.1. For each estimation of $\xi_{cc}(r)$, 20 random catalogues were used.

The radial co–moving distance, R, to each cluster is related to its redshift by

$$R = \frac{c}{H_o q_o^2 (1+z)} \left[q_o z + (1-q_o)(1-\sqrt{2q_o z + 1}) \right] , \qquad (5.4)$$

(Mattig 1958) for the standard Friedmann cosmology. Assuming $q_o = \frac{1}{2}$, the separation r, between clusters (real or random) was determined using the cosine rule as the angle

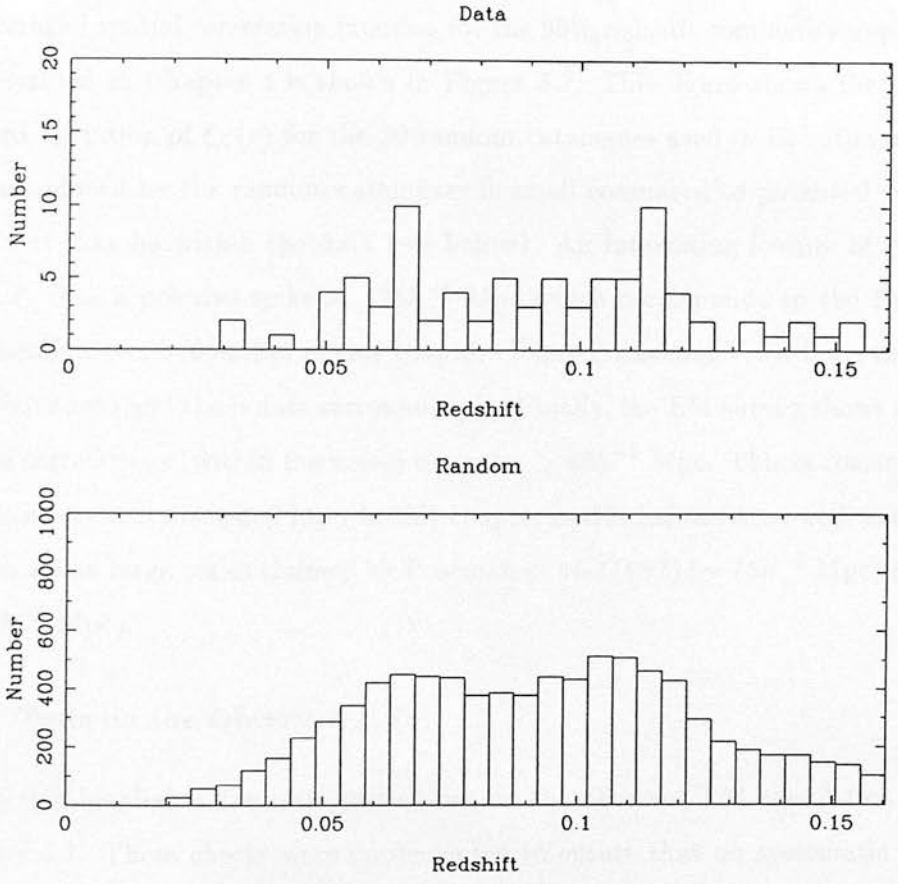

Figure 5.6: The redshift histograms for the data catalogue and the corresponding random catalogue. See text for details on the construction of the random catalogue.

between the two clusters was known. These separations were binned as a function of r to obtain the required quantities n_{dd} and n_{dr} in equation 5.2. Logarithmic bins were used in preference to linear bins ($\Delta r = \Delta \log_{10} r = 0.2$) as this increased the signal–to–noise at large scales where the clustering signal was weaker. The centre of the bins were defined in log space as $r - \Delta r/2 < r < r + \Delta r/2$. The differences between the logarithmic and linear bins was well within the errors (Figure 5.7).

The averaged spatial correlation function for the 90% redshift complete sample of clusters described in Chapter 4 is shown in Figure 5.7. This figure shows the mean and standard deviation of $\xi_{cc}(r)$ for the 20 random catalogues used in its estimation. The noise introduced by the random catalogues is small compared to potential systematic errors that may be within the data (see below). An interesting feature of Figure 5.7 is that ξ_{cc} has a positive spike at $128h^{-1}$ Mpc which corresponds to the Broadhurst phenomenon described earlier in this chapter. Using Poissonian error bars, the spike is $\sim 2\sigma$ above zero and the points surrounding it. Finally, the EM survey shows no sign of positive correlations (within the noise) on scales $> 40h^{-1}$ Mpc. This is consistent with the anisotropy test discussed later in this chapter and is inconsistent with the positive correlations on large scales claimed by Postman *et al.* (1992) ($\sim 75h^{-1}$ Mpc) and BS83 ($\sim 150h^{-1}$ Mpc).

5.3.2 Tests on the Observed $\xi_{cc}(r)$

This section highlights five tests carried out on the observed EM correlation function in Figure 5.7. These checks were implemented to ensure that no systematic errors or biases were introduced by the techniques used in deriving the observed function.

1. The data catalogue was replaced by a random catalogue and the correlation function computed. As expected, the correlation function was zero within the noise.

2. The correlation function was computed using different data limits to those shown in Table 5.1 to check whether the constraints on the data coordinates where fair. New angular limits were set at ten degrees further into the sample, while the redshift limits were set at 0.0 and 0.13 (the upper limit corresponds to the completeness limit of the EDCC, see Figure 3.4 and section 4.5.11). The new

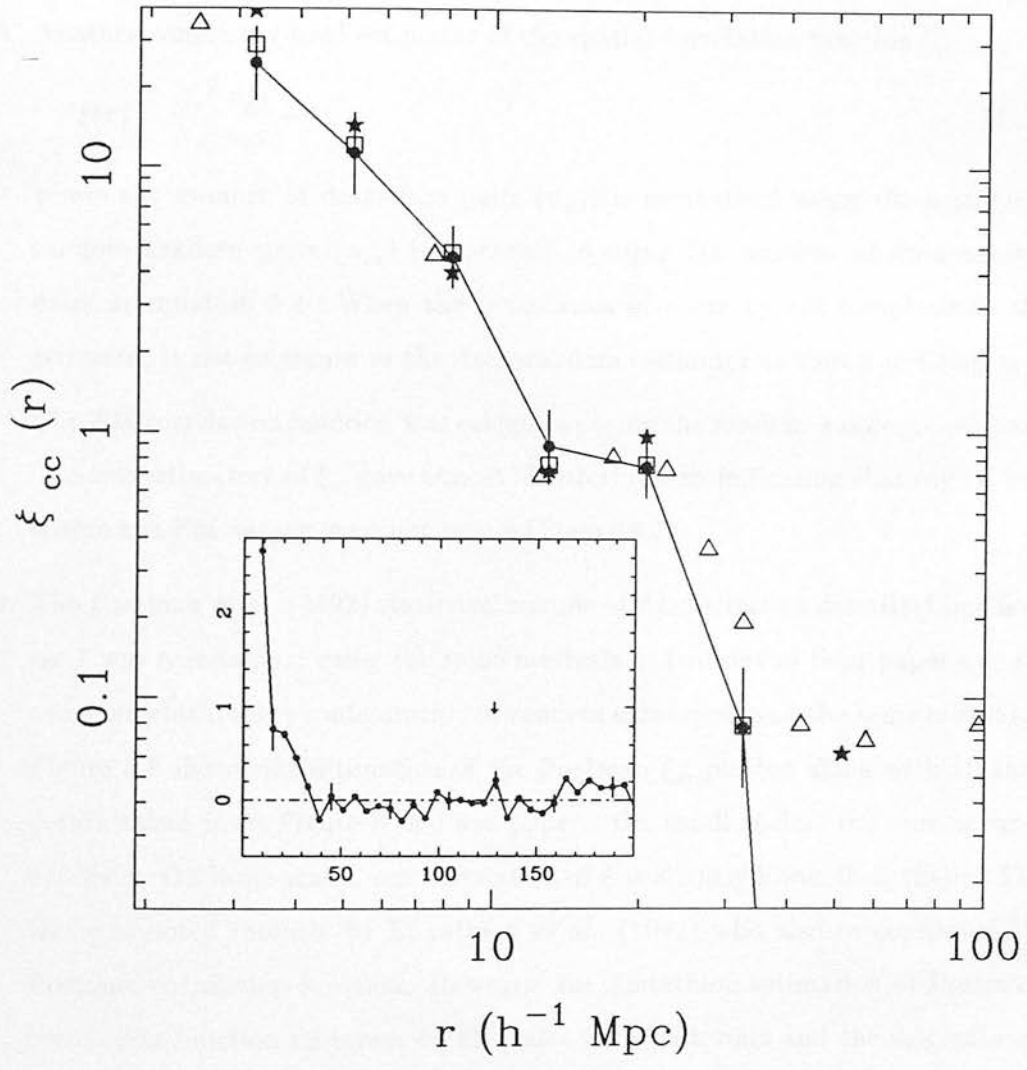

Figure 5.7: The spatial correlation function derived from the EM survey 90% redshift complete sample. The joined line is ξ_{cc} averaged over 20 random catalogues and the error bars are the standard deviation between these random catalogues. The □ symbols are ξ_{cc} estimated using the random–random estimator and the ⋆ symbols are ξ_{cc} estimated for a smaller area of the EM survey (see text). Finally, △ symbols are linear bins and inset is a linear plot of ξ_{cc} which is plotted out to a scale of $200h^{-1}$ Mpc. The arrow marks the scale of periodicity reported by Broadhurst *et al.* (1990) and coincides with a positive peak in ξ_{cc}. The error bars are Poissonian, only every fifth bar is plotted.

correlation function (67 clusters) is plotted in Figure 5.7 and there is no significant difference, within the error, between the correlation functions.

3. Another commonly used estimator of the spatial correlation function is

$$\xi(r) = \frac{{N_r}^2}{{N_d}^2}\frac{n_{dd}}{n_{rr}} - 1\,, \qquad (5.5)$$

where the number of data–data pairs (n_{dd}) is normalised using the number of random–random pairs (n_{rr}) in contrast to using the number of data–random pairs in equation 5.2. When the boundaries of a survey are complicated, this estimator is not as secure as the data–random estimator as shown in Chapter 2.

The EM correlation function was calculated using the random–random estimator. The two estimators of ξ_{cc} gave almost identical results indicating that edge effects within the EM survey were not severe (Figure 5.7).

4. The Postman *et al.* (1992) statistical sample of Abell clusters described in Chapter 1 was re–analysed using the same methods as laid out in their paper *i.e.* the same binwidth, same configuration of random catalogues and the same estimator. Figure 5.8 shows our estimation of the Postman ξ_{cc} plotted along with all their points taken from Figure 8 of their paper. On small scales, the agreement is excellent. On large scales, our estimation of ξ is slightly lower than theirs. This fact was noted recently by Efstathiou *et al.* (1992) who also re–computed the Postman correlation function. However, the Efstathiou estimation of Postmans correlation function disagrees on all scales with both ours and the original estimation (Figure 5.8). Part of our disagreement on large scales is due to the fact that Postman does not connect the data points with a line and therefore, does not indicate the presence of low or negative points that are not plotted. There are clearly points missing on large scales from Figure 8 of their paper and these missing points are negative in our estimation of their ξ_{cc}. This oversight leads to a false impression of large scale power in their correlation function.

The agreement with Postman on small scales is encouraging as it indicates that the methods being used to estimate ξ_{cc} for different samples of clusters are consistent. Any differences in the observed correlation functions for different samples cannot be due to different estimation techniques.

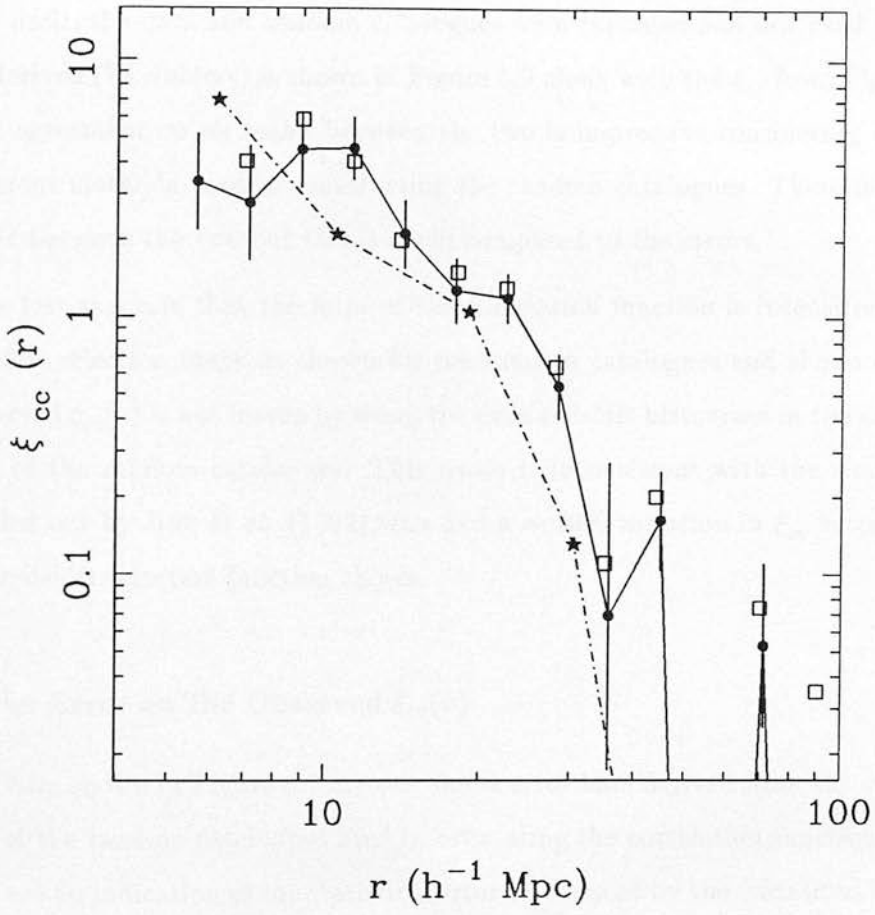

Figure 5.8: The spatial correlation function derived by us for the Postman *et al.* (1992) statistical sample (•). Also shown are all the data points from Figure 8 of their paper (□) and the re–analysis of the Postman data carried out by Efstathiou *et al.* (1992) (⋆). The error bars are Poissonian.

5. The final test was carried out by Luigi Guzzo. He independently estimated the correlation function for the EM 90% redshift complete sample of clusters using an alternative method of constructing the random catalogues. He assumed that the EM survey was volume–limited to a redshift of $z = 0.13$ and generated the random catalogues with a constant number density out to this redshift. Beyond this limit, the data and random catalogues were curtailed and not used. The ξ_{cc} he derived (73 clusters) is shown in Figure 5.9 along with the ξ_{cc} from Figure 5.7. The agreement on all scales between the two is impressive considering the very different methods used in constructing the random catalogues. There is a slight offset between the two but this is small compared to the errors.

   This test suggests that the form of the correlation function is insensitive to the redshift selection function chosen for the random catalogues and shows that the observed $\xi_{cc}(r)$ is not biased by using the data redshift histogram in the construction of the random catalogues. This result is inconsistent with the simulations carried out by Jing *et al.* (1992) who find a $\sim 30\%$ variation in ξ_{cc} according to the redshift selection function chosen.

5.3.3 The Error on the Observed $\xi_{cc}(r)$

The error bars shown in Figure 5.7 are one sigma error bars derived from the standard deviation of the random catalogues used in estimating the correlation function. These error bars are an indication of the statistical error introduced by the variations between the random catalogues and have little bearing on possible systematic errors in the data. The simplest way of estimating the error on the observed cluster correlation function would be to measure $\xi_{cc}(r)$ for several distinct areas of the sky or by splitting the sample of clusters into separate, independent sub–samples. The standard deviation derived from the average of these ξ_{cc} would be a measure of possible systematic errors in the data (*i.e.* differential extinction across the survey) and the statistical error in estimating the correlation function (*i.e.* whether the sample was large enough to be a fair sample of the universe). However, this would require a huge sample of clusters with measured redshifts which presently does not exist.

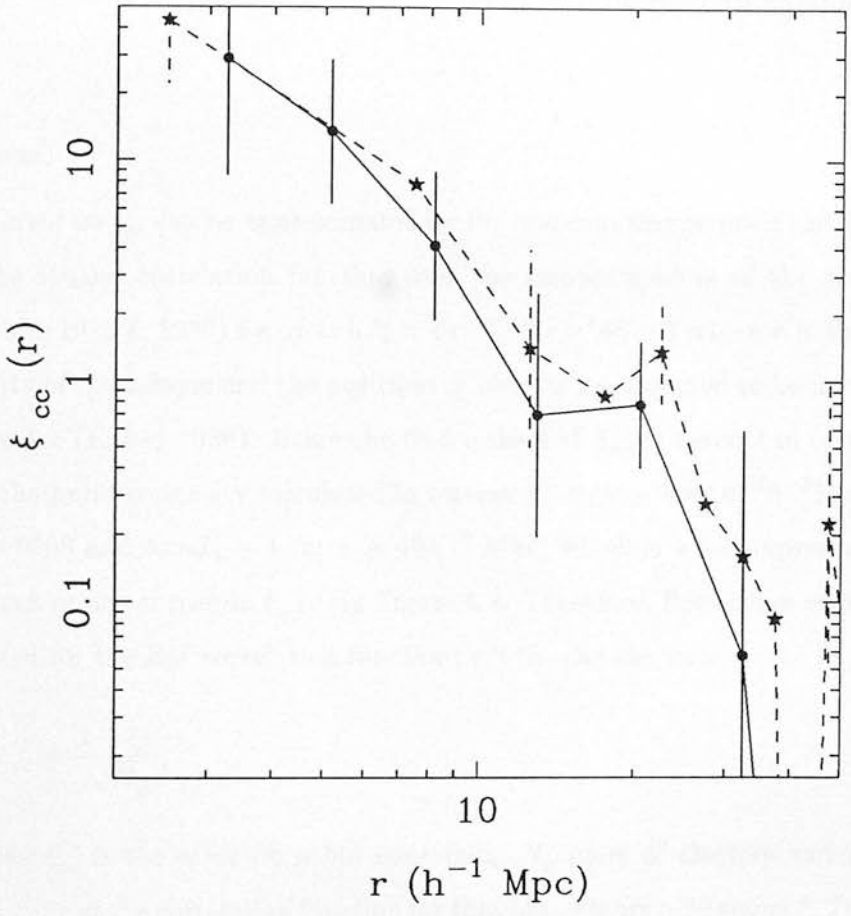

Figure 5.9: The comparison between the ξ_{cc} computed using the methods outlined in this chapter (•) and the ξ_{cc} independently calculated by Luigi Guzzo for the same data set ($\star$). Both sets of error bars are bootstrap errors (see below) and every other error bar on the Guzzo ξ_{cc} is plotted.

The statistical uncertainty on a single correlation function can be written down, but it is a complicated function of the two, three and four–point correlation functions (Peebles 1980). However, there are two methods available in estimating the error on a single correlation function which are Poisson errors calculated from the number of pairs in each correlation bin and the bootstrap re–sampling technique described by Ling *et al.* (1986).

- Poisson

  The error on ξ_{cc} can be approximated by Poisson counting errors if the J_3 integral of the spatial correlation function over the sample used is of the order unity (Peebles 1973 & 1980) *i.e.* if $4\pi n J_3 = 4\pi n \int_0^x \xi(r) r^2 dr \sim 1$ where n is the number density of the sample and the positions of objects are assumed to be uncorrelated beyond x (Kaiser 1986). Using the fit for the EM $\xi_{cc}(r)$ derived in section 5.3.4 and the number density calculated in section 5.3.6 ($n \sim 1 \times 10^{-5} h^{-3}\mathrm{Mpc}^3$), then $J_3 \sim 9000$ and $4\pi n J_3 \sim 1$ for $x = 40h^{-1}$ Mpc, which is a fair representation of the lack of power seen in $\xi_{cc}(r)$ in Figure 5.7. Therefore, Poissonian error bar can be used for the EM correlation function, which take the form

$$\delta\xi_{cc} = \frac{1 + \xi_{cc}}{\sqrt{N_p}} \qquad (56)$$

  where $\delta\xi_{cc}$ is the error on a bin containing N_p pairs of clusters and ξ_{cc} is the amplitude of the correlation function for that bin. Figure 5.10 shows $\xi_{cc}(r)$ plotted with Poissonian error bars.

  The major disadvantage of this method of estimating the error on $\xi_{cc}(r)$ is that the value of the J_3 integral is dependent on the form of the correlation function used. In addition, an assumption is made upon the amplitude of clustering on large scales in the form of x. If the form of the observed ξ_{cc} on large scales was due to some systematic error, this method would not accurately assess the error since the large scale form of the correlation function is assumed at the beginning of the calculation. Finally, this method neglects the possible bias introduced by using the mean number density, n, derived from the sample itself.

This method assesses whether the sample in question is a fair sample of the universe for estimating the correlation function *i.e.* whether a large enough volume of space has been surveyed to accurately derive the correlation function on scales of x. However, the form of the correlation function must be partly assumed, especially on large scales where the function is very noisy.

- Bootstrap re–sampling

  This method of estimating the error for a single sample of clusters is explained by Ling *et al.* 1986. They were solely concerned with the sampling uncertainties associated with the computation of the correlation function using statistical re–sampling techniques. This involved generating many pseudo data sets from the original data and examining the variance of these samples. The technique can neither assess the magnitude of any possible systematic error within the data nor can it address the question of whether the sample is a 'fair sample' (above). However, it can indicate the robustness of the data for evaluating a statistical quantity like ξ_{cc} and measures the individual contribution each cluster makes to the observed correlation function.

  The optimal method of re–sampling for cluster data sets is the bootstrap re–sampling technique. This is achieved by generating N pseudo data sets from the original data with replacement. If the original data has n objects, then each pseudo data set is constructed by selecting n objects from the data at random, allowing any object to be selected as many times as it is picked. Therefore, several clusters in each data set will be double counted or completely missed.

  As prescribed by Ling *et al.* (1986), each data set is treated in exactly the same way as the real data. The actual value of N, the number of pseudo data sets, is governed by equation 5 of their paper, but obviously more data sets gives a better estimate of the error. They found that $N = 100$ was adequate for an original sample containing 100 clusters. For the EM survey, $N = 600$ was chosen on the basis of computer time. The spatial correlation function for each sample was calculated using one random catalogue 100 times larger. There was no need to average each ξ_{cc} over several random catalogues since the statistical error introduced by using one catalogue (or a small number of random objects)

was small compared to the error from the re–sampling. Also, since all the data sets are very similar, when they are averaged together to derive the mean and standard deviation, ξ_{cc} is effectively being averaged over 600 random catalogues as well.

Figure 5.10 shows the observed cluster correlation function for the EM survey 90% redshift complete sample of clusters with errors estimated by the re–sampling technique. The re–sampling technique can only be used to estimate the internal variance of a sample and the mean derived from the N data sets is not a good estimate of the true mean. Therefore, Figure 5.10 shows ξ_{cc} evaluated in the normal way described above, while the error bars are taken from re–sampling.

The two methods of estimating the internal error on the observed ξ_{cc} are shown together in Figure 5.10 (one set of error bars has been shifted slightly). The Poissonian errors represent the best case errors, while the re–sampling errors are the worst case. The ideal way of evaluating the error on the observed correlation function is from a large number of independent samples.

5.3.4 The Fitting of the Observed $\xi_{cc}(r)$

The observed value of r_o has been at the heart of the debate over the true form of the cluster spatial correlation function. As shown at the beginning of this chapter and in Chapter 1, r_o is the value where $\xi(r) = 1$. Therefore, the observed ξ_{cc} (Figure 5.10) was fitted in log space using the formula

$$\xi_{cc}(r) = \frac{c}{r^{\gamma}} \qquad (5.7)$$

or,

$$\log_{10}\xi_{cc}(r) = \log_{10}c - \gamma\log_{10}r\,. \qquad (5.8)$$

The value of r_o is related to the constant c by,

$$r_o = 10^{\frac{c}{\gamma}}\,, \qquad (5.9)$$

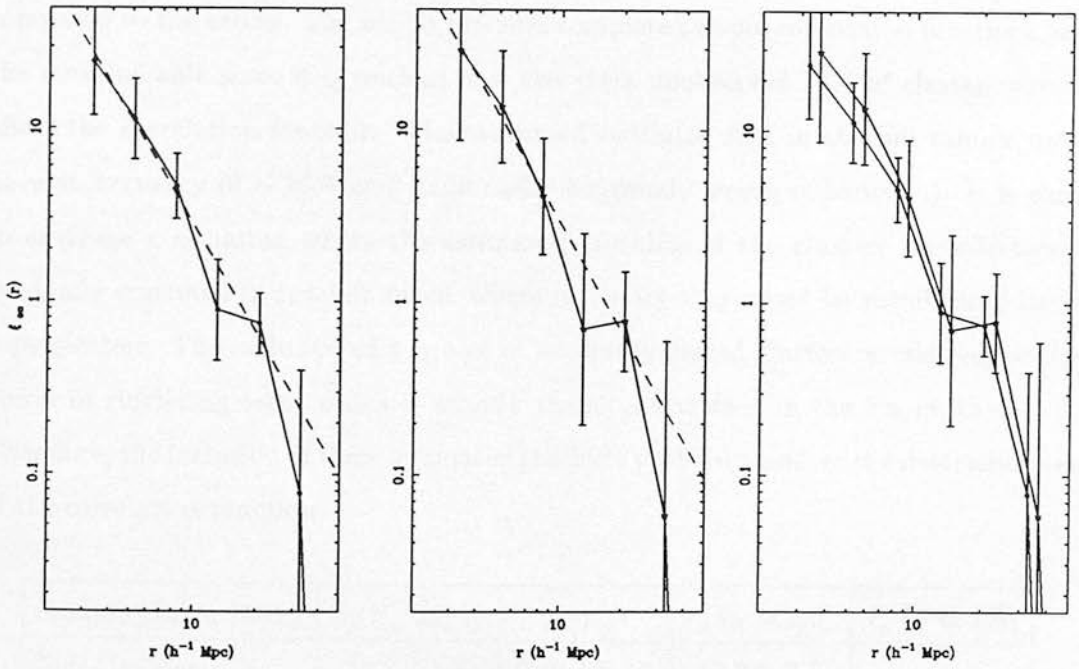

Figure 5.10: Plots of ξ_{cc} for Poissonian and Bootstrap errors. The fits from section 5.3.4 are also shown. The third plot is a comparison of the two sets of error bars. The Bootstrap ξ_{cc} has been artificially shifted by 0.05 in log space to show both sets of error bars simultaneously. Note: the data points are slightly different as the two functions shown represent different estimations of the correlation function for the 90% redshift complete sample. The small differences between these estimations are insignificant compared to the errors.

which is dependent upon the slope of the correlation function. Table 5.2 contains the fits to various correlation functions calculated from different configurations of the small Abell radius selection of clusters described in Chapter 4. These configurations were; *i)* only the 79 observed clusters with Poisson error bars, *ii)* only the 79 observed clusters with re–sampled errors, *iii)* the full small Abell radius sample shown in Appendix F (89 selected clusters with estimated redshifts included but with phantom clusters removed) with Poisson errors and *iv)* the full sample with re–sampling errors. The fits were obtained using χ^2 minimisation over the range $3.0 < r < 30.0h^{-1}$ Mpc. The difference between the full sample and the 90% redshift complete sample is small when compared to the errors. The fits to the 90% complete sample correlation functions are the more reliable since it is unclear how the extra unobserved 10% of clusters would affect the correlation function. The estimated redshifts used in the full sample only have an accuracy of $\sim 20\%$ and could easily be grossly wrong (Chapter 4). It is easy to envisage a situation where the estimated redshifts of the clusters are effectively randomly scattered in redshift space, where in reality they could be members of large superclusters. The inclusion of a subset of randomly placed clusters would reduce the power of clustering seen, which is exactly the situation seen in the fits in Table 5.2. Therefore, the inclusion of these estimated redshifts probably hinders the determination of the correlation function.

Sample (Error Bars)	$r_o(h^{-1}\text{Mpc})$	γ	r_o ($\gamma = 2.0$)	r_o ($\gamma = 1.8$)
Full (Poisson)	14.7 ± 2.6	2.13 ± 0.14	15.3 ± 2.8	
Full (Bootstrap)	14.5 ± 4.0	2.15 ± 0.27	15.7 ± 4.5	
90% (Poisson)	16.2 ± 2.6	2.06 ± 0.16	16.6 ± 2.9	17.9 ± 3.0
90% (Bootstrap)	16.4 ± 4.3	2.11 ± 0.26	16.9 ± 4.5	17.7 ± 4.4

Table 5.2: The parameter fits for various combinations of the sample and error bars. Fits of r_o are included when the slope was fixed at $\gamma = 2.0$ and 1.8.

As discussed above, the most reliable fit for ξ_{cc} from Table 5.2 is $r_o = 16.4h^{-1}$ Mpc with an error of $4.3h^{-1}$ Mpc (Bootstrap) or $2.6h^{-1}$ Mpc (Poisson) for a slope of $\gamma = 2.06$ with an error of 0.26 (Bootstrap) or 0.16 (Poisson). These fits are shown in Figure 5.10.

However, as shown above, the value of r_o is dependent on the slope of the correlation function, so each of the correlation functions were fitted again using a fixed slope of $\gamma = 2.0$ and $\gamma = 1.8$. The values for these fits are shown in Table 5.2. This allowed the EM ξ_{cc} to be easily compared to other observed ξ_{cc} in the astronomical literature with different slopes.

5.3.5 Redshift Anisotropy

As mentioned in Chapter 1, Sutherland (1988) suggested that the high amplitude of the cluster correlation function seen by BS83 was due to projection effects, where distant clusters were boosted into the sample by foreground contamination of nearby clusters. He came to this conclusion by studying the correlation function as a function of angular and radial separation and found that many close angular pairs of clusters had very different redshifts, thus leading to correlations on large scales. He claimed that all these correlations were due to projection effects and corrected ξ_{cc} for them. Since then, the whole question of projection effects and spurious clustering has been debated extensively in the literature, with no clear answer. Sutherland (1988), Sutherland & Efstathiou (1990) and Efstathiou *et al.* (1992) argue that the effect is highly significant, while numerous authors discard it as either insignificant, real line–of–sight clustering or peculiar velocities (Bahcall *et al.* 1986 Szalay *et al.* 1989, Huchra *et al.* 1990, Jing *et al.* 1992). In addition, Dekel *et al.* 1989 and Olivier *et al.* 1990 claim that the statistical uncertainties involved in the deprojection technique of Sutherland are too great, resulting in an ξ_{cc} that cannot be used to constrain theories of galaxy formation. Since the EM survey was objectively constructed with rigorous selection criteria designed to minimise projection effects, it will provide an important check on the reality of these projection effects and their effect on ξ_{cc}.

The correlation function was calculated as a function of transverse and radial separation. The separation between each pair of clusters was divided into its radial (r_z) and transverse components (r_p) as described below,

$$r = \sqrt{r_z^2 + r_p^2}, \qquad (5.10)$$

with,

$$r_z \simeq \frac{c}{H_o}(z_1 - z_2)\,, \tag{5.11}$$

where z_1 and z_2 are the redshifts of the two clusters. Equation 5.11 comes from equation 5.4 with the approximation that the redshifts are small compared to $z = 1$. The correlation function now becomes a function of two separations ($\xi_{cc}(r_z, r_p)$) instead of the usual one ($\xi_{cc}(r)$).

Figure 5.11 is a plot of all the individual pairs of clusters as a function of their transverse and radial separations calculated using the 90% redshift complete sample. Each point represents one pair of data clusters and shows the relative values of r_p and r_z for that pair. The points are effectively randomly scattered over the plane of the diagram and show no signs of an excess of pairs with a small r_p compared to r_z, as seen in the Abell catalogue (Sutherland 1988). These pairs were used in the determination of $\xi_{cc}(r_z, r_p)$ using the standard formula,

$$\xi_{cc}(r_z, r_p) = \frac{2N_r}{N_d}\frac{n_{dd}}{n_{dr}} - 1\,, \tag{5.12}$$

where N_r and N_d are the number of random and data clusters used. In this equation, n_{dd} and n_{dr} are the number of data-data pairs and data-random pairs respectively as a function of r_z and r_p. Each data-data pair was binned into a matrix of separations, thus making a 2–D array of pair counts. This was compared to a similar array constructed from the data-random pairs.

$\xi_{cc}(r_z, r_p)$ is shown in Figure 5.11 as a contour plot. The x axis shows the transverse separations while the y axis is radial separations. The value of the contours (*i.e.* $\xi_{cc}(r_z, r_p)$) are presented in the Figure caption. Clearly, the EM $\xi_{cc}(r_z, r_p)$ is effectively isotropic on scales of the most interest to ξ_{cc} ($\leq 30h^{-1}$ Mpc) with a slight anisotropy in the $\xi_{cc}(r_z, r_p) = 1$ contour of $r_z = 25h^{-1}$ Mpc against $r_p = 15h^{-1}$ Mpc. By comparison, the same contour in the $\xi_{cc}(r_z, r_p)$ for the Abell catalogue is increased by over a factor of three, with $r_z = 100h^{-1}$ Mpc against $r_p = 20h^{-1}$ Mpc (Sutherland 1988). This

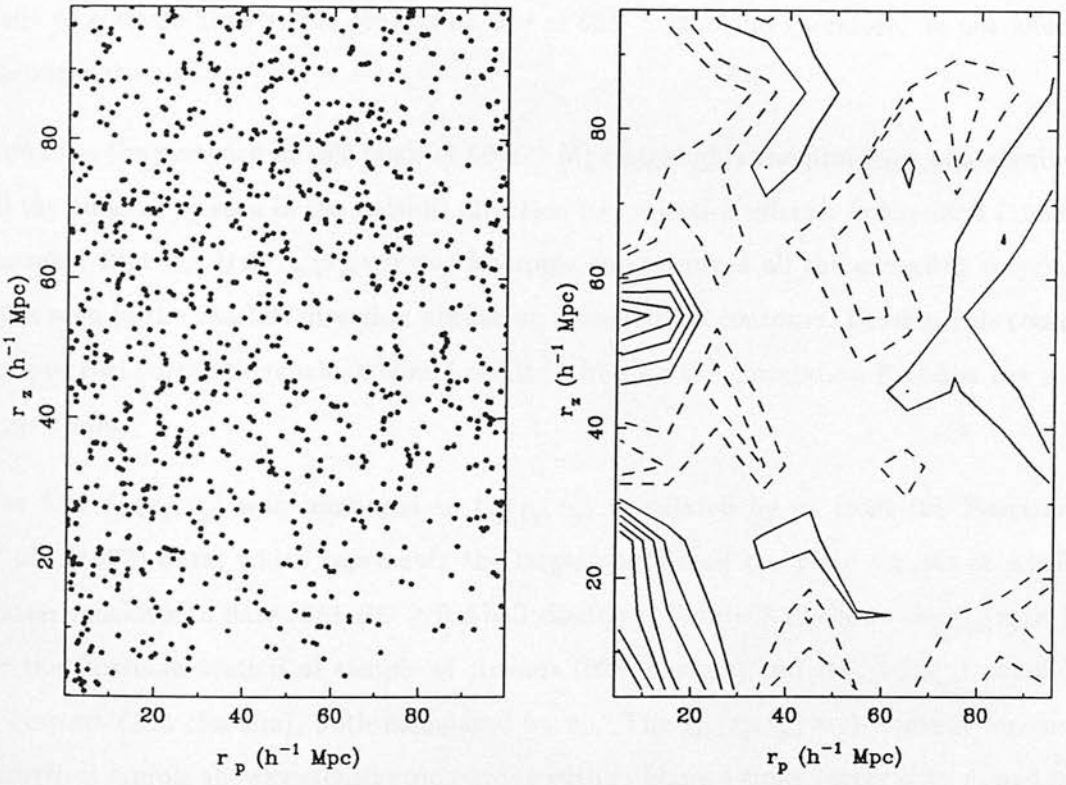

Figure 5.11: The scatter of the individual pairs as a function of their radial r_p and transverse r_p components for the EM survey 90% redshift complete sample and $\xi_{cc}(r_z, r_p)$ calculated using these pairs. The contour values are 3.0, 2.0, 1.0, 0.8, 0.6, 0.4, 0.2, -0.2, -0.4, with the negative contours dashed.

contour is the most anisotropic of the EM $\xi_{cc}(r_z, r_p)$ and after it the contours become symmetrical.

The peak seen along the r_z axis at $r_z \sim 60h^{-1}$ Mpc is due to the alignment along the line–of–sight of the two superclusters mentioned earlier in this chapter. Although the centres of these two structures are separated by a distance of $\sim 100h^{-1}$ Mpc, their extended envelopes combine to give many pairs of clusters with a separation of $\sim 50h^{-1}$ Mpc. This peak plays no role in the interpretation of r_o for the EM survey, since these pairs of clusters have a true separation of $r \simeq 60h^{-1}$ Mpc and therefore, do not affect the estimation of r_o.

However, the presence of this peak at $60\,h^{-1}$ Mpc highlights the problems of assigning all the anisotropy seen in the redshift direction to projection effects. Sutherland (1988) assumed that the true $\xi_{cc}(r_z, r_p)$ was isotropic and removed all the extended correlations seen in the redshift direction producing symmetrical contours. Clearly, this could remove real correlations which would result in biasing the correlation function low on large scales.

The EM $\xi_{cc}(r_z, r_p)$ was compared to $\xi_{cc}(r_z, r_p)$ calculated by us from the Postman *et al.* (1992) data, which represents the largest published complete sample of Abell cluster redshifts to date (351 $RC \geq 0$ Abell clusters). Figure 5.12 shows the $\xi_{cc}(r_z, r_p)$ for the Postman statistical sample of clusters (298 clusters) and the $RC \geq 1$ sample of clusters (136 clusters), both calculated by us. The $\xi_{cc}(r_z, r_p) = 1$ contour for the statistical sample shows extensive anisotropy with r_z being 4 times larger than r_p and is comparable to that found by Sutherland for the BS83 data set. Efstathiou *et al.* (1992) also analysed the Postman statistical sample of clusters and found exactly the same amount of anisotropy as that shown in Figure 5.12. In addition to the Postman *et al.* statistical sample, we calculated $\xi_{cc}(r_z, r_p)$ for the Postman $RC \geq 1$ data as the number density of this subset is $n \simeq 1.0 \times 10^{-5} h^3 \mathrm{Mpc}^{-3}$ (Postman *et al.* 1992) and is very similar to that of the EM survey (section 5.3.6). The difference between the EM survey and Abell catalogue is immediately noticeable. The Postman $RC \geq 1$ $\xi_{cc}(r_z, r_p) = 1$ contour is extended by a factor of 3 in the redshift direction with $r_z = 60h^{-1}$ Mpc compared to $r_p = 20h^{-1}$ Mpc. For the EM survey in Figure 5.11, the same contour is

only extended by a factor of 1.5 and is certainly the worst contour.

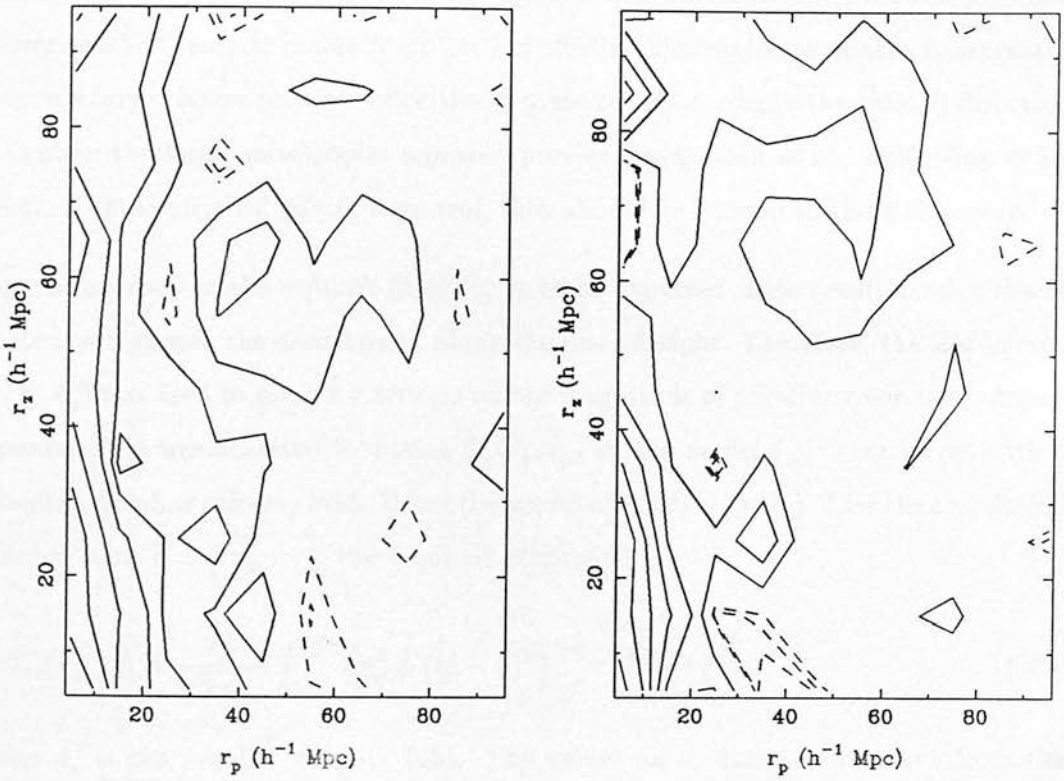

Figure 5.12: $\xi_{cc}(r_z, r_p)$ calculated by us for the Postman *et al.* (1992) sample of Abell clusters. The Postman statistical sample of clusters (left) and the Postman $RC \geq 1$ (right) sample of clusters are shown. The contour values are 5.0, 3.0, 2.0, 1.0, 0.5, 0.2, -0.1, -0.2, -0.3 and 12.0, 8.0, 6.0, 4.0, 2.0, 1.0, -0.1, -0.2, -0.3 respectively, with negative contours dashed.

Throughout the construction of the EDCC and EM survey much effort was invested in reducing projection effects. The three main methods of doing this were: *i)* the clusters were selected completely objectively removing the unquantifiable systematics in visually constructed catalogues; *ii)* the clusters were debelended twice to reduce projection effects as discussed by Sutherland (1988); *iii)* over 80% of the observed clusters have $\sim$ 10 galaxy redshift measurements which removes any phantom clusters ($\sim$ 10%,

Chapter 4). In addition, multiple cluster redshift measurements substantially reduced the probability of measuring the redshift of an interloper and therefore, introducing spurious large scale line–of–sight correlations (Chapter 4).

Clearly, the isotropy of the EM survey suggests that the anisotropy seen in previous cluster redshift samples is due to projection effects. This no longer makes it necessary to invoke large cluster peculiar velocities or preferred clustering in the redshift direction to explain the large anisotropies reported previously (Bahcall *et al.* 1986, Jing *et al.* 1992). If these physical effects were real, they should be present in the EM survey.

Some anisotropy in the redshift direction is to be expected since peculiar velocities of clusters will spread the distribution along the line–of–sight. Therefore, the EM survey $\xi_{cc}(r_z, r_p)$ was used to place a constrain on the magnitude of peculiar velocities between clusters. This was achieved by fitting $\xi_{cc}(r_z, r_p)$ with a model $\xi_{cc}(r)$ convolved with a Gaussian peculiar velocity field. Using the model of $\xi_{cc}(r) = (r/r_o)^{-\gamma}$ for the correlation function with $r = \sqrt{r_p^2 + r_z^2}$, the required expression is

$$\xi_{cc}(r_z, r_p) = \frac{r_o^\gamma}{\sqrt{2\pi}\sigma_v} \int_{-\infty}^{+\infty} \left(r_p^2 + (r_z - x)^2\right)^{-\frac{\gamma}{2}} e^{-\frac{x^2}{2\sigma_v^2}} dx \,, \tag{5.13}$$

where σ_v is the peculiar velocity field. The values for r_o and γ were taken from the fit to the EM correlation function and the values of r_p were constrained to the range $0 \leq r_p \leq 10h^{-1}$ Mpc. Figure 5.13 shows $\xi_{cc}(r_z, r_p)$ for this slice of r_p (Poissonian error bars). In addition, the 3 curves shown correspond to the model above for peculiar velocities of 300, 1000 and 2000 km s^{-1}. The best visual fit of the three is plainly 300 km s^{-1}. To place a constraint on the observed peculiar velocities of clusters, values of χ^2 were calculated for various values of the peculiar velocity field ($\sigma_v = 100 \rightarrow 2400$). Only the first five bins in Figure 5.13 were used, since beyond this all the models are effectively equal. These values are shown in Table 5.3.

The minimum χ^2 is for peculiar velocities of ~ 300 km s^{-1}, which gives a reasonable fit to the data (reduced $\chi^2 \simeq 1$). Peculiar velocities of 1000 km s^{-1} are ruled out at the 95% confidence level ($\sim 2\sigma$), while 1500 km s^{-1} is ruled out at the 99.99% confidence limit ($\sim 3\sigma$). The data cannot be used to put a lower limit on the peculiar velocities and are consistent with zero peculiar velocities.

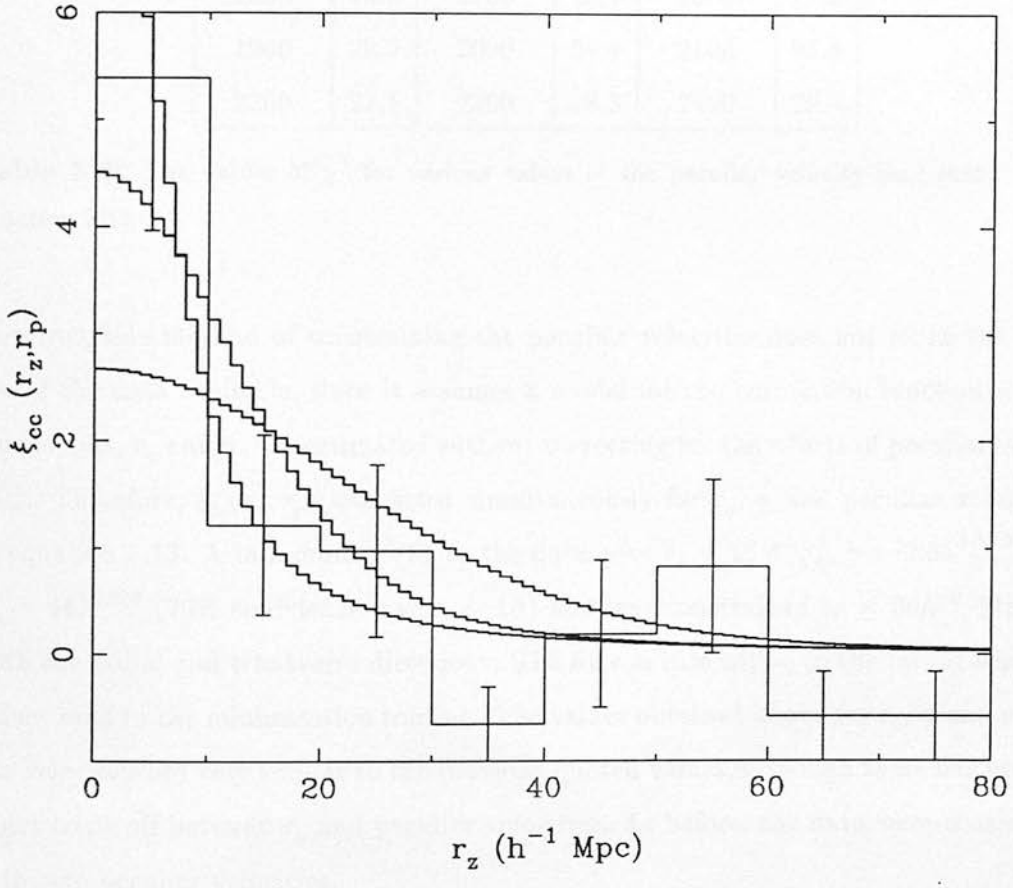

Figure 5.13: $\xi_{cc}(r_z, r_p)$ for the EM survey constrained to $0 < r_p < 10h^{-1}$ Mpc with Poisson error bars. The curves are for peculiar velocities of 300, 1000 and 2000 $\mathrm{km\,s^{-1}}$(flattest curve). See text for discussion.

Pec. Vel	χ^2	Pec. Vel	χ^2	Pec. Vel	χ^2
100	7.1	200	7.0	300	7.0
400	7.0	500	7.1	600	7.3
700	7.7	800	8.3	900	9.0
1000	9.9	1100	10.9	1200	12.1
1300	13.4	1400	14.9	1500	16.4
1600	18.0	1700	19.7	1800	21.3
1900	22.9	2000	24.4	2100	25.8
2200	27.1	2300	28.3	2400	29.4

Table 5.3: The values of χ^2 for various values of the peculiar velocity field ($\mathrm{km\,s^{-1}}$) in equation 5.13

However, this method of constraining the peculiar velocities does not make the best use of the data available, since it assumes a model for the correlation function whose parameters, r_o and γ, are estimated without correcting for the effects of peculiar velocities. Therefore, $\xi_{cc}(r_z, r_p)$ was fitted simultaneously for r_o, γ and peculiar velocities in equation 5.13. A minimum χ^2 fit to the data gave $r_o = 15.4^{+1.8}_{-1.6}$, $\gamma = 2.05^{+0.19}_{-0.32}$ and $\sigma_v = 442^{+398}$ (70% confidence levels, $\sim 1\sigma$) and was constrained to $\leq 30h^{-1}$ Mpc in both the radial and transverse directions. The fit was insensitive to the initial starting values used in the minimisation routine. The values obtained above for r_o, γ and peculiar velocities are very similar to the previous quoted values, although there has been a slight trade off between r_o and peculiar velocities. As before, the data were consistent with zero peculiar velocities.

Bahcall *et al.* (1986) claimed that the elongation in the redshift direction seen in their original data (BS83) was due to large peculiar velocities of clusters ($\sim 2000\mathrm{km\,s^{-1}}$). The fit to the EM survey data is clearly inconsistent with this value and is in good agreement with independent estimates of the peculiar velocities of clusters *i.e.* Aaronson *et al.* (1989) puts an upper limit on cluster peculiar velocities of $400\mathrm{km\,s^{-1}}$, while Lucey & Carter (1988) claim that observed cluster peculiar velocities are consistent with zero.

5.3.6 Comparison with Previous Observations

Table 5.4 summarises the parameter fits in equation 5.3 for various observed $\xi_{cc}(r)$ in the astronomical literature. There are 4 main points to be note from this table: *i)* ξ_{cc} estimates from the Abell catalogue all have an $r_o \geq 20.0\, h^{-1}$ Mpc; *ii)* the two automated catalogues have lower values of r_o; *iii)* projection corrections reduce the amplitude of r_o in line with the objective catalogues; *iv)* the slope of ξ_{cc} varies significantly between samples which ,in principle, could affect the observed value of r_o. However, the EM ξ_{cc} was fitted with a slope of 1.8 and the value of r_o only increased to $17.7h^{-1}$Mpc, which is still inconsistent with the estimations of r_o from the Abell catalogue.

Dalton *et al.* (1992) have estimated the correlation function for a cluster survey constructed objectively from the APM galaxy survey, which is similar to the EDSGC and was constructed automatically using the APM plate measuring machine. The EM survey has two major advantages over the APM cluster survey. Firstly, the original APM galaxy data was not deblended which can lead to mergers of galaxies in rich cores of clusters (Beard *et al.* 1990). Secondly, of the 220 cluster redshifts they possess, 144 were measured by themselves based on only one or two galaxy redshifts. The rest of their sample was constructed from a literature search. As highlighted in Chapter 4, it is extremely dangerous to sample so few galaxies per cluster, even in the cores of clusters. This is reinforced by the fact that they do not remove any of their clusters as phantom clusters.

To make a fair comparison between the EM survey and other cluster catalogues, it is important to determine the number density of the EM survey. Clearly, if the number densities between catalogues vary dramatically, then it suggests that different catalogues are sampling different populations of clusters. Therefore, the number density of the EM survey was calculated using the RA and Declination limits specified in section 4.6. The redshift limits were set at $0.02 < z < 0.13$, as this corresponded to the completeness limits of the EDCC (Chapter 4). The volume of the EM survey was found to be $1.0 \times 10^7 h^{-3}\mathrm{Mpc}^3$ and the number of clusters within the full small Abell radius selection used to calculate the correlation function that satisfy these constraints was 92 (with or without a redshift). Therefore, the number density of the

Survey	**No.**	r_o (h^{-1} Mpc)	n_c (h^3Mpc^{-3})	γ
Bahcall & Soneira 1983	104	25.0	0.6	1.8
Ling *et al.* 1986	104	$21.9^{+7.1}_{-5.1}$	0.6	1.7 ± 0.17
Postman *et al.* 1986	136	$20.0^{+4.6}_{-5.7}$		1.8
Postman *et al.* 1986	1207	$24.0^{+2.3}_{-3.0}$		1.8
Postman *et al.* 1986	370	$42.0^{+8.0}_{-9.1}$		1.8
Sutherland 1988	533	$14.0^{+4.0}_{-3.0}$	0.6	1.8
Dekel *et al.* 1989	102	~ 15.0		1.8
Lahav *et al.* 1989	53	21.0 ± 7.0		1.8
Huchra *et al.* 1990	145	$20.3^{+4.8}_{-5.1}$	~ 1.0	1.8
West & van der Bergh 1991	64	22.1 ± 6.8		1.7 ± 0.5
Sutherland & Efstathiou 1991	113	9.0	~ 3.0	1.8
Sutherland & Efstathiou 1991	145	14.0	0.7	1.8
Postman *et al.* 1992	351	$20.0^{+4.6}_{-4.0}$	1.2	2.5 ± 0.2
Postman *et al.* 1992	156	$23.7^{+7.9}_{-9.0}$	~ 1.0	1.8 ± 0.2
Dalton *et al.* 1992	220	12.9 ± 1.4	2.4	1.9 ± 0.3
Dalton *et al.* 1992	93	14.4 ± 4.0	1.1	2.0
Efstathiou *et al.* 1992	298	~ 13	1.4	~ 2.0
Nichol *et al.* 1992	79	$15.4^{+1.8}_{-1.6}$	1.0	$2.05^{+0.19}_{-0.32}$

Table 5.4: The parameter fits in equation 5.3 for observed $\xi_{cc}(r)$ quoted in the literature. Table 5.5 contains information on the individual surveys.

Survey	Comments
Bahcall & Soneira 1983	$RC \geq 1$, $D \leq 4$ Abell clusters.
Ling *et al.* 1986	same data as above.
Postman *et al.* 1986	Abell statistical sample $z \leq 0.1$.
Postman *et al.* 1986	All Abell $RC \geq 1$ clusters (80% estimated redshifts).
Postman *et al.* 1986	All Abell $RC \geq 2$ clusters (75% estimated redshifts).
Sutherland 1988	Abell catalogue + projection correction.
Dekel *et al.* 1989	$RC \geq 1$, $D \leq 4$ Abell clusters + projection correction.
Lahav *et al.* 1989	EXOSAT X-ray clusters.
Huchra *et al.* 1990	Deep Abell survey.
West & van der Bergh 1991	cD Abell clusters.
Sutherland & Efstathiou 1991	Shectman (1985) clusters + projection correction.
Sutherland & Efstathiou 1991	Huchra *et al.* (1990) survey + projection correction.
Postman *et al.* 1992	All Abell clusters $m_{10} \geq 16.5$.
Postman *et al.* 1992	$RC \geq 1$ Abell clusters $m_{10} \geq 16.5$.
Dalton *et al.* 1992	APM survey, $R \geq 20$.
Dalton *et al.* 1992	APM survey, $R \geq 35$.
Efstathiou *et al.* 1992	Postman *et al.* (1992) survey + projection correction.
Nichol *et al.* 1992	EDSGC survey, $R \geq 22$. This thesis.

Table 5.5: Details of the surveys used in estimating the correlation functions listed in Table 5.4.

sample was $\simeq 1.0 \times 10^{-5} h^3 \mathrm{Mpc}^{-3}$.

Efstathiou *et al.* (1992) computed the number densities of both the APM cluster survey and the Postman *et al.* (1992) Abell survey. They found that the number density of the Postman $RC \geq 1$ sample was $7.0 \times 10^{-6} h^3 \mathrm{Mpc}^{-3}$ and the $RC \geq 0$ sample was $\simeq 1.5 \times 10^{-5} h^3 \mathrm{Mpc}^{-3}$. The EM survey number density of clusters is therefore, midway between the Abell $RC \geq 0$ and $RC \geq 1$ samples and any differences in the clustering seen between the EM survey and the Abell catalogue cannot be explained by the differences in the number densities. In addition, Efstathiou *et al.* quotes $2.4 \times 10^{-5} h^3 \mathrm{Mpc}^{-3}$ for the number density of the whole APM cluster survey, while $\simeq 1.1 \times 10^{-5} h^3 \mathrm{Mpc}^{-3}$ for the richer $R \geq 35$ APM sample of clusters. Therefore, using the relative number densities of these samples, the EM survey should be compared with the richer APM sample and the Abell $RC \geq 1$ sample of clusters.

Figure 5.14 shows the correlation functions for the Postman *et al.* sample of Abell $RC \geq 1$ clusters, the APM $R \geq 35$ sample (Dalton *et al.* 1992) and the EM 90% redshift complete sample (Chapter 4). As stated above, all these samples have approximately the same number density ($n \sim 1.0 \times 10^{-5} h^3 \mathrm{Mpc}^{-3}$). The EM survey points are systematically below the Abell estimate of the correlation function, especially on large scales. Although the error bars on all the ξ_{cc} makes it hard to statistically argue the relative differences in the functions, it is encouraging that both the objective catalogues are *systematically* below the estimate of ξ_{cc} from the Abell catalogue. This is complemented by the fact that all the estimates of the correlation function in Table 5.4 for the Abell catalogue put $r_o > 20.0 h^{-1} \mathrm{Mpc}$, while the two automated surveys find lower values.

The motivation behind the construction of the EM survey was to remove possible systematic effects that may be present in other optical cluster catalogues. The lack of anisotropy in the EM survey compared to the Abell catalogue show that a definite systematic error exist within the Abell catalogue. Therefore, the lower value of r_o can be argued as significant and used to place new constraints on theory. Therefore, the work presented in this thesis represents the best optical estimation of ξ_{cc} to date. As demonstrated earlier in this chapter, the Abell catalogue contains spurious line–of–sight

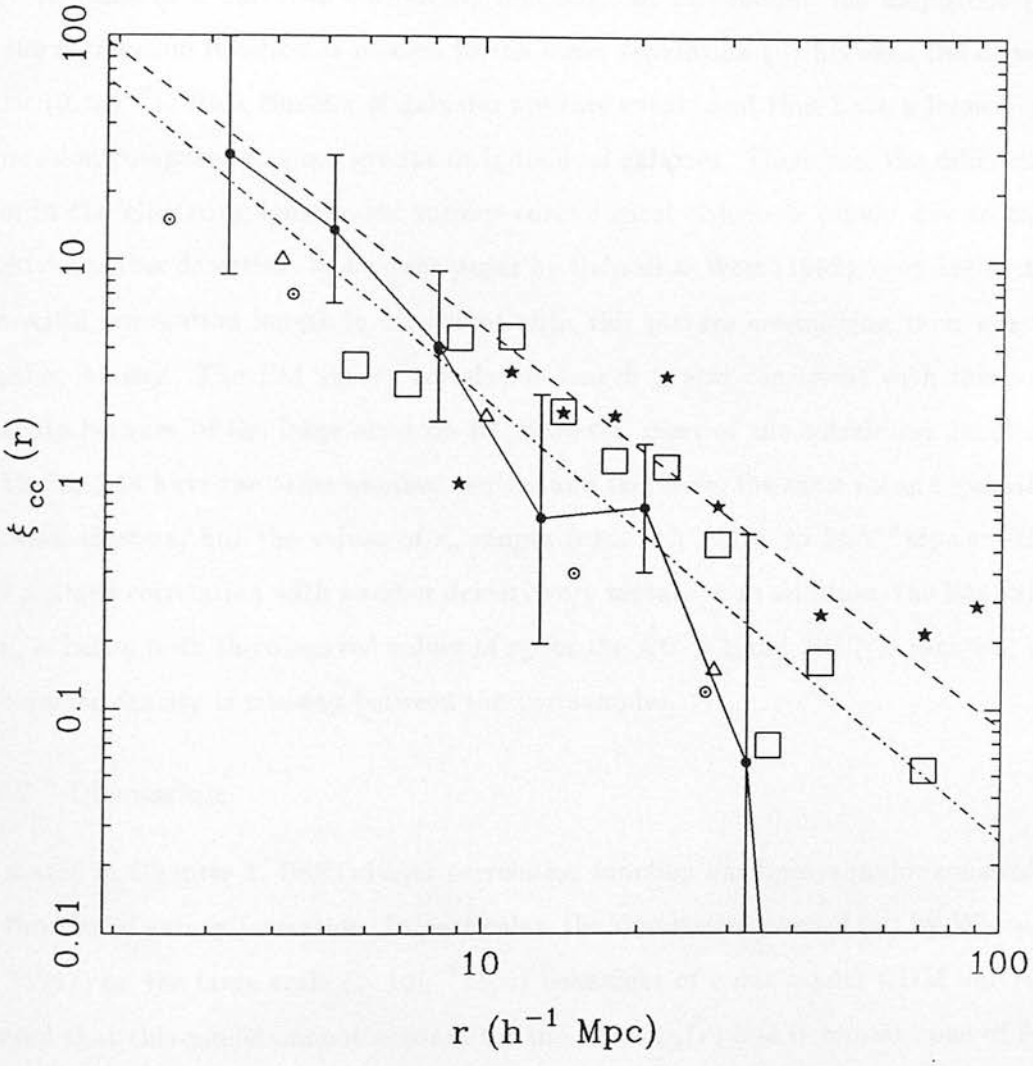

Figure 5.14: $\xi_{cc}(r)$ for the EM survey with Bootstrap error bars (•) and the best fit power law (dot–dash). Also shown are the Postman *et al.* (1992) ξ_{cc} for their statistical sample (□) and their $RC \geq 1$ sample (⋆). The best fit power law for the BS83 correlation function is plotted as the dashed line. Finally, the ξ_{cc} for the APM $R \geq 20$ sample (⊙) and the APM $R \geq 35$ sample (△) are shown as well (Dalton *et al.* (1992)).

correlations probably due to a combination of the subjective nature of the catalogue, single redshift measurements and projection effects.

Finally, Bahcall (1988) has tried to understand the differences in the correlation length (r_o) in terms of a universal correlation function. In this model, the amplitude (A) of the correlation function is related to the mean separation (d) between the objects ($A = (0.4d)^{1.8}$). Rich clusters of galaxies are rare events and thus have a large mean separation compared to poor groups or individual galaxies. Therefore, the differences seen in the clustering lengths for various cosmological objects is purely due to their relative number densities. In a recent paper by Bahcall & West (1992), they argue that the APM correlation length is consistent with this picture considering their greater number density. The EM survey correlation length is also consistent with this relationship because of the large error on it. However, most of the correlation functions in Figure 5.14 have the same number density and therefore, the same mean separation between clusters, but the values of r_o ranges from $14\,h^{-1}$Mpc to $24\,h^{-1}$Mpc making any claimed correlation with number density very tentative. In addition, the EM value of r_o is below both the observed values of r_o for the $RC \geq 1$ and $RC \geq 0$ samples, yet its number density is midway between the two samples.

5.3.7 Discussion

As stated in Chapter 1, BS83 cluster correlation function has been a major constraint on theories of galaxy formation. In particular, the simulations carried out by White *et al.* (1987) on the large scale ($> 10h^{-1}$Mpc) behaviour of a flat biased CDM universe showed that this model cannot account for the BS83 $\xi_{cc}(r)$ and it remains one of few observations of the large–scale structure in the universe that the CDM models cannot predict.

Figure 5.15 shows the EM correlation function along with the BS83 data points taken from Figure 1.3. Also plotted are the simulations of White *et al.* (1987) mentioned above and new simulations carried out by Dalton *et al.* (1992) using a different method of locating the clusters in the simulations and a different biasing parameter (see figure caption). As stated, the BS83 result is in clear disagreement with these simulations. However, the EM correlation function, within the errors, is in good agreement on all

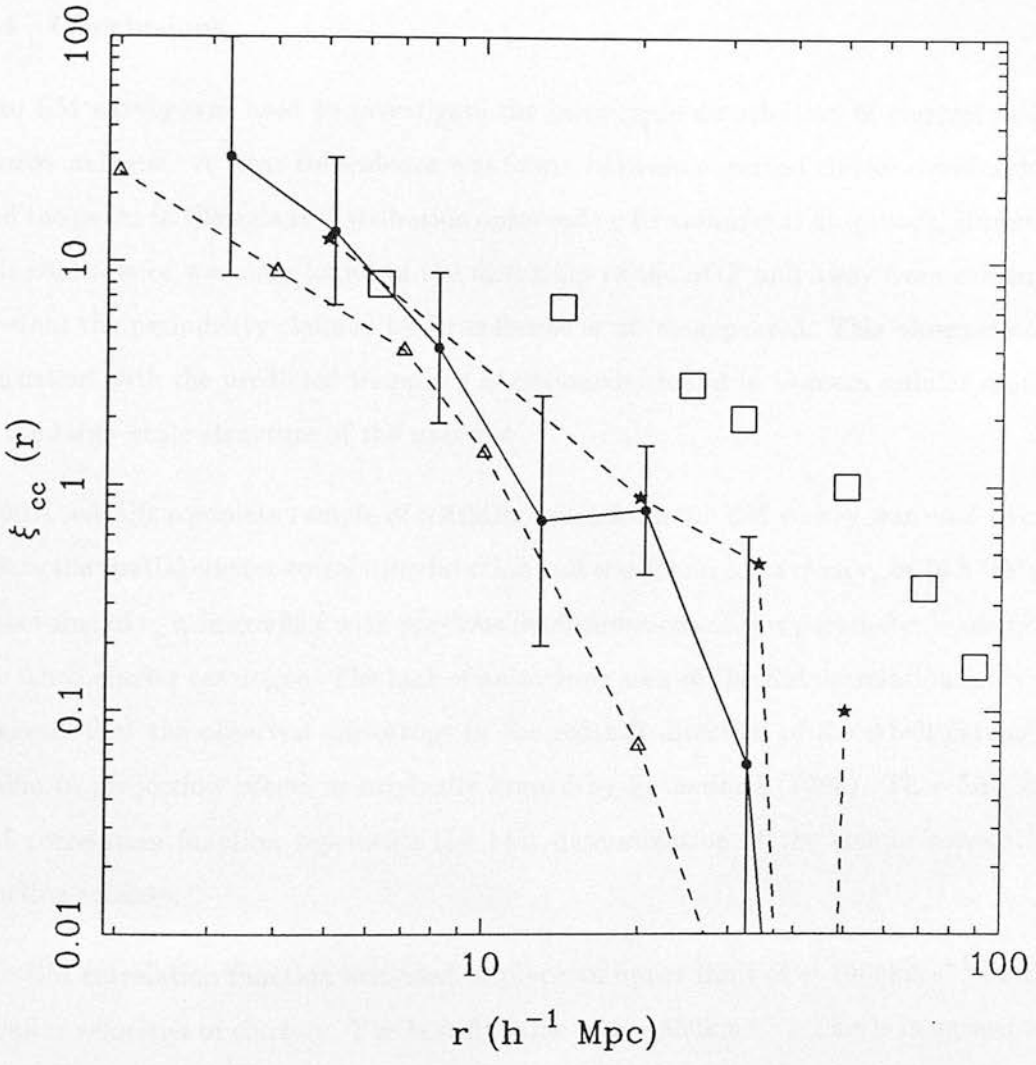

Figure 5.15: $\xi_{cc}(r)$ for the EM survey with Bootstrap error bars (•) taken from Figure 5.14. Also shown are the data points of the BS83 correlation function taken from Figure 1.3 (□). The two dotted lines are the simulations of White *et al.* (1987) (⋆) with a biasing parameter of $b = 2.5$ and Dalton *et al.* (1992) (△) for a biasing parameter of $b = 1.7$.

NOTE:— THE WHITE ET AL (1987) CURVE IS FOR $H_0 = 100$ KM S^{-1} MPC^{-1}
THE DALTON ET AL (1992) CURVE IS FOR $H_0 = 50$ KM S^{-1} MPC^{-1}
THEREFORE, SHIFT WHITE ET AL CURVE TO DALTON ET AL CURVE TO ACCOUNT FOR DIFFERENCES IN H_0

scales with both sets of simulations. In addition, White *et al.* (1987) predicted that the peculiar velocities of clusters in a CDM universe should be $\sim 500\mathrm{km\,s^{-1}}$ which are in good agreement with the observed peculiar velocities obtained from the fitting of the EM correlation function.

5.4 Conclusions

The EM survey was used to investigate the large scale distribution of clusters in the nearby universe. A clear coincidence was found between observed cluster overdensities and the peaks in the galaxy distribution observed by Broadhurst *et al.* (1990). However, this coincidence was only found in the directions of the SGP and away from this line–of–sight the periodicity claimed by Broadhurst *et al.* disappeared. This observation is consistent with the predicted frequency of periodicity found in Voronoi cellular models of the large–scale structure of the universe.

A 90% redshift complete sample of redshifts taken from the EM survey was used to calculate the spatial cluster correlation function and was found to have an r_o of $16\,h^{-1}$Mpc. This value of r_o is in conflict with previous determinations of this parameter made from the Abell cluster catalogue. The lack of anisotropy seen in the EM correlation function suggests that the observed anisotropy in the redshift direction of the Abell catalogue is due to projection effects as originally argued by Sutherland (1988). Therefore, the EM correlation function represents the best determination of the cluster correlation function to date.

The EM correlation function was used to place an upper limit of $\sim 1000\mathrm{km\,s^{-1}}$ on the peculiar velocities of clusters. The best fit value was $\sim 450\mathrm{km\,s^{-1}}$. This is in agreement with independent measures of cluster peculiar velocities and agrees with the predictions of CDM. Finally, the lower amplitude of the EM correlation function is consistent with predictions from CDM models of galaxy formation.

Chapter 6

Discussion and Conclusions

6.1 Discussion

One of the most controversial results in observational cosmology over the last decade has been the high amplitude of the spatial correlation function of clusters compared to that for the galaxies. As shown in Chapter 1, previous studies of these two statistics have put the discrepancy between the two functions at $\xi_{cc} \simeq 15\xi_{gg}$ over the same spatial scales. A consequence of this result is that both the clusters and the galaxies cannot be fair tracers of the underlying mass distribution. This result prompted Kaiser (1984) to suggest a general scenario in which clusters are proposed to have only formed at the highest peaks in the galaxy distribution and which, in principle, could account for the observed difference, $\xi_{clusters} \simeq (9-16)\,\xi_{density}$.

Kaiser's idea was incorporated into CDM models of galaxy formation by Davis *et al.* (1985), but was used to bias the galaxies instead. In these models, galaxies were identified with peaks in the density field that were 2.5σ above the mean of the density field after it had been smoothed with a Gaussian low–pass filter and resulted in lowering the amount of evolution seen in their simulations. This provided good agreement between the predicted and observed distribution of galaxies and their peculiar velocities. However, biased CDM was unable to explain the observed difference between the galaxy correlation function and the cluster correlation function, which was predicted to be $\xi_{cc} \simeq 4\,\xi_{gg}$ (White *et al.* 1987).

In light of the new observations presented in this thesis, the discrepancy between the observed spatial correlation functions of the galaxies and the clusters can be examined. Before such a comparison can be made, the large scale power seen in the EDSGC angular correlation function (Chapter 2) must be converted to an appropriate spatial correlation function, which can be achieved using Limber's equation. Following the prescription detailed by Peebles (1980) and using a selection function derived from the observed luminosity function of bright APM galaxies (Loveday 1991, $M^* = -19.7$, $\alpha = -0.95$), the amplitude of a model spatial correlation functions, $\xi_{gg}(r) = (r/r_o)^2$, was varied until it best matched the observed EDSGC $w(\theta)$. This was found to be $r_o \simeq 6.5h^{-1}$ Mpc, which was in good agreement with the spatial correlation function derived by Loveday (1991) for the bright APM galaxies used in the calculation of the

selection function.

Using this form for the spatial galaxy correlation function and the best fitted form of the spatial cluster correlation function from Chapter 5 ($\xi_{cc}(r) = (r_o/r)^{\gamma}$ with $r_o = 15.4^{+1.8}_{-1.6}h^{-1}$Mpc and $\gamma = 2.05^{+0.19}_{-0.32}$), the difference in amplitude of the two functions is reduced to $\xi_{cc} \simeq 5\xi_{cc}$. However, the error on this relationship is hard to quantify because of the difficulty in obtaining an error on the spatial galaxy correlation function via Limber's equation. An alternative to this approach is to compare the J_3 integrals ($J_3 \propto \int_0^{\infty} \xi(r) d^3r$) for the respective functions over the same volume of space, which would provide an estimate of the error on the above relationship.

As described in Chapter 2, the J_3 integral for the spatial galaxy correlation function can be obtained from $w(\theta)$ using the method detailed by Clutton–Brook & Peebles (1981). Using the model fit for the EDSGC $w(\theta)$ given at the end of Chapter 2, the derived J_3 integral for the galaxies is $J_3 = 2500e^{\pm 0.22}h^{-3}\text{Mpc}^3$ integrating out to scales of $R = 65h^{-1}$Mpc. Using the best fit cluster correlation function given above and assuming $\xi_{cc}(r) = 0.0$ on scales greater than $40h^{-1}$Mpc (Figure 5.7), then $J_3 = 9500^{+3200}_{-1700}h^{-3}\text{Mpc}^3$ for the clusters on the same scale. These values translate to $\xi_{cc} = 3.8^{+2.2}_{-1.3}\xi_{gg}$ (one sigma errors), which is consistent with the relationship given above for biased CDM models. Therefore, the lowering of the amplitude of the cluster spatial correlation function has removed one of the last conflicting observations with the popular theory of biased CDM.

However, new observations of the galaxy angular correlation function shown in Chapter 2 are in clear disagreement with this model and have now become one of the major constraints on CDM models. Chapter 2 highlighted several suggested alternatives for reconciling $w(\theta)$ with CDM. One such alternative was the lowering of the biasing to ~ 1 compared to 2.5 used in previous biased CDM models. Couchman & Carlberg (1992) showed that this could account for the new observations of $w(\theta)$. However, it is unclear whether a lower biasing can reproduce the new observations of the cluster correlation function and the observed galaxy peculiar velocities. Preliminary work on the predicted cluster correlation function in low biased CDM models indicate that these models can explain the new observations (Mann, private communication), while velocity bias has

been put forward to explain the difference between the observed and predicted galaxy peculiar velocities (Carlberg *et al.* 1990).

6.2 Conclusions

A clear conclusion of the work presented in this thesis is that previous visually compiled galaxy and cluster catalogues have given us a false view of the distribution of these objects in the nearby universe. Chapters 2, 3 and 5 demonstrate that the Abell and Lick catalogues, the two largest visually compiled catalogues, have systematic errors associated with the methods used in their construction and as a consequence, the clustering studies derived from these catalogues are also in error.

Chapter 1 presented a detailed description of the EDSGC, which is a new objective catalogue constructed to overcome the systematic errors in previous catalogues. Chapter 2 presented the galaxy angular correlation function for the EDSGC and was found to have significant power on scales $\theta \simeq 10^{\circ}$. This is in disagreement with the Lick determination of $w(\theta)$ and with the predictions of the standard $\Omega = 1$ high biased CDM model.

Chapter 3 and Chapter 4 described the objective construction of the EDCC and the EM cluster redshift survey. When these databases were compared to the Abell catalogue of clusters, substantial differences were found: *i)* the Abell catalogue systematically over–estimated the richness of individual clusters and only one sixth of the statistical sample of Abell clusters had the required 50 members to satisfy the original definition of this sample; *ii)* to the respective completeness limits of the EDCC and the Abell catalogue, $\sim$ 80% of the Abell clusters were found in the EDCC, while only $\sim$ 50% of the EDCC clusters were in the Abell catalogue; iii) from the extensive redshift information available in the EM survey, $\sim$ 10% of clusters were found to be the result of spurious line–of–sight projections and $\sim$ 25% of measured galaxy redshifts towards the cores of rich clusters were found to be interlopers, which is a much greater level of contamination than deduced from previous studies based on the Abell catalogue (Struble & Rood 1991); iv) finally, the elongations seen in the redshift direction of ξ_{cc} computed from the Abell catalogue (Bahcall *et al.* 1986, Sutherland 1988) were not

seen in the EM survey and strongly suggest that these line–of–sight correlations are a clear systematic error in the Abell catalogue.

The spatial cluster correlation function derived from the EM survey has a much lower amplitude than that of functions computed from the Abell catalogue. This is due to the objective manner in which the EM survey was constructed and the extensive redshift information it contains. The consequence of this lower amplitude, especially on scales greater than r_o, is that the cluster correlation function is now consistent with CDM models of galaxy formation and has removed one of the major problems with these models.

The new observations presented in this thesis provide a strong observational framework within which to test theories of galaxy formation. Presently, no one model can predict all these observations, but derivatives of the CDM model of galaxy formation are the most hopeful.

6.3 Future Work on the Catalogues

The EDCC has already been released to the astronomical community (Lumsden *et al.* 1992) and the EDSGC will be released soon (Collins & Nichol 1992). These databases will hopefully be extensively used and provided an comprehensive observational framework within which to test models of galaxy formation.

Future work will centre around the unique EM cluster redshift survey. There are three main projects planned using this survey:

1. Velocity dispersions of clusters

   The distribution of velocity dispersions of clusters is a strong galaxy formation indicator as well as a tight constraint on certain galaxy formation models (*e.g.* Lilje 1990). For example, the existence of a large fraction of high velocity dispersion clusters would be contrary to the predictions of biased CDM (Frenk *et al.* 1990). The extensive redshift information available within the EM survey means that for the first time, the distribution of velocity dispersions for a statistically significant

sample of cluster can be constructed and compared to predictions already in the astronomical literature.

2. The cluster luminosity function

   The existence of a universal cluster luminosity function (LF) would also be an important galaxy formation indicator, as differences between individual cluster LFs would indicate an environmental dependence on galaxy formation. Dressler (1978) and Colless (1989) find evidence for a 'general' cluster LF, yet their respective samples are small ($\sim$ 10 clusters). Colless (1989) details the need for a homogeneous cluster sample with $N_c > 1000$ (where N_c is the number of galaxies in the composite LF brighter than $\langle M^* \rangle + 1$) to constrain variations in a composite LF to ~ 0.2 mag in M^* and ~ 0.1 in α and thus greatly advance our knowledge of the cluster LF beyond previous studies. The EM survey is the only database that satisfies the above requirements.

3. Alignments of clusters

   There is much controversy in the astronomical literature over the suggested alignment of galaxy clusters in space. Many authors have found a tendency for clusters to be elongated towards their nearest neighbour, which suggests that the clusters either condensed out of a larger coherent structure or have experienced tidal interactions (Sastry 1968, Carter & Metcalfe 1980, Binggeli 1982). West (1991) recently claimed that clusters were aligned on scales as great as $50h^{-1}$Mpc. If these alignments exist, they would be extremely important indicators of certain galaxy formation scenarios (Oort 1983). For example, numerical simulations of CDM models cannot explain alignments of clusters beyond $20\,h^{-1}$Mpc (West *et al.* 1989). However, many authors have questioned the reality of these alignments (Struble & Peebles 1985, Ulmer *et al.* 1989) and West's sample of clusters was ill–defined, using only clusters from the Abell catalogue whose problems are well–documented. The unbiased nature of the EM survey makes it an ideal database for studying the reality and frequency of these alignments.

6.4 Future Work on the Large–Scale Structure in the Universe

Over the next decade, the number of measured galaxy redshifts will increase significantly allowing us to map the spatial distribution of galaxies over cosmologically interesting volumes of space. There are numerous large galaxy redshift surveys underway and the EDSGC is supporting 3 such surveys: Broadbent *et al.* (1992) at Durham using the FLAIR multi–fibre instrument on the UK Schmidt Telescope; Parker (1992) at the AAO also using FLAIR; Vettolani *et al.* at Bologna using the multi–fibre system OPTOPUS on the 3.6m telescope at ESO. However, the most ambition project of this kind is a plan to construct a digitised sky survey of the Northern Galactic Cap. Using a dedicated 2.5m telescope at Apache Point in New Mexico, a large collaboration of American astronomers hope to construct a catalogue of 10^8 objects to a limiting magnitude of $B = 23$ over half the northern sky. This will be supplemented with redshifts for a million galaxies and a hundred thousand quasars. They hope to finish the survey by the end of century and if successful, this project will clearly revolutionise our understanding of the large–scale structure in the universe.

The satellites COBE (Cosmic Background Explorer) and ROSAT (Roentgensatellit) will undoubtably have a large impact on our understanding of the universe. COBE was launched in 1989 and was designed to survey the CMB looking for temperature fluctuation of the order 10^{-6} from the mean CMB temperature. As explained in Chapter 1, the detection of such fluctuations would be a direct observation of the seeds from which the large–scale structure we see today formed. ROSAT was launched in 1990 to carry out a dedicated X–ray survey of the sky and a majority of the sources it will detect will be clusters of galaxies and active galactic nuclei out to high redshifts. In conjunction with this work, the Royal Observatory Edinburgh has constructed a digitised survey of the southern sky which contains over 500 million objects covering over 400 UK Schmidt survey plates. This catalogue will be primarily used to find the optical counterparts to the ROSAT X–ray detections, but the volume of optical information it contains will be important in its own respect. Projects are already underway in Edinburgh and Milano (Collins *et al.*, Guzzo *et al.*) to construct large cluster redshift surveys based on X–ray selected cluster catalogues. These catalogues have the benefit of objective selection, a clear physical definition of a cluster in terms of the hot gas in the potential well and

no projection effects.

Clearly, the volume of data on the large–scale structure will increase dramatically over the next few years. The first results from the ROSAT survey and the optical follow–up projects are expected within a year. By the end of the century, we should know the spatial distribution of galaxies and clusters over many hundreds of megaparsecs.

References

Aaronson, M., Bothun, G.D., Cornell, M.E., Dawe, J.A., Dickens, R.J., Hall, P.J., Han Ming Sheng, Huchra, J.P., Lucey, J.R., Mould, J.R., Murnoy, J.D., Schommen, R.A. & Wright, A.E., 1989. *Astrophys. J.*, **338**, 654.

Abell, G.O., 1958. *Astrophys. J. Suppl.*, **3**, 211.

Abell, G.O., Corwin, H.G. & Olowin, R.P., 1989. *Astrophys. J. Suppl.*, **70**, 1. (ACO)

Arp, H.C., Burbridge, G., Hoyle, F., Narlikar, J.V., & Wickramasinghe, N.C., 1990. *Nature.* **346**, 807.

Bahcall, N.A., & Soneira, R.M. 1983. *Astrophys. J.*, **277**, 27.

Bahcall, N.A., Soneira, R.M. & Burgett, W.S., 1986 *Astrophys. J.*, **311**, 15.

Bahcall, N.A., 1988. *Ann. Rev. Astr. Ap.*, **26**, 631.

Bahcall, N.A. 1991. *Astrophys. J.*, **376**, 43.

Bahcall, N.A. & West, M.J., 1992. *Astrophys. J.*, preprint.

Barrow, J.D., 1980. *Phil. Trans. R. Soc. Lond.* **296**, 273.

Beard, S.M., MacGillivray, H.M. & Thanisch, P.F., 1990. *Mon. Not. R. astr. Soc.*, **247**, 311.

Binggeli, B., 1982. *Ap. Astr.*, **107**, 338.

Bond, J.R. & Szalay, A.S., 1983. *Astrophys. J.*, **274**, 443.

Bond, J.R. & Couchman, H., 1988. *Proceedings of the Second Canadian Conference in General Relativity and Relativistic Astrophysics.* eds. Coly, A. & Dyer, C., World Scientific Press, Singapore.

Bond, J.R. & Efstathiou, G., 1991. *Phys. Lett. B.* **265**, 245

Brandenberger, R., 1990. *Physics of the Early Universe.* eds. Peacock, J.A., Heavens, A.F. & Davies, A.T., Proc. of the Thirty Sixth Scottish Universities Summer School in Physics, Edinburgh.

Broadhurst, T.J., Ellis, R.S., Koo, D.C., & Szalay, A.S. 1990. *Nature,* **343**, 726

Broadbent, A., Hale–Sutton, D., Shanks, T., Fong, D., Oates, A.P., Watson, F., Collins, C.A., MacGillivray, H.T., Parker, Q.A. & Nichol, R.C., 1992. *Digitised Optical Sky Surveys.* eds. MacGillivray, H.T. & Thomson, E.B., Kluwer Academic Publishers, London.

Bruck, M.T. & Waldron, J.D., 1984. *Astronomical Photography, Occ. Rep. R. Obs. Edin.*, **14**, Royal Observatory Edinburgh.

Burstein, D. & Heiles, C., 1978. *Astrophys. J.*, **225**, 40. (BH)

Cannon, R.D., Hawarden, T.G., Sim, M.E. & Tritton, S.B., 1978. *The UK 1.2m Schmidt Telescope & Southern Sky Survey II–Photographic Techniques, Occ. Rep. R. Obs. Edin.*, **4**, Royal Observatory Edinburgh.

Cappi, A., Focardi, P., Gergorini, L. & Vettolani, G., 1991. *Astron. Astrophys.* **246**, 290.

Carter, D. & Metcalfe, N., 1980. *Mon. Not. R. astr. Soc.*, **191**, 325.

Clutton–Brook, M. & Peebles, P.J.E., 1981. *Astron. J.* **86**, 1115.

Coles, P., 1990. *Nature,* **346**, 446.

Colless, M. & Hewett, P., 1987. *Mon. Not. R. astr. Soc.*, **224**, 453.

Colless, M., 1989. *Mon. Not. R. astr. Soc.*, **237**, 799.

Collins, C.A., Joseph., R.D. & Robertson, N.A., 1986. *Nature.* **320**, 506.

Collins, C.A., Heydon-Dumbleton, N.H. & MacGillivray, H.T., 1988. *Mon. Not. R. astr. Soc.*, **236**, 7P.

Collins, C.A., Nichol, R.C. & Lumsden, S.L. 1992. *Mon. Not. R. astr. Soc.*, **254**, 295.

Collins, C.A. & Nichol, R.C., 1992. *Mon. Not. R. astr. Soc.,* in preparation.

Corwin, H.G. & Emerson, D., 1982. *Mon. Not. R. astr. Soc.*, **200**, 621.

Costero, R. & Osterbrook, D.E., 1977. *Astrophys. J.*, **211**, 675.

Carlberg, R.G., Couchman, H.M.P. & Thomas, P.A., 1990. *Astrophys. J.*, **352**, L29.

Couchman, H.M.P. & Carlberg, R.G., 1992. *Astrophys. J.*, **389**, 453.

Da Costa, L.N., Pellegrini, P.S., Nunes, M.A., Willmer, C. & Latham, D.W., 1984. *Astron. J.* **89**, 1310.

Da Costa, L.N., Pellegrini, P.S., Davis, M., Meiksin, A., Sargent, W.L.W & Tonry, J., 1991. *Astrophys. J. Suppl.* **75**, 135.

de Lapparent, V., Kurtz, M.J. & Geller, M.J., 1986. *Astrophys. J.*, **304**, 585.

Dalton, G.B., Efstathiou, G., Maddox, S.J. & Sutherland, W., 1992. *Astrophys. J.*, submitted.

Davis, M. & Peebles, P.J.E., 1983. *Astrophys. J.*, **267**, 465.

Davis, M., Efstathiou, G., Frenk, C.S. & White, S.D.M., 1985. *Astrophys. J.*, **292**, 371.

Davis, M., Efstathiou, G., Frenk, C.S. & White, S.D.M., 1992. *Nature.* in press.

Dekel, A., Blumenthal, G.R., Primack, J.R. & Olivier, S., 1989. *Astrophys. J.*, **338**, L5.

Dickey, J.M. & Lockman, F.J., 1990. *Ann. Rev. Astron. Astro.* **28**, 215.

Dodds, R.J. & MacGillivray, H.M.G., 1986. *Astron. J.* **92**, 706.

Dressler, A., 1978. *Astrophys. J.*, **223**, 351.

Dressler, A., Faber, S.M., Burstein, D., Davies, R.L., Lynden–Bell, D., Terlevich, R.J. & Wegner, G., 1987. *Astrophys. J.*, **313**, L37.

Lynden–Bell, D., Faber, S.M., Burstein, D., Davies, R.L., Dressler, A., Terlevich, R.J. & Wegner, G., 1987. *Astrophys. J.*, **326**, 19.

Efstathiou, G. & Bond, J.R., 1987. *Mon. Not. R. astr. Soc.*, **227**, 33p.

Efstathiou, G., 1990. *Physics of the Early Universe.* eds. Peacock, J.A., Heavens, A.F. & Davies, A.T., Proc. of the Thirty Sixth Scottish Universities Summer School in Physics, Edinburgh.

Efstathiou, G., Sutherland, W. & Maddox, S.J., 1990. *Nature.* **348**, 705.

Efstathiou, G., Dalton, G.B., Maddox, S.J. & Sutherland, W., 1992. *Mon. Not. R. astr. Soc.*, preprint.

Fesenko, B.I., 1979. *Soviet Astron.*, **23**, 6.

Frenk, C., 1986. *Phil. Trans. R. Soc. Lond.* **330**, 517.

Frenk, C.S., White, S.D.M., Efstathiou, G. & Davis, M., 1990. *Astrophys. J.*, **351**, 10.

Gamov, G., 1946. *Phys. Rev.* **70**, 572.

Gamov, G., 1948. *Nature.* **152**, 680.

Geller, M.J., de Lapparent, V. & Kurtz, M.J., 1984. *Astrophys. J.*, **287**, L55.

Geller, M.J. & Huchra, J.P., 1989. *Science.* **246**, 897.

Glazebrook, K., 1991. *Ph.D. Thesis.* University of Edinburgh.

Groth, E.J. & Peebles, P.J.E., 1977. *Astrophys. J.*, **217**, 385. (GP77)

Groth, E.J. & Peebles, P.J.E., 1986a. *Astrophys. J.*, **310**, 499.

Groth, E.J. & Peebles, P.J.E., 1986b. *Astrophys. J.*, **310**, 507.

Guth, A.H., 1981. *Phys. Rev.* **D23**, 347.

Guth, A.H., 1986. *Inner Space/Outer Space. The Interface between Cosmology and Particle Physics.* eds. Kolb, E.W., Turner, M.S., Lindley, D., Olive, K. & Seckel, D. University of Chicago Press.

Guzzo, L., Collins., C.A., Nichol, R.C., & Lumsden, S.L., 1992. *Astrophys. J.,* in press.

Hale–Sutton, D., Shanks, T. & Fong, R., 1992. *Digitised Optical Sky Surveys.* eds. MacGillivray, H.T. & Thomson, E.B., Kluwer Academic Publishers, London.

Harrison, E.R., 1970. *Phys. Rev. D.* **1**, 2726.

Hauser, M.G. & Peebles, P.J.E., 1973. *Astrophys. J.,* **185**, 757.

Hewitt, P.C., 1982. *Mon. Not. R. astr. Soc.,* **201**, 867.

Heydon-Dumbleton, N.H., Collins,C.A., & MacGillivray, H.T., 1989. *Mon. Not. R. astr. Soc.,* **238**, 379.

Heydon–Dumbleton, N.H., 1989. *Ph.D. Thesis.* University of Edinburgh.

Huchra, J.P., Henry, J.P., Postman, M. & Geller, M.J., 1990. *Astrophys. J.,* **365**, 66.

Ikeuchi, S., & Turner, E.L. 1991. *Mon. Not. R. astr. Soc.,* **250**, 519.

Jelley, R., 1986. *Phil. Trans. R. Soc. Lond.* **330**, 517.

Jing, Y.P., Plionis, M. & Valdarnini, R., 1992. *Astrophys. J.,* **389**, 499.

Kaiser, N., 1984. *Astrophys. J.,* **284**, L9.

Kaiser, N., 1986. *Mon. Not. R. astr. Soc.,* **219**, 785.

Kaiser, N., & Peacock, J.A. 1991. *Astrophys. J.,* **379**, 482.

Kurki-Suonio, H., Mathews, G.J., & Fuller, G.M. 1990. *Astrophys. J.,* **356**, L5.

Lahav, O., Edge, A., Fabian, A.C. & Putney, A., 1989. *Mon. Not. R. astr. Soc.,* **238**, 881.

Landau, L.D. & Lifshitz, E.M., 1959. *Fluid Mechanics.* Pergamon, London.

Lilje, P. B., 1990. *Astrophys. J.,* **351**, 1.

Limber, D.N., 1953. *Astrophys. J.,* **117**, 134.

Ling, E.N., Frenk, C.S. & Barrow, J.D., 1986. *Mon. Not. R. astr. Soc.,* **223**, 21p.

Loveday, J., 1991. *Ph.D. Thesis.* University of Cambridge.

Lucey, J.R., 1983. *Mon. Not. R. astr. Soc.,* **204**, 33.

Lucey, J.R. & Carter, D., 1988. *Mon. Not. R. astr. Soc.,* **235**, 1177.

Lubimov, V.A., Novikov, E.G., Nozik, V.Z., Tretyakov, E.F. & Kozik, V.S., 1980. *Phys. Lett.* **94**, 266.

Lumsden, S.L., Nichol, R.C., Collins, C.A., & Guzzo, L., 1992. *Mon. Not. R. astr. Soc.,* in press.

MacGillivray, H.T. & Dodd, R.J., 1982. *Workshop on Astronomical Measuring Machines, Occ. Rep. R. Obs. Edin.,* **10**, Royal Observatory Edinburgh.

MacGillivray, H.T. & Stobie, R.S., 1984. *Vista Astr.,* **24**, 433.

Maddox, S.J., Efstathiou, G. & Loveday, J., 1988. *Large Scale Structures of the Universe, IAU Symp. No. 130.* eds Audouze, J., Pelletan, M.C. & Szalay, A., Kluwer Academic Publishers, Dordrecht, Holland.

Maddox, S.J., Efstathiou, G., Sutherland, W. & Loveday, J., 1990. *Mon. Not. R. astr. Soc.,* **242**, 43p.

Maddox, S.J., Efstathiou, G. & Sutherland, W., 1990b. *Mon. Not. R. astr. Soc.,* **246**, 433.

Mather, J.S., 1990. *Ann. Rev. Astron. Astro.* **28**, 37.

Mather, J.C., *et al.* 1990. *Astrophys. J.,* **354**, L37.

Matherson, D.S., Ford, V.L. & Buchhorn, M., 1992. *Astrophys. J.,* **389**, L5.

Mattig, W., 1958. *Astron. Nach.,* **284**, 109.

Meszaros, P., 1975. *Astron. Astrophys.* **38**, 5.

Muriel, H., Nicotra, M. & Lambas, D.G., 1990. *Astron. J.* **100**, 339.

Nichol, R.C., Collins, C.A., Guzzo, L., & Lumsden, S.L. 1992. *Mon. Not. R. astr. Soc.,* **255**, 21p.

Nicholson, D., 1991. *Ph.D. Thesis.* University of Edinburgh.

Olivier, S., Dekel, A., Blumenthal, G.R., Primack, J.R. & Stanhill, D., 1990. *Astrophys. J.,* **356**, 1.

Olowin, R., Da Souza, R.E. & Chincarini, G., 1988. *Astron. Astrophys. Suppl.* **73**, 125.

Oort, J.H., 1983. *Ann. Rev. Astr. Ap.,* **21**, 373.

Parker, Q.A., Beard, S.M. & MacGillivray, H.T., 1987. *Astron. Astrophys.* **173**, L5.

Parker, O.A., 1992. *Digitised Optical Sky Surveys.* eds. MacGillivray, H.T. & Thomson, E.B., Kluwer Academic Publishers, London.

Peebles, P.J.E., 1973. *Astrophys. J.,* **185**, 413.

Peebles, P.J.E., 1974a. *Astron. & Astrophys.* **32**, 391.

Peebles, P.J.E., 1974b. *Astrophys. J.,* **189**, L51.

Peebles, P.J.E., 1980. *The Large-Scale Structure of the Universe,* Princeton University Press, Princeton, New Jersey.

Peebles, P.J.E., 1981. *Astrophys. J.*, **248**, 885.

Peebles, P.J.E., Schramm, D.N., Turner, E.L., & Kron, R,G., 1991. *Nature.* **352**, 769.

Picard, A., 1991. *Astrophys. J.*, **368**, L7.

Postman, M., Geller, M.J. & Huchra, J.P., 1986. *Astron. J.*, **91**, 1267.

Postman, M., Huchra, J.P. & Geller, M.J., 1992. *Astrophys. J.*, **384**, 404.

Rainey, G.W., 1977. *Ph.D. Thesis.* University of California.

Robertson, H.P., 1935. *Astrophys. J.*, **82**, 284.

Rowan–Robinson, M., 1985. *The Cosmological Distance Ladder: Distance and Time in the Universe.* Freeman, New York.

Rowan–Robinson, M., Hughes, J., Leech, K., Vedi, K. & Walker, D., 1991. *Mon. Not. R. astr. Soc.*, **248**, 111.

Rubin, V.C., Ford, W.K., Thonnard, N., Roberts, M.S. & Graham, J.A., 1976a. *Astron. J.* **81** 687.

Rubin, V.C., Thonnard, N., Ford, W.K. & Roberts, M.S. 1976b. *Astron. J.* **81** 719.

Sachs, R.K. & Wolfe, A.M., 1967. *Astrophys. J.*, **147**, 73.

Sastry, G. N., 1968. *Pub. A.S.P.*, **80**, 252.

Saunders, W., Frenk, C.S., Rowan–Robertson, R., Efstathiou, G., Lawrence, A., Kaiser, N., Ellis, R., Crawford, J., Xia, X.Y. & Parry, I., 1991. *Nature.* **349**, 32.

Savage, A., 1978. *Astron. J.* **83**, 904.

Scaramella, R., Zamorani, G., Vettolani, G. & Chincarini, G., 1991. *Astron. J.* **101**, 342.

Schuecker, P., & Ott, H.A. 1991. *Astrophys. J.*, **378**, L1.

Seitter, W.C., Ott, H.A., Duemmler, R., Schuecker, P. & Horstmann, H., 1989. *Lecture Notes in Physics, Vol. 322, Morphological Cosmology.* eds. Flin, P. & Duerkbeck, H.W., Springer, Berlin.

Seldner, M., 1977. *Ph.D. Thesis.* Princeton University.

Seldner, M., Siebers, B., Groth, E.J. & Peebles, P.J.E., 1977. *Astron. J.*, **82**, 249.

Shane, C.D. & Wirtanen, C.A., 1967. *Publs. Lick Obs.* **22**, Part 1.

Shanks, T., Fong, R., Ellis, R.S. & MacGillivray, H.T., 1980. *Mon. Not. R. astr. Soc.*, **192**, 209.

Shectman, S.A., 1985. *Astrophys. J. Suppl.*, **57**, 77.

Stark, A.A., Gammie, C.F., Wilson, R.W., Balley, J., Linke, R.A., Heiles, C. & Hurwity, M., 1992. *Astrophys. J. Suppl.* **79**, 77.

Sharp, N.A., 1979. *Astron. Astrophys.* **74**, 308.

Stevenson, P.R.F., 1985. *Ph.D. Thesis.* University of Durham.

Stevenson, P.R.F., Shanks, T., Fong, R. & MacGillivray, H.T., 1985. *Mon. Not. R. astr. Soc.,* **213**, 953.

Stevenson, P.R.F., Fong, R. & Shanks, T., 1988. *Mon. Not. R. astr. Soc.,* **234**, 801.

Stobie, R.S., 1980. *Journal Brit. Interplanetary Soc.,* **33**, 323.

Struble, M.F. & Rood, H.J., 1984. *Astron. J.* **89**, 1487.

Struble, M. F. & Peebles, P. J. E., 1985. *Astrophys. J.,* **90**, 582.

Struble, M.F. & Rood, H.J., 1991. *Astrophys. J.,* **374**, 395.

Sutherland, W., 1988. *Mon. Not. R. astr. Soc.,* **234**, 159.

Sutherland, W. & Eftathiou, G., 1991. *Mon. Not. R. astr. Soc.,* **248**, 159.

Szalay, A.S., Hollosi, J. & Toth, G. 1989. *Astrophys. J.,* **239**, L5.

Teague, P., Carter, D. & Gray, P.M., 1990. *Astrophys. J. Suppl.* **72**, 715.

Thanisch, P., McNally, B.V. & Robin, A., 1984. *Image Vis. Comput.,* **2**, 4.

Tonry, J. & Davis, M., 1977. *Astron. J.* **84**, 1511.

Totsuji, H. & Kihara, T., 1969. *Publ. Astron. Soc. Japan.* **21**, 221.

Tully, R.B., Scaramella, R., Vettolani, G., & Zamorani, G. 1992. *Astrophys. J.,* **388**, 9.

Ulmer, M. P., McMillan, S. L. W. & Kowalski, M. P., 1989. *Astrophys. J.,* **338**, 711.

United Kingdom Schmidt Telescope Unit (UKSTU) Handbook, 1983. Royal Observatory Edinburgh.

Uson, J.M. & Wilkinson, D.T., 1984. *Nature.* **312**, 427.

van de Weygaert, R. 1991. *Mon. Not. R. astr. Soc.,* **249**, 159.

Vettolani, G., Cappi, A., Chincarini, G., Focardi, P., Garilli, B., Gergorini, L. & Maccagini, D., 1989. *Astron. Astrophys. Suppl.* **79**, 147.

Wagoner, R.V., 1973. *Astrophys. J.,* **179**, 343.

Walker, A.G., 1936. *Proc London Math Soc.* **42**, 90.

Weinberg, S., 1972. *Gravitation and Cosmology.* New York: Wiley.

Weinberg, S., 1977. *The First Three Minuites: A Modern View of the Origin of the Universe.* London: Andre Deutsch.

West, M.J., Dekel, A. & Oemler A., 1989. *Astrophys. J.*, **336**, 46.

West, M.J., 1991. *Astrophys. J.*, **379**, 19.

West, M.J. & van den Bergh, S., 1991. *Astrophys. J.*, **373**, 1.

Williams, B., 1992 *Ph.D. Thesis.* Edinburgh University.

White, S.D.M., Frenk, C.S. & Davis, M., 1983. *Astrophys. J.*, **274**, L1.

White, S.D.M., Davis, M. & Frenk, C.S., 1984. *Mon. Not. R. astr. Soc.*, **209**, 27.

White, S.D.M., 1986. *Inner Space/Outer Space. The Interface between Cosmology and Particle Physics.* eds. Kolb, E.W., Turner, M.S., Lindley, D., Olive, K. & Seckel, D. University of Chicago Press.

White, S.D.M, Frenk, C.S., Davis, M. & Efstathiou, G., 1987. *Astrophys. J.*, **313**, 505.

Willick, J.A., 1990. *Astrophys. J.*, **351**, L5.

Wilson, M.L. & Silk, J., 1981. *Astrophys. J.*, **243**, 14.

Yang, J., Turner, M.S., Steigman, G., Schramm, D.N., & Olive, K.A., 1984. *Astrophys. J.*, **281**, 493.

Zabludoff, A., Huchra, J.P. & Geller, M.J., 1990. *Astrophys. J. Suppl.* **74**, 1.

Zamorani, G., Scaramella, R., & Vettolani, G., 1991. *Astrophys. J.*, , preprint.

Zel'dovich, Y.B., 1972. *Mon. Not. R. astr. Soc.*, **160**, 1p.

Appendix A

The Edinburgh/Durham Cluster Catalogue

This Appendix contains the final cluster list of the Edinburgh/Durham Cluster Catalogue (EDCC). Full details of how these clusters were selected can be found in Chapter 3. All the clusters were visually scanned and a small percentage of the clusters (4%) were rejected as obvious mistakes. These are presented in Table A.2 at the end of this Appendix. If a cluster has zero magnitudes for its m_1, m_3 or m_{10} values, then most of its galaxies were deblended into an adjacent cluster, leaving too few galaxies to calculate the background subtracted magnitudes. Possible errors in the values of m_{10} and richness, noted during the visual inspection of the clusters, have been marked with a $*$. A '?' against the cluster identification number means that no obvious overdensity could be found at the cluster position (43 clusters). These flags are meant only as guides to individual clusters and may be highly subjective.

Column Number	Description
1	Sequential cluster identification number.
2	Right Ascension of the final cluster centroid (Epoch 1950).
3	Declination of the final cluster centroid (Epoch 1950).
4	Magnitude of the brightest galaxy in the cluster (m_1).
5	Magnitude of the 3rd brightest galaxy in the cluster (m_3).
6	Magnitude of the 10th brightest galaxy in the cluster (m_{10}). The above 3 magnitudes were all background corrected.
7	Number of galaxies within the Abell radius between m_3 and $m_3 + 2$ after background correlation (n_{clus}).
8	The number of estimated background/foreground galaxies within the same magnitude limits as above (n_{back}).
9	The Abell radius in degrees calculated from the corrected m_{10}.
10	The UK Schmidt survey field number that the cluster was detected on.
11	The number of times in a particular run the cluster was detected *i.e.* 121 means the cluster was detected once in run 1, twice in run 2, etc.
12	Whether the cluster was deblended in the final analysis.
13	Abell identification number. For a match–up, the cluster centroids had to be within each others Abell radii. For numbers in brackets, the Abell radii just overlapped.

Table A.1: Description of the columns in Table A.2.

EDCC	R.A.			Dec.			m_1	m_3	m_{10}	n_{clus}	n_{back}	θ_A	Field	runs	Deb.	Abell
	h	m	s	°	′	″										
1	21	26	47.4	−22	29	39.0	17.28	18.13	19.58	21	40	0.151	F531	111	d	2347
2	21	27	17.3	−22	40	41.5	16.88	17.02	18.76	11	19	0.196	F531	010	d	
3	21	28	1.9	−24	1	1.9	15.68	17.62	17.99	40	70	0.269	F531	110	d	
4	21	29	27.7	−24	9	40.9	14.65	17.33	18.12	47*	44	0.255	F531	111	d	
5	21	29	33.9	−22	53	2.0	15.95	17.38	18.56	15	71	0.212	F531	011	d	3778
6	21	29	59.3	−23	1	14.0	15.63	16.78	19.05	8	32	0.178	F531	121	d	
7	21	30	37.5	−23	57	14.8	18.29	18.37	19.04	24*	95	0.179	F531	010	d	
8	21	30	54.0	−26	0	24.8	16.12	18.10	0.00	0	0	0.000	F531	011	d	
9	21	31	31.3	−27	18	28.2	15.24	15.87	17.22	15	7	0.370	F531	110	d	
10	21	31	46.7	−26	15	51.2	15.52	16.22	17.62	22	11	0.313	F531	100	d	
11	21	32	55.6	−26	53	59.2	15.11	16.11	18.17	8	5	0.249	F531	100	d	
12	21	33	55.8	−23	29	41.7	16.42	17.88	18.45	48	67	0.222	F531	011		2357
13	21	36	40.9	−27	19	50.7	17.54	18.27	18.65	38	62	0.205	F531	010		3797
14	21	36	53.1	−26	49	41.3	14.09	17.32	18.15	13	34	0.252	F531	100	d	
15	21	37	31.8	−23	5	51.3	14.41	15.77	17.15	23	10	0.381	F531	113	d	(S 963)
16?	21	37	38.6	−32	37	11.7	17.34	17.39	18.33	33	15	0.233	F466	012	d	(3795)
17?	21	37	56.5	−31	16	30.7	14.55	19.72	20.27	22	16	0.120	F466	001		
18	21	38	6.7	−23	4	21.4	0.00	0.00	0.00	0	0	0.000	F531	001	d	
19?	21	38	11.0	−32	6	50.5	16.00	16.83	18.38	14	9	0.229	F466	100	d	
20	21	38	15.1	−27	0	33.2	17.09	18.14	19.38	28	36	0.161	F531	011	d	
21	21	38	17.2	−29	13	16.2	15.49	16.45	17.90*	7	11	0.279	F466	110		
22?	21	38	22.8	−28	39	24.5	16.95	17.77	18.17	43	52	0.249	F466	011		
23?	21	39	37.7	−31	36	23.8	18.42	18.75	19.84	48	24	0.138	F466	001	d	
24?	21	39	39.8	−31	55	35.3	17.09	18.02	18.33	69	39	0.233	F466	110	d	
25?	21	39	47.0	−32	34	40.3	16.34	17.40	18.36	34	18	0.231	F466	010	d	
26	21	40	35.1	−25	26	13.5	13.67	17.31	18.20	19	40	0.245	F531	100		
27	21	41	0.0	−31	19	51.3	15.86	18.16	18.49	59*	46	0.211	F466	001		
28?	21	41	33.4	−32	28	58.4	17.41	18.03	18.71	48	32	0.200	F466	100	d	
29	21	41	33.5	−24	37	17.4	18.57	19.39	20.12	21	39	0.127	F531	001	d	
31	21	42	27.7	−24	23	33.7	15.89	17.61	18.46	55	45	0.221	F531	011	d	2371
32	21	42	42.3	−27	30	52.0	17.04	19.26	19.69	34*	54	0.145	F531	001		
33	21	42	44.6	−22	42	53.5	16.55	17.31	18.63	15	30	0.207	F531	111		
34	21	42	51.5	−26	10	10.3	17.63	17.77	18.89	50*	38	0.188	F531	011		3805
35	21	43	2.7	−30	9	11.5	15.41	18.02	18.89	34	50	0.188	F466	001	d	
36?	21	43	25.2	−31	7	54.8	17.05	17.50	18.46	19	33	0.221	F466	100	d	

EDCC	R.A.			Dec.			m_1	m_3	m_{10}	n_{clus}	n_{back}	θ_A	Field	runs	Deb.	Abell
	h	m	s	°	′	″										
37	21	44	57.1	−30	49	45.3	17.44	17.88	18.13	54*	73	0.254	F466	111	d	
38?	21	45	39.3	−31	58	49.7	17.36	17.87	18.39	40	55	0.228	F466	011		3813
39	21	45	42.2	−28	27	12.9	16.94	17.25	18.34	22	26	0.217	F466	100		
40	21	45	53.1	−27	55	42.8	16.47	16.82	18.65	13	13	0.205	F466	110		
42	21	46	21.9	−30	56	37.8	16.18	17.55	18.21	87	55	0.245	F466	111	d	3814
43	21	46	34.6	−35	54	25.7	16.10	16.73	17.55	30	18	0.323	F404	010	d	
44?	21	46	37.2	−37	36	3.9	16.05	16.36	18.39	6	4	0.228	F404	011	d	
45	21	46	40.2	−34	2	11.8	16.52	16.71	17.78	18	21	0.293	F404	111		(3815)
46	21	46	40.3	−37	6	4.5	16.01	17.06	17.78	57*	17	0.293	F404	111	d	
47?	21	46	45.7	−30	9	10.9	16.65	17.64	18.60	19	40	0.207	F466	100		
48	21	47	32.9	−35	7	5.5	12.70	15.64	17.72	6	4	0.301	F404	220	d	
49?	21	47	34.6	−26	56	12.5	16.57	17.87	18.16	67	75	0.250	F531	110		
50	21	49	2.7	−31	53	30.5	17.39	17.54	18.10	47*	55	0.257	F466	101	d	
51	21	49	22.2	−29	8	1.7	16.35	16.76	17.78	17	30	0.293	F466	111		
52	21	50	12.6	−23	48	46.8	18.60	18.72	19.01	82	71	0.180	F532	011		2385
53	21	50	12.8	−31	47	36.5	17.34	17.83	19.15	16	47	0.172	F466	011	d	
54	21	50	45.7	−42	25	48.9	15.40	16.34	17.87	11	6	0.282	F344	110		(S 978)
55	21	52	4.7	−37	51	18.1	15.88	17.74	17.87	69*	45	0.282	F344	110		
57	21	53	30.9	−30	23	0.4	17.29	18.05	18.19	31	96	0.248	F466	110	d	
58	21	53	38.9	−35	9	38.5	17.25	18.19	18.79	61*	48	0.194	F404	011	d	
59	21	53	42.8	−32	53	38.5	18.29	18.38	19.49	38	44	0.155	F404	001		
60	21	53	47.4	−24	10	5.9	17.04	19.09	19.65	28	57	0.147	F532	001		
61	21	53	59.4	−30	19	37.9	18.24	18.31	0.00	0	0	0.000	F466	001	d	
62	21	54	2.5	−40	10	41.8	15.91	16.08	17.45	16	6	0.336	F344	110	d	
64	21	54	17.0	−38	22	15.8	15.11	16.11	18.09	10*	6	0.257	F344	110		
65	21	54	54.9	−26	57	12.8	17.08	18.58	19.32	53*	56	0.163	F532	001		(3824)
66	21	55	2.0	−39	41	39.2	16.02	16.14	18.02	8	6	0.265	F344	110	d	
67	21	55	35.2	−30	9	33.4	17.58	19.20	19.67	34	60	0.145	F466	001	d	
68	21	55	36.5	−31	7	54.8	16.01	17.08	17.76	34	49	0.296	F466	121		
69	21	55	37.0	−28	49	33.2	13.33	14.54	16.27	8	5	0.594	F466	100		
70	21	56	9.5	−25	26	51.0	16.61	17.51	18.92	12	24	0.186	F532	010		
72	21	56	56.9	−42	20	24.0	16.17	16.84	17.94	47*	24	0.274	F344	110		
73	21	57	16.8	−24	43	45.1	15.53	16.70	18.45	11	12	0.223	F532	100		
75	21	58	7.7	−24	21	16.1	18.45	18.65	18.84	23	79	0.193	F532	010		
76	21	58	41.5	−32	9	44.5	11.92	14.87	17.72	2	1	0.287	F466	100		

EDCC	R.A.			Dec.			m_1	m_3	m_{10}	n_{clus}	n_{back}	θ_A	Field	runs	Deb.	Abell
	h	m	s	°	′	″										
77	21	59	10.6	−22	59	33.9	0.00	0.00	0.00	0	0	0.000	F532	021	d	
78	21	59	15.3	−29	56	21.4	18.37	18.49	19.34	18	53	0.164	F466	010		
79	21	59	21.3	−37	46	52.3	15.45	16.65	18.70	4	10	0.200	F404	010		
80	21	59	25.2	−22	48	38.6	14.63	14.79	16.69	10	3	0.461	F532	110	d	S 987
81	21	59	37.5	−30	19	29.4	17.98	18.83	19.53	23	60	0.157	F466	001		
82	21	59	45.7	−41	24	48.0	14.13	16.95	18.05	20*	25	0.262	F344	100		
83	22	0	3.9	−28	37	58.0	16.75	17.33	19.08	7	18	0.170	F466	001		
84	22	0	19.0	−34	47	30.0	17.73	18.21	19.56	21	32	0.144	F404	001		
85	22	2	5.0	−25	29	37.9	17.06	17.67	19.75	6	18	0.143	F532	001		2416
86	22	2	25.6	−30	45	48.0	16.26	17.35	18.73	16	25	0.202	F467	010		3833
87	22	2	41.5	−33	58	25.7	18.74	19.09	19.41	41*	71	0.157	F404	001		
88	22	3	24.2	−39	24	18.7	17.00	17.14	18.31	13	28	0.235	F344	111		S 993
89	22	3	46.7	−36	37	55.4	16.71	17.49	19.42	10	18	0.158	F404	001	d	
90	22	4	9.6	−42	1	18.3	16.25	17.83	18.40	23	52	0.226	F344	110	d	
91	22	4	55.8	−24	39	44.3	17.71	18.56	19.52	29	50	0.153	F532	001		2417
92	22	5	18.0	−41	47	45.2	16.22	17.00	18.26	10	25	0.240	F344	100	d	
93	22	5	25.9	−26	44	38.1	17.58	18.49	18.88	35	80	0.189	F532	011		
94	22	5	35.4	−26	22	5.7	17.16	18.51	19.05	50	69	0.178	F532	010		(2418)
95	22	5	39.3	−36	45	45.2	16.35	16.90	18.12	23	28	0.255	F404	110	d	
96	22	6	9.7	−35	21	37.2	14.57	15.11	17.11	9	4	0.387	F404	101		S 997
97	22	6	10.8	−32	19	53.3	17.60	19.11	20.48	10	32	0.112	F467	001		
98	22	6	30.3	−28	43	20.2	17.79	18.17	19.49	19	32	0.145	F467	001		
99	22	6	34.9	−27	33	24.0	14.39	14.99	17.67	4	2	0.307	F532	111		3837
100	22	7	17.3	−28	20	34.5	18.20	18.53	19.19	16	55	0.161	F467	001		3838
101	22	7	33.6	−40	6	23.8	16.28	16.38	18.84	2	6	0.191	F344	010		3840
102	22	7	40.2	−30	27	43.3	16.08	18.79	20.24	18	32	0.122	F467	001		
103	22	8	6.3	−28	42	40.5	19.09	19.40	20.30	20	44	0.120	F467	001		
104	22	8	25.3	−33	15	37.0	17.22	17.32	18.38	25	26	0.219	F404	100		
105	22	8	40.5	−39	2	19.3	17.83	18.50	18.63	45	87	0.206	F344	001	d	3842
106	22	8	53.4	−33	55	34.2	16.32	17.62	18.57	21	36	0.211	F404	100	d	S1000
107	22	9	18.5	−34	19	57.5	14.84	15.82	18.04	2	4	0.263	F404	100	d	
108	22	9	49.0	−38	45	4.7	14.81	16.63	18.72	7	10	0.198	F344	010	d	
110	22	9	55.3	−29	15	23.1	18.02	18.41	19.48	21	45	0.158	F467	001		
111	22	9	58.1	−27	15	51.2	16.03	17.80	18.24	42	64	0.242	F532	110		
112	22	10	10.0	−32	49	10.4	16.67	18.46	19.30	39	46	0.167	F404	001		

EDCC	R.A.			Dec.			m_1	m_3	m_{10}	n_{clus}	n_{back}	θ_A	Field	runs	Deb.	Abell
	h	m	s	°	′	″										
113	22	10	51.4	−36	37	9.5	0.00	0.00	0.00	0	0	0.000	F404	100	d	
114	22	11	8.7	−36	54	40.2	15.34	16.82	17.15	57	55	0.381	F404	122	d	S1005
115	22	11	9.1	−35	13	31.2	15.66	17.25	18.58	10	24	0.210	F405	001		(3844)
116	22	11	27.2	−34	42	33.7	16.64	16.97	19.45	4	8	0.148	F404	001		
117	22	12	19.5	−27	21	12.5	16.17	17.09	18.58	12	22	0.212	F533	010		(3846)
118	22	13	18.5	−41	19	4.9	15.34	16.41	18.03	5	12	0.264	F344	010		
119	22	13	21.8	−25	51	52.6	15.77	15.94	18.28	6	6	0.238	F533	111		
120	22	13	35.0	−39	31	55.6	18.20	18.31	18.75	28	67	0.192	F344	001		3853
121	22	13	51.5	−25	24	43.5	16.24	16.53	20.04	2	4	0.136	F533	001		
122	22	14	22.9	−38	36	27.2	17.45	17.69	19.22	18	24	0.161	F344	010		
123	22	14	37.1	−26	31	26.3	16.38	16.96	18.87	8*	18	0.189	F533	011	d	(S1008)
124	22	14	43.9	−35	57	33.1	17.07	18.04	18.46	109	63	0.221	F405	011		3854
125	22	15	6.5	−41	50	55.9	16.15	16.59	18.47	11	11	0.220	F344	100		
126	22	15	8.8	−30	19	50.2	16.18	17.20	18.28	17	28	0.240	F467	100		
127	22	15	41.0	−39	8	55.9	16.38	17.49	18.09	53	52	0.257	F344	111		3856
128	22	15	56.3	−28	34	41.1	16.73	17.95	20.32	2	17	0.120	F467	100		
129	22	16	2.1	−24	26	56.1	14.77	16.34	16.75	36*	31	0.449	F533	111		
130	22	16	6.2	−26	47	19.5	14.42	15.75	17.62	12	7	0.313	F533	111	d	(S1010)
131	22	16	39.2	−34	56	27.0	16.73	17.90	18.18	66	63	0.249	F405	111		3858
132	22	17	5.3	−39	46	11.4	16.06	17.30	18.05	20	40	0.262	F344	100		
133	22	17	37.6	−22	39	45.2	16.52	19.18	20.12	19	39	0.127	F533	001		
134	22	17	40.6	−35	23	52.5	17.67	18.61	19.28	27	50	0.158	F405	001		3866
135	22	18	26.4	−26	17	15.3	15.76	17.87	18.85	16	36	0.180	F533	100		
136	22	18	52.3	−29	3	37.1	16.16	17.60	18.89	40*	25	0.188	F467	011		
137	22	19	17.9	−38	52	56.0	15.80	16.26	19.15	5	4	0.170	F345	101		S1016
139	22	21	21.4	−26	27	16.2	16.70	17.44	18.50	15	31	0.218	F533	011		(S1018)
140	22	21	22.6	−42	3	5.8	16.34	17.33	18.23	10	31	0.243	F345	100		
141	22	22	50.9	−35	11	46.4	16.62	18.77	19.17	38	61	0.175	F405	001		
142	22	23	1.5	−31	21	17.7	14.02	14.84	16.43	10	5	0.526	F467	212	d	
143	22	23	48.5	−42	40	58.4	16.72	18.37	19.42	27	42	0.158	F345	010		
144	22	24	3.2	−32	13	26.3	17.30	18.21	19.08	19	33	0.168	F467	001		3878
145	22	24	56.7	−30	51	11.0	15.07	16.27	16.91	34	27	0.421	F467	111	d	3880
146	22	24	59.8	−24	3	54.5	0.00	0.00	0.00	0	0	0.000	F533	001	d	(2444)
147	22	25	28.0	−24	17	24.5	16.18	17.28	17.69	28	46	0.305	F533	100	d	
148	22	25	39.2	−24	42	57.9	15.89	16.43	18.96	7	10	0.183	F533	001	d	

EDCC	R.A.			Dec.			m_1	m_3	m_{10}	n_{clus}	n_{back}	θ_A	Field	runs	Deb.	Abell
	h	m	s	°	′	″										
149?	22	26	24.6	−32	15	32.2	16.88	18.01	18.55	51	41	0.205	F468	010		
150	22	26	28.8	−36	39	4.9	15.67	17.30	19.98	5	10	0.133	F405	001		(3882)
151?	22	27	22.4	−24	10	52.0	17.19	17.28	17.55	12	50	0.323	F533	100	d	
152?	22	27	47.2	−24	34	53.0	17.48	17.64	18.47	5	36	0.220	F533	100	d	
153	22	29	19.8	−31	27	51.9	15.55	16.06	17.30	11	9	0.358	F468	101		
154	22	29	23.4	−39	0	52.5	16.76	18.27	19.78	19	44	0.141	F345	001	d	
155	22	29	26.3	−25	40	49.1	13.28	16.05	16.77	10	20	0.446	F533	111		
156	22	29	53.3	−39	16	50.4	16.88	18.58	19.20	53	76	0.170	F345	001	d	3887
158	22	30	45.3	−36	2	11.7	17.72	19.13	19.29	39*	75	0.166	F405	011		
159	22	31	7.4	−39	19	53.2	19.63	19.63	19.94	22	62	0.134	F345	001	d	
160	22	31	32.4	−37	59	54.1	15.42	16.30	18.00	10	14	0.268	F345	011		3888
161	22	32	54.3	−38	59	17.3	16.23	16.63	17.72	18	26	0.301	F345	011		S1042
162	22	33	4.7	−37	36	45.1	14.87	15.88	18.54	5	5	0.214	F405	010		
163	22	33	6.1	−40	40	55.4	18.09	18.12	18.91	19	56	0.187	F345	010		
164	22	33	17.2	−41	43	42.2	15.86	16.67	17.49	14	28	0.331	F345	100		
165	22	33	35.6	−24	36	25.3	14.88	16.27	17.28	26	18	0.361	F534	111		S1043
166	22	34	4.8	−38	17	43.8	16.56	18.27	18.98	56	77	0.182	F345	011		S1045
168	22	34	22.7	−39	26	53.0	15.80	16.67	19.30	4	15	0.164	F345	011	d	S1047
169	22	34	44.9	−39	45	14.8	17.31	17.53	17.98	19	68	0.270	F345	110	d	
170	22	35	9.7	−30	56	26.5	15.98	17.43	18.48	15	23	0.219	F468	001		3892
171	22	35	11.0	−24	9	40.5	17.74	18.01	18.92	26	37	0.189	F534	001		3893
172	22	35	50.4	−37	9	50.4	14.80	15.65	17.05	21	15	0.397	F405	122	d	3895
173	22	35	57.3	−36	39	56.2	16.23	16.52	17.78	18	43	0.293	F406	022	d	
174?	22	36	17.9	−22	48	45.5	15.92	16.34	18.09	14	10	0.258	F534	121		
175	22	36	27.4	−38	5	29.3	16.21	17.53	18.40	42	59	0.227	F345	112		S1051
176	22	36	54.3	−36	26	25.4	0.00	0.00	0.00	0	0	0.000	F406	110	d	(S1050)
177	22	37	27.4	−24	8	2.7	17.87	18.82	19.42	31*	54	0.163	F534	001		3900
178	22	37	50.6	−34	14	33.4	16.42	17.67	18.22	35*	43	0.241	F406	010		
179	22	38	58.7	−36	33	51.5	16.04	19.29	20.29	8	39	0.119	F406	001		
180?	22	39	7.7	−29	27	43.4	16.16	16.74	17.54	21	21	0.327	F468	100		
181	22	39	29.2	−38	51	44.5	18.95	19.32	19.44	95	78	0.156	F345	001		
182	22	39	42.1	−25	15	16.3	15.75	16.44	18.06	12	9	0.261	F534	111		
183	22	40	6.8	−38	20	35.0	18.62	18.73	19.31	35	82	0.166	F345	001		
184	22	40	33.3	−23	43	11.2	16.15	16.86	19.00	5	8	0.181	F534	100		
185	22	41	14.0	−40	7	40.6	13.35	15.90	17.23	15	16	0.376	F345	100		S1055

EDCC	R.A.			Dec.			m_1	m_3	m_{10}	n_{clus}	n_{back}	θ_A	Field	runs	Deb.	Abell
	h	m	s	°	′	″										
186	22	42	28.1	−38	4	2.0	17.32	17.86	18.87	14	51	0.187	F345	100		S1056
187	22	43	23.9	−34	15	32.2	16.36	16.74	17.71	16	26	0.302	F406	100	d	
188	22	43	39.4	−36	21	46.7	15.20	16.29	17.50	29	23	0.329	F406	112		3912
189	22	44	0.9	−39	29	1.8	16.74	16.91	19.70	3	10	0.144	F346	001		
190	22	44	30.4	−41	9	45.4	16.45	17.01	18.41	17	24	0.226	F346	010	d	
191	22	44	41.1	−34	35	46.6	16.95	17.33	19.31	9	21	0.164	F406	001	d	
192?	22	45	18.6	−31	29	26.7	17.67	18.03	18.52	18	48	0.216	F468	010	d	
194	22	45	44.1	−28	51	51.6	16.78	17.58	19.11	23*	18	0.175	F468	011		3918
195	22	46	14.1	−28	21	50.2	15.87	16.92	18.71	10	10	0.200	F468	001		
196	22	46	15.2	−33	5	43.8	16.12	16.50	18.54	7	9	0.214	F406	001	d	S1064
197	22	46	16.1	−37	41	58.6	13.66	15.82	16.70	19	23	0.459	F406	100		S1065
198	22	46	29.7	−41	10	2.1	18.17	18.60	18.76	61	86	0.196	F346	010	d	3920
199	22	46	39.9	−38	55	49.0	16.44	18.98	19.69	12	62	0.147	F346	001		
200	22	46	42.4	−23	47	57.0	17.38	18.90	19.18	62	56	0.171	F534	011		2488
201	22	47	13.5	−31	26	25.6	17.15	17.71	18.10	46*	50	0.257	F468	111	d	
202	22	48	2.1	−33	3	2.8	16.52	16.61	17.81	22	20	0.289	F406	100	d	
203	22	48	13.2	−26	20	35.4	17.81	18.04	18.37	31*	44	0.230	F534	111		2493
204	22	48	32.8	−35	18	5.4	17.08	17.32	18.19	23	32	0.231	F406	100		
205	22	48	43.9	−34	35	42.0	14.98	17.14	18.50	15	22	0.217	F406	100		
206	22	48	59.1	−33	40	16.2	16.72	18.57	19.47	58	52	0.156	F406	001	d	3926
207	22	49	13.2	−32	28	0.5	15.68	17.39	18.95	13	19	0.186	F469	010		3929
208	22	49	18.6	−39	31	20.0	17.51	19.56	19.92	16	51	0.141	F346	001		
209	22	49	31.7	−33	49	22.9	17.00	18.98	19.47	34	64	0.156	F406	011	d	3928
210	22	49	56.5	−31	24	10.6	16.37	17.28	19.51	7	10	0.152	F469	100		3930
211	22	50	0.9	−26	17	17.0	17.58	18.96	19.17	81*	56	0.171	F534	011		2499
212	22	50	7.4	−23	15	45.8	17.86	19.19	19.78	30*	49	0.143	F534	001		
213	22	50	29.0	−28	37	38.0	17.31	17.76	19.87	8	13	0.137	F469	001		
214	22	50	35.9	−35	35	1.6	16.91	18.93	19.43	31	59	0.158	F406	001		
215	22	50	38.9	−29	48	46.9	16.39	16.83	18.49	8	12	0.219	F469	100		
216	22	50	40.5	−25	47	13.6	16.86	17.39	17.98*	79	34	0.270	F534	111		2500
217	22	50	42.2	−30	24	50.8	16.78	16.90	17.82	25*	21	0.275	F469	100		
218	22	50	42.7	−29	8	36.1	16.55	16.94	18.69	10	11	0.201	F469	011		
219	22	51	12.1	−37	17	9.6	15.71	16.97	19.40	2	12	0.166	F406	001		
220	22	51	39.3	−24	45	2.8	16.26	18.70	19.54	17	38	0.149	F534	001		
221	22	52	19.9	−38	55	31.1	17.95	18.41	19.95	19	35	0.133	F346	001		

EDCC	R.A.			Dec.			m_1	m_3	m_{10}	n_{clus}	n_{back}	θ_A	Field	runs	Deb.	Abell
	h	m	s	°	′	″										
222	22	52	43.4	−34	10	54.4	14.09	15.66	17.40	10	8	0.343	F406	100		(3934)
223	22	52	52.9	−42	29	40.8	15.22	16.12	18.27	7	7	0.239	F346	110		
224	22	53	22.5	−38	2	44.4	16.29	17.32	18.48	15	33	0.219	F346	100		
225	22	53	30.8	−28	41	33.3	16.97	17.54	18.78	20	20	0.186	F469	001		3943
226?	22	54	14.2	−27	8	41.1	15.19	16.24	17.67	25	9	0.307	F534	111		(3948)
227	22	55	4.7	−39	21	54.3	16.68	17.67	19.52	10	24	0.151	F346	001		3945
228	22	55	38.9	−31	5	19.5	0.00	0.00	0.00	0	0	0.000	F469	110	d	(S1075)
229	22	56	2.3	−30	58	13.7	14.36	16.62	17.37	39	24	0.348	F469	111	d	
230	22	56	32.8	−31	7	11.7	0.00	0.00	0.00	0	0	0.000	F469	001	d	
231	22	58	5.1	−24	26	44.0	16.50	17.67	18.65	21	28	0.204	F535	011		2518
232	22	58	14.0	−26	33	2.2	18.69	18.78	18.95	10	62	0.178	F535	010		
234	22	59	37.6	−29	28	18.4	18.03	18.46	19.25	26*	43	0.172	F469	001		3958
235	22	59	55.3	−33	38	6.3	17.00	17.75	19.05	18	28	0.178	F407	001	d	3959
236?	23	0	5.0	−28	45	55.9	17.14	17.69	19.15	20	20	0.179	F469	010		
237	23	0	5.6	−35	12	12.7	16.55	18.78	19.38	30	57	0.161	F407	001		3960
239	23	0	50.6	−33	54	25.3	16.90	17.52	19.36	10	18	0.162	F407	100	d	
240	23	0	50.6	−42	35	23.4	16.95	17.38	18.64	18	29	0.206	F346	010		S1084
241	23	1	16.8	−32	6	31.0	16.25	17.21	17.95	26	34	0.273	F469	111	d	
242	23	1	42.5	−24	23	10.1	17.82	19.20	19.49	73*	68	0.155	F535	001		2526
243	23	2	14.2	−32	53	35.4	16.55	16.60	18.10	20	15	0.257	F469	111	d	S1086
244	23	2	36.8	−25	37	21.1	18.06	20.05	20.22	34	33	0.122	F535	001		2527
245	23	2	49.9	−32	28	18.2	15.74	16.55	18.56	8	9	0.212	F469	100	d	
246	23	2	53.2	−33	5	22.7	19.31	0.00	0.00	0	0	0.000	F407	001	d	
247	23	2	56.1	−39	22	14.5	16.49	17.92	18.35	57	65	0.232	F346	011		3968
248	23	2	59.6	−30	55	33.7	14.60	15.62	17.47	11	6	0.333	F469	111		
249	23	3	0.8	−29	21	39.5	16.58	18.94	0.00	0	0	0.000	F469	100	d	
250	23	3	8.6	−34	43	53.0	16.12	18.89	19.74	34	42	0.136	F407	001		
251	23	3	11.0	−35	45	39.8	17.13	18.34	19.67	18	34	0.149	F407	001		
252	23	3	59.1	−29	12	58.9	16.34	17.55	18.31	45	32	0.236	F469	001	d	
253	23	5	1.3	−22	52	46.4	17.69	18.31	18.69	73*	67	0.201	F535	002		2534
254	23	5	26.3	−42	32	39.0	16.45	16.79	17.78	4	34	0.313	F346	100		
255	23	6	0.0	−33	9	58.9	16.41	16.78	19.30	3	6	0.163	F407	001		
256	23	7	36.2	−23	12	39.6	16.93	17.86	18.48	51*	49	0.219	F535	011	d	2541
257	23	7	59.8	−34	22	27.4	16.64	17.10	18.86	11	13	0.190	F407	011		
258	23	8	1.3	−22	55	14.8	16.41	17.98	18.73	41	45	0.198	F535	011	d	2546

EDCC	R.A.			Dec.			m_1	m_3	m_{10}	n_{clus}	n_{back}	θ_A	Field	runs	Deb.	Abell
	h	m	s	°	′	″										
259	23	8	14.0	−40	45	16.4	16.54	18.68	19.27	38	63	0.166	F346	010	d	(3977)
260	23	8	28.2	−28	59	43.2	11.84	16.39	17.88	20	11	0.281	F469	121	d	3978
261	23	9	9.4	−29	19	41.1	16.75	17.37	18.33	26	30	0.233	F469	111	d	S1096
262	23	9	17.9	−41	49	42.4	16.97	17.76	19.09	16	31	0.169	F346	010		
263	23	9	30.4	−41	2	39.1	16.58	17.21	18.67	20	27	0.203	F346	010	d	
264	23	9	38.0	−25	14	56.3	17.52	18.82	19.08	56	71	0.176	F535	011		2553
265	23	9	58.0	−39	25	31.7	16.63	18.69	19.28	39	63	0.166	F347	001		
266	23	10	19.5	−28	38	54.9	12.37	16.74	19.09	5*	5	0.176	F470	011		3980
267	23	10	24.1	−30	36	29.3	16.80	17.48	18.57	29*	25	0.211	F469	110		
268?	23	11	35.8	−26	46	7.1	17.73	19.01	19.65	44	54	0.147	F535	001		
269	23	12	32.5	−38	2	9.0	14.58	17.64	18.54	54	34	0.214	F347	011		3984
270	23	13	24.3	−23	39	58.8	16.67	17.48	18.27	21	37	0.239	F535	101		3985
271	23	13	28.7	−38	38	39.0	17.32	18.72	19.79	26	48	0.148	F347	001		
272	23	13	35.3	−39	12	1.8	15.99	16.26	18.80	2	5	0.193	F347	010	d	
273	23	14	23.0	−39	34	32.7	17.16	17.41	18.42	25	30	0.225	F347	101	d	
274	23	14	47.5	−37	28	32.7	18.53	18.74	19.74	19	38	0.134	F407	001		
275	23	14	52.5	−25	37	9.1	16.25	17.72	19.11	8	22	0.171	F535	001		
276	23	15	25.8	−35	54	41.1	18.46	18.75	19.50	50	46	0.155	F407	001		3989
277	23	15	34.9	−36	34	4.8	16.64	18.38	19.39	33	39	0.161	F407	001		S1109
278	23	15	40.9	−33	56	47.9	17.32	17.40	19.26	8	13	0.167	F407	001		
279	23	15	47.7	−27	47	16.6	16.23	17.53	18.34	37	30	0.232	F535	110		
281	23	16	23.3	−34	35	3.4	16.47	17.25	18.20	11	25	0.246	F407	100		
282	23	16	30.9	−37	43	57.9	18.71	19.62	20.03	24	44	0.134	F407	001		
283	23	16	37.6	−42	18	28.7	11.23	12.30	16.38	1*	0	0.548	F347	110	d	S1111
284	23	17	3.3	−22	44	31.0	17.98	18.38	19.45	31	50	0.167	F536	001		2576
285	23	18	12.7	−42	9	24.7	0.00	0.00	0.00	0	0	0.000	F347	110	d	(3998)
286	23	18	19.4	−29	8	48.3	16.47	17.49	20.06	6	8	0.128	F470	001		
287	23	18	39.1	−23	25	49.0	15.71	16.78	18.37	20	14	0.230	F536	112		2580
288	23	19	39.4	−40	57	9.3	16.48	16.64	18.73	8	10	0.209	F347	100		4000
289	23	20	16.0	−26	33	20.8	17.55	18.54	19.55	40	42	0.157	F536	001		2585
290	23	20	23.5	−31	41	47.7	15.99	18.33	19.00	29	45	0.176	F470	010		
291	23	21	30.0	−22	50	16.3	17.31	18.78	19.24	20	68	0.167	F536	010		(2587)
292	23	22	19.4	−30	35	45.6	16.45	17.07	18.32	14	17	0.235	F470	100	d	(S1119)
293	23	22	26.0	−23	41	59.2	14.79	17.59	18.24	27	45	0.242	F536	111		2596
294?	23	22	49.0	−29	47	51.8	15.76	17.92	18.16	27	53	0.249	F470	100		

EDCC	R.A.			Dec.			m_1	m_3	m_{10}	n_{clus}	n_{back}	θ_A	Field	runs	Deb.	Abell
	h	m	s	°	′	″										
295	23	23	30.3	−39	30	39.0	15.13	16.03	17.59	16	9	0.317	F347	110		
296	23	23	33.9	−30	49	59.8	15.98	16.75	0.00	0	0	0.000	F470	100	d	
297	23	23	46.2	−24	14	59.1	16.86	17.41	18.04	60*	38	0.263	F536	122		2599
298	23	24	5.9	−22	42	22.6	17.82	17.90	18.35	25	63	0.232	F536	111		2600
299	23	24	10.1	−32	0	0.0	17.51	18.79	19.63	43	45	0.143	F470	001		S1123
300?	23	25	32.8	−25	10	58.2	17.96	18.13	18.73	17	48	0.198	F536	010		
301	23	25	39.6	−29	25	39.6	16.80	17.07	18.89	16	10	0.188	F470	011		S1127
302	23	25	42.1	−36	41	48.4	16.17	18.07	18.54	21	60	0.227	F408	010		
303	23	26	20.5	−23	39	26.9	16.63	17.03	18.38	12	19	0.229	F536	111		2605
304	23	26	43.1	−30	25	58.3	17.24	18.26	19.48	9	33	0.158	F470	001		
305	23	26	53.8	−31	22	14.1	15.46	16.02	18.45	6	3	0.221	F470	100		S1129
306	23	27	9.6	−36	2	34.8	16.33	17.28	17.88	21	41	0.286	F408	100		
307	23	27	31.1	−39	33	24.8	14.88	16.16	17.72	11	10	0.301	F347	111		4008
308	23	27	42.9	−35	13	24.0	15.26	15.93	17.09	26	12	0.391	F408	111	d	
309	23	27	57.2	−26	24	5.1	16.57	17.34	19.56	5	9	0.153	F536	001		2609
310	23	27	59.1	−29	31	52.8	16.49	17.92	18.69	38	32	0.201	F470	011		4009
311	23	28	36.0	−36	47	41.4	14.66	0.00	0.00	0	0	0.000	F408	011	d	(4010)
312	23	29	13.0	−34	22	0.5	16.64	17.13	17.85	24	33	0.285	F408	110	d	(4012)
313	23	29	18.9	−30	21	8.1	16.33	16.70	18.36	16	10	0.231	F470	110		
314	23	29	19.2	−34	41	12.1	16.86	17.53	19.13	17	33	0.174	F408	001	d	4011
315	23	29	20.2	−35	34	4.3	17.54	17.96	19.83	9	30	0.138	F408	001	d	4013
316	23	29	49.8	−36	31	28.1	15.92	16.51	17.03	96*	33	0.400	F408	110	d	
317	23	31	19.4	−33	55	41.1	17.29	18.69	19.20	26	64	0.172	F408	010		
318	23	31	52.7	−32	35	44.7	15.37	17.28	18.10	25	32	0.257	F470	010	d	
319	23	33	8.4	−38	47	46.7	16.45	17.26	18.29	7	26	0.237	F347	100		
320	23	33	26.2	−31	52	26.5	14.64	16.51	17.83	20	13	0.287	F470	111		S1136
321	23	33	30.3	−32	47	38.9	15.35	16.31	18.30	8	7	0.237	F408	111	d	
322	23	33	36.9	−36	12	10.9	16.47	17.13	18.58	27	20	0.210	F408	012		
323	23	33	51.4	−30	39	58.7	16.42	16.86	18.66	10	10	0.204	F470	011		
324	23	34	3.4	−24	29	17.2	18.20	18.22	19.00	33	41	0.181	F536	011		2628
325	23	34	52.0	−31	17	6.3	16.38	17.59	18.09	0	44	0.265	F471	100		
326	23	35	9.7	−38	29	18.9	15.64	16.82	18.46	17	13	0.221	F347	110		4021
327	23	35	26.5	−40	57	38.8	15.21	16.36	18.14	13	8	0.253	F347	110		
328	23	35	35.1	−31	47	24.6	16.23	17.65	19.48	13	16	0.156	F471	100		
329	23	38	11.4	−30	34	11.6	16.49	17.17	18.46	10	17	0.221	F471	100	d	S1142

EDCC	R.A.			Dec.			m_1	m_3	m_{10}	n_{clus}	n_{back}	θ_A	Field	runs	Deb.	Abell
	h	m	s	°	′	″										
330	23	38	12.9	−37	50	24.9	17.15	18.28	20.00	13	59	0.131	F348	010	d	4026
331	23	38	15.2	−25	8	28.6	17.10	19.44	19.62	78	60	0.148	F536	001		2641
332	23	39	4.3	−29	28	46.3	15.06	17.08	17.73	50*	31	0.299	F471	110		
333	23	39	8.4	−37	47	31.5	16.53	18.32	19.78	18	58	0.141	F348	011	d	
334	23	39	31.2	−42	21	48.6	16.32	17.52	18.53	17	23	0.224	F348	100		
335	23	39	36.3	−30	28	45.3	16.23	18.16	18.83	17	44	0.192	F471	111	d	
336	23	40	40.0	−36	31	17.6	14.79	15.36	16.48	12	14	0.504	F408	100		
338	23	41	5.9	−38	32	21.0	15.57	17.31	19.10	8	15	0.175	F348	001		4029
339	23	41	27.7	−34	46	32.7	15.65	17.43	17.94	20	43	0.256	F408	100		
341	23	42	20.2	−24	3	39.5	15.35	15.66	17.32	9	6	0.355	F537	101		
342	23	42	29.3	−26	17	35.6	16.75	17.02	17.68	19	26	0.306	F537	100	d	2660
343	23	42	33.3	−42	1	15.2	17.73	17.81	18.69	13	26	0.207	F348	010		
344	23	42	45.5	−24	45	52.8	16.43	18.84	19.84	26	40	0.136	F537	001		4031
345	23	43	34.3	−23	27	36.6	15.62	16.91	18.05	13	17	0.262	F537	110		S1146
346	23	43	45.3	−28	35	50.7	0.00	0.00	0.00	0	0	0.000	F471	001	d	
347	23	44	31.9	−33	53	46.3	17.71	18.63	19.38	38	50	0.156	F408	001		4035
348	23	44	33.7	−28	31	40.6	13.77	15.20	15.90	43*	24	0.783	F471	121	d	4037
349	23	45	9.8	−38	46	58.1	14.71	15.21	16.97	11	6	0.394	F348	100		
350	23	45	40.7	−36	32	37.9	19.54	19.72	19.91	54	47	0.138	F408	001		4039
351	23	46	21.8	−31	34	17.7	18.78	18.96	19.78	33	41	0.141	F471	001		4043
352	23	46	34.3	−35	15	21.6	16.06	16.59	18.06	19	15	0.249	F408	100		
353	23	46	51.1	−27	14	37.4	16.07	18.33	19.10	50	42	0.176	F537	011		4044
354	23	47	8.8	−29	23	54.1	15.01	15.64	17.38	10	7	0.346	F471	100	d	S1155
355	23	47	18.1	−25	0	13.5	18.65	18.87	19.39	40	56	0.158	F537	001		2663
356	23	47	21.2	−35	59	3.5	15.40	16.52	18.86	5	8	0.190	F408	001		
357?	23	47	51.2	−37	27	13.3	19.21	19.43	19.75	43	58	0.143	F348	001		
358	23	48	11.4	−39	5	2.6	15.22	17.55	18.41	11	28	0.209	F348	100		
359	23	48	26.6	−38	43	20.8	18.30	19.26	19.56	66	63	0.149	F348	001		4048
360	23	48	26.6	−34	41	56.4	16.16	0.00	0.00	0*	0	0.000	F349	100	d	
361	23	49	2.4	−28	37	44.0	14.17	15.34	17.04	17*	12	0.399	F471	100	d	4049
362	23	49	58.5	−34	40	29.5	15.09	16.53	17.32	36*	31	0.355	F349	112	d	S1157
363	23	50	7.6	−34	25	12.5	14.89	0.00	0.00	0	0	0.000	F349	001	d	
365	23	51	56.5	−32	51	53.5	16.96	17.91	19.51	1	24	0.153	F349	100		
366	23	52	19.6	−27	56	40.0	15.60	16.89	17.78	32	26	0.293	F471	111		4053
367	23	52	40.8	−28	49	9.8	17.16	18.70	18.87	54	69	0.190	F471	001		4054

EDCC	R.A.			Dec.			m_1	m_3	m_{10}	n_{clus}	n_{back}	θ_A	Field	runs	Deb.	Abell
	h	m	s	°	′	″										
368	23	53	0.7	−33	56	6.4	16.46	17.66	18.59	26	45	0.225	F349	010		S1161
369	23	53	28.3	−37	33	48.6	18.59	18.70	19.61	24	56	0.153	F348	001		4056
370	23	53	49.7	−31	38	26.1	14.62	16.59	17.56	9	20	0.321	F471	100		
371	23	54	4.4	−36	55	14.2	16.62	18.81	19.68	49	55	0.145	F349	010		4058
372	23	54	18.2	−34	54	40.8	13.86	14.89	16.48	14	7	0.508	F349	111	d	4059
373	23	54	37.1	−32	53	39.6	10.09	16.61	17.62	21	22	0.313	F349	111		
374	23	54	57.4	−37	53	8.8	16.44	16.76	18.64	9	10	0.206	F348	011		S1164
375	23	55	50.9	−24	41	34.5	18.49	18.64	19.30	41	46	0.164	F537	001		2685
376	23	56	5.6	−34	36	9.8	15.74	0.00	0.00	0	0	0.000	F349	122	d	
377	23	56	26.4	−32	9	31.6	15.17	17.26	17.48	60	61	0.332	F471	100	d	
378	23	56	45.7	−32	10	44.0	17.57	0.00	0.00	0	0	0.000	F471	011	d	
380?	23	56	54.5	−31	37	42.1	16.44	16.92	18.34	21	17	0.232	F471	111	d	
381	23	57	14.2	−39	45	34.2	16.71	18.00	18.50	64	47	0.218	F348	110		4068
382	23	57	37.7	−25	29	52.7	16.81	17.19	18.51	20	15	0.217	F537	111		2690
383	23	57	47.9	−30	39	55.6	16.74	19.31	19.61	46*	57	0.145	F409	001		4070
384?	23	58	14.3	−28	54	56.6	17.60	18.53	19.23	26	43	0.164	F409	010		
385	23	58	25.9	−37	5	11.1	18.90	18.94	19.64	24	57	0.149	F349	001		S1170
386	23	58	28.3	−38	56	36.9	15.30	17.83	18.47	24	42	0.220	F348	100		S1172
387	23	58	35.2	−36	39	0.0	15.80	17.63	18.55	35	43	0.213	F349	111	d	4074
388	23	58	53.9	−27	54	6.8	14.22	15.38	16.79	11	8	0.442	F409	110	d	S1171
389	23	58	56.2	−39	26	25.4	16.55	17.69	18.42	13	36	0.222	F348	100		
390	23	59	26.2	−25	23	58.5	16.05	17.55	19.15	12	16	0.171	F537	001		
391	23	59	43.6	−32	3	49.1	16.77	18.52	19.92	18	32	0.134	F409	001		
392	0	0	13.9	−34	56	38.4	17.65	17.73	18.33	42	60	0.233	F349	111		2715
393	0	0	30.3	−30	12	46.7	15.98	16.36	18.06	10	11	0.261	F409	110		S 2
394	0	0	32.1	−36	12	58.9	14.57	16.71	17.22	29	44	0.370	F349	111	d	2717
395	0	0	33.8	−28	10	9.8	15.77	17.45	0.00	0	0	0.000	F409	100	d	(S 3)
396	0	0	37.9	−27	28	15.6	15.97	17.44	18.64	16	31	0.206	F472	111	d	2716
397	0	1	0.8	−42	12	53.2	16.61	18.38	19.03	31	43	0.175	F293	010		2718
398	0	1	25.3	−23	25	15.7	17.09	18.13	18.76	34	42	0.196	F472	101		2719
399?	0	1	56.3	−42	35	23.9	16.89	18.66	19.14	36	60	0.181	F293	010		
400	0	3	39.1	−34	58	49.1	16.30	17.64	18.28	98	51	0.238	F349	111	d	2721
401	0	3	41.5	−39	1	25.8	18.80	19.34	20.09	34	43	0.127	F293	001		
402	0	3	53.0	−26	36	36.5	17.08	17.41	18.07	25	39	0.279	F472	100		
403	0	4	50.4	−34	57	44.5	18.42	18.51	18.98	40	90	0.182	F349	001	d	

EDCC	R.A.			Dec.			m_1	m_3	m_{10}	n_{clus}	n_{back}	θ_A	Field	runs	Deb.	Abell
	h	m	s	°	′	″										
404	0	5	17.7	−25	25	33.0	16.68	17.67	18.34	9	36	0.232	F472	100		
405	0	6	33.3	−42	4	13.9	17.33	18.09	18.52	16	51	0.210	F293	010		
406	0	6	34.0	−25	55	41.6	18.35	18.52	19.28	23	44	0.166	F472	001		
407	0	6	38.9	−35	35	0.2	15.08	16.53	17.78	16	17	0.293	F349	110	d	S 12
408	0	7	27.8	−35	56	8.6	16.85	18.13	18.45	52	78	0.222	F349	111	d	2730
409	0	8	41.1	−30	14	41.7	15.43	16.57	17.80	8	16	0.287	F409	100		
410	0	8	46.0	−29	7	35.1	15.03	16.15	17.44	25	12	0.337	F409	111		2734
411	0	10	23.1	−42	28	55.6	16.40	17.06	18.44	16	21	0.232	F293	010		2736
412	0	10	39.3	−35	46	6.4	15.87	16.40	17.42	24	18	0.340	F349	111		
413	0	10	54.4	−24	30	43.9	14.19	17.86	18.45	11*	63	0.222	F473	111	d	
414	0	11	11.7	−38	1	36.9	16.54	17.57	18.92	18	22	0.186	F294	001	d	S 17
415?	0	11	18.3	−37	35	50.0	15.29	17.36	17.74	42	44	0.298	F293	111	d	
416	0	11	23.6	−36	32	37.2	16.54	17.31	18.25	4	36	0.241	F349	111		
417	0	11	58.0	−24	30	44.7	0.00	0.00	0.00	0	0	0.000	F473	001	d	
418	0	12	30.2	−24	9	58.6	15.12	15.72	16.59	31	11	0.481	F473	121	d	0014
419	0	12	49.7	−26	21	9.9	17.05	18.12	18.75	48	41	0.197	F473	011		15
420	0	13	29.5	−37	25	8.2	18.38	18.65	19.03	71	65	0.179	F350	011		2750
421	0	13	35.9	−35	13	53.1	16.38	18.04	18.70	55	55	0.200	F350	001	d	2749
422	0	13	44.9	−39	44	10.1	15.79	16.68	18.39	13	9	0.213	F294	100		
423	0	13	56.0	−31	32	46.7	17.21	18.52	19.99	21*	62	0.131	F410	001	d	2751
424	0	14	5.9	−34	7	59.0	17.64	17.92	18.16	24	75	0.254	F350	010		
425	0	14	46.6	−26	55	8.2	16.14	18.33	18.82	45	43	0.186	F473	010		
426	0	14	56.2	−31	42	27.7	17.76	17.88	18.69	44	36	0.201	F410	010	d	
427	0	14	57.7	−24	28	49.9	15.17	16.64	18.07	14	14	0.260	F473	111	d	
428	0	15	9.5	−27	37	24.2	17.63	18.27	19.23	24	33	0.168	F473	001		
429	0	15	23.2	−35	25	2.5	16.81	17.52	17.91	109	55	0.277	F350	111	d	2755
430	0	16	6.0	−28	12	51.6	17.11	17.99	18.53	23	40	0.215	F410	111		
431	0	16	17.4	−42	1	24.3	16.35	16.66	18.14	24	15	0.253	F294	020	d	2758
432	0	16	20.1	−30	56	8.7	16.54	17.03	18.19	16	19	0.249	F410	100		2759
433	0	16	55.3	−25	55	1.4	0.00	0.00	0.00	0	0	0.000	F473	001	d	
434	0	17	29.9	−42	14	16.7	16.28	17.77	18.40	31	58	0.227	F294	010	d	2763
435	0	17	49.1	−40	43	41.9	17.69	17.88	18.96	14	31	0.183	F294	010		
436	0	18	0.9	−34	12	28.4	16.98	17.87	18.86	30	40	0.189	F350	011		
437	0	18	1.2	−25	54	26.3	17.50	17.83	17.97	124	59	0.271	F473	111	d	22
438	0	20	23.5	−38	24	12.6	17.12	17.56	18.63	33	26	0.207	F294	011		2767

EDCC	R.A.			Dec.			m_1	m_3	m_{10}	n_{clus}	n_{back}	θ_A	Field	runs	Deb.	Abell
	h	m	s	°	′	″										
439	0	21	48.8	−34	16	19.5	18.32	18.81	18.95	53*	71	0.178	F350	010		
440	0	21	50.3	−40	23	53.4	15.14	16.27	17.85	10	10	0.285	F294	010		2771
441	0	22	37.8	−38	16	5.7	18.14	18.15	18.59	40	51	0.209	F294	011		2772
442	0	22	52.2	−33	22	0.0	14.52	15.81	17.18	16	10	0.375	F350	110	d	
443	0	23	4.7	−33	17	38.6	15.60	17.36	0.00	0	0	0.000	F350	001	d	(S 41)
444	0	25	12.6	−36	59	48.2	16.01	17.88	18.59	23	35	0.209	F350	010		S 51
445	0	25	40.8	−27	51	7.2	16.37	17.23	18.18	4	21	0.236	F473	100		
446	0	25	44.0	−35	43	4.5	16.51	17.27	18.72	23	15	0.198	F350	011		
447	0	26	7.8	−23	54	4.3	16.67	17.80	18.26	77	48	0.241	F473	111		42
448	0	26	34.0	−30	26	26.8	16.84	17.56	18.19	51	35	0.248	F410	122		2778
449	0	26	35.8	−35	16	59.3	17.41	17.71	18.72	33	26	0.198	F350	111		
450?	0	27	23.4	−29	45	1.3	15.02	17.34	17.78	45	40	0.293	F410	110		2780
451	0	28	4.2	−24	27	29.3	19.12	19.18	19.61	34	61	0.156	F473	001		47
452	0	28	50.0	−23	1	32.4	14.67	15.48	18.63	2	2	0.207	F473	101		
453	0	29	11.5	−23	55	1.5	17.43	17.70	19.32	14	20	0.163	F473	011		0051
454	0	31	32.6	−34	32	46.7	15.14	18.56	20.01	23	23	0.124	F350	001		
455	0	32	52.2	−32	39	1.7	19.04	19.21	19.88	31	43	0.141	F350	001		
456	0	33	25.2	−24	4	3.4	16.65	17.54	18.00	33	45	0.268	F474	100		
457	0	33	35.7	−26	22	7.2	15.41	16.31	17.95	11	10	0.273	F474	111		
458	0	33	44.6	−28	32	56.5	0.00	0.00	0.00	0	0	0.000	F411	001	d	
459	0	34	7.1	−28	37	8.4	14.15	16.20	18.54	4	10	0.214	F411	010	d	
460	0	34	47.1	−28	44	47.4	16.94	17.83	18.53	27	70	0.215	F411	111	d	2798
461	0	35	10.7	−31	5	28.7	16.13	16.44	18.60	7	6	0.208	F411	111		(2794)
462	0	35	14.5	−39	23	42.4	15.82	16.81	17.37	45	26	0.348	F294	211		2799
463	0	35	28.5	−25	27	55.6	16.12	16.76	17.48	21	30	0.332	F474	110	d	2800
464	0	35	58.5	−29	19	51.5	15.37	16.59	18.57	8	11	0.211	F411	111	d	2801
465	0	36	21.3	−27	29	10.5	14.75	16.71	19.18	6	7	0.171	F474	010		
466	0	36	24.1	−31	53	26.9	16.82	18.72	19.27	50	46	0.171	F411	001		2802
468	0	36	46.3	−24	16	44.1	15.96	17.29	17.87	18	36	0.283	F474	110		(0080)
469	0	37	13.0	−29	10	20.8	14.34	16.79	18.24	17	16	0.242	F411	111	d	2804
470	0	37	26.4	−26	26	25.1	16.88	17.95	18.79	38	34	0.194	F474	011		
471	0	37	43.3	−24	56	48.3	16.67	16.76	17.51	36	27	0.328	F474	111		80
472	0	37	57.2	−31	49	9.2	17.23	17.83	19.86	7	13	0.137	F411	001		
473	0	40	3.7	−28	50	23.2	16.10	17.11	17.92	67	31	0.277	F411	121		2811
474	0	40	44.7	−26	19	53.9	16.84	17.03	17.54	44	36	0.324	F474	121		0088

EDCC	R.A.			Dec.			m_1	m_3	m_{10}	n_{clus}	n_{back}	θ_A	Field	runs	Deb.	Abell
	h	m	s	°	′	″										
475	0	41	6.0	−22	34	15.0	14.44	16.61	18.10	12	12	0.255	F474	100		
476	0	41	35.6	−25	41	28.9	17.11	17.88	18.49	8	40	0.219	F474	100		
477	0	43	14.9	−23	27	16.3	18.08	18.27	19.02	43	41	0.190	F474	001		0097
479	0	45	54.9	−38	45	19.6	16.83	17.91	19.47	16	19	0.149	F295	001		2822
480	0	45	56.6	−42	17	20.8	16.00	16.33	18.11	10	7	0.256	F295	110	d	
481	0	46	29.9	−34	29	4.6	16.06	16.33	17.28	14	14	0.360	F351	110		S 83
482	0	46	50.3	−29	47	22.0	17.15	17.68	18.06	61	54	0.261	F411	111		S 84
483	0	47	38.0	−42	10	1.3	17.03	17.58	0.00	0	0	0.000	F295	100	d	
484	0	48	20.4	−42	27	43.6	15.53	16.51	0.00	0	0	0.000	F295	100	d	
485	0	48	56.3	−28	46	50.4	16.44	16.70	17.63	19	24	0.312	F411	111		2829
486	0	49	7.9	−42	30	7.6	17.51	17.93	0.00	0	0	0.000	F295	010	d	
487	0	49	37.0	−34	14	31.0	16.86	17.41	18.25	23	28	0.243	F351	100		S 88
488	0	50	1.9	−35	16	59.5	14.90	17.00	17.60*	7*	42	0.315	F351	011	d	
489?	0	51	1.7	−35	28	9.7	14.94	16.60	17.14	44	29	0.382	F351	100	d	
490	0	51	5.5	−33	24	21.4	15.17	18.60	19.25	27	44	0.168	F351	001		
492	0	52	0.3	−31	20	0.5	13.84	17.09	17.86	26	30	0.284	F411	111	d	
493	0	52	41.6	−39	9	32.3	18.25	19.27	19.52	45	77	0.159	F295	001		
494	0	53	24.9	−37	36	35.8	15.35	16.13	17.51	15	7	0.327	F351	110		S 102
495	0	53	28.6	−26	36	9.4	15.86	16.31	17.61	25	8	0.315	F474	223	d	118
496	0	53	32.6	−29	9	31.4	16.58	17.11	17.76	29	31	0.301	F411	100		S 100
497	0	53	41.1	−22	49	56.5	17.11	17.24	18.05	24	23	0.262	F474	100	d	
498	0	53	43.7	−31	48	39.7	16.36	17.37	18.47	21*	24	0.219	F411	001		
499	0	53	51.4	−38	10	2.1	16.62	17.72	18.46	42	33	0.221	F295	011		S 106
500	0	53	59.7	−30	20	2.0	17.92	18.13	18.41	70	56	0.226	F411	111	d	2844
501	0	54	3.3	−24	18	43.5	19.01	19.05	19.83	42*	43	0.140	F475	001		2842
502	0	54	7.4	−27	45	55.0	16.49	17.82	18.71	30	28	0.200	F411	011	d	2843
503	0	54	21.7	−39	2	20.1	16.62	18.76	19.49	65	53	0.155	F295	001		2845
504	0	54	27.5	−22	32	32.9	16.92	17.15	19.05	10	8	0.178	F475	001	d	
505	0	54	38.9	−29	57	0.1	15.92	18.00	0.00	0	0	0.000	F411	110	d	(2846)
506	0	54	39.0	−31	7	10.9	14.87	15.70	17.58	8	5	0.319	F411	111	d	S 109
507	0	54	55.5	−26	33	35.6	16.41	18.17	19.23	19	36	0.168	F475	001	d	122
508	0	55	1.9	−29	58	31.7	18.84	18.90	19.83	26	88	0.138	F411	001	d	
509	0	55	3.0	−29	42	49.4	16.50	17.65	0.00	0	0	0.000	F411	010	d	(S 108)
511	0	55	50.0	−31	17	20.5	17.31	0.00	0.00	0*	0	0.000	F412	001	d	
512	0	56	8.0	−34	34	0.4	13.82	17.17	18.28	32*	19	0.238	F351	111		2847

EDCC	R.A.			Dec.			m_1	m_3	m_{10}	n_{clus}	n_{back}	θ_A	Field	runs	Deb.	Abell
	h	m	s	°	′	″										
513	0	56	48.1	−29	19	41.8	17.38	19.45	19.87	78	40	0.137	F412	001		2850
514?	0	57	23.4	−30	39	5.8	16.10	17.69	18.65	21	29	0.204	F412	001		2851
515?	0	58	17.5	−34	58	2.6	17.13	17.35	18.08	37	29	0.259	F351	100		
516	0	58	26.0	−40	30	22.6	13.62	15.68	17.39	12	6	0.345	F295	110		S 113
517	1	0	7.7	−33	36	54.6	16.39	17.23	18.60	20	14	0.195	F352	010		
518	1	0	57.9	−22	51	54.1	19.41	19.51	20.00	45	39	0.134	F475	001		0135
519	1	2	7.7	−40	6	22.4	16.53	17.27	17.97	45	33	0.271	F295	110		2860
520	1	2	11.5	−24	15	37.4	17.32	18.34	18.81	61	46	0.192	F475	011		0140
521	1	2	49.7	−39	14	18.1	15.28	16.13	18.13	8	6	0.254	F295	100		
522	1	3	12.1	−24	55	28.7	19.31	19.33	19.62	55	46	0.149	F475	001		0141
523	1	4	5.6	−33	14	29.0	18.51	18.57	19.95	20	26	0.133	F352	001		
524	1	5	39.9	−37	1	20.6	15.53	18.07	18.64	75	46	0.206	F352	011		2871
525	1	5	40.6	−40	20	12.4	17.03	17.76	18.65	25	31	0.205	F296	010	d	S 127
526	1	6	30.7	−40	37	19.6	16.96	18.21	18.58	88	58	0.210	F296	010	d	2874
527	1	7	42.0	−25	5	2.9	17.19	17.64	18.22	37	28	0.244	F475	111		155
528	1	7	57.7	−30	0	31.6	17.65	17.90	18.81	14	28	0.193	F412	100		2878
529	1	8	5.6	−40	44	52.6	17.61	18.06	0.00	0	0	0.000	F296	100	d	
530	1	10	12.5	−36	37	9.8	16.12	17.77	19.00	27	24	0.181	F352	001		2883
531	1	10	15.7	−35	57	51.4	17.13	19.50	20.09	34	55	0.134	F352	001		
532	1	10	32.1	−33	54	52.1	15.31	16.19	17.43	18	8	0.323	F352	100		
533	1	11	28.1	−32	1	20.5	13.83	0.00	0.00	0*	0	0.000	F412	100	d	(S 141)
534	1	11	30.1	−39	12	20.6	17.07	17.32	18.75	16	19	0.193	F296	001		2885
535	1	11	43.9	−31	59	50.2	12.91	15.04	0.00	0*	0	0.000	F412	011	d	
536	1	12	39.5	−30	4	54.6	15.90	17.15	18.20	15	17	0.246	F412	100		
537	1	13	56.9	−28	37	58.0	18.44	18.84	19.41	39	46	0.151	F412	001		
538	1	14	40.1	−37	19	12.3	15.79	18.10	18.97	31	39	0.178	F352	001		2892
539	1	15	16.1	−38	16	27.4	16.68	17.60	18.41	29	36	0.226	F296	112		S 144
540	1	15	55.7	−28	40	46.8	17.10	18.18	19.08	23	34	0.177	F412	010		
541	1	15	55.9	−27	15	13.8	15.93	16.75	17.80	17	13	0.290	F475	111	d	2895
542	1	16	15.4	−26	53	22.9	17.10	17.99	18.46	36*	40	0.220	F475	111	d	
543	1	17	9.3	−36	7	38.6	15.73	16.95	18.69	10	10	0.201	F352	010		
544	1	18	32.1	−30	42	15.6	18.31	18.47	19.03	57	49	0.179	F412	012		S 151
545	1	18	45.5	−31	20	28.4	15.05	16.78	18.85	5	7	0.190	F412	011		
546	1	19	45.7	−39	53	30.0	16.80	17.55	18.39	32	32	0.215	F296	010		
547	1	20	20.4	−33	4	11.8	14.66	17.48	18.43	22*	24	0.221	F352	100		

EDCC	R.A.			Dec.			m_1	m_3	m_{10}	n_{clus}	n_{back}	θ_A	Field	runs	Deb.	Abell
	h	m	s	°	′	″										
548	1	21	12.2	−27	17	34.3	16.27	17.16	19.16	8	9	0.169	F476	001		2906
549	1	21	38.4	−41	6	59.9	16.54	16.78	18.32	12	14	0.236	F296	100		
550	1	22	11.8	−37	37	50.7	14.66	17.85	18.78	47*	34	0.195	F352	011	d	2909
551	1	22	42.2	−37	55	40.1	18.35	18.84	19.35	−8	66	0.162	F296	010	d	
552	1	22	58.3	−26	21	8.4	17.48	17.61	18.96	19	20	0.183	F476	010		
553	1	23	9.0	−39	41	37.1	16.71	17.47	18.05	55*	41	0.262	F296	110		S 156
554	1	23	9.3	−33	35	11.0	15.07	17.36	19.29	8	13	0.166	F352	001	d	
555	1	23	24.9	−29	48	28.2	16.92	17.56	18.33	35	28	0.233	F413	111		
556	1	23	39.6	−33	46	37.1	16.99	18.09	19.98	11	23	0.133	F353	001	d	2910
557	1	23	46.9	−38	14	34.8	14.33	14.35	17.53	5	1	0.326	F296	111	d	2911
558	1	23	56.2	−40	40	22.9	16.85	17.35	18.60	10	23	0.213	F296	010		
559	1	24	54.7	−35	50	45.1	13.83	15.97	18.58	4*	2	0.203	F353	010		
560	1	25	0.9	−23	1	25.6	15.30	16.18	17.59	12	9	0.317	F476	100		
561	1	25	59.4	−29	14	42.1	15.83	17.16	18.76	14*	13	0.196	F413	011		2915
562	1	26	12.6	−25	54	9.3	19.28	19.29	19.53	35	39	0.148	F476	001		0206
563	1	26	37.6	−34	13	24.4	17.88	18.23	19.54	15	30	0.152	F353	001		(2913)
564	1	27	28.9	−33	9	24.1	14.58	16.22	17.59	13	9	0.317	F353	111		S 160
565	1	29	3.4	−41	27	37.8	14.81	16.53	18.37	9	9	0.231	F296	100		
567	1	29	42.3	−24	59	43.0	16.82	17.33	19.19	8	12	0.170	F476	010		2921
568	1	29	42.7	−35	5	59.9	16.10	19.01	19.37	35	62	0.161	F353	011		(2920)
569	1	29	53.8	−26	15	35.2	15.11	16.98	19.33	2*	7	0.166	F476	001		0210
570	1	30	7.7	−42	24	38.7	15.06	17.33	17.91	39*	36	0.278	F296	120		S 163
571	1	30	15.4	−31	20	3.7	15.65	17.16	18.65	18	14	0.205	F413	011		2923
572	1	30	35.6	−29	48	9.7	19.08	19.26	19.55	38*	59	0.145	F413	001		2922
573	1	30	46.5	−27	11	48.2	16.51	16.92	18.40	27	12	0.227	F476	110		2924
574	1	31	39.5	−32	45	54.1	17.53	19.88	0.00	0	0	0.000	F353	010	d	(S 165)
575	1	31	52.4	−27	47	19.3	16.66	17.05	17.87	35	23	0.283	F476	111	d	2926
576	1	31	54.1	−26	21	39.8	17.04	18.00	18.89	47	31	0.188	F476	001	d	214
577	1	32	11.5	−31	52	49.8	16.14	17.38	18.58	23	19	0.210	F413	010		S 166
578	1	32	16.2	−33	3	18.6	15.05	15.44	17.81	3	2	0.289	F353	110	d	S 167
579	1	32	45.4	−27	43	52.2	0.00	0.00	0.00	0	0	0.000	F476	001	d	(2928)
580	1	32	53.3	−23	44	3.9	17.66	18.38	18.82	41	45	0.191	F476	001		0215
581	1	33	4.1	−25	54	41.8	14.77	16.53	17.11	16	19	0.387	F476	111	d	(0214)
582	1	33	17.2	−22	58	15.9	15.29	16.23	17.54	15	10	0.329	F476	100		
583	1	34	8.8	−36	44	25.8	14.34	17.08	18.91	10	9	0.176	F353	001		

EDCC	R.A.			Dec.			m_1	m_3	m_{10}	n_{clus}	n_{back}	θ_A	Field	runs	Deb.	Abell
	h	m	s	°	′	″										
584	1	34	49.8	−34	58	24.4	17.17	18.67	19.45	23	43	0.156	F353	001		2930
585	1	35	25.3	−26	56	16.0	16.53	16.90	19.10	5	7	0.176	F476	011		
586	1	39	26.9	−30	50	23.3	17.75	19.22	19.72	29	62	0.145	F413	001		
587	1	39	46.9	−42	24	57.6	15.44	17.17	17.49	47	34	0.330	F297	110		S 180
588	1	40	37.0	−40	24	35.8	15.15	16.23	18.46	6	4	0.237	F297	100		
589	1	41	10.0	−36	33	30.0	13.91	16.44	18.17	14	7	0.249	F353	100		S 182
590	1	41	34.6	−32	43	30.6	18.74	18.83	19.73	30	49	0.152	F413	001		
591	1	41	46.0	−35	32	50.0	16.81	17.01	17.59	28	25	0.317	F353	111		S 186
592	1	43	8.5	−29	29	23.9	17.79	19.07	20.06	67*	42	0.130	F414	001		
593	1	43	36.3	−29	6	28.6	16.90	17.37	19.26	11	10	0.167	F414	010		S 189
594	1	44	4.6	−32	7	19.5	17.39	18.55	19.35	41	43	0.161	F414	001		
595	1	45	3.8	−40	19	6.8	17.24	17.24	18.91	16	9	0.181	F297	010		
596	1	46	3.8	−32	10	16.6	18.10	18.43	19.14	74	44	0.174	F414	011		2943
597	1	49	3.5	−36	25	28.6	14.27	16.34	18.59	3	4	0.209	F354	011	d	
598	1	49	37.2	−26	3	24.7	16.59	18.43	18.83	53	51	0.192	F477	011		0264
599	1	50	2.9	−36	7	8.7	15.90	16.67	18.45	13*	7	0.222	F354	010	d	
600	1	51	1.7	−33	52	36.5	17.89	18.28	19.33	42	34	0.163	F354	001		S 203
601	1	51	26.0	−33	22	6.1	16.51	17.66	18.77	16	23	0.195	F354	011		
602	1	51	29.8	−26	46	45.0	16.19	18.35	19.21	42	34	0.161	F477	001		2950
603	1	52	2.8	−35	55	56.4	14.81	16.09	18.23	4*	4	0.243	F354	011	d	2952
604	1	54	50.3	−24	14	20.6	18.69	19.17	19.85	26	45	0.137	F477	001		2956
605	1	57	51.6	−31	27	59.8	16.84	18.52	19.73	20	34	0.151	F414	001		2961
606	1	58	27.2	−33	11	15.2	17.19	17.56	17.90	45*	42	0.278	F354	120		2962
607	1	58	49.6	−25	20	34.8	14.14	16.83	19.43	5	4	0.158	F477	001		2964
608	1	58	54.9	−40	39	57.9	16.29	16.76	18.31	22	9	0.236	F298	110		2965
609	1	58	57.8	−36	9	52.1	17.28	17.80	18.46	44	40	0.221	F354	111	d	2963
610	1	59	26.1	−37	15	45.5	18.66	19.01	19.47	22*	60	0.158	F354	001		S 216
611	1	59	43.1	−36	3	14.8	0.00	0.00	0.00	0	0	0.000	F354	001	d	(S 219)
612	1	59	45.4	−35	24	14.9	18.10	18.14	19.12	18	36	0.172	F354	001		
613	1	59	55.2	−25	50	32.6	18.66	19.10	19.73	81	48	0.143	F477	001	d	0297
614	2	0	29.7	−34	31	24.2	17.68	17.74	19.00	33	25	0.181	F354	011		
615	2	0	36.3	−28	31	1.0	17.80	18.23	18.96	21	39	0.183	F414	011		2967
616	2	0	59.0	−25	48	43.8	18.68	18.98	19.71	14	50	0.144	F477	001	d	
617	2	1	19.5	−27	14	52.3	16.50	17.42	17.99	45*	35	0.268	F478	110		2968
618	2	1	28.8	−41	20	44.7	16.86	17.81	18.31	68	44	0.236	F298	110		2969

EDCC	R.A.			Dec.			m_1	m_3	m_{10}	n_{clus}	n_{back}	θ_A	Field	runs	Deb.	Abell
	h	m	s	°	′	″										
619	2	2	23.7	−35	55	52.8	17.46	17.95	18.96	43	34	0.187	F354	001		2970
620	2	3	5.4	−32	33	28.2	14.74	17.60	20.13	4	10	0.128	F414	001		
621	2	3	42.9	−27	23	49.4	17.33	17.64	18.77	42	25	0.195	F478	011		2972
622	2	3	51.3	−36	22	22.1	15.37	16.66	17.87	30	14	0.283	F354	100		
623	2	4	12.1	−28	38	46.5	14.89	16.96	17.79	42	22	0.292	F414	110	d	
624?	2	4	43.5	−28	53	16.9	16.53	18.56	19.14	−6	90	0.174	F414	010	d	2975
625	2	5	3.7	−35	56	14.8	14.96	17.41	18.39	24	24	0.216	F354	100		
626	2	6	2.8	−32	10	44.5	17.15	18.06	18.48	44*	49	0.219	F414	110		2978
627	2	6	11.2	−28	42	56.7	16.58	17.16	19.65	4*	7	0.147	F415	001	d	
628	2	6	42.1	−26	36	23.6	17.22	18.01	19.26	15	29	0.167	F478	011		2979
629	2	7	12.0	−37	36	40.7	16.49	17.83	18.47	27	43	0.220	F354	011		(S 223)
630	2	8	6.4	−33	55	0.3	18.45	18.63	19.56	48	45	0.152	F354	001		S 227
631	2	8	15.7	−33	14	26.8	13.67	18.45	19.74	20	30	0.137	F354	001		2983
632	2	9	33.9	−40	31	42.1	15.86	17.99	18.73	51	42	0.198	F298	010	d	2984
633	2	10	40.2	−26	23	31.9	17.88	18.48	19.89	26	31	0.136	F478	001		0327
634	2	10	49.9	−25	32	17.6	16.67	19.33	19.59	84	72	0.156	F478	001		0325
635	2	11	4.5	−34	38	6.8	16.10	16.90	19.04	1	7	0.174	F355	001		S 233
636	2	11	29.4	−40	18	56.7	15.91	17.44	17.96	31	37	0.272	F298	100	d	
637	2	12	10.5	−30	46	2.3	16.95	17.25	18.82	14	12	0.187	F415	010		2990
638	2	12	24.3	−26	1	24.2	18.07	18.48	19.55	24	37	0.152	F478	001		2991
639	2	12	48.9	−26	52	58.6	16.10	17.41	19.33	8	12	0.161	F478	001		2992
640	2	12	54.2	−36	47	44.6	18.45	18.56	19.86	32*	33	0.138	F355	001		2993
641	2	13	51.9	−27	46	47.1	17.12	17.40	18.51	21*	23	0.217	F415	011		
642	2	14	8.3	−29	15	17.0	16.87	18.39	19.27	18	45	0.172	F415	001		
643?	2	17	42.1	−28	36	59.4	17.23	18.36	19.03	33	42	0.169	F415	001		S 245
644	2	18	40.9	−26	50	54.5	16.83	17.38	19.31	10	12	0.166	F478	010		
645	2	23	11.7	−29	43	24.8	15.86	16.04	17.14	25	9	0.383	F415	111	d	S 258
646	2	23	27.6	−35	1	26.5	18.23	18.83	19.61	23	43	0.148	F355	010		
647	2	23	50.1	−42	10	29.4	15.49	17.08	18.80	10*	9	0.191	F299	010		3017
648	2	24	8.5	−23	37	36.4	14.61	16.16	18.05	7	6	0.262	F479	100	d	S 263
649	2	24	54.3	−26	43	7.3	15.89	17.44	18.32	43	25	0.235	F479	110		
650	2	24	54.4	−23	8	46.5	15.51	16.28	17.62	13*	9	0.313	F479	100	d	
651	2	24	56.3	−29	4	55.0	17.72	19.25	19.61	79	51	0.140	F415	001		(S 266)
652	2	25	11.6	−29	49	30.8	16.65	16.72	19.13	4*	7	0.174	F415	010	d	
653	2	27	16.9	−33	41	37.0	15.23	16.47	18.09	17	8	0.258	F355	111	d	

EDCC	R.A.			Dec.			m_1	m_3	m_{10}	n_{clus}	n_{back}	θ_A	Field	runs	Deb.	Abell
	h	m	s	°	′	″										
654	2	27	52.7	−36	59	52.0	18.75	18.99	19.77	41	46	0.141	F355	001		3026
655	2	28	3.9	−24	49	29.9	17.26	17.40	17.85	36	35	0.283	F479	100		
656	2	28	13.0	−39	8	10.0	17.32	18.98	19.76	34	56	0.141	F299	001	d	S 271
657	2	28	19.7	−32	4	59.7	16.68	17.44	18.38	19	23	0.229	F415	100	d	
658	2	28	34.9	−33	17	55.5	16.26	16.82	17.91	29	15	0.278	F355	111	d	3027
659	2	29	0.5	−38	55	27.1	17.54	18.31	19.28	30	36	0.166	F299	001	d	3029
660	2	29	12.5	−23	5	47.4	15.30	15.85	18.07	6	3	0.260	F479	101		
661?	2	29	59.1	−32	13	26.3	16.65	17.77	18.40	38	32	0.227	F416	100	d	
662	2	30	1.2	−36	55	10.5	14.02	18.81	19.81	39	38	0.140	F355	001		
663	2	30	56.5	−23	22	54.1	17.53	18.63	19.20	33	42	0.170	F479	001		
664	2	31	16.7	−33	4	32.6	15.58	17.46	18.39	18	22	0.224	F355	100		
665	2	32	18.3	−33	52	39.2	14.98	16.32	17.86	11	9	0.284	F355	101		S 278
666	2	32	24.0	−37	42	55.3	15.95	17.18	18.38	14	15	0.229	F299	100		S 279
667	2	32	57.4	−24	44	4.5	17.77	19.75	20.17	31	26	0.124	F479	001		
668	2	33	45.7	−41	58	17.2	17.23	18.03	18.52	36	45	0.214	F299	010		3033
669	2	34	3.7	−22	40	31.2	17.44	18.60	19.11	25	38	0.169	F479	010		
670	2	34	47.0	−24	49	6.8	17.32	17.99	19.05	25	28	0.178	F479	010		
671	2	34	51.9	−25	35	29.7	16.14	17.27	18.20	10	25	0.246	F479	100		
672	2	35	10.9	−26	35	42.5	15.63	16.55	20.07	0	5	0.128	F479	001	d	
673	2	35	23.1	−26	44	13.5	16.45	17.11	19.77	3	11	0.141	F479	101	d	368
675	2	36	6.5	−32	34	12.0	19.26	19.38	19.90	21	47	0.138	F416	001		
676	2	36	7.7	−32	55	2.1	17.10	17.71	19.13	14	20	0.174	F356	010		
677	2	36	25.3	−33	48	47.1	15.13	16.25	18.49	6	5	0.221	F356	010		
678	2	36	48.0	−27	12	5.5	16.65	18.45	19.33	30	37	0.155	F479	001		
679	2	38	58.9	−25	59	37.4	17.14	18.54	19.02	24*	48	0.174	F479	001		
680	2	39	13.0	−28	51	33.9	17.37	18.45	18.89	55	45	0.177	F416	001		3041
681	2	41	29.6	−35	22	55.9	16.50	16.75	18.50	16	11	0.218	F356	110		
682	2	41	31.3	−28	5	8.0	16.77	18.43	19.10	40*	47	0.176	F416	011		3044
683	2	42	26.6	−26	31	10.7	15.78	17.08	17.99	43	25	0.269	F479	112		0380
684	2	42	29.6	−25	7	40.3	17.22	17.75	20.81	2	13	0.101	F479	100	d	
685	2	42	38.5	−28	58	16.2	17.19	17.91	19.21	12	19	0.162	F416	001		(3043)
686	2	43	44.3	−24	55	22.1	14.35	16.67	18.23	11	9	0.243	F479	100	d	
688	2	45	2.6	−42	32	34.1	14.89	16.68	18.21	19	16	0.245	F299	110	d	S 296
689	2	45	14.2	−34	11	48.3	19.05	19.09	19.48	32	54	0.156	F356	001	d	3053
690	2	45	19.2	−27	46	27.8	17.03	17.39	18.32	24	26	0.235	F480	011	d	3052

EDCC	R.A.			Dec.			m_1	m_3	m_{10}	n_{clus}	n_{back}	θ_A	Field	runs	Deb.	Abell
	h	m	s	°	′	″										
691	2	45	21.8	−34	55	44.4	16.96	18.52	19.01	34	56	0.189	F356	001		
692	2	45	34.2	−22	51	49.6	14.65	17.22	18.37	15	17	0.229	F480	110		
693	2	45	51.1	−42	3	37.9	16.04	16.69	16.90	24	35	0.422	F299	110	d	S 297
694	2	46	14.7	−27	53	52.0	17.01	18.43	0.00	0*	0	0.000	F416	100	d	(3054)
695	2	46	58.4	−31	23	15.8	14.67	14.75	16.04	16	3	0.706	F416	110		S 301
696	2	48	30.6	−40	33	10.2	17.37	17.85	18.38	27	48	0.229	F299	100		
697	2	48	54.0	−35	13	38.0	14.70	15.51	16.79	12	9	0.442	F356	100	d	
698	2	49	7.4	−35	45	11.6	17.42	19.58	20.18	11	23	0.124	F356	001	d	
699	2	49	17.9	−25	9	1.2	16.25	16.58	18.09	28	11	0.257	F480	111		0389
700	2	49	39.5	−25	47	15.5	15.15	17.39	18.33	42	24	0.233	F480	110	d	
701	2	50	6.1	−36	54	24.9	16.92	18.65	18.98	51*	56	0.182	F356	001		3063
702	2	50	8.9	−25	32	42.3	19.13	19.43	19.87	38	66	0.137	F480	001	d	3062
703	2	50	32.4	−41	23	27.3	17.24	18.08	0.00	0	0	0.000	F300	010	d	
704?	2	50	38.5	−33	5	28.7	16.69	17.27	18.23	23	19	0.232	F356	100		
705	2	50	41.7	−42	28	23.8	17.21	18.00	18.28	28	71	0.238	F300	110		
706	2	51	18.1	−26	46	54.6	16.50	18.01	18.96	22	33	0.186	F480	001		
707	2	51	30.2	−33	41	40.2	15.54	16.81	17.83	27*	20	0.287	F356	111		3064
708	2	51	36.4	−41	24	21.8	16.75	17.52	18.76	22	25	0.196	F300	110	d	S 306
709	2	53	7.9	−35	38	35.0	16.04	16.30	17.68	19	15	0.306	F356	111	d	
710	2	53	42.0	−22	51	29.8	16.59	17.75	18.60	37	25	0.208	F480	011		3069
711	2	54	0.6	−40	30	6.9	18.50	18.88	19.33	40	76	0.171	F300	010		
712	2	54	19.6	−24	55	51.1	16.33	17.65	18.40	34	30	0.226	F480	011		3070
713	2	55	28.3	−35	49	27.5	15.11	16.77	17.81	13	23	0.289	F356	101	d	
714	2	56	20.9	−26	46	42.2	18.34	18.45	19.24	27	43	0.172	F480	001		
715?	2	56	26.2	−41	8	4.0	16.72	18.23	18.91	41	54	0.187	F300	010		
716?	2	58	51.3	−36	46	46.4	16.13	16.91	17.66	20	35	0.308	F356	100	d	
717	2	58	55.5	−37	14	56.6	14.88	16.30	17.18	21	26	0.376	F356	110	d	S 316
718	2	58	56.3	−38	22	35.4	16.44	16.67	18.65	9	12	0.205	F300	011		
719	2	58	56.8	−33	24	56.2	16.01	17.22	17.81	12	24	0.270	F356	100		
720	2	59	49.3	−25	31	35.5	15.36	16.59	18.43	8	7	0.229	F480	010		
721	3	1	2.3	−34	27	50.6	17.09	18.19	18.81	21	34	0.182	F357	010		
722	3	1	3.9	−37	7	47.2	16.61	16.76	17.07	58	46	0.394	F357	112	d	(3084)
723	3	2	52.4	−37	47	6.4	16.69	17.08	18.37	9	25	0.230	F300	100		
724	3	3	20.5	−39	17	33.2	13.31	16.45	17.71	20	19	0.302	F300	100	d	
725	3	3	55.0	−38	16	11.0	16.23	17.18	18.12	16	34	0.256	F300	100		

EDCC	R.A.			Dec.			m_1	m_3	m_{10}	n_{clus}	n_{back}	θ_A	Field	runs	Deb.	Abell
	h	m	s	°	′	″										
726	3	4	43.0	−39	1	47.3	17.43	18.41	18.64	36	81	0.206	F300	111	d	
727	3	6	2.6	−23	8	22.6	13.94	16.34	18.98*	5	3	0.182	F481	100		
728	3	6	13.3	−36	53	32.2	16.03	16.18	17.30	28	21	0.358	F357	111		3089
729	3	6	15.5	−23	53	8.7	15.78	16.68	17.45	34	18	0.336	F481	111		419
731?	3	7	5.5	−37	45	6.1	17.66	18.14	18.99	23	40	0.177	F300	010		
732	3	7	23.7	−24	43	39.9	15.45	17.50	20.91	3	4	0.097	F481	100		
733	3	8	9.2	−38	29	39.0	17.86	18.06	19.84	9	24	0.140	F300	001		
734	3	8	31.3	−26	17	16.1	17.32	17.35	18.49	19	18	0.219	F481	001		
735	3	9	23.7	−27	5	34.3	17.39	17.70	18.43	2	60	0.224	F481	001	d	3094
736	3	9	42.8	−27	11	11.7	15.79	16.03	17.39	20	8	0.345	F481	110	d	
737	3	10	9.4	−22	33	54.3	17.17	17.62	18.15	25*	28	0.243	F481	100		
739	3	10	41.6	−36	44	10.9	16.66	17.42	19.01	17	20	0.181	F357	010		
742	3	11	52.2	−38	30	34.7	15.21	16.51	17.89	26*	19	0.280	F300	111		3098
743	3	11	54.5	−37	54	39.0	17.82	17.86	20.98	6	8	0.095	F300	100		
744	3	12	14.1	−42	10	39.7	16.68	16.98	18.99	7	11	0.178	F300	010		
745?	3	12	16.8	−32	28	20.6	17.05	17.77	18.62	49	22	0.207	F417	011	d	3101
746?	3	12	44.0	−42	37	55.9	16.44	18.67	19.27	27	58	0.164	F300	010		3105
747	3	13	2.4	−41	21	9.0	16.10	17.25	18.51	14	23	0.217	F300	010	d	
748	3	13	9.5	−29	24	14.2	15.74	16.58	17.25	39	14	0.365	F417	111		S 333
749	3	14	24.6	−37	13	39.9	16.91	18.25	19.96	9	20	0.127	F357	100		
751?	3	14	59.5	−42	12	3.5	17.19	17.40	18.30	29	29	0.229	F300	100		
752	3	15	7.0	−38	24	31.9	16.09	17.56	18.95	18	22	0.180	F301	001		
754	3	16	19.3	−39	18	37.1	17.23	19.11	19.70	69	50	0.143	F301	001		3114
755	3	18	23.9	−24	52	30.0	17.02	18.24	18.99	45*	29	0.181	F481	011		
756	3	18	42.3	−27	21	47.7	16.41	16.48	17.81	21	9	0.289	F481	110		S 340
757	3	19	46.0	−34	28	45.4	17.53	17.99	18.44	48	32	0.223	F357	121		3118
758	3	20	22.1	−41	30	46.8	15.74	16.99	17.55	51	33	0.321	F301	110		3122
759	3	21	23.1	−40	29	4.8	16.34	17.90	20.64	5	10	0.107	F301	100		
761	3	26	4.2	−26	38	15.0	16.73	17.54	18.83	21	7	0.181	F481	001		
762	3	32	15.2	−39	8	9.1	15.78	16.34	17.25	39	14	0.364	F301	110	d	3135
763	3	32	55.2	−39	38	0.9	16.35	17.52	18.36	23	31	0.230	F301	011	d	S 364
764	3	33	22.4	−42	36	8.3	15.45	17.24	18.63	9	15	0.210	F301	010		S 365
765	3	34	50.6	−39	53	15.6	16.01	16.71	17.95	30	15	0.273	F301	110	d	3142
766	3	36	2.3	−38	11	32.8	17.17	18.16	19.18	30	21	0.163	F301	001		3145
767	3	37	7.6	−40	44	57.6	16.67	17.27	18.62	18	18	0.204	F301	010		
768	3	37	55.9	−40	9	58.6	15.74	18.42	18.83	36	61	0.197	F301	010		
769	3	38	34.0	−38	3	8.0	15.56	16.91	18.75	13	7	0.194	F301	010		S 376

Table A2: The Edinburgh/Durham Cluster Catalogue

EDCC	R.A.			Dec.			m_1	m_3	m_{10}	n_{clus}	n_{back}	θ_A	Field	runs	Deb.	Object
	h	m	s	°	′	″										
30	21	41	48.8	−30	8	16.9	15.42	16.70	18.21	16	14	0.245	F466	112	d	Gal
41	21	46	10.5	−35	30	51.0	18.04	18.39	18.87	50	42	0.189	F404	100	d	d.s
56	21	52	36.1	−33	14	48.9	16.95	18.19	19.30	17	41	0.164	F404	011		d.s.
63	21	54	3.2	−34	48	23.3	12.89	17.52	18.89	18	25	0.188	F404	010	d	Gal
71	21	56	46.1	−25	58	35.2	15.93	17.26	18.80	19	19	0.193	F532	011		d.s.
74	21	57	57.7	−35	42	4.1	16.03	18.00	19.02	14	39	0.180	F404	111		Star
109	22	9	49.9	−38	25	29.5	14.57	18.39	19.79	10	37	0.140	F344	001	d	Gal
138	22	20	31.3	−42	30	40.4	16.84	18.11	18.72	53	47	0.192	F345	010		Gal
157	22	30	7.8	−24	48	26.6	16.99	18.92	19.24	33	68	0.168	F533	001		Star
167	22	34	14.7	−25	30	13.0	17.42	17.93	19.19	11	28	0.175	F534	001		Gal
193	22	45	38.0	−22	39	24.0	12.31	16.52	17.96	20	9	0.271	F534	100		Gal
233	22	59	32.1	−39	49	40.4	15.71	16.00	17.17	23	16	0.378	F346	110		Gal
238	23	0	5.8	−37	22	15.5	14.16	18.05	18.34	47	70	0.232	F406	100		Gal
280	23	15	59.9	−32	45	7.0	16.73	17.89	18.92	21	31	0.186	F470	011		Star
337	23	40	50.6	−33	21	32.3	17.16	17.37	19.40	7	13	0.158	F408	010		d.s.
340	23	42	3.4	−25	55	45.8	17.44	18.42	19.67	1	37	0.145	F537	100	d	d.s.
364	23	51	37.2	−42	36	30.9	15.85	16.52	18.46	11	7	0.221	F348	100		Star
379	23	56	51.0	−32	29	40.3	0.00	0.00	0.00	0	0	0.000	F471	011	d	Star
467	0	36	27.5	−25	50	54.2	16.31	16.80	18.18	12	17	0.249	F474	110	d	Star
478	0	44	39.9	−38	16	51.1	18.64	18.83	20.05	17	33	0.128	F295	001		Star
491	0	51	32.2	−27	25	13.7	15.18	17.38	19.31	9	13	0.170	F474	001		Gal
510	0	55	18.3	−27	44	59.9	13.15	18.84	19.45	54	57	0.157	F411	001	d	Gal
566	1	29	39.7	−33	22	32.1	16.78	17.43	18.96	12	17	0.185	F353	001		Gal
674	2	35	32.1	−36	22	40.1	16.63	18.61	20.34	11	22	0.117	F355	001		d.s.
687	2	43	45.3	−34	7	13.0	17.07	17.29	17.86	39	35	0.284	F356	110	d	d.s.
730	3	6	52.6	−32	42	34.2	16.52	16.88	17.89	21	16	0.280	F417	101		s.t.
738	3	10	32.3	−32	34	4.2	17.09	17.73	18.59	34	23	0.209	F417	001	d	Star
740	3	10	44.4	−31	40	17.6	16.36	17.39	19.09	11	10	0.176	F417	011		Gal
741	3	11	29.9	−25	23	31.0	15.61	17.63	18.15	9	34	0.252	F481	111		Gal
750	3	14	32.0	−35	45	12.0	15.89	16.53	17.00	60	32	0.405	F357	211		d.s.
753	3	15	21.8	−41	16	36.9	11.10	17.72	18.35	50	41	0.231	F301	110	d	Gal
760	3	22	48.1	−36	32	25.6	11.77	16.50	18.05	14	8	0.262	F357	110		Gal

Table A.3: Objects misidentified as clusters: Gal; galaxy: Star; star(s): s.t.; satelite trail: d.s.; diffraction spike(s).

Appendix B

Templates

This Appendix contains details of the templates observed and used in the estimation of the EM survey galaxy redshifts. Plots are shown of all the 17 templates observed at ESO and the 3 others obtained from elsewhere (*i.e.* Parker *et al* 1987). The spectra have been continuum subtracted and smoothed to zero at the edges in preparation for cross–correlation, but have not been logarithmically binned. Table B.1 contains the results of cross–correlating all the ESO templates with each other, while the scatter plots present the differences, Δv, between the published redshifts of the templates and the estimated redshifts using the other 16 templates. The number of the template from Table B.1 is plotted on the x–axis and Δv is plotted on the y–axis.

By inspecting Table B.1 and the scatter plots, rogue templates were easily spotted. Clearly, there was a problem with templates N5566, N5806, IC5175 and HD8779. Quentin Parker (Private Communication) also observed a $\sim 200\mathrm{km\,s^{-1}}$ shift between the observed and published redshift of IC5175. HD8779 was a low signal–to–noise spectrum. No plausible explanation could be found for the differences seen in templates N5566 and N5806. Several of the other templates showed a systematic shift of $\Delta v \sim 100\mathrm{km\,s^{-1}}$ (*i.e.* N5134, N6909, 223311), while templates N5746 and N5796 were observed twice. This left templates N5740, N5746, N5921, N6070, N6118, N7793 and N6958 whose typical scatter was $\Delta v \sim 50\mathrm{km\,s^{-1}}$, which was comparable to the wavelength calibration error. These 7 templates, along with HD35410 and HD171391 obtained from Quentin Parker and A4038 observed with AUTOFIB created the final library of cross–correlation templates. The templates were not shifted to account for the small scatter seen because the direction of the shift was unknown, *i.e.* no one template had a secure enough redshift to zero–point the shifts. Finally, the templates were not shifted back to zero redshift as it was felt to be advantageous to have the template features shifted nearer to the observed galaxy features.

	N5134	N5740	N5746	N5746	N5796	N5796	N5806	N5921	N6070	N6118	N5566	IC5175	N6909	N7793	N6958	223311	HD8779	z
N5134	1695	1794	1840	1826	1791	1791	1550	1765	1773	1786	1407	1598	1888	1794	1733	1707	1714	1696 ± 90
N5740	1471	1573	1597	1566	1557	1541	1400	1557	1565	1624	1270	1333	1703	1555	1582	1482	1455	1575 ± 20
N5746	1654	1775	1801	1789	1750	1748	1538	1752	1751	1824	1434	1540	1897	1751	1759	1702	1696	1801 ± 33
N5746	1669	1788	1810	1801	1761	1756	1558	1767	1773	1840	1458	1563	1918	1749	1774	1720	1692	1801 ± 33
N5796	2850	2958	2997	2985	2945	2944	2775	2982	2982	3003	2598	2760	3020	2998	3024	2928	2940	2946 ± 90
N5796	2850	2973	2998	2990	2946	2945	2774	2974	2970	3000	2624	2755	3039	2956	3003	2915	2894	2946 ± 90
N5806	1438	1468	1558	1540	1460	1462	1297	1477	1505	1505	1084	1285	1570	1531	1509	1398	1198	1301 ± 65
N5921	1405	1494	1524	1513	1449	1454	1300	1478	1494	1543	1168	1285	1621	1543	1476	1413	1351	1480 ± 10
N6070	1920	2010	2050	2028	1959	1971	1795	1985	2003	1983	1673	1770	2097	2013	2015	1950	1832	2005 ± 7
N6118	1430	1526	1549	1528	1510	1511	1369	1510	1594	1577	1309	1330	1652	1489	1633	1464	1388	1578 ± 15
N5566	1800	1819	1881	1859	1844	1823	1730	1825	1845	1783	1517	1651	1972	1839	1889	1724	1609	1518 ± 68
IC5175	10828	10976	10996	10972	10916	10932	10742	10927	10968	10981	10590	10727	11055	10883	10904	10902	10810	10731 ± 30
N6909	2652	2715	2762	2740	2785	2765	2583	2706	2768	2775	2392	2539	2659	2783	2720	2611	2498	2680 ± 90
N7793	130	247	275	278	168	207	-2	163	219	316	-90	80	298	230	149	46	-75	231 ± 7
N6958	2703	2725	2782	2768	2661	2682	2524	2736	2717	2670	2354	2569	2879	2816	2739	2631	2363	2742 ± 150
223311	-54	49	52	36	-26	-13	-143	23	2	65	-247	-212	201	134	65	-43	-100	-43 ± 1
HD8779	-37	109	86	89	-14	34	85	109	155	171	-100	-98	340	280	85	39	-17	$-17 \pm ?$
	1	2	3	4	5	6	7	8	9	10	11	12	13	14	15	16	17	

Table B.1: The array of ESO EM observed templates. Each template has been cross-correlated against all the other templates in the table. The published redshifts in the last column were taken from Da Costa *et al.* 1984 or the Astronomical Almanac. The typical internal error on the cross-correlated redshifts was $\Delta v \sim 40 \mathrm{km\,s^{-1}}$, but this obviously depended upon the error on the published velocity. All the velocities shown are in $\mathrm{km\,s^{-1}}$ and the numbers in the last row of the table are referenced to in the scatter plots of Δv against template.

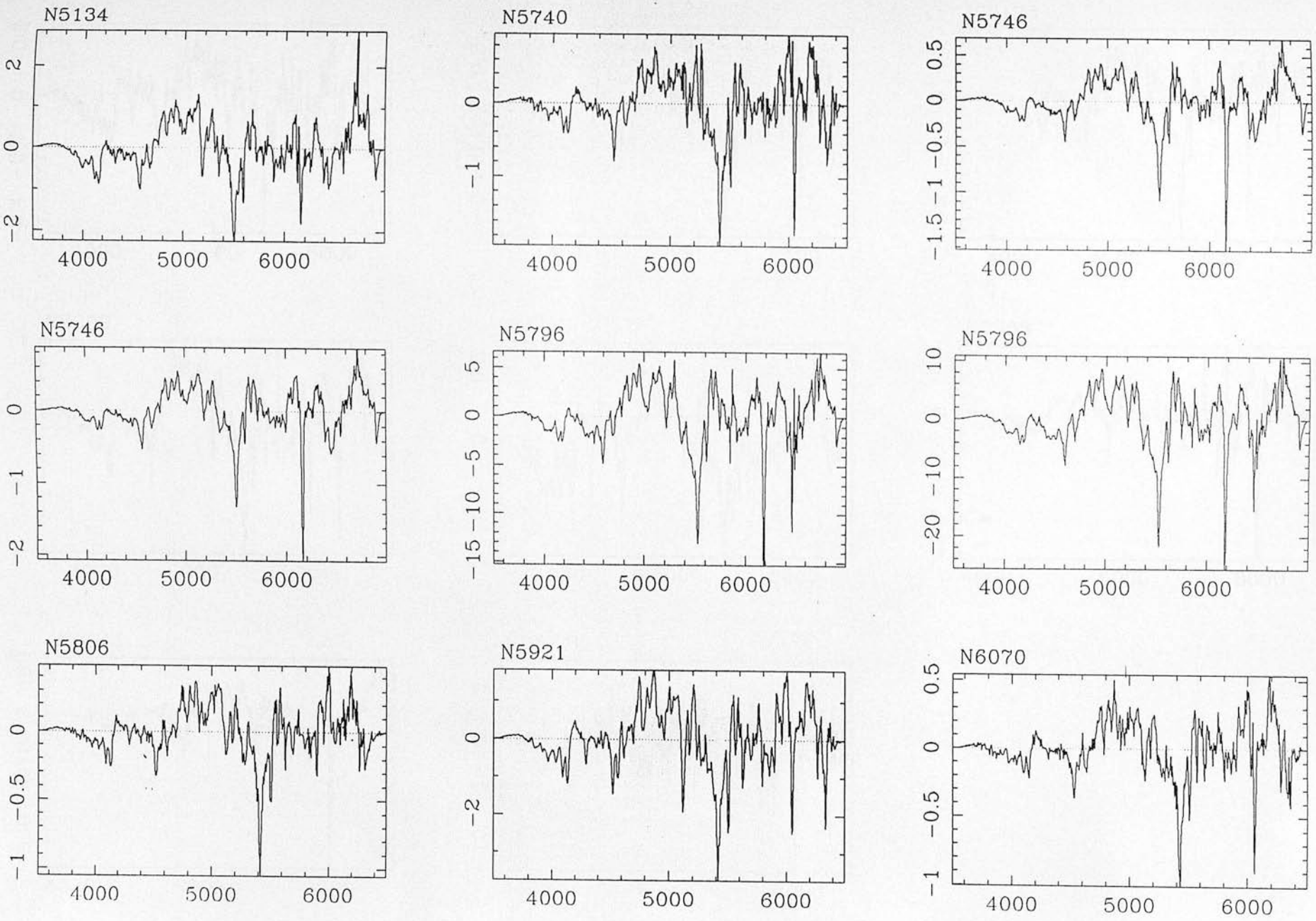
N5134
N5740
N5746
N5746
N5796
N5796
N5806
N5921
N6070
4000
5000
6000

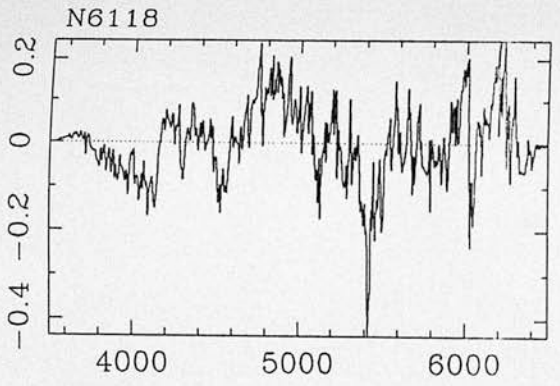
N6118
0.2
0
−0.2
−0.4
4000
5000
6000

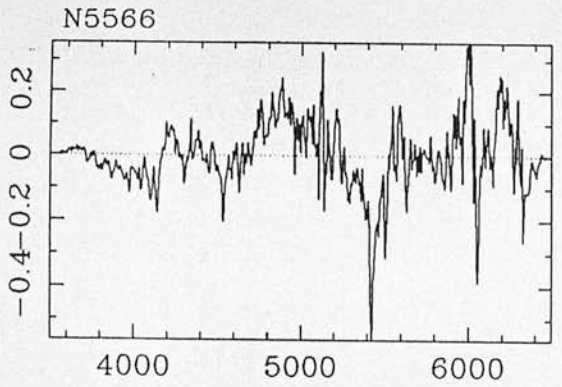
N5566
0.2
0
−0.2
−0.4
4000
5000
6000

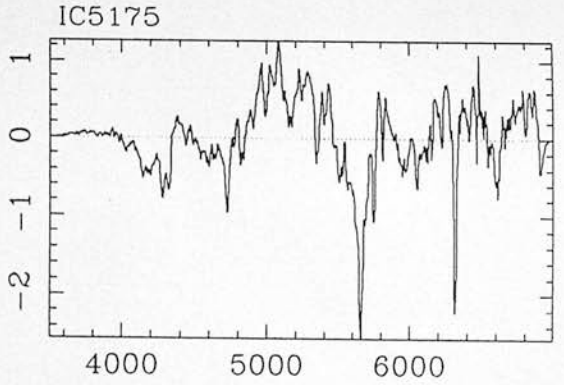
IC5175
1
0
−1
−2
4000
5000
6000

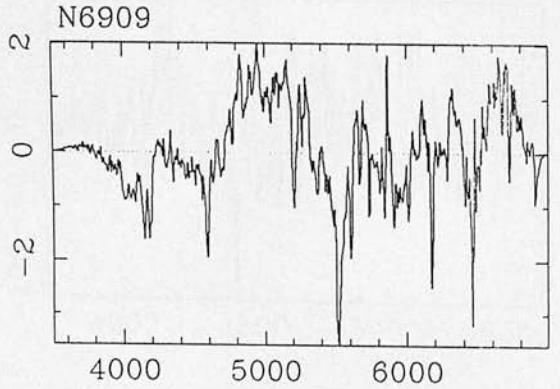
N6909
2
0
−2
4000
5000
6000

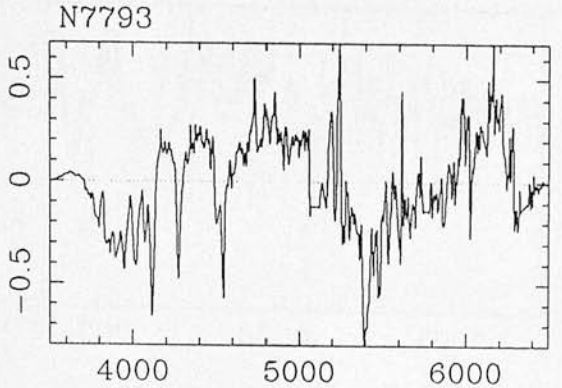
N7793
0.5
0
−0.5
4000
5000
6000

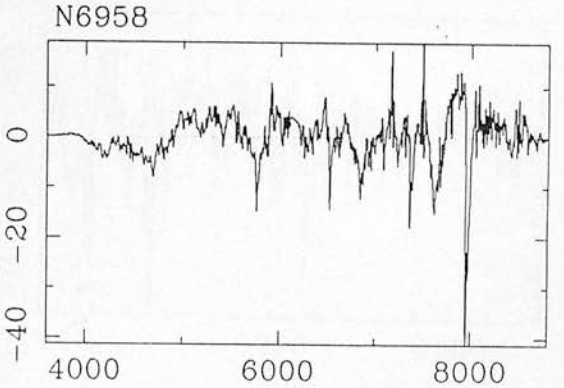
N6958
0
−20
−40
4000
6000
8000

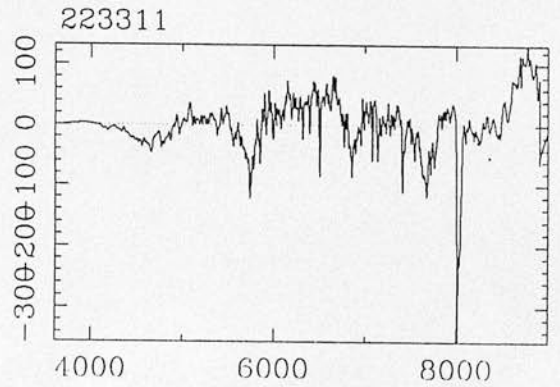
223311
100
0
−100
−200
−300
4000
6000
8000

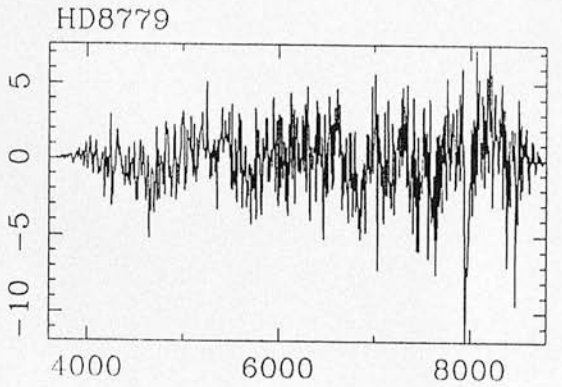
HD8779
5
0
−5
−10
4000
6000
8000

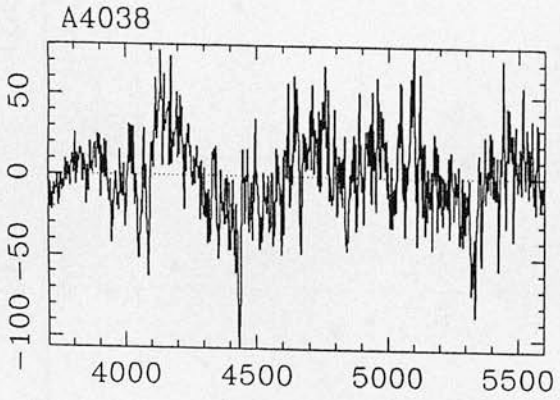
A4038
50
0
−50
−100
4000
4500
5000
5500

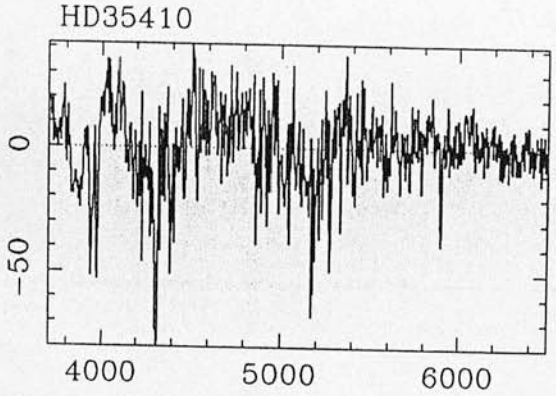
HD35410
0
−50
4000
5000
6000

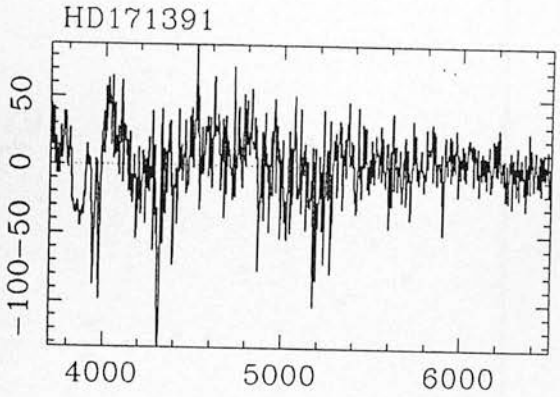
HD171391
50
0
−50
−100
4000
5000
6000

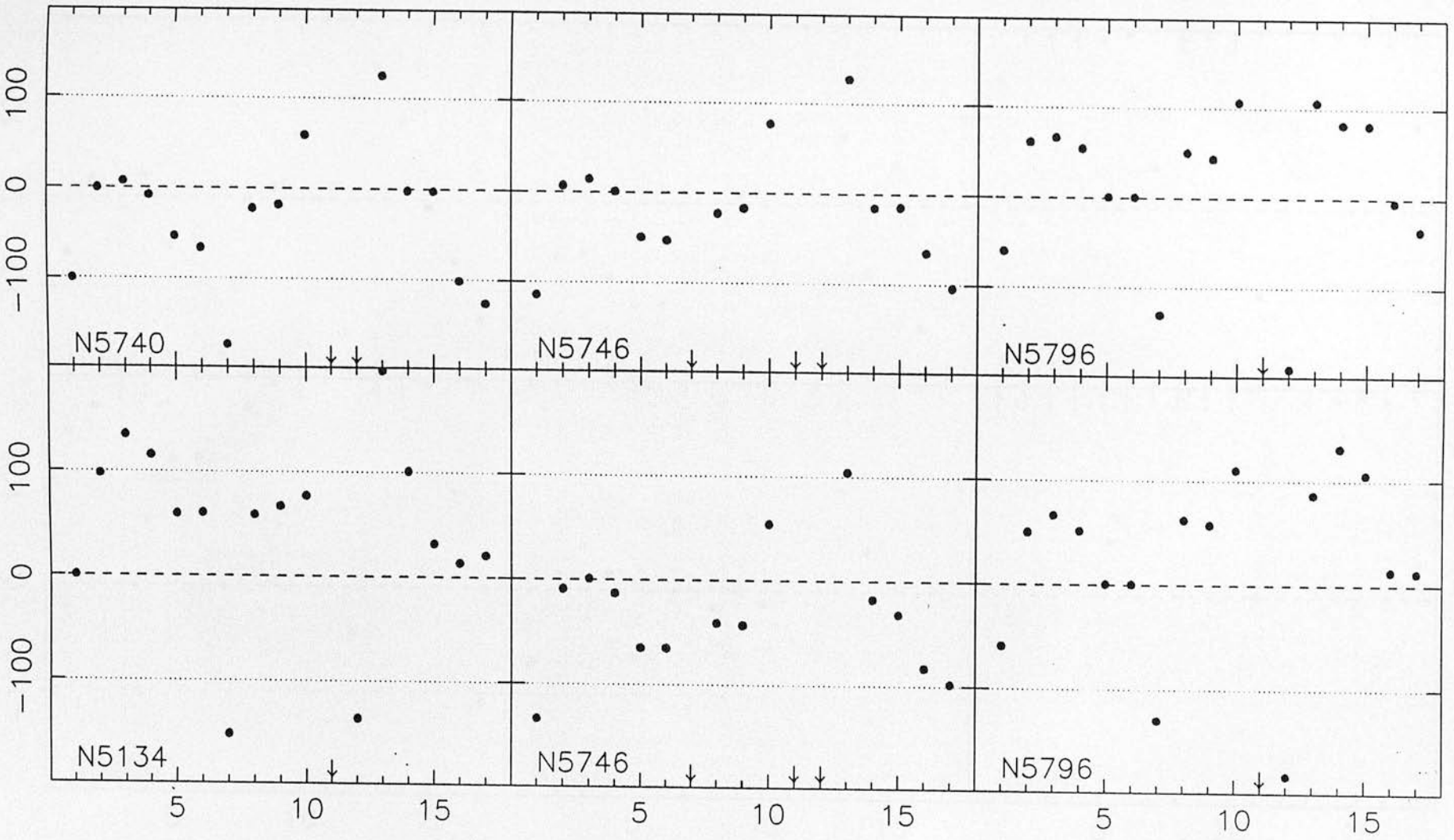
100
0
−100
N5740
N5746
N5796
100
0
−100
N5134
N5746
N5796
5
10
15
5
10
15
5
10
15

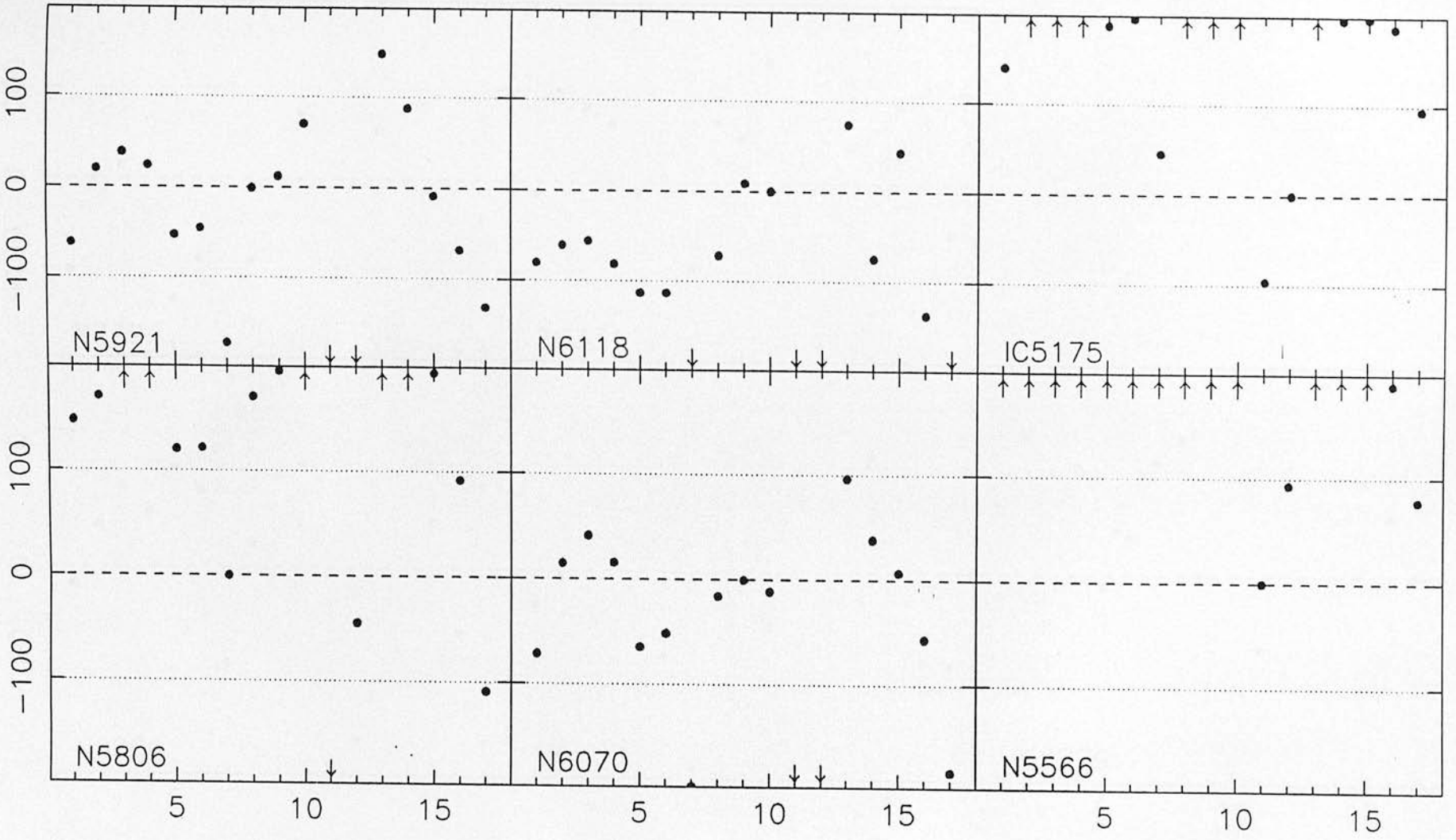
N5921
N6118
IC5175
N5806
N6070
N5566
100
0
−100
5
10
15

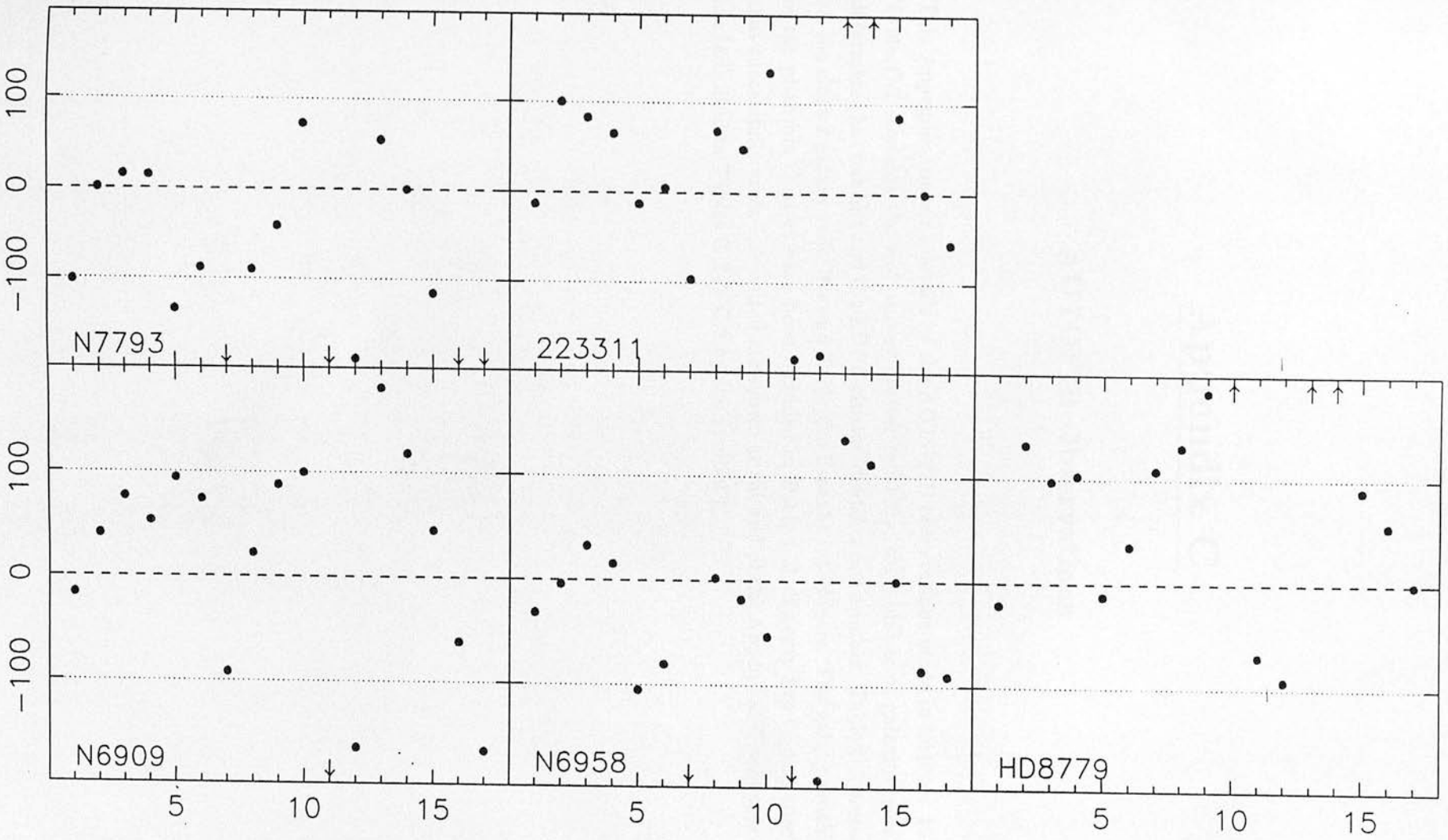
N7793
223311
N6909
N6958
HD8779
100
0
−100
5
10
15

Appendix C

AUTOFIB Observations

This Appendix contains details of the AUTOFIB observations made in October 1989. Table C.1 contains the EM survey cluster redshifts, the number of galaxies used to determine that redshift and the EDCC cluster identification number. Table C.2 presents all the cluster galaxy redshifts and Table C.3 lists the interlopers. The galaxy redshifts of the phantom clusters have been included in Table C.2. Twenty five typical spectra that successfully cross–correlated are shown at the end of the Appendix. These spectra are indicated in Tables C.2 & C.3 by the symbol †.

EDCC	RA (hrs)	Dec. (°)	z	Δz	Field	No. z
80	21.9972	-23.0500	0.07068	0.00283	532	20
127	22.2608	-39.1375	Proj.	Proj.	344	14
145	22.4156	-30.8283	0.05697	0.00350	467	16
166	22.5692	-38.2817	0.05933	0.00160	345	5
269	23.2075	-38.0267	Proj.	Proj.	347	12
348	23.7517	-28.4167	0.02920	0.00182	471	32
418	0.2125	-24.1083	0.06575	0.00236	473	9
419	0.2128	-26.3617	0.12887	0.00407	473	4
437	0.2997	-25.8683	0.06337	0.00318	473	5
460	0.5828	-28.7667	0.11308	0.00141	410	12
482	0.7792	-29.7961	0.10844	0.00213	411	14
519	1.0428	-40.0733	0.10730	0.00300	295	15
553	1.3889	-39.7033	0.08791	0.00217	296	15
658	2.4758	-33.3033	0.07636	0.00352	355	22
712	2.9067	-24.9167	0.11093	0.00185	480	14
728	3.1039	-36.8833	0.06748	0.00050	357	8

Table C.1: Table of the AUTOFIB EM clusters observed. The first column contains the EDCC cluster number, while the last two columns contains the Field number of the cluster and number of galaxies used to determine the cluster redshift. The interlopers have been placed in Table C.3 and the individual galaxy redshifts are presented in Table C.2. The low number of galaxy redshifts for certain clusters is mainly due to the bad weather experienced on various nights during the run. Projection effects are indicated and their galaxy redshifts have been included in Table C.2

RA (hrs)	Dec. (°)	z	Δz	Mag.	ID	RA (hrs)	Dec. (°)	z	Δz	Mag.	ID
22.4169	-30.8178	0.05600	0.00017	-5.20	145	22.4181	-30.8153	0.06316	0.00017	-5.00	145
22.4344	-30.8850	0.05963	0.00018	-4.40	145	22.4250	-30.8928	0.05662	0.00022	-4.90	145
22.4289	-30.9389	0.05710	0.00019	-4.40	145	22.4211	-30.8794	0.05131	0.00045	-5.20	145
22.4186	-30.9542	0.06073	0.00025	-5.30	145	22.4178	-30.8875	0.05940	0.00019	-5.10	145
22.4217	-31.0208	0.05557	0.00015	-4.60	145	22.4186	-30.9542	0.05895	0.00020	-5.70	145†
22.4156	-30.9908	0.04926	0.00020	-5.50	145	22.4153	-30.9544	0.05597	0.00028	-5.60	145
22.3953	-30.8453	0.05374	0.00022	-4.70	145	22.4014	-30.7775	0.05623	0.00015	-4.10	145
22.4094	-30.7508	0.05863	0.00036	-6.00	145	22.4125	-30.7292	0.05928	0.00025	-5.90	145
0.0000	0.0000	0.06416	0.00027	-0.00	418	0.0000	0.0000	0.06568	0.00042	-0.00	418
0.0000	0.0000	0.06792	0.00018	-0.00	418	0.0000	0.0000	0.06337	0.00019	-0.00	418
0.0000	0.0000	0.06795	0.00166	-0.00	418	0.0000	0.0000	0.06620	0.00019	-0.00	418
0.0000	0.0000	0.06942	0.00021	-0.00	418	0.0000	0.0000	0.06478	0.00018	-0.00	418
0.0000	0.0000	0.06228	0.00024	-0.00	418	0.0000	0.0000	0.06594	0.00015	-0.00	728
0.0000	0.0000	0.06715	0.00013	-0.00	728	0.0000	0.0000	0.06599	0.00030	-0.00	728
0.0000	0.0000	0.06662	0.00012	-0.00	728	0.0000	0.0000	0.06644	0.00013	-0.00	728
0.0000	0.0000	0.06847	0.00033	-0.00	728	0.0000	0.0000	0.06814	0.00019	-0.00	728
0.0000	0.0000	0.06896	0.00022	-0.00	728	22.2611	-39.1458	0.13993	0.00019	-3.20	127
22.2647	-39.2150	0.13820	0.00030	-3.70	127†	22.2603	-39.1425	0.13687	0.00041	-2.80	127
22.2597	-39.0031	0.13702	0.00047	-3.00	127	22.2817	-39.0997	0.03998	0.00014	-4.30	127
22.2653	-39.3303	0.04413	0.00032	-3.70	127	22.2553	-39.1431	0.04749	0.00028	-4.40	127
22.2397	-39.1356	0.03963	0.00000	-3.60	127	22.2550	-39.2192	0.05453	0.00024	-4.10	127
22.2469	-39.2306	0.07171	0.00000	-3.00	127	22.2353	-39.0100	0.06370	0.00000	-3.40	127
22.2778	-39.2692	0.08480	0.00020	-4.80	127	22.2722	-39.2903	0.09427	0.00044	-4.70	127
22.2692	-39.2642	0.14959	0.00029	-3.30	127	0.3042	-25.7575	0.06650	0.00060	-4.30	437
0.3031	-25.8244	0.06424	0.00017	-4.40	437	0.2931	-26.0067	0.06481	0.00018	-4.40	437
0.2989	-25.8589	0.05810	0.00000	-4.30	437	0.2892	-25.8953	0.06319	0.00012	-4.40	437
2.9069	-24.9100	0.11052	0.00010	-6.10	712	2.9142	-24.7886	0.11140	0.00018	-2.80	712
2.9100	-24.8797	0.10687	0.00011	-4.90	712	2.9119	-24.9364	0.11140	0.00017	-4.10	712
2.9097	-24.9194	0.11193	0.00020	-3.10	712	2.9089	-24.9353	0.11141	0.00011	-3.10	712
2.9058	-24.9731	0.10973	0.00014	-4.10	712	2.9058	-24.9086	0.11116	0.00049	-4.20	712
2.9036	-24.9794	0.11300	0.00027	-4.50	712	2.9050	-24.8958	0.11473	0.00012	-3.20	712
2.9033	-24.9250	0.10847	0.00032	-2.60	712	2.9056	-24.8825	0.11052	0.00014	-3.00	712
2.8964	-24.8653	0.11098	0.00017	-3.40	712	2.9022	-24.7861	0.11095	0.00012	-3.80	712
22.0122	-22.9608	0.07388	0.00019	-4.70	80	22.0019	-22.9739	0.07355	0.00025	-4.70	80
22.0039	-22.9561	0.06825	0.00097	-3.70	80	22.0056	-23.0428	0.07324	0.00030	-4.50	80†
22.0067	-23.1206	0.06827	0.00021	-4.70	80	22.0181	-23.1903	0.06876	0.00052	-5.00	80
22.0083	-23.1397	0.07019	0.00023	-3.90	80	22.0022	-23.2258	0.07104	0.00030	-4.90	80
21.9936	-23.1942	0.07021	0.00018	-5.80	80	21.9933	-23.1572	0.07193	0.00019	-5.10	80
21.9953	-23.1319	0.06984	0.00000	-5.20	80	21.9936	-23.1281	0.07177	0.00000	-5.10	80
21.9972	-23.0267	0.07282	0.00015	-4.20	80	21.9944	-23.0394	0.06457	0.00012	-5.70	80
21.9800	-22.9864	0.07155	0.00034	-5.40	80	21.9786	-22.9475	0.06397	0.00041	-4.60	80
21.9861	-22.8961	0.07024	0.00033	-5.20	80	21.9886	-22.8500	0.07276	0.00027	-3.80	80
21.9936	-22.7756	0.07269	0.00041	-5.30	80	21.9964	-22.9667	0.07411	0.00084	-4.10	80

RA (hrs)	Dec. (°)	z	Δz	Mag.	ID	RA (hrs)	Dec. (°)	z	Δz	Mag.	ID
0.7817	-29.7486	0.10784	0.00022	-3.40	482	0.7808	-29.7794	0.10792	0.00016	-3.10	482†
0.7831	-29.7956	0.10867	0.00014	-3.50	482	0.7844	-29.7636	0.11364	0.00011	-3.60	482
0.7842	-29.8011	0.11049	0.00015	-2.80	482†	0.7881	-29.8433	0.10857	0.00014	-3.60	482
0.7922	-29.8739	0.10771	0.00010	-3.50	482	0.7842	-29.8414	0.10690	0.00018	-3.30	482
0.7906	-29.8639	0.11062	0.00028	-4.40	482	0.7817	-29.8233	0.10913	0.00013	-2.90	482†
0.7772	-29.8719	0.10833	0.00016	-3.30	482	0.7747	-29.9561	0.10714	0.00009	-3.50	482
0.7753	-29.7356	0.10640	0.00015	-2.60	482	0.7778	-29.7144	0.10486	0.00021	-3.00	482
2.4992	-33.1947	0.08033	0.00010	-3.70	658	2.4789	-33.3006	0.07340	0.00020	-4.10	658
2.5003	-33.3181	0.07224	0.00021	-4.10	658	2.4967	-33.3233	0.07094	0.00011	-4.70	658
2.4944	-33.3303	0.07857	0.00009	-4.00	658	2.4850	-33.4103	0.07561	0.00007	-3.70	658†
2.4778	-33.4036	0.07506	0.00010	-3.60	658	2.4767	-33.4406	0.07810	0.00017	-4.30	658
2.4675	-33.5422	0.07990	0.00025	-4.00	658	2.4681	-33.4400	0.08077	0.00022	-4.80	658
2.4783	-33.3250	0.07859	0.00011	-5.70	658†	2.4675	-33.4136	0.07778	0.00006	-4.30	658
2.4636	-33.3992	0.07948	0.00015	-5.90	658	2.4764	-33.2786	0.07778	0.00009	-3.90	658
2.4692	-33.2083	0.07750	0.00009	-4.70	658	2.4789	-33.2639	0.07447	0.00006	-3.90	658
2.4747	-33.1908	0.07670	0.00006	-3.70	658	2.4717	-33.0742	0.07218	0.00010	-3.60	658
2.4744	-33.0642	0.07265	0.00013	-4.60	658	2.4783	-33.1872	0.08371	0.00015	-3.30	658
2.4803	-33.0989	0.07313	0.00024	-4.90	658	2.4867	-33.1914	0.07108	0.00008	-4.10	658
22.5875	-38.0925	0.05931	0.00028	-3.50	166	22.5908	-38.4897	0.06065	0.00008	-4.70	166†
22.5575	-38.3864	0.06118	0.00033	-3.70	166	22.5644	-38.2792	0.05801	0.00009	-3.10	166
22.5628	-38.0211	0.05751	0.00012	-3.80	166	0.2086	-26.5372	0.13183	0.00027	-4.20	419
0.2106	-26.6314	0.13061	0.00027	-4.60	419	0.2086	-26.5369	0.13018	0.00013	-4.20	419
0.2128	-26.3192	0.12286	0.00012	-3.80	419	1.3908	-39.7375	0.08806	0.00008	-5.60	553†
1.4047	-39.7522	0.08691	0.00009	-3.80	553	1.3944	-39.7467	0.08690	0.00012	-4.40	553
1.4100	-39.8353	0.08825	0.00025	-3.70	553	1.3964	-39.7936	0.08954	0.00009	-4.80	553†
1.3967	-39.8158	0.08826	0.00013	-4.10	553	1.3917	-39.7556	0.08795	0.00010	-4.70	553
1.3892	-39.7450	0.08865	0.00009	-3.80	553	1.3889	-39.8733	0.08862	0.00016	-4.90	553
1.3875	-39.7967	0.08976	0.00043	-3.20	553	1.3853	-39.7556	0.08070	0.00008	-4.60	553†
1.3878	-39.7586	0.08907	0.00022	-4.40	553	1.3853	-39.7772	0.08946	0.00059	-3.50	553
1.3872	-39.7372	0.08888	0.00027	-4.20	553	1.3861	-39.7392	0.08764	0.00006	-4.40	553
1.0550	-39.9011	0.10879	0.00013	-4.60	519	1.0467	-39.9967	0.11369	0.00021	-4.60	519
1.0428	-40.0289	0.10654	0.00017	-4.60	519	1.0597	-40.1186	0.10546	0.00021	-4.30	519
1.0444	-40.0753	0.10599	0.00018	-4.50	519	1.0506	-40.1819	0.10575	0.00024	-4.70	519
1.0381	-40.2306	0.10658	0.00017	-4.10	519	1.0414	-40.1108	0.11018	0.00019	-3.70	519
1.0353	-40.1800	0.10820	0.00017	-4.30	519†	1.0317	-40.1881	0.09972	0.00023	-4.00	519
1.0344	-40.1156	0.10928	0.00037	-4.90	519	1.0292	-40.1078	0.10752	0.00013	-4.10	519
1.0294	-40.0511	0.10666	0.00051	-5.80	519	1.0322	-40.0458	0.10894	0.00020	-4.50	519
1.0306	-40.0225	0.10627	0.00014	-4.00	519	23.1967	-38.0286	0.09390	0.00016	-3.90	269
23.1925	-38.0000	0.09347	0.00010	-4.50	269	23.2036	-38.0331	0.09198	0.00020	-3.60	269†
23.2014	-38.0072	0.09375	0.00025	-5.20	269†	23.1944	-37.8275	0.09415	0.00013	-4.20	269
23.2317	-38.2050	0.06304	0.00013	-4.60	269	23.2158	-38.2008	0.06702	0.00012	-4.60	269
23.2028	-38.3289	0.06050	0.00010	-5.20	269	23.1978	-37.9692	0.06763	0.00028	-3.20	269
23.2147	-38.0025	0.17891	0.00028	-4.20	269	23.2172	-38.0692	0.17786	0.00010	-4.30	269
23.2050	-38.0547	0.18512	0.00025	-3.20	269	0.5850	-28.6989	0.11444	0.00019	-4.20	460

RA (hrs)	Dec. (°)	z	Δz	Mag.	ID	RA (hrs)	Dec. (°)	z	Δz	Mag.	ID
0.5839	-28.8039	0.11126	0.00018	-4.70	460	0.5858	-28.8442	0.11366	0.00018	-4.60	460
0.5842	-28.8714	0.11362	0.00013	-2.90	460	0.5808	-28.7878	0.11373	0.00009	-2.90	460
0.5692	-28.7989	0.11292	0.00017	-2.90	460†	0.5597	-28.8678	0.11307	0.00016	-4.30	460
0.5639	-28.8056	0.11022	0.00013	-3.70	460	0.5578	-28.5275	0.11192	0.00018	-4.50	460
0.5719	-28.6258	0.11260	0.00014	-4.30	460	0.5856	-28.7203	0.11490	0.00015	-2.90	460
0.5758	-28.6022	0.11465	0.00015	-3.90	460	23.7528	-28.3856	0.02690	0.00009	-4.20	348
23.7689	-28.4214	0.02599	0.00030	-7.60	348	23.7625	-28.3942	0.02957	0.00009	-6.30	348†
23.7564	-28.4197	0.02455	0.00005	-5.70	348	23.7583	-28.5567	0.02712	0.00007	-5.80	348
23.7550	-28.4433	0.03003	0.00005	-4.90	348†	23.7536	-28.5692	0.02957	0.00008	-4.20	348
23.7519	-28.4506	0.02749	0.00009	-5.80	348	23.7481	-28.3864	0.02656	0.00011	-8.20	348
23.7431	-28.5181	0.02569	0.00010	-4.10	348	23.7519	-28.4344	0.02639	0.00010	-4.10	348
23.7439	-28.4706	0.02921	0.00007	-5.40	348	23.7522	-28.4169	0.02834	0.00008	-8.60	348
23.7447	-28.4017	0.02937	0.00007	-5.70	348	23.7497	-28.4033	0.03064	0.00006	-5.30	348
23.7481	-28.3864	0.02706	0.00029	-8.20	348	23.7511	-28.3808	0.03056	0.00008	-4.00	348
23.7456	-28.3406	0.02767	0.00010	-5.00	348	23.7439	-28.3078	0.02743	0.00015	-4.40	348
23.7486	-28.3208	0.02723	0.00010	-4.80	348	23.7461	-28.2533	0.02441	0.00005	-5.20	348
23.7508	-28.2906	0.02613	0.00008	-4.90	348	23.7539	-28.4197	0.03201	0.00005	-5.70	348
23.7619	-28.4567	0.03498	0.00007	-5.60	348	23.7569	-28.4411	0.03202	0.00007	-4.30	348
23.7539	-28.4817	0.03184	0.00006	-5.00	348	23.7539	-28.4300	0.03260	0.00010	-4.60	348
23.7478	-28.5494	0.03370	0.00010	-5.00	348	23.7497	-28.4322	0.03202	0.00007	-4.40	348
23.7464	-28.3967	0.03218	0.00006	-5.80	348	23.7436	-28.2950	0.03326	0.00008	-5.40	348
23.7178	-28.2797	0.03216	0.00010	-4.20	348						

Table C.2: This table presents the cluster galaxy redshifts used to define the AUTOFIB EM cluster redshifts. Galaxy redshifts for projection effects have been included. The ID column contains the cluster number and the Mag. column contains the m_{cos} magnitude of the galaxy (Chapter 1). Galaxies that could not be identified in the EDSGC, have zero RA, Dec and magnitudes. Galaxies marked with the symbol † are shown in the plots at the end of this Appendix. The galaxies have not been sorted.

RA (hrs)	Dec. (°)	z	Δz	Mag.	ID	RA (hrs)	Dec. (°)	z	Δz	Mag.	ID
0.0000	0.0000	0.04432	0.00020	-0.00	728	0.0000	0.0000	0.10379	0.00031	-0.00	418
0.0000	0.0000	0.16015	0.00018	-0.00	418	0.1939	-26.4564	0.08661	0.00013	-4.60	419
0.2094	-26.4944	0.11875	0.00048	-4.67	419	0.2097	-26.4972	0.06296	0.00018	-4.60	419
0.2106	-26.3792	0.11937	0.00025	-4.20	419	0.2131	-26.1156	0.08957	0.00014	-3.90	419
0.2139	-26.3519	0.14510	0.00019	-4.50	419†	0.2850	-25.7606	0.11974	0.00030	-4.30	437
0.2850	-25.9164	0.11260	0.00029	-4.80	437	0.2889	-26.1461	0.14395	0.00028	-4.80	437
0.2947	-26.0658	0.02918	0.00018	-4.00	437	0.3017	-25.6342	0.14385	0.00034	-4.80	437
0.3033	-25.9847	0.14076	0.00044	-5.30	437	0.3044	-25.7347	0.08963	0.00031	-4.40	437
0.5608	-28.5814	0.08864	0.00013	-4.10	460	0.5614	-28.6003	0.02365	0.00023	-4.00	460
0.5636	-28.8714	0.09143	0.00016	-3.20	460	0.5661	-28.5744	0.07408	0.00017	-5.40	460
0.5675	-28.5664	0.07422	0.00016	-4.50	460	0.5681	-28.5392	0.07419	0.00011	-3.70	460
0.5719	-28.4764	0.07400	0.00030	-3.80	460	0.5731	-28.6419	0.02371	0.00006	-7.40	460†
0.5781	-28.5453	0.07267	0.00019	-4.90	460	0.5786	-28.7889	0.13514	0.00034	-3.00	460
0.5856	-28.6131	0.14328	0.00023	-2.90	460	0.5869	-28.8039	0.06163	0.00019	-3.90	460
0.5956	-28.5942	0.07267	0.00009	-2.90	460†	0.7647	-29.7389	0.07678	0.00030	-3.70	482
0.7664	-29.7531	0.07491	0.00015	-3.30	482	0.7753	-29.7903	0.07509	0.00020	-3.20	482
0.7761	-29.8964	0.07586	0.00014	-4.20	482	0.7794	-29.6894	0.07612	0.00011	-4.00	482
0.7814	-29.6628	0.02351	0.00015	-2.10	482	0.7822	-29.8539	0.07571	0.00024	-3.10	482
0.7869	-29.9489	0.07574	0.00009	-2.80	482	1.0175	-40.1222	0.09433	0.00028	-5.30	519
1.0225	-40.1461	0.03023	0.00005	-5.80	519†	1.0239	-40.1767	0.09131	0.00018	-5.00	519
1.0350	-40.1422	0.12725	0.00016	-4.20	519	1.0375	-40.3722	0.09286	0.00014	-4.90	519
1.0419	-39.8475	0.07674	0.00016	-4.10	519	1.0478	-40.1792	0.09173	0.00011	-4.40	519
1.0483	-40.2983	0.09264	0.00025	-5.10	519	1.3825	-39.7606	0.12341	0.00039	-3.90	553†
1.3953	-39.8878	0.03504	0.00009	-3.80	553	2.4558	-33.4681	0.03214	0.00065	-6.90	658
2.4678	-33.2306	0.03784	0.00012	-3.90	658	2.4792	-33.2869	0.10432	0.00010	-3.40	658
2.4800	-33.4158	0.11207	0.00024	-4.20	658	2.4833	-33.3567	0.11365	0.00024	-4.10	658
2.8992	-24.9875	0.08623	0.00011	-4.80	712	2.9011	-24.9511	0.08630	0.00016	-3.80	712
2.9028	-24.9606	0.08617	0.00010	-4.50	712	2.9075	-24.8219	0.15975	0.00020	-3.50	712
2.9108	-24.7542	0.09606	0.00015	-4.80	712	2.9119	-24.8681	0.12594	0.00019	-2.60	712
2.9150	-24.7514	0.08611	0.00011	-4.30	712	2.9150	-24.9486	0.12833	0.00017	-5.00	712
2.9172	-24.8625	0.13456	0.00013	-3.50	712	21.9825	-23.1900	0.10952	0.00026	-5.00	80
21.9942	-22.9339	0.03399	0.00144	-3.50	80	21.9997	-22.9756	0.10901	0.00035	-4.00	80
22.0025	-22.8811	0.04619	0.00029	-4.20	80	22.0067	-23.0561	0.05404	0.00024	-5.60	80
22.4144	-30.8450	0.02858	0.00015	-4.80	145	22.4244	-30.6825	0.02569	0.00013	-4.20	145
22.5628	-38.2331	0.15781	0.00048	-4.30	166†	22.5739	-38.3058	0.17144	0.00042	-4.70	166
22.5758	-38.2419	0.07755	0.00022	-3.40	166	22.5792	-38.2381	0.10424	0.00014	-4.10	166
22.5853	-38.2714	0.07308	0.00006	-4.10	166	22.5872	-38.2842	0.15356	0.00039	-4.30	166
23.7436	-28.4908	0.06318	0.00009	-3.90	348†						

Table C.3: The table of AUTOFIB interlopers defined using the objective criteria outlined in Chapter 4. The ID column contains the cluster number and the Mag. column is the m_{cos} magnitude of the galaxy (Chapter 1). Zero values for the RA, Dec and magnitude of a galaxy mean that the information is not available within the EDSGC. Galaxies marked with the symbol † are shown at the end of this Appendix. The galaxies have been sorted in RA.

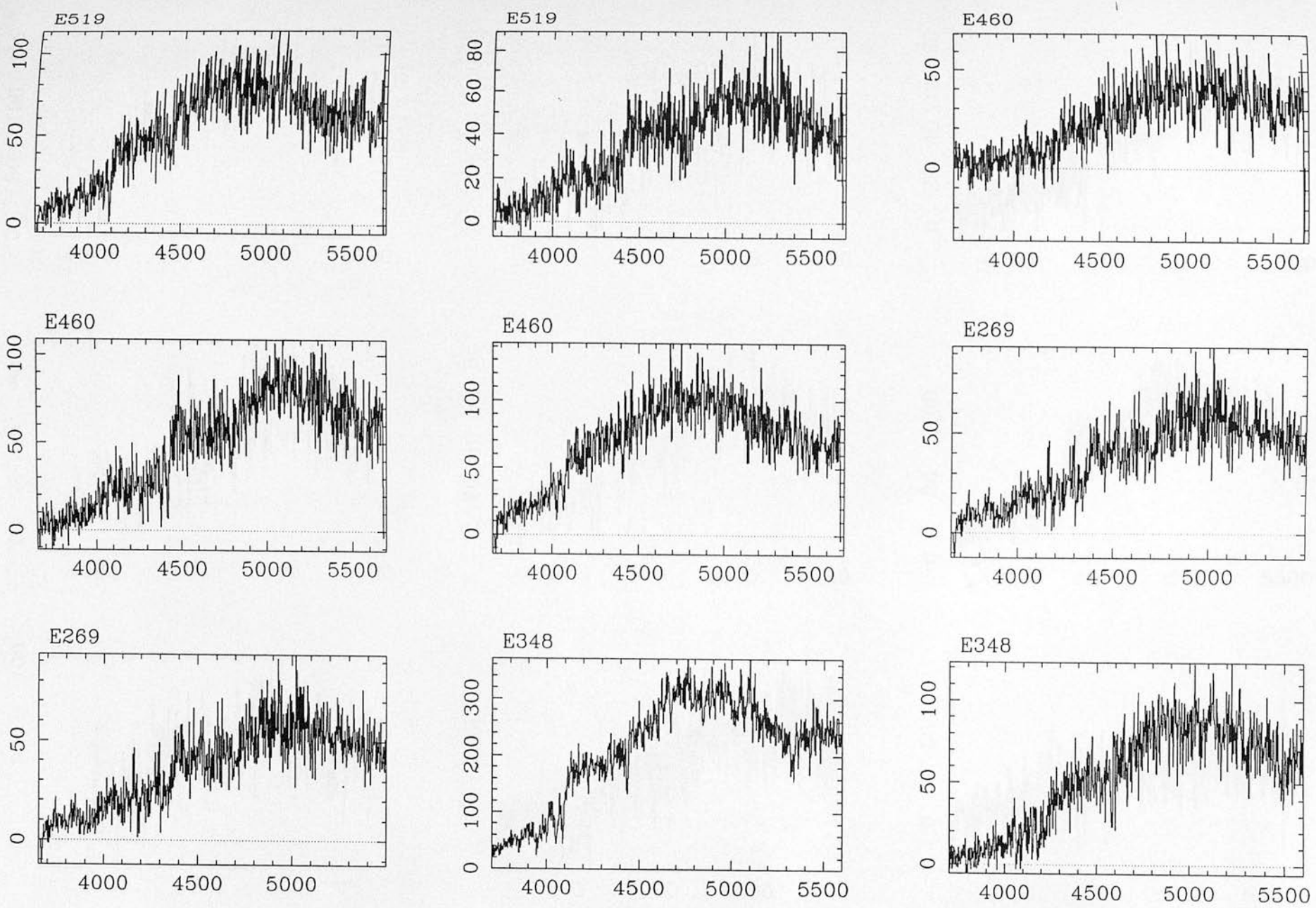
E519
E519
E460
E460
E460
E269
E269
E348
E348

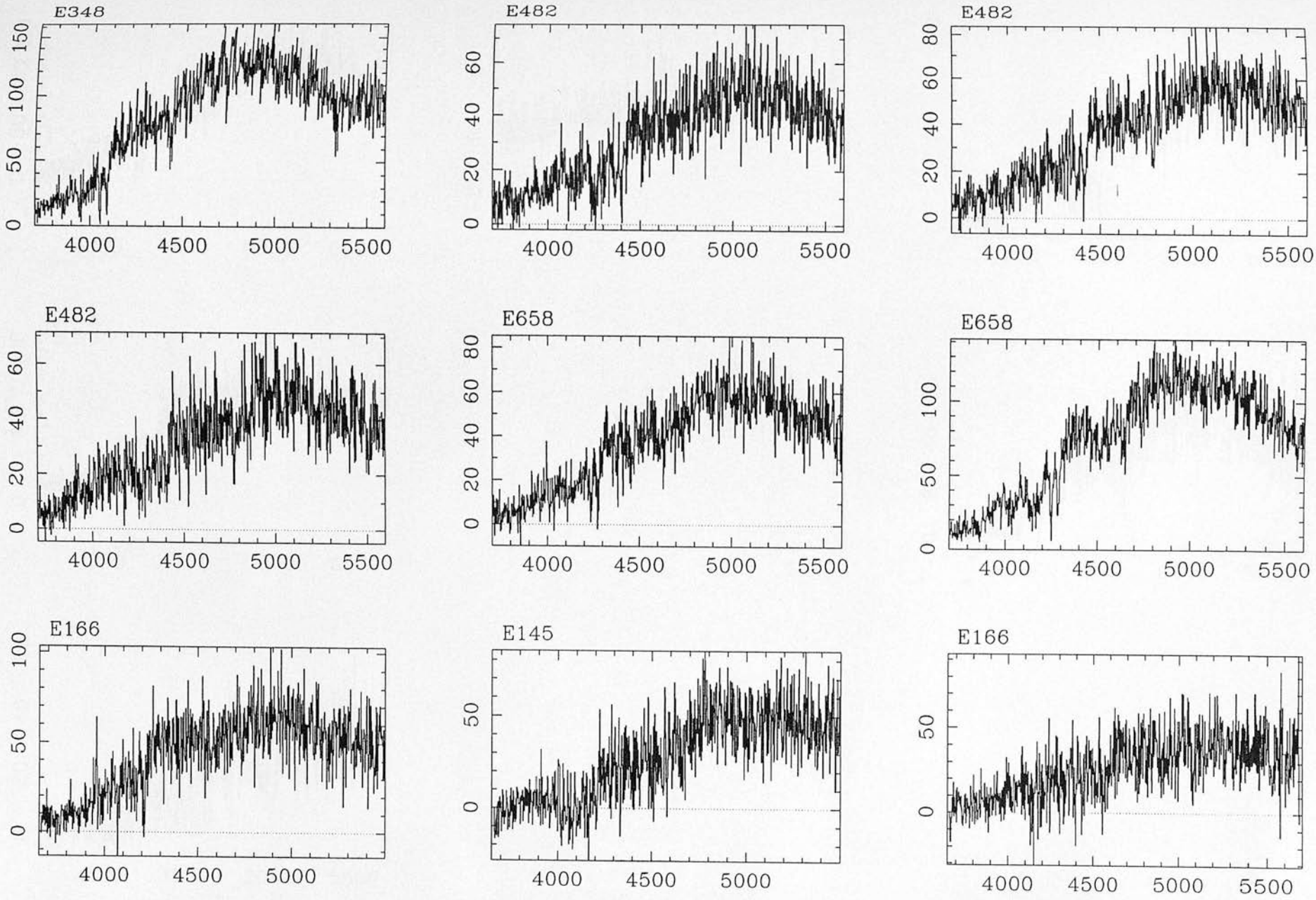
E348
E482
E482
E482
E658
E658
E166
E145
E166

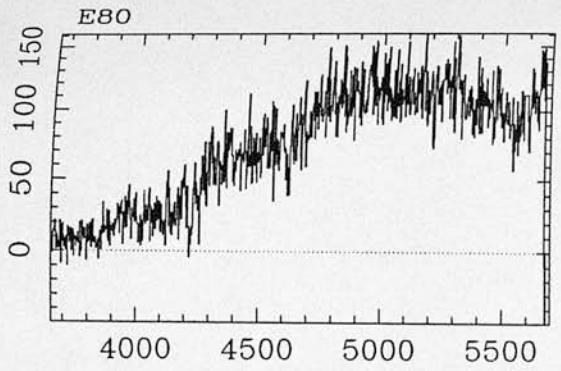
E80
0
50
100
150
4000
4500
5000
5500

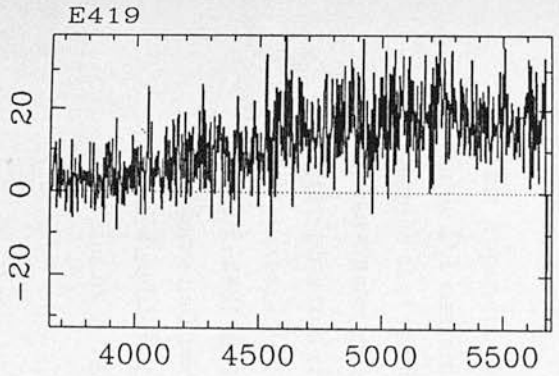
E419
−20
0
20
4000
4500
5000
5500

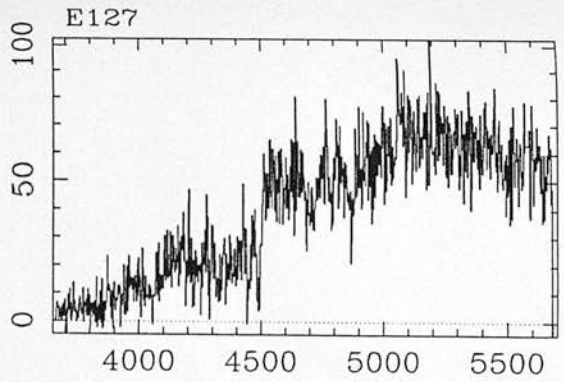
E127
0
50
100
4000
4500
5000
5500

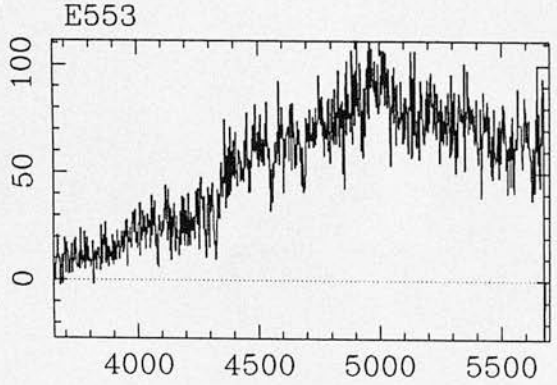
E553
0
50
100
4000
4500
5000
5500

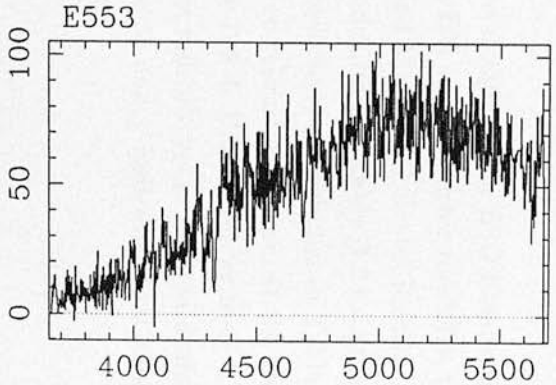
E553
0
50
100
4000
4500
5000
5500

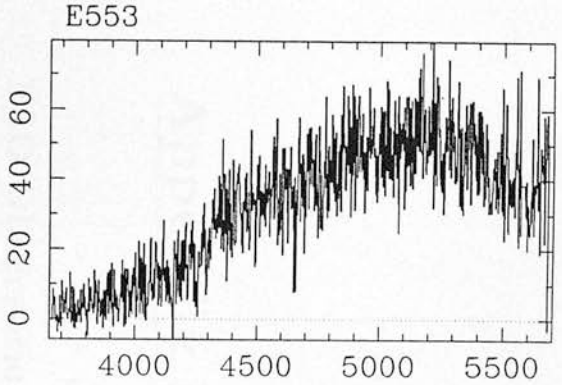
E553
0
20
40
60
4000
4500
5000
5500

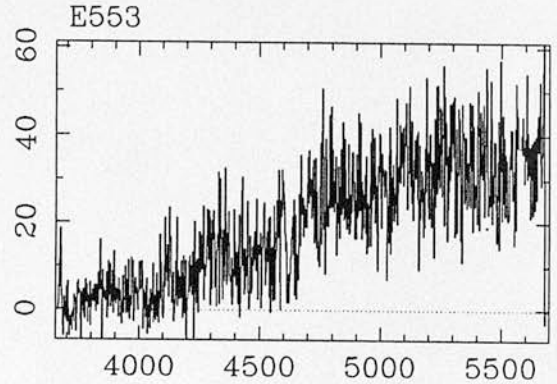
E553
0
20
40
60
4000
4500
5000
5500

Appendix D

ESO Observations

This Appendix contains details of the ESO observations made over the entire project. Table D.1 contains the EM survey cluster redshifts, the number of galaxies used to determine that redshift and the EDCC cluster identification number. Table D.2 presents all the cluster galaxy redshifts and Table D.3 lists the interlopers. The galaxy redshifts of the phantom clusters have been included in Table D.2. Twenty five typical spectra that successfully cross–correlated are shown at the end of the Appendix. These spectra are indicated in Tables D.2 & D.3 by the symbol †. The symbol $*$ indicates clusters that have had two large redshift peaks merged during the objective estimation of the clusters redshift (Stage 5) and $_a$ indicated that these clusters were also observed in Australia by AUTOFIB.

EDCC	RA (hrs)	Dec. (°)	z	Δz	Field	No. z
5	21.4933	-22.8667	0.11238	0.00271	531	4
42	21.7700	-30.9333	0.11949	0.00248	466	7
51	21.8239	-29.1400	0.09270	0.00109	466	4
57	21.8889	-30.3961	0.09257	0.00065	466	4
80_a^*	21.9872	-22.6867	0.06939	0.00286	532	11
99	22.1067	-27.5667	Proj.	Proj.	467	5
114	22.1864	-36.9683	0.03396	0.00009	404	2
115	22.1767	-35.0000	0.07300	0.00033	404	3
124	22.2467	-35.9667	0.14661	0.00332	405	8
131	22.2789	-34.9483	0.15711	0.00125	405	3
172	22.5989	-37.0117	0.05766	0.00102	406	2
175	22.6083	-38.1000	0.15354	0.00104	345	3
178	22.6305	-34.2425	0.04971	0.00037	406	2
198	22.7747	-41.1683	Proj.	Proj.	346	6
201	22.7867	-31.4500	Proj.	Proj.	468	4
216	22.8450	-25.8267	Proj.	Proj.	534	5
230	22.9367	-31.1217	0.10979	0.00288	469	2
235	22.9950	-33.6667	Proj.	Proj.	407	5
247	23.0494	-39.3917	0.16605	0.00028	346	2
256	23.1278	-23.2233	Proj.	Proj.	535	4
260	23.1497	-29.3675	Proj.	Proj.	469	5
261	23.1525	-29.3280	0.11709	0.00222	469	3
285	23.3064	-42.1217	Proj.	Proj.	347	4
297	23.3989	-24.2017	Proj.	Proj.	536	5
307	23.4600	-39.6000	0.05459	0.00178	347	3
311	23.4750	-36.7833	0.09544	0.00041	408	5
316	23.4997	-36.5067	0.09459	0.00108	408	4
326	23.5917	-38.3833	0.10893	0.00071	347	4
332	23.6517	-29.4867	0.05176	0.00086	471	3
366	23.8700	-27.9500	0.07278	0.00247	471	7
372	23.9017	-34.9500	0.04228	0.00000	349	1

EDCC	RA (hrs)	Dec. (°)	z	Δz	Field	No. z
392	0.0033	-34.9500	0.11272	0.00148	349	5
394	0.0117	-36.2333	0.04902	0.00071	349	4
400	0.0600	-35.0000	0.11307	0.00412	349	5
408*	0.1233	-35.9667	0.11936	0.00354	349	14
410	0.1467	-29.1500	0.06153	0.00082	409	2
421	0.2250	-35.2333	0.14618	0.00448	350	5
424	0.2350	-34.1333	0.07548	0.00135	350	2
429	0.2500	-35.4667	0.09693	0.00291	350	17
438	0.3400	-38.4167	0.11919	0.00009	294	2
447	0.4336	-23.8961	0.11291	0.00183	473	4
448	0.4350	-30.5167	Proj.	Proj.	410	18
450	0.4467	-29.6667	Proj.	Proj.	410	6
460_a	0.5786	-28.7100	0.11220	0.00244	411	12
462	0.5850	-39.4000	0.06316	0.00183	294	15
470	0.6239	-26.4583	0.10975	0.00155	474	7
471	0.6286	-24.9450	0.11175	0.00079	474	6
473	0.6903	-28.5794	0.10799	0.00205	411	11
474	0.6722	-26.3533	0.11256	0.00133	474	8
475	0.6861	-26.2333	0.05436	0.00023	474	3
482_a	0.7828	-29.7989	0.10783	0.00303	474	8
485*	0.8150	-28.8000	0.11251	0.00164	411	6
494	0.8872	-37.5883	0.05582	0.00092	351	4
495	0.8842	-26.6667	0.11412	0.00151	474	14
499	0.8981	-38.1800	0.11697	0.00056	295	3
500	0.9011	-30.2117	0.11320	0.00036	411	3
520	1.0358	-24.2667	0.16030	0.00326	475	8
524*	1.0933	-37.0000	0.11751	0.00365	352	9
526*	1.1072	-40.6200	0.14085	0.00363	296	6
533	1.1911	-32.0222	0.019977	0.00245	412	15
555	1.3900	-29.7800	0.14182	0.00013	413	3
557	1.3967	-38.2333	0.07969	0.00112	296	6

EDCC	RA (hrs)	Dec. (°)	z	Δz	Field	No. z
570	1.4997	-42.4133	0.08786	0.00052	296	3
571	1.5000	-31.3500	0.07213	0.00085	413	3
575	1.5308	-27.7433	0.12545	0.00271	413	5
587	1.6627	-42.4160	0.076773	0.00341	297	7
591	1.6939	-35.5867	0.06762	0.00181	353	5
606*	1.9753	-33.2150	0.10045	0.00329	354	12
618	2.0250	-41.3333	0.12480	0.00265	298	6
629	2.1211	-37.6133	0.09048	0.00000	298	1
632	2.1567	-40.5167	0.10221	0.00156	298	3
649	2.4139	-26.7167	0.14644	0.00141	479	4
653*	2.4656	-33.5167	0.07924	0.00159	355	6
683	2.7081	-26.5250	0.13364	0.00073	479	3
693	2.7617	-42.1917	Proj.	Proj.	299	3
699	2.8203	-25.1383	0.11113	0.00094	480	4
710	2.8944	-22.8250	0.12552	0.00073	546	3
717	2.9803	-37.2717	0.06616	0.00086	356	3
722	3.0164	-37.0500	0.06664	0.00057	357	4
726	3.0783	-38.9967	0.08737	0.00037	300	4
735	3.1550	-27.1167	0.06826	0.00129	481	7
742*	3.1978	-38.5267	0.08384	0.00257	300	6
748	3.2200	-29.3483	0.06709	0.00084	417	6
758*	3.3417	-41.5167	0.06487	0.00221	301	9
762	3.5617	-35.9869	0.06217	0.00132	358	3
765	3.5817	-39.9667	0.10517	0.00083	301	4
x1	3.7414	-33.0967	0.11737	0.00114	358	7

Table D.1: Table of ESO EM cluster observations. The first column contains the EDCC identification number, while the last two columns are the Field number and number of galaxies used in determining the cluster redshift. Cluster interlopers have been placed in Table D.3 and the cluster galaxy redshifts in Table D.2. The symbols $*$ and $_a$ are explained at the beginning of this Appendix. Cluster x1 is outside the EDSGC and therefore has no EDCC identification number. Projection effects have been indicated and their galaxy redshifts have been included in Table D.2.

RA (hrs)	Dec. (°)	z	Δz	Mag.	ID	RA (hrs)	Dec. (°)	z	Δz	Mag.	ID
21.4874	-22.7866	0.10919	0.00057	18.75	5	21.4874	-22.7937	0.11160	0.00040	19.39	5
22.9971	-33.6190	0.08734	0.00027	18.62	235	22.9984	-33.6197	0.08747	0.00012	17.00	235
22.9984	-33.6197	0.08842	0.00025	17.23	235	23.0019	-33.6588	0.06578	0.00009	17.23	235
22.9970	-33.6076	0.06456	0.00046	19.41	235	23.5955	-38.4958	0.10804	0.00020	18.78	326
23.5970	-38.5241	0.10871	0.00012	19.22	326	23.5972	-38.4987	0.10931	0.00018	18.94	326†
0.0000	0.0000	0.10966	0.00023	0.00	326	21.7733	-30.9512	0.11876	0.00042	20.50	42
21.7731	-30.9409	0.11739	0.00028	18.09	42	21.7735	-30.9657	0.11738	0.00026	19.03	42
21.7750	-30.9577	0.11737	0.00046	18.61	42	21.7735	-30.9815	0.12390	0.00026	18.49	42
21.7754	-30.9924	0.12097	0.00113	20.30	42	21.7740	-30.9464	0.12068	0.00019	17.59	42
22.1084	-27.5518	0.06373	0.00013	17.75	99	22.1091	-27.5496	0.06383	0.00014	17.60	99
22.1064	-27.5740	0.09053	0.00013	17.23	99	22.1067	-27.5658	0.08842	0.00034	18.92	99
22.1062	-27.5750	0.10450	0.00043	17.94	99	22.1739	-34.9142	0.07279	0.00111	18.95	115
22.1762	-34.9168	0.07337	0.00019	17.77	115	22.1774	-34.9080	0.07283	0.00022	18.20	115
22.2448	-35.9661	0.14514	0.00035	17.97	124	22.2450	-35.9658	0.14044	0.00013	19.42	124
22.2454	-35.9689	0.14750	0.00066	20.12	124	22.2466	-36.0019	0.14840	0.00021	19.65	124
22.2494	-35.9660	0.15190	0.00032	0.00	124	22.2472	-35.9782	0.14559	0.00044	18.04	124
22.2481	-35.9806	0.14558	0.00016	18.34	124	22.2484	-35.9881	0.14831	0.00026	18.42	124
23.4767	-36.7876	0.09613	0.00012	0.00	311	23.4773	-36.7470	0.09536	0.00040	19.22	311
23.4773	-36.7475	0.09538	0.00028	0.00	311	23.4781	-36.7783	0.09533	0.00013	19.19	311
23.4794	-36.7710	0.09502	0.00054	17.87	311	23.8699	-27.9678	0.07532	0.00027	19.07	366
23.8697	-27.9596	0.07284	0.00016	16.89	366	23.8697	-27.9428	0.07234	0.00018	18.17	366
23.8696	-27.9393	0.06838	0.00111	18.24	366	23.8782	-27.9317	0.07147	0.00025	17.76	366
23.8707	-27.9306	0.07344	0.00010	17.75	366	23.8707	-27.9240	0.07569	0.00022	18.42	366
0.0609	-34.9958	0.11367	0.00036	19.42	400	0.0620	-34.9851	0.10825	0.00027	19.29	400
0.0629	-34.9595	0.11826	0.00031	19.02	400	0.0619	-34.9422	0.11548	0.00040	20.38	400
0.0628	-34.9478	0.10967	0.00049	19.88	400	0.0007	-34.9799	0.11304	0.00104	19.25	392
0.0010	-34.9672	0.11481	0.00024	19.49	392	0.0034	-34.5587	0.11142	0.00021	18.02	392
0.0030	-34.2968	0.11117	0.00018	18.70	392	0.0046	-34.9375	0.11317	0.00018	18.53	392
0.1233	-35.9532	0.11747	0.00048	19.51	408	0.1236	-35.9555	0.11698	0.00038	0.00	408
0.1239	-35.9470	0.11603	0.00018	0.00	408	0.1241	-35.9425	0.11420	0.00038	17.42	408
0.0000	0.0000	0.12028	0.00025	0.00	408	0.1245	-35.9479	0.11839	0.00028	19.29	408
0.1247	-35.9447	0.11435	0.00030	0.00	408	0.0000	0.0000	0.11591	0.00025	0.00	408
0.1238	-35.9771	0.12385	0.00017	18.97	408	0.1238	-35.9523	0.12271	0.00025	18.91	408
0.1235	-35.9591	0.12221	0.00017	19.09	408	0.1238	-35.9522	0.12254	0.00017	18.81	408
0.1225	-35.9729	0.12289	0.00018	19.41	408	0.1385	-35.9771	0.12330	0.00022	18.97	408
0.2515	-35.4576	0.09872	0.02000	18.46	429	0.2512	-35.4612	0.09531	0.00030	16.80	429
0.2504	-35.4762	0.09848	0.00013	17.76	429	0.2526	-35.4642	0.09242	0.00028	19.04	429
0.2506	-35.4849	0.09878	0.00019	18.41	429	0.2516	-35.4802	0.09633	0.00021	17.95	429
0.2521	-35.4775	0.09857	0.00063	18.97	429	0.2542	-35.4864	0.10170	0.00019	18.96	429
0.2515	-35.4889	0.09160	0.00019	18.55	429	0.2529	-35.4778	0.09591	0.00060	16.77	429
0.2514	-35.4940	0.09631	0.00015	18.06	429	0.2532	-35.4798	0.09132	0.00021	18.41	429
0.2517	-35.4973	0.09783	0.00016	17.33	429	0.2516	-35.5011	0.09743	0.00018	18.49	429
0.2542	-35.4323	0.09808	0.00018	18.08	429	0.2522	-35.5070	0.10006	0.00012	18.89	429
0.2529	-35.5083	0.09899	0.00027	19.32	429	0.5836	-28.8034	0.11416	0.00039	18.64	460
0.5840	-28.8040	0.11243	0.00033	16.87	460	0.5873	-28.7270	0.11139	0.00046	19.58	460

RA (hrs)	Dec. (°)	z	Δz	Mag.	ID	RA (hrs)	Dec. (°)	z	Δz	Mag.	ID
0.5846	-28.8076	0.11270	0.00060	17.02	460	0.5850	-28.8105	0.11004	0.00020	18.04	460
0.5860	-28.8292	0.11380	0.00011	18.53	460	0.5801	-39.4210	0.06240	0.00019	18.70	462
0.5824	-39.4285	0.06228	0.00021	19.40	462	0.5826	-39.4263	0.05957	0.00012	18.86	462
0.5831	-39.4216	0.05940	0.00008	18.29	462	0.5813	-39.4094	0.06563	0.00080	18.54	462
0.5830	-39.4133	0.06282	0.00008	17.29	462	0.5840	-39.4048	0.06343	0.00009	15.82	462
0.5833	-39.3955	0.06561	0.00010	17.83	462	0.5834	-39.3927	0.06340	0.00161	17.23	462
0.2275	-35.1720	0.15072	0.00043	19.74	421	0.2277	-35.1732	0.15022	0.00009	17.95	421
0.2279	-35.1867	0.14147	0.00057	19.63	421	0.2274	-35.2042	0.14164	0.00029	19.95	421
0.2281	-35.2053	0.14685	0.00023	18.21	421	0.0000	0.0000	0.06231	0.00010	0.00	762
0.0000	0.0000	0.06078	0.00011	0.00	762	0.0000	0.0000	0.06341	0.00012	0.00	762
0.0021	-36.2142	0.04987	0.00020	17.83	394	0.0029	-36.2078	0.04893	0.00010	17.82	394
0.0043	-36.1956	0.04814	0.00013	18.16	394	0.0110	-36.2153	0.04913	0.00016	14.57	394
0.4536	-29.7147	0.10231	0.00015	18.01	450	0.4549	-29.6927	0.10082	0.00015	18.74	450
0.4553	-29.6906	0.09570	0.00015	17.99	450	0.4569	-29.7002	0.09656	0.00011	18.31	450
0.4540	-29.7055	0.13176	0.00120	18.55	450	0.4554	-29.6832	0.12902	0.00014	0.00	450
1.3957	-38.2251	0.08028	0.00100	19.45	557	1.3970	-38.1993	0.07804	0.00015	18.81	557
1.3975	-38.2249	0.08037	0.00012	15.74	557	1.3987	-38.2046	0.08108	0.00013	17.44	557
1.3991	-38.2445	0.07877	0.00013	18.44	557	1.3999	-38.2015	0.07963	0.00010	19.37	557
1.5009	-31.3492	0.07117	0.00016	15.65	571	1.5032	-31.3180	0.07277	0.00021	17.08	571
1.5035	-31.3675	0.07245	0.00028	18.85	571	0.8138	-28.7974	0.11111	0.00015	17.46	485
0.8163	-28.7691	0.10993	0.00017	16.70	485	0.8169	-28.7763	0.11279	0.00017	18.12	485
0.8158	-28.7992	0.11335	0.00009	16.62	485	0.8124	-28.7711	0.11398	0.00009	17.25	485
0.8120	-28.7605	0.11392	0.00025	17.25	485	3.5821	-39.9652	0.10423	0.00013	16.00	765
3.5889	-39.9806	0.10487	0.00032	18.56	765	3.5890	-39.9806	0.10619	0.00019	16.73	765
3.5890	-39.9751	0.10539	0.00014	17.24	765	23.4497	-39.6974	0.05400	0.00016	16.85	307
23.4555	-39.6198	0.05319	0.00011	17.08	307	23.4543	-39.7275	0.05660	0.00013	16.89	307
0.0000	0.0000	0.10939	0.00009	0.00	473	0.0000	0.0000	0.10835	0.00010	0.00	473
0.0000	0.0000	0.11033	0.00011	0.00	473	2.0242	-41.3568	0.12374	0.00019	0.00	618
2.0251	-41.3317	0.12061	0.00017	18.98	618	2.0254	-41.3403	0.12709	0.00016	16.86	618
2.0263	-41.3713	0.12813	0.00012	18.62	618	2.0271	-41.3500	0.12454	0.00012	0.00	618
2.0274	-41.3615	0.12468	0.00022	20.35	618	2.1549	-40.5215	0.10137	0.00045	19.92	632
2.1566	-40.5282	0.10401	0.00013	18.86	632	2.1565	-40.5344	0.10124	0.00013	18.61	632
3.3422	-41.5403	0.06373	0.00019	15.74	758	3.3418	-41.5253	0.06468	0.00021	18.34	758
3.3432	-41.5280	0.06230	0.00010	18.20	758	3.3378	-41.5046	0.06386	0.00019	17.87	758
0.0000	0.0000	0.06496	0.00018	0.00	758	0.0000	0.0000	0.06225	0.00021	0.00	758
3.3412	-41.5198	0.06638	0.00022	15.50	758	3.3338	-41.5084	0.06896	0.00010	17.00	758
0.0000	0.0000	0.06688	0.00010	0.00	758†	21.9842	-22.6526	0.07244	0.00024	16.54	80
21.9846	-22.6530	0.07168	0.00020	16.74	80	21.9859	-22.6397	0.07321	0.00019	18.00	80
21.9880	-22.6369	0.07102	0.00019	17.65	80	21.9844	-22.7266	0.07095	0.00020	14.78	80
22.0000	-22.7145	0.07041	0.00016	15.00	80	21.9837	-22.6629	0.06719	0.00019	18.99	80
21.9850	-22.6748	0.06646	0.00013	15.04	80	21.9861	-22.6574	0.06839	0.00012	16.11	80
21.9857	-22.6439	0.06765	0.00022	18.95	80	21.9858	-22.6266	0.06399	0.00128	17.59	80
0.6860	-26.2336	0.05440	0.00019	17.79	474	0.6878	-26.2379	0.05458	0.00012	16.74	474
0.6894	-26.2888	0.05412	0.00012	17.29	474	0.6724	-26.3350	0.11461	0.00010	18.66	474
0.6730	-26.3530	0.10973	0.00008	17.20	474	0.6736	-26.3504	0.11265	0.00013	19.31	474†

RA (hrs)	Dec. (°)	z	Δz	Mag.	ID	RA (hrs)	Dec. (°)	z	Δz	Mag.	ID
0.6740	-26.3865	0.11277	0.00013	17.76	474	0.6744	-26.3576	0.11259	0.00008	17.53	474
0.6746	-26.3694	0.11266	0.00019	18.71	474	0.6735	-26.3495	0.11275	0.00013	19.58	474
0.6753	-26.3599	0.11273	0.00023	18.83	474	0.5836	-28.8034	0.10832	0.00029	18.64	460
0.5841	-28.8040	0.11169	0.00014	17.14	460†	0.5846	-28.8076	0.11097	0.00014	17.02	460
0.5849	-28.8143	0.11349	0.00012	18.16	460	0.5852	-28.7890	0.10929	0.00025	19.68	460
0.5866	-28.7713	0.11715	0.00053	19.10	460	0.5874	-28.8285	0.11412	0.00028	18.98	460
0.6213	-26.4985	0.11144	0.00015	18.19	470†	0.6216	-26.4992	0.10838	0.00009	18.70	470
0.6225	-26.4869	0.11208	0.00037	18.76	470	0.6230	-26.4602	0.10973	0.00023	17.31	470
0.6234	-26.4730	0.10847	0.00025	20.04	470	0.6242	-26.4865	0.10997	0.00010	16.88	470
0.6243	-26.5038	0.10817	0.00035	19.48	470	21.8244	-29.1110	0.09393	0.00015	16.37	51
21.8236	-29.1588	0.09140	0.00014	17.79	51	21.8246	-29.1661	0.09317	0.00022	17.76	51
21.8232	-29.0094	0.09231	0.00013	16.96	51	0.5795	-39.4547	0.06361	0.00010	17.01	462
0.5801	-39.4210	0.06332	0.00033	18.70	462	0.5819	-39.4312	0.06398	0.00014	19.02	462
0.5830	-39.4133	0.06369	0.00016	17.29	462	0.5834	-39.3927	0.06539	0.00022	17.28	462
0.5840	-39.4045	0.06292	0.00010	15.82	462	0.6305	-24.9620	0.11179	0.00044	20.34	471
0.6321	-25.0032	0.11148	0.00019	18.43	471	0.6314	-24.9834	0.11096	0.00029	18.59	471
0.6319	-24.9907	0.11236	0.00016	18.16	471	0.6321	-25.0032	0.11095	0.00018	18.45	471
0.6324	-24.9760	0.11295	0.00017	19.16	471	0.7801	-28.7809	0.10348	0.00018	20.00	482
0.7830	-29.7989	0.10767	0.00010	17.99	482	0.7830	-29.7989	0.10833	0.00026	17.99	482
0.7828	-29.7926	0.10492	0.00013	17.15	482	0.7834	-29.7733	0.10954	0.00008	19.85	482
0.7834	-29.7733	0.10614	0.00033	0.00	482	0.7843	-29.8013	0.11314	0.00014	18.77	482
0.7848	-29.7880	0.10945	0.00010	0.00	482	1.0946	-36.9996	0.11328	0.00487	18.41	524
1.0958	-37.0564	0.11860	0.00022	19.59	524	1.0964	-37.0556	0.11430	0.00014	18.34	524
1.0967	-37.0102	0.11386	0.00012	18.08	524	1.0970	-37.0130	0.11374	0.00013	18.91	524
1.0949	-37.0344	0.12136	0.00010	18.93	524	1.0962	-37.0234	0.12089	0.00019	18.97	524†
1.0973	-37.0390	0.11993	0.00010	19.61	524	1.0980	-36.9929	0.12171	0.00012	18.61	524
3.1572	-27.0849	0.06847	0.00015	16.04	735	3.1527	-27.0869	0.06991	0.00033	19.34	735
3.1538	-27.1018	0.06806	0.00006	17.96	735	3.1545	-27.1195	0.06830	0.00014	15.96	735
3.1537	-27.0747	0.06806	0.00016	18.76	735	3.1557	-27.1070	0.06926	0.00008	18.87	735
3.1546	-27.0457	0.06577	0.00014	18.24	735	0.6594	-28.8210	0.11045	0.00017	19.11	473
0.6588	-28.7927	0.10857	0.00043	18.62	473	0.6597	-28.8000	0.10448	0.00012	18.56	473
0.6603	-28.8072	0.10454	0.00009	18.09	473	0.6623	-28.8420	0.10747	0.00015	19.61	473
0.6615	-28.8097	0.10819	0.00008	16.10	473	0.6624	-28.8170	0.10947	0.00015	18.84	473
0.6629	-28.8238	0.10669	0.00010	18.96	473	0.8812	-26.6745	0.11399	0.00008	19.32	495
0.8837	-26.6575	0.11316	0.00009	18.92	495	0.8841	-26.6609	0.11308	0.00012	18.50	495
0.8844	-26.6668	0.11169	0.00009	18.41	495	0.8831	-26.6574	0.11280	0.00011	20.05	495
0.8851	-26.6713	0.11340	0.00008	19.01	495	0.8856	-26.7797	0.11240	0.00018	18.45	495
0.8888	-26.6054	0.11703	0.00020	17.42	495	0.8896	-26.6035	0.11473	0.00023	19.66	495
0.8882	-26.6438	0.11556	0.00024	19.61	495	0.8890	-26.6401	0.11579	0.00015	19.37	495
0.8900	-26.6359	0.11585	0.00012	17.28	495	0.8910	-26.6273	0.11433	0.00012	19.56	495
0.8912	-26.6312	0.11306	0.00017	18.31	495	1.0338	-24.2280	0.16112	0.00020	20.31	520
1.0339	-24.2238	0.16629	0.00012	19.33	520	1.0345	-24.2349	0.16314	0.00018	20.43	520
1.0345	-24.2270	0.15923	0.00013	19.16	520	1.0352	-24.2311	0.15656	0.00017	0.00	520
1.0354	-24.2639	0.15654	0.00010	18.89	520	1.0357	-24.2423	0.15959	0.00010	17.32	520
1.0365	-24.2312	0.15998	0.00030	20.83	520	3.7403	-33.0964	0.11657	0.00010	-3.32	x1

RA (hrs)	Dec. (°)	z	Δz	Mag.	ID	RA (hrs)	Dec. (°)	z	Δz	Mag.	ID
3.7405	-33.1124	0.11783	0.00016	-4.11	x1	3.7409	-33.0912	0.11807	0.00013	-3.01	x1
3.7415	-33.1051	0.11738	0.00010	-3.20	x1	3.7421	-33.1041	0.11597	0.00011	-4.02	x1
3.7463	-32.9581	0.11933	0.00008	-4.59	x1	3.7462	-32.9566	0.11665	0.00011	-5.67	x1
23.6495	-29.5138	0.05076	0.00015	15.46	332	23.6456	-29.4311	0.05224	0.00028	18.88	332
23.6480	-29.5980	0.05227	0.00013	15.06	332	0.4374	-30.3900	0.10179	0.00023	19.24	448
0.4382	-30.3827	0.10093	0.00014	19.36	448	0.4385	-30.3849	0.10419	0.00047	19.33	448
0.4390	-30.3835	0.10843	0.00039	20.07	448	0.4393	-30.3746	0.10258	0.00013	17.82	448
0.4393	-30.3746	0.10334	0.00203	17.82	448	0.4410	-30.3723	0.10277	0.00025	19.45	448
0.4413	-30.3607	0.10220	0.00024	18.04	448	0.4414	-30.3610	0.10328	0.00010	18.00	448
0.4306	-30.5220	0.10969	0.00031	18.60	448	0.4319	-30.5198	0.10400	0.00028	18.61	448
0.4381	-30.3731	0.12807	0.00013	18.49	448†	0.4384	-30.3816	0.12722	0.00013	18.99	448
0.4387	-30.3782	0.12914	0.00019	18.82	448	0.4396	-30.3522	0.11834	0.00015	18.64	448
0.4297	-30.5200	0.12090	0.00014	18.53	448	0.4300	-30.5370	0.12043	0.00022	18.85	448
0.4290	-30.4863	0.07116	0.00022	16.84	448	21.9009	-30.3492	0.09191	0.00019	20.32	57
21.9037	-30.3333	0.09251	0.00013	18.89	57	21.9011	-30.3179	0.09346	0.00016	17.94	57
21.8990	-30.3184	0.09242	0.00022	17.52	57	23.4016	-24.1600	0.08887	0.00025	18.94	297
23.3988	-24.1438	0.09044	0.00015	18.95	297	23.4009	-24.1291	0.08839	0.00012	17.18	297
23.4023	-24.1541	0.10998	0.00140	19.86	297	23.3981	-24.1525	0.11755	0.00023	19.75	297
1.1085	-40.6316	0.14022	0.00017	19.37	526	1.1105	-40.6242	0.13647	0.00016	18.08	526
1.1067	-40.5980	0.13708	0.00011	18.97	526	1.1082	-40.6045	0.14184	0.00019	19.29	526†
1.1060	-40.6040	0.14415	0.00011	0.00	526	1.1060	-40.5862	0.14535	0.00011	18.77	526
1.9748	-33.2266	0.09597	0.00059	3.85	606	1.9748	-33.2266	0.09510	0.00008	3.85	606
1.9759	-33.2515	0.09717	0.00020	4.54	606	1.9760	-33.2347	0.09683	0.00009	4.93	606
1.9764	-33.2421	0.09640	0.00010	5.17	606	1.9774	-33.2352	0.09719	0.00011	3.90	606
3.0124	-37.0784	0.06717	0.00013	18.58	722	3.0134	-37.0764	0.06611	0.00011	16.83	722
3.0110	-37.1130	0.06620	0.00013	17.60	722	3.0089	-37.0935	0.06710	0.00015	18.37	722
22.8467	-25.8221	0.07762	0.00010	16.86	216	22.8485	-25.7915	0.08629	0.00020	19.85	216
22.8462	-25.8174	0.08999	0.00019	18.68	216	22.8474	-25.8124	0.15602	0.00017	20.55	216
22.8476	-25.8044	0.15157	0.00013	19.99	216	23.1497	-29.3676	0.08620	0.00014	17.37	260
23.1481	-29.3590	0.08637	0.00009	17.81	260	23.1505	-29.3927	0.12222	0.00010	18.09	260
23.1493	-29.3827	0.11687	0.00027	17.14	260	23.1489	-29.3614	0.12241	0.00032	18.38	260
3.0794	-38.9440	0.08786	0.00012	17.51	726	3.0778	-38.9273	0.08695	0.00017	18.72	726
3.0837	-39.0590	0.08740	0.00017	19.09	726	3.0832	-39.0480	0.08728	0.00007	19.09	726
2.9732	-37.1185	0.06565	0.00014	14.88	717	2.9751	-37.2474	0.06715	0.00016	15.64	717
2.9735	-37.2389	0.06567	0.00021	16.74	717	0.4353	-23.9236	0.11080	0.00024	19.00	447
0.4351	-23.9156	0.11196	0.00009	17.80	447	0.4357	-23.8767	0.11465	0.00009	17.56	447
0.4364	-23.8801	0.11421	0.00013	18.12	447	1.5269	-27.7850	0.12349	0.00012	17.33	575†
1.5263	-27.7801	0.12627	0.00010	18.21	575	1.5258	-27.7734	0.12461	0.00012	17.02	575
1.5292	-27.7748	0.12312	0.00014	17.98	575	1.5273	-27.7510	0.12977	0.00010	18.25	575
1.6978	-35.5163	0.06970	0.00009	16.81	591	1.6986	-35.5669	0.06608	0.00023	17.09	591
1.6994	-35.5470	0.06819	0.00011	16.71	591	1.6984	-35.6008	0.06542	0.00009	17.77	591
1.7017	-35.5071	0.06871	0.00027	19.24	591†	2.4164	-26.6774	0.14687	0.00015	17.44	649
2.4172	-26.6682	0.14702	0.00010	18.32	649†	2.4174	-26.6703	0.14750	0.00028	19.28	649
2.4176	-26.6929	0.14435	0.00011	18.76	649	2.8174	-25.1354	0.11064	0.00027	19.84	699
2.8193	-25.1266	0.11045	0.00018	18.33	699	2.8228	-25.2506	0.11251	0.00010	17.78	699†

RA (hrs)	Dec. (°)	z	Δz	Mag.	ID	RA (hrs)	Dec. (°)	z	Δz	Mag.	ID
2.8207	-25.1599	0.11092	0.00014	18.87	699	3.1969	-38.4864	0.08543	0.00018	15.21	742
3.1939	-38.5479	0.08487	0.00023	17.50	742	3.1952	-38.5224	0.08547	0.00016	18.50	742
3.1975	-38.4774	0.08616	0.00016	18.91	742†	3.1966	-38.4954	0.08027	0.00034	18.14	742
3.1947	-38.5483	0.08087	0.00018	17.22	742	22.6043	-36.8517	0.05694	0.00011	16.23	172
22.5956	-37.0275	0.05838	0.00013	17.31	172	22.7801	-31.5334	0.10408	0.00009	17.15	201
22.7802	-31.5157	0.10683	0.00010	17.60	201	22.7863	-31.3996	0.11541	0.00016	18.08	201
22.7882	-31.3916	0.11305	0.00012	17.08	201	0.3375	-38.3940	0.11912	0.00028	17.94	438†
0.3380	-38.3917	0.11925	0.00015	17.12	438	0.8943	-38.1739	0.11762	0.00020	16.62	499
0.8957	-38.1647	0.11666	0.00015	18.24	499	0.8907	-38.2115	0.11664	0.00012	18.13	499
2.4784	-33.3251	0.07858	0.00012	16.41	653†	2.4540	-33.7527	0.07716	0.00012	15.24	653
2.4532	-33.7277	0.07791	0.00010	16.47	653	2.4806	-33.3450	0.08004	0.00020	18.43	653
2.4682	-33.5565	0.08057	0.00025	17.57	653	2.4674	-33.5422	0.08120	0.00034	18.09	653
22.2850	-34.8505	0.15842	0.00035	17.93	131	22.2795	-34.8340	0.15594	0.00009	17.50	131
22.2827	-34.8325	0.15697	0.00018	18.41	131	23.1313	-23.2055	0.09126	0.00011	18.26	256
23.1295	-23.2017	0.09054	0.00009	17.86	256	23.1307	-23.3108	0.10949	0.00011	18.10	256
23.1328	-23.2957	0.11034	0.00010	18.00	256	23.5022	-36.4827	0.09564	0.00016	17.24	316
23.5022	-36.4668	0.09320	0.00016	18.19	316	23.5028	-36.5181	0.09430	0.00012	17.92	316
23.5031	-36.5079	0.09523	0.00014	17.31	316	1.5041	-42.3684	0.08756	0.00010	16.91	570
1.4965	-42.4387	0.08756	0.00008	16.82	570	1.4970	-42.4297	0.08846	0.00011	17.91	570
1.9724	-33.1276	0.10279	0.00014	18.84	606	1.9723	-33.1223	0.10614	0.00011	19.06	606
1.9723	-33.1193	0.10413	0.00013	17.98	606	1.9723	-33.1145	0.10419	0.00012	18.38	606
1.9816	-33.1056	0.10505	0.00016	17.42	606	1.9809	-33.1048	0.10450	0.00023	18.75	606
2.7161	-26.6274	0.13444	0.00017	18.53	683	2.7169	-26.6162	0.13301	0.00028	18.18	683
2.7027	-26.4473	0.13348	0.00012	18.19	683	2.7637	-42.0664	0.07060	0.00018	17.77	693
2.7627	-42.0598	0.07124	0.00022	16.87	693	2.7606	-42.0443	0.13982	0.00020	17.39	693
3.2269	-29.5237	0.06637	0.00024	17.22	748	3.2251	-29.5102	0.06656	0.00013	16.68	748
3.2169	-29.3415	0.06635	0.00012	17.06	748	3.2148	-29.3529	0.06852	0.00019	17.66	748
3.2150	-29.4180	0.06730	0.00016	17.00	748†	3.2168	-29.4217	0.06741	0.00018	17.13	748
22.6132	-38.1182	0.15385	0.00014	17.91	175	22.6124	-38.1216	0.15439	0.00011	18.08	175
22.6000	-38.0989	0.15238	0.00013	17.55	175	22.7764	-41.1801	0.12672	0.00014	18.61	198
22.7758	-41.1757	0.12521	0.00016	18.72	198	22.7771	-41.1576	0.12630	0.00012	18.83	198†
22.7731	-41.1810	0.19076	0.00013	19.14	198	22.7728	-41.1843	0.19390	0.00020	19.15	198
22.7787	-41.1274	0.20977	0.00033	19.38	198	22.9333	-31.1414	0.11183	0.00014	17.81	230
22.9329	-31.1502	0.10775	0.00011	18.26	230	23.0498	-39.3508	0.16625	0.00018	18.35	247
23.0486	-39.3605	0.16585	0.00019	18.14	247†	23.2971	-42.0648	0.05715	0.00010	17.88	285†
23.2970	-42.0750	0.05510	0.00012	17.00	285	23.3190	-42.1798	0.08703	0.00014	17.74	285
23.3158	-42.1700	0.08984	0.00015	16.00	285	0.9009	-30.3269	0.11279	0.00024	18.60	500
0.9023	-30.3450	0.11336	0.00018	17.70	500	0.9038	-30.3273	0.11345	0.00017	18.18	500
0.8866	-37.5361	0.05690	0.00015	17.15	494	0.8902	-37.5619	0.05489	0.00012	16.78	494
0.8900	-37.5894	0.05626	0.00015	16.50	494	0.8900	-37.6789	0.05525	0.00016	15.35	494
1.3967	-29.8308	0.14187	0.00020	18.33	555	1.3963	-29.8382	0.14168	0.00023	18.45	555
1.3960	-29.8398	0.14191	0.00027	18.40	555	2.8957	-22.8668	0.12499	0.00013	17.74	710
2.8959	-22.8460	0.12522	0.00021	18.79	710	2.8940	-22.9000	0.12635	0.00025	19.00	710
23.9072	-34.9590	0.04228	0.00012	14.66	372	0.1470	-29.1327	0.06094	0.00011	15.03	410
0.1532	-29.2104	0.06210	0.00010	16.04	410	2.1207	-37.5609	0.09048	0.00018	16.32	629

RA (hrs)	Dec. (°)	z	Δz	Mag.	ID	RA (hrs)	Dec. (°)	z	Δz	Mag.	ID
22.1857	-36.9289	0.03396	0.00023	15.34	114	22.1876	-36.9435	0.03397	0.00018	15.96	114†
0.0000	0.00000	0.04945	0.00023	0.00	178	0.0000	0.00000	0.04998	0.00013	0.00	178
0.0000	0.00000	0.11456	0.00024	0.00	261	0.0000	0.00000	0.11871	0.00019	0.00	261
0.0000	0.00000	0.11802	0.00022	0.00	261	0.0000	0.00000	0.07452	0.00009	0.00	424
0.0000	0.00000	0.07644	0.00016	0.00	424						

Table D.2: Table of galaxy redshifts used in the determination of the ESO EM cluster redshifts. The ID column contains the cluster identification number and the Mag. column contains the b_j calibrated magnitude of the galaxy. Galaxy redshifts for cluster x1 have been included and their magnitudes have been quoted as m_{cos} magnitudes (Chapter 1). Zero values for the RA, Dec and magnitude of a galaxy means that the information is unavailable within the EDSGC. Galaxies marked with the symbol † are shown at the end of this Appendix.The galaxies have not been sorted in RA.

RA (hrs)	Dec. (°)	z	Δz	Mag.	ID	RA (hrs)	Dec. (°)	z	Δz	Mag.	ID
0.0000	0.0000	0.06148	0.00020	0.00	326	0.0018	-34.9717	0.11050	0.00019	18.99	392
0.0029	-34.9553	0.10891	0.00014	18.15	392	0.0032	-36.2085	0.04606	0.00019	19.09	394
0.0037	-34.9736	0.11966	0.00014	18.14	392	0.0048	-36.2020	0.05245	0.00026	18.90	394
0.0616	-34.9887	0.05721	0.00024	19.23	400	0.0619	-34.9641	0.12004	0.00015	18.26	400
0.0620	-34.9751	0.05926	0.00029	18.53	400	0.0628	-35.0089	0.28941	0.00228	19.02	400
0.0630	-34.9668	0.11867	0.00049	19.40	400	0.1236	-35.9539	0.12598	0.00125	19.68	408
0.2251	-35.1664	0.09738	0.00013	19.40	421	0.2275	-35.1634	0.32116	0.00192	20.00	421
0.2301	-35.1732	0.11207	0.00000	0.00	421	0.2513	-35.5331	0.12523	0.00042	19.22	429
0.2523	-35.4626	0.06449	0.00015	20.28	429	0.2528	-35.4961	0.12136	0.00020	19.28	429
0.3365	-38.4026	0.12288	0.00034	18.49	438	0.3368	-38.4004	0.11636	0.00015	18.61	438
0.4339	-23.9129	0.19370	0.00012	18.73	447	0.4359	-23.9093	0.10614	0.00010	19.19	447
0.5813	-39.4094	0.05424	0.00029	18.54	462	0.5822	-39.4279	0.14858	0.00039	19.95	462
0.5831	-28.7898	0.11625	0.00067	20.06	460	0.5834	-39.4121	0.11341	0.00035	18.95	462
0.5843	-39.4096	0.10870	0.00000	21.15	462	0.5846	-28.8236	0.12919	0.00023	20.53	460
0.5849	-28.8094	0.10901	0.00043	18.43	460	0.5858	-28.8197	0.10669	0.00020	19.31	460
0.5860	-28.8292	0.11875	0.00030	18.53	460	0.5870	-28.8039	0.06187	0.00018	17.67	460
0.5870	-28.8038	0.06254	0.00031	17.67	460	0.6218	-26.5037	0.10670	0.00009	18.12	470
0.6228	-26.5088	0.11501	0.00015	19.90	470	0.6281	-26.4859	0.11710	0.00013	18.89	470
0.6330	-24.9872	0.10485	0.00025	19.18	471	0.6337	-25.0046	0.11586	0.00020	18.16	471†
0.6604	-28.8300	0.09765	0.00032	19.46	473	0.6623	-28.7931	0.11062	0.00008	17.96	473
0.6632	-28.8226	0.11406	0.00019	20.03	473	0.6756	-26.3646	0.10022	0.00028	18.78	474
0.6759	-26.3860	0.10098	0.00011	19.56	474	0.6883	-26.2847	0.10028	0.00016	17.38	474
0.6913	-26.2951	0.12244	0.00018	19.28	474	0.7801	-28.7809	0.21652	0.00010	20.00	482
0.7822	-29.7988	0.16225	0.00015	19.55	482†	0.8840	-26.6583	0.11506	0.00035	18.33	495
0.8913	-26.6334	0.11280	0.00010	18.93	495	0.8918	-26.6353	0.11248	0.00025	19.17	495
0.8930	-38.2207	0.11442	0.00015	17.69	499	0.9009	-30.3071	0.09565	0.00019	18.86	500
0.9016	-30.3673	0.15801	0.00009	18.21	500	0.9016	-30.3777	0.16580	0.00017	18.95	500
0.9027	-30.3131	0.21473	0.00017	20.47	500	1.0352	-24.2646	0.18799	0.00025	19.20	520
1.0370	-24.2273	0.11521	0.00035	18.56	520	1.0373	-23.2323	0.19141	0.00014	20.58	520
1.0983	-36.9887	0.09284	0.00022	18.28	524	1.3862	-29.8099	0.09687	0.00014	18.50	555
1.3966	-38.2176	0.08619	0.00020	18.86	557	1.3975	-38.2250	0.07704	0.00006	15.74	557
1.5016	-31.3401	0.06941	0.00013	17.16	571	1.5020	-31.3319	0.07621	0.00033	18.41	571
1.5043	-42.3580	0.08364	0.00015	18.27	570	1.5251	-27.7469	0.09690	0.00047	18.08	575
1.5278	-27.7928	0.09264	0.00021	0.00	575	1.5300	-27.7752	0.13705	0.00014	18.24	575
1.6992	-35.5638	0.23681	0.00046	19.60	591	1.7008	-35.5690	0.15403	0.00014	19.56	591
1.7014	-35.5140	0.23539	0.00055	20.08	591	1.9803	-33.1050	0.06154	0.00013	19.50	606
2.0247	-41.3697	0.14535	0.00023	19.55	618	2.0259	-41.3354	0.11903	0.00011	17.95	618
2.0269	-41.3472	0.13432	0.00015	18.86	618	2.1552	-40.4971	0.10543	0.00014	20.02	632
2.1558	-40.5196	0.09853	0.00014	17.98	632	2.1562	-40.5353	0.09686	0.00029	19.02	632
2.1588	-40.5378	0.23900	0.00000	19.66	632	2.4149	-26.6999	0.05934	0.00008	17.84	649
2.4176	-26.6848	0.08291	0.00018	17.35	649	2.4184	-26.7021	0.03410	0.00015	16.68	649
2.7025	-26.4329	0.13773	0.00016	18.32	683	2.8181	-25.1304	0.03443	0.00019	19.28	699
2.8189	-25.1349	0.11820	0.00028	19.14	699	2.8253	-25.1770	0.11637	0.00013	19.60	699
2.8949	-22.8801	0.12240	0.00017	18.84	710	3.0143	-37.0525	0.06452	0.00044	18.48	722
3.1542	-27.0824	0.11581	0.00022	17.63	735†	3.1554	-27.0705	0.13486	0.00026	18.49	735

RA (hrs)	Dec. (°)	z	Δz	Mag.	ID	RA (hrs)	Dec. (°)	z	Δz	Mag.	ID
3.5799	-39.9570	0.06656	0.00012	16.00	765	3.5884	-39.9583	0.10092	0.00013	17.72	765
3.7392	-33.0975	0.09537	0.00016	-4.24	x1	3.7400	-33.1319	0.22197	0.00037	-4.42	x1
3.7449	-32.9244	0.21998	0.00015	-3.64	x1	3.7455	-32.9093	0.16379	0.00010	-3.44	x1
3.7466	-32.9126	0.16372	0.00020	-2.56	x1	21.4871	-22.7662	0.12797	0.00120	19.41	5
21.4877	-22.8092	0.13765	0.00185	20.36	5	21.7748	-30.9731	0.10960	0.00168	19.60	42
21.8241	-29.1246	0.09098	0.00011	16.76	51	21.8257	-29.2217	0.02308	0.00025	16.47	51
22.1769	-34.9101	0.15087	0.00022	18.19	115	22.2454	-35.9875	0.11982	0.00126	20.68	124
22.2467	-35.9686	0.16046	0.00016	18.96	124	22.2484	-35.9660	0.15366	0.00022	0.00	124
22.2855	-34.8719	0.15421	0.00021	18.03	131	22.5984	-37.0050	0.06021	0.00013	15.84	172
22.5987	-38.0885	0.18985	0.00013	18.29	175†	22.6013	-36.8878	0.07742	0.00016	16.73	172†
22.9262	-31.1170	0.08136	0.00022	17.19	230	22.9270	-31.1139	0.12616	0.00016	18.23	230
23.0494	-39.3356	0.08809	0.00014	18.67	247	23.0495	-39.3138	0.16939	0.00015	18.40	247
23.4754	-36.7915	0.10111	0.00029	18.58	311	23.4770	-36.7852	0.09895	0.00033	18.21	311
23.4789	-36.7542	0.08992	0.00014	20.16	311	23.5972	-38.5023	0.16522	0.00035	0.00	326
23.5982	-38.5023	0.16579	0.00023	18.91	326	23.5992	-38.5101	0.06537	0.00024	18.15	326
23.5993	-38.5031	0.23735	0.00020	19.59	326	23.8719	-27.9595	0.05257	0.00032	18.44	366
23.8719	-27.9564	0.18619	0.00161	19.18	366						

Table D.3: Table of interlopers defined by the objective criteria outlined in Chapter 4. The ID column contains the cluster identification number and the Mag. column contains the b_j calibrated magnitude of the galaxy. The interlopers of cluster x1 have been included and their magnitudes have been quoted as m_{cos} magnitudes (Chapter 1). Zero values for the RA, Dec and magnitude of a galaxy mean that the information is not available within the EDSGC. Galaxies marked with the symbol † are shown at the end of this Appendix. The galaxies have been sorted in RA.

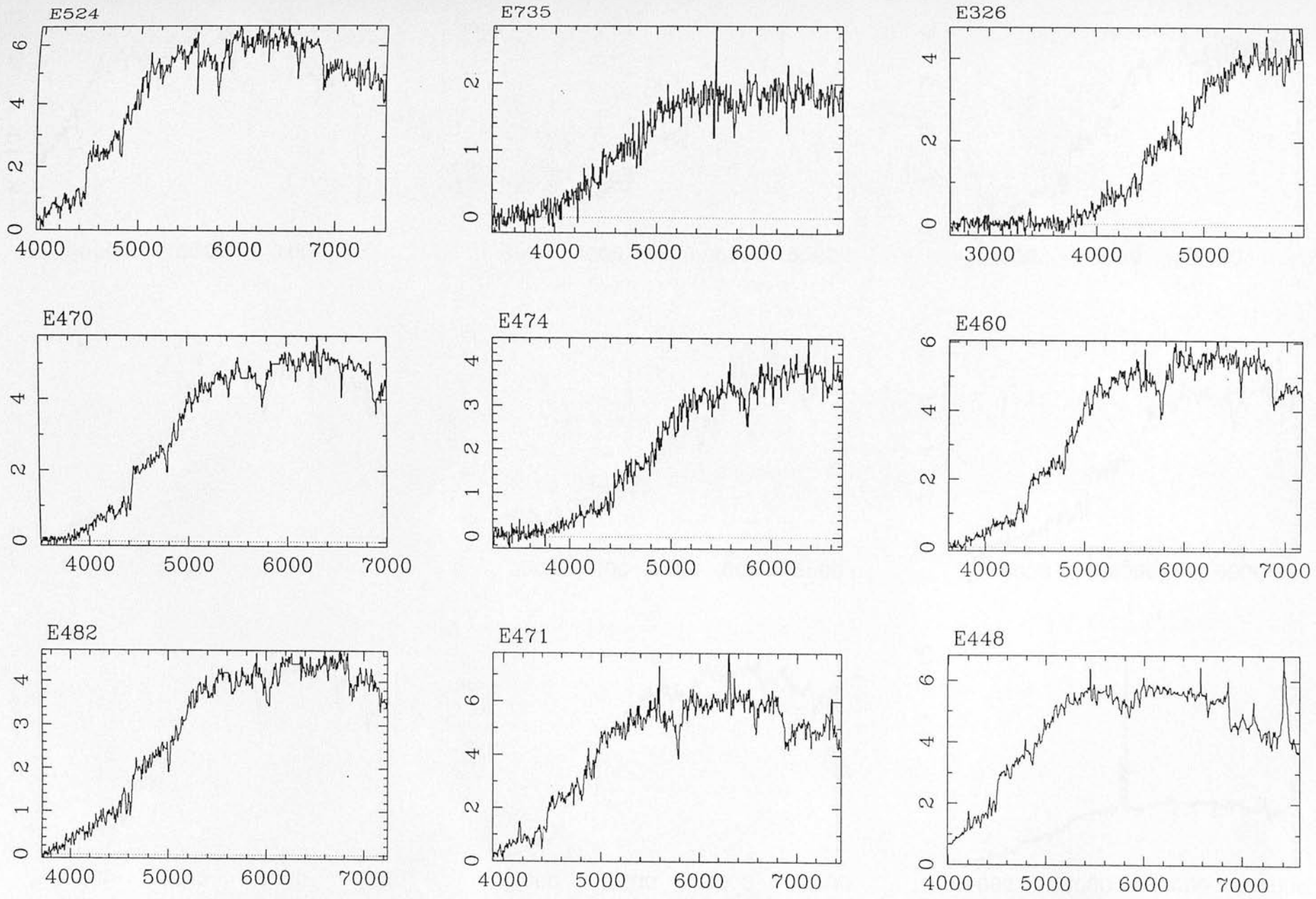
E524
E735
E326
E470
E474
E460
E482
E471
E448

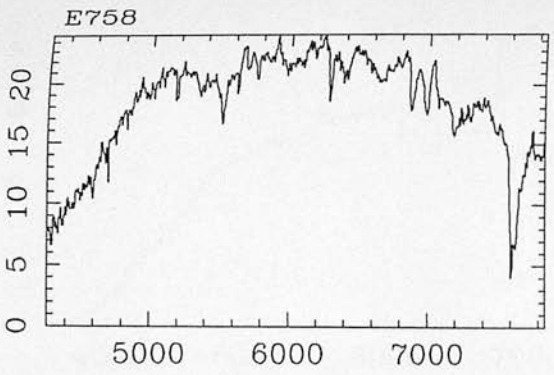
E758
0 5 10 15 20
5000 6000 7000

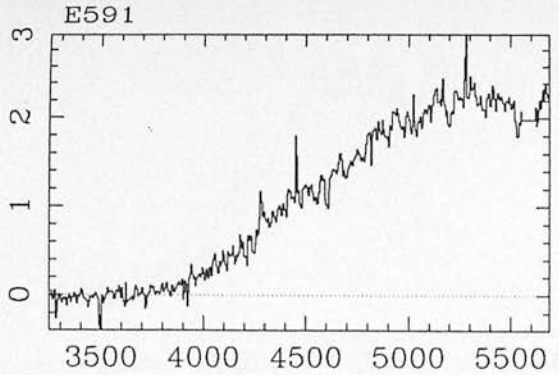
E591
0 1 2 3
3500 4000 4500 5000 5500

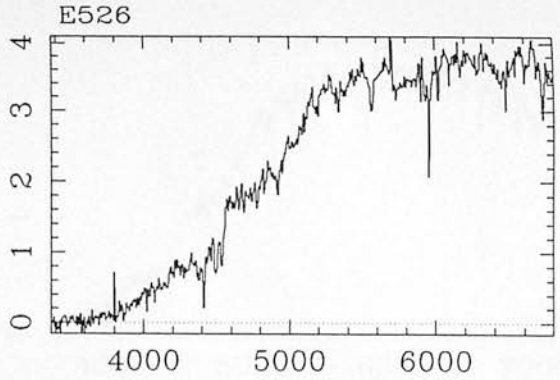
E526
0 1 2 3 4
4000 5000 6000

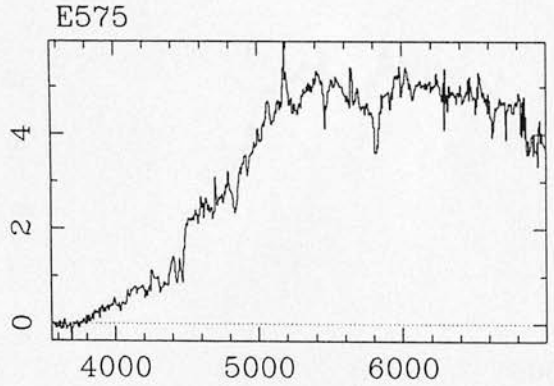
E575
0 2 4
4000 5000 6000

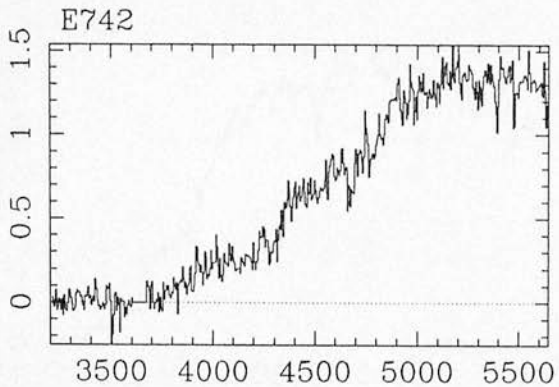
E742
0 0.5 1 1.5
3500 4000 4500 5000 5500

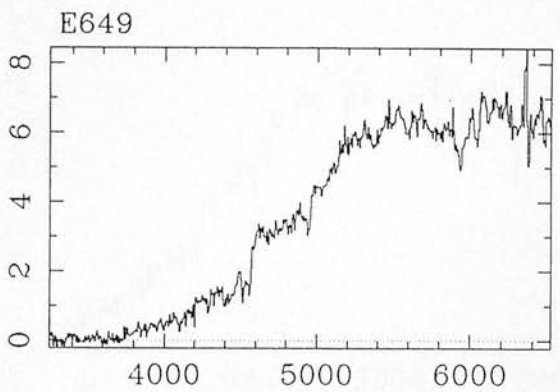
E649
0 2 4 6 8
4000 5000 6000

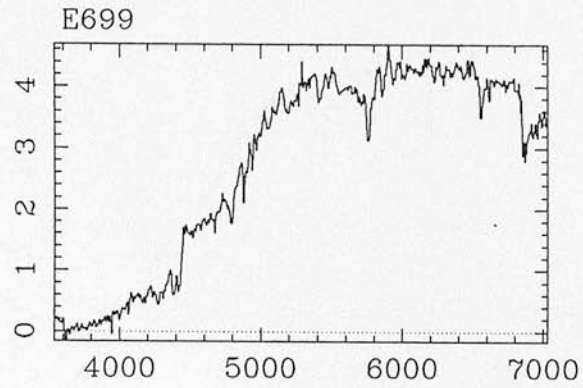
E699
0 1 2 3 4
4000 5000 6000 7000

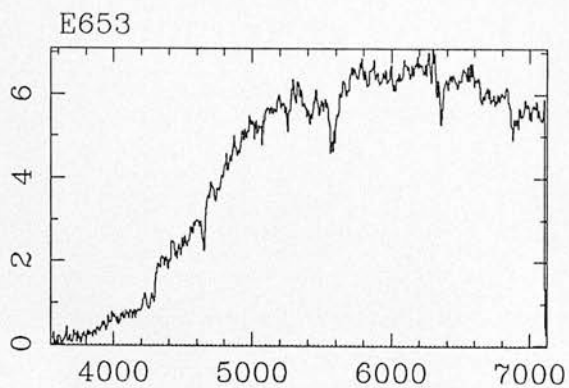
E653
0 2 4 6
4000 5000 6000 7000

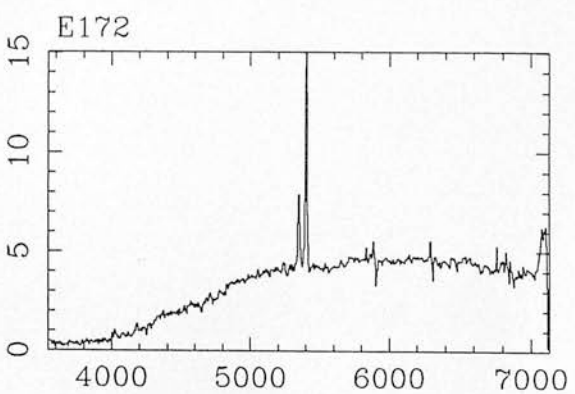
E172
0 5 10 15
4000 5000 6000 7000

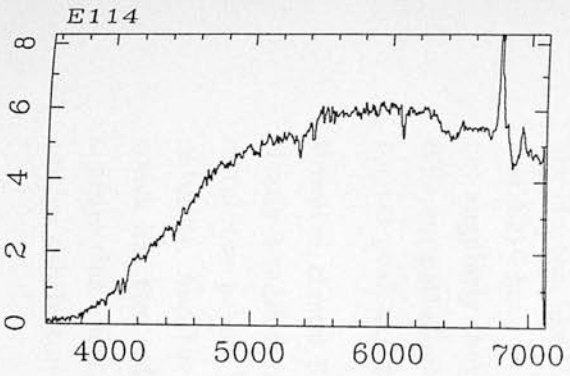
E114
0
2
4
6
8
4000
5000
6000
7000

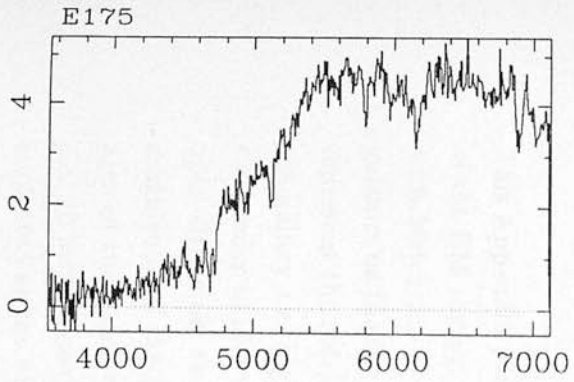
E175
0
2
4
4000
5000
6000
7000

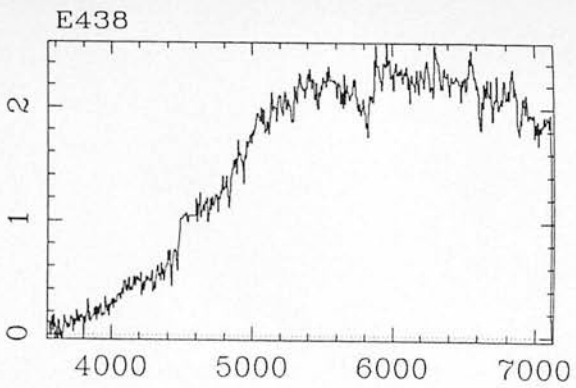
E438
0
1
2
4000
5000
6000
7000

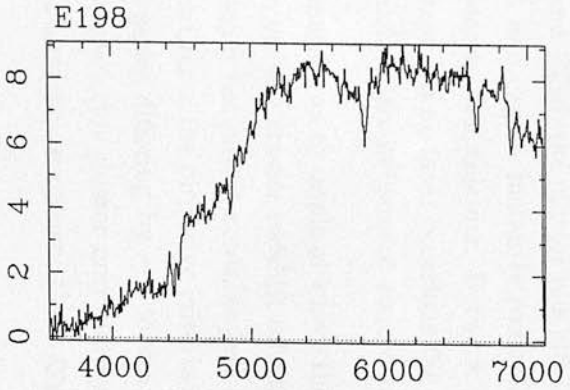
E198
0
2
4
6
8
4000
5000
6000
7000

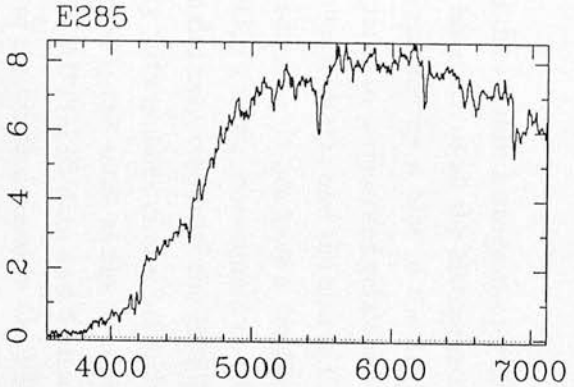
E285
0
2
4
6
8
4000
5000
6000
7000

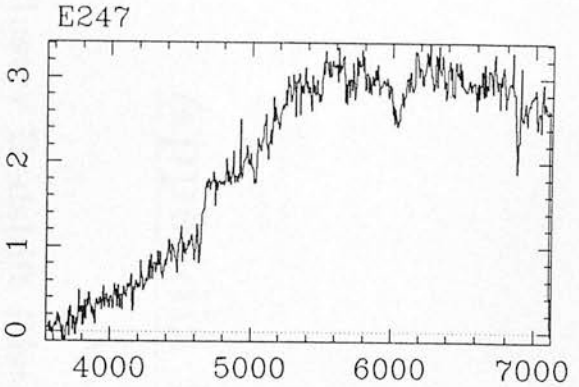
E247
0
1
2
3
4000
5000
6000
7000

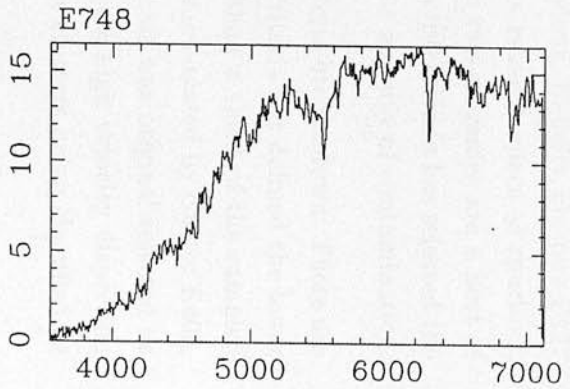
E748
0
5
10
15
4000
5000
6000
7000

Appendix E

Cluster Redshift Histograms

This Appendix presents the redshift histograms for 27 typical clusters observed as part of the EM survey. The binwidth of all the histograms is set at 700km s^{-1}. In addition, each histogram is accompanied by a plot of the angular distribution of the observed galaxies on the sky compared to unobserved galaxies within the EDSGC. The black dots represent the redshift measurements and the size of the dot is related to the redshift of the galaxy *i.e.* higher redshift galaxies have a smaller dot and vice versa. This allows the reader to identify which galaxies correspond to which peaks in the histogram. The open circles are the galaxies extracted from the EDSGC and their size is related to the magnitude of the galaxy with smaller circles being fainter to the limit $b_j = 20$. The area of the window plotted is the same as the window used for observing the clusters *i.e.* 40 arcminutes for the AUTOFIB data and 5 arcminutes for the ESO data. A star is plotted at the centre of cluster as defined in the EDCC.

These plots help to illustrate the objective criteria used to define the cluster redshift. For clusters like E712 and E658, the cluster redshift is obvious. Equally, clusters E127 and E216 have no peak and can be instantly recognised in redshift space as spurious, yet angularly they appear as real clusters. Between these two extremes are a host of different pathological cases, yet on most occasions the objective criteria has selected the correct peak and has made a fair judgement concerning the amount of contamination.

However, cluster E482 may be an example of where the criteria breaks down. There are clearly 2 redshift peaks, yet the cluster redshift selection criteria has defined the lower of the two as the interloper because it contains just less than a third of the sampled redshifts. Another limitation of the objective criteria is demonstrated by cluster E408, which has two redshift peaks differing by $\sim$ 1400km s^{-1} and was original selected as a projection effect. However, this cluster may simply have a high velocity dispersion and/or subclustering. Therefore, to prevent these types of clusters being classified as

projection effects, clusters with 2 or more peaks separated by less than 1500km s^{-1} were re–analysed using a single broad peak instead of the individual peaks. A full explanation of the cluster redshift selection criteria is given in Chapter 4.

(Note: For some of the plotted clusters, the number of black dots *i.e.* measured redshifts, does not match the number binned in the histograms. This is because some of the measured redshifts have not been identified within the EDSGC and therefore, have not been assigned an RA and Dec.)

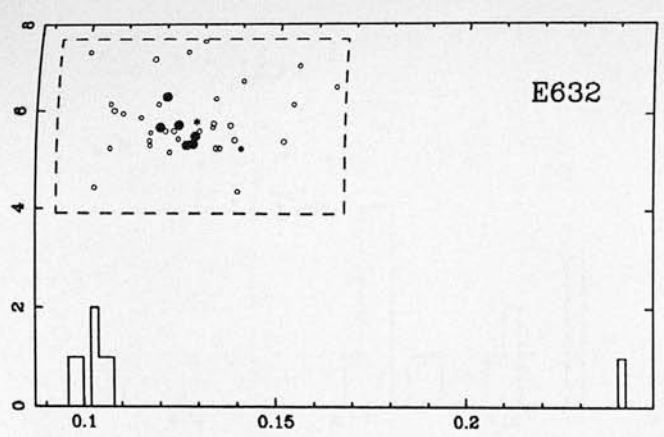
E632
0
2
4
6
8
0.1
0.15
0.2

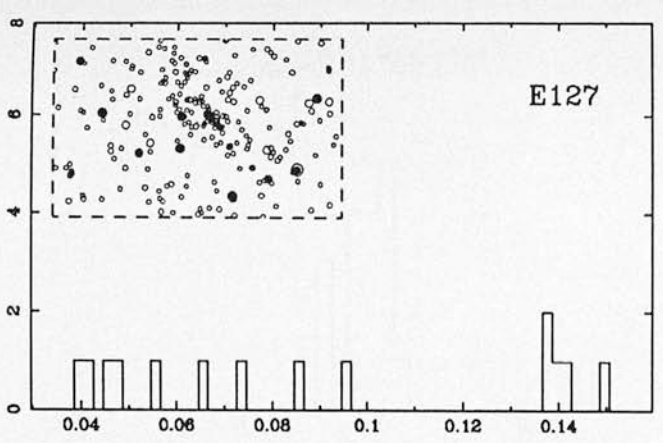
E127
0
2
4
6
8
0.04
0.06
0.08
0.1
0.12
0.14

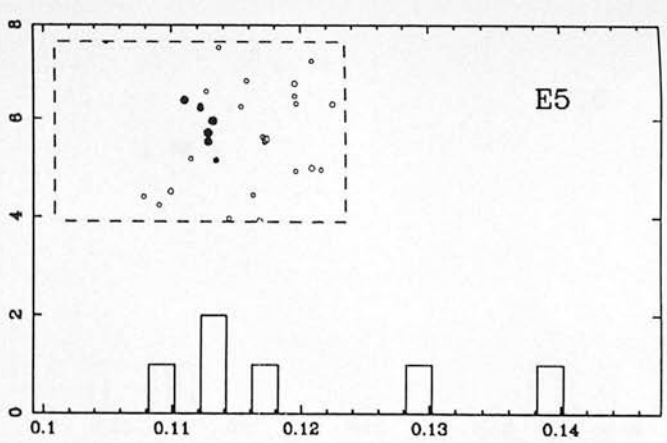
E5
0
2
4
6
8
0.1
0.11
0.12
0.13
0.14

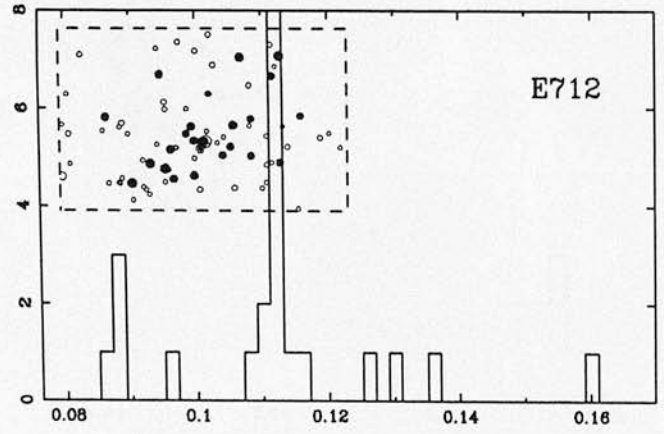
E712
0
2
4
6
8
0.08
0.1
0.12
0.14
0.16

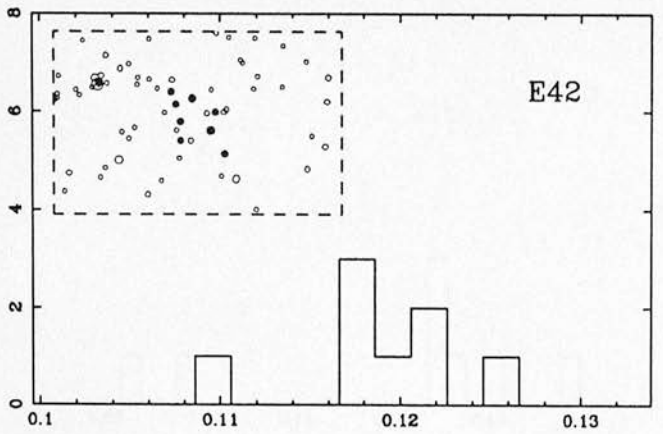
E42
0
2
4
6
8
0.1
0.11
0.12
0.13

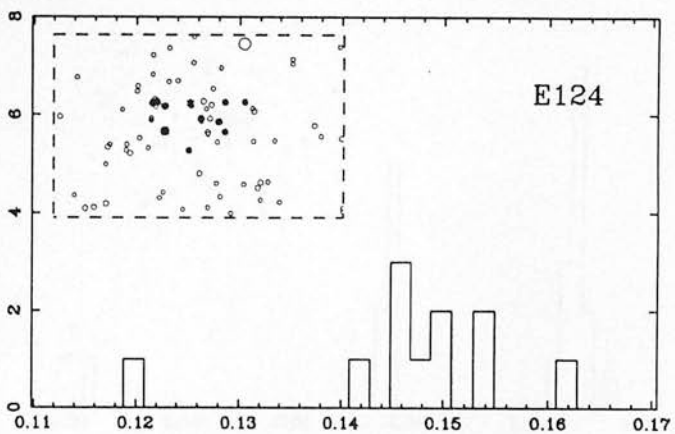
E124
0
2
4
6
8
0.11
0.12
0.13
0.14
0.15
0.16
0.17

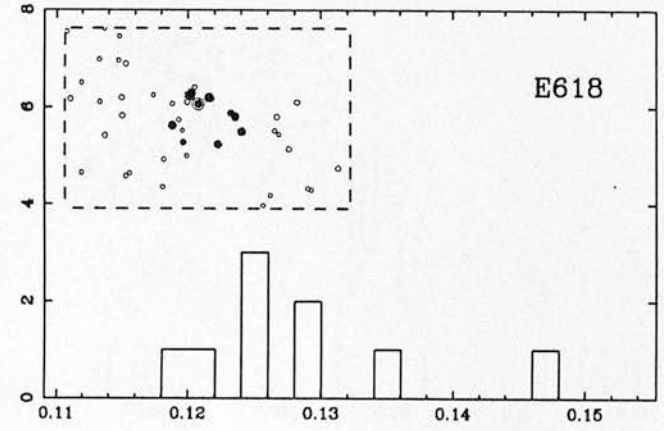
E618
0
2
4
6
8
0.11
0.12
0.13
0.14
0.15

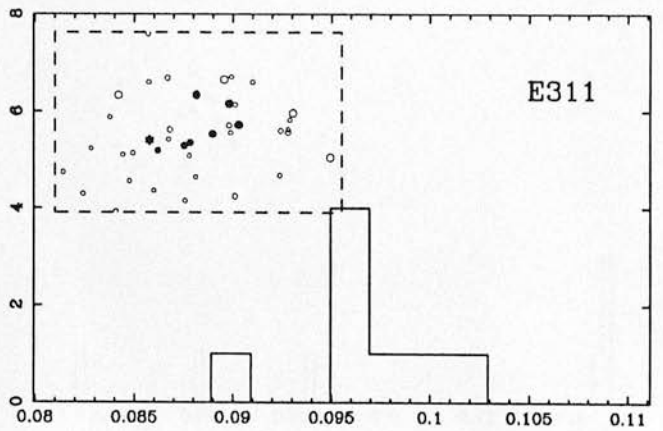
E311
0
2
4
6
8
0.08
0.085
0.09
0.095
0.1
0.105
0.11

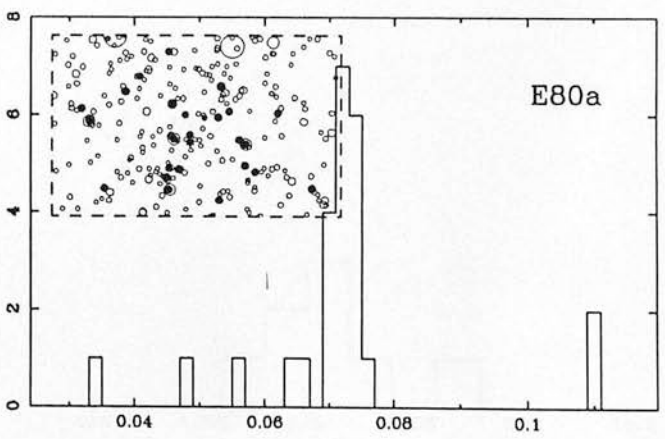
E80a
0
2
4
6
8
0.04
0.06
0.08
0.1

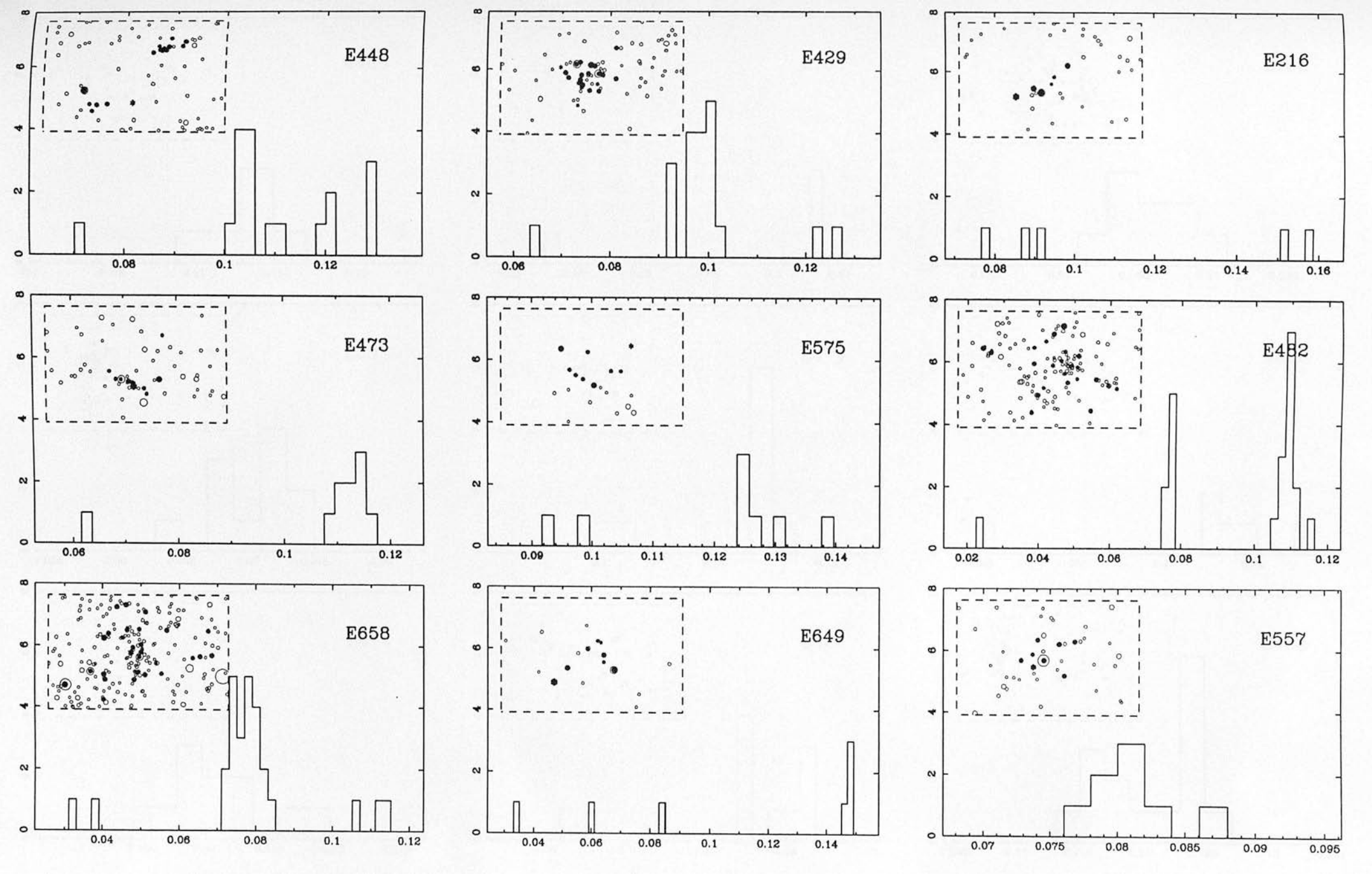
E448
E429
E216
E473
E575
E482
E658
E649
E557

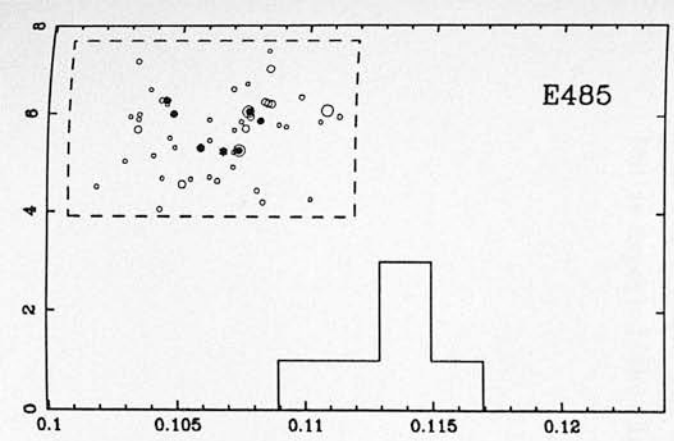
E485
0
2
4
6
8
0.1
0.105
0.11
0.115
0.12

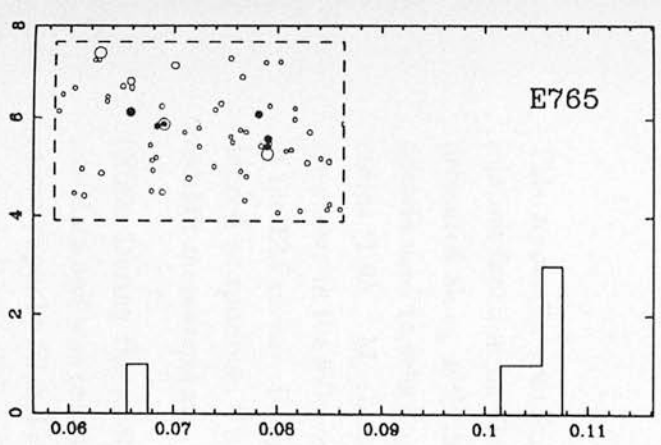
E765
0
2
4
6
8
0.06
0.07
0.08
0.09
0.1
0.11

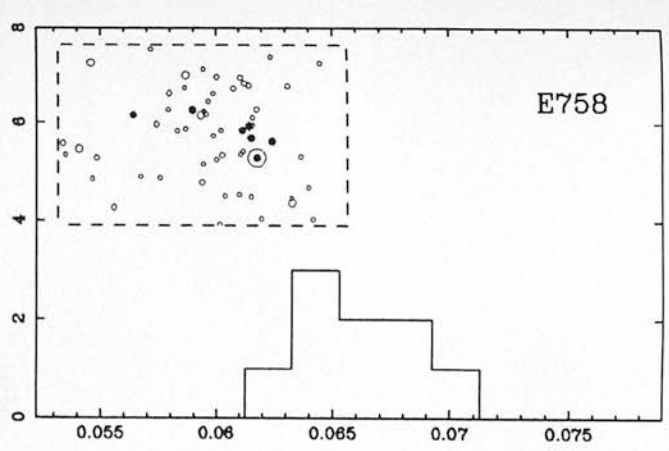
E758
0
2
4
6
8
0.055
0.06
0.065
0.07
0.075

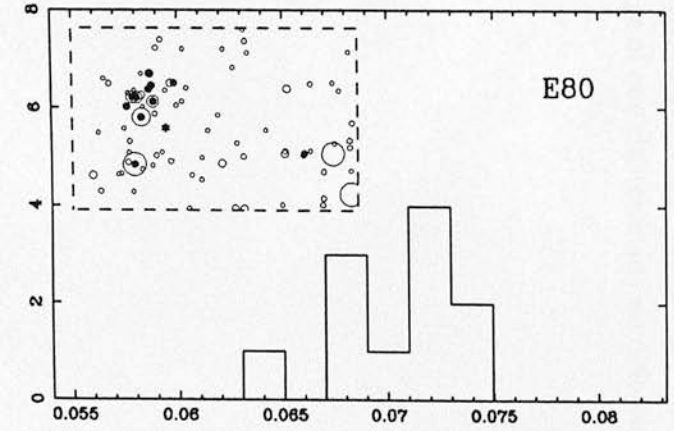
E80
0
2
4
6
8
0.055
0.06
0.065
0.07
0.075
0.08

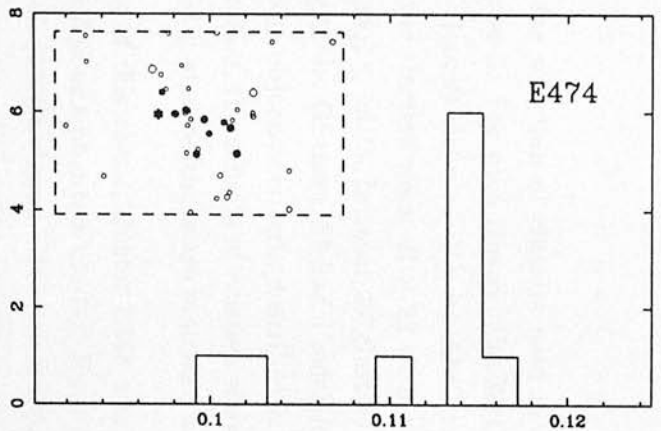
E474
0
2
4
6
8
0.1
0.11
0.12

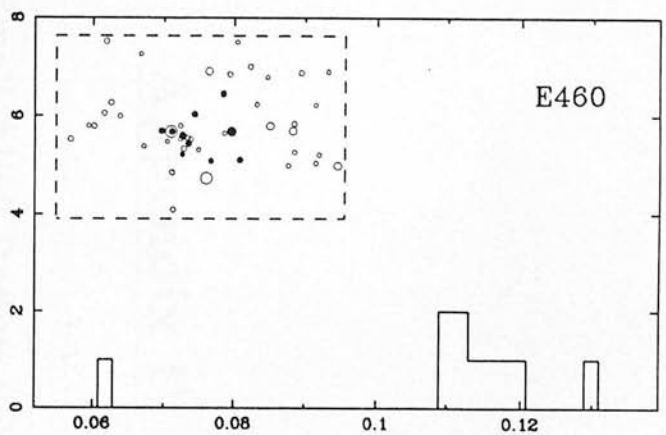
E460
0
2
4
6
8
0.06
0.08
0.1
0.12

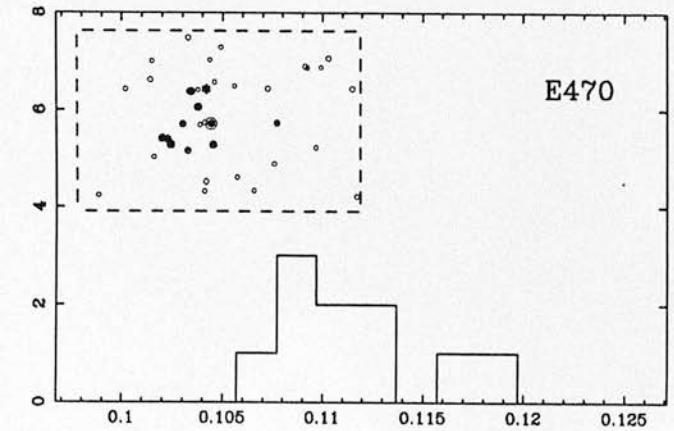
E470
0
2
4
6
8
0.1
0.105
0.11
0.115
0.12
0.125

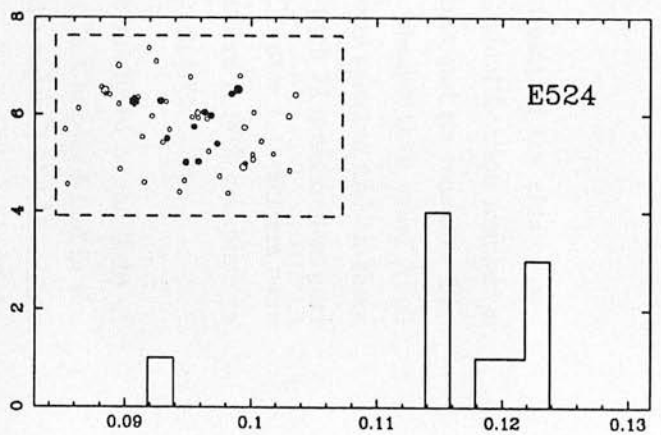
E524
0
2
4
6
8
0.09
0.1
0.11
0.12
0.13

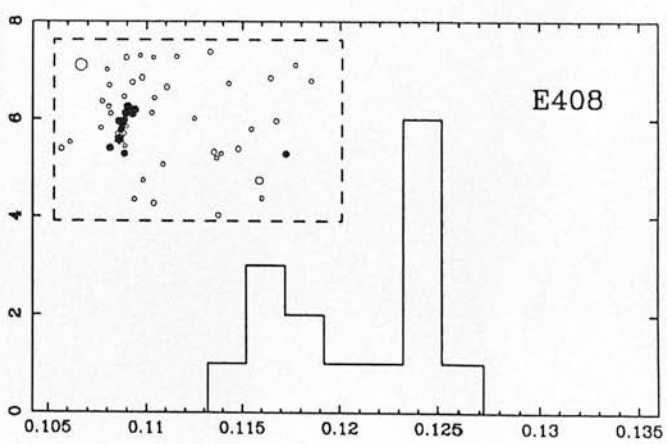
E408
0
2
4
6
8
0.105
0.11
0.115
0.12
0.125
0.13
0.135

Appendix F

The Small Abell Radius Selection

This Appendix contains the selection of clusters used in estimating the cluster correlation function in Chapter 5. For each cluster, the EDCC identification number is presented along with the clusters richness (R), its Abell radius and its redshift. The criteria used in selecting the clusters were: $R \geq 22$ within a smaller than usual Abell radius ($1.0h^{-1}$ Mpc); $m_{10}(b_j) \leq 18.75$. In total, 97 clusters were selected and all these are shown in the following table. Of these, 88 had a redshifts with 71 measured as part of the EM survey. Using the objective criteria described in Chapter 4, 9 clusters were defined as spurious. Therefore, the sample of clusters shown here is 90% complete in redshift measurements. Estimated redshifts are indicated as negative values.

(Note: During the writing of this thesis, cluster E448 was re–analysed in the light of new data and was re–classified as a phantom cluster. However, in Chapter 5 and in the recent paper by Nichol *et al.* (1992), cluster E448 was assigned a redshift of 0.103. This accounts for the different number of phantom clusters quoted in Nichol *et al.* (1992) to that quoted here. The correlation function was re–calculated with E448 as a phantom, but as expected, the change of one cluster made no difference.)

EDCC	R	RA (hrs)	Dec (°)	m_{10}	Rad.(°)	z
57	59	21.8929	-30.3894	18.1	0.172	0.09257
72	30	21.9529	-42.3415	18.3	0.157	-0.10179
80	26	21.9893	-22.6867	17.7	0.202	0.06939
86	26	22.0407	-30.7609	18.7	0.136	0.09401
114	24	22.1875	-36.9341	17.2	0.245	0.03396
124	75	22.2467	-35.9718	18.7	0.127	0.14661
127	67	22.2604	-39.1380	18.5	0.145	proj.
129	28	22.2662	-24.4540	16.8	0.300	0.03490
145	35	22.4161	-30.8406	17.0	0.271	0.05697
160	77	22.5228	-38.0097	18.7	0.138	0.15100
165	25	22.5602	-24.5798	17.7	0.197	-0.08276
172	25	22.5958	-37.0095	17.3	0.357	0.05766
173	31	22.5988	-37.3063	18.0	0.265	0.05690
175	34	22.6061	-38.0945	18.5	0.148	0.15354
176	35	22.6224	-36.3872	18.3	0.237	0.05700
178	28	22.6308	-34.2512	18.2	0.161	0.04971
188	35	22.7281	-36.3318	17.5	0.219	0.06710
201	37	22.7838	-31.4639	18.4	0.155	proj.
203	34	22.8016	-26.3320	18.3	0.153	-0.11590
216	58	22.8453	-25.7929	18.2	0.163	proj.
230	33	22.9367	-31.1217	18.6	0.141	0.10979
258	35	23.1330	-22.9033	18.7	0.131	0.11190
260	30	23.1412	-28.9869	18.7	0.131	proj.
261	22	23.1506	-29.3318	18.4	0.152	0.11700
263	29	23.1566	-41.0393	18.7	0.133	-0.10487
269	44	23.2080	-38.0204	18.6	0.140	proj.
279	22	23.2626	-27.7804	18.6	0.138	0.084
285	30	23.3082	-42.1218	17.7	0.199	proj.
297	42	23.4021	-24.1223	18.3	0.159	proj.
311	43	23.4760	-36.7978	18.1	0.253	0.09544
316	49	23.4990	-36.5579	17.4	0.343	0.09459
332	34	23.6500	-29.4983	17.8	0.194	0.05176

EDCC	R	RA (hrs)	Dec (°)	m_{10}	Rad.(°)	z
335	23	23.6602	-30.4931	18.7	0.136	0.07010
348	22	23.7416	-28.4315	16.2	0.430	0.02920
366	33	23.8713	-27.9481	17.7	0.205	0.07278
377	53	23.9462	-32.1652	17.8	0.185	0.05920
381	22	23.9538	-39.7623	18.5	0.145	0.10161
387	27	23.9722	-36.6634	18.6	0.134	-0.08888
392	34	0.0060	-34.9336	18.6	0.140	0.11272
394	24	0.0094	-36.2279	17.4	0.227	0.04902
396	22	0.0103	-27.4692	18.3	0.159	0.06780
398	29	0.0260	-23.4067	18.6	0.140	-0.11280
400	80	0.0628	-34.9861	18.5	0.147	0.11307
407	25	0.1091	-35.5799	17.7	0.196	0.04890
410	25	0.1469	-29.1237	17.4	0.225	0.06153
418	32	0.2117	-24.0956	17.1	0.264	0.06575
419	35	0.2134	-26.3345	18.7	0.133	0.12887
424	22	0.2337	-34.1191	18.4	0.141	0.07548
429	63	0.2519	-35.4238	18.0	0.176	0.09693
431	30	0.2687	-42.0268	18.2	0.166	0.09230
437	59	0.3023	-25.9316	18.5	0.145	0.06337
446	22	0.4283	-35.7348	18.7	0.130	0.10740
447	46	0.4343	-23.9006	18.4	0.152	0.11291
448	22	0.4390	-30.3569	18.7	0.181	proj.
450	26	0.4582	-29.7010	18.5	0.143	proj.
460	30	0.5783	-28.7047	17.9	0.183	0.11308
462	35	0.5841	-39.4290	18.5	0.147	0.06316
473	44	0.6623	-28.8368	18.0	0.265	0.10799
474	22	0.6873	-26.2889	18.6	0.203	0.11256
480	23	0.7649	-42.2769	18.5	0.141	0.05400
482	54	0.7812	-29.8069	18.0	0.177	0.10844
495	55	0.8830	-26.6521	18.1	0.176	0.11412
500	40	0.9017	-30.3112	18.8	0.134	0.11320
505	26	0.9086	-29.9664	18.5	0.147	-0.08819

EDCC	R	RA (hrs)	Dec (°)	m_{10}	Rad.(°)	z
507	23	0.9113	-26.5099	18.4	0.155	0.11300
519	37	1.0391	-40.0608	18.2	0.164	0.10730
520	70	1.0369	-24.2585	18.6	0.138	0.16038
524	55	1.0945	-37.0155	18.6	0.137	0.11752
546	27	1.3282	-39.8952	18.6	0.141	-0.10630
553	25	1.3897	-39.7377	18.1	0.168	0.08791
555	22	1.3897	-29.8039	18.4	0.148	0.14182
557	42	1.3985	-38.2354	18.1	0.168	0.07969
570	29	1.5017	-42.3986	17.9	0.185	0.08786
575	29	1.5297	-27.7723	18.0	0.175	0.12545
587	31	1.6618	-42.3926	17.6	0.214	0.07677
591	28	1.6961	-35.5665	17.6	0.211	0.06762
606	33	1.9777	-33.1235	18.0	0.179	0.10045
618	30	2.0225	-41.3508	18.4	0.153	0.12480
645	30	2.3885	-29.7384	18.1	0.170	-0.08134
653	30	2.4558	-33.6999	18.3	0.153	0.07924
658	43	2.4768	-33.3105	18.5	0.141	0.07636
683	22	2.7081	-26.4860	18.3	0.162	0.13364
699	65	2.8206	-25.1424	18.2	0.163	0.11113
700	27	2.8265	-25.8082	18.4	0.151	0.11200
707	26	2.8636	-33.6735	17.9	0.187	-0.0842
712	26	2.9064	-24.9128	18.6	0.138	0.11092
717	43	2.9982	-37.2044	17.3	0.241	0.06616
726	26	3.0774	-39.0101	18.5	0.143	0.08737
729	24	3.1048	-23.9127	17.4	0.225	0.06650
728	38	3.1064	-36.8876	17.3	0.237	0.06748
735	22	3.1631	-27.1850	17.4	0.230	0.06826
742	25	3.1970	-38.5115	17.9	0.187	0.08384
748	29	3.2186	-29.4178	17.7	0.202	0.06708
758	36	3.3398	-41.5052	17.9	0.187	0.06487
762	23	3.5386	-39.1318	17.3	0.236	0.06217
763	25	3.5484	-39.6623	18.2	0.152	0.10300
765	22	3.5847	-39.9365	18.0	0.177	0.10432

Appendix G

Published Papers

The work presented in this thesis has resulted in four papers published in the astronomical literature. These papers are presented in this Appendix.

Accepted for publication
in *The Astrophysical Journal Letters*

The Distribution of Rich Clusters of Galaxies in the South Galactic Pole Region*

Luigi Guzzo[1], Chris A. Collins[2],
Robert C. Nichol[3] & Stuart L. Lumsden[4]

[1] *Osservatorio Astronomico di Brera, Sezione di Merate, Via Bianchi 46, I-22055 Merate, Italy.*

[2] *Royal Observatory, Blackford Hill, Edinburgh EH9 3HJ, U.K.*

[3] *Department of Astronomy, University of Edinburgh, Blackford Hill, Edinburgh EH9 3HJ, U.K.*

[4] *Astrophysics Department, University of Oxford, Keble Road, Oxford OX1 3RH, U.K.*

* Based partly on data collected at the European Southern Observatory, La Silla, Chile.

ABSTRACT

We present the first results from the Edinburgh–Milano cluster redshift survey. This survey consists of ~ 800 galaxy redshifts for ~ 100 rich clusters contained in the Edinburgh/Durham Cluster Catalogue. The most striking result is the close correspondence between the maxima in the cluster redshift distribution and the periodic peaks discovered by Broadhurst *et al.* in their pencil beam galaxy survey at the south galactic pole. Particularly impressive is an elongated concentration of ~ 20 systems at $z \sim 0.11$, found to be responsible for giving rise to the 3^{rd} peak. These observations leave little doubt about the structural reality of the fluctuations observed by Broadhurst *et al.* .

Subject headings: cosmology – galaxies: clustering – clusters of galaxies

1. INTRODUCTION

Our view of the spatial distribution of matter in the universe has changed dramatically during the last decade. Essentially, this has been due to the increasingly large number of galaxies for which a redshift has been measured, allowing the reconstruction of their true three–dimensional distribution.

Wide–angle redshift surveys, like the Arecibo HI survey (Haynes & Giovanelli 1988) or the CfA survey (Geller & Huchra 1989) have clearly established the existence of both overdense (superclusters) and underdense (voids) regions, with sharp boundaries and sizes exceeding 50 h^{-1} Mpc. Some of the most striking results on this subject have come from deep ($\sim 10^3$ h^{-1} Mpc) "pencil beam" surveys (Koo & Kron 1987; Broadhurst, Ellis & Shanks 1988). These present a complementary approach to the wide–angle studies, presently limited to depths of $\sim 10^2$ h^{-1} Mpc. Combining the data from two beams lying in op-

posite directions, towards the north galactic pole and south galactic pole (SGP), Broadhurst *et al.* (1990, hereafter BEKS) have been able to show a remarkable periodicity in the distribution of galaxies along the z direction, spanning almost 2000 h^{-1} Mpc. The peaks shown in their redshift histogram are separated by a comoving distance of 128 h^{-1} Mpc, a measure confirmed by a one–dimensional power–spectrum and autocorrelation analysis. The authors suggest that the observation could be consistent with a cellular distribution of galaxies, where the phenomenon would be observed only along some preferential directions. In fact, statistical studies seem to show that if the galaxy distribution can be realistically modelled through a Voronoi tessellation model, then the BEKS result is statistically plausible (Coles 1990; Ikeuchi & Turner 1991; van de Weygaert 1991). On the other hand, other authors caution against the risks of over–interpreting the 128 h^{-1} Mpc periodicity as evidence for real 3D clustering power on similar scales (Kaiser & Peacock, 1991). In order to understand the real meaning of this result, it is crucial to study the galaxy distribution in different directions, in particular in regions adjacent to the deep probes where the periodicity has been detected.

All the surveys discussed above have involved the study of the galaxy distribution. An alternative approach to the study of the large–scale structure of the universe is to use galaxy clusters as tracers (see Bahcall 1988 for a review). The main advantage of this approach is the possibility of probing much larger scales than with galaxy redshift surveys. The practical benefit is the reduced number of redshifts to be measured, in comparison with a galaxy survey filling the same volume of space.

Until recently, there have been serious problems in using clusters as tracers of the large–scale structure. These have arisen from the selection biases and

incompleteness that are thought to affect presently available eye–compiled cluster catalogues (Abell 1958; Abell, Corwin & Olowin 1989 ACO), as discussed by several authors (e.g. Lucey 1983; Postman, Geller & Huchra 1986; Sutherland 1988; Dekel *et al.* 1989). The recent completion of the fully automated Edinburgh/Durham Cluster Catalogue (EDCC, Lumsden *et al.* 1992) provides an excellent opportunity to overcome these problems (Nichol *et al.* 1992). The full EDCC consists of 737 clusters selected from the Edinburgh/Durham Southern Galaxy Catalogue (Heydon–Dumbleton *et al.* 1989) and covers an area of $80° \times 20°$ centered at the SGP. We have obtained spectra of about 800 galaxies for a subsample of the EDCC comprising $\sim$ 100 clusters, with the aim of investigating their spatial distribution and correlation properties (e.g. Nichol *et al.* 1992). This database constitutes the Edinburgh–Milano cluster redshift survey.

This *Letter* presents a preliminary discussion of the spatial distribution of this cluster redshift sample. The most striking feature is the close correspondence between the peaks in our cluster redshift distribution and those evident in the BEKS galaxy data in the corresponding redshift range. In particular, the peak at $z \simeq 0.11$ is caused by a large concentration of about 20 clusters extending for more than 100 h^{-1} Mpc almost perpendicularly to the line of sight. This result, while confirming that the BEKS peaks are certainly due to real structure, also demonstrates further proof of the high degree of inhomogeneity still present on the scales of rich clusters.

2. THE DATA

The sample discussed here contains 104 clusters and is composed of the 90% complete $R \geq 22$ sample used in Nichol *et al.* (1992) for the correlation analysis,

together with another 25 clusters of lower richness which have also been observed as part of the redshift survey. One unique feature of our redshift survey is the fact that we have observed on average 10 galaxies in the direction of each cluster core. This observing strategy has two advantages. First, it allows us to reduce the error on the estimate of the cluster redshift. Secondly, and more importantly, we can identify galaxy interlopers and spurious clusters produced by projection effects. In fact, a total of 8 clusters were identified as spurious and removed from the Edinburgh-Milano survey. The completeness limit of the $R \geq 22$ cluster redshift sample which forms 80 % of the total number of redshifts, can be estimated from the results of Lumsden *et al.* (1992). In this paper it is shown that the EDCC number counts are Euclidean for $m_{10}(b_j) < 18.75$. Using the m_{10} vs. *log* z relation for our data (Nichol 1992), this magnitude corresponds to a completeness limit in redshift of $z \simeq 0.13$. In addition, we expect to be missing a few systems with $z < 0.03$ (Lumsden *et al.* 1992).

3. RESULTS AND DISCUSSION

Figure 1a shows the right ascension cone diagram for all the 104 clusters in our redshift sample. The declination range ($-22.5° < \delta < -42.5°$) has been compressed onto the plane of the figure. The most striking feature in this plot is the strong concentration of clusters around 0.5^h, at $z \simeq 0.11$, containing ~ 20 clusters. Inspection of the declination distribution in the right ascension range $23.4^h \leq \alpha \leq 1.2^h$, containing this structure (Figure 1b), shows that it is elongated in the declination direction. Also notable in both figures are the large regions of scale $\sim 100\ h^{-1}$ Mpc, where no rich clusters are detected.

Figure 2 shows the redshift histograms for wedges containing the central supercluster (b), and those on either side (a, c). The filled circles in Figure 2b

mark the position of the first four maxima observed in the BEKS pencil beam survey towards $\alpha = 0.9^h$ and $\delta = -27.5°$. The BEKS peaks and the structures delineated by the clusters in our survey show a striking one to one correspondence over the redshift range for which our data are expected to be reasonably complete ($0.03 < z < 0.13$). As a check on possible biases related to the incompleteness of the total sample, also shown in Figure 2 is the histogram for the complete $R \geq 22$ richness–limited sample. This clearly shows the same features as the total redshift sample.

These data represent confirmation of the reality of the structure seen in the SGP narrow probe. It is also clear from Figure 1 that the structures giving rise to the peaks in the redshift distribution, while of considerable extent, are nevertheless confined within a wedge of about $8° \times 20°$, corresponding to a linear size for the structure at $z = 0.11$ of $\sim 60\ h^{-1}$ Mpc in right ascension and $\sim 140\ h^{-1}$ Mpc in declination.

The coincidence of known superclusters with the BEKS peaks has been recently discussed by Bahcall (1991). This paper indicates that at the SGP the Perseus–Pisces Supercluster (Giovanelli, Haynes & Chincarini 1986) contributes at $z \sim 0.02$ and the spike near $z \sim 0.06$ is coincident with the Bahcall & Soneira (1984, BS) listed supercluster BS1. The structure isolated by us at $z \sim 0.11$ is not included in the BS supercluster catalogue (limited to $z \leq 0.08$), but corresponds to the known Sculptor Supercluster overdensity (Seitter *et al.* 1989). An attempt to identify the origin of the BEKS peaks in the Abell/ACO catalogues has been made by Tully *et al.* (1992), although the coincidence they find is much less apparent than can be seen in Figures 1 and 2. In a recent paper, Schuecker & Ott (1991), analyse the distribution of galaxies in an objective prism redshift survey of the southern sky. They find no evidence for periodic

peaks in the volume probed by the BEKS pencil beam. The clear detection of the peaks in our cluster survey suggests that most probably the periodic signal is washed out in their data by the large observational redshift errors.

Kaiser and Peacock (1991) model the BEKS data using a one-dimensional power-spectrum analysis. They claim that such an apparent periodicity in a pencil-beam survey can be understood as chance events associated with standard small-scale galaxy correlations. Our data seem to be inconsistent with this conclusion, since the discovery that clusters of galaxies trace the BEKS peaks provides a strong indication that the spike features are the result of real structure in the universe on scales $\sim 100\ h^{-1}$ Mpc.

Models of the large-scale structure which incorporate a cellular or foam type structure have tried to explain the BEKS periodicity as slices through the walls of a much larger structure (Coles 1990; Kurki-Suonio *et al.* 1990; Ikeuchi & Turner 1991; van de Weygaert 1991). In principle our data can distinguish between models of this kind by placing constraints on the frequency of the periodicity. For example, Kurki-Suonio *et al.* (1990), who analyse a model where the galaxies reside on the surface of bubbles or sheets, whose centers are anticorrelated, predict deviations of only $\sim 15\% - 20\%$ from regular periodicity along any line of sight. In the Voronoi cellular model of van de Weygaert (1991), on the other hand, there is a 15% probability of a beam showing a regular pattern in any random direction, with peaks separated by $\sim 100\ h^{-1}$ Mpc. From our data, the probability that a random line of sight direction will intersect both the structures at $z = 0.06$ and $z = 0.11$ and thereby produce a regular structure is $\simeq 20\%$. At face value our data therefore appear consistent with the Voronoi model and definitely inconsistent with the model discussed by Kurki-Suonio *et al.* (1990).

In summary, this work demonstrates the reality of the BEKS peaks. In the redshift range of the Edinburgh–Milano cluster survey, they appear to be associated with concentrations of rich clusters of galaxies. We have compared our data with the predictions of specific models proposed to explain the BEKS observations. In general, such cluster surveys appear to provide a strong observational framework with which to confront cosmological models.

ACKNOWLEDGMENTS

It is a pleasure to thank N. Heydon–Dumbleton for his contribution during the early phases of this project. We thank J. Huchra for the use of both published and unpublished data. Fruitful discussions with T. Broadhurst are gratefully acknowledged. This paper uses data from the COSMOS measuring machine facility.

References

Abell, G.O. 1958, *ApJ*, **3**, 211

Abell, G.O., Corwin, H.G., Olowin, R.P. 1989, *ApJS*, **70**, 1

Bahcall, N.A. 1988, Ann. Rev. Astron. Astrophys., **26**, 631

Bahcall, N.A. 1991, *ApJ*, **376**, 43

Bahcall, N.A., & Soneira, R.M. 1984, *ApJ*, **277**, 27

Broadhurst, T.J., Ellis, R.S., Koo, D.C., & Szalay, A.S. 1990, *Nature*, **343**, 726 (BEKS)

Broadhurst, T.J., Ellis, R.S., & Shanks, T. 1988, *MNRAS*, **235**, 827

Coles, P. 1990, *Nature*, **346**, 446

Dekel, A., Blumenthal, G.R., Primack, J.R., & Olivier, S. 1989, *ApJ*, **338** , L5

Geller, M., & Huchra, J.P. 1989, *Science*, **246**, 897

Giovanelli, R., Haynes, M.P., & Chincarini, G. 1986, *ApJ*, **300**, 77

Haynes, M.P., & Giovanelli, R. 1988, in *Large-Scale Motions in the Universe*, eds. Rubin V.C., & Coyne G.V. (Pontificia Academia Scientiarum, Vatican City & Princeton University Press, Princeton), p. 31

Heydon–Dumbleton, N.H., Collins, C.A., & MacGillivray, H.T. 1989, *MNRAS*, **238**, 379

Ikeuchi, S., & Turner, E.L. 1991, *MNRAS*, **250**, 519

Kaiser, N., & Peacock, J.A. 1991, *ApJ*, **379**, 482

Koo, D.C., & Kron, R. 1987, in *Observational Cosmology*, eds. Hewitt, A., Burbidge, G.R., & Fang, L.Z., (Reidel, Dordrecht), p. 383

Kurki-Suonio, H., & Mathews, G.J., & Fuller, G.M. 1990, *ApJ*, **356**, L5

Lucey, J.R. 1983, *MNRAS*, **204**, 33

Lumsden, S.L., Nichol, R.C., Collins, C.A., & Guzzo, L. 1992, *MNRAS*, in press

Nichol, R.C. 1992, PhD thesis, University of Edinburgh

Nichol, R.C., Collins, C.A., Guzzo, L., & Lumsden, S.L. 1992, *MNRAS*, in press

Postman, M., Geller, M.J., & Huchra, J.P. 1986, *AJ*, **91**, 1267

Seitter, W.C., Ott, H.A., Duemmler, R., Schuecker, P., & Horstmann, H. 1989, in *Lecture Notes in Physics, Vol. 322, Morphological Cosmology*, eds. Flin, P. & Duerbeck, H.W., (Springer, Berlin), p 3

Schuecker, P., & Ott, H.–A. 1991, *ApJ*, **378**, L1

Sutherland, W. 1988, *MNRAS*, **234**, 159

Tully, R.B., Scaramella, R., Vettolani, G., & Zamorani, G. 1992, *ApJ*, in press

van de Weygaert, R. 1991, *MNRAS*, **249**, 159

Figure Captions

Figure 1

a) Right ascension wedge diagram showing the whole sample of 104 clusters in the declination range $-22.5°$ to $-42.5°$. b) Declination wedge diagram showing only the central right ascension range $23.4^h \leq \alpha \leq 1.2^h$. The two structures giving rise to the 2^{nd} and 3^{rd} peaks of BEKS towards $\alpha = 0.9^h$ and $\delta = -27.5°$ are clearly evident.

Figure 2

Histograms of the redshift distribution in three right ascension ranges: a) $21.5^h \leq \alpha \leq 23.4^h$; b) $23.4^h \leq \alpha \leq 1.2^h$; c) $1.2^h \leq \alpha \leq 3.5^h$. Filled circles in panel b) mark the position of the observed peaks in the BEKS survey. The dot–dashed line shows the same histogram, but using only the clusters from the complete $R \geq 22$ richness–limited sample.

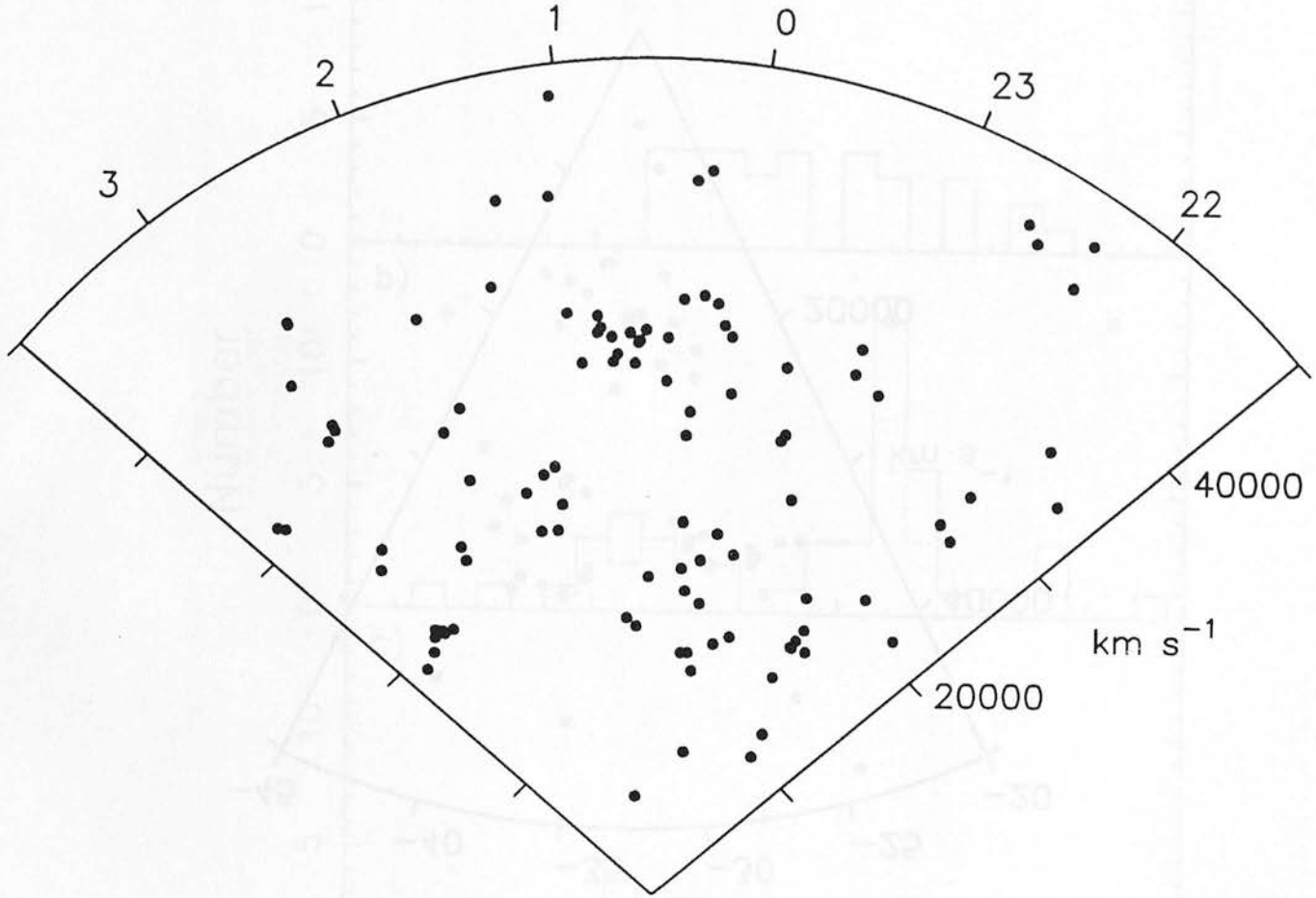

Fig. 1a

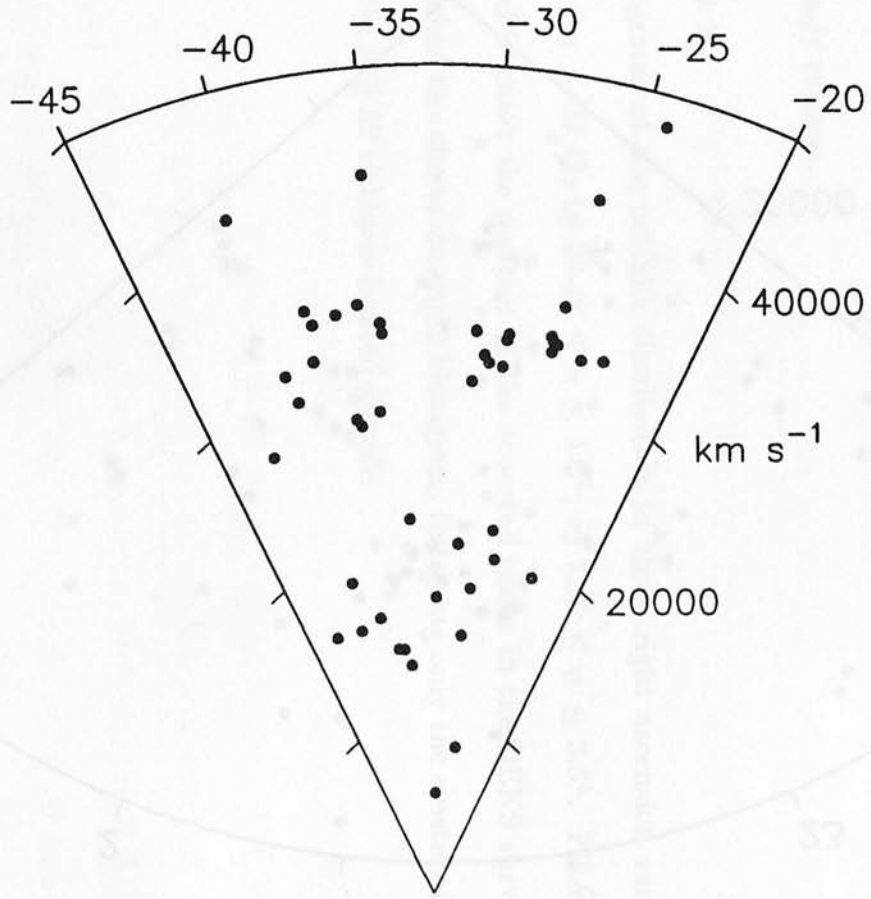

Fig. 16

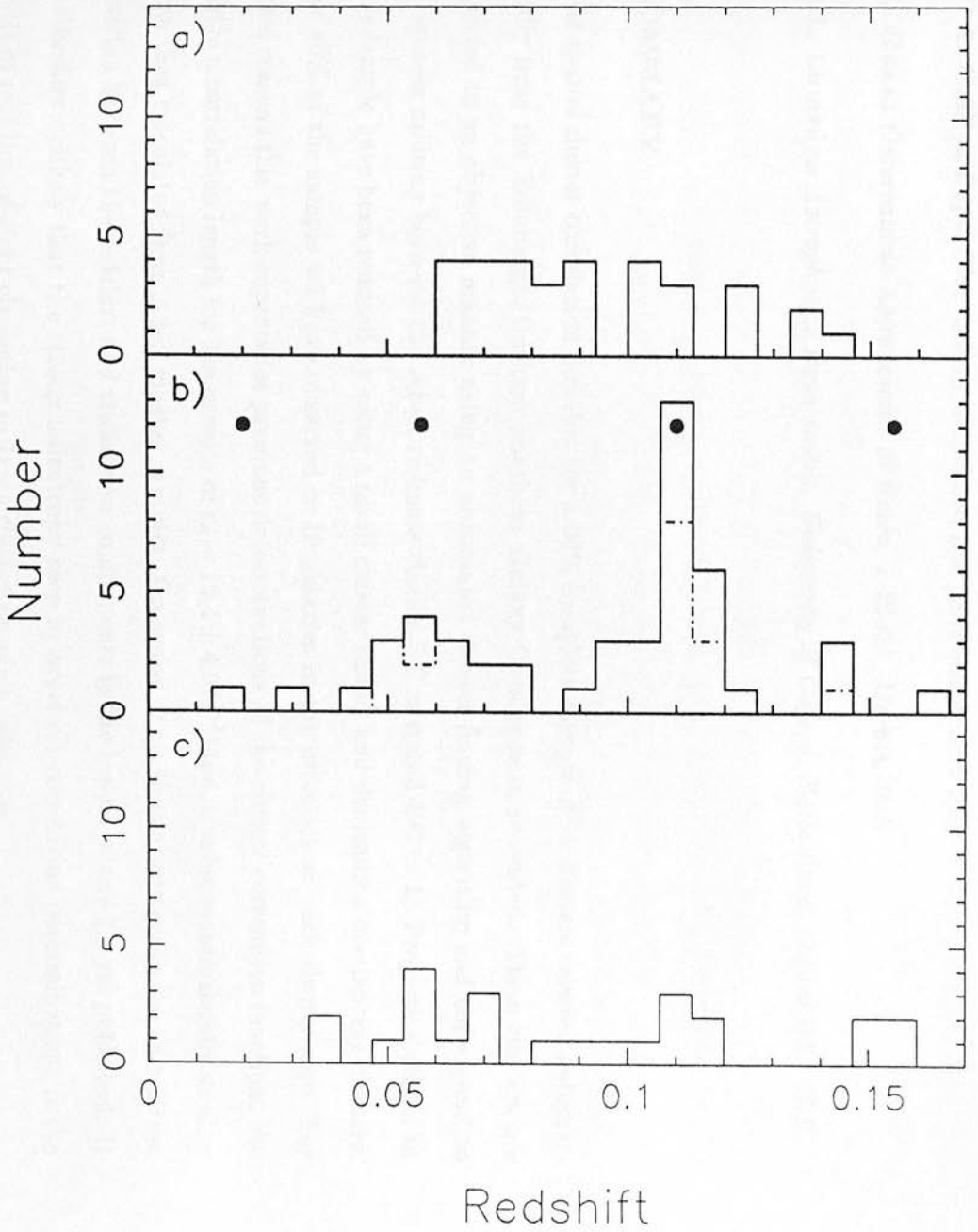

Fig 2

Accepted for publication
in *Monthly Notices of the Royal Astronomical Society*

The Edinburgh/Durham Southern Galaxy Catalogue - V. The Cluster Correlation Function†

R.C. Nichol *Department of Astronomy, University of Edinburgh, Blackford Hill, Edinburgh EH9 3HJ*

C.A. Collins *Royal Observatory, Blackford Hill, Edinburgh EH9 3HJ*

L. Guzzo *Osservatorio Astronomico di Brera, I–22055, Merate, Italy*

S.L. Lumsden *Astrophysics Department, University of Oxford, Keble Road, Oxford OX1 3RH*

SUMMARY

The spatial cluster correlation function for a 90% complete sample of 79 clusters selected automatically from the Edinburgh/Durham Southern Galaxy Catalogue is presented. These clusters are selected in an objective manner using an automated cluster finding algorithm and correspond to a richness midway between the Abell richness classes RC = 0 and RC = 1. Projection effects in this sample have been reduced by using a small cluster radius and deblending overlapping clusters. For 80% of the sample we have observed $\simeq$ 10 galaxies in the direction of each cluster core. For these reasons this work supercedes previous determinations of the cluster correlation function. We derive a correlation length for the sample of $r_0 = 16.4 \pm 4.0\, h^{-1}$Mpc, a value systematically smaller than that calculated from Abell cluster samples. On scales $\simeq r_0$, the anisotropy in the correlation function between the redshift and transverse components is the lowest of any ξ_{cc} yet published. It is therefore unlikely that the strong anisotropy seen in previous correlation determinations is the result of real line-of-sight clustering or large cluster peculiar velocities.

†Based in part on data collected at the European Southern Observatory, La Silla, Chile.

1 INTRODUCTION

One of the most controversial results in cosmology over the last decade has been the amplitude of the two-point spatial cluster-cluster correlation function (ξ_{cc}). The bench mark for such studies is the work of Bahcall & Soneira (1983), who use a statistical cluster sample consisting of 104 redshifts which constitute all the high galactic latitude RC $\geq$ 1, D $\leq$ 4 Abell clusters (Abell 1958). Their correlation function has the form $\xi_{cc}(r) = (r/r_0)^{-1.8}$, with $r_0 = 25\,h^{-1}$Mpc. If correct, this result provides a strong indication that clusters are $\simeq$ 15 times more clustered than galaxies on the same spatial scale. More recently, Postman, Huchra & Geller (1992; PHG) analyse a complete magnitude limited sample of 351 Abell clusters. They find a correlation scale-length of $20.0 \pm 4.0\,h^{-1}$Mpc. Correlation scale-lengths as large as this imply that galaxies and clusters cannot both be tracers of the large-scale matter distribution. One implication of a scale-length $r_0 \simeq 20\,h^{-1}$Mpc is that it is inconsistent with a flat universe dominated by cold dark matter (*e.g.* White *et al.* 1987). Although these results have had a major impact, the cluster samples in each case are based on the Abell (1958) cluster catalogue which has been the focus of substantial criticism. The Bahcall & Soneira (1983) result has been criticized on the grounds that the Abell cluster catalogue contains projection effects. Sutherland (1988) suggests that such effects cause spurious line-of-sight elongations of ξ_{cc}. When corrected for projection effects the correlation amplitude is much reduced to a scale length $r_0 = 14\,h^{-1}$Mpc, a value not too discordant with the cold dark matter model. However, Dekel *et al.* (1989) conclude that the uncertainties inherent in this decontamination procedure are too large for the resulting ξ_{cc} to constrain the standard theory. In any case the decontamination correction may over correct, since elongations in the redshift direction may be due to peculiar velocities $\simeq 2000\,\mathrm{km\,s^{-1}}$ or real geometry of the clusters in space (Bahcall, Soneira & Burgett 1986; Jing, Plionis & Valdarnini 1992). In addition to the uncertainties introduced by projection effects, it has been recognised for some time that the intrinsically subjective nature of the Abell catalogue gives rise to severe problems in homogeneity and statistical completeness (Postman, Geller & Huchra 1986).

In this paper we report on the ξ_{cc} for a sample of galaxy clusters selected automatically from the Edinburgh/Durham Southern Galaxy Catalogue (EDSGC). This is a digitised galaxy survey covering $\simeq 1400\,\mathrm{deg}^2$ at the South Galactic Cap. The advantage of using a machine-based cluster sample is that it provides a completely objective set of clusters. In addition, great care has been taken in the selection procedure to reduce the effects of cluster projection (see Section 2). Both these factors enable us to avoid the major criticisms which befall cluster samples that have been selected from the Abell catalogue.

2 THE CLUSTER SAMPLE

The details of the EDSGC and statistical results on the galaxy clustering are reported in earlier papers of this series (see Collins, Nichol & Lumsden 1992; Paper-III). Lumsden *et al.* (1992) present the complete sample of 737 clusters selected from the EDSGC along with a detailed description of the cluster-finding algorithm.

There are two aspects to the selection of clusters which are specifically designed to reduce projection effects. Firstly, the sample was corrected by deblending clusters which had overlapping radii. Galaxies in the overlap region were assigned to the appropriate cluster based on a Gaussian fit to the cluster density profiles. Secondly, to select the sample for the correlation function a radius $r_A = 1\,h^{-1}$Mpc was used in place of the $r_A = 1.5\,h^{-1}$Mpc value adopted by Abell. This reduced the number of cluster blends, since the galaxies defining each cluster are constrained to lie closer to the cluster core. If the standard Abell radius had been used, $\simeq 30\%$ of the clusters would be deblended. This is consistent with the level of contamination in Abell clusters estimated by Lucey (1983). For the smaller Abell radius, 8% of the clusters were deblended.

The cluster sample used in this paper to determine ξ_{cc} corresponds to a subsample of the full 737 clusters selected according to the following criteria: richness $R \geq 22$ inside a radius corresponding to $r_A = 1\,h^{-1}$Mpc, where R is the number of cluster galaxies between the limits m_3 and $m_3 + 2$ as defined by Abell (1958); clusters having an $m_{10}(b_j) \leq 18.75$; clusters within the area $\alpha = 21^h\,53^m$ to $\alpha = 03^h\,35^m$ and $\delta = -22^\circ\,53'$ to $\delta = -42^\circ\,12'$. The number of clusters satisfying these selection criteria is 97.

In total we have taken redshifts for 96 clusters from the full list of 737, using both the European Southern Observatory 3.6m and the Anglo-Australian Telescope. On average, for the clusters we observed ourselves, redshifts of 10 galaxies towards each cluster core were taken. These 96 observed clusters constitute the Edinburgh-Milano cluster redshift survey. Results from this sample will be discussed in other papers (*e.g.* Guzzo *et al.* 1992). Of these, 71 satisfy the selection criteria described above and we supplement these with 16 from the literature. Therefore we have cluster redshifts for 87 of the 97 selected clusters. From the 71 clusters we observed, 8 were rejected as projection effects using strict objective criteria based entirely on the redshift distributions (Nichol 1992). Therefore the final statistical sample used to determine ξ_{cc} corresponds to 79 out of 89 clusters and represents a completeness of 90%.

From a comparison between the clusters in the EDSGC sample ($R \geq 22$, 97 clusters) and the southern Abell catalogue (Abell, Corwin & Olowin 1989), we find that our sample is equivalent to an Abell richness of $R = 40$, i.e. between the Abell richness classes $RC = 1$ and $RC = 0$. This comparison is consistent with the spatial number density of the cluster samples (n_c). For the EDSGC sample, $n_c = 1 \times 10^{-5} h^3 \mathrm{Mpc}^{-3}$ compared to $n_c = 1.2 \times 10^{-5} h^3 \mathrm{Mpc}^{-3}$ for the PHG $RC \geq 0$ sample. On these criteria alone we would expect to see a clustering amplitude close to that reported by PHG.

3 CALCULATION and RESULTS

The correlation function was calculated by comparing the observed distribution of cluster pairs with that of a random distribution within an identical volume. ξ_{cc} can then be estimated from

$$\xi_{cc}(r) = 2\frac{n_r}{n_d}\frac{N_{dd}}{N_{dr}} - 1, \qquad (1)$$

where n_d and n_r are the number density of data and random points respectively ($n_r >> n_d$). N_{dd} and N_{dr} are the number of data-data pairs and data-random pairs respectively (Davis & Peebles 1983). In order to account for the redshift selection function the random dataset was constructed by selecting angular positions randomly from within the survey area and assigning them redshifts taken from our own observed redshift distribution, smoothed with a Gaussian of width $3000\,\mathrm{km\,s^{-1}}$. The final result was insensitive to the exact smoothing width used. The calculated correlation function is shown in Fig. 1. Also shown in this figure are the points of the PHG correlation functions recalculated by us for their $RC \geq 0$ statistical sample and $RC \geq 1$ sample using the technique they prescribe. The stability of the EDSGC correlation function was checked using an estimator which depends on the number of random-random pairs and an identical result to that in Fig. 1 was found.

One possible systematic effect of using the observed redshift distribution to generate the random catalogue is that the large structures in the redshift direction of our survey (Guzzo *et al.* 1992) cause ξ_{cc} to be underestimated. To check this a random catalogue was constructed based on the assumption that our cluster sample is volume limited to a redshift $z = 0.13$. Excellent agreement was obtained between the resulting correlation function and the points in Fig. 1.

The error bars shown are estimated from the bootstrap method described by Ling, Frenk & Barrow (1987). These estimates are more conservative than simple Poissonian errors but are more realistic given that we have a partially incomplete sample. Assuming $\xi_{cc}(r) = (r/r_0)^{-\gamma}$, a least-squares fit to our correlation function over the range $3-35\,h^{-1}\mathrm{Mpc}$ gives $r_0 = 16.4 \pm 4.0\,h^{-1}\mathrm{Mpc}$ and $\gamma = 2.1 \pm 0.3$.

If the error bars are Poissonian, $r_0 = 16.2 \pm 2.3\, h^{-1}$Mpc and $\gamma = 2.0 \pm 0.2$. This compares with the PHG correlation length of $20.0 \pm 4.0\, h^{-1}$Mpc for their complete RC ≥ 0 statistical sample and $23.7 \pm 8.0\, h^{-1}$Mpc for their RC ≥ 1 sample.

In order to characterize the line-of-sight elongations in the correlation functions we followed the procedure described by Sutherland (1988) and computed ξ_{cc} as a function of both radial (r_z) and transverse (r_p) separations. Contour values of $\xi_{cc}(r_z, r_p)$ for the EDSGC data and the PHG RC ≥ 1 sample are shown in Fig. 2.

4 DISCUSSION

The correlation function of the EDSGC clusters is systematically below the Bahcall & Soneira (1983) result and both the PHG RC ≥ 0 and RC ≥ 1 cluster samples, although the difference between our correlation length of $r_0 = 16.4 \pm 4.0\, h^{-1}$Mpc and the values given by PHG are not statistically significant. Fig. 2a demonstrates there is little anisotropy detected for our sample on scales $\leq 30\, h^{-1}$Mpc. The contours are virtually spherical on these scales. In comparison, the PHG sample (Fig. 2b) shows considerable anisotropy. The $\xi_{cc}(r_z, r_p)$ contours are extended by a ratio of 3 to 1 in the redshift direction compared to the transverse direction on scales $\leq 30\, h^{-1}$Mpc. A similar result for the RC ≥ 0 statistical sample of PHG was found recently by Efstathiou *et al.* (1992).

The lack of anisotropy in Fig. 2a compared to Fig. 2b should not be surprising as our data represent a substantial advance over existing samples used for cluster correlation studies. There are three main differences to note: firstly, our clusters are selected in a completely objective manner from the EDSGC and are not subject to unquantifiable systematics introduced by "Abell's eye". Secondly, precautions have been taken to avoid including clusters which would otherwise be spuriously selected due to projection effects (Section 2). Thirdly, for 71 clusters in our sample we have taken redshifts for $\simeq 10$ galaxies in the direction of each cluster core. This significantly reduces the possibility of inducing spurious peculiar velocities to the clusters. For the PHG data, 43% of the cluster redshifts are based on 1 or 2 galaxies. These effects point towards a natural explanation of the anisotropy in Fig. 2b in terms of projection effects. It is unnecessary to invoke either line-of-sight clustering or large cluster peculiar velocities as the explanation for the anisotropy evident in the cluster samples selected from the Abell catalogue (Section 1).

The isotropy seen in Fig. 2a enables a direct constraint to be placed on the cluster peculiar velocities. We fitted $\xi_{cc}(r_z, r_p)$ to a model in which $\xi_{cc}(r) = (r/16\,h^{-1}\mathrm{Mpc})^{-2}$, convolved with a Gaussian peculiar velocity field (Nichol 1992). From this analysis peculiar velocities between clusters as large as $1000\,\mathrm{km\,s^{-1}}$ are ruled out at about the 2 sigma level, although our data are consistent with zero peculiar velocities. Similar values for r_0, γ, and the rms cluster peculiar velocity were obtained when a simultaneous fit was made to all three parameters.

5 CONCLUSIONS

A nearly complete cluster sample selected from the EDSGC has been used to calculate ξ_{cc}. The resulting correlation length has a value $r_0 = 16\,h^{-1}$Mpc. The anisotropy of ξ_{cc} between the radial and transverse directions is significantly smaller than that found in Abell cluster samples of comparable richness on scales $\leq 30\,h^{-1}$Mpc. This is a consequence of minimising the projection effects in the cluster search algorithm and measuring multiple redshifts for most clusters. This result suggests that such effects are not due to real structure or large peculiar velocities as suggested by some authors. We derive an upper limit to the rms peculiar velocities for clusters of $\simeq 1000\,\mathrm{km\,s^{-1}}$. We are aware of similar work underway using clusters selected from the APM cluster catalogue (Dalton *et al.* 1992).

ACKNOWLEDGEMENTS

We thank the supporting staff of the Anglo-Australian Telescope and particularly the European Southern Observatory for their excellent assistance in making the observations. Neil Heydon-Dumbleton carried out some of the observations and was instrumental in constructing the EDSGC and carrying out the ground-work on automated cluster detection. His contribution is warmly acknowledged. We thank John Huchra for the use of both published and unpublished data and for useful discussions. RCN thanks Lance Miller and John Peacock for discussions and both RCN and SLL acknowledge financial support from the SERC. This paper is based on data from the COSMOS measuring machine.

REFERENCES

Abell, G.O., 1958. *Astrophys. J. Suppl.*, **3**, 211.

Abell, G.O., Corwin, H.G. & Olowin, R.P., 1989. *Astrophys. J.*, **70**, 1.

Bahcall, N.A. & Soneira, R.M., 1983. *Astrophys. J.*, **262**, 20.

Bahcall, N.A., Soneira, R.M. & Burgett, W.S., 1986 *Astrophys. J.*, **311**, 15.

Collins, C.A., Nichol, R.C. & Lumsden, S.L., 1992 *Mon. Not. R. astr. Soc.*, **254**, 295 (Paper-III).

Dalton, G.B., Efstathiou, G., Maddox, S.J. & Sutherland, W., 1992. *Astrophys. J.*, submitted.

Davis, M. & Peebles, P.J.E., 1983. *Astrophys. J.*, **267**, 465.

Dekel, A., Blumenthal, G.R., Primack, J.R. & Olivier, S., 1989. *Astrophys. J.*, **338**, L5.

Efstathiou, G., Dalton, G.B., Sutherland, W. & Maddox, S.J., 1992. *Mon. Not. R. astr. Soc.*, preprint.

Guzzo, L., Collins, C.A., Nichol, R.C. & Lumsden, S.L., 1992. *Astrophys. J.*, submitted.

Jing, Y.P., Plionis, M. & Valdarnini, R., 1992. *Astrophys. J.*, in press.

Ling, E.N., Frenk, C.S. & Barrow, J.D., 1986. *Mon. Not. R. astr. Soc.*, **223**, 21p.

Lucey, J.R., 1983. *Mon. Not. R. astr. Soc.*, **204**, 33.

Lumsden, S.L., Nichol, R.C., Collins, C.A. & Guzzo, L., 1992. *Mon. Not. R. astr. Soc.*, in press.

Nichol, R.C., 1992. *Ph.D. Thesis* , University of Edinburgh.

Postman, M., Geller, M.J. & Huchra, J.P., 1986. *Astr. J.*, **91**, 1267.

Postman, M., Huchra, J.P. & Geller, M.J., 1992. *Astrophys. J.*, **384**, 404 (PHG).

Sutherland, W., 1988. *Mon. Not. R. astr. Soc.*, **234**, 159.

White, S.D.M., Frenk, C.S., Davis, M. & Efstathiou, G., 1987. *Astrophys. J.*, **313**, 505.

Figure Captions

Figure 1 The $\xi_{cc}(r)$ for the 79 EDSGC clusters ($\bullet$), the RC $\geq$ 0 statistical sample ($\Box$) and the RC $\geq$ 1 sample of PHG ($\star$). The dot-dashed line represents our best fit to $\xi_{cc}(r)$ (see text) and the single dashed line corresponds to the Bahcall & Soneira $r_0 = 25h^{-1}$Mpc correlation function. The bootstrap error bars are shown.

Figure 2 (a) A contour diagram of $\xi(r_z, r_p)$ for the 79 EDSGC clusters. No projection effect correction has been applied. The contour levels are 3.0, 2.0, 1.0, 0.8, 0.6, 0.4, 0.2, -0.2, -0.4. (b) Similar to (a) for the PHG RC $\geq$ 1 Abell cluster sample. The contour levels are 12.0, 8.0, 6.0, 4.0, 2.0, 1.0, -0.1, -0.2, -0.3. Negative contours are dashed.

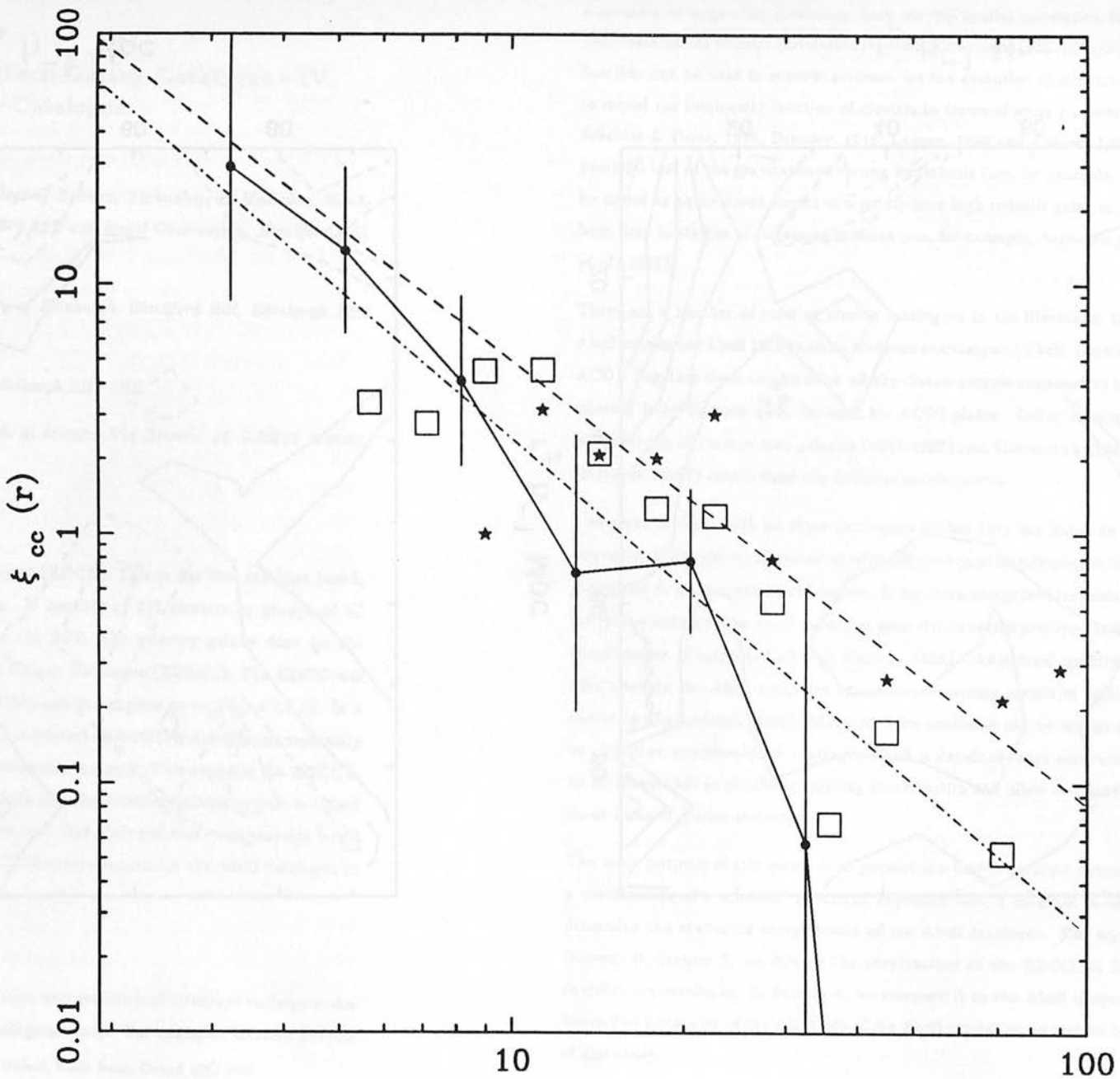

Fig. 1

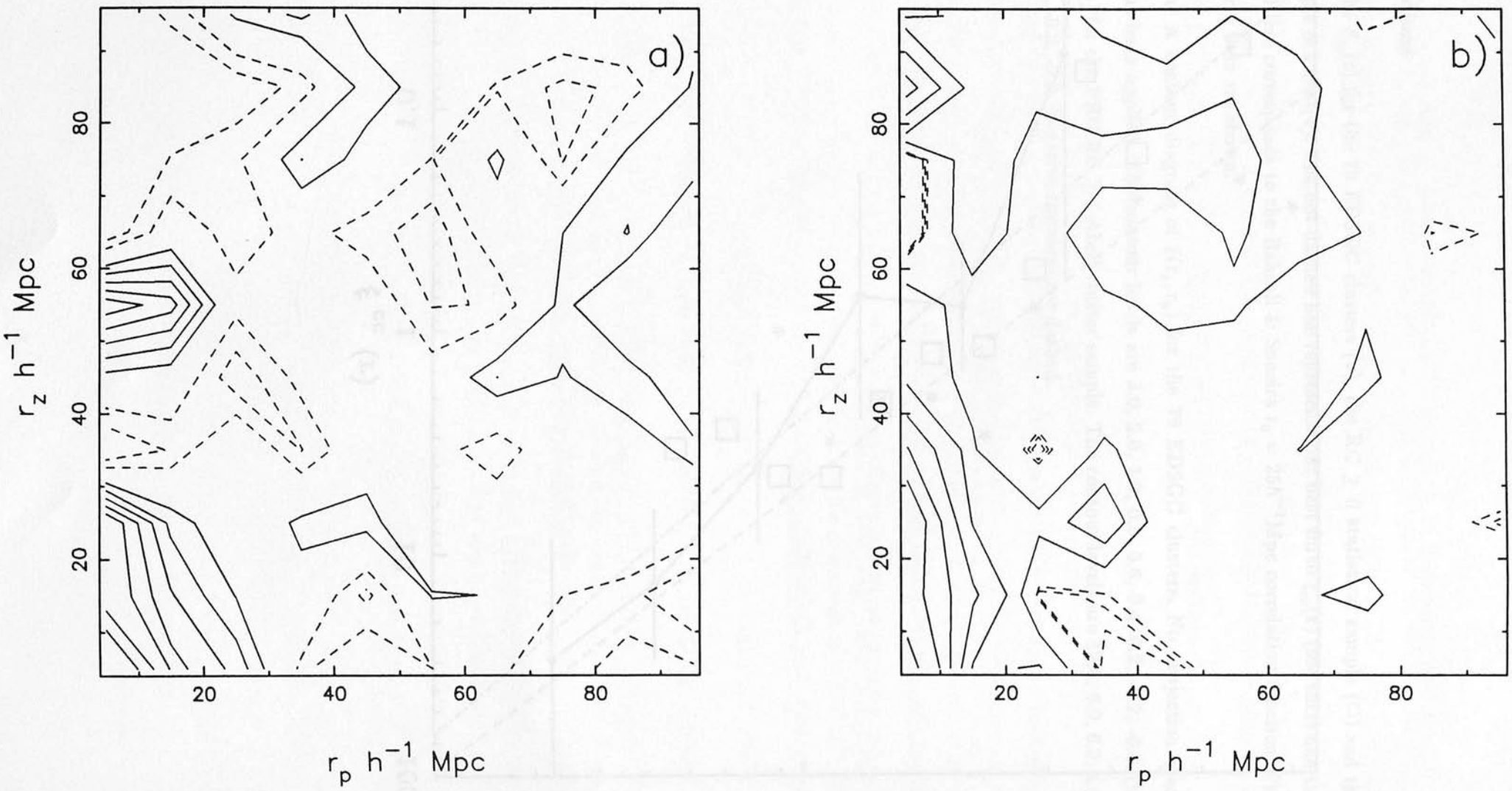

Fig. 2

Accepted for publication
in Monthly Notices of the Royal Astronomical Society

The Edinburgh/Durham Southern Galaxy Catalogue - IV. The Cluster Catalogue

S.L. Lumsden[†] *Astrophysics Group, Imperial College of Science, Technology & Medicine, Blackett Laboratories, Prince Consort Road, London SW7 2BZ and Royal Observatory, Blackford Hill, Edinburgh EH9 3HJ.*

R.C. Nichol *Department of Astronomy, University of Edinburgh, Blackford Hill, Edinburgh EH9 3HJ.*

C.A. Collins *Royal Observatory, Blackford Hill, Edinburgh EH9 3HJ.*

L. Guzzo *Osservatorio Astronomico di Brera, Sede di Merate, Via Bianchi 46, I-22055 Merate, Italy.*

SUMMARY

We present the Edinburgh/Durham Cluster Catalogue (EDCC). This is the first machine based, objectively selected sample of clusters of galaxies. It consists of 737 clusters or groups of all richnesses, over 0.5 steradians of sky, centered on the SGP. The primary galaxy data for the cluster survey is the Edinburgh/Durham Southern Galaxy Catalogue (EDSGC). The EDCC was constructed using an automatic peak finding algorithm and is complete to $m_{10}(b_j) = 18.75$. In a comparison with the Abell clusters in the same region, we detect 80% of their rich clusters nominally brighter than our completion limit in addition to many new systems. This suggests the EDCC is 90% complete for Abell-type clusters. We also conclude that the Abell magnitude system is biased towards bright magnitudes for most of their clusters, and that their richness estimates are prone to a larger uncertainty than they suggest. The EDCC therefore supercedes the Abell catalogue as a database for statistical studies of cluster properties.

1 MOTIVATION

Clusters of galaxies provide a powerful probe of the form and evolution of structure on large scales and have been used in many diverse areas of cosmological study. For example, clusters provide

[†]Present address: Astrophysics Department, University of Oxford, Keble Road, Oxford OX1 3RH.

a measure of large-scale clustering, both for the spatial correlation function (Bahcall & Soneira, 1983) and for the angular correlation function (Couchman, McGill & Olowin, 1989). The luminosity function can be used to provide evidence for the evolution of clusters. Attempts have been made to model the luminosity function of clusters in terms of some universal function (e.g. Abell, 1962, Schecter & Press, 1976, Dressler, 1978, Lugger, 1986 and Colless, 1989). Clusters also provide a powerful test of the gravitational lensing hypothesis (see, for example, Ellis, 1990), and hence may be useful as an unbiased source of serendipitous high redshift galaxies. Furthermore, clusters have been used in studies of streaming motions (see, for example, Aaronson *et al.*, 1986 and Lynden-Bell *et al.*, 1988).

There are a number of existing cluster catalogues in the literature: the most widely used is the Abell catalogue (Abell 1958) and its southern counterpart (Abell, Corwin & Olowin, 1989; hereafter ACO). Together these consist of an all-sky cluster sample supposed to be at redshifts less than 0.2, selected from Palomar (UK Schmidt for ACO) plates. Other catalogues include the Zwicky *et al.* catalogue of clusters and galaxies (1961-1968) and Shectman's (1985) analysis of the Shane & Wirtanen (1967) counts from the Palomar survey plates.

The main problem with all these catalogues is that they are based on data gathered from visual inspection of the galaxy distribution with different (and largely unquantifiable) selection procedures giving rise to heterogeneous catalogues. It has been recognised for some time that the intrinsically subjective nature of the Abell catalogue gives rise to severe problems in homogeneity and statistical completeness (Postman, Geller & Huchra, 1986). Additional problems arising from projection effects within the Abell catalogue render the clustering results of Bahcall & Soneira (1983) very uncertain (Sutherland, 1988). Many of these problems can be solved or at least quantified with an objective, machine-based catalogue. Such a database, with accurate photometry, would prove an invaluable aid in clarifying existing uncertainties and allow substantial progress to be made in many areas of cluster research.

The main purpose of this paper is to present the first large-scale automated cluster survey using a combination of a modified Shectman approach with a modified Abell analysis. From this we determine the statistical completeness of the Abell catalogue. The structure of this paper is as follows: In Section 2, we discuss the construction of the EDCC. In Section 3, we present and describe the catalogue. In Section 4, we compare it to the Abell clusters in the same region and hence find a measure of the reliability of the Abell catalogue. In section 5 we summarise the results of this study.

2 CONSTRUCTION OF THE CATALOGUE

2.1 The Galaxy Data

The source of our galaxy data is the Edinburgh/Durham Southern Galaxy Catalogue (hereafter EDSGC: Heydon-Dumbleton, Collins & MacGillivray, 1989, paper 3), which consists of COSMOS scans of sixty UK Schmidt survey plates. The EDSGC covers 0.5 steradians, centred on the South Galactic Pole. Accurate calibration and star-galaxy separation have resulted in a catalogue that is 95% complete to $b_j \sim 20.5$ with less than 10% stellar contamination, and a plate-to-plate zero-point variation of $\Delta m \sim 0.05$. The COSMOS image analysis package (Thanisch, McNally & Robin, 1984, Beard, MacGillivray & Thanisch, 1990) also contains a powerful deblending routine which we use to discriminate between the different galaxies in rich cluster cores. This is vital for our purposes since an underestimate of the number of galaxies in a rich compact core could easily result in that cluster being overlooked. The EDSGC is therefore an ideal tool for many large scale cosmological survey projects.

2.2 Finding Candidate Clusters

In this paper we utilise a similar approach to that of Abell in classifying clusters since our aim is to test the reliability of the Abell catalogue. We adopted a method of finding cluster candidates independent of any presumed cluster model and imposed the Abell classification at a later stage. We intend to consider the same candidate clusters in terms of non-Abell parameters in future papers. There are two well established mechanisms for carrying out this task. The one we used involves binning the galaxy data, and is modified from the work of Shectman (1985). The alternative is to use a percolation analysis. We decided not to use this method since it can in principle merge nearby candidate objects into a single structure. Consideration of the computer time involved also favours the binning method.

The catalogue was binned into equal area square bins on a true sky projection. The bin size was chosen such that the mean number of galaxies per bin was ~ 1. This procedure was carried out three times, for different magnitude limits; the actual limits and bin sizes used are given in Table 1. Each selection gives rise to a different set of candidates, although, as might be expected, there are large overlaps.

Once the data are binned, they are lightly smoothed with a Shectman (1985) filter to produce a 'Shectman' frame. This filter has the weights:

$$\begin{matrix} \frac{1}{16} & \frac{1}{8} & \frac{1}{16} \\ \frac{1}{8} & \frac{1}{4} & \frac{1}{8} \\ \frac{1}{16} & \frac{1}{8} & \frac{1}{16} \end{matrix}$$

The Shectman filter was chosen since it is effectively a Gaussian filter, and hence matches the cluster density profiles well (a point that we make use of again in the Abell analysis). Over-smoothing the data (using a top hat filter for example) reduces the likelihood of detecting real small scale structures, and not smoothing at all would make location of a peak dependent on its location with respect to the bin. Light smoothing reduces binning noise, ensuring that a true peak is located irrespective of where it lay in the original bins. The validity of this latter point will be discussed further in Section 2.5 when the errors in the catalogue are considered.

Shectman searched for peaks above a global threshold. However, since the EDSGC gives only a two dimensional representation of the actual galaxy density on the sky, it is impossible to find all clusters this way. A single threshold will find all clusters, however poor, in a region of generally high galaxy density and, conversely, miss those, however rich, in regions of low galaxy density. In order to overcome this problem, the large scale baseline was removed by following the background projected density (Dodds & MacGillivray, 1986). This background or 'sky' frame was calculated by smoothing the 'Shectman' frame using a square, mean filter of width between 1° and 2°. Tests showed that the clusters selected were actually quite resilient to the exact form of this 'sky' frame. Changing the scale on which the background is smoothed (within the range 40′ to 3°), and hence changing the effective background level, causes less than a 10% change in the final candidate centres. Most of the candidates that were sensitive to this change were found to be 'noise'.

The 'sky' frame was subtracted from the 'Shectman' frame. An image analysis package similar to the COSMOS image analyser (Thanisch, McNally & Robin, 1984, Beard, MacGillivray & Thanisch, 1990) was used to find pixels above a given threshold in this background subtracted image. The threshold was set according to the values given in Table 1. These values were set empirically as a compromise between rejecting real clusters while keeping the proportion of 'noise' images to a minimum. The threshold varies between runs since the number of such 'noise' images increases as the bin size is decreased. If the threshold was lowered it would be possible to counteract this by including an area cut but this was found to exclude some genuine distant clusters. Therefore from experiments on a small area of the data we chose thresholds which gave minimum contamination without discarding any of the clusters that we had previously detected by eye. Only 5% of the objects detected definitely proved not to be clusters or groups of galaxies on a further visual

inspection.

Thresholding the data is not sufficient to find all true density peaks. Clearly, neighbouring peaks can lie above the same threshold. We therefore deblended the data in density space to search for the true peaks and the saddle points between them. Failure to do his would have led to nearby groups being considered as a single unit. Applying an Abell classification to that single unit would give misleading results, since we would have no further information that there was in fact more than one peak in the density distribution at that position. Deblending before applying the Abell mechanism allows us to note that there are two or more overlapping Abell radii for the candidates, and hence to correct the counts again at a later point in the analysis. This is also the reason that we decided against using a percolation method for selecting candidate clusters. This helps to reduce the problem of projection effects which have been noted as a common occurrence in the Abell (1958) catalogue (Lucey, 1983, Sutherland, 1988). Since the background subtracted frame is analogous to a galaxy density, linear thresholding was used, in contrast to the COSMOS software used to deblend merged galaxy/star images in the construction of the EDSGC. We used twenty thresholds, starting at the thresholds given in Table 1 and ending at the peak in the actual structure. The other major difference between the procedure applied here and the COSMOS package was that each pixel was allocated to only one cluster. This is justified for two reasons. Firstly, there were very few instances in which pixels were equally shared. Secondly, since we later imposed the Abell classification and then deblended again, the small richness errors arising at this stage from this simplification were irrelevant. For every candidate, the locations of all pixels belonging to that object (which by definition must be connected), and the EDSGC catalogue information on all the galaxies within those pixels was stored for future use. The number of candidate clusters found for the different bin sizes are given in Table 1.

2.3 The Abell Analysis

The methods outlined by Abell (1958) are valuable for three reasons. They provide an opportunity to place the EDCC within a recognised framework, provide one method of giving additional information over that presented by the pseudo-'Shectman' analysis given above, and also allow us to make a direct comparison between our catalogue and that of Abell.

The candidate cluster centres were taken as initial centroids for the true Abell cluster. The magnitude of the tenth brightest galaxy, m_{10}, was taken from the list of galaxies contained within the pixels. This magnitude was converted into an Abell radius, θ_A, using the formula given by ACO; the Abell radius is the angle subtended on the sky by a circle of radius $1.5h^{-1}$Mpc at the cluster,

ignoring cosmological corrections.

$$\theta_A = \arctan\left(\frac{150}{cz}\right) \tag{1a}$$

where cz is given by equation 11 of ACO (the well known m_{10}–$\log cz$ relation), and a correction of

$$b_j - V = 0.77 \tag{1b}$$

has been made to convert from the EDSGC magnitude system (b_j) to the ACO system (V). This value was obtained from the calibration sequences used in the construction of the EDSGC (Heydon-Dumbleton, Collins & MacGillivray, 1989). It should also be noted that the ACO form of the m_{10}–$\log cz$ relation is in reasonable agreement with that found by Scaramella *et al.* (1990) for the same clusters and using updated redshifts.

Allowance must be made for the galaxies seen in projection on the cluster before the Abell radius can be calculated. An estimate of the contamination was derived from number counts of all the galaxies in a box of $4° \times 4°$ centred on the original candidate. These counts were then scaled down to the cluster area. The contribution of cluster galaxies to this count on each field is negligible once the counts are scaled down. Calculating the background in this way guards against only using an unrepresentative low density region, free from clusters, (as Abell did) and so should be more reliable. Since the cluster area is a function of m_{10}, this is an iterative process, but in general it converges rapidly. For the clusters presented here, convergence was taken to be the point at which the value of m_{10} was stable to within 1% between iterations.

For very distant clusters, it was sometimes the case that the 'true' m_{10} actually lay beyond the EDSGC magnitude limit. In that case, the candidate was discarded. Similarly, if the centroid moved in the iteration by more than a quarter of its initial Abell radius it was discarded (since such a cluster is likely to be too poor for the iterative process to be stable) and if the value of m_{10} failed to converge within ten tries it was also discarded. In this way 20%, 15% and 25% of the candidates from the respective runs were removed from further consideration. The high rejection rate for the smallest bin size was largely due to candidates whose magnitudes lay very near the plate limits, and that for the largest bin size because the low threshold allowed many poor nearby groups to be considered which consequently moved centroid in the analysis.

The centroid of the cluster was defined by using all the galaxies within the Abell radius since the background should be smooth across these scales. The richness is defined as the number of galaxies

in the magnitude range $[m_3, m_3 + 2]$, as in Abell, also corrected for the background contamination in the same manner that m_{10} was.

2.4 The Final Catalogue

The next step in the construction of the catalogue was to combine the data from the Abell analyses of each of the three runs using the different initial bin sizes. The first step in this process was to remove duplicate entries from the final list. Any cluster which overlapped with other clusters so that its centroid fell within the others Abell radius was flagged as being a possible duplicate. Any isolated clusters were passed straight into the final catalogue since they required neither merging nor deblending.

We used a two sided Kolmogorov-Smirnov (KS) test to compare the background subtracted magnitude distributions for those clusters found to be overlapping. This can also be viewed as comparing the luminosity functions of the two clusters through their apparent magnitude distributions but, crucially, places no constrictions on the form of the distribution. It is also formally independent of the number of objects under consideration (so it is useful for the poorer systems). A more conservative approach would have been to include every cluster from the different runs in the final catalogue, but this ignores the fact that many of the candidates from different runs were clearly the same cluster. The KS test is a relatively weak constraint (see below). Since some of the distinct peaks that we locate may be due to substructure we opted for these relatively loose constraints in combining the three original catalogues.

Where the apparent magnitude distribution was found to be the same, within a given significance level, we accepted these clusters as being the same. The level of significance that we used varied according to the separation of the clusters. This was found empirically on visual inspection of the candidates to be well behaved, whereas using only one threshold gave either too few or too many blends depending on which level of significance was chosen. For those clusters where both the centroids were within each other's Abell radius, clusters had to pass at the 10% level; for those where one centroid was within the other's Abell radii, clusters had to pass at the 20% level; and for those where only the Abell radii overlapped (those which had been grouped through a common third cluster that lay between them for example) the requirement was that the distribution should be the same at the 40% level of significance. To estimate how rigourous these limits were we selected a cluster with a richness of 40, and $m_{10} = 18$, typical of our catalogue and then varied the magnitude and the effective richness and compared it against itself. A shift in magnitude of 0.2 (roughly a difference in redshift of 0.01), or a change in richness by a factor of 60% caused a failure

at the 10% level. Therefore substructure on its own is unlikely to cause a failure, and only distinct clusters should be excluded by this test. Correspondingly smaller shifts would cause failure at the stricter levels for those clusters that only partially overlapped.

In cases where more than two clusters overlapped, we ranked them according to the size of their Abell radius. All the clusters were compared with the largest, and those that matched removed. The remaining set were then compared with the remaining largest cluster in the same manner. This process continued until all the clusters had been allocated to final distinct products. These final products were then reanalysed in order to determine their Abell characteristics. In the actual data set before the KS test was applied there were 425 clusters which existed in only one run, 154 clusters which were found in two distinct runs, 89 triplets in three distinct runs and 55 other combinations of more than three initial candidates (42 objects consisting of 211 initial candidates) or mergers where more than one of the components came from the same run (as happened for 10 triplets and 3 pairs). After the KS test, these numbers reduced to 461 singlets, 178 distinct pairs, 93 distinct triplets and 37 others (29 complex objects consisting of 126 initial candidates and two pairs and six triplets). Only the complex combinations were affected by the KS test since the other groups have virtually the same centres in the different runs, and hence almost exactly the same magnitude distributions. Clearly, from these figures the test has passed virtually all the clusters it should have, but has discriminated against large complex groupings which were actually blends of distinct clusters. In total therefore we reduced the three original runs to a final list of 769 clusters. Information on how many times a given cluster was detected in the individual runs is given in the catalogue (Table 3), from which the reliability of our procedure can be checked.

Finally, this single set of clusters was again checked for overlaps. Where overlaps were found, since the KS test had shown these clusters were distinct, deblending was applied to ensure that every galaxy could only appear in one distinct cluster. 255 clusters in 110 blended groups were treated in this way. This fraction (33%) compares favourably with previous estimates (Lucey, 1983) for the Abell catalogue. Only galaxies in the overlaps between clusters were tested, since testing all galaxies in a blended pair usually resulted in all the galaxies in very poor clusters being assigned to the richer system, which was found by visual inspection to be unrealistic. For simplicity, a Gaussian was fitted to the density profile of every cluster in a blend, and the cluster whose Gaussian fit had the largest amplitude at the location of any galaxy was assigned that galaxy. Once all the galaxies had been allocated to clusters, the cluster properties were again reanalysed (since the values of m_3 and m_{10} can change during the deblending process).

2.5 Error Estimates

The internal errors in the Abell parameters can be estimated by comparing the output from the three separate runs. We considered those overlapping clusters which passed the KS test to be essentially separate measurements on the same intrinsic cluster. Since there were cases of multiple blends, we used only the nearest clusters from the other two runs to a cluster in a given run (this avoids problems with using clusters which effectively sample largely different areas of the data). The scatter found in this way should give a realistic estimate of the underlying error in the final cluster catalogue. Fig. 1(a) shows a comparison of the derived m_{10}'s for all the clusters, Fig. 1(b) that for the m_{10}'s when only clusters with more than 30 members were considered and Fig. 1(c) a comparison of the richness values. This information is also summarised in Table 2, where the estimated intrinsic errors in the final catalogue are also given. The average differences between runs for any of the parameters given there were effectively consistent with zero (as can be seen from Fig. 1).

Some fairly obvious points can be made about these scatter plots. The scatter in the value of m_{10} is reduced when only the richer clusters are considered, as would be expected. Also, there appears to be a correlation between the size of the original bin and the final value of the m_{10} in the sense that larger bins give rise to brighter m_{10}'s. However, this is less evident in the richer clusters, probably indicating that some of the poorer clusters are not well defined. Note also that the scatter in the brighter magnitudes (m_1, m_3) are larger than in m_{10}, which would be expected since m_{10} is closer to the peak in the cluster luminosity function (so an error in selecting the actual tenth brightest galaxy is less likely to give rise to a large error in the magnitude). However, the scatter in richness is not reduced if only richer clusters are compared. This is largely due to a coupling between two effects. Overall, the scatter in m_3 is smaller for richer clusters, but the induced richness error is also proportional to the richness itself. For a Schechter style luminosity function it can be seen that such an error in m_3 leads to an error in the richness that is approximately equal to the product of the number of objects in the cluster and the error in the magnitude (*c.f.* Colless, 1989, equation 10). Since these two effects almost cancel we would expect the overall scatter for the richness to be approximately the same irrespective of the actual richness, as is observed.

Finally, removing those overlaps where the offset between the centroids is more than 2′ reduces the scatter considerably (see the final entry in Table 2). These errors must represent the irreducible minimum errors within the EDCC and can be seen to arise from the actual mechanics of the iteration process. Slight shifts in the initial centroid can lead to a slightly different initial value for

m_{10}. The iteration procedure ends when the m_{10}'s between successive iterations agree to within 1%, so potentially the final magnitudes can differ by 0.1 → 0.2 magnitudes. Hence, the minimal scatter is consistent with that expected from the iteration procedure.

One other possible source of error was the residual effect of the binning, not adequately accounted for by the Shectman filter. In order to test whether or not residual binning noise played any part in the selection procedure, the bin centres were offset by half a bin width and a re-selection made. This error might have been expected to dominate near the edge of the survey for instance, where background subtraction is more uncertain and small shifts in the centroid are more likely to have a correspondingly larger effect. In fact the resulting changes to the various cluster properties were consistent with the minimal measurement errors described above. In addition, the same density peaks were found in both the original and offset data indicating any residual effect of the binning was negligible.

3 THE CLUSTER CATALOGUE

Table 3 gives the measured properties for all the clusters in the EDCC. There were 769 clusters remaining after identifying duplicates. No restriction has been made on richness or distance (unlike ACO). The catalogue is based around detecting local peaks in the density distribution. Though the Abell classifications may be questionable (see below) in some cases, there were only a few instances (32 cases) in which the peak in the smoothed data did not appear to correlate with any visible cluster on the plates. Those which were judged to be outright errors are listed separately in Table 4. Details of the original peak locations (and other details of the original separate 'runs') will be made freely available on request for those who are interested. The table is sorted in right ascension and contains the following information: 1) Sequential EDCC cluster identification numbers. 2) Right ascension and declination (equinox 1950). 3) The magnitude of 1st, 3rd and 10th brightest members (m_1; m_3; m_{10}). 4) The number of galaxies within the Abell radius between m_3 and m_3+2 *after* the background galaxies have been removed (n_{clus}). 5) The number of background galaxies within the same radius to the same magnitude limit (n_{back}). The actual original counts within θ_A can be reconstructed from $n_{raw} = n_{clus} + n_{back}$. 6) The Abell radius ($\theta_A$) in degrees. 7) Schmidt J survey field number. 8) The number of times the cluster was located in each of the original runs. For example, 310 implies the cluster was found 3 times in run1, once in run 2 and not at all in run 3. 9) Whether or not the cluster was deblended (d or blank). 10) Abell identification number. An identification is defined as an Abell cluster centre within one Abell radii of an EDCC cluster. Where the Abell identification appears in brackets only the cluster's Abell radii overlap.

If the cluster entry has a zero magnitude then it implies that most of its members have been lost to a companion during deblending (so that the background subtracted magnitude cannot be defined). If $m_{10} = 0$ then the richness and background are taken to be zero by default (since the richness cannot be calculated if $\theta_A = 0$). These clusters are still included since they represent distinct peaks in the original catalogues as determined by the KS test, and also show where the centres are in a blend.

All of the clusters have been checked visually. Where a number is missing from the sequential identification described above, that cluster has been rejected on the basis of this check. Only 'obvious' errors are excluded such as residual diffraction spikes from faint stars, star-star mergers, or nearby, bright face-on spirals, where the nucleus and dense HII regions in the disk are detected as separate objects. As noted above, these objects are listed separately in Table 4. In this table the final column contains our assessment of the actual object detected.

We have also indicated possible errors in our richness and magnitude estimates in Table 3, where the visual inspection gave a clearly different result. These are flagged by a * in the m_{10} (4 clusters) or n_{clus} (82 clusters) columns. A '?' against the cluster identification in general indicates that such clusters could not be distinguished from the surrounding field (43 clusters). It follows that any quoted magnitudes or richness should equally be treated with caution for that cluster. These visual assessments are of course highly subjective and should be used only as a guide and not as absolutes. Most of these possible classification errors are in the richness. Partly, this is due to the greater ease with which such errors can be spotted visually compared to magnitude errors, but it is also in accord with the scatter found previously, whereby the richness values (dependent on m_3) were found to be more uncertain than the m_{10} values. These assessments are also included for those clusters which are deblended: in particular, where a cluster with zero richness and $m_{10} = 0$ has a flag against the richness, we assess this as being a good cluster.

The completeness of the catalogue can be estimated in several ways. The number-magnitude relation for the clusters is shown in Fig. 2. The differential and cumulative number counts for those EDCC clusters with more than 30 members and those ACO clusters with the same richness cut-off are shown. The EDCC is partially incomplete at very bright magnitudes (missing 3 clusters compared to ACO for $b_j < 17$). Two of these ACO clusters have been deblended in our catalogue and the third lies within a defocussed region that was excluded from the EDSGC. Deblending bright large clusters can lead to them being classified wrongly since they overlap with so may other potential centres. The dashed line shown in Fig. 2 has a slope of 0.65, but a value as low as 0.55

or as high as 0.75 cannot be ruled out on the basis of our data alone since only small changes in the numbers of clusters with $b_j < 17$ changes the slope significantly. If we were to assume that the ACO classification of the missing bright clusters in terms of richness and magnitude was accurate, then the slope will be more severely constrained around the the value of 0.65. It is encouraging that this value is close to the value of 0.6 expected for a homogeneous distribution at low redshift with minimal curvature or K-correction. We also estimate the completeness limit of the EDCC as $m_{10}(b_j) = 18.75$ since beyond this magnitude the differential counts decline. Given that a cluster must have $m_3 + 2 < 20.5$ for it to be found within the EDSGC, this value is in agreement with what is expected. The ACO clusters would appear to have a similar completeness limit, though the nature of the 'completeness' of the ACO catalogue will be discussed further in the next section.

The distribution of the number-richness relation is shown in Fig. 3. There is evidence from this plot for incompleteness in ACO at counts less than 40, since the number of clusters with fewer members declines. The expectation would be that these counts should continue to increase at smaller counts. The EDCC is therefore more complete at lower richnesses than the ACO supplementary catalogue, and there is no evidence for incompleteness in the EDCC with richness for counts above 0. An explanation for this is that ACO counts are generally overestimated. Then incompleteness in the ACO catalogue would only occur for the supplementary clusters, where no claim is made for any rigorous detection of all such clusters. This also agrees with the comparisons between the catalogues outlined below. This plot also shows that the EDCC does not suffer from any 'hidden' incompleteness such as might be expected if the poorer clusters were only found brighter than a certain magnitude, whereas the richer ones were visible to the quoted completeness limit of the EDCC.

Finally, as discussed in Section 2.2, the binning method imposes a selection criterion in terms of the size of the final cluster. The distribution of the Abell radii of the clusters found for the different initial sizes is shown in Fig. 4. Also plotted is the expected number of clusters with a given Abell radius if it was assumed that the number-magnitude distribution for the clusters had a slope of 0.6. Given the uncertainty in the actual slope of the number counts, the agreement between the observed and predicted distribution is another indication that there is no significant problem with the method adopted.

The sky distribution of the clusters is shown in Fig. 5. The clusters follow the general galaxy distribution well. Clusters within areas of low galaxy density are still located where genuine over-densities exist. There is no evidence for any systematic gradients or other effects in this plot. We

therefore conclude that the EDCC has no systematic incompleteness with position. A more detailed examination of the structures seen in this plot is given in Guzzo *et al.* (1992).

4 COMPARISON WITH THE ABELL CATALOGUE

4.1 Comparison Sample

All the Abell clusters from the sixty EDSGC fields were extracted from the ACO catalogue. These clusters included all the full ACO clusters (restricted to those clusters with richness greater than 30 and distance class less than or equal to 6: see ACO for the definition), all the supplementary ACO clusters, and those clusters that lay within the overlap region between the northern and southern catalogues. There were 339 full ACO clusters, 228 supplementary clusters and 87 within the overlap region. For the latter, both their original Abell (1958) classifications (as tabulated by ACO) and the newer southern classifications were considered. In order to carry out the comparison between these clusters and the catalogue presented here, both the V magnitude system of ACO and the R magnitude scale of Abell (1958) were converted to the photographic magnitude b_j. As noted previously, the relation $b_j - V = 0.77$ was adopted for transforming the raw ACO V magnitudes and a correction given by $b_j - R = 1.07$ was used for the northern clusters, following equation 9 of ACO. We have ignored the extinction corrections applied by Abell to the northern catalogue. This is valid since the measured extinction at the galactic latitudes covered by the EDCC is smaller than the errors within the catalogue.

In order to make a direct comparison between the EDCC and ACO clusters a consistent definition of the Abell parameters must be applied. One aspect of the ACO catalogue which remains very uncertain is their adopted background correction. ACO adopt a global background correction, and then force agreement with the northern Abell catalogue. As noted by ACO themselves, their global background subtraction is not realistic, since it can result in negative counts. Although our aim is to directly compare the selection methods of Abell and EDCC, our information is fully digitised and we can be more flexible in the definition of cluster parameters than ACO. Therefore, we estimated local background corrected counts for the ACO clusters by reconstructing their raw counts (using their data and equations 1, 6 &7 of ACO) and then calculating a new local background count from the EDSGC data. Only richness and magnitude comparisons are presented here. Comparisons with the more subjective parameters (*e.g.* classification of the cluster shape) quoted in ACO were not carried out.

4.2 The Comparison

As described above, all the Abell clusters within the EDCC area were used in the comparison, plus those within 20 arcminutes of the boundary. A match occurred when both the EDCC cluster centroid and the Abell cluster centroid lay within the other's Abell radius. Only one match was allowed per cluster. Those EDCC clusters that had fewer than 10 members after deblending were excluded (because of the impossibility of comparing magnitudes) but those ACO clusters with fewer than 10 members were included (since ACO still quote magnitudes for these clusters). In all, there were 308 matches between the combined ACO plus overlap catalogue and the EDCC.

As a test of the reliability of the comparison a maximum allowed offset, beyond which no matches were allowed, was considered. This did not seriously affect the scatter between the Abell and EDCC catalogues but did change the matching percentages. Table 5 gives values of the calculated scatter for both the complete comparison and this restricted set. This included 58 matches with clusters in the overlap region. When a maximum radius of $5'$ was imposed, the number of matches was reduced to 243. Since the average offset is $3'$, and the distribution of the offsets is approximately Gaussian, this change in the number of matches is not surprising. If more than one match was allowed per cluster, then an extra 9 clusters were detected from the full ACO and northern catalogues. Therefore, the condition that any one EDCC cluster can only match one ACO cluster is valid.

Scatter plots for Abell richness against EDCC richness, and the correlation between Abell m_{10} and EDCC m_{10} are shown in Figs. 6 and 7 respectively. The data are shown separately for the northern clusters, and for those classified by Olowin or Corwin. There are no clusters in the ACO sample classified by Abell. The ACO and northern magnitudes have been corrected to b_j using the relation given earlier. For clusters lying in the overlap region of the northern and southern catalogues both classifications have been plotted.

The obvious conclusion from Fig. 6 is the lack of any strong correlation between the richness values (though there is a weak correlation in the expected sense of overall ACO richness being proportional to ours). This is also true when the local background corrected ACO counts are used and so this lack of correlation reflects a real difference between the catalogues. In addition, there is a systematic tendency for the ACO clusters to have higher richnesses. This seems to be particularly reflected in the northern counts and Corwin's ACO southern counts. Given the steep dependence of the number-richness counts shown in Fig. 3, this explains the apparent greater number of Abell clusters with counts greater than 30 compared to the EDCC (467 as opposed to 249). It is important to stress that this lack of correlation between our richnesses and theirs applies to all clusters. We

find all bar 5 of the 'statistical sample' of Abell (distance class less than, or equal to, 4 and more than 50 members). However, of those we find, only one third have more than 30 members and only one sixth more than 50. Clearly, even this sample is prone to a large scatter, sufficient to move the clusters more than one richness class. This is contrary to the analysis of Struble & Rood (1991) who attempt an internal analysis of the Abell catalogues, and must also place in doubt clustering statistics derived from such samples (see Postman, Geller & Huchra, 1992).

The magnitude differences between the EDCC and the ACO clusters can best be characterised by the straight line fit shown in Fig. 7 (though the scatter about this is large, $\sigma \sim 0.7$):

$$m_{10}(\mathrm{EDCC}) - m_{10}(\mathrm{ACO}, b_j) = 0.31 + 0.03(m_{10}(\mathrm{EDCC}) - 18). \quad (2)$$

This is effectively consistent with a slight constant offset in the ACO clusters. By comparison, the faint northern Abell clusters ($R > 17$) shown in Fig. 7 follow a slope close to 45° indicating they have almost no dependence on true magnitude. As noted by ACO, they all have magnitudes near $R \sim 17$ regardless of their correct magnitude, a value defined largely by the limit of the Palomar Sky Survey plates. This also explains the reason why so many clusters with $z > 0.2$ (the nominal redshift limit of the Abell catalogue) were detected by Abell, since the $m_{10} - cz$ relation breaks down for northern catalogue clusters with true magnitudes fainter than $R \sim 17$. This difference in the magnitudes between the catalogues is also partially responsible for the much greater richnesses found in ACO. Since a change in magnitude of 0.25 is approximately equivalent to changing the Abell radius by 2′ at $b_j = 17$, and the Abell radius is 20′, the change in the counting area is 20%. Therefore, we would expect to see greater richnesses in ACO from this argument.

For the full ACO cluster list only, the number of matches found were 222 out of 417 (185 out of 413 for the 5′ matching radius). Therefore, the percentage of full clusters found is 53% and of the supplementary clusters, 36%. Fig. 8 shows a scatter plot of m_{10} against richness for those clusters detected which are in common between the EDCC and Abell catalogues, Fig. 9 a plot of those Abell clusters not found and Fig. 10 a plot of those EDCC clusters not found within the Abell catalogue. The magnitudes of the northern clusters have been transformed into the V-band using equations 8 and 9 of ACO. Since the magnitude scale is unreliable beyond $R \sim 17$, it is not surprising that this transformation leaves many northern clusters fainter than $V \sim 20$. The supplementary catalogue limits are marked as dashed lines. In both cases the values plotted for magnitude and richness are taken from ACO (using their corrected richness but uncorrected $m_{10}(V)$ data).

Fig. 11 shows the percentage of ACO clusters found to any given magnitude within four richness

bands. At the nominal completeness limit of the ACO catalogue ($V \sim 17$), 70% of the rich ACO clusters are found within the EDCC. All the bright ($V < 16$) rich clusters are found. In total, 65% of all ACO clusters brighter than the completeness limit of the ACO catalogue are located within the EDCC. Within the completeness limit of the EDCC (assumed to be $V \sim 18$), 80% of the full ACO cluster list are still found (though the rate of detections is dropping rapidly at the limit as shown by Fig. 11). Many of the Abell clusters are considerably fainter in the EDCC survey (since if the EDCC clusters are restricted to $b_j \sim 17.75$ and this comparison carried out again, then only 30% of the ACO clusters are found and 38% of the northern clusters). This is consistent with the relation between the ACO and EDCC magnitude systems derived above. However, the overall detection rates for all clusters only drop sharply for magnitudes fainter than the completeness limit of the EDCC. The overall detection rate of the northern clusters is 70%. This rate does not vary strongly with magnitude given the problems with the northern Abell magnitude system.

By comparison, truncating the EDCC at our completeness limit and comparing with the total ACO catalogue results in only 42% of the EDCC clusters being found. Even if only clusters with more than 30 members within the EDCC are considered, this value only rises to 58%. Clearly, there are many more new clusters in the EDCC that are not in the Abell catalogue.

We have visually checked all those missing ACO clusters with $n_{clus} > 30$ and distance class less than 5 (see Table 2A of ACO for the definition of distance class - the limit corresponds approximately to 17.9 in V for clusters near the SGP). Most of these are either close to the threshold used in the peak-finding algorithm (Section 2.2) or distant. Some of those clusters examined are near areas removed from the EDSGC (satellite trails or bright stars near the centre of the cluster field), or were found to be marginal detections (in terms of finding a peak above the local background). Others also appear to have wildly inaccurate magnitude estimates and may actually lie outside the completeness limit of the EDSGC. In a few cases, no cluster was evident on the plate.

The richnesses for the ACO clusters were also corrected to a local background as described above and a second comparison carried out. This is shown in Table 6. Corwin has systematically larger richnesses (as in Fig. 6 for the global background: a fact they note themselves in ACO in their internal comparisons), whereas for Olowin's clusters the scatter has no systematic trend. The large scatter still found in the richness after correcting to local background counts is partly due to the difficulties of transforming from b_j counts to V counts; however, it is likely that the much of the error arises from the quoted errors both for the EDCC and the ACO catalogues (which predict a scatter of about 23 counts - the residual discrepancy between this value and that given in Table 6

is probably due to the differences in background estimation). The difficulty in estimating richness for a purely visual survey such as ACO should not be underestimated (see also Scaramella *et al.*, 1990, for a discussion of the richness of ACO clusters).

There are also indications that the Corwin clusters have larger true scatters in their magnitude estimates. The scatter is larger than might be expected purely from the quoted errors in the ACO and EDCC surveys. One might expect, for example, a scatter of 0.35 magnitudes for the m_{10} comparison from the estimates of Table 5. Even allowing for a large intrinsic scatter in the galaxies colours, the $b_j - V$ correction cannot explain the observed discrepancy. However, this may be partly due to chance, since the actual distribution of the most outlying points on the scatter diagram for the Abell/Corwin clusters is mostly the same as that for the Olowin clusters. Part of the scatter in m_{10} probably arises from the difference in definition of m_{10} between ACO and the methods presented here (especially the iterative background removal procedure).

5 SUMMARY

The EDCC is the first automated, objectively selected cluster catalogue. Its success rate in finding 80% of the full Abell clusters in the ACO catalogue suggests that, within the quoted completeness limit, the EDCC is at least 90% complete for the Abell sub-sample (assuming that 10% of all Abell clusters are seriously in error in their classification as appears to be the case from the visual check carried out of those bright ACO clusters not found in the EDCC as described in Section 4.2). By comparison, almost 70% of the clusters in the EDCC brighter than the completeness limit of $m_{10}(b_j) \sim 18.5$ are new clusters. This lends credence to the idea (already stated by both Abell and ACO) that the Abell catalogue is not useful as a statistical database.

Furthermore, we find magnitude and richness errors in the Abell catalogues which are sufficient to move such clusters by more than one richness or distance class (in terms of their Abell, 1958, definition). This clearly makes the Abell catalogue unsuitable for calculating any large scale clustering properties. In contrast, the EDCC is statistically complete within the limits and for the selection procedures described.

The extent of the data available will also allow tests of non-Abell classification schemes, or of modifications to the Abell classification scheme (*e.g.* McGill & Couchman, 1990, Sutherland, 1989). This will be discussed in detail in a future paper. In order to utilise this new catalogue to its fullest extent, we have also undertaken a large redshift survey program, using a slightly modified Abell method for our selection. One hundred of the richest clusters with $m_{10} < 18.5$ have been observed.

On average, 10 redshifts per cluster were obtained. This will enable a rigorous determination of the spatial correlation function (Nichol *et al.*, 1992), free from many of the contaminating projection effects notable in previous estimations (*e.g.* Bahcall & Soneira, 1983). The wealth of redshift information will also enable a major analysis of the cluster LF. Since the EDCC covers 5% of the whole sky, it will allow advances in the statistical study of clusters. All these aspects of the catalogue will also be discussed in future papers.

Acknowledgements

We would like to thank Harvey MacGillivray for his comments on an early draft of this paper, and the anonymous referee for valuable comments which helped us to clarify the text. We would also like to thank Neil Heydon-Dumbleton for his contributions to the early stages of this project. RCN thanks Roberto Scaramella for enlightening discussions. SLL is grateful to the Royal Observatory Edinburgh for providing the facilities with which much of this work was carried out and would like to thank Bob Joseph for allowing him to carry on the work at Imperial College. SLL acknowledges receipt of an SERC postdoctoral fellowship during the latter stages of this work and RCN acknowledges receipt of an SERC studentship. This paper is based on data from the COSMOS measuring machine.

References

Aaronson, M., Bothun, G., Mould, J., Huchra, J., Schommer, R.A. & Cornell, M.E., 1986. *Astrophys. J.*, **302**, 536.

Abell, G.O., 1958. *Astrophys. J. Suppl.*, **3**, 211.

Abell, G.O., 1962. In: *Problems of Extragalactic Research, IAU Symp. No. 15*, p.213, ed. McVittie, G.C., MacMillan, New York.

Abell, G.O., Corwin, H.G. & Olowin, R.P., 1989. *Astrophys. J. Suppl.*, **70**, 1.

Bahcall, N.A. & Soneira, R.M., 1983. *Astrophys. J.*, **270**, 20.

Beard, S.M., MacGillivray, H.M. & Thanisch, P.F., 1990. *Mon. Not. R. astr. Soc.*, **247**, 311.

Colless, M., 1989. *Mon. Not. R. astr. Soc.*, **237**, 799.

Couchman, H.M.P., McGill, C. & Olowin, R.P., 1989. *Mon. Not. R. astr. Soc.*, **239**, 513.

Dodds, R.J. & MacGillivray, H.M.G., 1986. *Astr. J.* **92**, 706.

Dressler, A., 1978. *Astrophys. J.*, **223**, 765.

Ellis, R.S., 1990. In: *Gravitational Lenses*, p236, eds. Mellier, Y., Fort, B. & Soucail, G., Springer-Verlag, Berlin.

Guzzo, L., Nichol, R.C., Collins, C.A. & Lumsden, S.L., 1992. In preparation.

Heydon-Dumbleton, N.H., Collins,C.A., & MacGillivray, H.T., 1989. *Mon. Not. R. astr. Soc.*, **238**, 379.

Lucey, J.R., 1983. *Mon. Not. R. astr. Soc.*, **204**, 33.

Lugger, P.M., 1986. *Astrophys. J.*, **303**, 535.

Lynden-Bell, D., Faber, S.M., Burstein, D., Davies, R.L., Dressler, A., Terlevich, R.J. & Wegner, G., 1988. *Astrophys. J.*, **326**, 19.

McGill, C. & Couchman, H.M.P., 1990. *Astrophys. J.*, **364**, 426.

Nichol, R.C., Collins, C.A., Guzzo, L. & Lumsden, S.L., 1992. In preparation.

Postman, M., Geller, M.J. & Huchra, J.P., 1986. *Astr. J.*, **91**, 1267.

Postman, M., Geller, M.J. & Huchra, J.P., 1992. *Astrophys. J.*, , in press.

Scaramella, R., Zamorani, G., Vettolani, G. & Chincarini, G., 1990. preprint.

Schechter, P. & Press, W.H., 1976. *Astrophys. J.*, **203**, 557.

Shane, C.D. & Wirtanen, C.A., 1967. *Publs Lick Obs.*, No. 22, Part 1.

Shectman, S.A., 1985. *Astrophys. J. Suppl.*, **57**, 77.

Struble, M.F. & Rood, H.J., 1991. *Astrophys. J.*, **374**, 395.

Sutherland, W., 1988. *Mon. Not. R. astr. Soc.*, **234**, 159.

Sutherland, W., 1989. PhD. thesis, University of Cambridge.

Thanisch, P., McNally, B.V. & Robin, A., 1984. *Image Vis. Comput.*, **2**, 4

Zwicky, F., Herzog, E., Wild, P., Karpowicz, M. & Kowal, C.T., 1961-1968. *Catalogue of Galaxies & Clusters of Galaxies*, 6 volumes, Calif. Inst. Technol., Pasadena.

Figure Captions

Figure 1: Scatter plots showing the comparison of (a) m_{10} values for all EDCC clusters, (b) m_{10} values for those with more than 30 members and (c) richness values for all EDCC clusters. Symbols are (+) for run 1 against run 2, (□) for run 1 against run 3 and (∗) for run 2 against run 3. In all cases the lower numbered run is on the X-axis.

Figure 2: Number-magnitude counts for the EDCC and ACO. Differential counts are indicated by • (EDCC) and ⋆ (ACO). The solid line is the cumulative EDCC counts, and the dotted line the cumulative ACO counts. The dashed straight line fit has a slope of 0.65 ± 0.05, and is fitted to the EDCC data between $b_j \sim 15.9$ and $b_j \sim 18.9$. The error bars on the differential EDCC counts are Poissoinian.

Figure 3: Number-richness counts for the EDCC and ACO. Symbols as in Fig. 2.

Figure 4: Comparison of the expected size distribution of Abell clusters (dotted line) compared to that found for the EDCC. The expected size distribution of the Abell clusters was calculated assuming a slope for the differential number-magnitude counts of 0.6.

Figure 5: Sky distribution of the EDCC clusters. Filled circles have richness > 30, open circles richness < 30.

Figure 6: Comparison of the richness for clusters found in common between the EDCC and Abell catalogues. • denotes a Corwin cluster, ∗ an Olowin cluster and + a Northern Abell catalogue cluster.

Figure 7: As for Fig. 6 except for m_{10} values. ACO V magnitudes and northern R magnitudes have been corrected to b_j.

Figure 8: Scatter plot of m_{10} against richness for all those Abell clusters that match up with the EDCC. The dashed lines show the limits of the supplementary catalogue. Symbols as in Fig. 6.

Figure 9: As for Fig. 8 except for those clusters in the Abell catalogue that do not match up with the EDCC. Symbols as in Fig. 6.

*Figure 10: As for Fig. 9 except for those clusters in the EDCC that do not match up with the Abell catalogue. * denotes an EDCC cluster.*

Figure 11: The detection rate of ACO clusters with different richnesses (where richness is denoted by c). The data has been binned into one magnitude wide bins.

Table 1: Values used in the binning routines.

run no.	magnitude limit	bin size (arcmin)	threshold (galaxies/bin)	number of cands
1	18.5	8	$1.5\,(2.3\sigma, \sigma = 0.65)$	438
2	19.5	5	$2.5\,(3.9\sigma, \sigma = 0.64)$	491
3	20.5	3	$3\,(4.6\sigma, \sigma = 0.65)$	633

Table 2: Error estimates.

Sample	σ_1	σ_3	σ_{m10}	σ_{counts}
All clusters: run 1 v 2	0.54	0.36	0.24	10.4
All clusters: run 1 v 3	0.52	0.31	0.34	9.2
All clusters: run 2 v 3	0.42	0.31	0.26	9.5
$c > 30$: run 1 v 2	0.57	0.24	0.15	10.4
$c > 30$: run 1 v 3	0.60	0.24	0.19	8.2
$c > 30$: run 2 v 3	0.46	0.16	0.15	9.5
Final catalogue	0.34	0.23	0.18	6.9
Final catalogue: $c > 30$	0.38	0.15	0.15	6.5
Final catalogue: offset $< 2'$	0.32	0.14	0.08	4.6

Table 5: Comparison of EDCC and Abell catalogues.

Sample	σ_{m_1}	σ_{m_3}	$\sigma_{m_{10}}$	σ_{counts}
All ACO clusters	1.30	0.93	0.79	34.7
ACO clusters with offset $< 5'$	1.21	0.88	0.74	34.4
Full ACO custers only	1.34	0.90	0.72	36.7
All Northern clusters			0.78	40.4

Table 6: Comparison of EDCC and Olowin and Corwin clusters.

Sample	σ_{m_1}	σ_{m_3}	$\sigma_{m_{10}}$	σ_{counts}(local)
Olowin's clusters (local counts)	1.24	0.87	0.56	38.7
Corwin's clusters (local counts)	1.55	1.26	0.98	50.6

Table 7: Estimates of the internal errors in the ACO catalogue.

Sample	σ_{m_1}	σ_{m_3}	$\sigma_{m_{10}}$	σ_{counts}
All clusters	1.28	0.98	0.82	33.0

EDCC	R.A. h	m	s	Dec. °	′	″	m_1	m_3	m_{10}	n_{clus}	n_{back}	θ_A	Field	runs	Deb.	Abell
1	21	26	47.4	−22	29	39.0	17.28	18.13	19.58	21	40	0.151	F531	111	d	2347
2	21	27	17.3	−22	40	41.5	16.88	17.02	18.76	11	19	0.196	F531	010	d	
3	21	28	1.9	−24	1	1.9	15.68	17.62	17.99	40	70	0.269	F531	110	d	
4	21	29	27.7	−24	9	40.9	14.65	17.33	18.12	47*	44	0.255	F531	111	d	
5	21	29	33.9	−22	53	2.0	15.95	17.38	18.56	15	71	0.212	F531	011	d	3778
6	21	29	59.3	−23	1	14.0	15.63	16.78	19.05	8	32	0.178	F531	121	d	
7	21	30	37.5	−23	57	14.8	18.29	18.37	19.04	24*	95	0.179	F531	010	d	
8	21	30	54.0	−26	0	24.8	16.12	18.10	0.00	0	0	0.000	F531	011	d	
9	21	31	31.3	−27	18	28.2	15.24	15.87	17.22	15	7	0.370	F531	110	d	
10	21	31	46.7	−26	15	51.2	15.52	16.22	17.62	22	11	0.313	F531	100	d	
11	21	32	55.6	−26	53	59.2	15.11	16.11	18.17	8	5	0.249	F531	100	d	
12	21	33	55.8	−23	29	41.7	16.42	17.88	18.45	48	67	0.222	F531	011		2357
13	21	36	40.9	−27	19	50.7	17.54	18.27	18.65	38	62	0.205	F531	010		3797
14	21	36	53.1	−26	49	41.3	14.09	17.32	18.15	13	34	0.252	F531	100	d	
15	21	37	31.8	−23	5	51.3	14.41	15.77	17.15	23	10	0.381	F531	113	d	(S 963)
16?	21	37	38.6	−32	37	11.7	17.34	17.39	18.33	33	15	0.233	F466	012	d	(3795)
17?	21	37	56.5	−31	16	30.7	14.55	19.72	20.27	22	16	0.120	F466	001		
18	21	38	6.7	−23	4	21.4	0.00	0.00	0.00	0	0	0.000	F531	001	d	
19?	21	38	11.0	−32	6	50.5	16.00	16.83	18.38	14	9	0.229	F466	100	d	
20	21	38	15.1	−27	0	33.2	17.09	18.14	19.38	28	36	0.161	F531	011	d	
21	21	38	17.2	−29	13	16.2	15.49	16.45	17.90*	7	11	0.279	F466	110		
22?	21	38	22.8	−28	39	24.5	16.95	17.77	18.17	43	52	0.249	F466	011		
23?	21	39	37.7	−31	36	23.8	18.42	18.75	19.84	48	24	0.138	F466	001	d	
24?	21	39	39.8	−31	55	35.3	17.09	18.02	18.33	69	39	0.233	F466	110	d	
25?	21	39	47.0	−32	34	40.3	16.34	17.40	18.36	34	18	0.231	F466	010	d	
26	21	40	35.1	−25	26	13.5	13.67	17.31	18.20	19	40	0.245	F531	100		
27	21	41	0.0	−31	19	51.3	15.86	18.16	18.49	59*	46	0.211	F466	001		
28?	21	41	33.4	−32	28	58.4	17.41	18.03	18.71	48	32	0.200	F466	100	d	
29	21	41	33.5	−24	37	17.4	18.57	19.39	20.12	21	39	0.127	F531	001	d	
31	21	42	27.7	−24	23	33.7	15.89	17.61	18.46	55	45	0.221	F531	011	d	2371
32	21	42	42.3	−27	30	52.0	17.04	19.26	19.69	34*	54	0.145	F531	001		
33	21	42	44.6	−22	42	53.5	16.55	17.31	18.63	15	30	0.207	F531	111		
34	21	42	51.5	−26	10	10.3	17.63	17.77	18.89	50*	38	0.188	F531	011		3805
35	21	43	2.7	−30	9	11.5	15.41	18.02	18.89	34	50	0.188	F466	001	d	
36?	21	43	25.2	−31	7	54.8	17.05	17.50	18.46	19	33	0.221	F466	100	d	

Table 8: The Edinburgh/Durham Cluster Catalogue.

EDCC	R.A.			Dec.			m_1	m_3	m_{10}	n_{clus}	n_{back}	θ_A	Field	runs	Deb.	Abell
	h	m	s	°	′	″										
37	21	44	57.1	−30	49	45.3	17.44	17.88	18.13	54*	73	0.254	F466	111	d	
38?	21	45	39.3	−31	58	49.7	17.36	17.87	18.39	40	55	0.228	F466	011		3813
39	21	45	42.2	−28	27	12.9	16.94	17.25	18.34	22	26	0.217	F466	100		
40	21	45	53.1	−27	55	42.8	16.47	16.82	18.65	13	13	0.205	F466	110		
42	21	46	21.9	−30	56	37.8	16.18	17.55	18.21	87	55	0.245	F466	111	d	3814
43	21	46	34.6	−35	54	25.7	16.10	16.73	17.55	30	18	0.323	F404	010	d	
44?	21	46	37.2	−37	36	3.9	16.05	16.36	18.39	6	4	0.228	F404	011	d	
45	21	46	40.2	−34	2	11.8	16.52	16.71	17.78	18	21	0.293	F404	111		(3815)
46	21	46	40.3	−37	6	4.5	16.01	17.06	17.78	57*	17	0.293	F404	111	d	
47?	21	46	45.7	−30	9	10.9	16.65	17.64	18.60	19	40	0.207	F466	100		
48	21	47	32.9	−35	7	5.5	12.70	15.64	17.72	6	4	0.301	F404	220	d	
49?	21	47	34.6	−26	56	12.5	16.57	17.87	18.16	67	75	0.250	F531	110		
50	21	49	2.7	−31	53	30.5	17.39	17.54	18.10	47*	55	0.257	F466	101	d	
51	21	49	22.2	−29	8	1.7	16.35	16.76	17.78	17	30	0.293	F466	111		
52	21	50	12.6	−23	48	46.8	18.60	18.72	19.01	82	71	0.180	F532	011		2385
53	21	50	12.8	−31	47	36.5	17.34	17.83	19.15	16	47	0.172	F466	011	d	
54	21	50	45.7	−42	25	48.9	15.40	16.34	17.87	11	6	0.282	F344	110		(S 978)
55	21	52	4.7	−37	51	18.1	15.88	17.74	17.87	69*	45	0.282	F344	110		
57	21	53	30.9	−30	23	0.4	17.29	18.05	18.19	31	96	0.248	F466	110	d	
58	21	53	38.9	−35	9	38.5	17.25	18.19	18.79	61*	48	0.194	F404	011	d	
59	21	53	42.8	−32	53	38.5	18.29	18.38	19.49	38	44	0.155	F404	001		
60	21	53	47.4	−24	10	5.9	17.04	19.09	19.65	28	57	0.147	F532	001		
61	21	53	59.4	−30	19	37.9	18.24	18.31	0.00	0	0	0.000	F466	001	d	
62	21	54	2.5	−40	10	41.8	15.91	16.08	17.45	16	6	0.336	F344	110	d	
64	21	54	17.0	−38	22	15.8	15.11	16.11	18.09	10*	6	0.257	F344	110		
65	21	54	54.9	−26	57	12.8	17.08	18.58	19.32	53*	56	0.163	F532	001		(3824)
66	21	55	2.0	−39	41	39.2	16.02	16.14	18.02	8	6	0.265	F344	110	d	
67	21	55	35.2	−30	9	33.4	17.58	19.20	19.67	34	60	0.145	F466	001	d	
68	21	55	36.5	−31	7	54.8	16.01	17.08	17.76	34	49	0.296	F466	121		
69	21	55	37.0	−28	49	33.2	13.33	14.54	16.27	8	5	0.594	F466	100		
70	21	56	9.5	−25	26	51.0	16.61	17.51	18.92	12	24	0.186	F532	010		
72	21	56	56.9	−42	20	24.0	16.17	16.84	17.94	47*	24	0.274	F344	110		
73	21	57	16.8	−24	43	45.1	15.53	16.70	18.45	11	12	0.223	F532	100		
75	21	58	7.7	−24	21	16.1	18.45	18.65	18.84	23	79	0.193	F532	010		
76	21	58	41.5	−32	9	44.5	11.92	14.87	17.72	2	1	0.287	F466	100		

EDCC	R.A.			Dec.			m_1	m_3	m_{10}	n_{clus}	n_{back}	θ_A	Field	runs	Deb.	Abell
	h	m	s	°	′	″										
77	21	59	10.6	−22	59	33.9	0.00	0.00	0.00	0	0	0.000	F532	021	d	
78	21	59	15.3	−29	56	21.4	18.37	18.49	19.34	18	53	0.164	F466	010		
79	21	59	21.3	−37	46	52.3	15.45	16.65	18.70	4	10	0.200	F404	010		
80	21	59	25.2	−22	48	38.6	14.63	14.79	16.69	10	3	0.461	F532	110	d	S 987
81	21	59	37.5	−30	19	29.4	17.98	18.83	19.53	23	60	0.157	F466	001		
82	21	59	45.7	−41	24	48.0	14.13	16.95	18.05	20*	25	0.262	F344	100		
83	22	0	3.9	−28	37	58.0	16.75	17.33	19.08	7	18	0.170	F466	001		
84	22	0	19.0	−34	47	30.0	17.73	18.21	19.56	21	32	0.144	F404	001		
85	22	2	5.0	−25	29	37.9	17.06	17.67	19.75	6	18	0.143	F532	001		2416
86	22	2	25.6	−30	45	48.0	16.26	17.35	18.73	16	25	0.202	F467	010		3833
87	22	2	41.5	−33	58	25.7	18.74	19.09	19.41	41*	71	0.157	F404	001		
88	22	3	24.2	−39	24	18.7	17.00	17.14	18.31	13	28	0.235	F344	111		S 993
89	22	3	46.7	−36	37	55.4	16.71	17.49	19.42	10	18	0.158	F404	001	d	
90	22	4	9.6	−42	1	18.3	16.25	17.83	18.40	23	52	0.226	F344	110	d	
91	22	4	55.8	−24	39	44.3	17.71	18.56	19.52	29	50	0.153	F532	001		2417
92	22	5	18.0	−41	47	45.2	16.22	17.00	18.26	10	25	0.240	F344	100	d	
93	22	5	25.9	−26	44	38.1	17.58	18.49	18.88	35	80	0.189	F532	011		
94	22	5	35.4	−26	22	5.7	17.16	18.51	19.05	50	69	0.178	F532	010		(2418)
95	22	5	39.3	−36	45	45.2	16.35	16.90	18.12	23	28	0.255	F404	110	d	
96	22	6	9.7	−35	21	37.2	14.57	15.11	17.11	9	4	0.387	F404	101		S 997
97	22	6	10.8	−32	19	53.3	17.60	19.11	20.48	10	32	0.112	F467	001		
98	22	6	30.3	−28	43	20.2	17.79	18.17	19.49	19	32	0.145	F467	001		
99	22	6	34.9	−27	33	24.0	14.39	14.99	17.67	4	2	0.307	F532	111		3837
100	22	7	17.3	−28	20	34.5	18.20	18.53	19.19	16	55	0.161	F467	001		3838
101	22	7	33.6	−40	6	23.8	16.28	16.38	18.84	2	6	0.191	F344	010		3840
102	22	7	40.2	−30	27	43.3	16.08	18.79	20.24	18	32	0.122	F467	001		
103	22	8	6.3	−28	42	40.5	19.09	19.40	20.30	20	44	0.120	F467	001		
104	22	8	25.3	−33	15	37.0	17.22	17.32	18.38	25	26	0.219	F404	100		
105	22	8	40.5	−39	2	19.3	17.83	18.50	18.63	45	87	0.206	F344	001	d	3842
106	22	8	53.4	−33	55	34.2	16.32	17.62	18.57	21	36	0.211	F404	100	d	S1000
107	22	9	18.5	−34	19	57.5	14.84	15.82	18.04	2	4	0.263	F404	100	d	
108	22	9	49.0	−38	45	4.7	14.81	16.63	18.72	7	10	0.198	F344	010	d	
110	22	9	55.3	−29	15	23.1	18.02	18.41	19.48	21	45	0.158	F467	001		
111	22	9	58.1	−27	15	51.2	16.03	17.80	18.24	42	64	0.242	F532	110		
112	22	10	10.0	−32	49	10.4	16.67	18.46	19.30	39	46	0.167	F404	001		

EDCC	R.A.	Dec.	m_1	m_3	m_{10}	n_{clus}	n_{back}	θ_A	Field	runs	Deb.	Abell
	h m s	° ′ ″										
113	22 10 51.4	−36 37 9.5	0.00	0.00	0.00	0	0	0.000	F404	100	d	
114	22 11 8.7	−36 54 40.2	15.34	16.82	17.15	57	55	0.381	F404	122	d	S1005
115	22 11 9.1	−35 13 31.2	15.66	17.25	18.58	10	24	0.210	F405	001		(3844)
116	22 11 27.2	−34 42 33.7	16.64	16.97	19.45	4	8	0.148	F404	001		
117	22 12 19.5	−27 21 12.5	16.17	17.09	18.58	12	22	0.212	F533	010		(3846)
118	22 13 18.5	−41 19 4.9	15.34	16.41	18.03	5	12	0.264	F344	010		
119	22 13 21.8	−25 51 52.6	15.77	15.94	18.28	6	6	0.238	F533	111		
120	22 13 35.0	−39 31 55.6	18.20	18.31	18.75	28	67	0.192	F344	001		3853
121	22 13 51.5	−25 24 43.5	16.24	16.53	20.04	2	4	0.136	F533	001		
122	22 14 22.9	−38 36 27.2	17.45	17.69	19.22	18	24	0.161	F344	010		
123	22 14 37.1	−26 31 26.3	16.38	16.96	18.87	8*	18	0.189	F533	011	d	(S1008)
124	22 14 43.9	−35 57 33.1	17.07	18.04	18.46	109	63	0.221	F405	011		3854
125	22 15 6.5	−41 50 55.9	16.15	16.59	18.47	11	11	0.220	F344	100		
126	22 15 8.8	−30 19 50.2	16.18	17.20	18.28	17	28	0.240	F467	100		
127	22 15 41.0	−39 8 55.9	16.38	17.49	18.09	53	52	0.257	F344	111		3856
128	22 15 56.3	−28 34 41.1	16.73	17.95	20.32	2	17	0.120	F467	100		
129	22 16 2.1	−24 26 56.1	14.77	16.34	16.75	36*	31	0.449	F533	111		
130	22 16 6.2	−26 47 19.5	14.42	15.75	17.62	12	7	0.313	F533	111	d	(S1010)
131	22 16 39.2	−34 56 27.0	16.73	17.90	18.18	66	63	0.249	F405	111		3858
132	22 17 5.3	−39 46 11.4	16.06	17.30	18.05	20	40	0.262	F344	100		
133	22 17 37.6	−22 39 45.2	16.52	19.18	20.12	19	39	0.127	F533	001		
134	22 17 40.6	−35 23 52.5	17.67	18.61	19.28	27	50	0.158	F405	001		3866
135	22 18 26.4	−26 17 15.3	15.76	17.87	18.85	16	36	0.180	F533	100		
136	22 18 52.3	−29 3 37.1	16.16	17.60	18.89	40*	25	0.188	F467	011		
137	22 19 17.9	−38 52 56.0	15.80	16.26	19.15	5	4	0.170	F345	101		S1016
139	22 21 21.4	−26 27 16.2	16.70	17.44	18.50	15	31	0.218	F533	011		(S1018)
140	22 21 22.6	−42 3 5.8	16.34	17.33	18.23	10	31	0.243	F345	100		
141	22 22 50.9	−35 11 46.4	16.62	18.77	19.17	38	61	0.175	F405	001		
142	22 23 1.5	−31 21 17.7	14.02	14.84	16.43	10	5	0.526	F467	212	d	
143	22 23 48.5	−42 40 58.4	16.72	18.37	19.42	27	42	0.158	F345	010		
144	22 24 3.2	−32 13 26.3	17.30	18.21	19.08	19	33	0.168	F467	001		3878
145	22 24 56.7	−30 51 11.0	15.07	16.27	16.91	34	27	0.421	F467	111	d	3880
146	22 24 59.8	−24 3 54.5	0.00	0.00	0.00	0	0	0.000	F533	001	d	(2444)
147	22 25 28.0	−24 17 24.5	16.18	17.28	17.69	28	46	0.305	F533	100	d	
148	22 25 39.2	−24 42 57.9	15.89	16.43	18.96	7	10	0.183	F533	001	d	

EDCC	R.A.	Dec.	m_1	m_3	m_{10}	n_{clus}	n_{back}	θ_A	Field	runs	Deb.	Abell
	h m s	° ′ ″										
149?	22 26 24.6	−32 15 32.2	16.88	18.01	18.55	51	41	0.205	F468	010		
150	22 26 28.8	−36 39 4.9	15.67	17.30	19.98	5	10	0.133	F405	001		(3882)
151?	22 27 22.4	−24 10 52.0	17.19	17.28	17.55	12	50	0.323	F533	100	d	
152?	22 27 47.2	−24 34 53.0	17.48	17.64	18.47	5	36	0.220	F533	100	d	
153	22 29 19.8	−31 27 51.9	15.55	16.06	17.30	11	9	0.358	F468	101		
154	22 29 23.4	−39 0 52.5	16.76	18.27	19.78	19	44	0.141	F345	001	d	
155	22 29 26.3	−25 40 49.1	13.28	16.05	16.77	10	20	0.446	F533	111		
156	22 29 53.3	−39 16 50.4	16.88	18.58	19.20	53	76	0.170	F345	001	d	3887
158	22 30 45.3	−36 2 11.7	17.72	19.13	19.29	39*	75	0.166	F405	011		
159	22 31 7.4	−39 19 53.2	19.63	19.63	19.94	22	62	0.134	F345	001	d	
160	22 31 32.4	−37 59 54.1	15.42	16.30	18.00	10	14	0.268	F345	011		3888
161	22 32 54.3	−38 59 17.3	16.23	16.63	17.72	18	26	0.301	F345	011		S1042
162	22 33 4.7	−37 36 45.1	14.87	15.88	18.54	5	5	0.214	F405	010		
163	22 33 6.1	−40 40 55.4	18.09	18.12	18.91	19	56	0.187	F345	010		
164	22 33 17.2	−41 43 42.2	15.86	16.67	17.49	14	28	0.331	F345	100		
165	22 33 35.6	−24 36 25.3	14.88	16.27	17.28	26	18	0.361	F534	111		S1043
166	22 34 4.8	−38 17 43.8	16.56	18.27	18.98	56	77	0.182	F345	011		S1045
168	22 34 22.7	−39 26 53.0	15.80	16.67	19.30	4	15	0.164	F345	011	d	S1047
169	22 34 44.9	−39 45 14.8	17.31	17.53	17.98	19	68	0.270	F345	110	d	
170	22 35 9.7	−30 56 26.5	15.98	17.43	18.48	15	23	0.219	F468	001		3892
171	22 35 11.0	−24 9 40.5	17.74	18.01	18.92	26	37	0.189	F534	001		3893
172	22 35 50.4	−37 9 50.4	14.80	15.65	17.05	21	15	0.397	F405	122	d	3895
173	22 35 57.3	−36 39 56.2	16.23	16.52	17.78	18	43	0.293	F406	022	d	
174?	22 36 17.9	−22 48 45.5	15.92	16.34	18.09	14	10	0.258	F534	121		
175	22 36 27.4	−38 5 29.3	16.21	17.53	18.40	42	59	0.227	F345	112		S1051
176	22 36 54.3	−36 26 25.4	0.00	0.00	0.00	0	0	0.000	F406	110	d	(S1050)
177	22 37 27.4	−24 8 2.7	17.87	18.82	19.42	31*	54	0.163	F534	001		3900
178	22 37 50.6	−34 14 33.4	16.42	17.67	18.22	35*	43	0.241	F406	010		
179	22 38 58.7	−36 33 51.5	16.04	19.29	20.29	8	39	0.119	F406	001		
180?	22 39 7.7	−29 27 43.4	16.16	16.74	17.54	21	21	0.327	F468	100		
181	22 39 29.2	−38 51 44.5	18.95	19.32	19.44	95	78	0.156	F345	001		
182	22 39 42.1	−25 15 16.3	15.75	16.44	18.06	12	9	0.261	F534	111		
183	22 40 6.8	−38 20 35.0	18.62	18.73	19.31	35	82	0.166	F345	001		
184	22 40 33.3	−23 43 11.2	16.15	16.86	19.00	5	8	0.181	F534	100		
185	22 41 14.0	−40 7 40.6	13.35	15.90	17.23	15	16	0.376	F345	100		S1055

EDCC	R.A.			Dec.			m_1	m_3	m_{10}	n_{clus}	n_{back}	θ_A	Field	runs	Deb.	Abell
	h	m	s	°	′	″										
186	22	42	28.1	−38	4	2.0	17.32	17.86	18.87	14	51	0.187	F345	100		S1056
187	22	43	23.9	−34	15	32.2	16.36	16.74	17.71	16	26	0.302	F406	100	d	
188	22	43	39.4	−36	21	46.7	15.20	16.29	17.50	29	23	0.329	F406	112		3912
189	22	44	0.9	−39	29	1.8	16.74	16.91	19.70	3	10	0.144	F346	001		
190	22	44	30.4	−41	9	45.4	16.45	17.01	18.41	17	24	0.226	F346	010	d	
191	22	44	41.1	−34	35	46.6	16.95	17.33	19.31	9	21	0.164	F406	001	d	
192?	22	45	18.6	−31	29	26.7	17.67	18.03	18.52	18	48	0.216	F468	010	d	
194	22	45	44.1	−28	51	51.6	16.78	17.58	19.11	23*	18	0.175	F468	011		3918
195	22	46	14.1	−28	21	50.2	15.87	16.92	18.71	10	10	0.200	F468	001		
196	22	46	15.2	−33	5	43.8	16.12	16.50	18.54	7	9	0.214	F406	001	d	S1064
197	22	46	16.1	−37	41	58.6	13.66	15.82	16.70	19	23	0.459	F406	100		S1065
198	22	46	29.7	−41	10	2.1	18.17	18.60	18.76	61	86	0.196	F346	010	d	3920
199	22	46	39.9	−38	55	49.0	16.44	18.98	19.69	12	62	0.147	F346	001		
200	22	46	42.4	−23	47	57.0	17.38	18.90	19.18	62	56	0.171	F534	011		2488
201	22	47	13.5	−31	26	25.6	17.15	17.71	18.10	46*	50	0.257	F468	111	d	
202	22	48	2.1	−33	3	2.8	16.52	16.61	17.81	22	20	0.289	F406	100	d	
203	22	48	13.2	−26	20	35.4	17.81	18.04	18.37	31*	44	0.230	F534	111		2493
204	22	48	32.8	−35	18	5.4	17.08	17.32	18.19	23	32	0.231	F406	100		
205	22	48	43.9	−34	35	42.0	14.98	17.14	18.50	15	22	0.217	F406	100		
206	22	48	59.1	−33	40	16.2	16.72	18.57	19.47	58	52	0.156	F406	001	d	3926
207	22	49	13.2	−32	28	0.5	15.68	17.39	18.95	13	19	0.186	F469	010		3929
208	22	49	18.6	−39	31	20.0	17.51	19.56	19.92	16	51	0.141	F346	001		
209	22	49	31.7	−33	49	22.9	17.00	18.98	19.47	34	64	0.156	F406	011	d	3928
210	22	49	56.5	−31	24	10.6	16.37	17.28	19.51	7	10	0.152	F469	100		3930
211	22	50	0.9	−26	17	17.0	17.58	18.96	19.17	81*	56	0.171	F534	011		2499
212	22	50	7.4	−23	15	45.8	17.86	19.19	19.78	30*	49	0.143	F534	001		
213	22	50	29.0	−28	37	38.0	17.31	17.76	19.87	8	13	0.137	F469	001		
214	22	50	35.9	−35	35	1.6	16.91	18.93	19.43	31	59	0.158	F406	001		
215	22	50	38.9	−29	48	46.9	16.39	16.83	18.49	8	12	0.219	F469	100		
216	22	50	40.5	−25	47	13.6	16.86	17.39	17.98*	79	34	0.270	F534	111		2500
217	22	50	42.2	−30	24	50.8	16.78	16.90	17.82	25*	21	0.275	F469	100		
218	22	50	42.7	−29	8	36.1	16.55	16.94	18.69	10	11	0.201	F469	011		
219	22	51	12.1	−37	17	9.6	15.71	16.97	19.40	2	12	0.166	F406	001		
220	22	51	39.3	−24	45	2.8	16.26	18.70	19.54	17	38	0.149	F534	001		
221	22	52	19.9	−38	55	31.1	17.95	18.41	19.95	19	35	0.133	F346	001		

EDCC	R.A.			Dec.			m_1	m_3	m_{10}	n_{clus}	n_{back}	θ_A	Field	runs	Deb.	Abell
	h	m	s	°	′	″										
222	22	52	43.4	−34	10	54.4	14.09	15.66	17.40	10	8	0.343	F406	100		(3934)
223	22	52	52.9	−42	29	40.8	15.22	16.12	18.27	7	7	0.239	F346	110		
224	22	53	22.5	−38	2	44.4	16.29	17.32	18.48	15	33	0.219	F346	100		
225	22	53	30.8	−28	41	33.3	16.97	17.54	18.78	20	20	0.186	F469	001		3943
226?	22	54	14.2	−27	8	41.1	15.19	16.24	17.67	25	9	0.307	F534	111		(3948)
227	22	55	4.7	−39	21	54.3	16.68	17.67	19.52	10	24	0.151	F346	001		3945
228	22	55	38.9	−31	5	19.5	0.00	0.00	0.00	0	0	0.000	F469	110	d	(S1075)
229	22	56	2.3	−30	58	13.7	14.36	16.62	17.37	39	24	0.348	F469	111	d	
230	22	56	32.8	−31	7	11.7	0.00	0.00	0.00	0	0	0.000	F469	001	d	
231	22	58	5.1	−24	26	44.0	16.50	17.67	18.65	21	28	0.204	F535	011		2518
232	22	58	14.0	−26	33	2.2	18.69	18.78	18.95	10	62	0.178	F535	010		
234	22	59	37.6	−29	28	18.4	18.03	18.46	19.25	26*	43	0.172	F469	001		3958
235	22	59	55.3	−33	38	6.3	17.00	17.75	19.05	18	28	0.178	F407	001	d	3959
236?	23	0	5.0	−28	45	55.9	17.14	17.69	19.15	20	20	0.179	F469	010		
237	23	0	5.6	−35	12	12.7	16.55	18.78	19.38	30	57	0.161	F407	001		3960
239	23	0	50.6	−33	54	25.3	16.90	17.52	19.36	10	18	0.162	F407	100	d	
240	23	0	50.6	−42	35	23.4	16.95	17.38	18.64	18	29	0.206	F346	010		S1084
241	23	1	16.8	−32	6	31.0	16.25	17.21	17.95	26	34	0.273	F469	111	d	
242	23	1	42.5	−24	23	10.1	17.82	19.20	19.49	73*	68	0.155	F535	001		2526
243	23	2	14.2	−32	53	35.4	16.55	16.60	18.10	20	15	0.257	F469	111	d	S1086
244	23	2	36.8	−25	37	21.1	18.06	20.05	20.22	34	33	0.122	F535	001		2527
245	23	2	49.9	−32	28	18.2	15.74	16.55	18.56	8	9	0.212	F469	100	d	
246	23	2	53.2	−33	5	22.7	19.31	0.00	0.00	0	0	0.000	F407	001	d	
247	23	2	56.1	−39	22	14.5	16.49	17.92	18.35	57	65	0.232	F346	011		3968
248	23	2	59.6	−30	55	33.7	14.60	15.62	17.47	11	6	0.333	F469	111		
249	23	3	0.8	−29	21	39.5	16.58	18.94	0.00	0	0	0.000	F469	100	d	
250	23	3	8.6	−34	43	53.0	16.12	18.89	19.74	34	42	0.136	F407	001		
251	23	3	11.0	−35	45	39.8	17.13	18.34	19.67	18	34	0.149	F407	001		
252	23	3	59.1	−29	12	58.9	16.34	17.55	18.31	45	32	0.236	F469	001	d	
253	23	5	1.3	−22	52	46.4	17.69	18.31	18.69	73*	67	0.201	F535	002		2534
254	23	5	26.3	−42	32	39.0	16.45	16.79	17.78	4	34	0.313	F346	100		
255	23	6	0.0	−33	9	58.9	16.41	16.78	19.30	3	6	0.163	F407	001		
256	23	7	36.2	−23	12	39.6	16.93	17.86	18.48	51*	49	0.219	F535	011	d	2541
257	23	7	59.8	−34	22	27.4	16.64	17.10	18.86	11	13	0.190	F407	011		
258	23	8	1.3	−22	55	14.8	16.41	17.98	18.73	41	45	0.198	F535	011	d	2546

EDCC	R.A.			Dec.			m_1	m_3	m_{10}	n_{clus}	n_{back}	θ_A	Field	runs	Deb.	Abell
	h	m	s	°	′	″										
259	23	8	14.0	−40	45	16.4	16.54	18.68	19.27	38	63	0.166	F346	010	d	(3977)
260	23	8	28.2	−28	59	43.2	11.84	16.39	17.88	20	11	0.281	F469	121	d	3978
261	23	9	9.4	−29	19	41.1	16.75	17.37	18.33	26	30	0.233	F469	111	d	S1096
262	23	9	17.9	−41	49	42.4	16.97	17.76	19.09	16	31	0.169	F346	010		
263	23	9	30.4	−41	2	39.1	16.58	17.21	18.67	20	27	0.203	F346	010	d	
264	23	9	38.0	−25	14	56.3	17.52	18.82	19.08	56	71	0.176	F535	011		2553
265	23	9	58.0	−39	25	31.7	16.63	18.69	19.28	39	63	0.166	F347	001		
266	23	10	19.5	−28	38	54.9	12.37	16.74	19.09	5*	5	0.176	F470	011		3980
267	23	10	24.1	−30	36	29.3	16.80	17.48	18.57	29*	25	0.211	F469	110		
268?	23	11	35.8	−26	46	7.1	17.73	19.01	19.65	44	54	0.147	F535	001		
269	23	12	32.5	−38	2	9.0	14.58	17.64	18.54	54	34	0.214	F347	011		3984
270	23	13	24.3	−23	39	58.8	16.67	17.48	18.27	21	37	0.239	F535	101		3985
271	23	13	28.7	−38	38	39.0	17.32	18.72	19.79	26	48	0.148	F347	001		
272	23	13	35.3	−39	12	1.8	15.99	16.26	18.80	2	5	0.193	F347	010	d	
273	23	14	23.0	−39	34	32.7	17.16	17.41	18.42	25	30	0.225	F347	101	d	
274	23	14	47.5	−37	28	32.7	18.53	18.74	19.74	19	38	0.134	F407	001		
275	23	14	52.5	−25	37	9.1	16.25	17.72	19.11	8	22	0.171	F535	001		
276	23	15	25.8	−35	54	41.1	18.46	18.75	19.50	50	46	0.155	F407	001		3989
277	23	15	34.9	−36	34	4.8	16.64	18.38	19.39	33	39	0.161	F407	001		S1109
278	23	15	40.9	−33	56	47.9	17.32	17.40	19.26	8	13	0.167	F407	001		
279	23	15	47.7	−27	47	16.6	16.23	17.53	18.34	37	30	0.232	F535	110		
281	23	16	23.3	−34	35	3.4	16.47	17.25	18.20	11	25	0.246	F407	100		
282	23	16	30.9	−37	43	57.9	18.71	19.62	20.03	24	44	0.134	F407	001		
283	23	16	37.6	−42	18	28.7	11.23	12.30	16.38	1*	0	0.548	F347	110	d	S1111
284	23	17	3.3	−22	44	31.0	17.98	18.38	19.45	31	50	0.167	F536	001		2576
285	23	18	12.7	−42	9	24.7	0.00	0.00	0.00	0	0	0.000	F347	110	d	(3998)
286	23	18	19.4	−29	8	48.3	16.47	17.49	20.06	6	8	0.128	F470	001		
287	23	18	39.1	−23	25	49.0	15.71	16.78	18.37	20	14	0.230	F536	112		2580
288	23	19	39.4	−40	57	9.3	16.48	16.64	18.73	8	10	0.209	F347	100		4000
289	23	20	16.0	−26	33	20.8	17.55	18.54	19.55	40	42	0.157	F536	001		2585
290	23	20	23.5	−31	41	47.7	15.99	18.33	19.00	29	45	0.176	F470	010		
291	23	21	30.0	−22	50	16.3	17.31	18.78	19.24	20	68	0.167	F536	010		(2587)
292	23	22	19.4	−30	35	45.6	16.45	17.07	18.32	14	17	0.235	F470	100	d	(S1119)
293	23	22	26.0	−23	41	59.2	14.79	17.59	18.24	27	45	0.242	F536	111		2596
294?	23	22	49.0	−29	47	51.8	15.76	17.92	18.16	27	53	0.249	F470	100		

EDCC	R.A.			Dec.			m_1	m_3	m_{10}	n_{clus}	n_{back}	θ_A	Field	runs	Deb.	Abell
	h	m	s	°	′	″										
295	23	23	30.3	−39	30	39.0	15.13	16.03	17.59	16	9	0.317	F347	110		
296	23	23	33.9	−30	49	59.8	15.98	16.75	0.00	0	0	0.000	F470	100	d	
297	23	23	46.2	−24	14	59.1	16.86	17.41	18.04	60*	38	0.263	F536	122		2599
298	23	24	5.9	−22	42	22.6	17.82	17.90	18.35	25	63	0.232	F536	111		2600
299	23	24	10.1	−32	0	0.0	17.51	18.79	19.63	43	45	0.143	F470	001		S1123
300?	23	25	32.8	−25	10	58.2	17.96	18.13	18.73	17	48	0.198	F536	010		
301	23	25	39.6	−29	25	39.6	16.80	17.07	18.89	16	10	0.188	F470	011		S1127
302	23	25	42.1	−36	41	48.4	16.17	18.07	18.54	21	60	0.227	F408	010		
303	23	26	20.5	−23	39	26.9	16.63	17.03	18.38	12	19	0.229	F536	111		2605
304	23	26	43.1	−30	25	58.3	17.24	18.26	19.48	9	33	0.158	F470	001		
305	23	26	53.8	−31	22	14.1	15.46	16.02	18.45	6	3	0.221	F470	100		S1129
306	23	27	9.6	−36	2	34.8	16.33	17.28	17.88	21	41	0.286	F408	100		
307	23	27	31.1	−39	33	24.8	14.88	16.16	17.72	11	10	0.301	F347	111		4008
308	23	27	42.9	−35	13	24.0	15.26	15.93	17.09	26	12	0.391	F408	111	d	
309	23	27	57.2	−26	24	5.1	16.57	17.34	19.56	5	9	0.153	F536	001		2609
310	23	27	59.1	−29	31	52.8	16.49	17.92	18.69	38	32	0.201	F470	011		4009
311	23	28	36.0	−36	47	41.4	14.66	0.00	0.00	0	0	0.000	F408	011	d	(4010)
312	23	29	13.0	−34	22	0.5	16.64	17.13	17.85	24	33	0.285	F408	110	d	(4012)
313	23	29	18.9	−30	21	8.1	16.33	16.70	18.36	16	10	0.231	F470	110		
314	23	29	19.2	−34	41	12.1	16.86	17.53	19.13	17	33	0.174	F408	001	d	4011
315	23	29	20.2	−35	34	4.3	17.54	17.96	19.83	9	30	0.138	F408	001	d	4013
316	23	29	49.8	−36	31	28.1	15.92	16.51	17.03	96*	33	0.400	F408	110	d	
317	23	31	19.4	−33	55	41.1	17.29	18.69	19.20	26	64	0.172	F408	010		
318	23	31	52.7	−32	35	44.7	15.37	17.28	18.10	25	32	0.257	F470	010	d	
319	23	33	8.4	−38	47	46.7	16.45	17.26	18.29	7	26	0.237	F347	100		
320	23	33	26.2	−31	52	26.5	14.64	16.51	17.83	20	13	0.287	F470	111		S1136
321	23	33	30.3	−32	47	38.9	15.35	16.31	18.30	8	7	0.237	F408	111	d	
322	23	33	36.9	−36	12	10.9	16.47	17.13	18.58	27	20	0.210	F408	012		
323	23	33	51.4	−30	39	58.7	16.42	16.86	18.66	10	10	0.204	F470	011		
324	23	34	3.4	−24	29	17.2	18.20	18.22	19.00	33	41	0.181	F536	011		2628
325	23	34	52.0	−31	17	6.3	16.38	17.59	18.09	0	44	0.265	F471	100		
326	23	35	9.7	−38	29	18.9	15.64	16.82	18.46	17	13	0.221	F347	110		4021
327	23	35	26.5	−40	57	38.8	15.21	16.36	18.14	13	8	0.253	F347	110		
328	23	35	35.1	−31	47	24.6	16.23	17.65	19.48	13	16	0.156	F471	100		
329	23	38	11.4	−30	34	11.6	16.49	17.17	18.46	10	17	0.221	F471	100	d	S1142

EDCC	R.A.			Dec.			m_1	m_3	m_{10}	n_{clus}	n_{back}	θ_A	Field	runs	Deb.	Abell
	h	m	s	°	′	″										
330	23	38	12.9	−37	50	24.9	17.15	18.28	20.00	13	59	0.131	F348	010	d	4026
331	23	38	15.2	−25	8	28.6	17.10	19.44	19.62	78	60	0.148	F536	001		2641
332	23	39	4.3	−29	28	46.3	15.06	17.08	17.73	50*	31	0.299	F471	110		
333	23	39	8.4	−37	47	31.5	16.53	18.32	19.78	18	58	0.141	F348	011	d	
334	23	39	31.2	−42	21	48.6	16.32	17.52	18.53	17	23	0.224	F348	100		
335	23	39	36.3	−30	28	45.3	16.23	18.16	18.83	17	44	0.192	F471	111	d	
336	23	40	40.0	−36	31	17.6	14.79	15.36	16.48	12	14	0.504	F408	100		
338	23	41	5.9	−38	32	21.0	15.57	17.31	19.10	8	15	0.175	F348	001		4029
339	23	41	27.7	−34	46	32.7	15.65	17.43	17.94	20	43	0.256	F408	100		
341	23	42	20.2	−24	3	39.5	15.35	15.66	17.32	9	6	0.355	F537	101		
342	23	42	29.3	−26	17	35.6	16.75	17.02	17.68	19	26	0.306	F537	100	d	2660
343	23	42	33.3	−42	1	15.2	17.73	17.81	18.69	13	26	0.207	F348	010		
344	23	42	45.5	−24	45	52.8	16.43	18.84	19.84	26	40	0.136	F537	001		4031
345	23	43	34.3	−23	27	36.6	15.62	16.91	18.05	13	17	0.262	F537	110		S1146
346	23	43	45.3	−28	35	50.7	0.00	0.00	0.00	0	0	0.000	F471	001	d	
347	23	44	31.9	−33	53	46.3	17.71	18.63	19.38	38	50	0.156	F408	001		4035
348	23	44	33.7	−28	31	40.6	13.77	15.20	15.90	43*	24	0.783	F471	121	d	4037
349	23	45	9.8	−38	46	58.1	14.71	15.21	16.97	11	6	0.394	F348	100		
350	23	45	40.7	−36	32	37.9	19.54	19.72	19.91	54	47	0.138	F408	001		4039
351	23	46	21.8	−31	34	17.7	18.78	18.96	19.78	33	41	0.141	F471	001		4043
352	23	46	34.3	−35	15	21.6	16.06	16.59	18.06	19	15	0.249	F408	100		
353	23	46	51.1	−27	14	37.4	16.07	18.33	19.10	50	42	0.176	F537	011		4044
354	23	47	8.8	−29	23	54.1	15.01	15.64	17.38	10	7	0.346	F471	100	d	S1155
355	23	47	18.1	−25	0	13.5	18.65	18.87	19.39	40	56	0.158	F537	001		2663
356	23	47	21.2	−35	59	3.5	15.40	16.52	18.86	5	8	0.190	F408	001		
357?	23	47	51.2	−37	27	13.3	19.21	19.43	19.75	43	58	0.143	F348	001		
358	23	48	11.4	−39	5	2.6	15.22	17.55	18.41	11	28	0.209	F348	100		
359	23	48	26.6	−38	43	20.8	18.30	19.26	19.56	66	63	0.149	F348	001		4048
360	23	48	26.6	−34	41	56.4	16.16	0.00	0.00	0*	0	0.000	F349	100	d	
361	23	49	2.4	−28	37	44.0	14.17	15.34	17.04	17*	12	0.399	F471	100	d	4049
362	23	49	58.5	−34	40	29.5	15.09	16.53	17.32	36*	31	0.355	F349	112	d	S1157
363	23	50	7.6	−34	25	12.5	14.89	0.00	0.00	0	0	0.000	F349	001	d	
365	23	51	56.5	−32	51	53.5	16.96	17.91	19.51	1	24	0.153	F349	100		
366	23	52	19.6	−27	56	40.0	15.60	16.89	17.78	32	26	0.293	F471	111		4053
367	23	52	40.8	−28	49	9.8	17.16	18.70	18.87	54	69	0.190	F471	001		4054

EDCC	R.A.			Dec.			m_1	m_3	m_{10}	n_{clus}	n_{back}	θ_A	Field	runs	Deb.	Abell
	h	m	s	°	′	″										
368	23	53	0.7	−33	56	6.4	16.46	17.66	18.59	26	45	0.225	F349	010		S1161
369	23	53	28.3	−37	33	48.6	18.59	18.70	19.61	24	56	0.153	F348	001		4056
370	23	53	49.7	−31	38	26.1	14.62	16.59	17.56	9	20	0.321	F471	100		
371	23	54	4.4	−36	55	14.2	16.62	18.81	19.68	49	55	0.145	F349	010		4058
372	23	54	18.2	−34	54	40.8	13.86	14.89	16.48	14	7	0.508	F349	111	d	4059
373	23	54	37.1	−32	53	39.6	10.09	16.61	17.62	21	22	0.313	F349	111		
374	23	54	57.4	−37	53	8.8	16.44	16.76	18.64	9	10	0.206	F348	011		S1164
375	23	55	50.9	−24	41	34.5	18.49	18.64	19.30	41	46	0.164	F537	001		2685
376	23	56	5.6	−34	36	9.8	15.74	0.00	0.00	0	0	0.000	F349	122	d	
377	23	56	26.4	−32	9	31.6	15.17	17.26	17.48	60	61	0.332	F471	100	d	
378	23	56	45.7	−32	10	44.0	17.57	0.00	0.00	0	0	0.000	F471	011	d	
380?	23	56	54.5	−31	37	42.1	16.44	16.92	18.34	21	17	0.232	F471	111	d	
381	23	57	14.2	−39	45	34.2	16.71	18.00	18.50	64	47	0.218	F348	110		4068
382	23	57	37.7	−25	29	52.7	16.81	17.19	18.51	20	15	0.217	F537	111		2690
383	23	57	47.9	−30	39	55.6	16.74	19.31	19.61	46*	57	0.145	F409	001		4070
384?	23	58	14.3	−28	54	56.6	17.60	18.53	19.23	26	43	0.164	F409	010		
385	23	58	25.9	−37	5	11.1	18.90	18.94	19.64	24	57	0.149	F349	001		S1170
386	23	58	28.3	−38	56	36.9	15.30	17.83	18.47	24	42	0.220	F348	100		S1172
387	23	58	35.2	−36	39	0.0	15.80	17.63	18.55	35	43	0.213	F349	111	d	4074
388	23	58	53.9	−27	54	6.8	14.22	15.38	16.79	11	8	0.442	F409	110	d	S1171
389	23	58	56.2	−39	26	25.4	16.55	17.69	18.42	13	36	0.222	F348	100		
390	23	59	26.2	−25	23	58.5	16.05	17.55	19.15	12	16	0.171	F537	001		
391	23	59	43.6	−32	3	49.1	16.77	18.52	19.92	18	32	0.134	F409	001		
392	0	0	13.9	−34	56	38.4	17.65	17.73	18.33	42	60	0.233	F349	111		2715
393	0	0	30.3	−30	12	46.7	15.98	16.36	18.06	10	11	0.261	F409	110		S 2
394	0	0	32.1	−36	12	58.9	14.57	16.71	17.22	29	44	0.370	F349	111	d	2717
395	0	0	33.8	−28	10	9.8	15.77	17.45	0.00	0	0	0.000	F409	100	d	(S 3)
396	0	0	37.9	−27	28	15.6	15.97	17.44	18.64	16	31	0.206	F472	111	d	2716
397	0	1	0.8	−42	12	53.2	16.61	18.38	19.03	31	43	0.175	F293	010		2718
398	0	1	25.3	−23	25	15.7	17.09	18.13	18.76	34	42	0.196	F472	101		2719
399?	0	1	56.3	−42	35	23.9	16.89	18.66	19.14	36	60	0.181	F293	010		
400	0	3	39.1	−34	58	49.1	16.30	17.64	18.28	98	51	0.238	F349	111	d	2721
401	0	3	41.5	−39	1	25.8	18.80	19.34	20.09	34	43	0.127	F293	001		
402	0	3	53.0	−26	36	36.5	17.08	17.41	18.07	25	39	0.279	F472	100		
403	0	4	50.4	−34	57	44.5	18.42	18.51	18.98	40	90	0.182	F349	001	d	

EDCC	R.A.			Dec.			m_1	m_3	m_{10}	n_{clus}	n_{back}	θ_A	Field	runs	Deb.	Abell
	h	m	s	°	′	″										
404	0	5	17.7	−25	25	33.0	16.68	17.67	18.34	9	36	0.232	F472	100		
405	0	6	33.3	−42	4	13.9	17.33	18.09	18.52	16	51	0.210	F293	010		
406	0	6	34.0	−25	55	41.6	18.35	18.52	19.28	23	44	0.166	F472	001		
407	0	6	38.9	−35	35	0.2	15.08	16.53	17.78	16	17	0.293	F349	110	d	S 12
408	0	7	27.8	−35	56	8.6	16.85	18.13	18.45	52	78	0.222	F349	111	d	2730
409	0	8	41.1	−30	14	41.7	15.43	16.57	17.80	8	16	0.287	F409	100		
410	0	8	46.0	−29	7	35.1	15.03	16.15	17.44	25	12	0.337	F409	111		2734
411	0	10	23.1	−42	28	55.6	16.40	17.06	18.44	16	21	0.232	F293	010		2736
412	0	10	39.3	−35	46	6.4	15.87	16.40	17.42	24	18	0.340	F349	111		
413	0	10	54.4	−24	30	43.9	14.19	17.86	18.45	11*	63	0.222	F473	111	d	
414	0	11	11.7	−38	1	36.9	16.54	17.57	18.92	18	22	0.186	F294	001	d	S 17
415?	0	11	18.3	−37	35	50.0	15.29	17.36	17.74	42	44	0.298	F293	111	d	
416	0	11	23.6	−36	32	37.2	16.54	17.31	18.25	4	36	0.241	F349	111		
417	0	11	58.0	−24	30	44.7	0.00	0.00	0.00	0	0	0.000	F473	001	d	
418	0	12	30.2	−24	9	58.6	15.12	15.72	16.59	31	11	0.481	F473	121	d	0014
419	0	12	49.7	−26	21	9.9	17.05	18.12	18.75	48	41	0.197	F473	011		15
420	0	13	29.5	−37	25	8.2	18.38	18.65	19.03	71	65	0.179	F350	011		2750
421	0	13	35.9	−35	13	53.1	16.38	18.04	18.70	55	55	0.200	F350	001	d	2749
422	0	13	44.9	−39	44	10.1	15.79	16.68	18.39	13	9	0.213	F294	100		
423	0	13	56.0	−31	32	46.7	17.21	18.52	19.99	21*	62	0.131	F410	001	d	2751
424	0	14	5.9	−34	7	59.0	17.64	17.92	18.16	24	75	0.254	F350	010		
425	0	14	46.6	−26	55	8.2	16.14	18.33	18.82	45	43	0.186	F473	010		
426	0	14	56.2	−31	42	27.7	17.76	17.88	18.69	44	36	0.201	F410	010	d	
427	0	14	57.7	−24	28	49.9	15.17	16.64	18.07	14	14	0.260	F473	111	d	
428	0	15	9.5	−27	37	24.2	17.63	18.27	19.23	24	33	0.168	F473	001		
429	0	15	23.2	−35	25	2.5	16.81	17.52	17.91	109	55	0.277	F350	111	d	2755
430	0	16	6.0	−28	12	51.6	17.11	17.99	18.53	23	40	0.215	F410	111		
431	0	16	17.4	−42	1	24.3	16.35	16.66	18.14	24	15	0.253	F294	020	d	2758
432	0	16	20.1	−30	56	8.7	16.54	17.03	18.19	16	19	0.249	F410	100		2759
433	0	16	55.3	−25	55	1.4	0.00	0.00	0.00	0	0	0.000	F473	001	d	
434	0	17	29.9	−42	14	16.7	16.28	17.77	18.40	31	58	0.227	F294	010	d	2763
435	0	17	49.1	−40	43	41.9	17.69	17.88	18.96	14	31	0.183	F294	010		
436	0	18	0.9	−34	12	28.4	16.98	17.87	18.86	30	40	0.189	F350	011		
437	0	18	1.2	−25	54	26.3	17.50	17.83	17.97	124	59	0.271	F473	111	d	22
438	0	20	23.5	−38	24	12.6	17.12	17.56	18.63	33	26	0.207	F294	011		2767

EDCC	R.A.			Dec.			m_1	m_3	m_{10}	n_{clus}	n_{back}	θ_A	Field	runs	Deb.	Abell
	h	m	s	°	′	″										
439	0	21	48.8	−34	16	19.5	18.32	18.81	18.95	53*	71	0.178	F350	010		
440	0	21	50.3	−40	23	53.4	15.14	16.27	17.85	10	10	0.285	F294	010		2771
441	0	22	37.8	−38	16	5.7	18.14	18.15	18.59	40	51	0.209	F294	011		2772
442	0	22	52.2	−33	22	0.0	14.52	15.81	17.18	16	10	0.375	F350	110	d	
443	0	23	4.7	−33	17	38.6	15.60	17.36	0.00	0	0	0.000	F350	001	d	(S 41)
444	0	25	12.6	−36	59	48.2	16.01	17.88	18.59	23	35	0.209	F350	010		S 51
445	0	25	40.8	−27	51	7.2	16.37	17.23	18.18	4	21	0.236	F473	100		
446	0	25	44.0	−35	43	4.5	16.51	17.27	18.72	23	15	0.198	F350	011		
447	0	26	7.8	−23	54	4.3	16.67	17.80	18.26	77	48	0.241	F473	111		42
448	0	26	34.0	−30	26	26.8	16.84	17.56	18.19	51	35	0.248	F410	122		2778
449	0	26	35.8	−35	16	59.3	17.41	17.71	18.72	33	26	0.198	F350	111		
450?	0	27	23.4	−29	45	1.3	15.02	17.34	17.78	45	40	0.293	F410	110		2780
451	0	28	4.2	−24	27	29.3	19.12	19.18	19.61	34	61	0.156	F473	001		47
452	0	28	50.0	−23	1	32.4	14.67	15.48	18.63	2	2	0.207	F473	101		
453	0	29	11.5	−23	55	1.5	17.43	17.70	19.32	14	20	0.163	F473	011		0051
454	0	31	32.6	−34	32	46.7	15.14	18.56	20.01	23	23	0.124	F350	001		
455	0	32	52.2	−32	39	1.7	19.04	19.21	19.88	31	43	0.141	F350	001		
456	0	33	25.2	−24	4	3.4	16.65	17.54	18.00	33	45	0.268	F474	100		
457	0	33	35.7	−26	22	7.2	15.41	16.31	17.95	11	10	0.273	F474	111		
458	0	33	44.6	−28	32	56.5	0.00	0.00	0.00	0	0	0.000	F411	001	d	
459	0	34	7.1	−28	37	8.4	14.15	16.20	18.54	4	10	0.214	F411	010	d	
460	0	34	47.1	−28	44	47.4	16.94	17.83	18.53	27	70	0.215	F411	111	d	2798
461	0	35	10.7	−31	5	28.7	16.13	16.44	18.60	7	6	0.208	F411	111		(2794)
462	0	35	14.5	−39	23	42.4	15.82	16.81	17.37	45	26	0.348	F294	211		2799
463	0	35	28.5	−25	27	55.6	16.12	16.76	17.48	21	30	0.332	F474	110	d	2800
464	0	35	58.5	−29	19	51.5	15.37	16.59	18.57	8	11	0.211	F411	111	d	2801
465	0	36	21.3	−27	29	10.5	14.75	16.71	19.18	6	7	0.171	F474	010		
466	0	36	24.1	−31	53	26.9	16.82	18.72	19.27	50	46	0.171	F411	001		2802
468	0	36	46.3	−24	16	44.1	15.96	17.29	17.87	18	36	0.283	F474	110		(0080)
469	0	37	13.0	−29	10	20.8	14.34	16.79	18.24	17	16	0.242	F411	111	d	2804
470	0	37	26.4	−26	26	25.1	16.88	17.95	18.79	38	34	0.194	F474	011		
471	0	37	43.3	−24	56	48.3	16.67	16.76	17.51	36	27	0.328	F474	111		80
472	0	37	57.2	−31	49	9.2	17.23	17.83	19.86	7	13	0.137	F411	001		
473	0	40	3.7	−28	50	23.2	16.10	17.11	17.92	67	31	0.277	F411	121		2811
474	0	40	44.7	−26	19	53.9	16.84	17.03	17.54	44	36	0.324	F474	121		0088

EDCC	R.A.	Dec.	m_1	m_3	m_{10}	n_{clus}	n_{back}	θ_A	Field	runs	Deb.	Abell
	h m s	° ′ ″										
475	0 41 6.0	−22 34 15.0	14.44	16.61	18.10	12	12	0.255	F474	100		
476	0 41 35.6	−25 41 28.9	17.11	17.88	18.49	8	40	0.219	F474	100		
477	0 43 14.9	−23 27 16.3	18.08	18.27	19.02	43	41	0.190	F474	001		0097
479	0 45 54.9	−38 45 19.6	16.83	17.91	19.47	16	19	0.149	F295	001		2822
480	0 45 56.6	−42 17 20.8	16.00	16.33	18.11	10	7	0.256	F295	110	d	
481	0 46 29.9	−34 29 4.6	16.06	16.33	17.28	14	14	0.360	F351	110		S 83
482	0 46 50.3	−29 47 22.0	17.15	17.68	18.06	61	54	0.261	F411	111		S 84
483	0 47 38.0	−42 10 1.3	17.03	17.58	0.00	0	0	0.000	F295	100	d	
484	0 48 20.4	−42 27 43.6	15.53	16.51	0.00	0	0	0.000	F295	100	d	
485	0 48 56.3	−28 46 50.4	16.44	16.70	17.63	19	24	0.312	F411	111		2829
486	0 49 7.9	−42 30 7.6	17.51	17.93	0.00	0	0	0.000	F295	010	d	
487	0 49 37.0	−34 14 31.0	16.86	17.41	18.25	23	28	0.243	F351	100		S 88
488	0 50 1.9	−35 16 59.5	14.90	17.00	17.60*	7*	42	0.315	F351	011	d	
489?	0 51 1.7	−35 28 9.7	14.94	16.60	17.14	44	29	0.382	F351	100	d	
490	0 51 5.5	−33 24 21.4	15.17	18.60	19.25	27	44	0.168	F351	001		
492	0 52 0.3	−31 20 0.5	13.84	17.09	17.86	26	30	0.284	F411	111	d	
493	0 52 41.6	−39 9 32.3	18.25	19.27	19.52	45	77	0.159	F295	001		
494	0 53 24.9	−37 36 35.8	15.35	16.13	17.51	15	7	0.327	F351	110		S 102
495	0 53 28.6	−26 36 9.4	15.86	16.31	17.61	25	8	0.315	F474	223	d	118
496	0 53 32.6	−29 9 31.4	16.58	17.11	17.76	29	31	0.301	F411	100		S 100
497	0 53 41.1	−22 49 56.5	17.11	17.24	18.05	24	23	0.262	F474	100	d	
498	0 53 43.7	−31 48 39.7	16.36	17.37	18.47	21*	24	0.219	F411	001		
499	0 53 51.4	−38 10 2.1	16.62	17.72	18.46	42	33	0.221	F295	011		S 106
500	0 53 59.7	−30 20 2.0	17.92	18.13	18.41	70	56	0.226	F411	111	d	2844
501	0 54 3.3	−24 18 43.5	19.01	19.05	19.83	42*	43	0.140	F475	001		2842
502	0 54 7.4	−27 45 55.0	16.49	17.82	18.71	30	28	0.200	F411	011	d	2843
503	0 54 21.7	−39 2 20.1	16.62	18.76	19.49	65	53	0.155	F295	001		2845
504	0 54 27.5	−22 32 32.9	16.92	17.15	19.05	10	8	0.178	F475	001	d	
505	0 54 38.9	−29 57 0.1	15.92	18.00	0.00	0	0	0.000	F411	110	d	(2846)
506	0 54 39.0	−31 7 10.9	14.87	15.70	17.58	8	5	0.319	F411	111	d	S 109
507	0 54 55.5	−26 33 35.6	16.41	18.17	19.23	19	36	0.168	F475	001	d	122
508	0 55 1.9	−29 58 31.7	18.84	18.90	19.83	26	88	0.138	F411	001	d	
509	0 55 3.0	−29 42 49.4	16.50	17.65	0.00	0	0	0.000	F411	010	d	(S 108)
511	0 55 50.0	−31 17 20.5	17.31	0.00	0.00	0*	0	0.000	F412	001	d	
512	0 56 8.0	−34 34 0.4	13.82	17.17	18.28	32*	19	0.238	F351	111		2847

EDCC	R.A.	Dec.	m_1	m_3	m_{10}	n_{clus}	n_{back}	θ_A	Field	runs	Deb.	Abell
	h m s	° ′ ″										
513	0 56 48.1	−29 19 41.8	17.38	19.45	19.87	78	40	0.137	F412	001		2850
514?	0 57 23.4	−30 39 5.8	16.10	17.69	18.65	21	29	0.204	F412	001		2851
515?	0 58 17.5	−34 58 2.6	17.13	17.35	18.08	37	29	0.259	F351	100		
516	0 58 26.0	−40 30 22.6	13.62	15.68	17.39	12	6	0.345	F295	110		S 113
517	1 0 7.7	−33 36 54.6	16.39	17.23	18.60	20	14	0.195	F352	010		
518	1 0 57.9	−22 51 54.1	19.41	19.51	20.00	45	39	0.134	F475	001		0135
519	1 2 7.7	−40 6 22.4	16.53	17.27	17.97	45	33	0.271	F295	110		2860
520	1 2 11.5	−24 15 37.4	17.32	18.34	18.81	61	46	0.192	F475	011		0140
521	1 2 49.7	−39 14 18.1	15.28	16.13	18.13	8	6	0.254	F295	100		
522	1 3 12.1	−24 55 28.7	19.31	19.33	19.62	55	46	0.149	F475	001		0141
523	1 4 5.6	−33 14 29.0	18.51	18.57	19.95	20	26	0.133	F352	001		
524	1 5 39.9	−37 1 20.6	15.53	18.07	18.64	75	46	0.206	F352	011		2871
525	1 5 40.6	−40 20 12.4	17.03	17.76	18.65	25	31	0.205	F296	010	d	S 127
526	1 6 30.7	−40 37 19.6	16.96	18.21	18.58	88	58	0.210	F296	010	d	2874
527	1 7 42.0	−25 5 2.9	17.19	17.64	18.22	37	28	0.244	F475	111		155
528	1 7 57.7	−30 0 31.6	17.65	17.90	18.81	14	28	0.193	F412	100		2878
529	1 8 5.6	−40 44 52.6	17.61	18.06	0.00	0	0	0.000	F296	100	d	
530	1 10 12.5	−36 37 9.8	16.12	17.77	19.00	27	24	0.181	F352	001		2883
531	1 10 15.7	−35 57 51.4	17.13	19.50	20.09	34	55	0.134	F352	001		
532	1 10 32.1	−33 54 52.1	15.31	16.19	17.43	18	8	0.323	F352	100		
533	1 11 28.1	−32 1 20.5	13.83	0.00	0.00	0*	0	0.000	F412	100	d	(S 141)
534	1 11 30.1	−39 12 20.6	17.07	17.32	18.75	16	19	0.193	F296	001		2885
535	1 11 43.9	−31 59 50.2	12.91	15.04	0.00	0*	0	0.000	F412	011	d	
536	1 12 39.5	−30 4 54.6	15.90	17.15	18.20	15	17	0.246	F412	100		
537	1 13 56.9	−28 37 58.0	18.44	18.84	19.41	39	46	0.151	F412	001		
538	1 14 40.1	−37 19 12.3	15.79	18.10	18.97	31	39	0.178	F352	001		2892
539	1 15 16.1	−38 16 27.4	16.68	17.60	18.41	29	36	0.226	F296	112		S 144
540	1 15 55.7	−28 40 46.8	17.10	18.18	19.08	23	34	0.177	F412	010		
541	1 15 55.9	−27 15 13.8	15.93	16.75	17.80	17	13	0.290	F475	111	d	2895
542	1 16 15.4	−26 53 22.9	17.10	17.99	18.46	36*	40	0.220	F475	111	d	
543	1 17 9.3	−36 7 38.6	15.73	16.95	18.69	10	10	0.201	F352	010		
544	1 18 32.1	−30 42 15.6	18.31	18.47	19.03	57	49	0.179	F412	012		S 151
545	1 18 45.5	−31 20 28.4	15.05	16.78	18.85	5	7	0.190	F412	011		
546	1 19 45.7	−39 53 30.0	16.80	17.55	18.39	32	32	0.215	F296	010		
547	1 20 20.4	−33 4 11.8	14.66	17.48	18.43	22*	24	0.221	F352	100		

EDCC	R.A.			Dec.			m_1	m_3	m_{10}	n_{clus}	n_{back}	θ_A	Field	runs	Deb.	Abell
	h	m	s	°	′	″										
548	1	21	12.2	−27	17	34.3	16.27	17.16	19.16	8	9	0.169	F476	001		2906
549	1	21	38.4	−41	6	59.9	16.54	16.78	18.32	12	14	0.236	F296	100		
550	1	22	11.8	−37	37	50.7	14.66	17.85	18.78	47*	34	0.195	F352	011	d	2909
551	1	22	42.2	−37	55	40.1	18.35	18.84	19.35	−8	66	0.162	F296	010	d	
552	1	22	58.3	−26	21	8.4	17.48	17.61	18.96	19	20	0.183	F476	010		
553	1	23	9.0	−39	41	37.1	16.71	17.47	18.05	55*	41	0.262	F296	110		S 156
554	1	23	9.3	−33	35	11.0	15.07	17.36	19.29	8	13	0.166	F352	001	d	
555	1	23	24.9	−29	48	28.2	16.92	17.56	18.33	35	28	0.233	F413	111		
556	1	23	39.6	−33	46	37.1	16.99	18.09	19.98	11	23	0.133	F353	001	d	2910
557	1	23	46.9	−38	14	34.8	14.33	14.35	17.53	5	1	0.326	F296	111	d	2911
558	1	23	56.2	−40	40	22.9	16.85	17.35	18.60	10	23	0.213	F296	010		
559	1	24	54.7	−35	50	45.1	13.83	15.97	18.58	4*	2	0.203	F353	010		
560	1	25	0.9	−23	1	25.6	15.30	16.18	17.59	12	9	0.317	F476	100		
561	1	25	59.4	−29	14	42.1	15.83	17.16	18.76	14*	13	0.196	F413	011		2915
562	1	26	12.6	−25	54	9.3	19.28	19.29	19.53	35	39	0.148	F476	001		0206
563	1	26	37.6	−34	13	24.4	17.88	18.23	19.54	15	30	0.152	F353	001		(2913)
564	1	27	28.9	−33	9	24.1	14.58	16.22	17.59	13	9	0.317	F353	111		S 160
565	1	29	3.4	−41	27	37.8	14.81	16.53	18.37	9	9	0.231	F296	100		
567	1	29	42.3	−24	59	43.0	16.82	17.33	19.19	8	12	0.170	F476	010		2921
568	1	29	42.7	−35	5	59.9	16.10	19.01	19.37	35	62	0.161	F353	011		(2920)
569	1	29	53.8	−26	15	35.2	15.11	16.98	19.33	2*	7	0.166	F476	001		0210
570	1	30	7.7	−42	24	38.7	15.06	17.33	17.91	39*	36	0.278	F296	120		S 163
571	1	30	15.4	−31	20	3.7	15.65	17.16	18.65	18	14	0.205	F413	011		2923
572	1	30	35.6	−29	48	9.7	19.08	19.26	19.55	38*	59	0.145	F413	001		2922
573	1	30	46.5	−27	11	48.2	16.51	16.92	18.40	27	12	0.227	F476	110		2924
574	1	31	39.5	−32	45	54.1	17.53	19.88	0.00	0	0	0.000	F353	010	d	(S 165)
575	1	31	52.4	−27	47	19.3	16.66	17.05	17.87	35	23	0.283	F476	111	d	2926
576	1	31	54.1	−26	21	39.8	17.04	18.00	18.89	47	31	0.188	F476	001	d	214
577	1	32	11.5	−31	52	49.8	16.14	17.38	18.58	23	19	0.210	F413	010		S 166
578	1	32	16.2	−33	3	18.6	15.05	15.44	17.81	3	2	0.289	F353	110	d	S 167
579	1	32	45.4	−27	43	52.2	0.00	0.00	0.00	0	0	0.000	F476	001	d	(2928)
580	1	32	53.3	−23	44	3.9	17.66	18.38	18.82	41	45	0.191	F476	001		0215
581	1	33	4.1	−25	54	41.8	14.77	16.53	17.11	16	19	0.387	F476	111	d	(0214)
582	1	33	17.2	−22	58	15.9	15.29	16.23	17.54	15	10	0.329	F476	100		
583	1	34	8.8	−36	44	25.8	14.34	17.08	18.91	10	9	0.176	F353	001		

EDCC	R.A.			Dec.			m_1	m_3	m_{10}	n_{clus}	n_{back}	θ_A	Field	runs	Deb.	Abell
	h	m	s	°	′	″										
584	1	34	49.8	−34	58	24.4	17.17	18.67	19.45	23	43	0.156	F353	001		2930
585	1	35	25.3	−26	56	16.0	16.53	16.90	19.10	5	7	0.176	F476	011		
586	1	39	26.9	−30	50	23.3	17.75	19.22	19.72	29	62	0.145	F413	001		
587	1	39	46.9	−42	24	57.6	15.44	17.17	17.49	47	34	0.330	F297	110		S 180
588	1	40	37.0	−40	24	35.8	15.15	16.23	18.46	6	4	0.237	F297	100		
589	1	41	10.0	−36	33	30.0	13.91	16.44	18.17	14	7	0.249	F353	100		S 182
590	1	41	34.6	−32	43	30.6	18.74	18.83	19.73	30	49	0.152	F413	001		
591	1	41	46.0	−35	32	50.0	16.81	17.01	17.59	28	25	0.317	F353	111		S 186
592	1	43	8.5	−29	29	23.9	17.79	19.07	20.06	67*	42	0.130	F414	001		
593	1	43	36.3	−29	6	28.6	16.90	17.37	19.26	11	10	0.167	F414	010		S 189
594	1	44	4.6	−32	7	19.5	17.39	18.55	19.35	41	43	0.161	F414	001		
595	1	45	3.8	−40	19	6.8	17.24	17.24	18.91	16	9	0.181	F297	010		
596	1	46	3.8	−32	10	16.6	18.10	18.43	19.14	74	44	0.174	F414	011		2943
597	1	49	3.5	−36	25	28.6	14.27	16.34	18.59	3	4	0.209	F354	011	d	
598	1	49	37.2	−26	3	24.7	16.59	18.43	18.83	53	51	0.192	F477	011		0264
599	1	50	2.9	−36	7	8.7	15.90	16.67	18.45	13*	7	0.222	F354	010	d	
600	1	51	1.7	−33	52	36.5	17.89	18.28	19.33	42	34	0.163	F354	001		S 203
601	1	51	26.0	−33	22	6.1	16.51	17.66	18.77	16	23	0.195	F354	011		
602	1	51	29.8	−26	46	45.0	16.19	18.35	19.21	42	34	0.161	F477	001		2950
603	1	52	2.8	−35	55	56.4	14.81	16.09	18.23	4*	4	0.243	F354	011	d	2952
604	1	54	50.3	−24	14	20.6	18.69	19.17	19.85	26	45	0.137	F477	001		2956
605	1	57	51.6	−31	27	59.8	16.84	18.52	19.73	20	34	0.151	F414	001		2961
606	1	58	27.2	−33	11	15.2	17.19	17.56	17.90	45*	42	0.278	F354	120		2962
607	1	58	49.6	−25	20	34.8	14.14	16.83	19.43	5	4	0.158	F477	001		2964
608	1	58	54.9	−40	39	57.9	16.29	16.76	18.31	22	9	0.236	F298	110		2965
609	1	58	57.8	−36	9	52.1	17.28	17.80	18.46	44	40	0.221	F354	111	d	2963
610	1	59	26.1	−37	15	45.5	18.66	19.01	19.47	22*	60	0.158	F354	001		S 216
611	1	59	43.1	−36	3	14.8	0.00	0.00	0.00	0	0	0.000	F354	001	d	(S 219)
612	1	59	45.4	−35	24	14.9	18.10	18.14	19.12	18	36	0.172	F354	001		
613	1	59	55.2	−25	50	32.6	18.66	19.10	19.73	81	48	0.143	F477	001	d	0297
614	2	0	29.7	−34	31	24.2	17.68	17.74	19.00	33	25	0.181	F354	011		
615	2	0	36.3	−28	31	1.0	17.80	18.23	18.96	21	39	0.183	F414	011		2967
616	2	0	59.0	−25	48	43.8	18.68	18.98	19.71	14	50	0.144	F477	001	d	
617	2	1	19.5	−27	14	52.3	16.50	17.42	17.99	45*	35	0.268	F478	110		2968
618	2	1	28.8	−41	20	44.7	16.86	17.81	18.31	68	44	0.236	F298	110		2969

EDCC	R.A.			Dec.			m_1	m_3	m_{10}	n_{clus}	n_{back}	θ_A	Field	runs	Deb.	Abell
	h	m	s	°	′	″										
619	2	2	23.7	−35	55	52.8	17.46	17.95	18.96	43	34	0.187	F354	001		2970
620	2	3	5.4	−32	33	28.2	14.74	17.60	20.13	4	10	0.128	F414	001		
621	2	3	42.9	−27	23	49.4	17.33	17.64	18.77	42	25	0.195	F478	011		2972
622	2	3	51.3	−36	22	22.1	15.37	16.66	17.87	30	14	0.283	F354	100		
623	2	4	12.1	−28	38	46.5	14.89	16.96	17.79	42	22	0.292	F414	110	d	
624?	2	4	43.5	−28	53	16.9	16.53	18.56	19.14	−6	90	0.174	F414	010	d	2975
625	2	5	3.7	−35	56	14.8	14.96	17.41	18.39	24	24	0.216	F354	100		
626	2	6	2.8	−32	10	44.5	17.15	18.06	18.48	44*	49	0.219	F414	110		2978
627	2	6	11.2	−28	42	56.7	16.58	17.16	19.65	4*	7	0.147	F415	001	d	
628	2	6	42.1	−26	36	23.6	17.22	18.01	19.26	15	29	0.167	F478	011		2979
629	2	7	12.0	−37	36	40.7	16.49	17.83	18.47	27	43	0.220	F354	011		(S 223)
630	2	8	6.4	−33	55	0.3	18.45	18.63	19.56	48	45	0.152	F354	001		S 227
631	2	8	15.7	−33	14	26.8	13.67	18.45	19.74	20	30	0.137	F354	001		2983
632	2	9	33.9	−40	31	42.1	15.86	17.99	18.73	51	42	0.198	F298	010	d	2984
633	2	10	40.2	−26	23	31.9	17.88	18.48	19.89	26	31	0.136	F478	001		0327
634	2	10	49.9	−25	32	17.6	16.67	19.33	19.59	84	72	0.156	F478	001		0325
635	2	11	4.5	−34	38	6.8	16.10	16.90	19.04	1	7	0.174	F355	001		S 233
636	2	11	29.4	−40	18	56.7	15.91	17.44	17.96	31	37	0.272	F298	100	d	
637	2	12	10.5	−30	46	2.3	16.95	17.25	18.82	14	12	0.187	F415	010		2990
638	2	12	24.3	−26	1	24.2	18.07	18.48	19.55	24	37	0.152	F478	001		2991
639	2	12	48.9	−26	52	58.6	16.10	17.41	19.33	8	12	0.161	F478	001		2992
640	2	12	54.2	−36	47	44.6	18.45	18.56	19.86	32*	33	0.138	F355	001		2993
641	2	13	51.9	−27	46	47.1	17.12	17.40	18.51	21*	23	0.217	F415	011		
642	2	14	8.3	−29	15	17.0	16.87	18.39	19.27	18	45	0.172	F415	001		
643?	2	17	42.1	−28	36	59.4	17.23	18.36	19.03	33	42	0.169	F415	001		S 245
644	2	18	40.9	−26	50	54.5	16.83	17.38	19.31	10	12	0.166	F478	010		
645	2	23	11.7	−29	43	24.8	15.86	16.04	17.14	25	9	0.383	F415	111	d	S 258
646	2	23	27.6	−35	1	26.5	18.23	18.83	19.61	23	43	0.148	F355	010		
647	2	23	50.1	−42	10	29.4	15.49	17.08	18.80	10*	9	0.191	F299	010		3017
648	2	24	8.5	−23	37	36.4	14.61	16.16	18.05	7	6	0.262	F479	100	d	S 263
649	2	24	54.3	−26	43	7.3	15.89	17.44	18.32	43	25	0.235	F479	110		
650	2	24	54.4	−23	8	46.5	15.51	16.28	17.62	13*	9	0.313	F479	100	d	
651	2	24	56.3	−29	4	55.0	17.72	19.25	19.61	79	51	0.140	F415	001		(S 266)
652	2	25	11.6	−29	49	30.8	16.65	16.72	19.13	4*	7	0.174	F415	010	d	
653	2	27	16.9	−33	41	37.0	15.23	16.47	18.09	17	8	0.258	F355	111	d	

EDCC	R.A.			Dec.			m_1	m_3	m_{10}	n_{clus}	n_{back}	θ_A	Field	runs	Deb.	Abell
	h	m	s	°	′	″										
654	2	27	52.7	−36	59	52.0	18.75	18.99	19.77	41	46	0.141	F355	001		3026
655	2	28	3.9	−24	49	29.9	17.26	17.40	17.85	36	35	0.283	F479	100		
656	2	28	13.0	−39	8	10.0	17.32	18.98	19.76	34	56	0.141	F299	001	d	S 271
657	2	28	19.7	−32	4	59.7	16.68	17.44	18.38	19	23	0.229	F415	100	d	
658	2	28	34.9	−33	17	55.5	16.26	16.82	17.91	29	15	0.278	F355	111	d	3027
659	2	29	0.5	−38	55	27.1	17.54	18.31	19.28	30	36	0.166	F299	001	d	3029
660	2	29	12.5	−23	5	47.4	15.30	15.85	18.07	6	3	0.260	F479	101		
661?	2	29	59.1	−32	13	26.3	16.65	17.77	18.40	38	32	0.227	F416	100	d	
662	2	30	1.2	−36	55	10.5	14.02	18.81	19.81	39	38	0.140	F355	001		
663	2	30	56.5	−23	22	54.1	17.53	18.63	19.20	33	42	0.170	F479	001		
664	2	31	16.7	−33	4	32.6	15.58	17.46	18.39	18	22	0.224	F355	100		
665	2	32	18.3	−33	52	39.2	14.98	16.32	17.86	11	9	0.284	F355	101		S 278
666	2	32	24.0	−37	42	55.3	15.95	17.18	18.38	14	15	0.229	F299	100		S 279
667	2	32	57.4	−24	44	4.5	17.77	19.75	20.17	31	26	0.124	F479	001		
668	2	33	45.7	−41	58	17.2	17.23	18.03	18.52	36	45	0.214	F299	010		3033
669	2	34	3.7	−22	40	31.2	17.44	18.60	19.11	25	38	0.169	F479	010		
670	2	34	47.0	−24	49	6.8	17.32	17.99	19.05	25	28	0.178	F479	010		
671	2	34	51.9	−25	35	29.7	16.14	17.27	18.20	10	25	0.246	F479	100		
672	2	35	10.9	−26	35	42.5	15.63	16.55	20.07	0	5	0.128	F479	001	d	
673	2	35	23.1	−26	44	13.5	16.45	17.11	19.77	3	11	0.141	F479	101	d	368
675	2	36	6.5	−32	34	12.0	19.26	19.38	19.90	21	47	0.138	F416	001		
676	2	36	7.7	−32	55	2.1	17.10	17.71	19.13	14	20	0.174	F356	010		
677	2	36	25.3	−33	48	47.1	15.13	16.25	18.49	6	5	0.221	F356	010		
678	2	36	48.0	−27	12	5.5	16.65	18.45	19.33	30	37	0.155	F479	001		
679	2	38	58.9	−25	59	37.4	17.14	18.54	19.02	24*	48	0.174	F479	001		
680	2	39	13.0	−28	51	33.9	17.37	18.45	18.89	55	45	0.177	F416	001		3041
681	2	41	29.6	−35	22	55.9	16.50	16.75	18.50	16	11	0.218	F356	110		
682	2	41	31.3	−28	5	8.0	16.77	18.43	19.10	40*	47	0.176	F416	011		3044
683	2	42	26.6	−26	31	10.7	15.78	17.08	17.99	43	25	0.269	F479	112		0380
684	2	42	29.6	−25	7	40.3	17.22	17.75	20.81	2	13	0.101	F479	100	d	
685	2	42	38.5	−28	58	16.2	17.19	17.91	19.21	12	19	0.162	F416	001		(3043)
686	2	43	44.3	−24	55	22.1	14.35	16.67	18.23	11	9	0.243	F479	100	d	
688	2	45	2.6	−42	32	34.1	14.89	16.68	18.21	19	16	0.245	F299	110	d	S 296
689	2	45	14.2	−34	11	48.3	19.05	19.09	19.48	32	54	0.156	F356	001	d	3053
690	2	45	19.2	−27	46	27.8	17.03	17.39	18.32	24	26	0.235	F480	011	d	3052

EDCC	R.A.			Dec.			m_1	m_3	m_{10}	n_{clus}	n_{back}	θ_A	Field	runs	Deb.	Abell
	h	m	s	°	′	″										
691	2	45	21.8	−34	55	44.4	16.96	18.52	19.01	34	56	0.189	F356	001		
692	2	45	34.2	−22	51	49.6	14.65	17.22	18.37	15	17	0.229	F480	110		
693	2	45	51.1	−42	3	37.9	16.04	16.69	16.90	24	35	0.422	F299	110	d	S 297
694	2	46	14.7	−27	53	52.0	17.01	18.43	0.00	0*	0	0.000	F416	100	d	(3054)
695	2	46	58.4	−31	23	15.8	14.67	14.75	16.04	16	3	0.706	F416	110		S 301
696	2	48	30.6	−40	33	10.2	17.37	17.85	18.38	27	48	0.229	F299	100		
697	2	48	54.0	−35	13	38.0	14.70	15.51	16.79	12	9	0.442	F356	100	d	
698	2	49	7.4	−35	45	11.6	17.42	19.58	20.18	11	23	0.124	F356	001	d	
699	2	49	17.9	−25	9	1.2	16.25	16.58	18.09	28	11	0.257	F480	111		0389
700	2	49	39.5	−25	47	15.5	15.15	17.39	18.33	42	24	0.233	F480	110	d	
701	2	50	6.1	−36	54	24.9	16.92	18.65	18.98	51*	56	0.182	F356	001		3063
702	2	50	8.9	−25	32	42.3	19.13	19.43	19.87	38	66	0.137	F480	001	d	3062
703	2	50	32.4	−41	23	27.3	17.24	18.08	0.00	0	0	0.000	F300	010	d	
704?	2	50	38.5	−33	5	28.7	16.69	17.27	18.23	23	19	0.232	F356	100		
705	2	50	41.7	−42	28	23.8	17.21	18.00	18.28	28	71	0.238	F300	110		
706	2	51	18.1	−26	46	54.6	16.50	18.01	18.96	22	33	0.186	F480	001		
707	2	51	30.2	−33	41	40.2	15.54	16.81	17.83	27*	20	0.287	F356	111		3064
708	2	51	36.4	−41	24	21.8	16.75	17.52	18.76	22	25	0.196	F300	110	d	S 306
709	2	53	7.9	−35	38	35.0	16.04	16.30	17.68	19	15	0.306	F356	111	d	
710	2	53	42.0	−22	51	29.8	16.59	17.75	18.60	37	25	0.208	F480	011		3069
711	2	54	0.6	−40	30	6.9	18.50	18.88	19.33	40	76	0.171	F300	010		
712	2	54	19.6	−24	55	51.1	16.33	17.65	18.40	34	30	0.226	F480	011		3070
713	2	55	28.3	−35	49	27.5	15.11	16.77	17.81	13	23	0.289	F356	101	d	
714	2	56	20.9	−26	46	42.2	18.34	18.45	19.24	27	43	0.172	F480	001		
715?	2	56	26.2	−41	8	4.0	16.72	18.23	18.91	41	54	0.187	F300	010		
716?	2	58	51.3	−36	46	46.4	16.13	16.91	17.66	20	35	0.308	F356	100	d	
717	2	58	55.5	−37	14	56.6	14.88	16.30	17.18	21	26	0.376	F356	110	d	S 316
718	2	58	56.3	−38	22	35.4	16.44	16.67	18.65	9	12	0.205	F300	011		
719	2	58	56.8	−33	24	56.2	16.01	17.22	17.81	12	24	0.270	F356	100		
720	2	59	49.3	−25	31	35.5	15.36	16.59	18.43	8	7	0.229	F480	010		
721	3	1	2.3	−34	27	50.6	17.09	18.19	18.81	21	34	0.182	F357	010		
722	3	1	3.9	−37	7	47.2	16.61	16.76	17.07	58	46	0.394	F357	112	d	(3084)
723	3	2	52.4	−37	47	6.4	16.69	17.08	18.37	9	25	0.230	F300	100		
724	3	3	20.5	−39	17	33.2	13.31	16.45	17.71	20	19	0.302	F300	100	d	
725	3	3	55.0	−38	16	11.0	16.23	17.18	18.12	16	34	0.256	F300	100		

EDCC	R.A.			Dec.			m_1	m_3	m_{10}	n_{clus}	n_{back}	θ_A	Field	runs	Deb.	Abell
	h	m	s	°	′	″										
726	3	4	43.0	−39	1	47.3	17.43	18.41	18.64	36	81	0.206	F300	111	d	
727	3	6	2.6	−23	8	22.6	13.94	16.34	18.98*	5	3	0.182	F481	100		
728	3	6	13.3	−36	53	32.2	16.03	16.18	17.30	28	21	0.358	F357	111		3089
729	3	6	15.5	−23	53	8.7	15.78	16.68	17.45	34	18	0.336	F481	111		419
731?	3	7	5.5	−37	45	6.1	17.66	18.14	18.99	23	40	0.177	F300	010		
732	3	7	23.7	−24	43	39.9	15.45	17.50	20.91	3	4	0.097	F481	100		
733	3	8	9.2	−38	29	39.0	17.86	18.06	19.84	9	24	0.140	F300	001		
734	3	8	31.3	−26	17	16.1	17.32	17.35	18.49	19	18	0.219	F481	001		
735	3	9	23.7	−27	5	34.3	17.39	17.70	18.43	2	60	0.224	F481	001	d	3094
736	3	9	42.8	−27	11	11.7	15.79	16.03	17.39	20	8	0.345	F481	110	d	
737	3	10	9.4	−22	33	54.3	17.17	17.62	18.15	25*	28	0.243	F481	100		
739	3	10	41.6	−36	44	10.9	16.66	17.42	19.01	17	20	0.181	F357	010		
742	3	11	52.2	−38	30	34.7	15.21	16.51	17.89	26*	19	0.280	F300	111		3098
743	3	11	54.5	−37	54	39.0	17.82	17.86	20.98	6	8	0.095	F300	100		
744	3	12	14.1	−42	10	39.7	16.68	16.98	18.99	7	11	0.178	F300	010		
745?	3	12	16.8	−32	28	20.6	17.05	17.77	18.62	49	22	0.207	F417	011	d	3101
746?	3	12	44.0	−42	37	55.9	16.44	18.67	19.27	27	58	0.164	F300	010		3105
747	3	13	2.4	−41	21	9.0	16.10	17.25	18.51	14	23	0.217	F300	010	d	
748	3	13	9.5	−29	24	14.2	15.74	16.58	17.25	39	14	0.365	F417	111		S 333
749	3	14	24.6	−37	13	39.9	16.91	18.25	19.96	9	20	0.127	F357	100		
751?	3	14	59.5	−42	12	3.5	17.19	17.40	18.30	29	29	0.229	F300	100		
752	3	15	7.0	−38	24	31.9	16.09	17.56	18.95	18	22	0.180	F301	001		
754	3	16	19.3	−39	18	37.1	17.23	19.11	19.70	69	50	0.143	F301	001		3114
755	3	18	23.9	−24	52	30.0	17.02	18.24	18.99	45*	29	0.181	F481	011		
756	3	18	42.3	−27	21	47.7	16.41	16.48	17.81	21	9	0.289	F481	110		S 340
757	3	19	46.0	−34	28	45.4	17.53	17.99	18.44	48	32	0.223	F357	121		3118
758	3	20	22.1	−41	30	46.8	15.74	16.99	17.55	51	33	0.321	F301	110		3122
759	3	21	23.1	−40	29	4.8	16.34	17.90	20.64	5	10	0.107	F301	100		
761	3	26	4.2	−26	38	15.0	16.73	17.54	18.83	21	7	0.181	F481	001		
762	3	32	15.2	−39	8	9.1	15.78	16.34	17.25	39	14	0.364	F301	110	d	3135
763	3	32	55.2	−39	38	0.9	16.35	17.52	18.36	23	31	0.230	F301	011	d	S 364
764	3	33	22.4	−42	36	8.3	15.45	17.24	18.63	9	15	0.210	F301	010		S 365
765	3	34	50.6	−39	53	15.6	16.01	16.71	17.95	30	15	0.273	F301	110	d	3142
766	3	36	2.3	−38	11	32.8	17.17	18.16	19.18	30	21	0.163	F301	001		3145
767	3	37	7.6	−40	44	57.6	16.67	17.27	18.62	18	18	0.204	F301	010		
768	3	37	55.9	−40	9	58.6	15.74	18.42	18.83	36	61	0.197	F301	010		
769	3	38	34.0	−38	3	8.0	15.56	16.91	18.75	13	7	0.194	F301	010		S 376

EDCC	R.A.			Dec.			m_1	m_3	m_{10}	n_{clus}	n_{back}	θ_A	Field	runs	Deb.	Object
	h	m	s	°	′	″										
30	21	41	48.8	−30	8	16.9	15.42	16.70	18.21	16	14	0.245	F466	112	d	Gal
41	21	46	10.5	−35	30	51.0	18.04	18.39	18.87	50	42	0.189	F404	100	d	d.s
56	21	52	36.1	−33	14	48.9	16.95	18.19	19.30	17	41	0.164	F404	011		d.s.
63	21	54	3.2	−34	48	23.3	12.89	17.52	18.89	18	25	0.188	F404	010	d	Gal
71	21	56	46.1	−25	58	35.2	15.93	17.26	18.80	19	19	0.193	F532	011		d.s.
74	21	57	57.7	−35	42	4.1	16.03	18.00	19.02	14	39	0.180	F404	111		Star
109	22	9	49.9	−38	25	29.5	14.57	18.39	19.79	10	37	0.140	F344	001	d	Gal
138	22	20	31.3	−42	30	40.4	16.84	18.11	18.72	53	47	0.192	F345	010		Gal
157	22	30	7.8	−24	48	26.6	16.99	18.92	19.24	33	68	0.168	F533	001		Star
167	22	34	14.7	−25	30	13.0	17.42	17.93	19.19	11	28	0.175	F534	001		Gal
193	22	45	38.0	−22	39	24.0	12.31	16.52	17.96	20	9	0.271	F534	100		Gal
233	22	59	32.1	−39	49	40.4	15.71	16.00	17.17	23	16	0.378	F346	110		Gal
238	23	0	5.8	−37	22	15.5	14.16	18.05	18.34	47	70	0.232	F406	100		Gal
280	23	15	59.9	−32	45	7.0	16.73	17.89	18.92	21	31	0.186	F470	011		Star
337	23	40	50.6	−33	21	32.3	17.16	17.37	19.40	7	13	0.158	F408	010		d.s.
340	23	42	3.4	−25	55	45.8	17.44	18.42	19.67	1	37	0.145	F537	100	d	d.s.
364	23	51	37.2	−42	36	30.9	15.85	16.52	18.46	11	7	0.221	F348	100		Star
379	23	56	51.0	−32	29	40.3	0.00	0.00	0.00	0	0	0.000	F471	011	d	Star
467	0	36	27.5	−25	50	54.2	16.31	16.80	18.18	12	17	0.249	F474	110	d	Star
478	0	44	39.9	−38	16	51.1	18.64	18.83	20.05	17	33	0.128	F295	001		Star
491	0	51	32.2	−27	25	13.7	15.18	17.38	19.31	9	13	0.170	F474	001		Gal
510	0	55	18.3	−27	44	59.9	13.15	18.84	19.45	54	57	0.157	F411	001	d	Gal
566	1	29	39.7	−33	22	32.1	16.78	17.43	18.96	12	17	0.185	F353	001		Gal
674	2	35	32.1	−36	22	40.1	16.63	18.61	20.34	11	22	0.117	F355	001		d.s.
687	2	43	45.3	−34	7	13.0	17.07	17.29	17.86	39	35	0.284	F356	110	d	d.s.
730	3	6	52.6	−32	42	34.2	16.52	16.88	17.89	21	16	0.280	F417	101		s.t.
738	3	10	32.3	−32	34	4.2	17.09	17.73	18.59	34	23	0.209	F417	001	d	Star
740	3	10	44.4	−31	40	17.6	16.36	17.39	19.09	11	10	0.176	F417	011		Gal
741	3	11	29.9	−25	23	31.0	15.61	17.63	18.15	9	34	0.252	F481	111		Gal
750	3	14	32.0	−35	45	12.0	15.89	16.53	17.00	60	32	0.405	F357	211		d.s.
753	3	15	21.8	−41	16	36.9	11.10	17.72	18.35	50	41	0.231	F301	110	d	Gal
760	3	22	48.1	−36	32	25.6	11.77	16.50	18.05	14	8	0.262	F357	110		Gal

Table 4: Objects misidentified as clusters: Gal; galaxy: Star; star(s): s.t.; satelite trail: d.s.; diffraction spike(s).

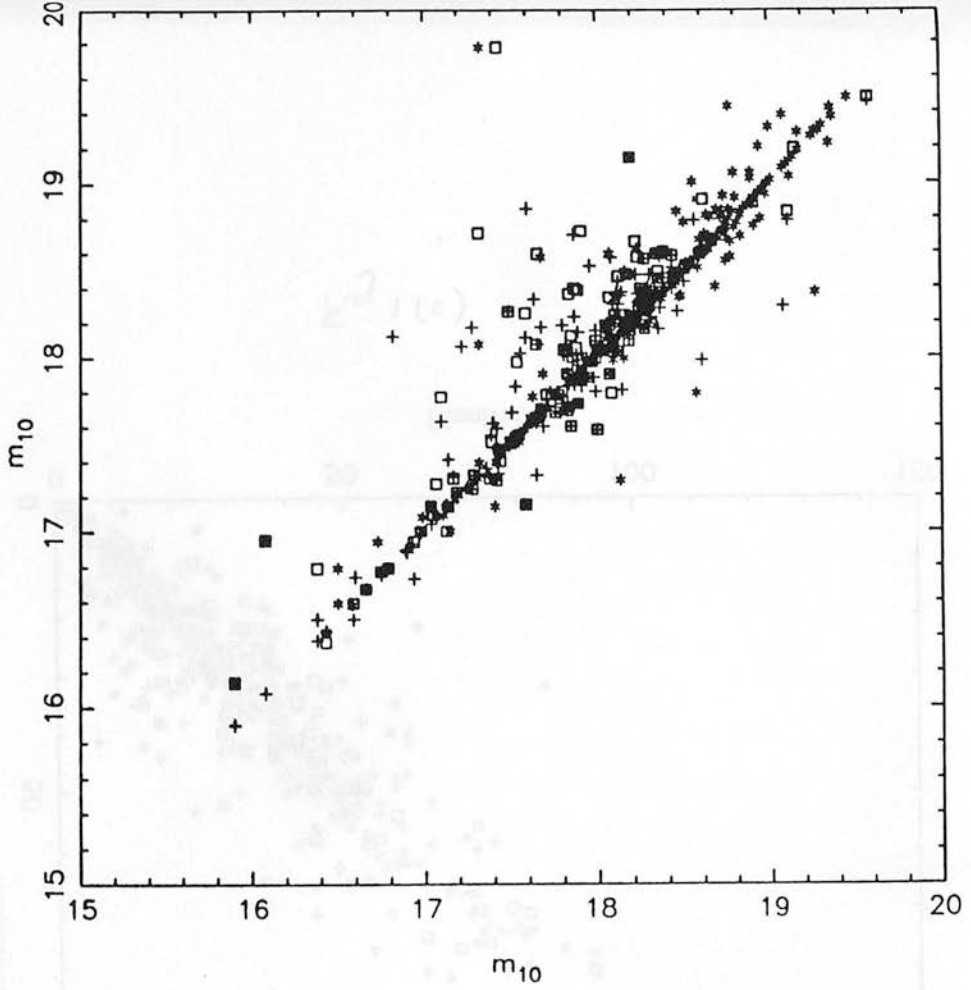

Fig 1(a)

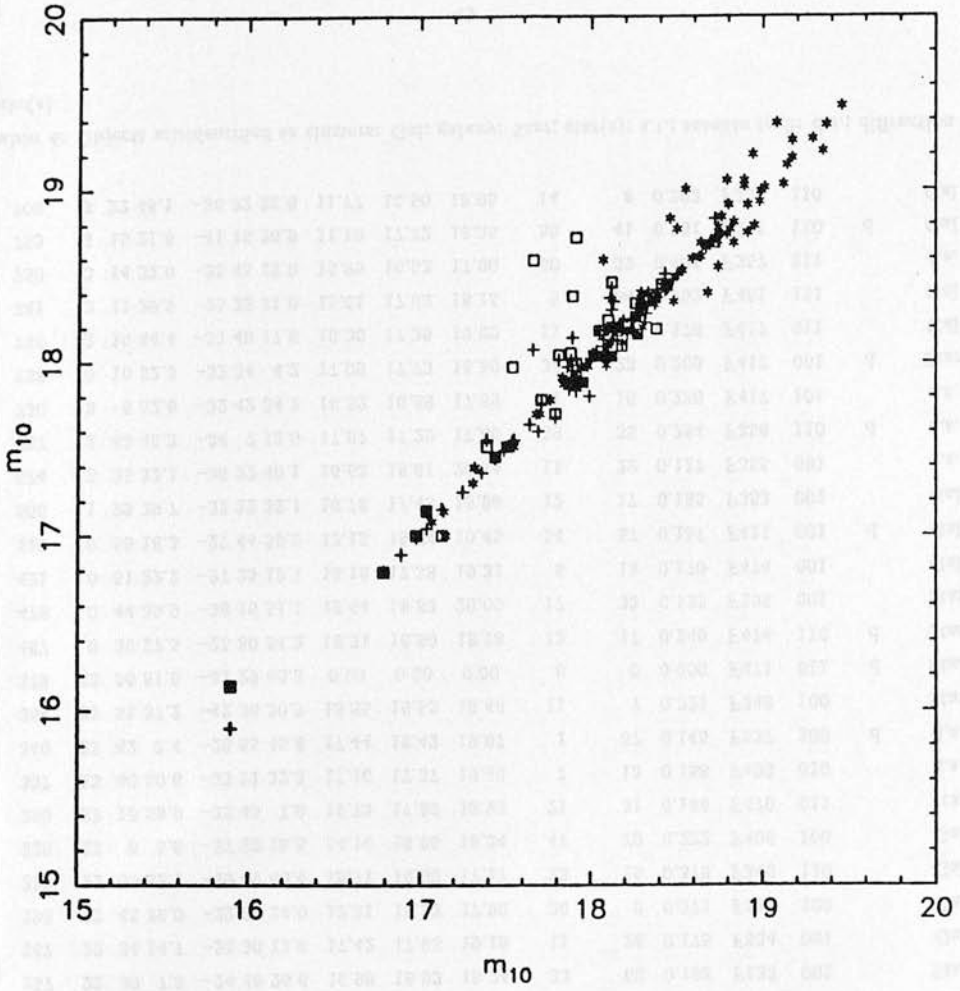
20
19
18
17
16
15
m_{10}
15
16
17
18
19
20
m_{10}

Fig 1 (b)

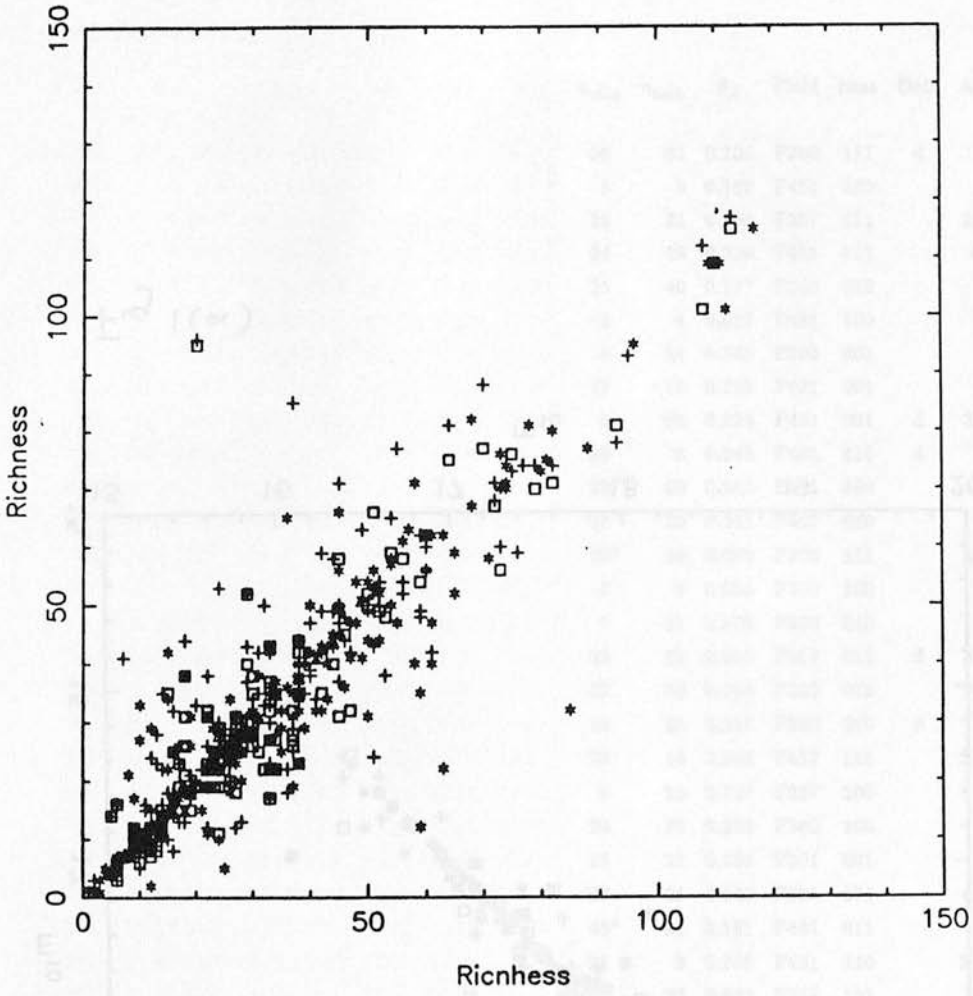
150
100
50
0
Richness
0
50
100
150
Ricnhess

Fig 1 (c)

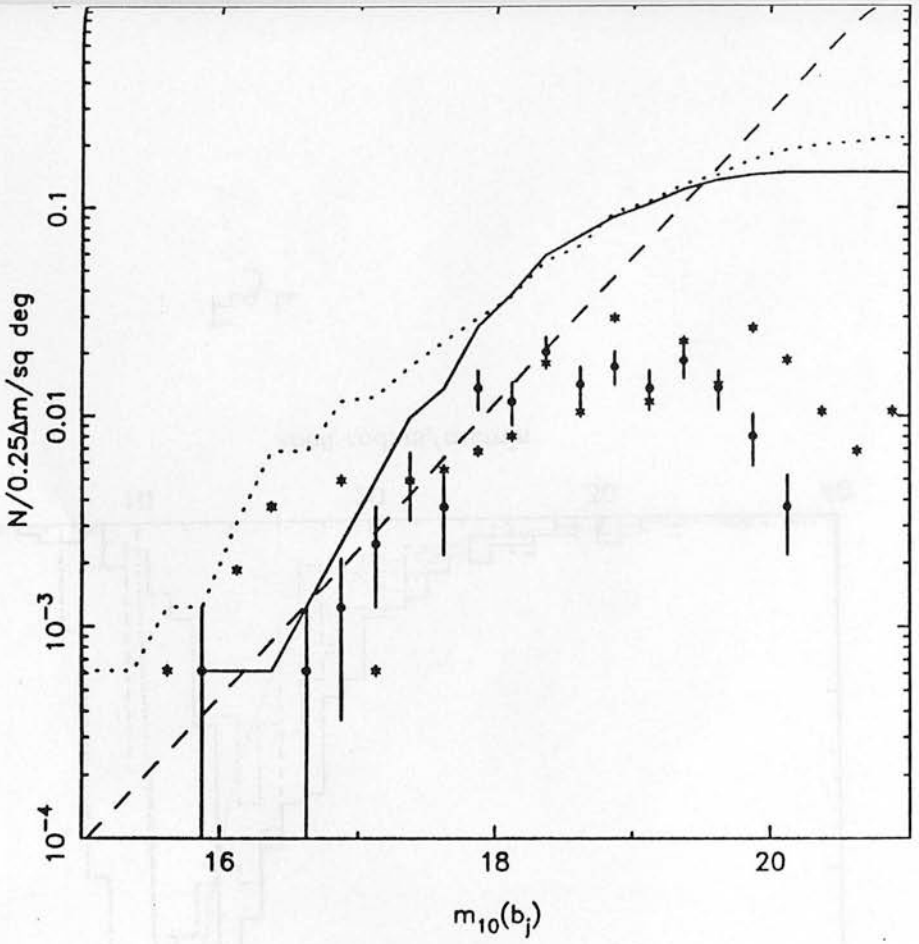
N/0.25Δm/sq deg
0.1
0.01
10^{-3}
10^{-4}
16
18
20
$m_{10}(b_j)$

Fig 2

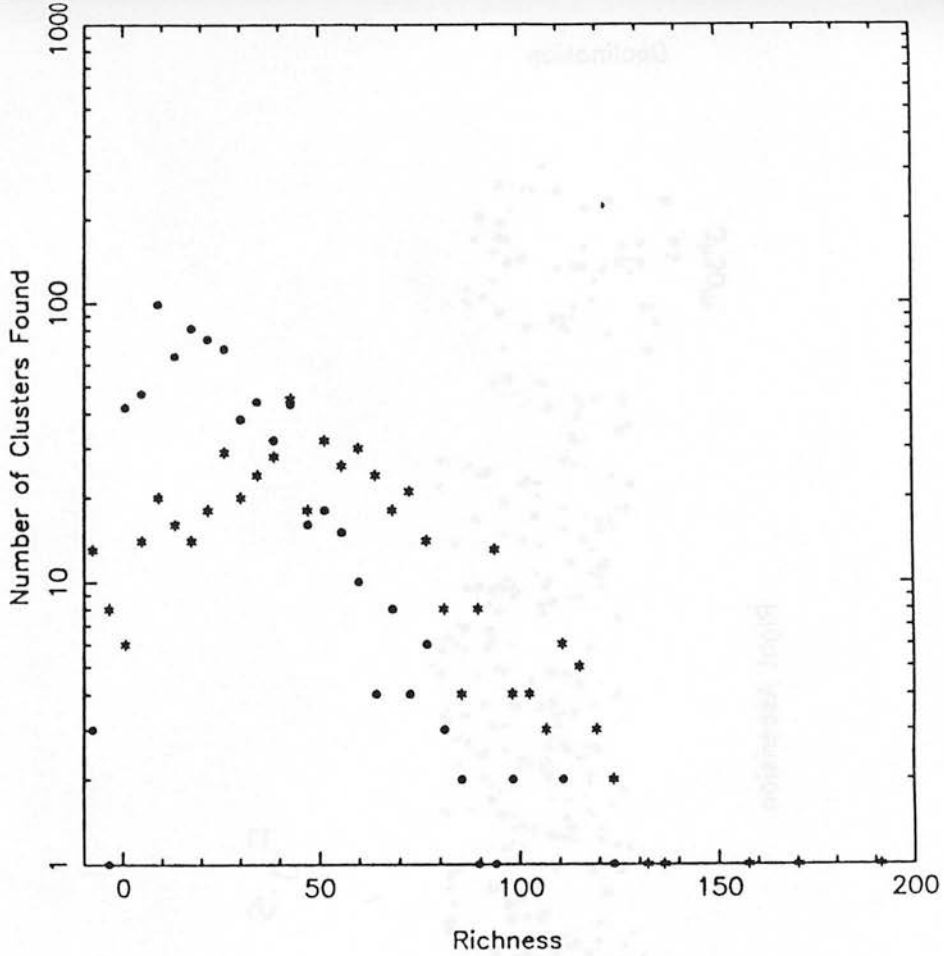
Number of Clusters Found
1000
100
10
1
0
50
100
150
200
Richness

Fig 3

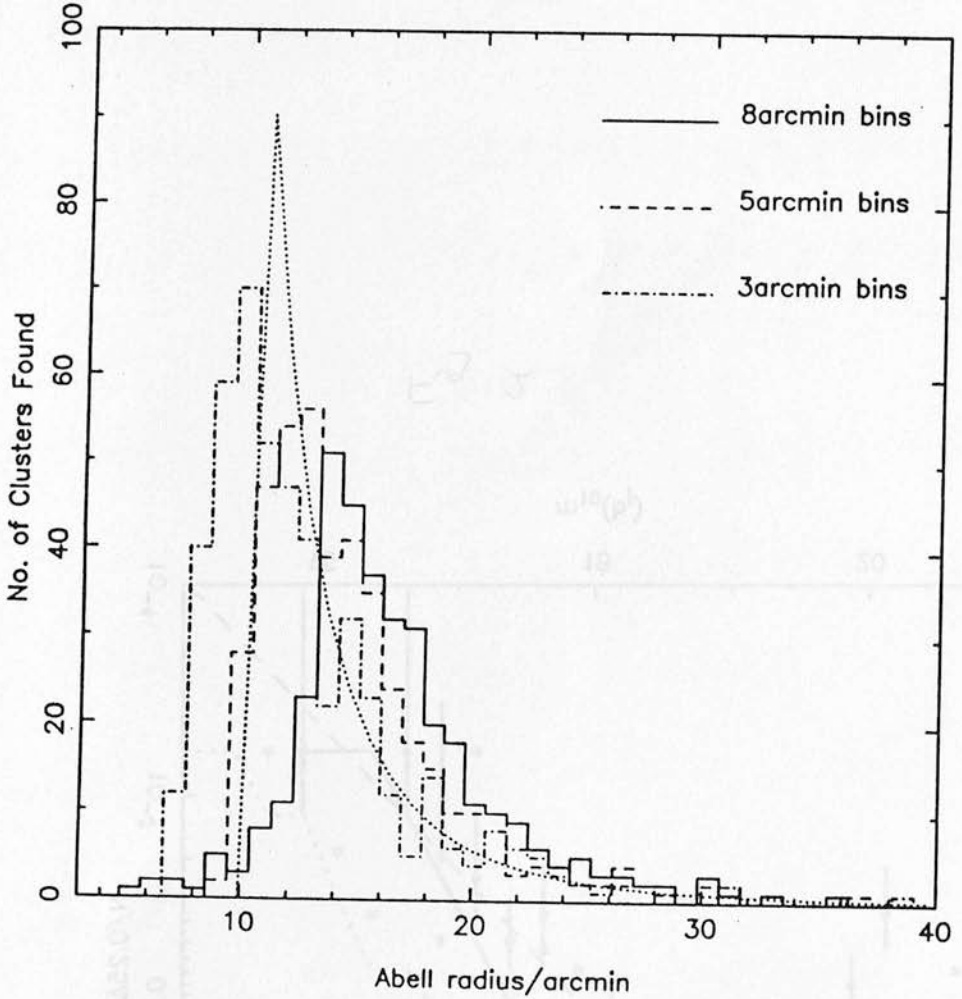
8arcmin bins
5arcmin bins
3arcmin bins
No. of Clusters Found
0
20
40
60
80
100
10
20
30
40
Abell radius/arcmin

Fig 4


−22.5°
−42.5°
21h30m
3h30m
Right Ascension
Declination

Fig 5

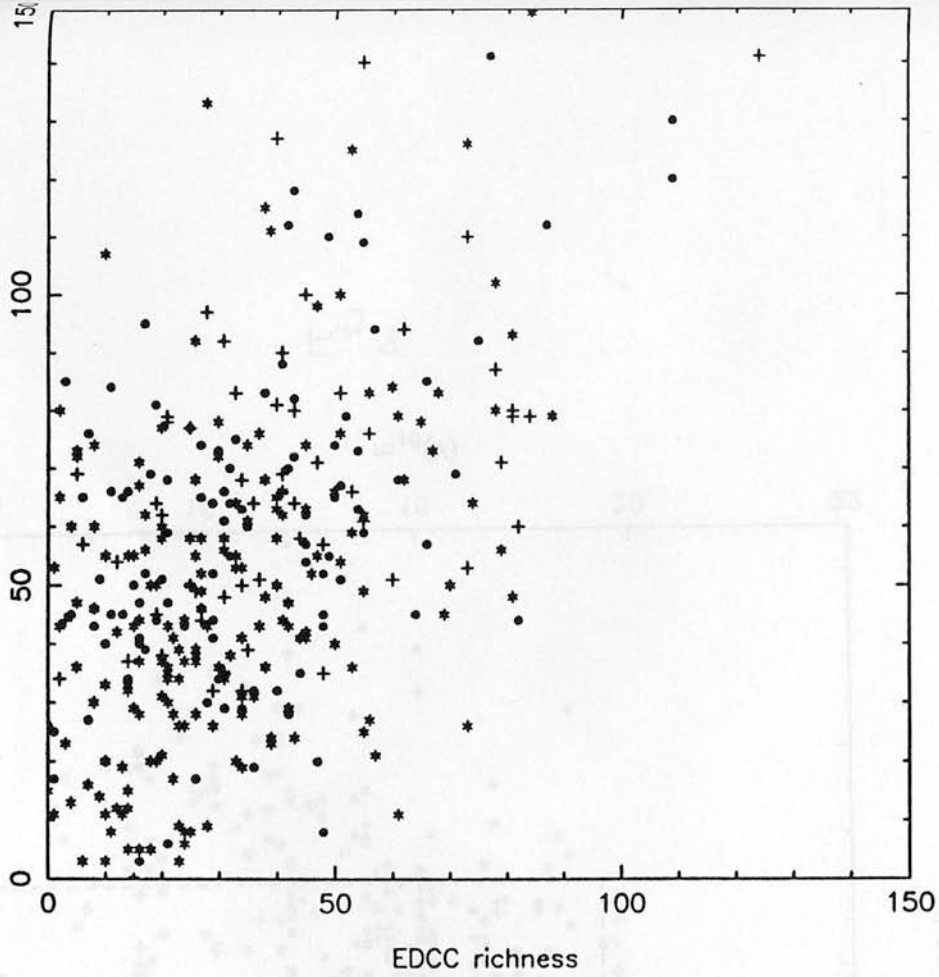
ACO richness
0
50
100
150
EDCC richness

Fig 6

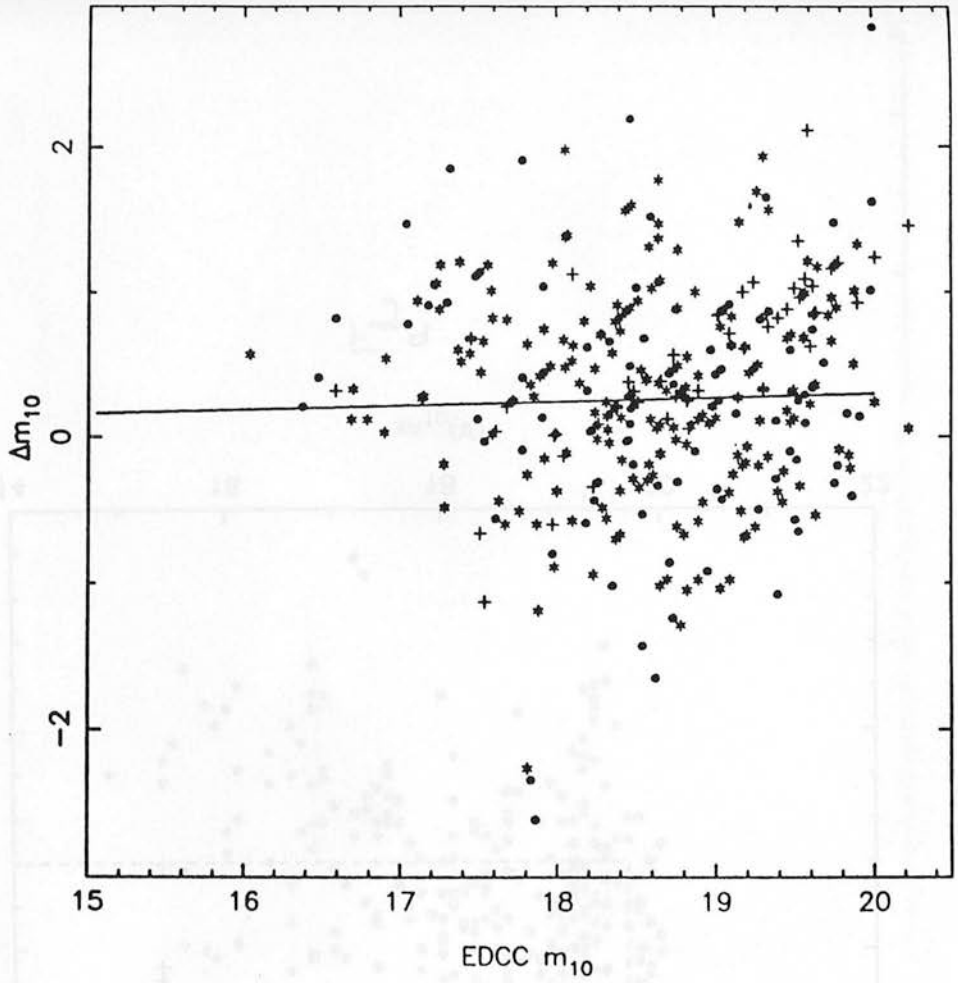
Δm_{10}
2
0
−2
15
16
17
18
19
20
EDCC m_{10}

Fig 7.

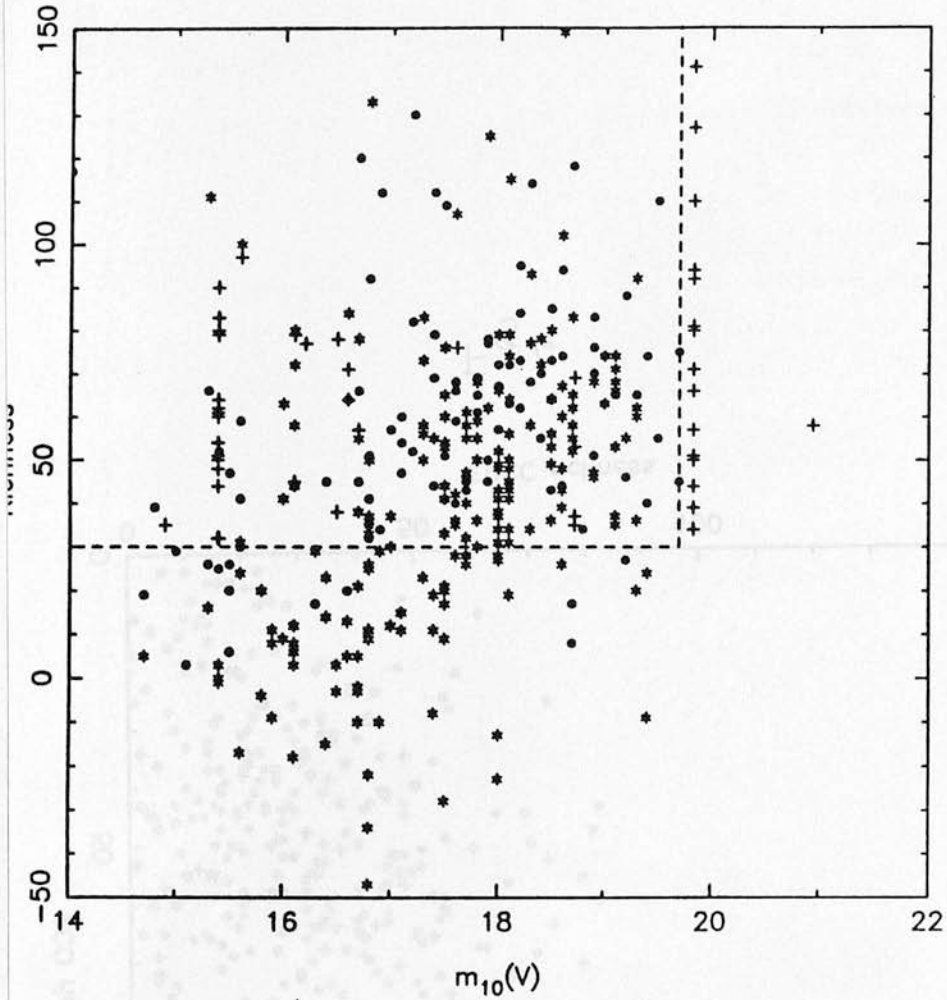
150
100
50
0
−50
14
16
18
20
22
m_{10}(V)

Fig 8

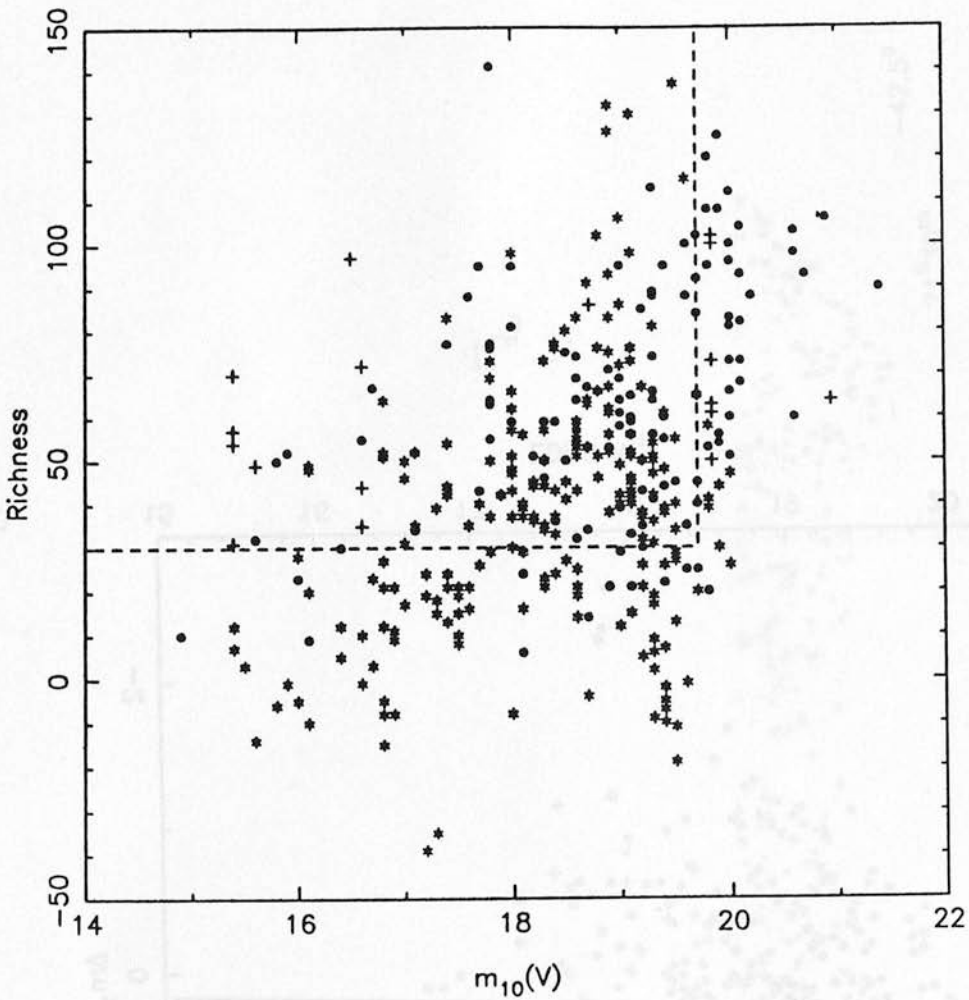
Richness
150
100
50
0
−50
14
16
18
20
22
m_{10}(V)

Fig 9

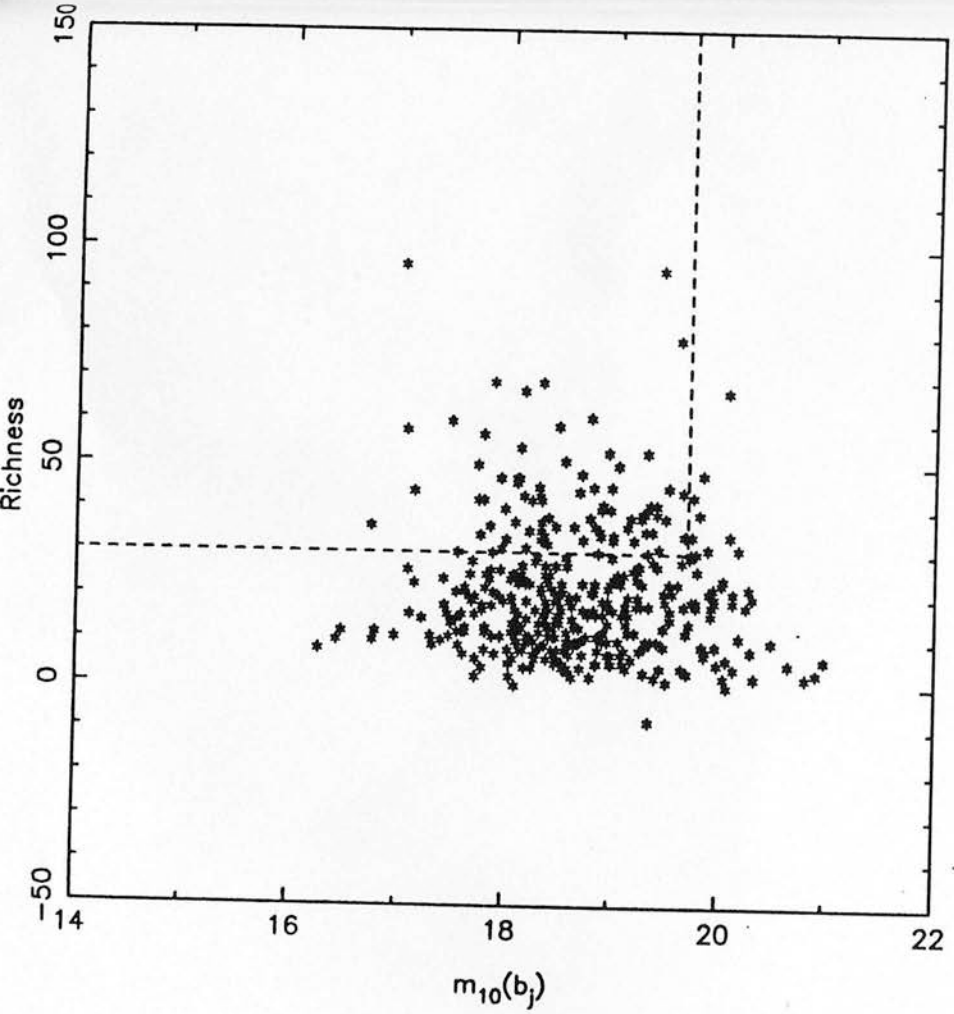
Richness
150
100
50
0
−50
14
16
18
20
22
$m_{10}(b_j)$

Fig 10

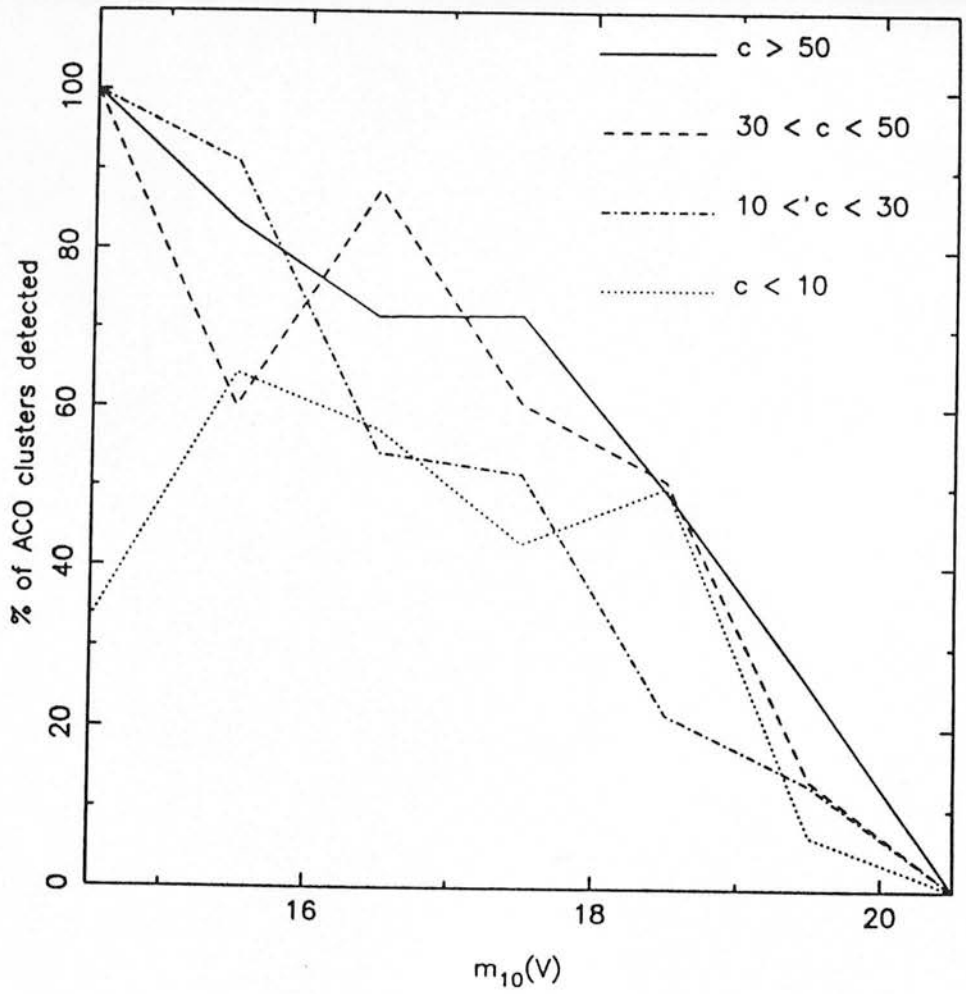
% of ACO clusters detected
100
80
60
40
20
0
16
18
20
$m_{10}(V)$
c > 50
30 < c < 50
10 < c < 30
c < 10

Fig 11